This thesis has been accepted for the award of the degree in the Faculty of Engineering

CONSTITUTIVE MODELS FOR CARBONATE SAND AND THEIR APPLICATION TO FOOTING PROBLEMS

by

Mohammed Kabirul Islam
BSc, MSE

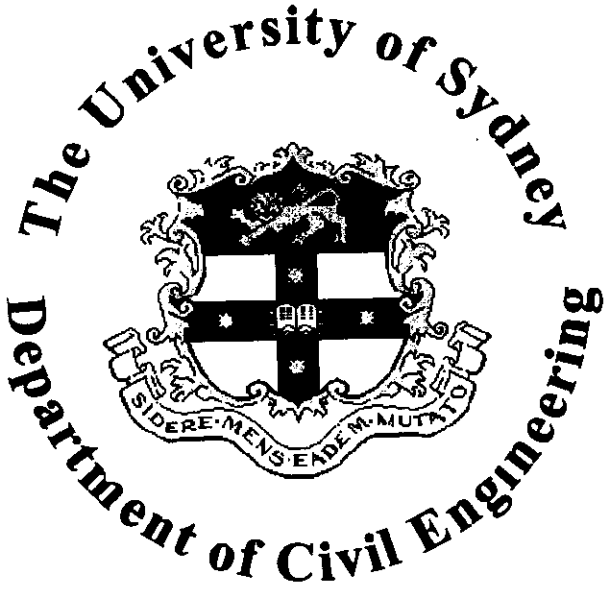

A thesis submitted for the degree of
Doctor of Philosophy

December 1999

CONTENTS

ABSTRACT

A numerical study was carried out to model the stress-strain or constitutive behaviour of carbonate sands. Several existing critical state models were used to simulate the triaxial response of both cemented and uncemented carbonate sands under drained conditions. Two new models were proposed as relatively simple modifications of the Cam Clay and Modified Cam Clay model respectively. It was observed that the proposed as well as several existing critical state models, which correctly take into account the yield, plastic stress-dilatancy and volumetric compression behaviour of carbonate sands, can predict reasonably well their triaxial response. The effect of cementation was simulated in the proposed models by the increased preconsolidation pressure occurring as a result of cementation. The triaxial behaviour of dense artificially cemented carbonates could be predicted quite well using this approach. However the stress-strain behaviour of loose cemented carbonates perhaps was not predicted very well using any of the existing critical state models including the proposed ones.

All of these critical state models were implemented in a finite element procedure. The models were then used to simulate the drained pressure-displacement response of circular footings resting on artificially cemented carbonate sand. It was observed that some of the models could predict quite well, both qualitatively and quantitatively, the drained pressure-displacement responses of circular footings resting on cemented carbonate sand.

One of proposed models (called here the SU2 model) was used to predict the centrifuge pressure-displacement data of surface circular footings as well as of model-scale footings embedded in carbonate sand. It was observed that the proposed model gives reasonable predictions of footing behaviour in both cases. A parametric study of the pressure-displacement behaviour of surface circular footings and of footings embedded in carbonate sand was carried out using the model. The effect of model parameters on footing response was investigated and simplified design charts were proposed for an assumed idealised soil profile below the footing. The proposed

design charts may be used to obtain approximate bilinear bearing pressure curves for circular footings on carbonate sand subjected to vertical load. Separate design charts were proposed for circular footings resting on normally consolidated carbonate sand.

Finally, the pressure-displacement response of circular footings subjected to inclined load was simulated using the proposed SU2 model in a semi-analytical three dimensional finite element procedure. Satisfactory predictions of the pressure-displacement behaviour of an experimental model-scale circular footing resting on cemented carbonate sand and subjected to inclined load could be made using the proposed model. However, similar predictions for uncemented carbonate sands were not satisfactory. A simplified footing model was proposed to predict the pressure-displacement response of circular footings subjected to inclined load without the use of a 3D finite element procedure. The simplified footing model could simulate quite well the response for footings obtained using the 3D finite element procedure.

PREFACE

The work described in this thesis was undertaken by the candidate during the period 1995 through 1999 in the Department of Civil Engineering, University of Sydney. During this period, the candidate was supervised by Professor J. P. Carter.

The By-Laws of the University of Sydney require a candidate for the degree of Doctor of Philosophy to indicate which sections of the thesis are original. In accordance with the By-Laws, information or ideas obtained or used from other sources have been acknowledged in the text. The Author claims the work described in the following sections of this thesis to be original:

In Chapter 3, constitutive models proposed for carbonate sands as modifications of the Cam Clay and Modified Cam Clay model are claimed to be original. The prediction of the triaxial response of cemented and uncemented carbonate sands using several critical state constitutive models including those proposed, and their comparison with laboratory data is also claimed as original.

In Chapter 4, the implementation of the proposed constitutive models in a finite element procedure is claimed to be original. The comparison of finite element predictions of several constitutive models including those proposed, of the pressure-displacement response of a model-scale circular footing with laboratory data, is also claimed as original.

In Chapter 5, the parametric study of the pressure-displacement response of surface circular footings on carbonate sand using the proposed constitutive model and the development of simplified design charts for such footings is claimed as original.

In Chapter 6, the parametric study of the pressure-displacement response of circular footings embedded in carbonate sand using the proposed model and the development

of simplified design charts for determining the bearing response of such footings is claimed as original.

In Chapter 7, the implementation of the proposed model in 3D semi-analytical finite element procedure and the finite element prediction of the pressure-displacement response of circular footings subjected to inclined load is claimed to be original. The development of a simplified footing model for predicting the response of circular footing on carbonate sand subjected to inclined is also claimed as original.

The following technical papers were published by the candidate during the period of the Author's candidature, viz.,

Islam, M.K., Carter J.P. and Airey D.W. (1999). A constitutive model for carbonate sediments, *Proceedings, 8th Australia New Zealand Conference on Geomechanics*, Hobart, Vol. 1, pp. 961-967.

Vafeian, M., Airey, D.W., Carter, J.P. and Islam, M.K. (1999). Analysis of pressuremeter tests in calcareous soils, *Engineering for calcareous sediments, Al-Shafei (ed.)*, Balkema, Rotterdam, pp.283-290.

Islam, M.K., Carter J.P. and Airey D.W. (1998). Model simulation of uncemented and cemented calcareous sediments, *The Geotechnics of Hard Soils-Soft Rocks, Evangelista & Picarelli (eds)*, Balkema, Rotterdam, pp. 561-569.

Carter, J.P., Bransby, M.F. , Taiebat, H., and Islam, M.K. (1998). Recent developments in the analysis of offshore foundations, *Computer Methods and Advances in Geomechanics, Yuan (ed.)*, Wuhan, Balkema, Rotterdam, pp.2435-2444.

Several other papers are currently under preparation.

ACKNOWLEDGEMENT

The work described in this thesis was supported by the Centre for Geotechnical Research (CGR) at the University of Sydney and the Centre for Offshore foundation Systems (COFS) established by the Australian Research Council.

I wish to express my gratitude and very sincere thanks to my supervisor, Professor John P. Carter and my co-supervisor Dr. David W. Airey for their encouragement, enthusiasm, guidance and support throughout the course of my candidature.

I would also like to extend my thanks to my fellow candidates: Hossein, Pan, Takashi, and Ezzat for their help and friendship.

Personally, I would like to give my special thanks to my wife, Shipa, my daughter, Samreen and my mother, for their encouragement, understanding, and support throughout the period of my candidature. I dedicate this thesis to them.

Mohammed Kabirul Islam

NOTATION

a	parameter for simplified footing model
A	Molenkamp model scaling parameter for elastic stiffness
AP	Molenkamp model curvature parameter for elastic stiffness
B	[4][5][6][7]footing diameter/least plan dimension of footing
B	[3][4] Molenkamp model scaling parameter for plastic stiffness
BP	Molenkamp model curvature parameter for plastic stiffness
B_e	Nova model elastic volumetric compliance
B_p	Nova model plastic volumetric compliance
C	Molenkamp model parameter for peak friction angle
CG	Molenkamp model parameter for dilatancy ratio other than triaxial
CP	Molenkamp model parameter for peak friction angle
CV	Molenkamp model parameter for dilatancy ratio other than triaxial
D	[6] Depth of embedment of footing
D	[3][4] Molenkamp model hardening parameter for deviator yield surface
DP	Molenkamp model curvature parameter for deviator yield surface
c	cohesion of soil
e	void ratio
e	constant approximately equal to 2.72
e_1	void ratio at unit mean effective pressure on normal consolidation line
e_2	void ratio at unit mean effective pressure on elastic rebound line
e_{cs}	void ratio at unit mean effective pressure at critical state line
e_{ij}	components of deviator stress tensor
E	drained Young's modulus of soil
E	[3][4] Molenkamp model parameter for plastic deviatoric stiffness
EP	Molenkamp model parameter for plastic deviatoric stiffness
f	yield function
f_j	applied nodal forces at wedge j

F_j	kth Fourier coefficient of externally applied load
F_c	cap yield function
F_d	deviator yield function
g	plastic potential function
G	shear modulus
G_c	cap plastic potential function
G_d	deviatoric plastic potential function
h'	horizontal displacement of footing normalised by footing diameter
h'_e	elastic component of horizontal displacement of footing normalised by footing diameter
h'_p	plastic component of horizontal displacement of footing normalised by footing diameter
H	[5][6] depth of cemented layer below footing
H	[7] horizontal component of applied traction
H'	[7] horizontal component of applied traction normalised by reference pressure
H_{mod}	plastic hardening modulus
I_1	1st invariant of effective stress tensor
I_1^*	1st invariant of effective stress tensor $\{\sigma'^*\}$
I_2	2nd invariant of effective stress tensor
I_3	3rd invariant of effective stress tensor
I_3^*	3rd invariant of effective stress tensor $\{\sigma'^*\}$
J_2	2nd invariant of deviator stress tensor
J_{2e}	2nd invariant of deviator strain tensor
$J_{2\eta}$	2nd transformed invariant of deviator stress tensor η'_{ij}
J_3	3rd invariant of deviator stress tensor
$J_{3\eta}$	3rd transformed invariant of deviator stress tensor η'_{ij}
J_{3e}	3rd invariant of deviator strain tensor
k	[3] shear intercept of Drucker-Prager envelope
k	[7] parameter in plastic potential function for simplified footing model
K_o	coefficient of earth pressure at rest

K_{he}	horizontal elastic stiffness of footing
K_{ve}	vertical elastic stiffness of footing
K_{vp}	vertical plastic stiffness of footing
L	length of footing
LB	Molenkamp model parameter for defining variation in plastic shear stiffness with isotropic stress
L_e	Nova model elastic shear compliance
M	critical state ratio
M_g	critical state ratio at triaxial compression plane
M^*	critical state ratio at $s' - t$ plane
N	[7]pressure intercept of unload-reload segment of pressure-displacement curve of footing under vertical load
N	[3][4] Molenkamp model parameter related to hardening of deviator yield surface
NU	Molenkamp model parameter related to dilatancy
N_c, N_q, N_γ	bearing capacity factors
p'	the mean effective stress
p'_a	effective atmospheric pressure
p'_g	reference mean effective pressure
p'_{cs}	the mean effective pressure on the critical state line (CSL)
p'_o	the mean effective stress on the normal consolidation line (NCL)
$PARCI$	Molenkamp model isotropic hardening parameter for cap
$PARDI$	[3][4] Molenkamp model hardening parameter for deviator yield surface
$PHICV$	Molenkamp model parameter for constant volume friction angle
$PHIMU$	Molenkamp model parameter for interparticle friction angle
q	deviator stress
q_{av}, q_o	average bearing pressure
q_{ref}	normalising reference pressure
r	the spacing ratio
R	footing radius

RT	Molenkamp model parameter defining shape of plastic potential surface in π plane
s'	hydrostatic stress proportional to mean effective pressure in Molenkamp model
s'_{ij}	components of the deviator stress tensor
S	plastic slope of vertical pressure-displacement curve
SCV	Molenkamp model parameter related to dilatancy
t	deviatoric stress measure proportional to 2nd deviatoric stress invariant in Molenkamp model
$(u_r, u_z, u_\theta)_j$	nodal displacements of wedge j in radial, vertical and angular direction
$(U_R, U_z, U_\theta)_K$	Kth Fourier coefficients of nodal displacements
v'	vertical displacement of footing normalised by footing diameter
v'_e	elastic component of vertical displacement of footing normalised by footing diameter
v'_p	plastic component of vertical displacement of footing normalised by footing diameter
V	vertical component of applied traction
VGC	Molenkamp model parameter related to dilatancy
VGP	Molenkamp model parameter related to dilatancy
V'	[7] vertical component of applied traction normalised by reference pressure
V_o	bearing capacity under vertical load
V^e	[3] elastic volumetric strain corresponding to mean pressure s'
V^p	[3] plastic volumetric strain corresponding to mean pressure s'
α	angle defining the slope of the Drucker-Prager envelope
β	[3] Nova model parameter for defining non-association of yield locus and plastic potential function
β	[7] parameter in yield locus for Nova footing model
δ	footing settlement
δ_{ij}	kronecker delta representing identity tensor

$\varepsilon, \varepsilon_{ij}^{p}$ tensor of total strains or its components

$\varepsilon^{p}, \varepsilon_{ij}^{p}$ tensor of plastic strains or its components

ε_{v}^{p} plastic volumetric strains

ε_{q}^{p} plastic deviator strains

ϕ, ϕ' friction angle

γ [3] Nova model parameter for critical state

γ' effective unit weight of soil

γ_{eq}^{p} plastic shear strains corresponding to shear stress t'

Γ pressure intercept of plastic segment of pressure-displacement curve of footing under vertical load

η stress ratio q / p'

η_{ij}' stress tensor s_{ij}' / p' or its components

κ slope of elastic rebound line in e : ln p' space

λ slope of normal consolidation line (NCL) in e : ln p' space

ν , μ Poisson's ratio

θ [3] lode angle

θ *[7] angle of load inclination with respect to vertical*

σ', σ_{ij}' the effective stress tensor or its elements

σ_{s}' hydrostatic stress tensor or its components in terms of stress s'

σ_{t}' deviatoric stress tensor or its components in terms of stress t'

σ_{v}' vertical effective stress or surcharge pressure

τ shear strength

ψ' dilation angle

$\zeta_c, \zeta_q, \zeta_\gamma$ correction factors for foundation shape

$\zeta_{ci}, \zeta_{qi}, \zeta_{\gamma i}$ correction factors for load inclination

1

INTRODUCTION

1.1 INTRODUCTION

Carbonate sands are present in many of the offshore regions of the world including Bass Strait, North West Shelf of Australia, India, Brazil and the Persian Gulf. Since the rapid growth of offshore oil and gas exploration in the last two decades, there has been a great need to safely design foundations for offshore structures. However, design of foundations in carbonate sand has presented considerable difficulties to geotechnical engineers. Computation of end bearing capacity using Terzaghi's general shear theory gave gross overpredictions. Terzaghi's local shear theory gave improved predictions, although it is still generally unsatisfactory. Spherical cavity expansion solutions presented by Ladanyi (1967) and Carter et al (1987) were found to correlate well with measured values of end bearing capacity, defined as the bearing pressure mobilised at a settlement of 10% of the footing diameter. However, no consistent method for relating spherical cavity expansion limit pressure to end bearing capacity was found. Datta (1980b) and Poulos (1980) also noted that conventional methods of geotechnical analysis were inadequate for predicting pile performance in calcareous soils.

McClelland (1988) reported several case histories of foundation problems in carbonate soils. Cases of piles failing by free fall under their own weight during driving, in offshore regions of the Arabian Gulf, Brazil and North West Shelf of Australia, have been described. Such foundation failures highlighted the need to better understand the stress-strain behaviour of carbonate sands. As a result, a large number of field and laboratory investigations were carried out to investigate their

fundamental behaviour (Huang and Airey (1998), Huang (1994), Coop and Atkinson (1990,1993), Airey, Randolph and Hyden (1988), Allman and Poulos (1988), Carter et al (1988), Poulos (1988) and others).

Previous research on carbonate sands was limited because they were considered as special soils and the problems encountered were generally explained as a result of their loose structure and consequent high compressibility. Cementation, which is often present, has been shown to significantly affect the behaviour of carbonate sands. While cementation may increase foundation capacity, it may also result in increased pile driving resistance and soil damage during driving. Huang's (1994) extensive experimental investigations showed that the triaxial stress-strain behaviour of both cemented and uncemented carbonate sands is quite similar to conventional soils. Huang (1994) concluded from his study that the general pattern of behaviour of carbonate sands could be described within the framework of critical state soil mechanics. Similar conclusions were reached independently by Novello (1988) and Coop and Atkinson (1990,1993). This pointed to the possibility of developing a constitutive model, within the framework of critical state soil mechanics specifically for carbonate sand. The model could be verified by calibrating against extensive triaxial test data that have now become available.

Constitutive modelling is one of the most important areas of research in geotechnical engineering today. A constitutive model defines the variation of strength and stiffness of a material under general conditions of stress and strain, using a series of governing or constitutive equations linked together in a mathematical framework. For a given stress path, a constitutive model gives a numerical approximation of the strain and vice versa. For the analysis of engineering structures such as a footing or a pile, a constitutive model is incorporated into a numerical algorithm such as a finite element procedure.

The formulation of stress-strain characteristics of soil using a constitutive model is quite difficult. The range of soil types and their properties often vary greatly. Thus constitutive models often analyse particular classes of soils (e.g. normally consolidated clays, loose sands, carbonate sands) under certain loading conditions (such as drained, undrained, monotonic, cyclic etc.). The numerical implementation

of a constitutive model is essential to demonstrate its usefulness in engineering practice. However, only a few models have been implemented into numerical algorithms for solving practical problems. Although several constitutive models have been used to predict the behaviour of foundations in carbonate sands, no detailed parametric study of a constitutive model has yet been carried out to investigate the effects of model parameters on foundation behaviour.

The problems of foundation behaviour on carbonate sand have been highlighted and consequently the need to model the triaxial as well as the response of footings resting on carbonate sand has been demonstrated.

1.2 AIMS, OBJECTIVES AND LIMITATIONS OF PROPOSED STUDY

In this section, the aims and objectives of the proposed research are elaborated and the limitations that were necessarily applicable to the scope of the study are described.

Extensive triaxial test data as well as results of model scale and centrifuge tests for footings on carbonate sand are now available. However, only limited numerical studies using critical state soil models have been carried out to investigate the triaxial behaviour of carbonate sand. Furthermore, limited numerical investigation of foundation behaviour has been made using such models. Acknowledging these facts, a study was initiated to investigate in detail the strengths and shortcomings of several critical state models to predict the triaxial behaviour of carbonate sands under drained conditions. The investigation was made in order to explore the possibility of developing a relatively simple model, within the framework of critical state soil mechanics, to predict the triaxial behaviour of carbonate sands. The model could then be incorporated in a finite element procedure to investigate the behaviour of surface and embedded circular footings in carbonate sand as well as that of circular footings subjected to inclined load at zero eccentricity. In summary, the specific aims of this research were:

- To investigate the possibility of developing a new constitutive model, within the framework of critical state soil mechanics, to predict the triaxial behaviour of cemented and uncemented carbonate sands under drained conditions.

- To compare the stress-strain and volumetric strain predictions of the new model with other critical state models as well as with available experimental data.

- To simulate the behaviour of an experimental model-scale footing resting on carbonate sediments using various constitutive models in a finite element procedure and compare the predictions with one another as well as with available experimental data.

- To conduct a detailed parametric study of surface circular footings and circular footings embedded in carbonate sand using an appropriate constitutive model in a finite element procedure and investigate the effects of various model parameters on footing behaviour.

- To develop simplified design charts from the results of the parametric study to predict the approximate bearing response of footings, without the use of sophisticated constitutive models in a finite element procedure.

- To simulate the behaviour of experimental model-scale circular footings subjected to inclined load at zero eccentricity using an appropriate constitutive model in a semi-analytical three dimensional finite element procedure, and to compare the results with available experimental data.

Limitations that were necessarily applied to the scope of this study were:

- Cementation was simulated in the constitutive models only by the increased preconsolidation pressure of cemented carbonate sands. As a first approximation, increase in elastic stiffness, development of cohesion and tensile strength and the change in size and shape of the yield loci due to cementation were not considered.

- The breakdown of cementation with plastic strains was not considered in the constitutive models used for simulating carbonate sand behaviour.

- The parametric study for surface circular footings and footings embedded in carbonate sand was carried out only for idealised soil profiles assumed to exist below the footing.

- The embedment of footings in carbonate sand was simulated only by the overburden pressure acting on the surface of the soil upon which the footings were assumed to be resting.

- The bearing response of footings on carbonate sand was idealised to be bilinear in the development of simplified design charts for the footings.

- No interface elements with separate constitutive properties were considered in the analysis of circular footings subjected to inclined load at zero eccentricity.

1.3 OULINE OF THESIS

In sections 1.1 and 1.2, the aims and objectives for carrying out this research work have been specified. They are described in detail in the following chapters of this thesis.

Chapter 2 presents a literature review of carbonate sand behaviour, of selected elastoplastic models used to model sand behaviour and the response of experimental model-scale circular footings, field plate load tests and some corresponding model predictions.

Chapter 3 presents a detailed investigation of the triaxial stress-strain and volumetric strain behaviour of both cemented and uncemented carbonate sands of low and high density, using several critical state models. Two constitutive models are proposed as simple modifications of Cam Clay and Modified Cam Clay models respectively, to

predict carbonate sand behaviour. The predictions of these models are compared with each other as well as with available experimental data.

Chapter 4 presents the simulation of the pressure-displacement response of an experimental model-scale footing in carbonate sand using five critical state models including those proposed. The predictions of the footing response of the various models are compared with one another as well as with available experimental data. The validation of one of the proposed constitutive model (called the SU2 model) with centrifuge and model-scale test data for surface circular footings and footings embedded in carbonate sand is also presented.

Chapters 5 and 6 presents a detailed parametric study carried out to investigate the effect of model parameters on the pressure-displacement response of such footings. Finally, simplified design charts are proposed providing approximate pressure-displacement curves of circular footings in carbonate sand.

Chapter 7 compares the predictions of the response of model-scale experimental circular footings resting on carbonate sand subjected to inclined load at zero eccentricity, with available experimental data. The proposed SU2 model was used in a semi-analytical three-dimensional finite element procedure to obtain the predictions. A simplified footing model is also proposed. The simplified model can be used to predict the traction mobilised by circular footings on carbonate sand subjected to inclined load, without using sophisticated constitutive models in a 3D finite element procedure.

Chapter 8 summarises the main findings of this study and presents recommendations for further research.

2

LITERATURE REVIEW

2.1 INTRODUCTION

In recent years, a series of geotechnical events have generated significant interest in the study of mechanical response of carbonate sand to imposed loads. Major problems have been encountered with foundations constructed on carbonate sediments in offshore locations. King and Lodge (1988) described the significantly low shaft resistance encountered in piles driven in natural calcarenite deposit at the North Rankin site of Australia. The mechanical behaviour of uncemented and cemented carbonate sand has thus been studied extensively in recent years.

In the first section of this chapter, a review of carbonate sand behaviour is undertaken. In the subsequent section, a review is made of selected elastoplastic models currently used for sands. Such a review helps to understand whether the current constitutive models are adequate for describing carbonate sand behaviour, or whether there exists a need to modify existing models or to develop a new one. In the final section, a review of the pressure-displacement response of model circular footings, field plate load tests and corresponding model predictions are carried out.

2.2 BEHAVIOUR OF CARBONATE SAND IN TRIAXIAL TESTS

It is necessary to have a clear understanding of the significant features of carbonate sand behaviour to select or develop suitable mathematical models of their behaviour. For this purpose, a review of the relevant literature describing the structure, origin,

isotropic consolidation and triaxial shear response of cemented and uncemented carbonate sand is carried out below.

2.2.1 STRUCTURE AND ORIGIN OF CARBONATE SAND

Fookes (1988) noted that carbonate sands encountered in nature originate from biological, mechanical or chemical depositional environments. Both Fookes (1988) and Poulos (1989) observed that carbonate deposits in offshore locations are mainly biological in origin, consisting primarily of skeletal remains of marine organisms. Carbonate sands were described by Semple (1988) as consisting of crushable particles with high angularity, which resulted in a high void ratio. Natural calcarenites are frequently cemented. Fookes and Higginbottom (1975) state that, as a result of the cementation, the initial loose structure of the sand may remain intact even after the sediment becomes subject to the high pressures of subsequent deposition. This leads to a high in-situ void ratio for a given overburden stress. Thus many naturally cemented carbonate sands exist in a loose state. Cementation in natural carbonate sand deposits is highly variable and undisturbed sampling is difficult. Thus Simpson (1970) used artificially cemented specimens for laboratory testing. Subsequently, different cementing agents have been used in the laboratory by various authors. Clough et al (1981) and Allman and Poulos (1988) used Portland cement, Boey (1990), Coop and Atkinson (1993) and Huang (1994) used Gypsum plaster. In each case, the investigators reported that, artificially cemented sand samples provide a reasonable approximation of the behaviour of naturally cemented soils.

2.2.2 CONSOLIDATION BEHAVIOUR OF CARBONATE SAND

Carter et al (1988) conducted a series of isotropic consolidation tests on specimens of cemented natural calcerinite. Their experimental studies indicated a high initial volumetric stiffness or bulk modulus. The existence of an apparent preconsolidation pressure could be identified. Beyond the preconsolidation pressure, the compressibility of carbonate sand increased significantly. Figure 2.1 shows the initial

stiff behaviour and the subsequent high compressibility of the soil. The response can be described by two distinct straight lines in logarithm of mean effective pressure versus void ratio space. The two lines are described respectively by the following equations:

$$e = e_1 - \kappa \ln p' \tag{2.1}$$

$$e = e_2 - \lambda \ln p' \tag{2.2}$$

where e is the void ratio at mean effective pressure of p', e_1 and e_2 are constants representing void ratio at unit mean effective pressure, and λ and κ are respectively the slopes of equations (2.1) and (2.2). Similar equations may be used to describe the consolidation response of uncemented carbonate sand (Huang, 1994). The primary effect of cementation was to shift the consolidation line of the uncemented carbonate sand to the right in *e-ln p'* space .

The typical range of values for the plastic slope λ was 0.18 – 0.24. The typical value for the elastic slope κ was found to be about 0.0065. This is similar to the compressibility values reported for London clays by Schofield and Wroth (1968). The ratio λ/κ, which can be taken to be a measure of relative compressibility, was reported to be approximately 30. This is significantly higher than for silica sand. Coop (1990) reported a value of 45 for the relative compressibility of carbonate sand. Allman and Poulos (1988), Coop and Atkinson (1993) and Huang (1994) have reported similar values. Poulos (1988) reported high values of compressibility for carbonate sand in one-dimensional oedeometer and K_o consolidation tests. Airey, Randolph and Hyden (1988) concluded that the high compressibility of carbonate sand is a result of the angularity of its particles, as well as the weak nature of the grains and the presence of intraparticle voids.

Huang (1994) observed that, the initial position of the isotropic consolidation line of carbonate sand varied as a function of its initial or formation void ratio. However, at high isotropic pressures, the consolidation lines converged to a unique straight line in semi-logarithmic space. Pestana and Whittle (1995) have reported a similar result for

quartz sand. The experimental data of Huang (1994), Coop and Atkinson (1993), Carter (1988) and Poulos (1988) show that the isotropic consolidation response of both uncemented and artificially cemented carbonate sand can be sufficiently approximated by the conventional semi-logarithmic equations of consolidation behaviour.

2.2.3 SHEAR BEHAVIOUR OF CARBONATE SAND

Extensive experimental studies have been carried out in recent years to investigate the drained response of carbonate sands in triaxial shearing. Allman and Poulos (1988) carried out a series of triaxial tests on dense uncemented and artificially cemented North Rankin carbonate sand. Figure 2.2 shows some results of these tests. It is interesting to observe that dense uncemented carbonate sands show volumetric compression behaviour even at low cell pressures. The volumetric compression is accompanied by a strain hardening response. In contrast, in medium dense and dense silica sand, the initial strain-hardening response is often associated with volumetric expansion. Figure 2.3 shows such behaviour of dense silica sand in triaxial shearing, as reported by Yeung and Carter (1988).

Many plastic volumetric strain hardening models always predict hardening with compression and softening with volumetric expansion. Consequently, these models are generally not considered suitable to predict the behaviour of medium and dense silica sand. Huang (1994) carried out triaxial shear tests on carbonate sand. It was observed that for both loose and dense, as well as cemented and uncemented carbonate sand, strain-hardening behaviour was always associated with volumetric compression, while expansive volumetric behaviour was accompanied by strain softening. Carter et al (1988) observed that during triaxial shear of natural calcarenite, the peak deviator stress developed generally at axial strains greater than 10%, with associated strain-hardening and volumetric compression. For heavily overconsolidated specimens, the peak values were attained at approximately 1% axial strain, with subsequent strain-softening and expansive dilatancy. The association of hardening with compression and softening with expansion, for both loose and dense carbonate sand, appears to be indicative that volumetric strain

hardening models may be quite appropriate to describe the stress-strain response of these soils.

2.2.4 EFFECT OF CEMENTATION ON CARBONATE SAND

Allman and Poulos (1988) concluded from the results of triaxial consolidation and shear tests on artificially cemented carbonate sand that the primary influence of cementation on carbonate sand behaviour is to provide an apparent preconsolidation pressure to the soil. Increased cell pressure in triaxial tests on cemented calcarenite shows a transition from brittle to ductile behaviour. It was observed that compressibility of cemented carbonate sand beyond the apparent preconsolidation pressure was of the same order of magnitude as for normally consolidated specimens of uncemented carbonate sand. Coop and Atkinson (1993) reported that addition of up to 30% cement did not significantly change the value of this plastic slope. These experimental results indicate that plastic volumetric strain-hardening models may be suitable for describing the behaviour of cemented carbonate sand.

Allman and Poulos (1988) also observed that there was an increase in soil stiffness, peak strength and dilation at failure due to cementation. The Mohr-Coulomb failure parameters such as the soil cohesion increased with the degree of cementation, while the ultimate friction angle remained relatively constant. Huang and Airey (1998) correlated the unconfined compression strength and preconsolidation pressure to the cement content of artificially cemented carbonate sand. It can be inferred from their correlations that increase in soil cohesion with cementation implies an increase of the apparent preconsolidation pressure of the soil.

Lagioia and Nova (1995) reported the identification of distinct phases during the triaxial testing of a strongly cemented natural calcarenite. An initial quasi-linear reversible elastic phase was observed. Beyond this phase, axial strain steadily increased at constant stress, which is suggestive of destructurisation. Hardening resumed when the structure of a loose granular soil was established. The ultimate state locus, conceptually similar to the critical state locus, was reached at very large strains. Carter et al (1988) also observed a short strain softening and destructurisation

phase during the initial breakdown of cementation, with subsequent strain hardening. However, most of the other authors referred to in this section did not either observe such a distinct destructurisation phase, or observed only slight strain softening and destructurisation during the triaxial shear of cemented carbonate sand.

Semple (1988) and Coop (1990) noted that although carbonate sands are generally thought to display unusual behaviour, experimental data indicate that their performance is comparable to conventional soils at similar void ratios. The effect of cementation on shearing and volume change compressibility was comparable to the effect of relative density on sands and overconsolidation on clays. Cementation influences the cohesive strength and preconsolidation pressure of the soil. This in turn affects the small strain rather than the large strain behaviour. A cemented soil has increased stiffness and strength, but becomes very brittle. Very large strains are required to develop the high frictional resistance indicated by the high friction angle. At critical state no stress changes are seen and negligible volume changes occur for continued shearing. For soils loaded beyond the preconsolidation pressure, the cementation breaks down and highly compressible behaviour is observed. In their view, theoretical treatments that incorporate soil compressibility appear to provide reasonable predictions for bioclastic sands.

2.2.5 ELASTIC PROPERTIES OF CARBONATE SAND

A short review of the elastic properties of carbonate sand is now presented. Drained triaxial tests on natural and artificially cemented sand by Clough et al (1981), Carter et al (1988), Poulos (1989), Coop and Atkinson (1993), Huang (1994) all indicate that cementation increases the initial elastic stiffness of the soil. Huang (1994) observed the elastic modulus of the soil to be pressure dependent for uncemented calcarenite, from the initiation of loading. Beyond yield, the elastic modulus of cemented carbonate sand also showed pressure dependent behaviour.

Airey, Randolph and Hyden (1988) found the Young's modulus of carbonate sand to be proportional to the square root of the mean effective pressure. They found this relation to correlate well with the elastic bulk modulus obtained from isotropic

unloading test. This relation is similar to non-linear elastic relations obtained in the Cam Clay models. Results of Hull, Poulos and Alehossein (1988) show that the Young's modulus as well as the Poisson's ratio of carbonate sand vary as a function of the initial confining pressure in triaxial tests. Balmer (1958) and Hull et al (1988) reported the value of elastic Poisson's ratio to be in the range of 0.1-0.3. Allman and Poulos (1988) reported a decrease of elastic Poisson's ratio for artificially cemented carbonate sand. O'Rourke and Crespo (1988) reported similar elastic behaviour for cemented volcanic soil, as did Lama and Vutukuri (1979) for limestone, sandstone and claystone.

2.2.6 CRITICAL STATE FRAMEWORK FOR CARBONATE SAND

Extensive triaxial experiments conducted on uncemented and artificially cemented carbonate sands by Huang (1994), Coop and Atkinson (1990,1993) and Novello (1988) show that their mechanical behaviour can be described within the critical state framework, using strain-hardening elastoplasticity concepts. Their experimental data show the existence of approximately parallel normal consolidation and critical state lines, an elliptical yield locus, a separate and non-associated plastic potential function, a unique state boundary surface and a stress-dilatancy relation similar to that given by the Modified Cam Clay model.

Figure 2.4 shows that the normal consolidation and critical state line obtained for carbonate sand, are approximately parallel in void ratio and semi-logarithm of mean effective pressure space. This parallelism is assumed in the critical state framework. However, the actual distance between the experimental lines, appear to be significantly greater than that assumed in the Cam Clay models.

Huang (1994) obtained an approximately elliptical shaped yield locus for a uncemented carbonate sand (Figure 2.5). The experimental elliptical locus is considerably flatter than the ellipse predicted by the Modified Cam Clay model. The figure shows that increased cementation increases the size of the ellipse. Cementation enlarges the size of the ellipse in the deviator direction, particularly in the case of low-density carbonates. Kavvadas et al (1993) obtained approximately

isotropic and elliptical yield locus in $p' - q$ space for Corinth marl and other structured soils. These soils show mechanical behaviour similar to carbonate sand.

Huang (1994) observed that carbonate sands in general obey a non-associated flow rule. Figure 2.6 show that the vectors of incremental plastic strain are not normal to the experimental yield locus. For a non-associated flow rule, the yield locus and the plastic potential determining the direction of plastic strain increment vectors, are given by separate functions. Experimental work by Pooroshasb, Holubec and Sherbourne (1966, 1967) has shown that, a non-associated flow rule is generally applicable for silica sand. Clays, in contrast, generally obey an associated flow rule. Thus while the compressibility behaviour of carbonate sands is similar to clays, its plastic flow behavior is comparable to sands.

Airey, Randolph and Hyden (1988) have shown that Rowe's (1962) stress-dilatancy function giving the relationship between the mobilised angle of friction at constant volume shearing and rate of dilation, show good agreement with the observed response of some carbonate sands. High ultimate, or constant volume shearing, friction angles, generally between 35° to 45°, have been obtained for most carbonate sands by many researchers, including Poulos, Uesugi and Young (1982), Allman and Poulos (1988), Hull, Poulos and Alehossein (1988), Airey, Randolph and Hyden (1988) and Huang (1994).

Thus it can be concluded that the major elements of the critical state framework are applicable to carbonate sand. The critical state framework has been observed to be applicable for other soils as well, which are similar to natural calcarenite. Atkinson and Little (1988) observed it to be applicable for glacial till (1984), Chiu and Johnstone (1984) for Ohyya tuff and mudstone and Elliot and Brown (1985) for high porosity Bathstone.

It is reasonable to conclude form this review that it should be possible to predict the drained triaxial response of cemented and uncemented carbonate sand using isotropic, volumetric strain-hardening elasto-plastic models, formulated within the critical state framework.

2.3 MODELLING THE MECHANICAL BEHAVIOUR OF SAND

It is well known that many soils, including carbonate sand, deform inelastically immediately upon the application of stress. The complex stress-strain response of sand in the inelastic range can be realistically modelled using the incremental theory of hardening plasticity In this section some selected elastoplastic models are investigated in detail, and the strengths and weaknesses in predicting carbonate sand behaviour are critically evaluated. The objective of such a review is to choose some of these models for subsequent study in detail. Such an evaluation helps to determine whether the current models are adequate, or they need to be modified or new models need to be developed to predict carbonate sand behaviour.

2.3.1 GENERAL FRAMEWORK FOR INCREMENTAL PLASTICITY

This section describes in general the framework upon which incremental theories of elasto-plasticity are based. The existence of a convex yield surface in stress space is first assumed. It is defined as a scalar function f of the stress tensor $\{\sigma'\}$ as follows:

$$f(\sigma') = f_c(\varepsilon^p) \tag{2.3}$$

In equation (2.3) f_c is a constant for perfect plasticity. Perfect plasticity gives a first approximation of real soil behaviour. Experimental evidence shows that for many soils the yield surface changes in size, shape and location during the process of plastic deformation. This is termed as strain hardening. A hardening rule is generally defined, which describes the evolution of subsequent yield surfaces represented by variation of f_c with plastic strains $\{\varepsilon^p\}$.

For stress states on the yield surface, the directions of the incremental plastic strains are in general assumed to be normal to a plastic potential function $g(\sigma')$. The incremental plastic strains are thus given by the following equation:

$$\{d\varepsilon^p\} = d\lambda \left\{\frac{\partial g}{\partial \sigma'}\right\} \tag{2.4}$$

In equation (2.4), $d\lambda$ is a constant of proportionality representing the magnitude of incremental plastic strains while the vector $\left\{\frac{\partial g}{\partial \sigma'}\right\}$ represents their direction. If $g = f$, then the flow rule is said to be associated. Otherwise, the flow rule is said to be non-associated. This describes briefly the framework upon which the incremental theories of elastoplasticity are based. Some models existing based on the framework of incremental elasto-plasticity, and their applicability for simulating carbonate sand behaviour, is described in greater detail below.

2.3.2 ELASTIC PERFECTLY-PLASTIC MODELS

The Mohr-Coulomb model of perfect plasticity is still widely used to characterize limit state behaviour of sand. The Mohr-Coulomb model states that the shear strength τ is a function of the mean effective normal stress σ'_n acting on the failure plane and they satisfy the following relationship:

$$\tau = c + \sigma'_n \tan\phi \tag{2.5}$$

where c and ϕ denotes respectively the cohesion and friction angle of the soil. In terms of the principal stresses such that $\sigma'_1 > \sigma'_2 > \sigma'_3$, the Mohr-Coulomb model is defined by the following equation:

$$\frac{1}{2}(\sigma'_1 - \sigma'_3) = \frac{1}{2}(\sigma'_1 + \sigma'_3)\sin\phi + c\cos\phi \tag{2.6}$$

Figure 2.7 shows that the Mohr-Coulomb model plots as an irregular hexagonal pyramid in principal stress space. It plots as an inclined straight line with a shear intercept in the $\tau - \sigma'$ plane.

The Mohr-Coulomb model has been widely used to obtain limit state solutions for many important problems in geotechnical engineering. However, when used with the associated flow rule, it predicts excessive expansive dilatancy for soils. This is unrealistic for carbonate sands, which show primarily compressive volume change during shear. This model cannot predict plastic volume compression observed during the isotropic loading of carbonate sand. The assumption of perfect plasticity is unrealistic for carbonate sands, which show a significant strain hardening response.

The Mohr-Coulomb failure function exhibits singularities in stress space. This gives rise to difficulties in numerical analysis. Despite its shortcomings, the Mohr-Coulomb model is widely used in numerical analysis because of its simplicity, its ability to give realistic solutions for many problems and for judging the relative performance of other models in predicting soil behaviour.

Drucker and Prager (1952) approximated the Mohr-Coulomb yield envelope by a smooth function in principal stress space. Its equation is given as follows:

$$f = \alpha I_1 + \sqrt{J_2} - k = 0 \tag{2.7}$$

where

$$I_1 = \sigma'_{11} + \sigma'_{22} + \sigma'_{33} \tag{2.8}$$

$$J_2 = \frac{1}{6}\left[(\sigma'_{11} - \sigma'_{22})^2 + (\sigma'_{22} - \sigma'_{33})^2 + (\sigma'_{33} - \sigma'_{11})^2\right] + \sigma'^{\,2}_{12} + \sigma'^{\,2}_{23} + \sigma'^{\,2}_{31} \tag{2.9}$$

I_1 is the first invariant of the stress tensor, J_2 is the second invariant of the stress deviator and σ' are the components of the effective stress tensor, α and k are material constants.

Figure 2.8 shows the Drucker-Prager yield function as a right circular cone, symmetric about the hydrostatic axis in principal stress space. In the p' - q plane this

function is identical to the Mohr-Coulomb model. p' is the mean effective stress and q the deviator stress given as follows:

$$p' = I_1/3 \tag{2.10}$$

$$q = \sqrt{3J_2} \tag{2.11}$$

The lack of corners in the Drucker-Prager yield function overcomes numerical difficulties encountered in the Mohr-Coulomb model. However, it still retains other shortcomings associated with the Mohr-Coulomb model in predicting real soil behaviour.

Both the Mohr-Coulmb and Drucker-Prager model are generally unsuited to predict carbonate sand behaviour, which is characterized by significant volumetric compression and little or no expansive dilatancy.

2.3.3 TWO SURFACE SINGLE HARDENING MODELS

DiMaggio and Sandler (1971), to overcome the shortcomings of the Mohr-Coulomb and Drucker-Prager model, added a strain hardening cap to the perfectly plastic modified Drucker-Prager envelope. The Cap model thus has two yield surfaces. The first is a perfectly plastic modified Drucker-Prager yield surface. This surface becomes asymptotically parallel to the isotropic axis at high pressures, forming a Von-Mises surface. The second yield surface is a volumetric strain-hardening elliptic cap. Figure 2.9 shows the complete Cap model in the deviator plane.

The modified Drucker-Prager and cap yield surface envelope is assumed to obey the associated flow rule. For a stress point on the modified Drucker-Prager envelope, the associated flow rule predicts expansive dilatancy. This contracts the cap. As the cap contracts due to expansive volume changes, the stress point remains fixed on the modified Drucker-Prager envelope and ultimately coincides with the corner of the contracted cap. At this stage, the direction of the incremental plastic strain vectors

becomes normal to the cap, which is parallel to the deviator stress axis in the deviator plane. Thus no further plastic volumetric strains are predicted. Thus the amount of expansive dilatancy is controlled and matches more closely with real soil behaviour. The strain-hardening cap predicts plastic volumetric compression in hydrostatic loading as observed in carbonate sand and many other soils. Thus the model overcomes some of the major shortcomings of the elastic perfectly plastic models.

The Cap model follows the associated flow rule and satisfies Drucker's (1956, 1959) theoretical requirements of stability and uniqueness. Huang's (1994) experimental results shows that carbonate sand exhibit a non-associative behaviour. Experimental results of Lade, Nelson and Ito (1988) show that granular frictional material exhibit simultaneous non-associated flow and stable behaviour, in contradiction to Drucker's (1959) stability postulates. Theoretical studies by these authors show that Drucker's stability postulates are a sufficient but not a necessary condition for stable soil behaviour. The Cap model can not simulate the non-associated behaviour of carbonate sand. It therefore can not give a true representation of its plastic response.

The Cap model cannot predict strain-softening behaviour under drained conditions. On other hand, cemented carbonates show significant strain softening in triaxial tests at low cell pressures. The material parameters of the Cap model have to be generally determined using a trial and error procedure. This is a significant shortcoming for the use of a constitutive model in practice. The existence of intersecting yield surfaces also causes numerical difficulties in its computer implementation.

Nova and Wood (1978) proposed an isotropic single-hardening model for sand with two intersecting yield surfaces. This model is closer in concept to the Cam Clay model. An isotropic plastic volumetric strain-hardening cap with associated flow rule was proposed. The deviator yield surface was assumed to be non-associated. The expressions proposed for the yield and plastic potential function are similar to the Cam Clay model. Both plastic shear and volumetric isotropic strain hardening were assumed for the deviator yield surface. Both the cap and deviator yield surface was assumed to expand omothetically about the origin of axes. The model gives realistic predictions of the triaxial response of both loose and dense silica sand. The behaviour of loose silica sand is quite similar to that of carbonates (Semple, 1988).

The single hardening two surface model of Nova and Wood (1978) illustrates the possibility of using the Cam Clay framework to give realistic predictions of carbonate sand behaviour.

2.3.4 TWO SURFACE DOUBLE HARDENING MODELS

Models with two intersecting and hardening yield surfaces were first proposed by Lade and Duncan (1977) to model the triaxial behaviour for medium dense and dense silica sands. Later Vermeer (1978), Nova and Wood (1978) and Molenkamp (1981) proposed double hardening critical state models with intersecting yield surfaces. These models have been successfully used to predict the triaxial behaviour of medium dense and dense silica sands in particular and silica sands in general. The models are discussed and their probable use for predicting carbonate sand behaviour is investigated.

Lade and Duncan (1973) performed cubical triaxial tests on sand. Based on their experimental data and that of Tatsuoka and Ishihara (1974) and Pooroshasb, Houlebec and Sherbourne (1973), Lade and Duncan (1975) proposed an isotropic, elastoplastic, work-hardening model for sand. The yield surface equation is given as follows:

$$f = I_1^3 - kI_3 = 0 \tag{2.12}$$

where I_1 and I_3 are stress invariants and the value of k varied from 27 at hydrostatic stress to a constant value k_1 at shear failure. I_1 is given by equation (2.8) and I_3 is defined as follows:

$$I_3 = \begin{vmatrix} \sigma'_{11} & \sigma'_{12} & \sigma'_{13} \\ \sigma'_{21} & \sigma'_{22} & \sigma'_{23} \\ \sigma'_{31} & \sigma'_{32} & \sigma'_{33} \end{vmatrix} \tag{2.13}$$

σ' are the components of the effective stress tensor

The results of Pooroshasb, Houlebec and Sherbourne (1966, 1967) and those of Lade and Duncan (1973) showed that the normality condition was not satisfied by the failure surface of sand in the triaxial plane. Thus a geometrically similar but separate plastic potential function g was proposed. This function satisfies the normality condition in the triaxial plane. The equation for the plastic potential function is given as follows:

$$g = I_1^3 - k_2 I_3 = 0 \tag{2.14}$$

where the value of k_2 is a function of the current stress level and is generally different from k.

Figure 2.10 shows the shape of the Lade-Duncan yield surface and plastic potential function to be conical in principal stress space. Their trace in the deviator plane is a straight line passing through the origin. An empirical work-hardening function was postulated. This function asymptotically reaches a constant value at the ultimate stress or yield condition.

Lade (1977) subsequently proposed a curved deviator yield surface and added an isotropic cap obeying an associated flow rule. The cap was added to overcome the shortcomings of the Lade-Duncan (1975) model in predicting volumetric compression during isotropic loading. The major strength of the Lade (1975, 1977) model lies in its ability to predict a hardening response concurrently with expansive volumetric strains. It has been shown in section 2.2.3 and Figure. 2.3 that this type of behaviour is generally encountered in medium dense and dense silica sands.

Carbonate sand generally has a loose structure. Neither loose nor dense carbonate sand exhibit hardening behaviour with concurrent expansive dilatation, in contrast to dense and medium dense silica sands. Carbonate sands also exhibit substantial volumetric compression with hardening. This behaviour is modelled only by the cap part of the Lade (1977) model. The Lade cap and deviator yield surface can only expand. They cannot contract. Consequently, the model cannot predict strain softening under drained conditions. Such strain softening behaviour is generally observed in triaxial tests of cemented carbonates at low cell pressures. The model

also has intersecting yield surfaces and associated difficulties with their computer implementation. Thus the Lade (1975,1977) model has some significant shortcomings in predicting the behaviour of carbonate sand.

Vermeer (1978) and Molenkamp (1981) also proposed double hardening critical state models with intersecting deviator and cap yield surfaces. These models are conceptually similar to the Lade (1977) model. However, instead of work hardening, the Vermeer (1978) and Molenkamp (1981) models postulate shear strain hardening for the deviator yield surface. In these models, the plastic potential function is derived for the deviator yield surface using the Lade (1973, 1977) approach but imposing the additional condition that Rowe's stress-dilatancy relation is satisfied. Most of the strengths and shortcomings associated with the Lade (1977) model in predicting carbonate sand behaviour are generally valid for these models as well. The double-hardening models generally have a large number of material parameters (the Molenkamp model has 23). Many of the model parameters have to be determined using a curve fitting approach. It is reasonable to assume that investigation of any one of the double-hardening models in detail would help to understand the strengths and weaknesses of these models as a whole.

The Molenkamp (1981) model was used by Woodside Petroleum Pty. Ltd. to predict the behaviour of end-bearing foundations resting on carbonate sand. However, little work has been done in investigating the performance of double hardening sand models, including the Molenkamp, in predicting the triaxial behaviour of carbonate sand.

Two surface double hardening models give realistic predictions of the triaxial response of silica sands. However, no detailed study is yet available regarding their ability to predict the triaxial response of carbonate sands. Such an investigation will allow the evaluation of the capability of such models for predicting carbonate sand behaviour.

2.3.5 SINGLE SURFACE STRAIN HARDENING MODELS

After a review and evaluation of experimental data on a variety of frictional materials, Kim and Lade (1988) and Lade and Kim (1988a) proposed a single isotropic yield surface for modelling the triaxial behaviour of sand.

Figure 2.11 shows that the single yield surface is shaped like an axisymmetric tear drop with a pointed apex at the origin. Away from the origin, it intersects the hydrostatic axis in an orthogonal fashion. The plastic work due to plastic shear and volumetric strains is computed to determine the hardening function. The yield surfaces themselves are defined as contours of constant plastic work in stress space. Rowe (1962) stress-dilatancy relation is used to determine the plastic potential function.

Experimental data of Lade and Prabucki (1995) on sand at four relative densities show that the model captures with good accuracy sand behaviour both in the hardening and softening regimes. The experimental data show coupling effects to exist in the hardening regime between mean effective stress and plastic shear strains, and between shear stress and plastic volumetric strains. Such coupling effects cannot be handled properly, if the yield locus is separated into two separate surfaces with shear/work and volumetric hardening components. They concluded it is more appropriate to use a single yield surface to predict both the isotropic and shear behaviour of sand.

Frankitzionis, Desai and Somasundaram (1986) proposed a single surface, non-associated model for cohesionless, granular soil. Combined volumetric and shear hardening was assumed. Their results show that the model gives satisfactory predictions of granular soil behaviour.

Nova (1988) proposed a single surface isotropic, strain-hardening, non-associated, critical state model for sand. The model, in general, assumes both plastic shear and volumetric strain hardening. The ultimate or critical state is defined by the Matsuoka-Nakai (1974) criterion for failure.

Nova (1992) and Lagioia and Nova (1993, 1995) extended the Nova (1988) model to predict the mechanical response of soft rocks. Their predictions show good agreement with the triaxial test data for natural and artificially cemented calcarenites and marl. In their model, soft rocks were assumed to have an uncemented soil component and a cementation component. It was assumed that they contribute separately to the total preconsolidation pressure of the soil. The uncemented soil part was characterised by a preconsolidation pressure, which was assumed to undergo plastic volumetric strain hardening with volumetric compression and strain softening with expansive volume change. The cementation part was characterised both by isotropic tensile strength and a part contributing to the increase in preconsolidation strength of the carbonate sand. The tensile and preconsolidation strength component due to cementation was assumed to always degrade with plastic volumetric strains, either expansive or compressive.

The Lagioia and Nova (1993) model was quite successful in predicting carbonate sand behaviour. However, it is important to investigate how much of the successful predictions are due to the strengths of the Nova (1988) model alone and how much is due to the aspects of cementation and degradation of cementation added to this model. This suggests the need to first investigate the basic Nova (1988) model predictions, with additional experimental data that has become available for carbonate sand (eg. Huang, 1994). It also appears to be worthwhile to investigate the role of the non-associatedness of yield and plastic potential functions in simulating carbonate sand behaviour. The Lagioia and Nova model (1993) captures quite well carbonate sand behaviour using a single yield locus and plastic volumetric strain hardening only. This seems to suggest that the Cam Clay framework may also be suitable for predicting the stress-strain behaviour of carbonate sand.

From the forgoing discussion it can be reasonably concluded that single yield surface, non-associated, elastoplastic models may provide satisfactory predictions of carbonate sand behaviour.

2.3.6 CAM CLAY MODELS

It is relevant at this stage to discuss the appropriateness of the Cam Clay models to predict behaviour of sands in general and carbonate sands in particular. The Cam Clay model was formulated by Roscoe et al (1963) as a single surface, volumetric strain hardening, and critical state model. The model was developed to predict the triaxial response behaviour of normally consolidated and lightly overconsolidated clays. The details of this model are available in Schofield and Wroth (1968). The isotropic yield locus of the original Cam Clay is given by the following equation:

$$q = Mp' \ln \frac{p'_o}{p'} \tag{2.15}$$

p'_o determines the position of the current yield locus. It is also the hardening parameter, which is a function of the plastic volumetric strains. The model assumes an associated flow rule.

Figure 2.12 shows the Cam Clay yield locus in the principal stress space as well as its projection in the deviator plane. A critical state line is postulated. This defines the frictional and pressure dependent behaviour of the material. The critical state defines the ultimate state of stress at which the material deforms continuously at constant state of stress and volume. Experimental data on many soils show that the critical state is one of the fundamental features of real soil behaviour.

The model correctly predicts the stress-history dependent response of real soils. Gens and Potts (1988) discussed the discontinuity of the yield surface of the Cam Clay model at the isotropic axis. This gives rise to a singularity and associated numerical problems. As associated flow is assumed, non-zero shear strain is predicted at the discontinuity on the yield surface under isotropic loading. This shortcoming was overcome by adopting an elliptical yield locus in the Modified Cam Clay model. The Modified Cam Clay yield locus is given by the following equation:

$$q^2 = Mp'^2 \left(p'_o - p'\right) \tag{2.16}$$

Figure 2.13 shows the Cam Clay and Modified Cam yield locus in the $p' - q$ plane. The Cam Clay models define a unique state boundary surface, beyond which no state of the soil is permissible. They also define a unique void ratio-critical state relationship. This is in accordance with experimental observations in soils by Rendulic (1936) and Henkel (1960).

One of the major weaknesses of the Cam Clay models in predicting the behaviour of dense silica sands is that expansive dilatancy always produces softening. Dense silica sands, on the other hand, show strain hardening concurrently with expansive dilatancy. Secondly, non-associated plastic flow behaviour is observed in all sands including carbonates. The Cam Clay models however assume an associated flow rule. As a result, the Cam Clay models cannot correctly predict the undrained behaviour of loose sands such as carbonates, which exhibit a peak before the critical state is reached. The Cam Clay yield locus has also been generally observed to significantly overpredict failure stresses of many soils on the supercritical side.

Nova and Wood (1978) state that Cam Clay models can predict reasonably well the drained behaviour of loose sands. Carbonate sands generally exist in a loose condition and strain softening is associated with expansive dilatancy and strain hardening with compressive volume change. This type of behaviour is generally well predicted by plastic volumetric strain-hardening models such as Cam Clay and Modified Cam Clay.

Atkinson and Bransby (1978) state that a major reason for the lack of success of the Cam Clay models in predicting sand behaviour is the difficulty associated with obtaining normal consolidation and critical state lines. However, high pressure consolidation and triaxial tests have been able to isolate both the normal and critical state lines of silica (Pestana and Whittle, 1995) and carbonate sand (Carter et al, 1988, Allman and Poulos, 1988 Huang, 1994 etc.). In such a case it may be realistic to model the triaxial response of carbonate sands within the Cam Clay framework.

Yu (1995) and Drescher et al (1995) formulated non-associated models using modifications of the Cam Clay and Modified Cam Clay respectively to predict the

triaxial response of silica sands and soft rocks similar to carbonate sands. Reasonable predictions were obtained in both cases. This suggests that the Cam Clay framework may be suitable for predicting carbonate sand behaviour.

Several isotropic, strain hardening, critical state, elasto-plastic models were reviewed. It was observed that strain-hardening models obeying a non-associated flow rule appear to predict the triaxial response of carbonate sands quite well. The performance of some of these models in predicting carbonate sand behaviour needs to be investigated in greater detail. It appears that the Cam Clay model or some modification of it may be suitable for predicting carbonate sand behaviour.

2.4 FOUNDATION RESPONSE IN CARBONATE SAND

The ultimate aim of developing a constitutive model is to use it in a numerical technique such as the finite element method to obtain solutions for practical problems in geotechnical engineering. In this section, the experimental results for the pressure-displacement response of circular footing on carbonate sand are first reviewed. The finite element and cavity expansion predictions of the bearing response given by selected constitutive models are then evaluated. Such an evaluation helps to identify which type of constitutive model may be appropriate for predicting foundation response in carbonate sand. It may also indicate whether the constitutive models need to be modified, improved or reformulated.

2.4.1 MODEL-SCALE FOOTING TESTS

Poulos and Chua (1985) compared the drained response of circular model footings on carbonate and silica sand. The bearing capacity was defined as the average mobilised pressure at a settlement of 10% relative to the footing diameter. Their experimental results in Figure. 2.14 and 2.15 show that despite the high friction angle, the stiffness and bearing capacity of circular footings on carbonate sand are significantly smaller than on silica sand. Semple (1988) re-plotted some published data of bearing capacity of carbonate and silica sand, as a function of the void ratio.

The results plot close to a single curve for both sands (Figure 2.16). He concluded that the lower bearing capacity of circular footings on carbonate sand is primarily a consequence of their initial loose structure or high void ratio. This result in significant volumetric compression of the soil as the footing is loaded and can be contrasted with the volumetric expansion exhibited by dense silica sand.

Figures 2.17 and 2.18 show the results of model footing tests described by Allman, Poulos, Carter and Yeung (1988) and carried out on uncemented and artificially cemented carbonate sand. The average pressure mobilised by the footing was plotted up to 20% settlement relative to the footing diameter. The pressures continued to increase with settlement. This is consistent with punching shear failure observed in a compressible, non-dilating soil. Yeoh and Airey (1996) reported similar results for artificially cemented carbonate sand, isotropically consolidated to a predefined cell pressure. It is seen that both the stiffness and the bearing capacity of the footings increase with overburden pressure for K_o consolidated conditions. Figure 2.18 shows that cementation increases the stiffness and bearing pressure mobilised by the footings.

2.4.2 CENTRIFUGE TESTS

Finnie (1993) and Finnie and Randolph (1994) carried out centrifuge tests to investigate the drained response of surface circular footings on normally consolidated carbonate sand. Figure 2.19 shows that the mobilised bearing pressure increases with foundation size, when the settlements are plotted relative to the foundation diameter. Figure 2.20 shows that an approximately single linear curve independent of foundation size is obtained, when the bearing pressure is plotted in terms of footing settlement.

A typical soil profile in offshore locations is that of a cemented layer close to the seabed, underlain by softer uncemented soil. The cemented crust increases the bearing modulus. But with increased loads the crust can fracture, allowing the foundation to punch through the softer material. Figure. 2.21 shows a typical

response in centrifuge tests of a shallow circular footing resting on layered strata, with a stronger crust.

2.4.3 PLATE LOAD TESTS

Figure 2.22 shows the results of eight in-situ downhole plate load test (PLT), reported by Goudever et al (1988) and Sharp and Seters (1988). The tests were carried out at the North Rankin platform, 112m and 141m below the mud line. The load-settlement response is bilinear. There was an initial stiff response up to yield, thereafter the stiffness decreased. The pressures continued to increase monotonically, with increased plate settlements. The field response was observed to be similar to model footing tests on carbonate sand. This suggests that the laboratory response of model footings may be representative of real footing behaviour. Reasonable predictions of PLT results were obtained by assuming an equivalent cone penetration value for the layered soil. This suggests that an assumption of equivalent uniform strata can approximate footing behaviour in layered carbonates. This may have practical implications in predicting foundation behaviour in real situations using approximate methods.

2.4.4 BEARING CAPACITY AND CAVITY EXPANSION THEORY

The bearing pressure mobilised by model-scale footings on carbonate sand has been predicted using bearing capacity and cavity expansion theory by various authors. The predictions and their comparison with experimental data are presented in this section.

Figure 2.23 shows comparison of the bearing capacity obtained for a model-scale footing on carbonate sand at various overburden pressures with Terzaghi general shear, Terzaghi local shear and cavity expansion theory (Poulos and Chua, 1988). Both Terzaghi general and local shear theories are observed to overestimate the bearing capacity of carbonate sand. The cavity expansion theory of Vesic (1972) was used with a perfectly plastic curved Mohr-Coulomb envelope and an empirical plastic volume compressibility relation for carbonate sand. The bearing capacity of

the footing was assumed to be equal to the computed limit pressures. The bearing capacity was defined as the bearing pressure mobilised by the footing at a settlement of 10% relative to the footing diameter. The predicted bearing capacity shows good agreement with the experimental data. This implies that taking into account the plastic volume compressibility results in significant improvement in predictions of the bearing pressure mobilised by footings in carbonate sand. However, it is not clear that why the limit pressures computed from cavity expansion should be related to the bearing pressure mobilised by footings at a displacement of 10% relative to the footing diameter.

Yeung and Carter (1989) computed the limit pressures in spherical cavity expansion using the elastic, perfectly plastic Mohr-Coulomb and elastoplastic Lade (1977) model. The closed form cavity expansion solution proposed by Carter et al. (1986) was used for the elastic, perfectly plastic model. A numerical solution scheme proposed for cavity expansion problems by Carter and Yeung (1985) was used for the Lade (1977) model. Figure 2.24 shows that the limit pressures computed using the Lade (1977) model are in good agreement with the experimental bearing capacity of circular footings resting on carbonate sand. It has to be acknowledged that the spherical cavity expansion method provides an indirect and approximate method of computing the bearing capacity. Because of the limitations of existing approaches, finite element analysis, with appropriate constitutive models, is more likely to provide realistic and accurate predictions of bearing pressure mobilised by foundations resting on carbonate sand.

2.4.5 FINITE ELEMENT PREDICTIONS

Smith et al (1988) reported the predictions of a plate load test using the Vermeer (1978), Molenkamp (1981), Mohr-Coulomb, and the Drucker-Prager (DP) and Von-Mises (VM) models and a formulation of Sweet's (1988) Crush-up constitutive model. Fully drained behaviour was assumed, and the compressibility and ultimate shear resistance characteristics were obtained from oedometer, unconfined compression and isotropic consolidation tests.

Figure 2.25 shows that the Crush-up (VM) model results are in good agreement with experimental data, up to a settlement of 50% relative to the footing diameter. In the Crush-up model, the crushing behaviour of rock is characterised by significant volume compression experienced by the soil in response to increased confining stress. This underscores the fact that the Cam Clay framework based on plastic volumetric strain hardening, may be appropriate to predict the bearing response of footings resting on this sand. Figure 2.26 shows the displacement vectors and deformed mesh obtained using the Molenkamp (1981) model, at a settlement of 20% relative to the footing diameter. It can be seen that due to the high compressibility, compaction occurs locally directly under the loaded area of the footing. Smith et al (1988) state that the main application of the Molenkamp (1981) model is in undrained problems. In these cases, collapsing or liquefying behaviour is of major concern. For drained problems, the use of a complex model with 23 material parameters, may not lead to any greater ability to curve fit the field data.

2.5 CONCLUSION

The review of the relevant literature shows that there has been only a limited investigation of the performance of critical state models in predicting the behaviour of cemented and uncemented carbonate sand in triaxial tests. Thus there exists a clear need for a detailed evaluation and comparison of selected critical state models in predicting carbonate sand behaviour. Detailed analysis and evaluation of available experimental data is necessary for the modification of existing models or for the development of a new constitutive model for carbonate sand. Surface and deep circular footings are frequently constructed on carbonate sand in offshore locations. The load-settlement response of these foundations may be simulated by elastoplastic finite element analysis. Detailed parametric study of footing response using appropriate constitutive models needs to be undertaken for a better understanding of the properties and mechanisms affecting foundation behaviour in carbonate sand.

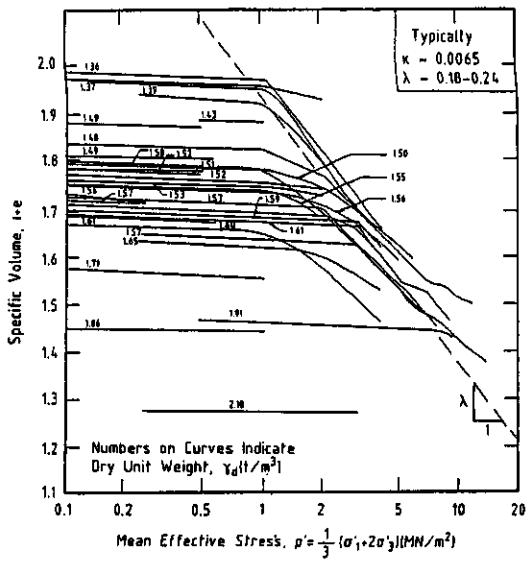

Figure 2.1 Behaviour of carbonate sand during isotropic consolidation (Carter et al., 1988)

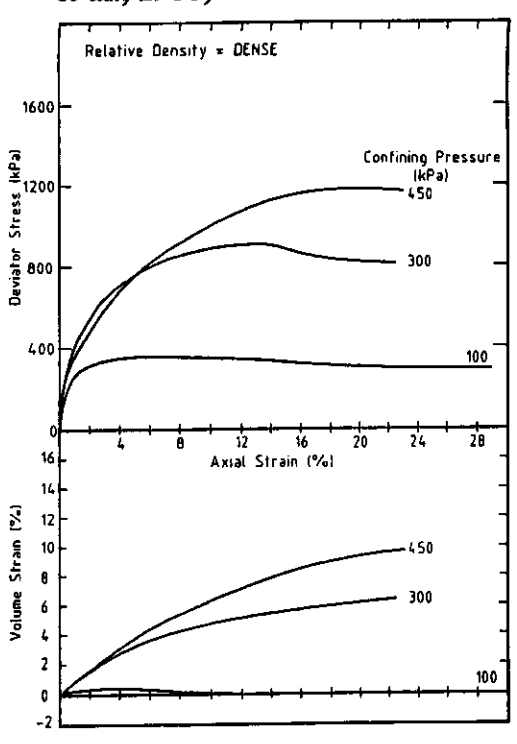

(a) Uncemented

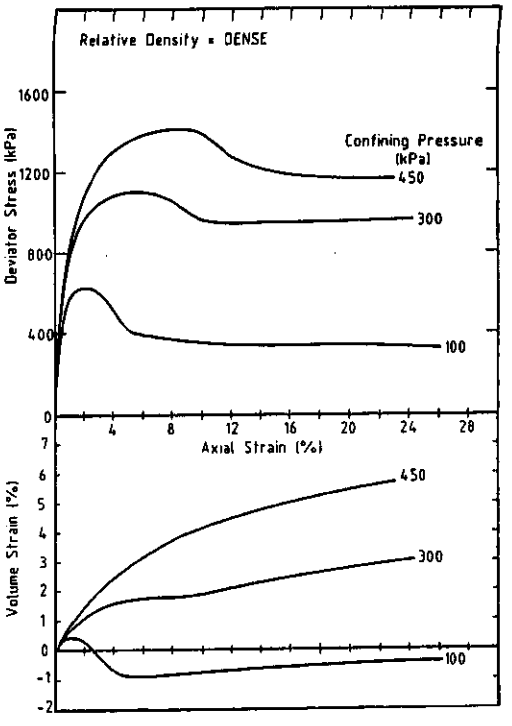

(b) Cemented

Figure 2.2 Stress-strain curves for dense uncemented and artificially cemented carbonate sand with 4% cement content (Allman and Poulos, 1988)

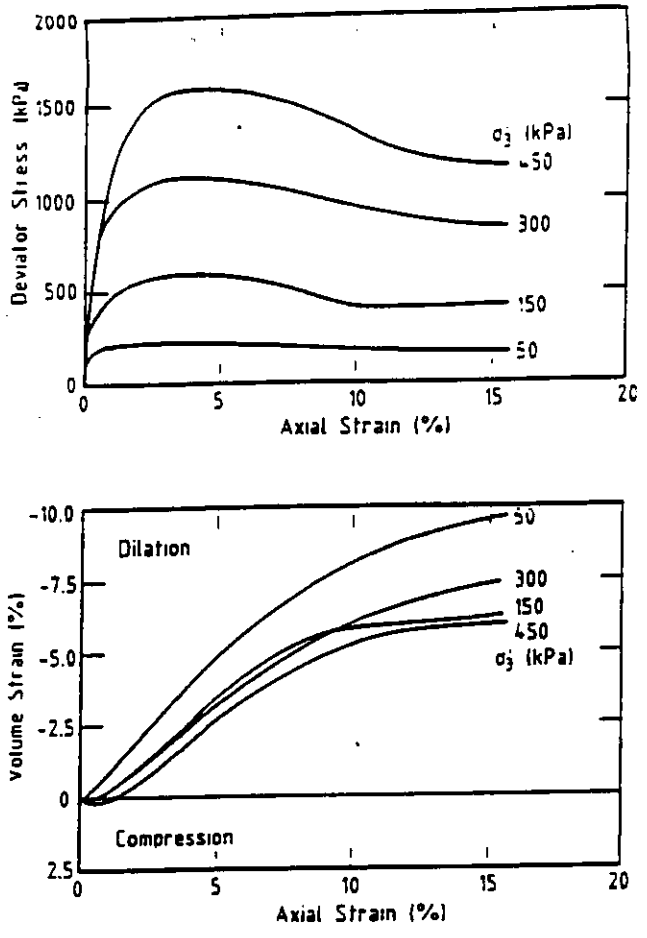

Figure 2.3 Stress-strain curves for dense silica sand in triaxial compression tests (Yeung and Carter, 1988)

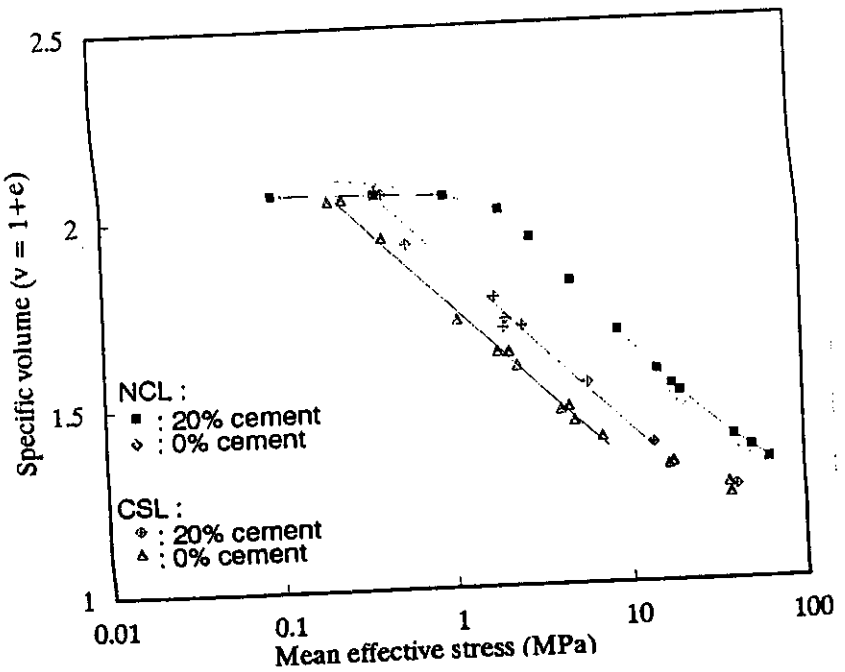

Figure 2.4 Normal consolidation line and critical state line of uncemented and cemented carbonate sand (Huang, 1994)

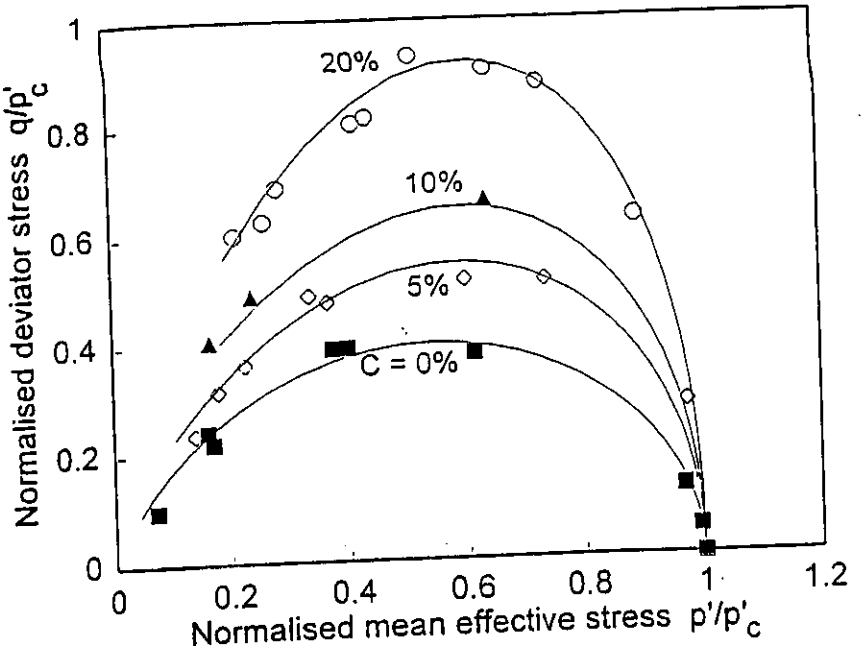

Figure 2.5 Normalised experimental yield loci for loose uncemented and cemented carbonate sand (Huang, 1994)

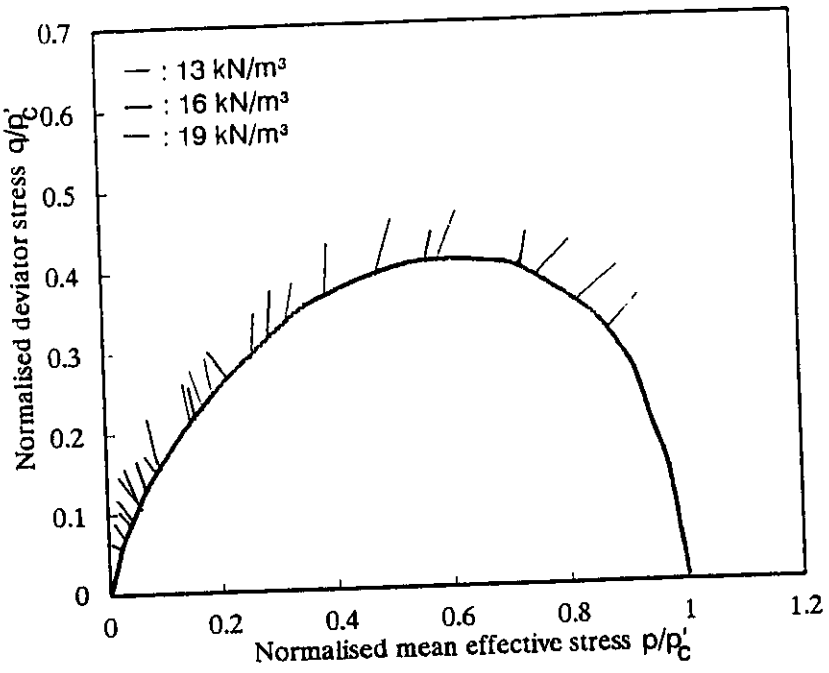

Figure 2.6 Incremental plastic strain vectors in yield locus of uncemented carbonate sand (Huang, 1994)

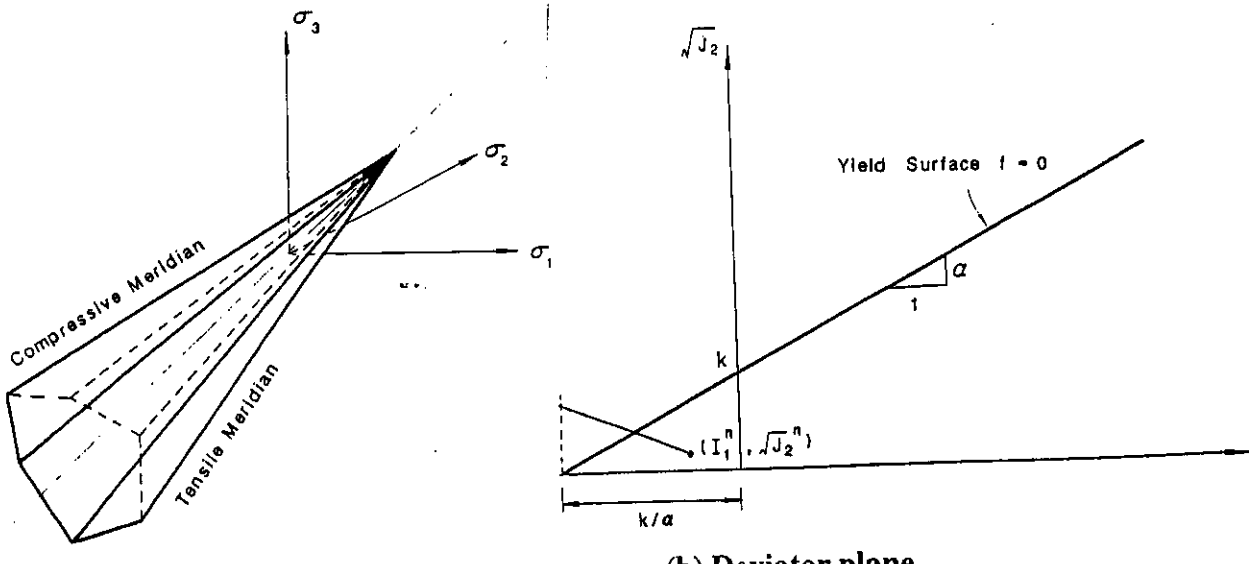

(a) Principal stress space

(b) Deviator plane

Figure 2.7 The Mohr-Coulomb model (Chen and Mizuno, 1990)

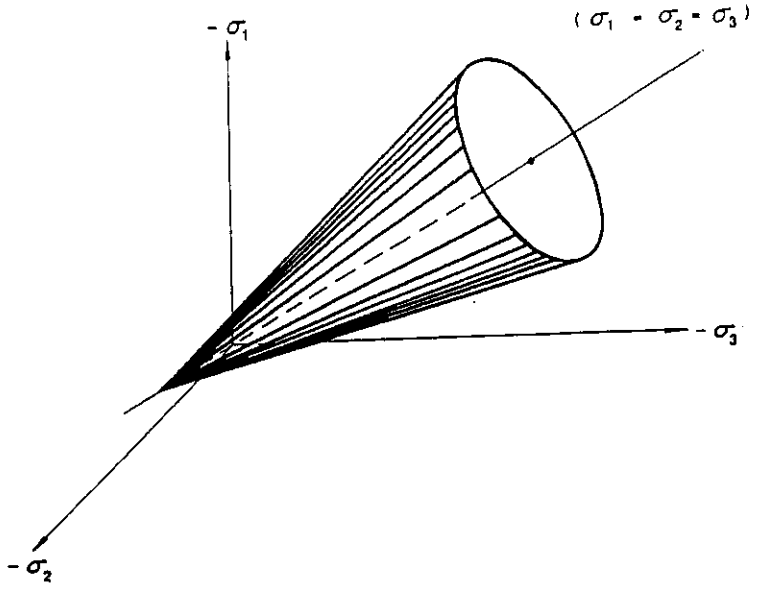

Figure 2.8 The Drucker-Prager model in principal stress space (Chen and Mizuno, 1990)

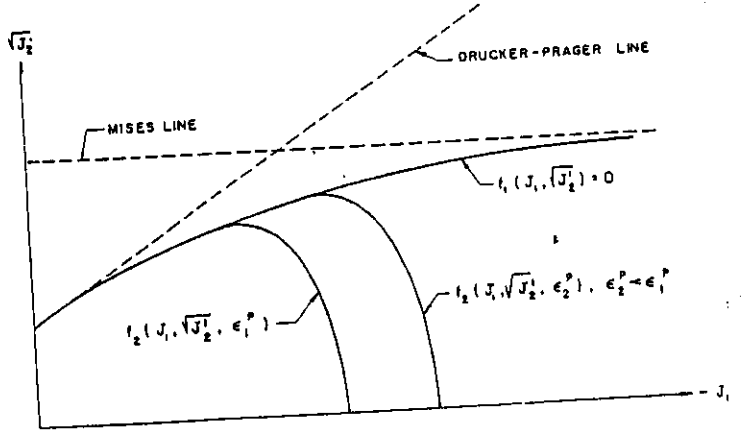

Figure 2.9 The Cap model in deviator plane (DiMaggio and Sandler, 1971)

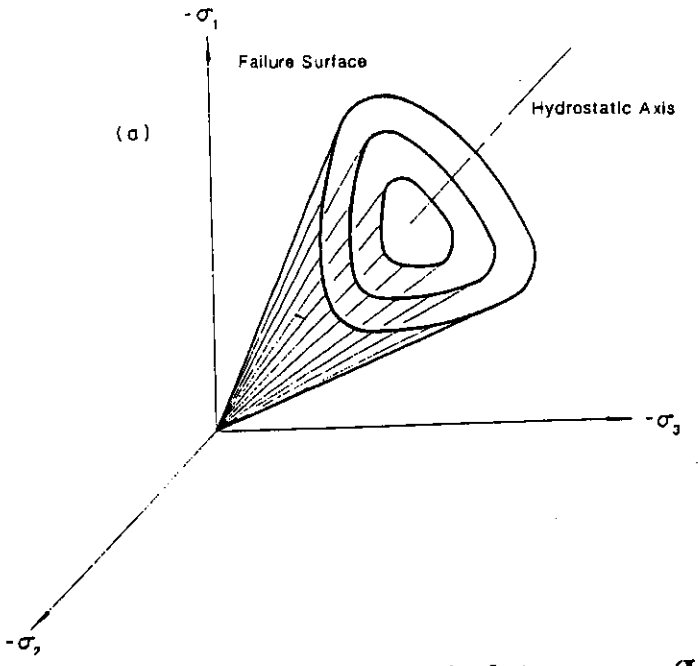

Figure 2.10 The Lade-Duncan model in principal stress space (Lade and Duncan, 1975)

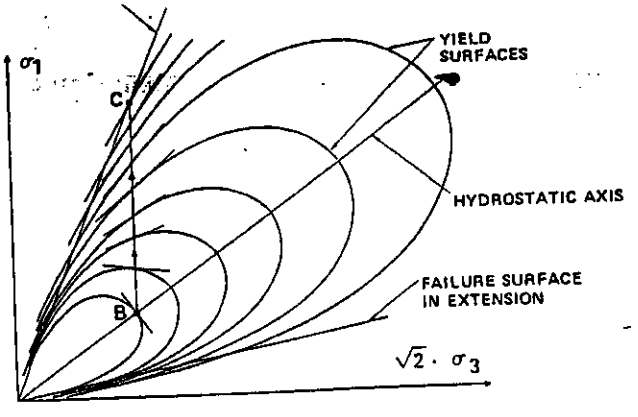

Figure 2.11 Proposed single yield surface for sands (Lade and Kim , 1988)

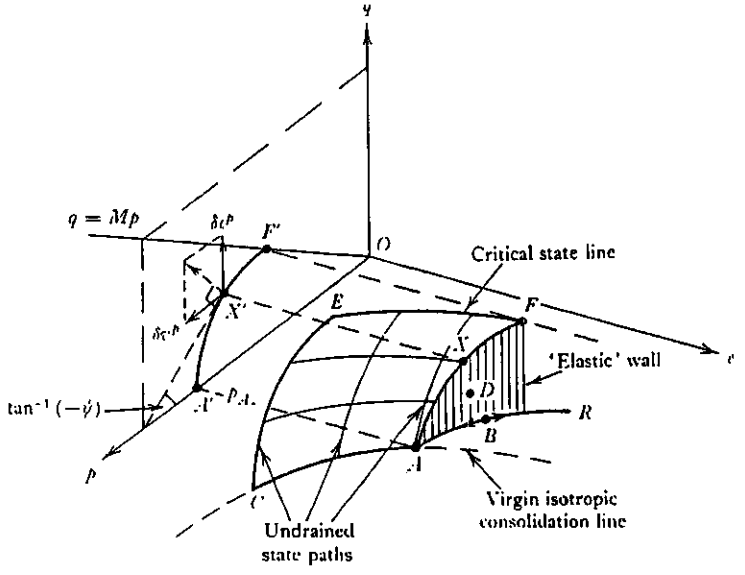

Figure 2.12 The Cam Clay state boundary surface in p', q, e space (Roscoe and Burland, 1968)

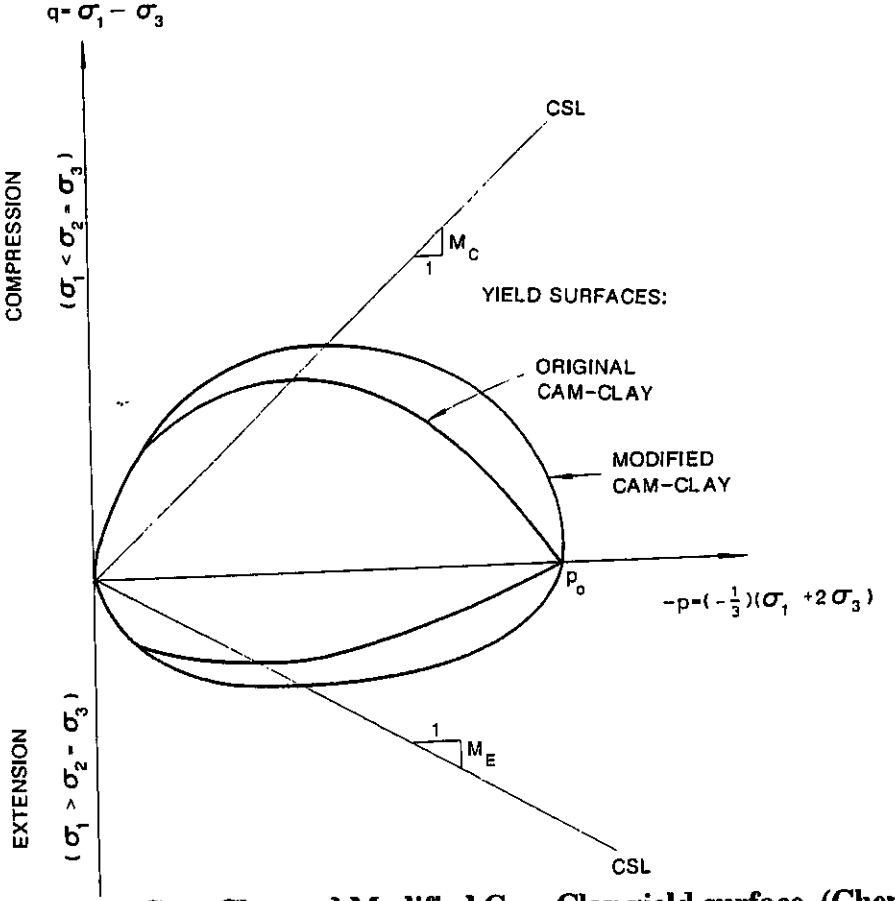

Figure 2.13 The Cam Clay and Modified Cam Clay yield surface (Chen and Mizuno , 1990)

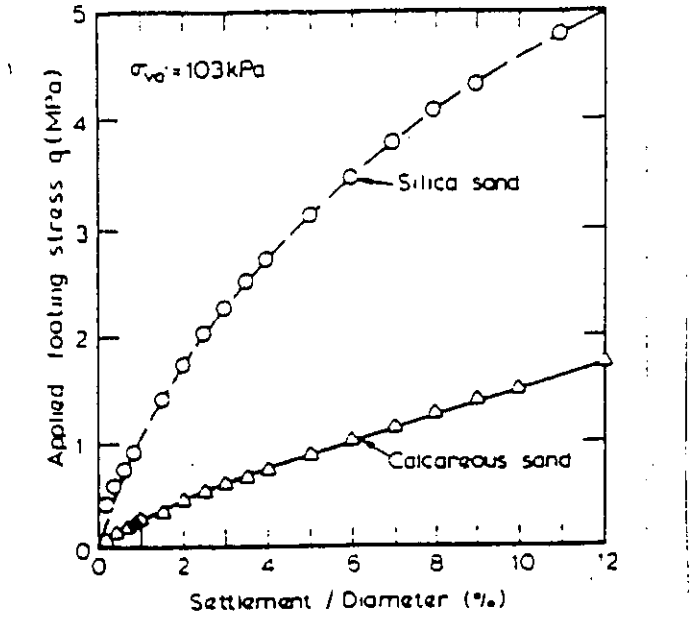

Figure 2.14 Comparison of typical load-settlement curves of foundations on carbonate and silica sand (Poulos and Chua, 1985)

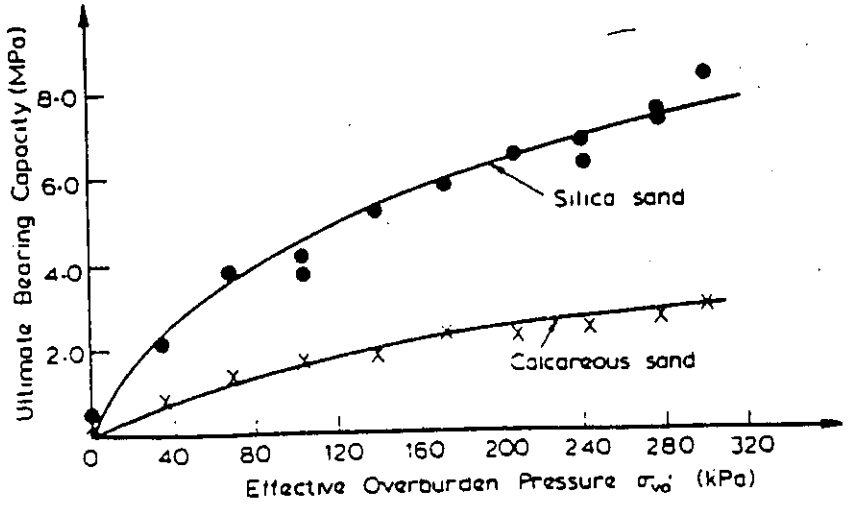

Figure 2.15 Comparison of the bearing capacity of foundations on carbonate and silica sand (Poulos and Chua, 1985)

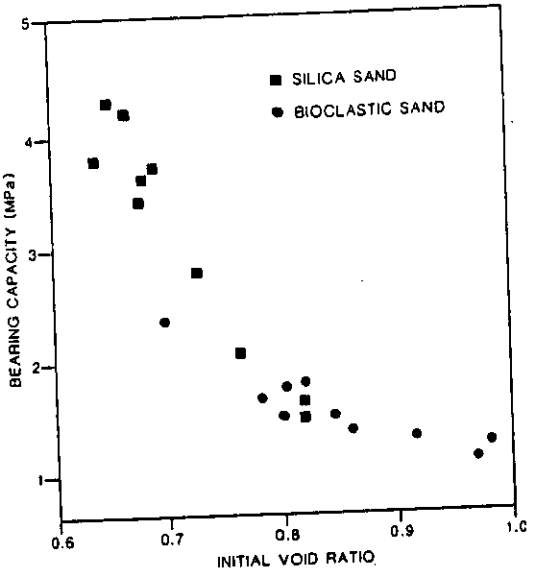

Figure 2.16 Bearing capacity versus initial void ratio for bioclastic and silica sand (Semple, 1988)

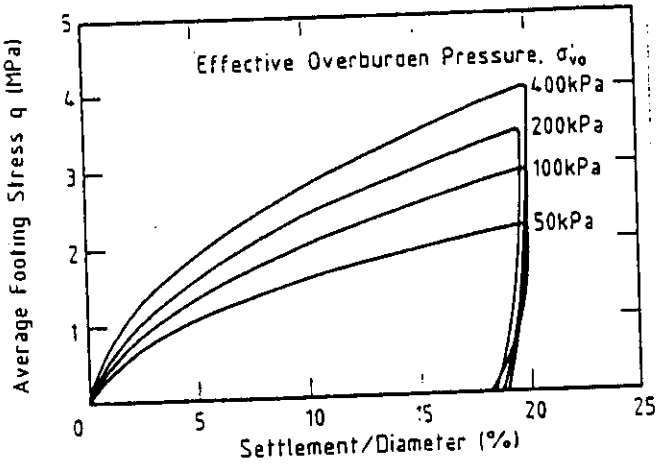

Figure 2.17 Pressure-settlement response of uncemented carbonate sand (Allman et al, 1988)

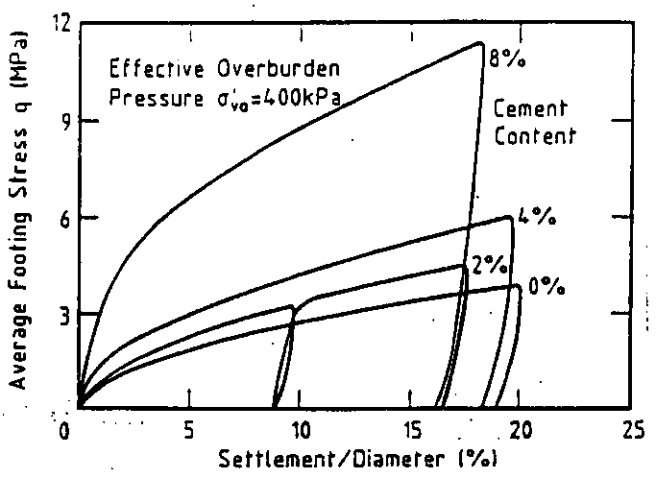

Figure 2.18 Pressure-settlement response of cemented carbonate sand (Allman et al, 1988)

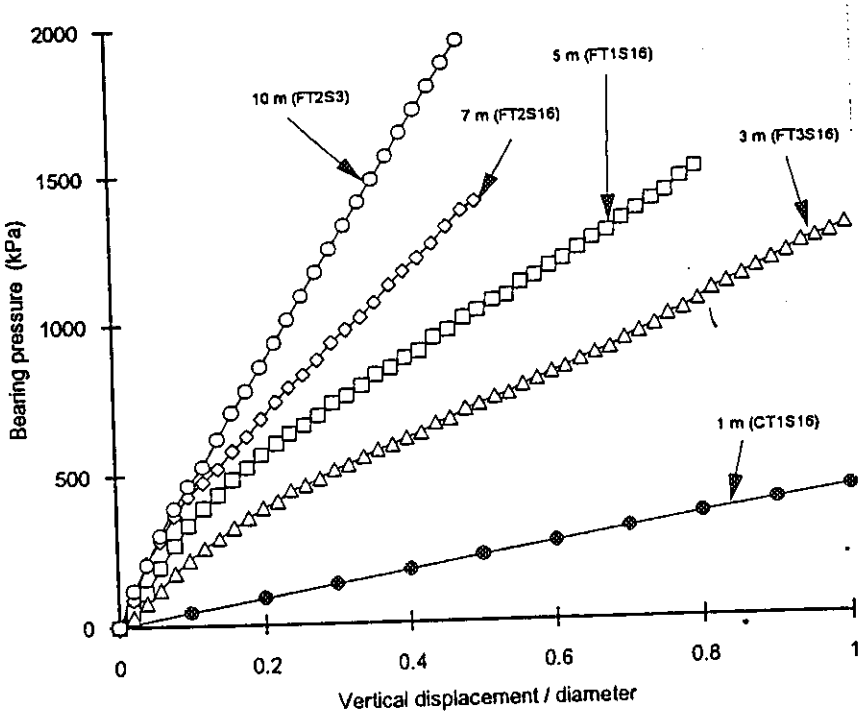

Figure 2.19 Centrifuge tests of model surface foundations in carbonate sand (Finnie, 1993)

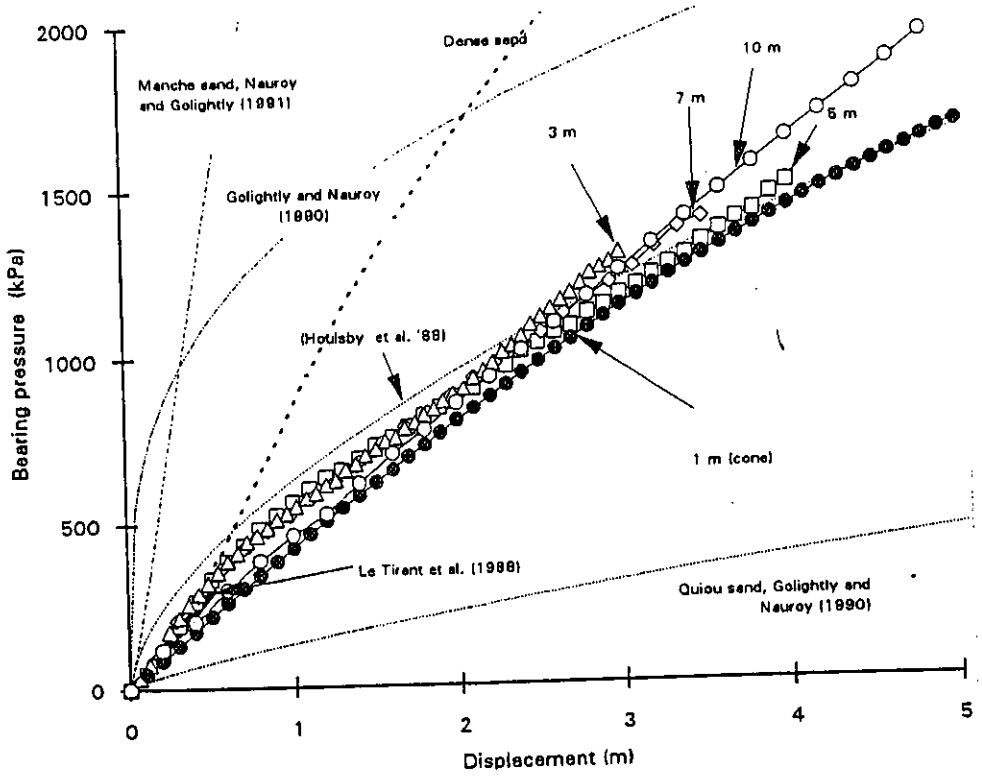

Figure 2.20 Comprison of centrifuge tests of model surface foundations in carbonates with silica sand (Finnie, 1993)

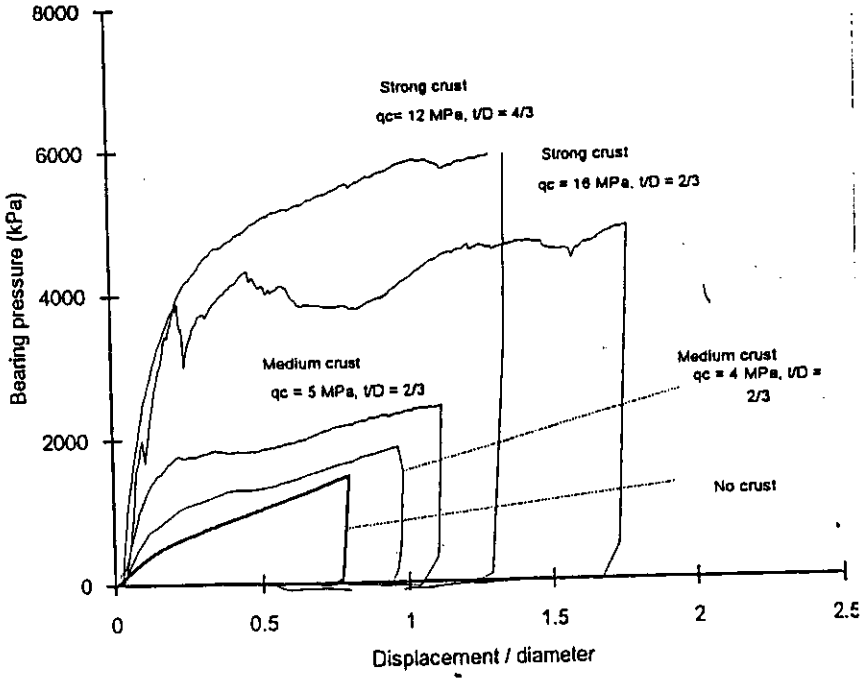

(a) Typical bearing response of a 3 m diameter foundation

Figure 2.21 Centrifuge tests of model surface foundation on layered carbonate strata (Finnie, 1993)

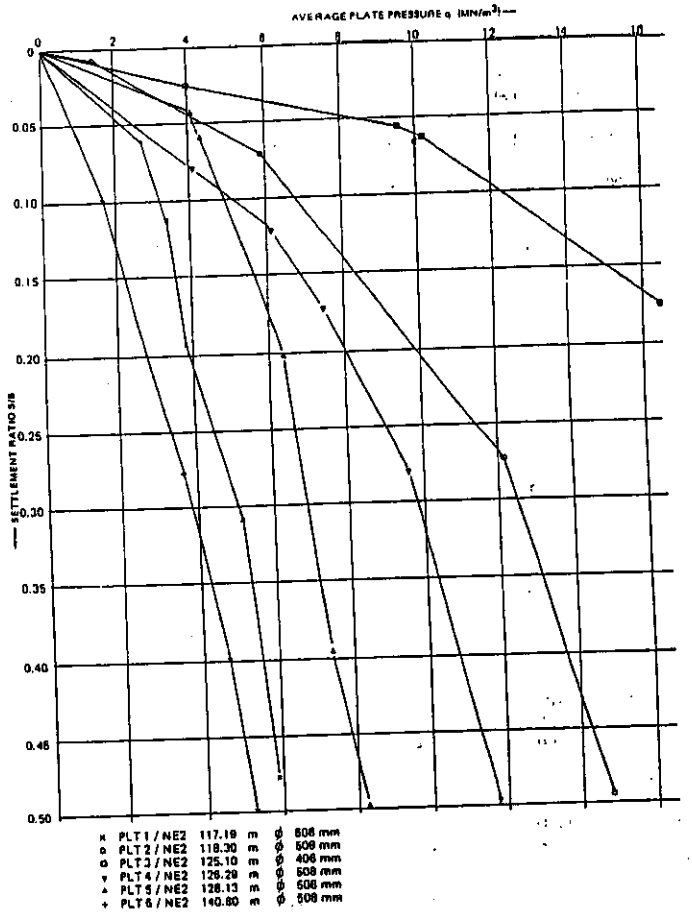

Figure 2.22 Plate load-settlement curves in carbonate sand (Goudoever et al,1988)

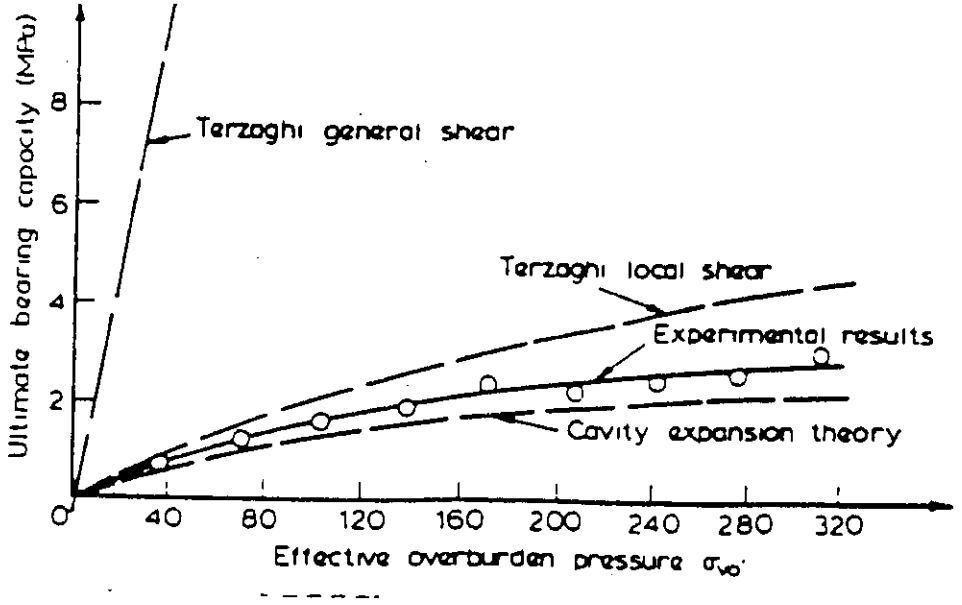

Figure 2.23 Comparison of the experimental and computed bearing capacity of model footings on carbonate sand (Poulos and Chua, 1988)

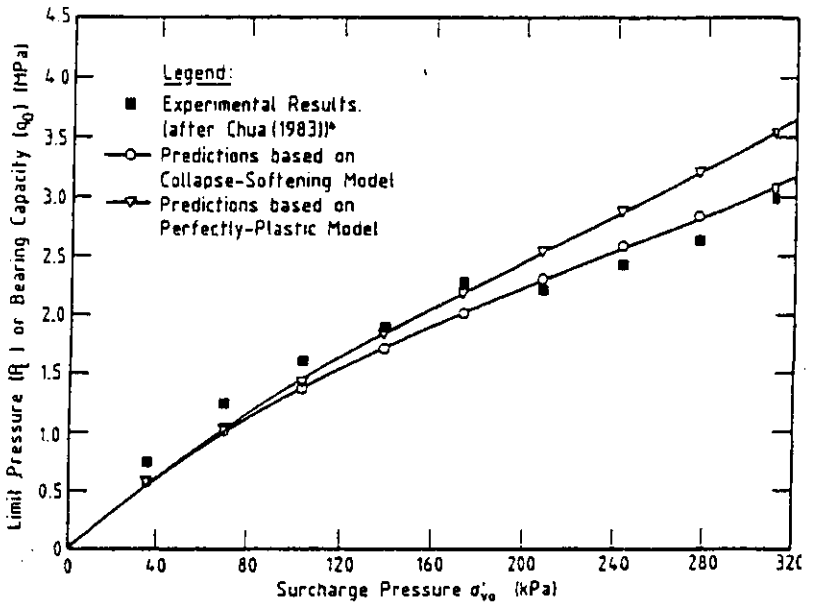

Figure 2.24 **Comparison of computed *limit pressures and measured bearing* capacities from model footings in carbonate sand (Yeung and Carter, 1989)**

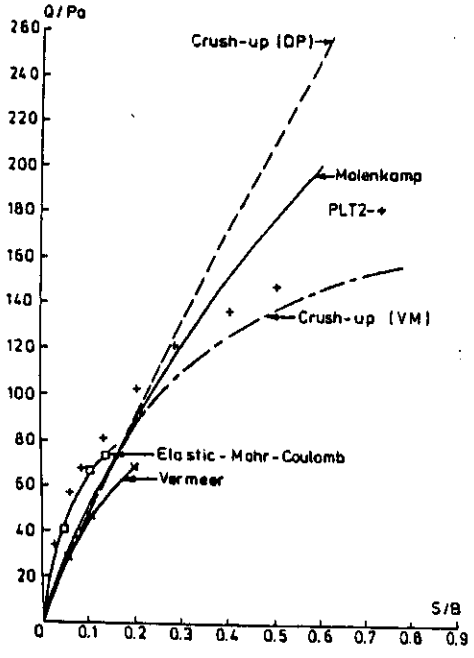

Figure 2.25 Predictions of drained plate load tests using various constitutive models(Smith et al, 1988)

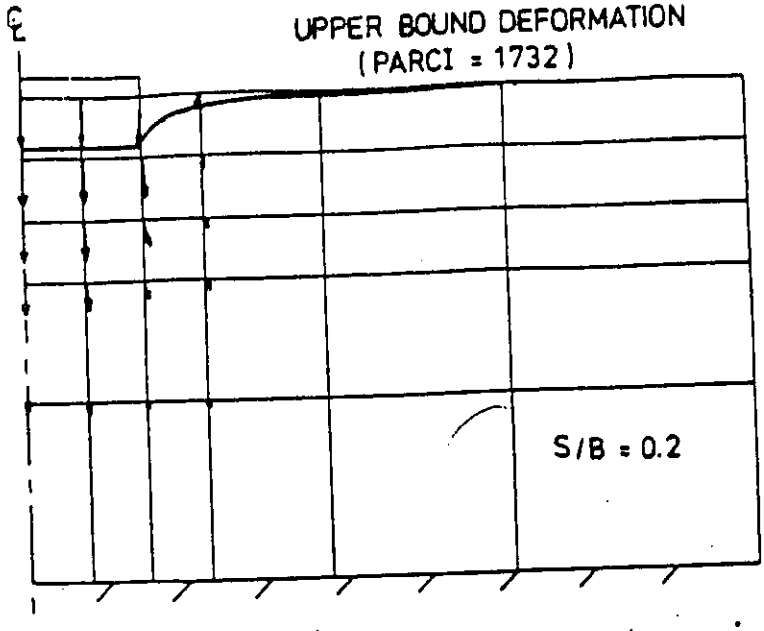

Figure 2.26 Displacement vectors in finite element analysis of plate load test using the Molenkamp model (Smith et al.,1988)

3

CONSTITUTIVE MODELS FOR CARBONATE SAND

3.1 INTRODUCTION

Cemented and uncemented carbonate sands are encountered in many offshore regions around Australia and in many other parts of the world. The mechanical response of these sands is quite complex and difficult to model. The high friction angles of these materials enables them to resist large loads, but unlike silica sands, these loads are resisted only after the material undergoes substantial deformations. This happens due to the high porosity and plastic compressibility of these soils. Despite the high plastic compressibility, carbonate sands and particularly cemented carbonates, exhibit a stiff initial elastic response. Cementation, which is often present in the natural sediments, further complicates their mechanical behaviour.

In order to understand clearly the observed experimental stress-strain response of carbonate sands, three critical state models, namely the Modified Cam Clay, the Molenkamp and the Nova models were chosen to simulate the material behaviour. The spacing ratio parameter is introduced in the Cam Clay and Modified Cam Clay model, which significantly improves their ability to predict the mechanical behaviour of carbonate sands. The modification of the Cam Clay model has been termed as the SU1 model. Similar changes to the Modified Cam Clay model are known as the SU2 model. The simulations of the Modified Cam Clay, Molenkamp, Nova, SU1 and SU2 model have been compared with the triaxial test data and these comparisons are analysed in detail. The results of the analyses are presented in this chapter.

3.2 TRIAXIAL TESTS

Huang (1994) carried out a series of isotropic consolidation and triaxial shear tests on carbonate sands. The model parameters were determined from, and model simulations matched with, the results of these tests. The method of sample preparation, the type of carbonate sand tested and the cell pressures at which the tests were carried out are described in this section.

The carbonate sand was obtained from the NorthWest shelf of Australia. It was composed of fine and medium sized sand grains with a specific gravity of 2.82 and carbonate content of 91%. Cylindrical uncemented and artificially cemented specimens were prepared by one-dimensional compression of mixtures of sand, distilled water and gypsum plaster to a predetermined unit weight. Specimens were transferred to a triaxial apparatus, saturated under a low confining pressure and compressed in isotropic conditions before shearing. The inherent variability of naturally cemented materials, as well as the difficulty in sampling, has led researchers to use artificially cemented specimens for laboratory testing. The results of the tests appear to indicate that artificially cemented specimens replicate the mechanical behaviour of natural cemented deposits quite well. The dry unit weights of the test samples were varied from loose (13kN/m^3) to dense (19kN/m^3), cement contents from 0% to 20% (by dry unit weight) and confining stress from low (0.1 MPa) to high (20 MPa). Triaxial tests for which model simulations were carried out are presented in summary form in Table 3.1 below.

Table 3.1 Summary of triaxial compression tests

Dry density (kN/m^3)	Cement content (%)	Yield stress (MPa)	Cell pressure			
			(MPa)	(MPa)	(MPa)	(MPa)
13	0	1.2	0.1	0.3	0.6	1.2
13	20	1.75	0.1	0.3	0.6	1.2
19	0	32	1.2	5	10	20
19	20	50	1.2	5	20	

The specimens were sheared at a constant axial strain rate of 5%/hr for undrained loading and 1%/hr for drained loading, often to axial strains of 50%. In the plots of the shearing tests, natural axial and volumetric strains were used. These tests provided a comprehensive set of data for examining and simulating the drained triaxial response of carbonate sands using complex, elasto-plastic soil models.

3.3 MODEL SELECTION AND NUMERICAL IMPLEMENTATION

The elasto-plastic models selected for simulating the triaxial behaviour of carbonate sands, the criteria for choosing them and their numerical implementation are discussed in this section.

Strain hardening-softening critical state soil models were chosen to simulate the triaxial response of carbonate sands. The reasons for choosing such models are now elaborated. Triaxial shear tests by Huang (1994) on carbonate sands indicated a stiff initial elastic response, subsequently a strain-hardening response and ultimately a perfectly plastic state. No true critical state condition, indicated by continuous plastic shearing at zero incremental volumetric strain, was observed even at large axial strains. However, the carbonate sand was close to or approaching critical state conditions by the end of most tests. Even at relatively low cell pressures, large

compressive volumetric strains were observed. The compressive volumetric strains corresponded with the observed strain-hardening behaviour. This indicates that volumetric strain-hardening models may be a good choice for simulating the mechanical behaviour of carbonate sands.

Modified Cam Clay (MCC) is one of the earliest and still widely used critical state formulations in computational applications (Gens and Potts, 1988). Selection of MCC provided a standard for comparing the relative strengths of other critical state models in simulating the triaxial behaviour of carbonate sands. The Nova (1988) model and its modifications, as described by Di Prisco, Mattioti and Nova (1992), Gens and Nova (1993) and Lagioia and Nova (1993, 1995), have been used to predict successfully the drained behaviour of carbonate sands. The selection of the Nova model for further investigation was thus a natural choice. The Molenkamp model was used to predict the response of triaxial specimens of carbonate sands and pile foundations resting on these soils at the NorthWest Shelf of Australia, eg. Smith et al (1988). A comparison of its predictions with those of the other models could provide a justification for choosing other relatively simple models, for future predictions. The SU1 and SU2 models were developed as modifications of the Cam Clay and Modified Cam Clay model respectively, by incorporating the spacing ratio, as explained below, as a model parameter. SU1 and SU2 are thus generalisations of the Cam Clay and Modified Cam Clay models respectively, and incorporate the original models as special cases.

The constitutive models were incorporated as element subroutines in the finite element program AFENA (Carter and Balaam, 1995). The SU1, SU2 and Nova model subroutines were implemented in AFENA by the author.

Displacement controlled tests, with single 8 node isoparametric quadrilateral elements, were used to simulate triaxial shear. As the constitutive models are highly non-linear, a tangent stiffness approach was used, with a large number of iterations, to obtain convergent results. Complete 3x3 element Gaussian integration was used in all cases.

The models selected for simulation of carbonate sand behaviour and their numerical implementation in AFENA have now been introduced. The subsequent subsections describe each of the constitutive models in more detail.

3.3.1 MODIFIED CAM CLAY MODEL

The Modified Cam Clay model was developed as a result of the work of the Cambridge group, including Roscoe and Burland (1968) and Roscoe, Schofield and Thurairajah (1963), etc. It is an isotropic, strain-hardening, critical state model obeying an associated flow rule.

In the Modified Cam Clay model, the yield and plastic potential functions are derived from energy considerations. It is assumed that the dissipation of plastic work is given by the following equation:

$$p'\delta\varepsilon_v^p + q\delta\varepsilon_q^p = p'\sqrt{\left(\delta\varepsilon_v^p\right)^2 + \left(M\delta\varepsilon_q^p\right)^2} \tag{3.1}$$

where

$$p' = I_1/3 \tag{3.2}$$

$$q = \sqrt{3J_2} \tag{3.3}$$

$$I_1 = \sigma'_{11} + \sigma'_{22} + \sigma'_{33} \tag{3.4}$$

$$J_2 = \frac{1}{6}\left[\left(\sigma'_{11} - \sigma'_{22}\right)^2 + \left(\sigma'_{22} - \sigma'_{33}\right)^2 + \left(\sigma'_{33} - \sigma'_{11}\right)^2\right] + \sigma'_{12}{}^2 + \sigma'_{23}{}^2 + \sigma'_{31}{}^2 \tag{3.5}$$

In the above equations, $\delta\varepsilon_v^p$ is the incremental plastic volumetric strain, $\delta\varepsilon_q^p$ is the incremental plastic shear strain, p' is the mean effective stress, q the deviator stress, M the stress ratio at critical state, I_1 the first invariant of the stress tensor, J_2 the

second invariant of the stress deviator and $\{\sigma'\}$ the components of the effective stress tensor.

The stress-dilatancy relation may be derived from equation (3.1) to give:

$$\frac{d\varepsilon_v^p}{d\varepsilon_q^p} = \frac{M^2 - \eta^2}{2\eta} \tag{3.6}$$

where

$$\eta = \frac{q}{p'} \tag{3.7}$$

In equation (3.6) $\frac{d\varepsilon_v^p}{d\varepsilon_q^p}$ is termed the dilatancy ratio and η is the current stress ratio.

The dilatancy ratio gives a measure of the relative direction of incremental plastic strains. Equation (3.6) shows that dilatancy is dependent on the current stress and independent of the direction of applied incremental stresses. It also shows that at the critical state where the stress ratio is *M*, the soil has zero dilatancy. The yield and plastic potential function of the MCC are obtained by integrating the stress-dilatancy equation which gives:

$$f = g = M^2 p'^2 - M^2 p' p'_o + q^2 = 0 \tag{3.8}$$

Equation (3.8) defines an ellipse in p' - q space as shown in Figures 3.1 and 3.2. Figure 3.1 shows that the MCC yield locus matches poorly the data for loose uncemented carbonates. However, good agreement is observed with the data for loose cemented carbonates, as shown in Figure 3.2. Different degrees of cementation will enlarge the yield locus of cemented carbonate sands to different extents in the deviator direction. Thus the agreement of the MCC yield locus with experimental data for cemented carbonate sand is likely to be coincidental, rather than a definitive demonstration of the ability of the model to capture the yielding behaviour of

cemented carbonates in general. Figures 3.3 and 3.4 shows that the stress-dilatancy relation given by equation (3.6) agrees quite well with the data for loose uncemented carbonates and reasonably well with data for loose cemented carbonates.

Stress changes within the yield locus are assumed to be associated with elastic behaviour. This assumption is reasonable for cemented carbonates, but less so for uncemented soils. Stress states on the yield locus satisfy the yield function and are associated with plastic behaviour. In the latter case, an increment of outward applied stress or plastic loading, results in enlargement of the yield locus, with a consequent increment of the hardening parameter p'_o. The new state of stress thus satisfies the yield function given by equation (3.8).

In the MCC model, the critical state line (CSL) represents the ultimate states of stress. At the critical state, the material is assumed to undergo continuous shear at constant volume and stress. The CSL is given by the following equations:

$$q = Mp' \tag{3.9}$$

$$e = e_{cs} - \lambda \ln p' \tag{3.10}$$

In equation (3.10), e is the void ratio, e_{cs} is a constant and λ is the slope of the CSL in $e - \ln p'$ space. M in equation (3.9) represents the slope of the CSL in $p' - q$ space. For triaxial compression, M may be obtained from the ultimate friction angle ϕ' by the following equation:

$$M = \frac{6Sin\phi'}{3 - Sin\phi'} \tag{3.11}$$

For the MCC, the CSL intersects the yield ellipse at its maximum point. The isotropic coordinate of the point of intersection is given as $p'_{cs} = p'_o / 2.0$.

The normal consolidation line (NCL) describes the elasto-plastic response of the soil during isotropic compression. A family of parallel unload-reload lines gives the elastic response. The NCL and elastic rebound line are defined respectively by the following equations:

$$e = N_1 - \lambda \ln p' \tag{3.12}$$

$$e = N_2 - \kappa \ln p' \tag{3.13}$$

In equations (3.12) and (3.13), e is the void ratio, λ and κ are the slopes of the NCL and the elastic unload-reload lines respectively and N_1 and N_2 are constants. The hardening function describes the change of the hardening parameter p'_o with plastic volumetric strain ε_v^p. It is derived from equations (3.12) and (3.13) as follows:

$$\frac{\partial p'_o}{\partial \varepsilon_v^p} = \frac{p'_o(1+e)}{\lambda - \kappa} \tag{3.14}$$

The non-linear elastic bulk modulus may be obtained from equation (3.13) as follows:

$$\frac{dp'}{d\varepsilon_v^e} = \frac{p'(1+e)}{\kappa} \tag{3.15}$$

The elastic bulk modulus is thus directly proportional to the mean pressure and inversely proportional to the elastic rebound parameter k. Originally the Modified Cam Clay model assumed infinite elastic shear modulus and zero elastic shear strains within the yield locus. A finite value for elastic shear modulus is now generally adopted for finite element calculations based on a stiffness formulation. In the current description of the MCC, the elastic shear modulus is obtained from the elastic bulk modulus using a constant value of the elastic Poisson's ratio ν.

The basic features of the Modified Cam Clay model have been described. The stress-dilatancy function and yield locus of the MCC have been compared with the data for

cemented and uncemented carbonate sand. The next section describes the significant features of the Molenkamp model.

3.3.2 MOLENKAMP MODEL

The Molenkamp model is a relatively complex, critical state, strain-hardening model with two intersecting yield surfaces. The complete Molenkamp model is described by 23 material parameters. In contrast, the number of model parameters in MCC is only 6. The significant features of the Molenkamp model are described in detail in this section.

A spherical cap-shaped surface, similar to that proposed by Lade (1977), defines one of the yield surfaces in I_1-I_2 space. The cap surface is associated primarily with compressive stresses. It is assumed to obey an associated flow rule. The equation for the cap function is given as follows:

$$F_c = G_c = I_1^2 + 2I_2 - k_c \tag{3.16}$$

$$I_2 = -\sigma'_{11}\sigma'_{22} - \sigma'_{22}\sigma'_{33} - \sigma'_{33}\sigma'_{11} + (\sigma'^2_{12} + \sigma'^2_{23} + \sigma'^2_{31}) \tag{3.17}$$

$\{\sigma'\}$ are the components of the effective stress tensor, I_1 and I_2 are stress invariants and k_c is a volumetric strain-hardening parameter related to the radius of the cap. I_1 has been defined in equation (3.4). The cap surface is elliptical in shape in $p' - q$ space. It is then defined by the following equation:

$$3p'^2 + \frac{2q^2}{3} = K_c \tag{3.18}$$

where K_c is a constant. Figure 3.5 illustrates the cap surface in $p' - q$ space. The cap is never allowed to contract. For stress states lying on the cap, the predominant strains are plastic and compressive.

The deviator yield surface is similar to that proposed by Lade and Duncan (1975), and a non-associated flow rule is assumed. Its equation is given as follows:

$$F_d = \frac{I_1^3}{I_3} - 27 - k_d = 0 \tag{3.19}$$

where

$$I_3 = \begin{vmatrix} \sigma'_{11} & \sigma'_{12} & \sigma'_{13} \\ \sigma'_{21} & \sigma'_{22} & \sigma'_{23} \\ \sigma'_{31} & \sigma'_{32} & \sigma'_{33} \end{vmatrix} \tag{3.20}$$

I_3 is a stress invariant given by equation (3.4), $\{\sigma'\}$ are the components of the effective stress tensor and k_d is a shear strain-hardening parameter defining the extent of the deviator yield surface. Figure 3.5 shows the deviator yield surface in $p' - q$ space. For stress states on the deviator yield surface, plastic shear strains are dominant. The deviator yield surface is assumed to harden with plastic shear strains only. It is never allowed to soften and contract. As the deviator yield surface hardens, it asymptotically approaches the failure surface.

Based on the data of Tatsuoka and Ishihara (1974) for sands, the failure surface is defined in the triaxial plane as follows:

$$\frac{t_f}{p_a} = C\left[\frac{s'}{p_a}\right]^{CP} \tag{3.21}$$

where

$$t = \sqrt{2J_2} \tag{3.22}$$

$$s' = \frac{I_1}{\sqrt{3}} \tag{3.23}$$

and

$$C = \frac{2\sqrt{2}Sin\phi'}{3 - Sin\phi'} \tag{3.24}$$

The isotropic stress s and shear stress t defined in the Molenkamp model are related to the stress invariants J_2 and I_1 by equations (3.22) and (3.23). $t = t_f$ at failure. C and CP are material parameters. C is related to the ultimate friction angle ϕ' by equation (3.24). The failure surface is equivalent to the CSL in $p' - q$ space (Figure 3.5). For stress ratios lower than failure, the deviator yield surface may be defined in the triaxial plane as follows:

$$\frac{t_y}{p_a} = D\left[\frac{s'}{p_a}\right]^{DP} \tag{3.25}$$

D and DP are material parameters. $t = t_y$ on the yield surface. A family of shear strain-hardening deviator yield surfaces, asymptotically approaching the failure surface in the limit, is then defined in the triaxial plane as follows:

$$\frac{t_d}{p_a} = \frac{t_y t_f}{\left[t_y^N + t_f^N\right]^{\frac{1}{N}}} \tag{3.26}$$

In equation (3.26), N is a material parameter.

The non-associated plastic potential function G_D, corresponding to the deviator yield locus F_D, is now defined. For stress states on the deviator yield surface, the direction of incremental plastic strains is given by the gradient of the plastic potential function G_D as follows:

$$\left\{\frac{\partial G_D}{\partial \sigma'}\right\} = \frac{1}{\sqrt{3}}\{I\}\frac{dV^p}{d\gamma^p} + \frac{\left\{\frac{\partial G_D'}{\partial \sigma'}\right\}}{\left[\left\{\frac{\partial G_D'}{\partial \sigma'}\right\}^T \left\{\frac{\partial G_D'}{\partial \sigma'}\right\}\right]^{0.5}} \tag{3.27}$$

where

$$\{I\} = \{1,1,1,0,0,0\} \tag{3.28}$$

The first term of equation (3.27) gives the isotropic component of the incremental plastic strain. Its magnitude is given by $\frac{dV^p}{d\gamma^p}$. In the Molenkamp model dV^p is defined as the incremental plastic volumetric strain and $d\gamma^p$ is defined as the incremental plastic shear strain. $d\gamma^p$ is proportional to the second invariant of the incremental plastic deviatoric strain tensor. The second term of equation (3.27) represents a unit deviator vector. The dilatancy ratio is thus given by $\frac{dV^p}{d\gamma^p}$. The dilatancy ratio in the triaxial plane may be obtained from Rowe's (1962, 1971) stress-dilatancy equation as follows:

$$\frac{dV^p_{eq}}{d\gamma^p_{eq}} = \frac{2\sqrt{2}Sin\phi'_o - \left[3 - Sin\phi'_o\right]\left(\frac{t}{s'}\right)}{\left[3 + Sin\phi'_o\right] - 2\sqrt{2}Sin\phi'_o\left(\frac{t}{s'}\right)} \tag{3.29}$$

The stress ratio at zero dilatancy or the critical state ratio is given as follows:

$$\frac{t}{s'} = \frac{2\sqrt{2}Sin\phi'_o}{3 - Sin\phi'_o} = M^* \tag{3.30}$$

In terms of the stress ratio η, Rowe's stress-dilatancy equation can be written as follows:

$$\frac{d\varepsilon^p_v}{d\varepsilon^p_q} = \frac{9(M - \eta)}{9 + 3M - 2M\eta} \tag{3.31}$$

In equation (3.31), η is the current stress ratio and M is the stress ratio at the critical state. Figure 3.6 plots Rowe's stress-dilatancy function. Figure 3.7 shows that the

Molenkamp deviator yield locus given by equation (3.25) may be made to agree quite well with the data for loose uncemented carbonate sand in $p'-q$ space. However Figure 3.8 shows poor agreement of the deviator yield locus with the data for cemented carbonate sand. By definition, the Molenkamp deviator yield locus cannot extend beyond (i.e. to the left of) the failure locus or critical state line. Thus it is impossible to match the experimental data points that extend beyond the critical state line by any amount of curve fitting exercise that may be undertaken, as seen in Figure 3.8, unless the position of the critical state line itself is shifted.

Figures 3.9 and 3.10 compares Rowe's stress-dilatancy relation with data for loose cemented and uncemented carbonate sand. Poor agreement is observed in both cases. The dilatancy ratio in the triaxial state may be converted to dilatancy for a general stress state as follows:

$$\frac{dV^p}{d\gamma^p} = \frac{f_v dV^p_{eq}}{f_\gamma d\gamma^p_{eq}} \tag{3.32}$$

where

$$f_v = \left[\frac{1+CV}{2}\right] + \left[\frac{-1+CV}{2}\right] Sin3\theta, CV \le 1 \tag{3.33}$$

$$f_\gamma = \left[\frac{1+CG}{2}\right] + \left[\frac{-1+CG}{2}\right] Sin3\theta, CG \le 1 \tag{3.34}$$

CG and CV are material parameters. A function F_D^* geometrically similar to the deviator yield function F_D is now defined as follows:

$$F_D^* = \frac{(I_1^*)^3}{I_3^*} - 27 - k_d^* = 0 \tag{3.35}$$

The invariants I_1^* and I_3^* are invariants of the stress state $\{\sigma'^*\}$ which is given as:

$$\{\sigma'^{*}\} = \{\sigma'_s\} + RT\{\sigma'_t\},\ 0 \le RT \le 1 \tag{3.36}$$

where

$$\{\sigma'\} = \{\sigma'_s\} + \{\sigma'_t\} \tag{3.37}$$

The isotropic component $\{\sigma'_s\}$ of $\{\sigma'^{*}\}$ and $\{\sigma'\}$ are the same, only their deviator component $\{\sigma'_t\}$ is different. RT is a material parameter, which determines the degree of non-association of the surface F_D^* from the yield surface F_D. Figure 3.11 illustrates the isotropic and deviatoric components of the incremental plastic strains. Figure 3.12 shows the deviator yield and plastic potential function F_D and G_D respectively in the π plane. The components of the incremental plastic deviator strains are shown superimposed on the plastic potential function. The gradient $\left\{\frac{\partial G_t^d}{\partial \sigma'}\right\}$ is now derived as follows:

$$\left\{\frac{\partial G_d^t}{\partial \sigma'}\right\} = \left\{\frac{\partial F_D^*}{\partial \sigma'}\right\} - \frac{\partial F_D^*}{\partial I}\left\{\frac{\partial I}{\partial \sigma'}\right\} \tag{3.38}$$

This completes the description of the deviator plastic potential function as given by the Molenkamp model.

The method of obtaining the hardening function for the deviator yield surface is now described. The hardening function gives the change of the deviator hardening parameter D with plastic shear strains. The plastic shear strains γ_{eq}^p exhibited by sand in constant mean stress tests carried out by Yamada and Ishihara (1979) were approximated in the Molenkamp model as follows:

$$\gamma_{eq}^p = E\left[\frac{t}{s'}\right]^{EP}\left[\frac{s'}{p_a}\right]^{LB} \tag{3.39}$$

E, EP and LB are material constants. In equation (3.39), the stress ratio $\left(\frac{t}{s'}\right)$ is substituted by the expression for the deviator yield surface in the triaxial plane given by equation (3.25). The following expression is obtained for the hardening function:

$$\gamma_{eq}^{p} = E\left[D\left[\frac{s'}{p_a}\right]^{DP-1}\right]^{EP}\left[\frac{s'}{p_a}\right]^{LB} \tag{3.40}$$

The incremental form of the hardening function is obtained from equation (3.40) as follows:

$$\frac{d\gamma_{eq}^{p}}{dD} = E.EP.D^{(EP-1)}\left[\frac{s'}{p_a}\right]^{((DP-1)EP+LB)} \tag{3.41}$$

The deviator hardening modulus H_{mod} may computed from the following expression:

$$H_{\text{mod}} = \frac{\partial F_d}{\partial\left(\frac{t}{s'}\right)}\frac{\partial\left(\frac{t}{s'}\right)}{\partial D}\frac{\partial D}{\partial\gamma_{eq}^{p}}\left\{\frac{\partial G_t^{D}}{\partial\sigma'}\right\} \tag{3.42}$$

The term $\frac{\partial\left(\frac{t}{s'}\right)}{\partial D}$ is computed from the expression:

$$D = \frac{C\left[\frac{s'}{p_a}\right]^{(CP-DP)}\left(\frac{t}{s'}\right)}{\left\{C^{N}\left[\frac{s'}{p_a}\right]^{(CP-1)N} - \left(\frac{t}{s'}\right)^{N}\right\}^{1/N}} \tag{3.43}$$

The term $\frac{\partial F_d}{\partial\left(\frac{t}{s'}\right)}$ is computed from the deviator yield surface equation F_D for triaxial states which is given as:

$$F_D = 27\left\{\frac{1}{\left[1+\sqrt{2}\left(\frac{t}{s'}\right)\right]\left[1-\frac{1}{\sqrt{2}}\left(\frac{t}{s'}\right)\right]}-1\right\}-k_d=0 \tag{3.44}$$

k_d may be computed for the current stress state $\{\sigma'\}$ using equation (3.19). For the current deviator yield surface, the stress ratio at triaxial stress states may then be obtained by solving the cubic in $\left(\frac{t}{s'}\right)$, given by equation (3.44). The stress ratio may then used to compute the hardening parameter D from equation (3.43). This completes the description of the method of obtaining the deviatoric hardening modulus for the Molenkamp model.

The equations for elasticity and isotropic consolidation are now described. The elastic compressive behaviour in isotropic loading is defined by the following equation:

$$V^e = A\left[\frac{s'}{p_a}\right]^{AP} \tag{3.45}$$

The plastic compressive behaviour in isotropic loading is given as follows:

$$V^p = B\left[\frac{s'}{p_a}\right]^{BP} \tag{3.46}$$

p_a *is* the atmospheric pressure. A, AP, B and BP are material parameters. The elastic bulk modulus can be obtained from equation (3.45).

The elastic shear modulus G is defined as follows:

$$G = G_o \left[\frac{\sigma'}{p_a} \right]^{n_v} \tag{3.47}$$

where

$$\sigma' = \frac{s'}{\sqrt{3}} \left[1 + \frac{(1+\nu)}{(1-2\nu)} \left[\frac{t}{s'} \right]^2 \right] \tag{3.48}$$

G_o, and n are material parameters and ν is the elastic Poisson's ratio.

The significant features of the Molenkamp model have been described in detail. The yield locus and stress-dilatancy relation of the Molenkamp model in the triaxial plane were compared with the test data for cemented and uncemented carbonate sand. It is obvious that the Molenkamp model is a relatively complex model with a large number of material parameters. Its use in boundary value problems would be justified only if significant improvement in predictions is obtained.

3.3.3 NOVA MODEL

The Nova (1988) model is an isotropic, volumetric strain hardening, critical state model following a non-associated flow rule. The ultimate surface of this model is defined by the failure criterion proposed by Matsuoka and Nakai (1974, 1976). The model is now described in detail.

The plastic potential function g is derived such that it satisfies critical state conditions at the Matsuoka-Nakai failure surface. The failure surface is defined by the following equation:

$$\frac{I_1 I_2}{I_3} = K \tag{3.49}$$

The stress invariants I_1, I_2 and I_3 have been defined before and K is a constant. In p', q, θ space the the Matsuoka-Nakai failure criteria may be written as follows:

$$(\gamma-1)\eta^2-\frac{2}{9}\gamma\eta^3 Sin3\theta-3(\gamma-3)=0 \tag{3.50}$$

In equation (3.50), γ is a constant and θ is the Lode angle. For triaxial compression, the following conditions are satisfied at the critical state:

$$\eta = M \tag{3.51}$$

and

$$Sin3\theta = 1 \tag{3.52}$$

Substituting the above values in equation (3.50), γ is computed as follows:

$$\gamma=\frac{9-M^2}{\frac{2}{9}M^3+3-M^2} \tag{3.53}$$

For a given value of γ, equation (3.50) may be utilised to obtain the critical stress ratio at any other Lode angle θ. Thus in the Matsuoka-Nakai failure surface, the critical state ratio varies with the Lode angle.

The method of obtaining the plastic potential function g for the Nova model is now described. It is assumed that the Matsuoka-Nakai criterion is satisfied at the critical state. This implies that at the critical state the following conditions are satisfied by the plastic potential function g:

$$\frac{\partial g}{\partial p'}=(\gamma-1)\eta^2-\frac{2}{9}\gamma\eta^3 Sin3\theta-3(\gamma-3) \tag{3.54}$$

and

$$\frac{\partial g}{\partial p'} = 0 \tag{3.55}$$

The plastic potential function g is chosen such that it satisfies equation (3.54) and (3.55). The Nova model plastic potential function g is thus given as follows:

$$g = 9(\gamma - 3)\ln\left(\frac{p'}{p'_g}\right) - \chi J_{3\eta} + \frac{9}{4}(\gamma - 1)J_{2\eta} = 0 \tag{3.56}$$

in which

$$J_{2\eta} = \eta'_{ij}\eta'_{ij} \tag{3.57}$$

$$J_{3\eta} = \eta'_{ij}\eta'_{jk}\eta'_{ki} \tag{3.58}$$

$$\eta_{ij} = \frac{s'_{ij}}{p'} \tag{3.59}$$

and

$$s'_{ij} = \sigma'_{ij} - p'\delta_{ij} \tag{3.60}$$

In equations (3.57) through (3.60), σ'_{ij} is the effective stress tensor, s'_{ij} the effective deviator stress tensor, δ_{ij} a unit tensor, p' the mean pressure and p'_g is a reference stress, included to provide an appropriate non-dimensionalisation. $J_{2\eta}$ and $J_{3\eta}$ are scalar invariants of the tensor η'_{ij}.

The yield function f is defined as follows:

$$f = 3\beta(\gamma - 3)\ln\left(\frac{p'}{p'_o}\right) - \gamma J_{3\eta} + \frac{9}{4}(\gamma - 1)J_{2\eta} \tag{3.61}$$

p'_o is the isotropic yield stress. The parameter β determines the degree of non-association of the yield and plastic potential functions. For $\beta = 3$, the yield and plastic potential functions become identical and the associated flow rule applies. For triaxial compression, the yield function f can be rewritten in terms of the mean pressure p' and the stress ratio η as follows:

$$p' = p'_o \exp\left[\frac{1}{A}\left(B\eta^3 - C\eta^2\right)\right] \tag{3.62}$$

where

$$A = 3\beta(\gamma - 3)$$

$$B = \frac{2\gamma}{9}$$

and

$$C = \frac{3(\gamma - 1)}{2}$$

Equation (3.62) was used to plot the yield locus and plastic potential function in $p' - q$ space. This is shown in Figure 3.13 for $\beta = 1.4$. The functions are seen to be non-convex with an abrupt change in values at $\eta \approx 3$. The model postulates a tension cut-off at these stress ratios to take care of this inconsistency.

The stress-dilatancy function may be computed from the plastic potential function as follows:

$$\frac{d\varepsilon_v^p}{d\varepsilon_q^p} = \frac{\partial g / \partial p'}{\partial g / \partial q} = \frac{3(\gamma - 3) + \frac{2}{9}\gamma\eta^3 Sin3\theta - (\gamma - 1)\eta^2}{(\gamma - 1)\eta} \tag{3.63}$$

For triaxial compression, the stress-dilatancy relation is obtained by substituting the value $Sin3\theta = 1$ in equation (3.63).

Figure 3.14 shows that for triaxial compression, the predicted stress-dilatancy is not a monotonic function of η, for stress ratios in the range $M \leq \eta \leq 3$. Thus convergence problems may occur if the strain-softening part of the model is used. Figure 3.15 shows that the Nova yield function agrees very well with data for loose uncemented carbonate sands. Figure 3.16 shows a much poorer agreement is obtained with the data for loose cemented carbonates. Figure 3.17 shows that good agreement of the stress-dilatancy is observed with data for loose uncemented carbonate sands. Figure 3.18 shows that the dilatancy function does not agree as well with the data for loose cemented sand.

The isotropic hardening function is given by the following general equation:

$$p'_o = p'_{oi} \exp\left[\frac{\varepsilon_{rs}^p \delta_{rs} + \xi (J_{2e})^{1/2} + \varphi (J_{3e})^{1/3}}{B_p}\right] \tag{3.64}$$

where

$$J_{2e} = e_{rs}^p e_{rs}^p \tag{3.65}$$

and

$$J_{3e} = e_{rs}^p e_{st}^p e_{tr}^p \tag{3.66}$$

ε_{rs}^p is the plastic strain tensor and e_{rs}^p is the plastic strain deviator. B_p is a material constant termed the plastic volumetric compliance. ξ and φ are additional material

constants. For volumetric strain hardening only, ξ and φ reduce to zero. The incremental plastic volumetric strain hardening relation is derived from equation (3.64) as follows:

$$\frac{dp'_o}{d\varepsilon_v^p} = \frac{p'_o}{B_p} \tag{3.67}$$

The incremental hardening function, the gradients of the yield and plastic potential functions and the consistency condition may be used to evaluate the plastic hardening modulus for any stress state on the yield locus.

All stress states within the yield function are assumed to be non-linear elastic. The non-linear elastic, volumetric and shear moduli are given as follows:

$$\frac{dp'}{d\varepsilon_v^e} = \frac{p'}{B_e} \tag{3.68}$$

$$\frac{ds'_{ij}}{de'_{ij}} = \frac{p'}{L} \tag{3.69}$$

B_e and L are material parameters defining elastic volumetric and shear compliance. Instead of equation (3.69), the elastic Poisson's ratio was used to determine the elastic shear modulus from the elastic bulk modulus given by equation (3.68). Lagioia and Nova (1993, 1995) incorporated the effect of cementation on the consolidation and tensile strength of soil and their breakdown with plastic volumetric strains. These additions to the Nova (1988) model were not considered in the present analysis.

The Nova (1988) model has been described. It is a relatively simple, isotropic, volumetric strain hardening, non-associated, critical state model based on the Matsuoka-Nakai failure criterion. The model has only 7 material parameters. The yield and the stress-dilatancy function for the Nova model was compared with experimental data for carbonate sands.

3.3.4 SU1 MODEL

The SU1 model is an isotropic, strain hardening, critical state model, based on the original Cam Clay model, but following a non-associated flow rule. The model is now described in detail.

Schofield and Wroth (1968) described the dissipation of plastic work in a frictional material by the following energy equation:

$$p'\delta\varepsilon_v^p + q\delta\varepsilon_q^p = Mp'\delta\varepsilon_q^p \tag{3.70}$$

The relevant terms of equation (3.70) have been defined previously. The stress-dilatancy relation of the SU1 model is obtained from equation (3.70) as follows:

$$\frac{d\varepsilon_v^p}{d\varepsilon_q^p} = M - \eta \tag{3.71}$$

$\frac{d\varepsilon_v^p}{d\varepsilon_q^p}$ is the dilatancy ratio, η is the current stress ratio and M is stress ratio at the critical state. The integration of the stress-dilatancy equation (3.70) gives the SU1 plastic potential function as follows:

$$\frac{q}{Mp'} = -\ln\left(\frac{p'}{p'_o}\right) \tag{3.72}$$

Equation (3.72) is identical to the original Cam Clay plastic potential function. p'_o gives the intersection of the plastic potential function with the isotropic axis, and can be determined from the current stress state. In the Cam Clay model, an associated flow law is assumed. Thus the plastic potential function defined by equation (3.72) becomes the equation of the Cam Clay yield locus. p'_o in that case becomes the isotropic preconsolidation stress.

Let (p'_{cs}, q_{cs}) denote the point of intersection of the critical state line (CSL) with the Cam Clay yield locus defined by equation (3.72). Substituting the relation $\frac{q_{cs}}{p'_{cs}} = M$ in equation (3.72) it can be shown that

$$\frac{p'_o}{p'_{cs}} = e \tag{3.73}$$

Equation (3.73) shows that in the Cam Clay model there is a fixed ratio of e 2.72, between the mean pressure p'_o on the normal consolidation line (NCL), and the mean pressure p'_{cs} on the critical state line (CSL), both measured along an elastic unload-reload line. This ratio is termed here as the spacing ratio. Figures 3.19 and 3.20 illustrate the spacing ratio concept. An elliptical yield locus has been used in this figure only for illustrative purposes. The spacing ratio concept may be used for other yield loci as well.

Experimental data indicate a spacing ratio between 5 to 6 to be appropriate for carbonate sands. A new yield locus is thus proposed with a variable spacing ratio. The SU1 yield locus is therefore given as follows:

$$\frac{q}{Mp'} = \frac{\ln\left(\frac{p'_o}{p'}\right)}{\ln r} \tag{3.74}$$

where

$$r = \frac{p'_o}{p'_{cs}} \tag{3.75}$$

In equation (3.74), r is the spacing ratio. It is assumed as an additional material parameter in the SU1 model. For $r = e$, the Cam Clay yield locus is recovered from equation (3.74). For $r > e$, a new yield locus scaled down in $p' - q$ space is obtained. Stress changes within the SU1 yield locus are assumed to be non-linear elastic.

Equation (3.74) giving the SU1 yield locus may be considered to be a special case of the yield locus of the CASM model proposed by Yu (1995, 1998), corresponding to a value of the CASM parameter $n = 1$.

The plastic potential function of the SU1 model is defined by equation (3.72), for all values of the spacing ratio r. In general, the SU1 model follows a non-associated flow rule. Figure 3.21 shows the yield locus and plastic potential for the SU1 model. Figure 3.22 illustrates the SU1 stress-dilatancy. Comparisons of the SU1 yield locus and plastic potential with those of the Nova model (Figure 3.13) indicate significant similarities. Non-association of the yield and plastic potential function is implemented in the SU1 model using the more rational concept of the spacing ratio.

The SU1 yield locus and stress-dilatancy relation are now compared with experimental data for carbonate sand. Figure 3.23 shows that the proposed yield locus agrees quite well with the data for loose uncemented carbonates. However, the yield locus compares poorly with data for loose cemented carbonates, as shown in Figure 3.24. Figures 3.25 and 3.26 show that the SU1 stress-dilatancy matches fairly well the data for loose cemented and uncemented carbonates. Figures 3.27 through 3.30 show the comparison of the SU1 yield locus and stress-dilatancy relation with data for dense uncemented and cemented carbonates. There is fairly good agreement with data for both.

The isotropic consolidation response of the SU1 model is defined by equation (3.12), the elastic unload-reload response by equation (3.13), the hardening function by equation (3.14) and the elastic bulk modulus by equation (3.15). The elastic shear modulus is obtained from the elastic bulk modulus using a constant value of the elastic Poisson's ratio. All these equations are identical to those of the original Cam Clay and the Modified Cam Clay models.

There are some similarities between the SU1 model and other models proposed in the literature. For example, Been and Jefferies (1985) and Jefferies (1993) proposed modifications of the Cam Clay yield locus utilising the concept of a variable spacing ratio for sands. Their model, unlike the SU1, follows an associated follow rule. The

state parameter is actually the hardening parameter in these models. The state parameter is defined as the difference between the current and critical state void ratio. The CASM model proposed by Yu (1995), used the spacing ratio and the state parameter explicitly in the formulation of the yield locus. CASM also follows a non-associated flow rule. The plastic potential is derived from Rowe's stress-dilatancy relation. The advantage of the SU1 model is its simplicity and improved predictive capability. It keeps intact the formulation of plastic potential function, volumetric strain hardening and most of the other aspects of the original Cam Clay model.

3.3.5 SU2 MODEL

The SU2 model is an isotropic, strain hardening, critical state model, following a non-associated flow rule. The stress-dilatancy equation is derived from an energy balance relation identical to that assumed in the Modified Cam Clay model, and given by equation (3.1). Thus the Modified Cam Clay and SU2 stress-dilatancy relation are both described by equation (3.2). As the SU2 model is central to this thesis, the stress-dilatancy equation is repeated below for completeness.

$$\frac{d\varepsilon_v^p}{d\varepsilon_q^p} = \frac{M^2 - \eta^2}{2\eta} \tag{3.6}$$

The integration of equation (3.6) gives the SU2 plastic potential function. Both the SU2 and Modified Cam Clay plastic potential function are described by the following equation:

$$\left(\frac{q}{Mp'}\right)^2 = \left(\frac{p'_o}{p'}\right) - 1 \tag{3.76}$$

Equation (3.76) is identical to the Modified Cam Clay plastic potential given by equation (3.8), but rearranged in a different form. p'_o is the intersection of the SU2 plastic potential with the isotropic stress axis, and can be determined from the current stress state. In the Modified Cam Clay model, equation (3.76) also defines the

equation of the yield locus. In that case p'_o becomes the isotropic preconsolidation stress.

Let (p'_{cs}, q_{cs}) denote the point of intersection of the critical state line (CSL) with the Modified Cam Clay yield locus, defined by equation (3.76). Substituting the relation $\frac{q_{cs}}{p'_{cs}} = M$ in equation (3.76), it can be shown that

$$\frac{p'_o}{p'_{cs}} = 2.0 \tag{3.77}$$

Thus in the MCC, there is a fixed ratio of 2.0 between the mean pressure p'_o on the normal consolidation line (NCL), and the mean pressure p'_{cs} on the critical state line (CSL), both measured along an elastic unload-reload line. This ratio has already been defined as the spacing ratio. It was stated earlier that, experimental data indicate a spacing ratio between 5 to 6 to be appropriate for carbonate sands. A new SU2 yield locus was thus proposed incorporating spacing ratio as an additional parameter. The yield locus is given as follows:

$$\frac{q}{Mp'} = \frac{\left(\frac{p'_o}{p'}\right) - 1}{r - 1} \tag{3.78}$$

where

$$r = \frac{p'_o}{p'_{cs}} \tag{3.75}$$

In equation (3.78), r is the spacing ratio. It is assumed as an additional material parameter in the SU2 model. For $r = 2$, the Modified Cam Clay yield locus is recovered from equation (3.78). For $r > 2$, a new elliptical yield locus scaled down in $p' - q$ space is obtained. Stress states within the SU2 yield locus are non-linear elastic. The plastic potential function of the SU2 model is defined by equation (3.76),

for all values of the spacing ratio r. The SU2 model thus follows a non-associated flow rule in the general case. The yield locus for SU2 model given by equation (3.78) is similar to the yield equation proposed by Brown and Yu (1988) for modelling soft rock.

The SU2 yield locus and stress-dilatancy relation are now compared with experimental data for carbonate sand. Figure 3.31 shows the yield locus and plastic potential of the SU2 model and Figure 3.32 illustrates the SU2 stress-dilatancy. Comparisons of the SU2 yield locus and plastic potential with those of the Nova model (Figure 3.13) indicate significant similarities. Similar to SU1, non-association of the yield and plastic potential is implemented in the SU2 model by using concept of the spacing ratio. Figure 3.33 shows that SU2 yield locus compares quite well with data for loose uncemented carbonates. However, the yield locus does not compare well with data for loose cemented carbonates, as shown in Figure 3.34. Figure 3.35 shows that the stress-dilatancy relation is in good agreement with the data for uncemented carbonates. Figure 3.36 shows that the stress-dilatancy also compares fairly well with the data for loose cemented carbonates. Figures 3.37 through 3.40 show that the SU2 yield locus and stress-dilatancy relation compares quite well with the data for dense uncemented and cemented carbonates.

The isotropic consolidation response of the SU2 model is defined by equation (3.12), the elastic unload-reload response by equation (3.13), the hardening function by equation (3.14) and the elastic bulk modulus by equation (3.15). The elastic shear modulus is obtained from the elastic bulk modulus using a constant value of the elastic Poisson's ratio. All these equations are identical to those of the Modified Cam Clay model.

Drescher et al (1995) and Shah (1997) used a critical state model with a Modified Cam Clay-type elliptical yield locus and plastic potential, to describe the elasto-plastic behaviour of brittle rocks. These models follow a non-associated flow rule. The non-association of the yield locus and plastic potential is implemented in these models by assuming separate parameters M_f and M_g for these functions. M_g is the critical state ratio and M_f is the stress ratio at the peak of the ellipse forming the

separate yield locus. Pastor and Zienkiewicz (1988, 1990, 1992) also used separate parameters M_g and M_f to generate the yield locus and plastic potential function for silica sands, in their non-associated critical state model. The ratio $\left(\frac{M_g}{M_f}\right)$ was assumed to depend on the relative density of sand. The critical state ratio M_g being known, the ratio M_f could be determined. The spacing ratio parameter in the SU2 model achieves effects similar to these models in a simpler and more meaningful way.

3.4 GENERALISATION OF THE SU1 AND SU2

The SU1 and SU2 models can be generalised for stress states other than triaxial compression by assuming a smooth Mohr-Coulomb-type variation of the critical state ratio M with Lode angle θ as follows:

$$M = \frac{18M_g}{18 + 3(1 - Sin3\theta)} \tag{3.79}$$

In equation (3.79), M_g is the critical stress ratio at triaxial compression. The Lode angle θ is given by the following expression:

$$-\frac{\pi}{6} \le \theta = \frac{1}{3} Sin^{-1}\left[\frac{3\sqrt{3}J_3}{2J_2^{1.5}}\right] \le \frac{\pi}{6} \tag{3.80}$$

where

$$J_3 = s'_{11}s'_{22}s'_{33} + 2s'_{12}s'_{23}s'_{31} - \left(s'_{11}s'^2_{23} + s'_{22}s'^2_{13} + s'_{33}s'^2_{12}\right) \tag{3.81}$$

The deviatoric effective stress tensor s'_{ij} is defined by equation (3.60). The deviator stress invariant J_2 has been defined in equation (3.5).

Further generalisations of the SU1 and SU2 models are also possible. The SU1 and SU2 yield loci can be generalised by adding an exponent n in the yield functions. This allows for enlargement of the yield locus in the deviator direction, which allows the possibility for a better fit with the data for cemented carbonates. The generalised yield loci of the SU1 and SU2 models, allowing for enlargement in the deviator direction, are given respectively as follows:

$$\left(\frac{q}{Mp'}\right)^n = \frac{\ln\left(\frac{p'_o}{p'}\right)}{\ln r} \tag{3.82}$$

$$\left(\frac{q}{Mp'}\right)^n = \frac{\left(\frac{p'_o}{p'}\right)-1}{r-1} \tag{3.83}$$

The parameter n in equations (3.82) and (3.83) is considered a material property, generally with $n \geq 2$. n may be assumed to vary with the degree of cementation as well as the initial density of the sand. Equation (3.82) is identical to the yield function of the CASM model proposed by Yu (1988).

The effect of cementation on the consolidation and tensile strength of soil and their breakdown with plastic volumetric strains may also be incorporated in the SU1 and SU2 model using an approach similar to Lagioia and Nova (1993, 1995). The generalisations that are suggested in this section have not been incorporated in the implementations of the SU1 and SU2 model used to predict the results presented in subsequent sections of this chapter. They are beyond the scope of the current work.

3.5 DETERMINATION OF MODEL PARAMETERS

Model parameters were determined for the Modified Cam Clay, Molenkamp, Nova, SU1 and the SU2 models. Huang (1994) carried out a series of isotropic consolidation and triaxial shear tests on specimens of loose and dense, cemented and uncemented

carbonate sands. The results of these tests were used to determine the model parameters.

The Modified Cam Clay model has 6 and the SU1 and SU2 each have 7 material parameters. Except for the spacing ratio, the remaining 6 parameters of these models are identical. The determination of the 6 common parameters of these models is described first.

The slope λ of the NCL and CSL and the slope κ of the elastic unload-reload line were determined from their plots in e-lnp space. Huang (1994) reported 2 sets of value for λ. One for $p'_o < 20$ MPa and the other for $p'_o \geq 20$ MPa. An appropriate value of λ was chosen depending on whether the pre-consolidation pressure p'_o was greater or less than 20 MPa. The pre-consolidation pressure p'_o was determined using the following procedure. A distinct break in the slope of the elastic consolidation line was selected as the pre-consolidation pressure. Otherwise, the point of maximum curvature in the isotropic consolidation line was selected.

The critical state ratio M_g was selected as the stress ratio at the perfectly plastic state when shearing of samples occurred at dilatancy ratios less than 0.003. This approach was adopted as it was observed that carbonate sands do not exhibit zero dilatancy, even at axial strains as large as 50%. In undrained tests, the critical stress ratio was measured as the stress ratio at constant stress and approaching critical state conditions as defined above.

A constant value of the elastic Poisson's ratio was chosen from the data. Although the elastic Poisson's ratio was observed to vary with the mean pressure, the variation was small for a significant range of mean pressures. The spacing ratio parameter r was computed by determining the mean pressures p'_o and p'_{cs} on the NCL and CSL respectively, along an elastic rebound line. The spacing ratio was then computed as the ratio of $\frac{p'_o}{p'_{cs}}$. The constant e_{cs} is the void ratio at unit pressure on the CSL. This

constant was computed using the semi-logarithmic equations of the NCL and CSL, the pre-consolidation pressure p'_o, the current void ratio e_o and the spacing ratio r. The elastic and plastic volumetric compliances B_p and B_e respectively of the Nova model, were computed from the current void ratio e_o, the slope λ of the NCL and the slope κ of the elastic rebound line. The ultimate state parameter γ was determined as a function of the critical state ratio M_g using equation (3.53). The parameter β was determined by fitting the Nova yield locus with data for loose uncemented carbonate sands. As β was considered a fundamental soil property, its value was kept unchanged for any increase of yield surface size occurring as a result of cementation.

The Molenkamp elastic and plastic volumetric compression parameters *A*, *AP*, *B* and *BP* were measured by fitting the corresponding consolidation equations with experimental data using a trial and error approach. *C* and *PHIMU* were computed from the value of the effective critical state friction angle ϕ'_o. As a linear failure surface in triaxial space was assumed, *CP* was given a value of 1.0. The curvature parameter *DP* and the deviator hardening parameter *D* or *PARDI* were obtained by fitting the deviator yield locus with the data for loose uncemented carbonates. A fixed value of *DP* was assumed for all cementation and soil densities. The plastic deviator hardening parameters *E* and *EP* were determined by trial and error by using the best fit of the triaxial shear simulation of the model with experimental data. For simplicity, identical values of *E* and *EP* were assumed for all densities and cementations. The parameter *PARCI* was computed as a function of the pre-consolidation pressure. A constant set of values was chosen for the rest of the Molenkamp parameters. The chosen values were identical to those suggested by Hicks (1990). Hicks found these values to be applicable for most sands.

Tables 3.2 to 3.5 provide a summary of the parameters of all the models adopted for loose and dense, cemented and uncemented carbonate sands. Due to their size, the tables have been placed at the end of this chapter. It is emphasised here that only a small subset of the available experimental data was used to determine model parameters. Thus most of the model "predictions" presented in the next section are genuine predictions, because the input parameters were determined from the results of separate tests.

3.6 MODEL PREDICTIONS

All the models discussed in this chapter were used to generate simulations for both loose and dense (corresponding to unit weights of 13kN/m^3 and 19kN/m^3 respectively) and uncemented and cemented samples (cement contents of 0% and 20%) of carbonate sand subjected to triaxial shearing, at various cell pressures. Thus four sets of material responses were simulated by these models, viz.,

13kN/m^3 density and 0% cement content
13kN/m^3 density and 20% cement content
19kN/m^3 density and 0% cement content
19kN/m^3 density and 20% cement content

Figures 3.41 to 3.70 illustrate the experimental data and the corresponding model simulations.

Figures 3.41 to 3.48 provide the stress-strain and volumetric strain predictions for loose uncemented carbonates. Figures 3.41 and 3.42 show that the SU1 and SU2 model predictions for triaxial shearing at 100 kPa cell pressure are in good agreement with the experimental data. The predictions of the Nova model appear to be quite good as well. The Molenkamp model parameters were chosen such that the failure state coincides with the line of zero volume change or critical state line. Thus no stress ratio beyond the critical state is possible. Thus the model predicts compressive volume strains at all cell pressures. As its deviator and cap surfaces are not allowed to shrink, no strain softening is predicted under drained conditions. Figures 3.43 and 3.44 show that at 300 kPa cell pressure the SU1, SU2 and Nova models give improved predictions of both the shear and volumetric behaviour compared to the MCC and Molenkamp model. A similar trend is noted in Figures 3.45 through 3.48.

Figures 3.49 to 3.56 give the shear and corresponding volumetric strain predictions for loose cemented carbonates. Figure 3.49 shows that the MCC model predicts well the peak shear stress at 100 kPa cell pressure. All other models under-predict the peak stress. This is a consequence of good correspondence of the MCC yield locus

with the experimental data. However, this correspondence is likely to be coincidental, rather than a demonstration of the ability of MCC to model well, the yield locus of cemented carbonates in general. Figure 3.50 shows that the MCC model substantially over-predicts the corresponding expansive volumetric strains. Figures 3.51 and 3.52 show that at 300 kPa cell pressure the MCC model again correctly predicts the peak shear stress. It predicts expansive volumetric strains in this case. However, the test data show compressive volumetric behaviour. The SU1, SU2 and Nova models predict this compression very well, although the peak shear is under-predicted by all these models.

Figures 3.57 to 3.64 give the stress-strain and volumetric strain predictions for dense uncemented carbonates. It is observed that the SU1, SU2 and Nova models provide good predictions, which match the experimental data better than the predictions of the MCC and the Molenkamp models. The low expansive volume strains exhibited by dense uncemented sands at low cell pressures, as seen in Figure 3.58, may be the result of strain localisation effects.

Figures 3.65 to 3.70 give the shear and volumetric predictions for dense uncemented carbonates. Unlike loose cemented carbonates, cementation does not cause a significant change in the shape and size of the yield locus in the deviator direction for dense carbonate sands. Thus the SU1, SU2 and the Nova models predict the peak shear stress better than the MCC model, for shearing at low cell pressures. At all other cell pressures, the predictions of the SU1, SU2 and Nova were observed to be similar and significantly better than the MCC and Molenkamp models.

3.7 DISCUSSION

The significant features of the experimental behaviour and model predictions for each of the models are now discussed in detail.

During the triaxial shearing, carbonate sands exhibit a lower peak stress and larger compressive volumetric strains at all cell pressures, as compared to silica sands.

Conventional critical state models such as the MCC model cannot predict this behaviour. The SU1 and SU2 models provide significantly better predictions of triaxial response by simply introducing the spacing ratio parameter in the Cam Clay and MCC models respectively. The spacing ratio can be obtained from routine laboratory tests. The corresponding improvement in predictions obtained can also be explained in a rational way. In general, the SU2 model shows improved prediction for stress-dilatancy, yield locus and triaxial shear of carbonate sands, compared to the other models. This is particularly true for uncemented carbonates. However, the predictions of all the models including those of the SU2, show significant deviation from experimental data when 20% cement was added to loose carbonates. For dense sands, this deviation was observed to be much smaller. Introducing additional parameters, and generalising the SU1 and SU2 for cementation effects, can possibly improve the model response. The SU2 is a simple generalisation of the MCC model, which is widely used for the numerical solution of many geotechnical problems. It is also free of numerical problems associated with corners in the yield loci and plastic potential. SU2 has only 7 model parameters, all of which can be obtained from routine laboratory tests.

The Nova model also provides reasonable predictions of the triaxial shear response of carbonate sands. However, its yield and plastic potential functions show non-convexity and abrupt changes in gradients at stress ratios greater than or equal to 3.0, for triaxial compression stress states. The stress-dilatancy relation shows non-monotonic behaviour even at stress ratios smaller than 3.0 in triaxial compression states.

The complete Molenkamp model has 23 model parameters. Many of the model parameters have to be obtained using a curve fitting approach. This process is time-consuming and requires considerable judgement. The physical significance of many of the parameters obtained in this fashion is often unclear. Although the model is sophisticated and complex, no significant improvements in prediction of the drained response of carbonate sands appear to have been obtained. It is likely that determination of the Molenkamp model parameters by exhaustive fitting with experimental data could result in improved predictions. This approach was not

adopted as its practical worth is questionable, and also because the Molenkamp model is not the central theme of this work.

It must be mentioned that the models taken from literature namely MCC, Molenkamp and Nova were originally conceived for simulating the behaviour of different materials, namely normally consolidated clays and uncemented carbonate sand. In this chapter, these models were used to simulate the triaxial response of cemented carbonate sands. The only modification considered in these models for simulating the behaviour of cemented carbonate sands, is the existence of an initial yield locus. The preconsolidation pressure of the initial yield locus is used as a measure of the bond or cementation strength. No other effect of cementation, such as tensile strength or the associated cohesion, was taken into account in the original form of these models. It is likely that taking these factors into account in these models may have had an effect on the predictions of the drained triaxial response for cemented carbonate sands. To have a standard yardstick for comparing the predictions of the proposed SU1 and SU2 models with the MCC, Molenkamp and Nova models, cohesion and tensile strength were not included in SU1 and SU2.

3.8 CONCLUSION

An elasto-plastic soil model must possess certain salient features to be useful in solving boundary value problems using the finite element method. First, it is essential that the model reproduce the salient features of the triaxial behaviour of the soil. The model should also be free from any numerical or mathematical inconsistencies under general stress paths. It is preferable that the model has a limited number of model parameters, all or most of which can be obtained using simple and routine laboratory tests. The SU2 model satisfies all these essential criteria. It was thus decided to select SU2 as the model of choice for further investigation in this thesis. The SU2 model was subsequently used to simulate the behaviour of carbonate sands in elasto-plastic boundary value problems using the finite element method. The results of these analyses are described in subsequent chapters.

APPENDIX 3.1 DERIVATION OF ELASTO-PLASTIC MATRIX FOR THE SU2 MODEL

The general incremental form of an elasto-plastic stress-strain constitutive equation may be written in tensor notation as follows:

$$d\sigma'_{ij} = \left[C_{ijmn} - \frac{\dfrac{\partial g}{\partial \sigma'_{kl}} C_{ijkl} \dfrac{\partial f}{\partial \sigma'_{rs}} C_{rsmn}}{H} \right] d\varepsilon_{mn} \tag{A3.1}$$

In equation (A3.1), the expression

$$\left[C_{ijmn} - \frac{\dfrac{\partial g}{\partial \sigma'_{kl}} C_{ijkl} \dfrac{\partial f}{\partial \sigma'_{rs}} C_{rsmn}}{H} \right] = \left[C_{ijmn} - \frac{H^*_{ij} H_{mn}}{H} \right] \tag{A3.2}$$

is the elasto-plastic constitutive matrix, where C_{ijkl} is the elastic constitutive matrix given in terms of the elastic bulk modulus K and elastic shear modulus G as follows:

$$C_{ijkl} = \begin{bmatrix} K+4G/3 & K-2G/3 & K-2G/3 & 0 \\ K-2G/3 & K+4G/3 & K-2G/3 & 0 \\ K-2G/3 & K-2G/3 & K+4G/3 & 0 \\ 0 & 0 & 0 & G \end{bmatrix} \tag{A3.3}$$

K and G may be constant or they may be dependent on the current state of stress. The tensors H^*_{ij} and H_{mn} and the scalar H in equation (A3.2), which is the expression for the elastic constitutive matrix, are given as follows:

$$H^*_{ij} = \frac{\partial g}{\partial \sigma'_{kl}} C_{ijkl} \tag{A3.4}$$

$$H_{mn} = \frac{\partial f}{\partial \sigma'_{rs}} C_{rsmn} \tag{A3.5}$$

$$H = H' + \frac{\partial f}{\partial \sigma'_{rs}} C_{rsmn} \frac{\partial g}{\partial \sigma'_{mn}} \tag{A3.6}$$

and

$$H' = -\frac{\partial f}{\partial a} \frac{\partial a}{\partial \varepsilon^p_{ij}} \frac{\partial g}{\partial \sigma'_{ij}} \tag{A3.7}$$

The scalar H' is generally defined as the plastic hardening modulus and a is defined as the strain-hardening parameter. In the above equations σ'_{ij} and $d\sigma'_{ij}$ are respectively the total and incremental effective stress tensor, $d\varepsilon_{mn}$ is the incremental total strain tensor, f and g are respectively the yield and plastic potential function and $\frac{\partial f}{\partial \sigma'_{ij}}$ and $\frac{\partial g}{\partial \sigma'_{ij}}$ are respectively the gradients of the yield and plastic potential function. Each of these components may be expressed in vector form in terms of their tensor components respectively as follows:

$$\{\sigma'\} = \begin{Bmatrix} \sigma'_{11} \\ \sigma'_{22} \\ \sigma'_{33} \\ \sigma'_{12} \\ \sigma'_{23} \\ \sigma'_{31} \end{Bmatrix} \tag{A3.8}$$

$$\{d\sigma'\} = \begin{Bmatrix} d\sigma'_{11} \\ d\sigma'_{22} \\ d\sigma'_{33} \\ d\sigma'_{12} \\ d\sigma'_{23} \\ d\sigma'_{31} \end{Bmatrix} \tag{A3.9}$$

$$\{d\varepsilon\} = \begin{Bmatrix} d\varepsilon_{11} \\ d\varepsilon_{22} \\ d\varepsilon_{33} \\ d\varepsilon_{12} \\ d\varepsilon_{23} \\ d\varepsilon_{31} \end{Bmatrix} \tag{A3.10}$$

$$\left\{\frac{\partial f}{\partial \sigma'}\right\} = \begin{Bmatrix} \dfrac{\partial f}{\partial \sigma'_{11}} \\ \dfrac{\partial f}{\partial \sigma'_{22}} \\ \dfrac{\partial f}{\partial \sigma'_{33}} \\ \dfrac{\partial f}{\partial \sigma'_{12}} \\ \dfrac{\partial f}{\partial \sigma'_{23}} \\ \dfrac{\partial f}{\partial \sigma'_{31}} \end{Bmatrix} \tag{A3.11}$$

$$\left\{\frac{\partial g}{\partial \sigma'}\right\} = \begin{Bmatrix} \dfrac{\partial g}{\partial \sigma'_{11}} \\ \dfrac{\partial g}{\partial \sigma'_{22}} \\ \dfrac{\partial g}{\partial \sigma'_{33}} \\ \dfrac{\partial g}{\partial \sigma'_{12}} \\ \dfrac{\partial g}{\partial \sigma'_{23}} \\ \dfrac{\partial g}{\partial \sigma'_{31}} \end{Bmatrix} \tag{A3.12}$$

It can be shown from tensor mathematics that the gradients of the yield and plastic potential function may be expressed in terms of the current stress and the invariants of the effective stress tensor as follows:

$$\frac{\partial f}{\partial \sigma'_{ij}} = \frac{\partial f}{\partial I'_1}\delta_{ij} + \frac{\partial f}{\partial J_2}s'_{ij} + \frac{\partial f}{\partial J_3}t'_{ij} \tag{A3.13}$$

$$\frac{\partial g}{\partial \sigma'_{ij}} = \frac{\partial g}{\partial I'_1}\delta_{ij} + \frac{\partial g}{\partial J_2}s'_{ij} + \frac{\partial g}{\partial J_3}t'_{ij} \tag{A3.14}$$

In equations (A3.13) and (A3.14) I'_1 is the first invariant of the effective stress tensor σ'_{ij}, δ_{ij} is the identity tensor, and J_2 and J_3 are respectively the 2nd and 3rd invariant of deviator stress tensor s'_{ij} where

$$\delta_{ij} = \frac{\partial I'_1}{\partial \sigma'_{ij}} \tag{A3.15}$$

$$s'_{ij} = \frac{\partial J_2}{\partial \sigma'_{ij}} = \sigma'_{ij} - \frac{I'_1}{3}\delta_{ij} \tag{A3.16}$$

and

$$t'_{ij} = \frac{\partial J_3}{\partial \sigma'_{ij}} = s'_{im}s'_{mj} - \frac{2}{3}J_2\delta_{ij} \tag{A3.17}$$

The terms H_{ij}, H^*_{mn} and $\frac{\partial f}{\partial \sigma'_{ij}}C_{ijkl}\frac{\partial g}{\partial \sigma'_{kl}}$ in the expression of the elasto-plastic constitutive matrix as shown in equation (A3.2) may be expressed as follows:

$$H_{ij} = 3KA_f\delta_{ij} + 2GB_f s'_{ij} + 2GC_f t'_{ij} \tag{A3.18}$$

$$H^*_{mn} = 3KA_g\delta_{mn} + 2GB_g s'_{mn} + 2GC_f t'_{mn} \tag{A3.19}$$

$$\frac{\partial f}{\partial \sigma'_{ij}} C_{ijkl} \frac{\partial g}{\partial \sigma'_{kl}} = 9KA_f A_g + 4GB_f B_g J_2 + 6GB_f C_g J_3 + 6GC_f B_g J_3 + 2GC_f C_g \left(s'_{im} s'_{mj} s'_{ik} s'_{kj} - \frac{4}{3} J_2^2 \right)$$

(A3.20)

Computing H_{ij} and H^*_{mn} from equations (A3.18) and (A3.19), the tensor product $H_{ij}H^*_{mn}$ in the expression of the elastic-plastic constitutive matrix as in equation (A3.2) may be computed as follows:

$$H^*_{ij}H_{mn} = \begin{Bmatrix} H^*_{11} \\ H^*_{22} \\ H^*_{33} \\ H^*_{12} \\ H^*_{23} \\ H^*_{31} \end{Bmatrix} \{ H_{11} \quad H_{22} \quad H_{33} \quad H_{12} \quad H_{23} \quad H_{31} \} \tag{A3.20a}$$

$$H^*_{ij}H_{mn} = \begin{bmatrix} H^*_{11}H_{11} & H^*_{11}H_{22} & H^*_{11}H_{33} & H^*_{11}H_{12} & H^*_{11}H_{23} & H^*_{11}H_{31} \\ H^*_{22}H_{11} & H^*_{22}H_{22} & H^*_{22}H_{33} & H^*_{22}H_{12} & H^*_{22}H_{23} & H^*_{22}H_{31} \\ H^*_{33}H_{11} & H^*_{33}H_{22} & H^*_{33}H_{33} & H^*_{33}H_{12} & H^*_{33}H_{23} & H^*_{33}H_{31} \\ H^*_{12}H_{11} & H^*_{12}H_{22} & H^*_{12}H_{33} & H^*_{12}H_{12} & H^*_{12}H_{23} & H^*_{12}H_{31} \\ H^*_{23}H_{11} & H^*_{23}H_{22} & H^*_{23}H_{33} & H^*_{23}H_{12} & H^*_{23}H_{23} & H^*_{23}H_{31} \\ H^*_{31}H_{11} & H^*_{3\cdot}H_{22} & H^*_{31}H_{33} & H^*_{31}H_{12} & H^*_{31}H_{23} & H^*_{31}H_{31} \end{bmatrix} \tag{A3.20b}$$

In equations (A3.18), (A3.19) and (A.20)

$$A_f = \frac{\partial f}{\partial I'_1} \tag{A3.21}$$

$$B_f = \frac{\partial f}{\partial J_2} \tag{A3.22}$$

$$C_f = \frac{\partial f}{\partial J_3} \tag{A3.23}$$

$$A_g = \frac{\partial g}{\partial I_1'} \tag{A3.24}$$

$$B_g = \frac{\partial g}{\partial J_2} \tag{A3.25}$$

$$C_g = \frac{\partial g}{\partial J_3} \tag{A3.26}$$

The elastic bulk and shear modulus K and G, the yield and plastic potential function f and g, the hardening function a and the current state of stress σ_{ij}' being known, the expressions (A3.18), (A3.19) and (A3.20) and subsequently the elasto-plastic matrix given by the expression (A3.2) can be calculated.

The yield and plastic potential function f and g respectively of the SU2 model may be expressed as follows:

$$f = \left(\frac{q}{Mp_{cs}'}\right)^2 - Ar\frac{p'}{p_{cs}'} + A\left(\frac{p'}{p_{cs}'}\right)^2 \tag{A3.28}$$

$$g = \left(\frac{q}{Mp_{cs}'}\right)^2 - 2\frac{p'}{p_{cs}'} + A\left(\frac{p'}{p_{cs}'}\right)^2 \tag{A3.29}$$

where

$$A = \frac{1}{r-1} \tag{A3.30}$$

and

$$r = \frac{p_o'}{p_{cs}'} \tag{A3.31}$$

In equations (A3.28) to (A3.31), p' is the mean effective stress, q is the deviator stress, p'_{cs} is the mean effective stress on the yield function at the critical stress ratio M, p'_o is the effective isotropic consolidation pressure and r is the spacing ratio. p'_{cs} or p'_o is used as the hardening parameter in the SU2 model. (p',q) represents the current state of stress. It can be shown that the stress invariants I'_1 and J_2 are related to the effective mean pressure p' and the deviator stress q as follows:

$$p' = \frac{I'_1}{3} \tag{A3.32}$$

$$q = \sqrt{3J_2} \tag{A3.33}$$

Using the equations of the yield and plastic potential function it can be shown that for the SU2 model:

$$\frac{\partial f}{\partial I'_1} = -\frac{A\left(r - 2\frac{p'}{p'_{cs}}\right)}{3p'_{cs}} \tag{A3.34}$$

$$\frac{\partial f}{\partial J_2} = \frac{3}{M^2 p'^2_{cs}} \tag{A3.35}$$

$$\frac{\partial f}{\partial J_3} = 0 \tag{A3.36}$$

$$\frac{\partial g}{\partial I'_1} = -\frac{2\left(1 - \frac{p'}{p'_{cs}}\right)}{3p'_{cs}} \tag{A3.37}$$

$$\frac{\partial g}{\partial J_2} = \frac{3}{M^2 p'^2_{cs}} \tag{A3.38}$$

$$\frac{\partial g}{\partial J_3} = 0 \tag{A3.39}$$

$$\frac{\partial f}{\partial p'_{cs}} = -\frac{Arp'}{p'^2_{cs}} \tag{A3.40}$$

In the SU2 model, isotropic consolidation and rebound are represented by the equations for the isotropic consolidation line and the elastic rebound line in $e - \ln p'$ space which are given as follows:

$$e = N_1 - \lambda \ln p' \tag{A3.41}$$

$$e = N_2 - k \ln p' \tag{A3.42}$$

In equations (A3.41) and (A3.42) e is the void ratio, N_1 and N_2 is the void ratio at unit mean effective pressure on the isotropic consolidation line and elastic rebound line respectively, and λ and κ are the slope of the isotropic consolidation line and elastic rebound line respectively. In the SU2 model, the elastic bulk modulus K is assumed to be dependent on the mean effective pressure p' as obtained from equation (A3.42) as follows:

$$K(p') = \frac{p'(1+e)}{\kappa} \tag{A3.43}$$

The elastic Poisson's ratio ν is used to compute the pressure dependent elastic shear modulus $G(p')$ from the elastic bulk modulus $K(p')$.

In the SU2 model, it is assumed the hardening parameter p'_{cs} changes with plastic volumetric strain ε_v^p only. The differential form of equations (A3.41) and (A3.42) and equation (A3.31) may be used to find the change of the hardening parameter p'_{cs} with plastic volumetric strain ε_v^p as follows:

$$\frac{\partial p'_{cs}}{\partial \varepsilon_v^p} = \frac{p'_{cs}(1+e)}{\lambda - \kappa} \tag{A3.44}$$

Equations (A3.40) and (A3.44) may be used to compute the plastic hardening modulus H' of the SU2 model given by equation (A3.7). Once the current stress state and the relevant model parameters λ, κ, M, r, e'_{cs} (void ratio on the critical state line at unit mean effective pressure), p'_o and the elastic Poisson' s ratio ν are known, the elasto-plastic constitutive matrix for the SU2 model may be calculated.

Table 3.2

Material: Uncemented carbonate sand.
Location: North West Shelf, Australia.
Density : 13 kN/ m^3. Cement content: 0 percent.

Modified Cam Clay

λ 0.209	κ 0.0075	M_g 1.6	e_{cs} 2.41	p'_o (kPa) 1200
ν 0.1				

Molenkamp

ν 0.1	*A* 0.000554	*AP* 0.8	*B* 0.0019	*BP* 0.8
C 0.75083	*CP* 1.0	*DP* 0.198	*PHIMU* 39	*PHICV* 39
SCV 1000	*VGC* 0.0	*VGP* 1.0	*NU* 0.0	*EE* 0.247
EP 2.7	*LB* 0.3	*N* 7	*CG* 0.8	*CV* 0.8
RT 0.3	*PARCI* 2078.5	*PARDI* 0.73		

Nova

B_p 0.096	B_e 0.0036	ν 0.1	γ 4.77	β 1.4
p'_o (kPa) 1750	ζ 0.0			

SU1 and SU2

λ 0.209	κ 0.0075	M_g 1.6	e_{cs} 2.21	p'_o (kPa) 1200
ν 0.1	r 5.0			

Table 3.3

Material: Artificially cemented carbonate sand.
Location: NorthWest Shelf, Australia.
Density : 13 kN/m^3. Cement content: 20 percent.

Modified Cam Clay

λ 0.213	κ 0.0072	M_g 1.6	e_{cs} 2.47	p'_o (kPa) 1750
ν 0.1				

Molenkamp

ν 0.1	A 0.000554	AP 0.8	B 0.0019	BP 0.8
C 0.75083	CP 1.0	DP 0.198	$PHIMU$ 39	$PHICV$ 39
SCV 1000	VGC 0.0	VGP 1.0	NU 0.0	EE 0.247
EP 2.7	LB 0.3	N 7	CG 0.8	CV 0.8
RT 0.3	$PARCI$ 3031.1	$PARDI$ 4.78		

Nova

B_p 0.098	B_e 0.0034	ν 0.1	γ 4.77	β 1.4
p'_o (kPa) 1750	ζ 0.0			

SU1 and SU2

λ 0.213	κ 0.0072	M_g 1.6	e_{cs} 2.28	p'_o (kPa) 1750
ν 0.1	r 5.0			

Table 3.4

Material: Uncemented carbonate sand.
Location: NorthWest Shelf, Australia.
Density : 19 kN/ m^3. Cement content: 0 percent.

Modified Cam Clay

λ 0.123	κ 0.0074	M_g 1.6	e_{cs} 1.57	p'_o (kPa) 32000.0
ν 0.2				

Molenkamp

ν 0.2	*A* 0.0015	*AP* 0.5	*B* 0.0005	*BP* 0.7
C 0.75083	*CP* 1.0	*DP* 0.198	*PHIMU* 39	*PHICV* 39
SCV 1000	*VGC* 0.0	*VGP* 1.0	*NU* 0.0	*EE* 0.10
EP 2.5	*LB* 0.3	*N* 7	*CG* 0.8	*CV* 0.8
RT 0.3	*PARCI* 55425.0	*PARDI* 17.69		

Nova

B_p 0.081	B_e 0.0052	ν 0.2	γ 4.77	β 1.4
p'_o (kPa) 32000.0	ζ 0.0			

SU1 and SU2

λ 0.123	κ 0.0074	M_g 1.6	e_{cs} 1.46	p'_o (kPa) 32000.0
ν 0.2	r 5.0			

Table 3.5

Material: Cemented carbonate sand.
Location: NorthWest Shelf, Australia.
Density : 19 kN/ m^3. Cement content: 20 percent.

Modified Cam Clay

λ 0.144	κ 0.0074	M_g 1.6	e_{cs} 1.84	p'_o (kPa) 50000.0
ν 0.2				

Molenkamp

ν 0.2	*A* 0.0015	*AP* 0.5	*B* 0.0005	*BP* 0.7
C 0.75083	*CP* 1.0	*DP* 0.198	*PHIMU* 39	*PHICV* 39
SCV 1000	*VGC* 0.0	*VGP* 1.0	*NU* 0.0	*EE* 0.10
EP 2.5	*LB* 0.3	*N* 7	*CG* 0.8	*CV* 0.8
RT 0.3	*PARCI* 86602.5	*PARDI* 45.6		

Nova

B_p 0.096	B_e 0.0052	ν 0.2	γ 4.77	β 1.4
p'_o (kPa) 50000.0	ζ 0.0			

SU1 and SU2

λ 0.144	κ 0.0074	M_g 1.6	e_{cs} 1.71	p'_o (kPa) 50000.0
ν 0.2	*r* 5.0			

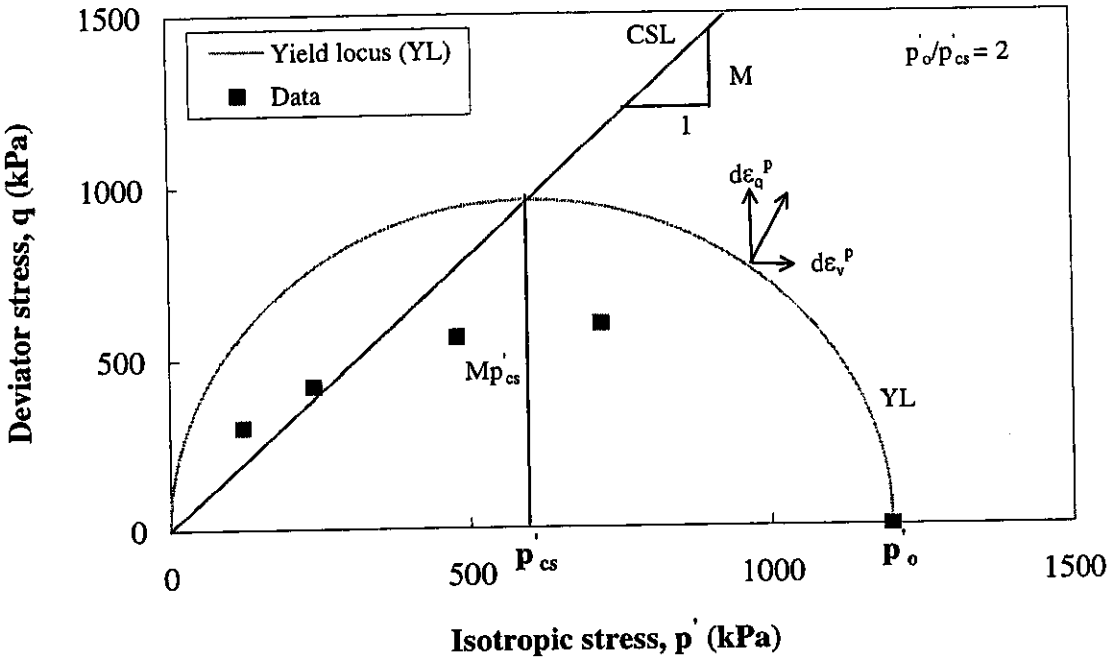

Figure 3.1 Comparison of Modified Cam Clay yield locus with data for loose uncemented carbonate sand

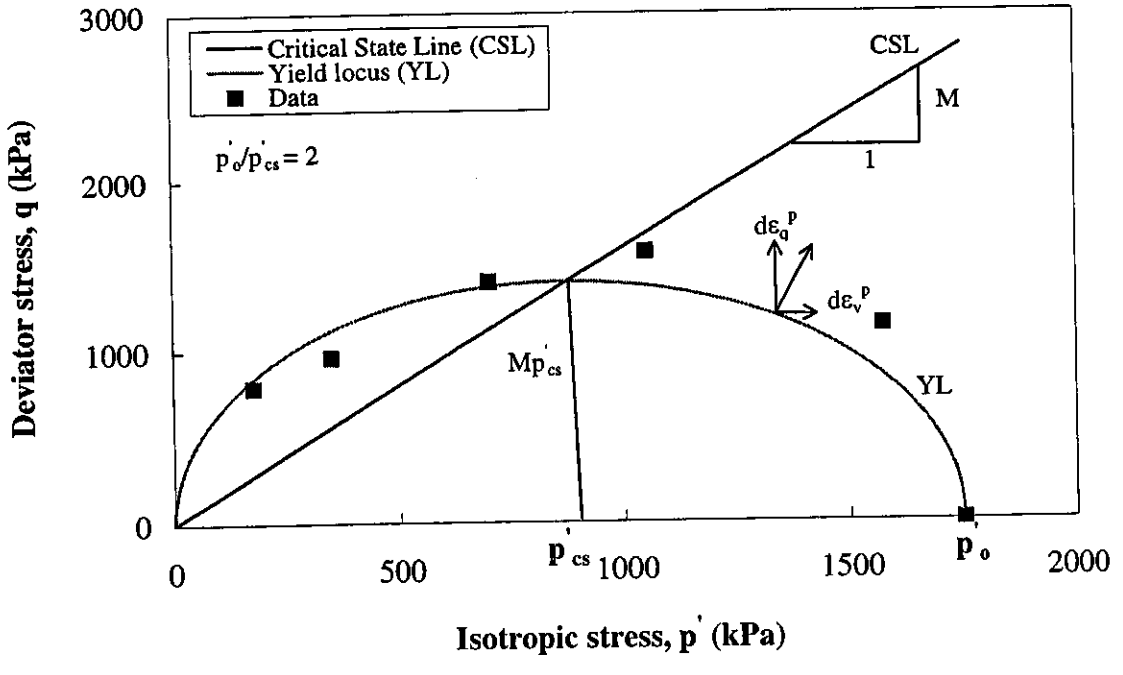

Figure 3.2 Comparison of Modified Cam Clay yield locus with data for loose cemented carbonate sand

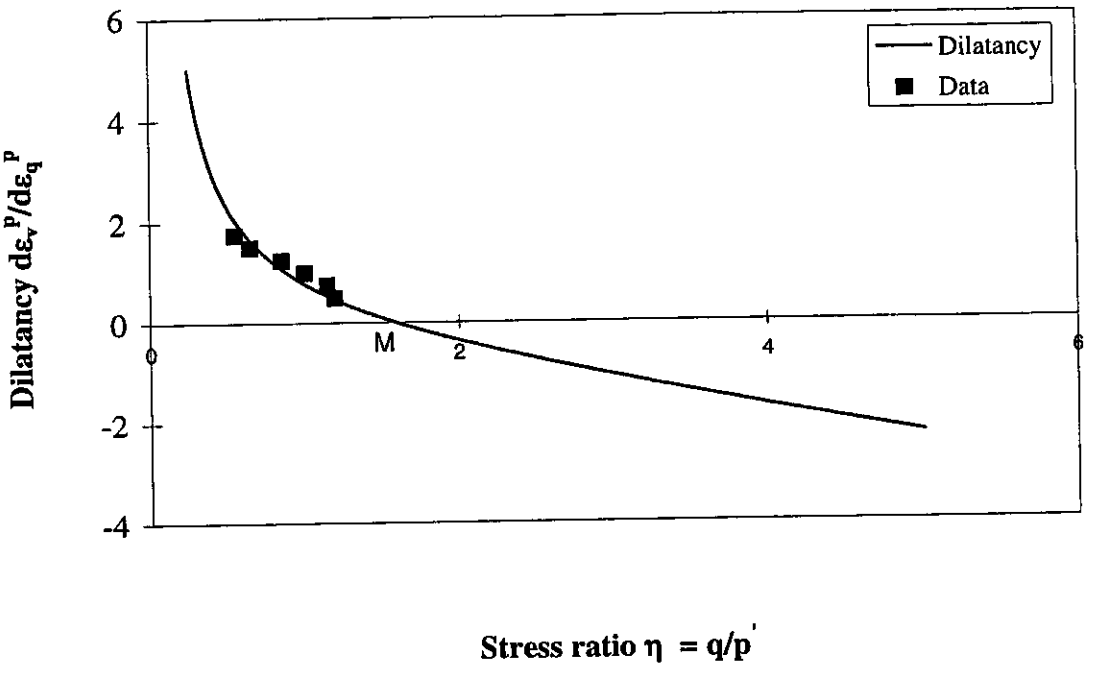

Figure 3.3 Comparison of Modified Cam Clay stress-dilatancy with data for loose uncemented carbonate sand

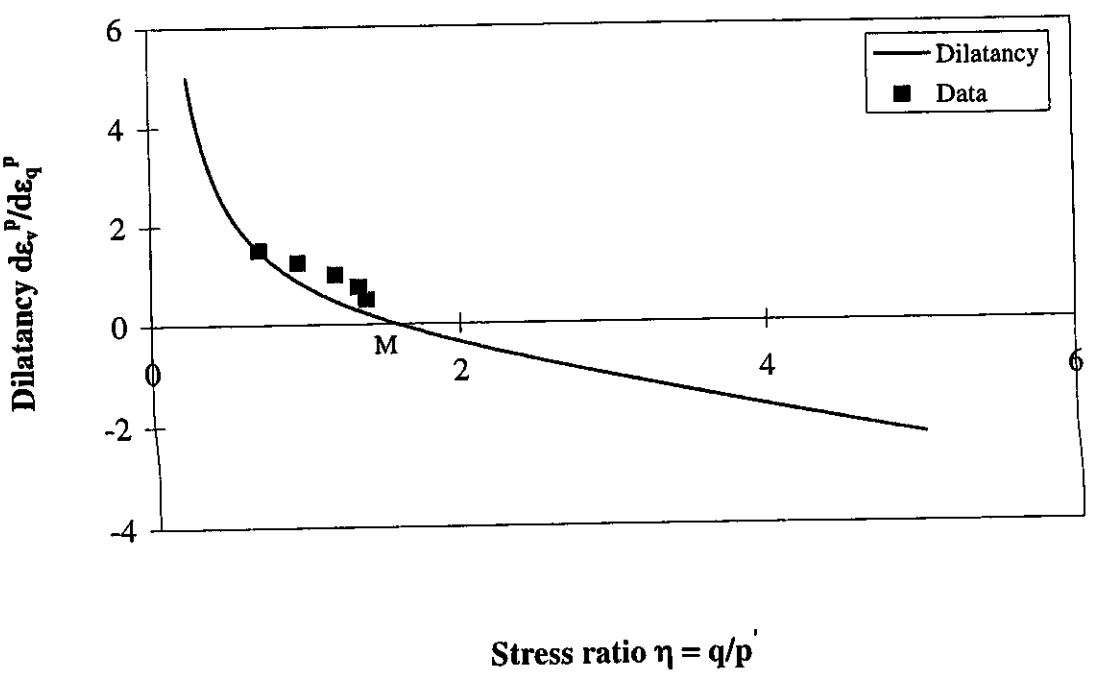

Figure 3.4 Comparison of Modified Cam Clay stress-dilatancy with data for **loose cemented carbonate sand**

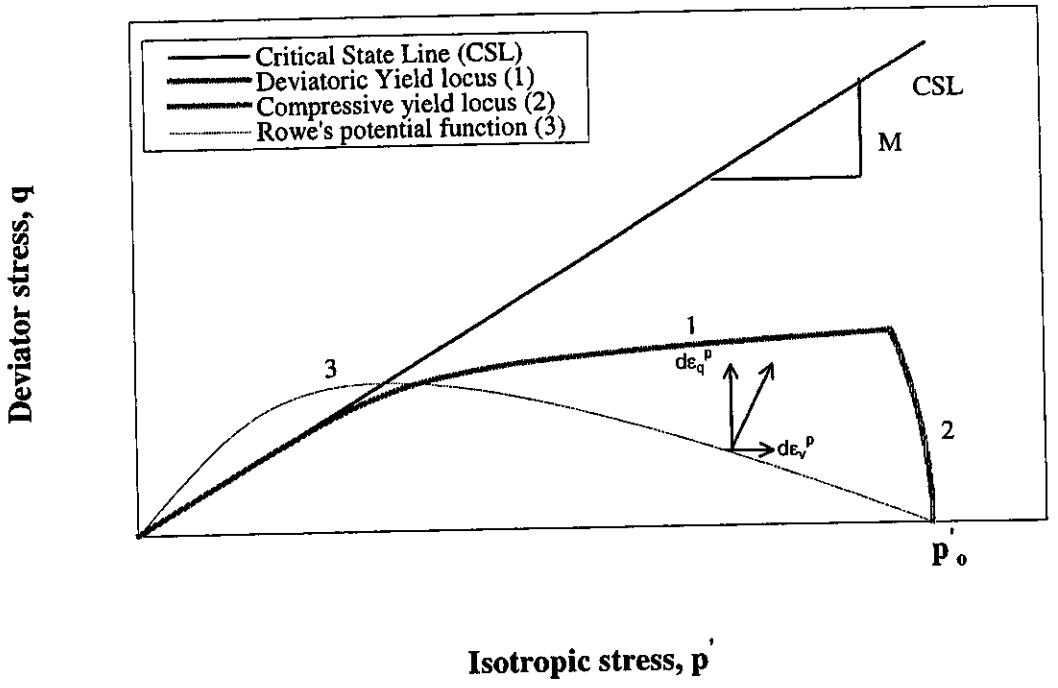

Figure 3.5 Molenkamp model yield locus and plastic potential function at triaxial compression plane

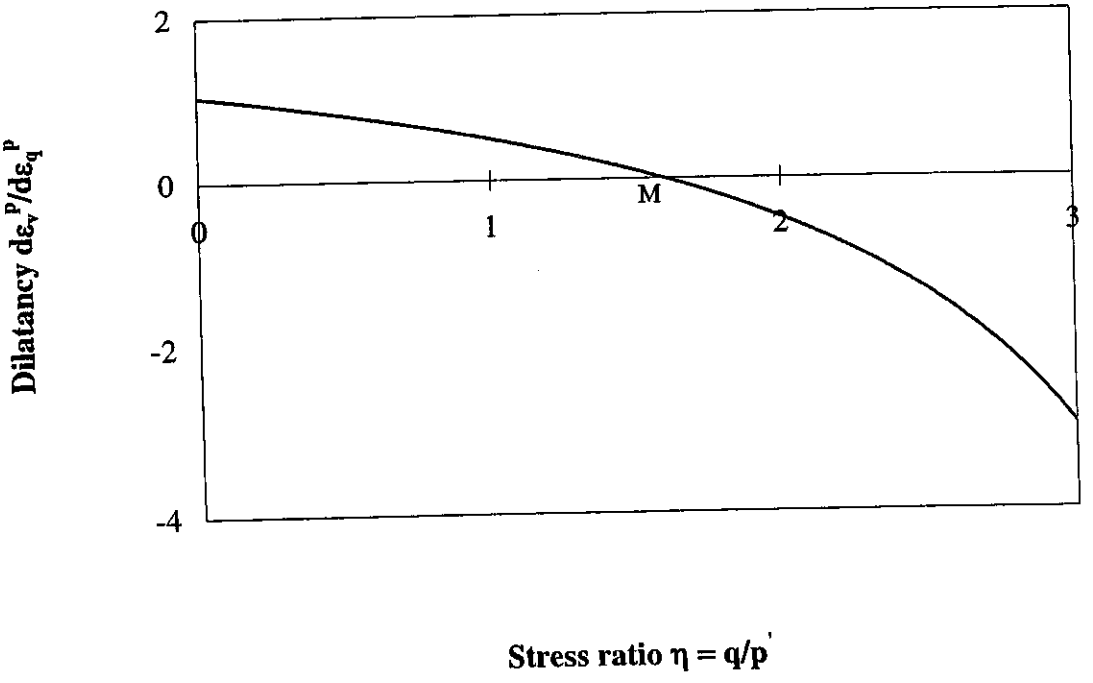

Figure 3.6 Rowe's stress-dilatancy function

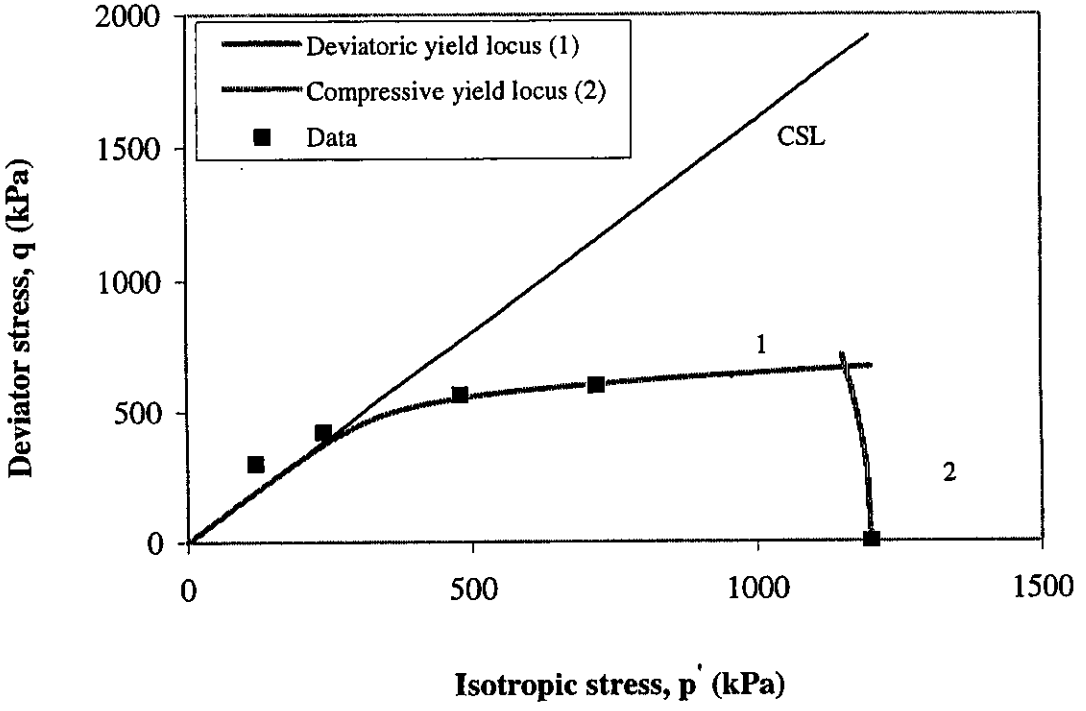

Figure 3.7 Comparison of Molenkamp yield locus with data for loose uncemented carbonate sand

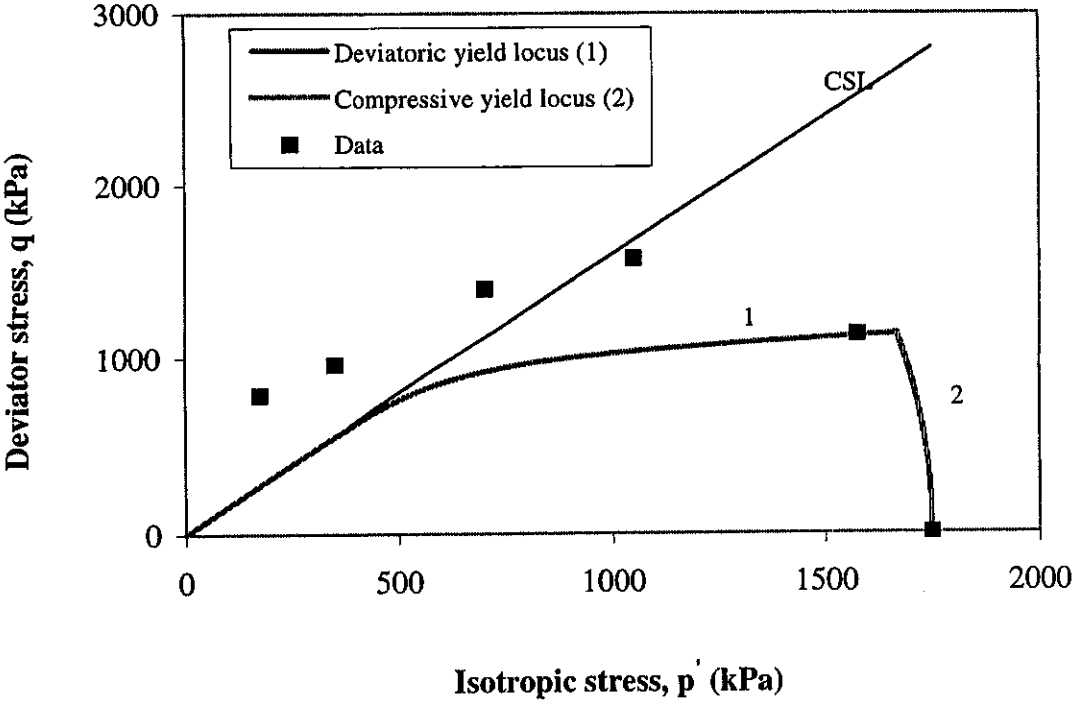

Figure 3.8 Comparison of Molenkamp yield locus with data for loose cemented carbonate sand

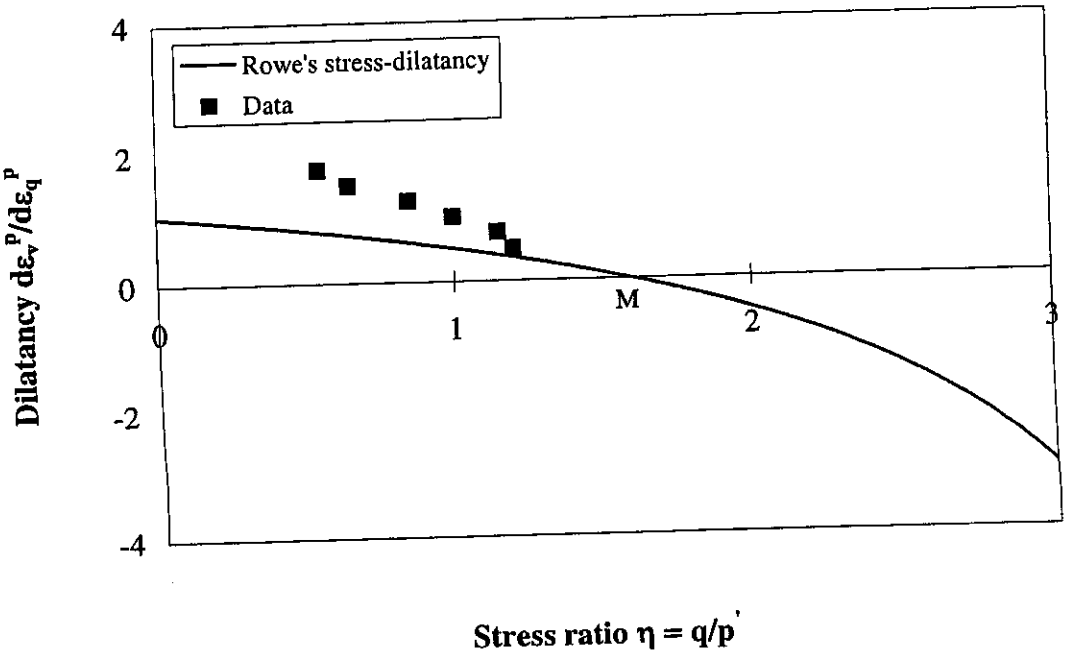

Figure 3.9 Comparison of Rowe's stress-dilatancy with data for loose uncemented carbonate sand

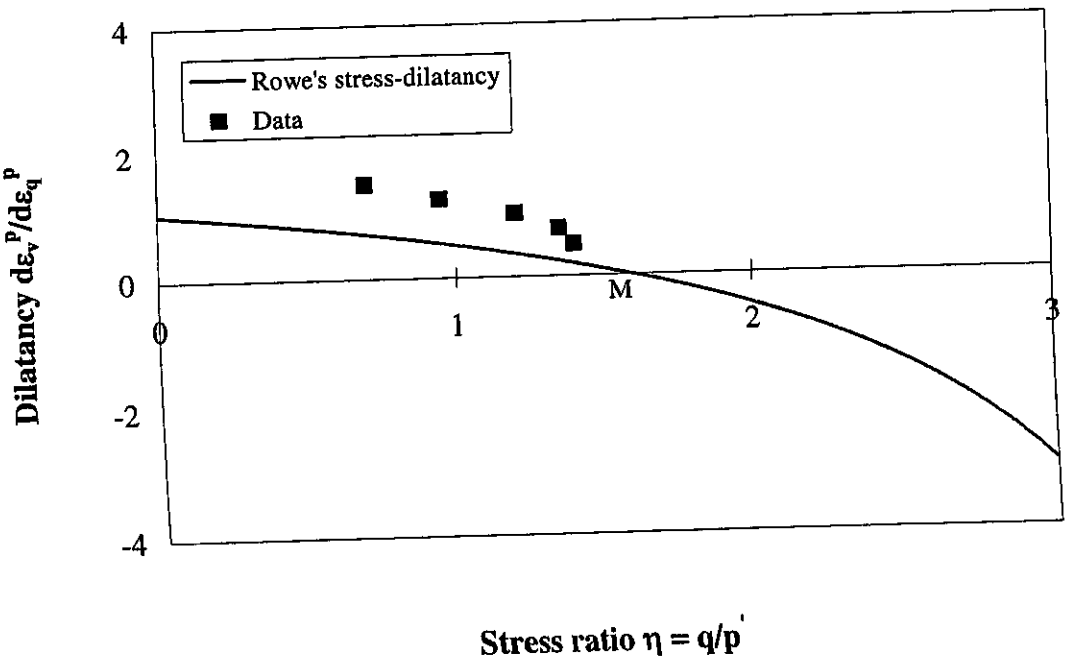

Figure 3.10 Comparison of Rowe's stress-dilatancy with data for loose cemented carbonate sand

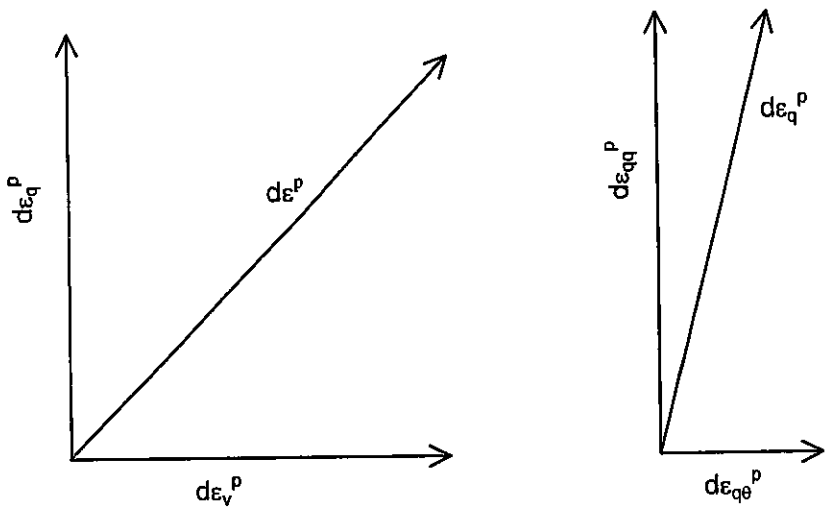

Figure 3.11 Components of total incremental plastic strains indicating effect of load angle

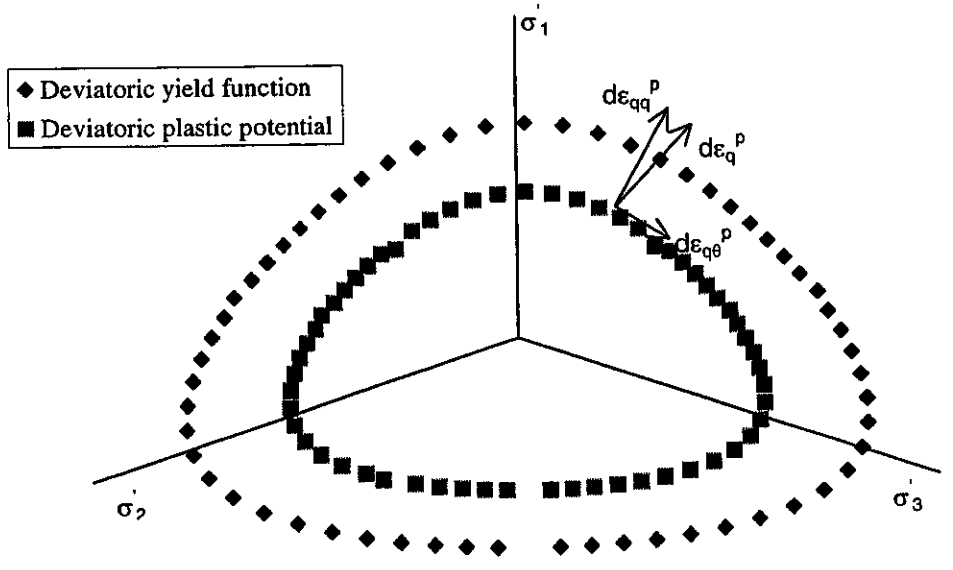

Figure 3.12 Molekamp model deviatoric yield surface and plastic potential function in the π plane

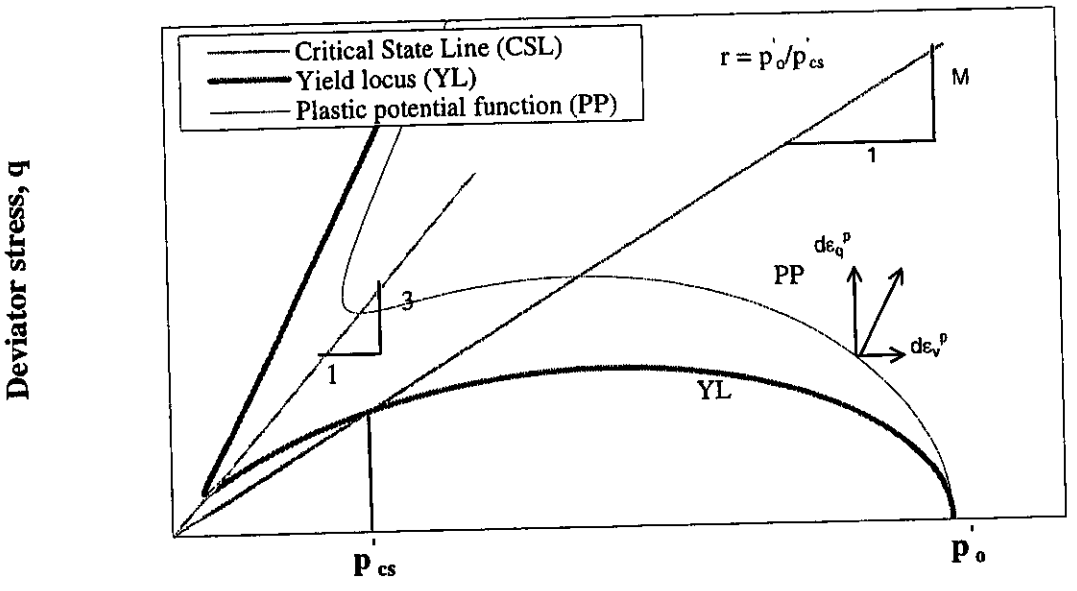

Figure 3.13 Nova model yield locus and plastic potential function on the triaxial compression plane

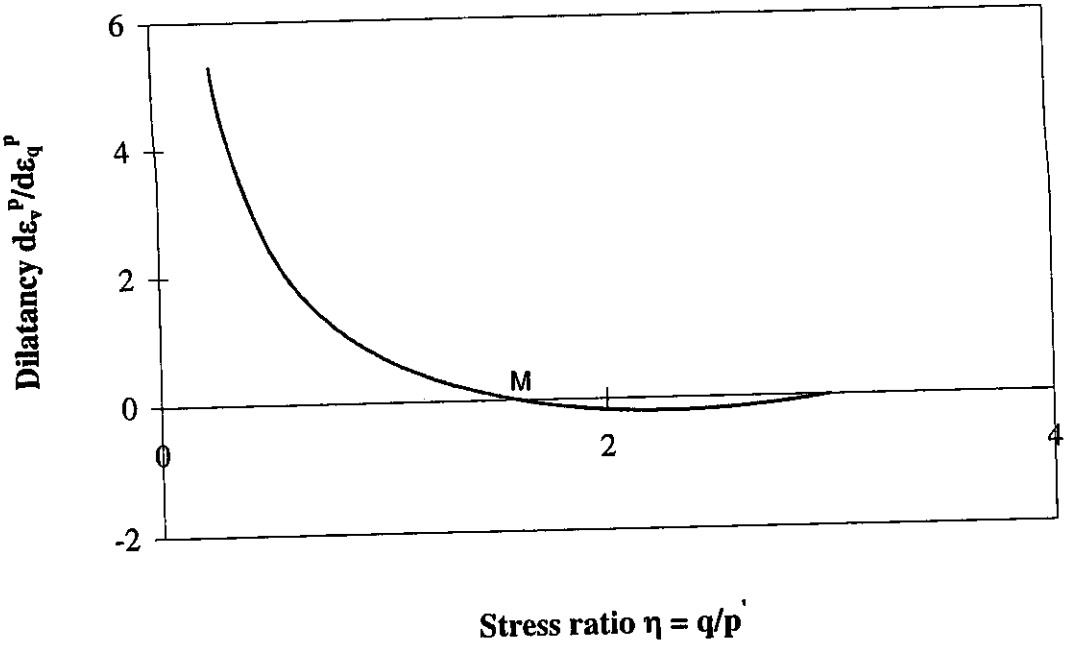

Figure 3.14 Nova model stress-dilatancy on the triaxial compression plane

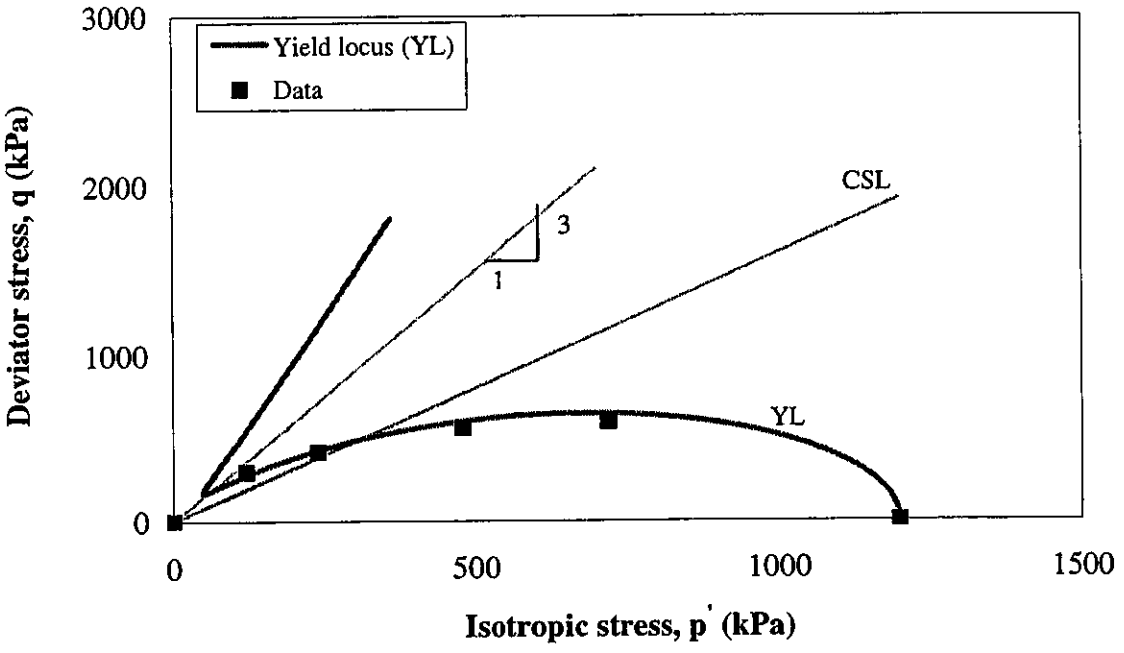

Figure 3.15 Comparison of Nova model yield locus with data for loose uncemented carbonate sand

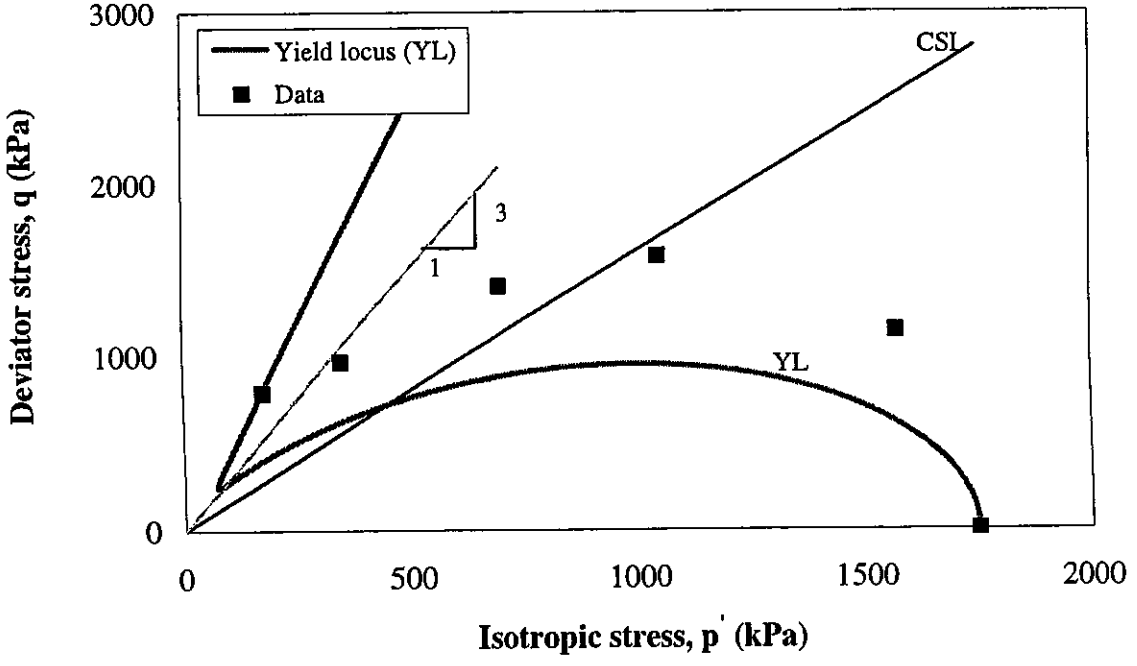

Figure 3.16 Comparison of Nova model yield locus with data for loose cemented carbonate sand

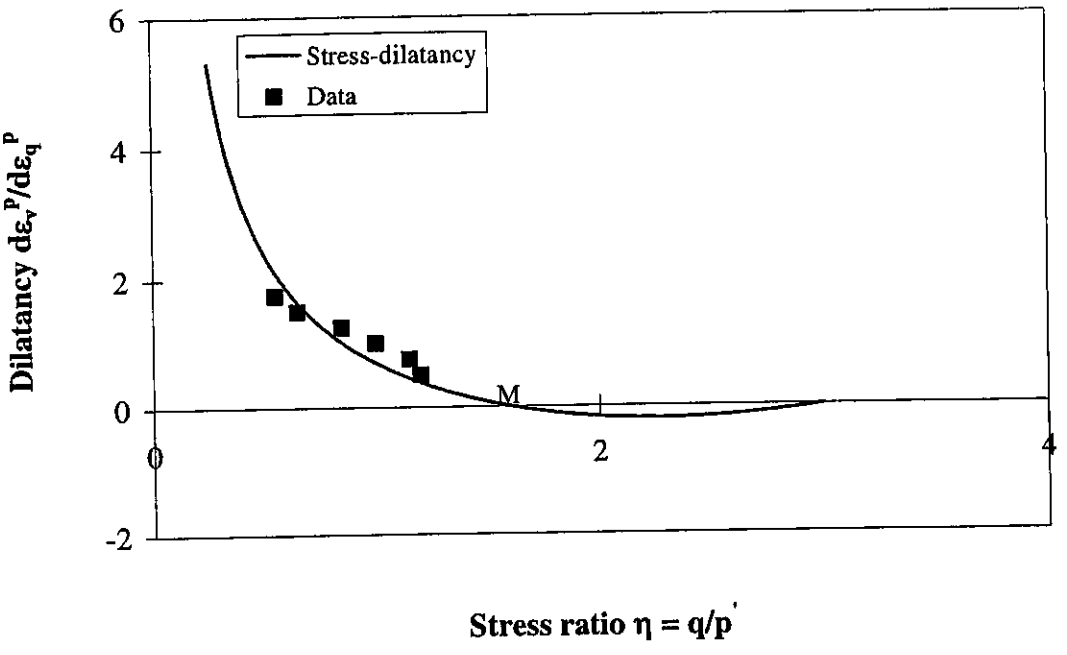

Figure 3.17 Comparison of Nova model stress-dilatancy with data for loose uncemented carbonate sand

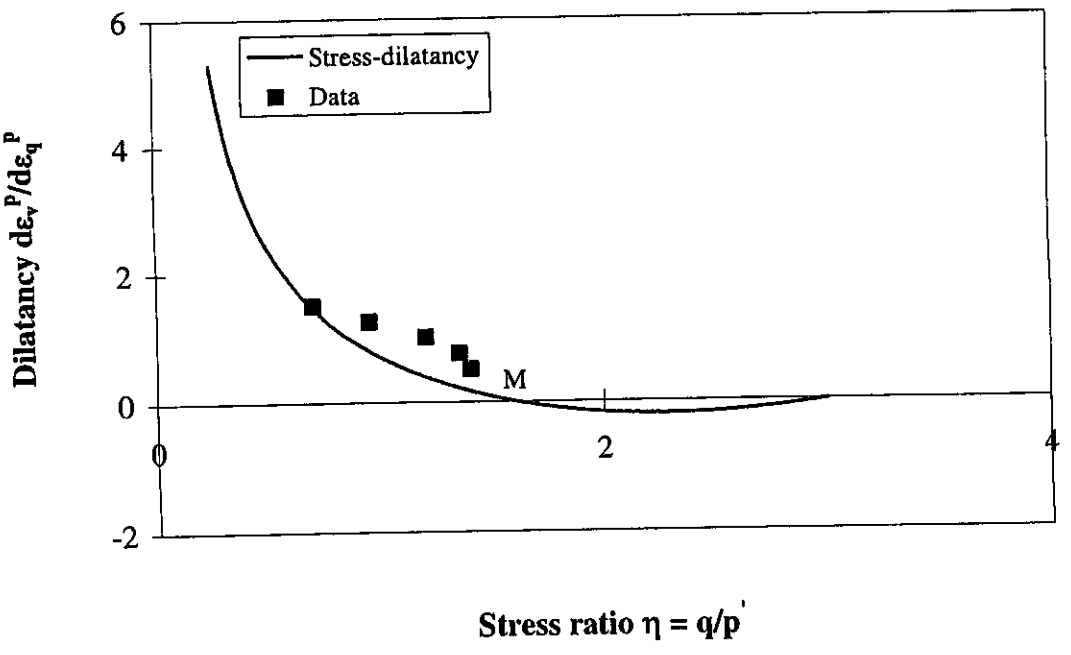

Figure 3.18 Comparison of Nova model stress-dilatancy with data for loose cemented carbonate sand

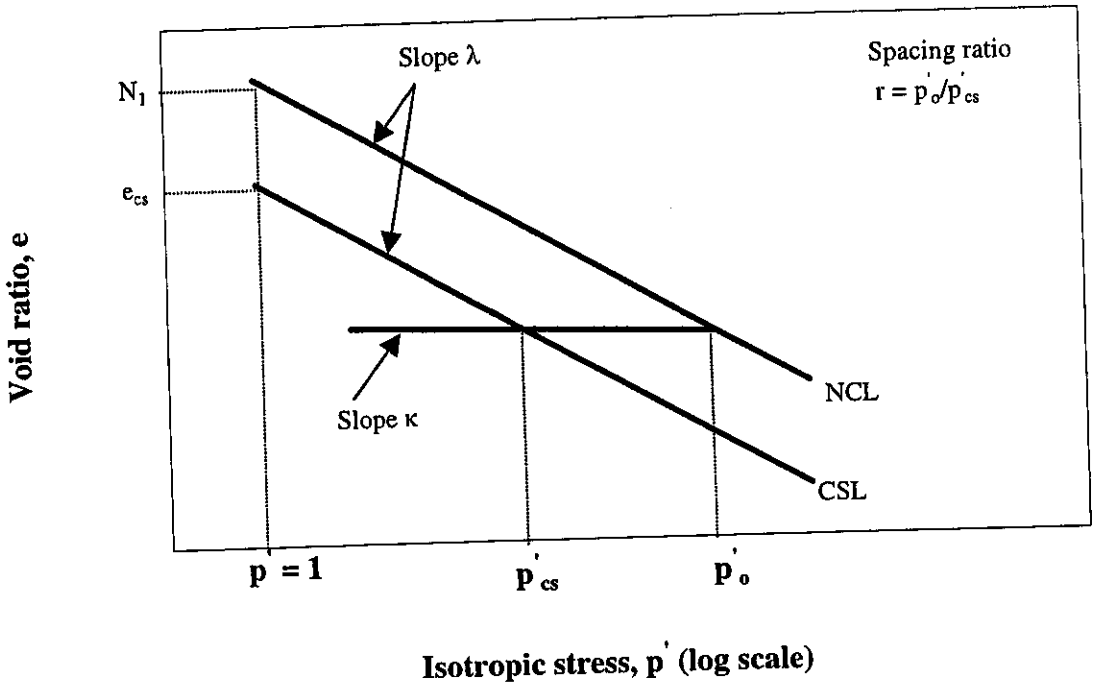

Figure 3.19 Illustration of the spacing ratio concept in the mean effective stress versus void ratio $(e - \ln p')$ space

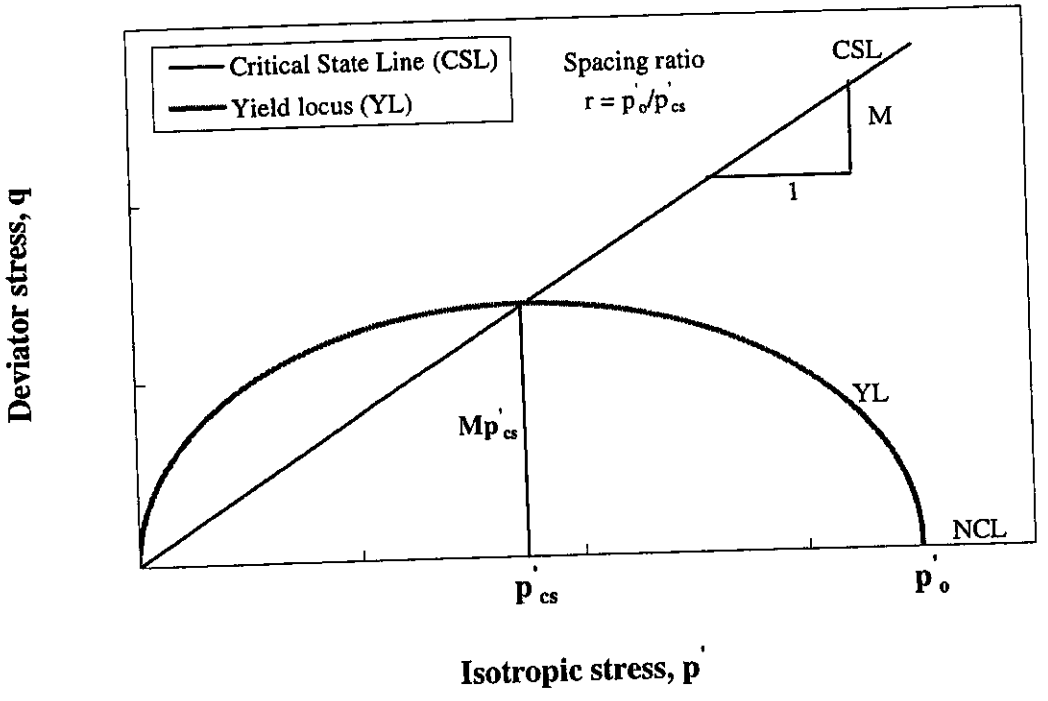

Figure 3.20 Illustration of the spacing ratio concept in the mean effective stress versus deviator stress $(p' - q)$ space

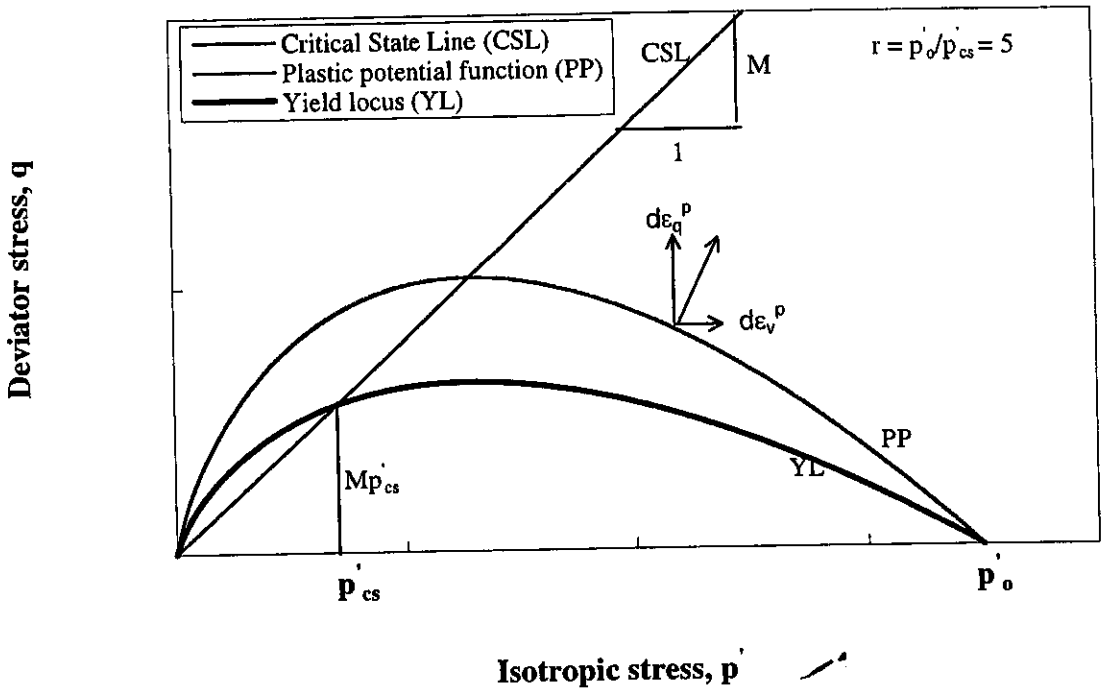

Figure 3.21 SU1 model yield locus and plastic potential function

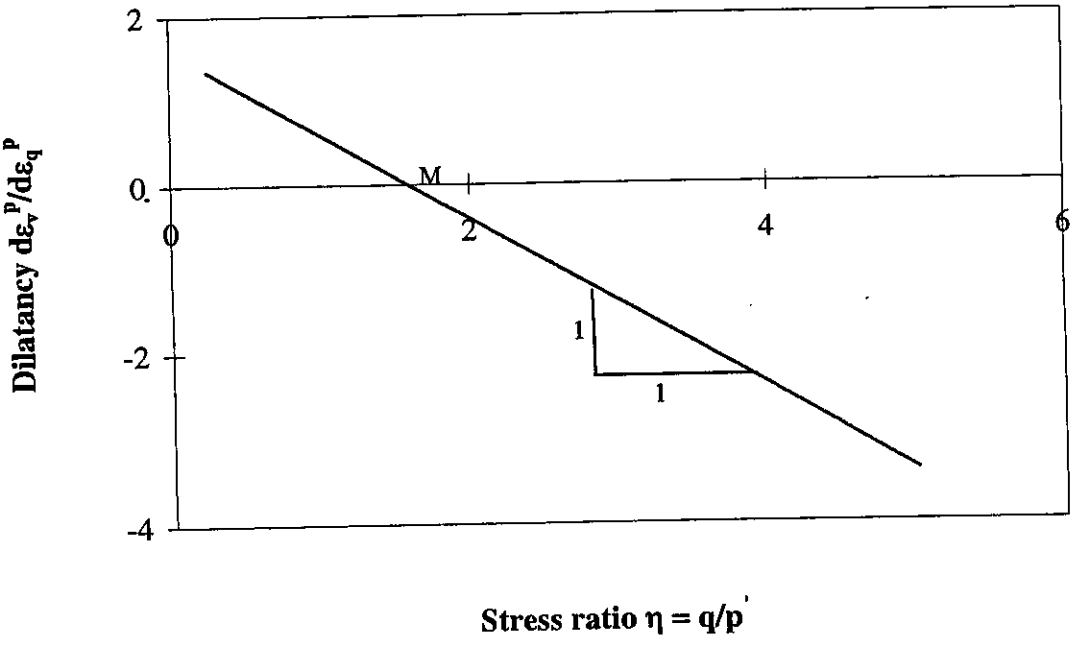

Figure 3.22 SU1 model stress-dilatancy function

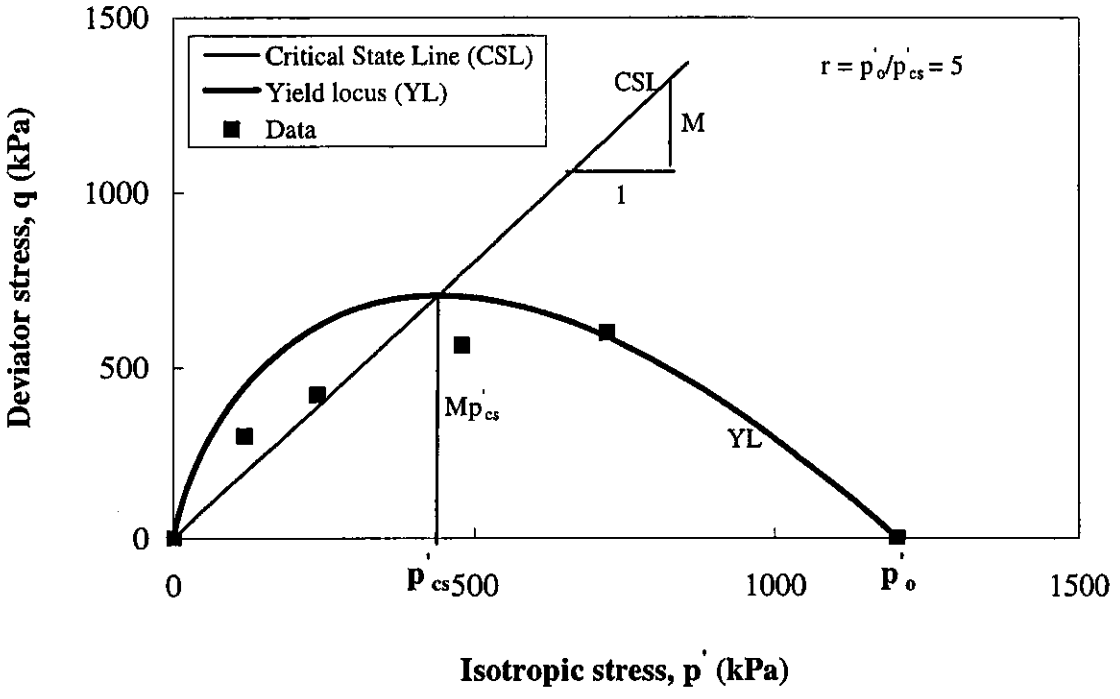

Figure 3.23 Comparison of SU1 yield locus with data for loose uncemented carbonate sand

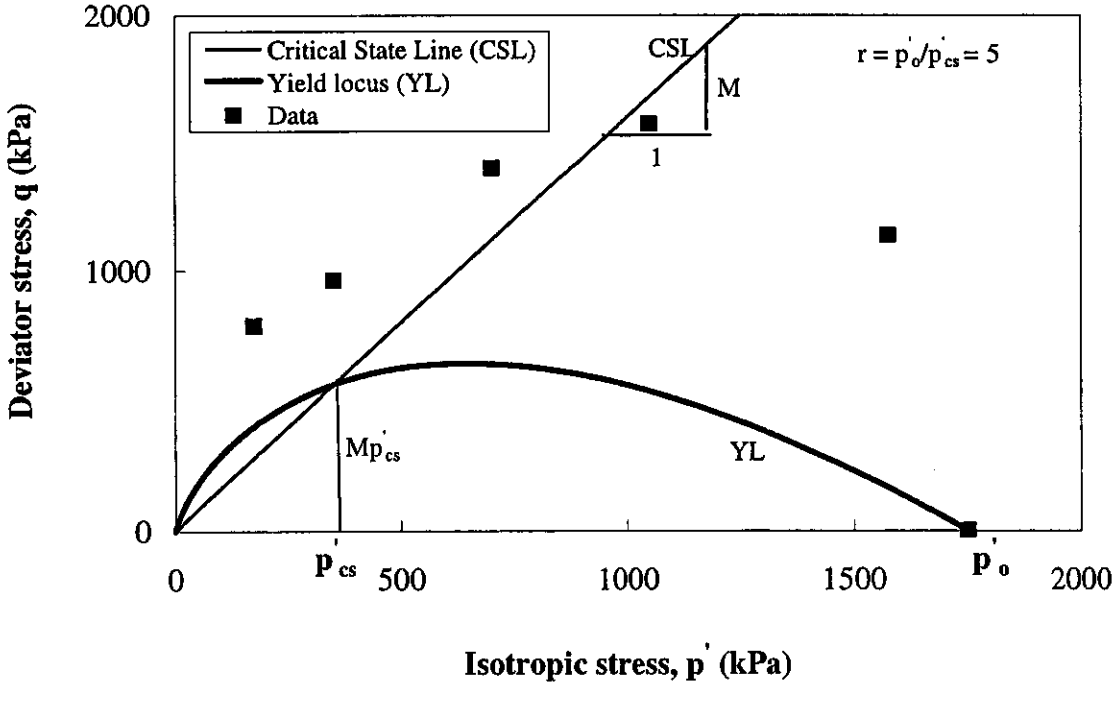

Figure 3.24 Comparison of SU1 yield locus with data for loose cemented carbonate sand

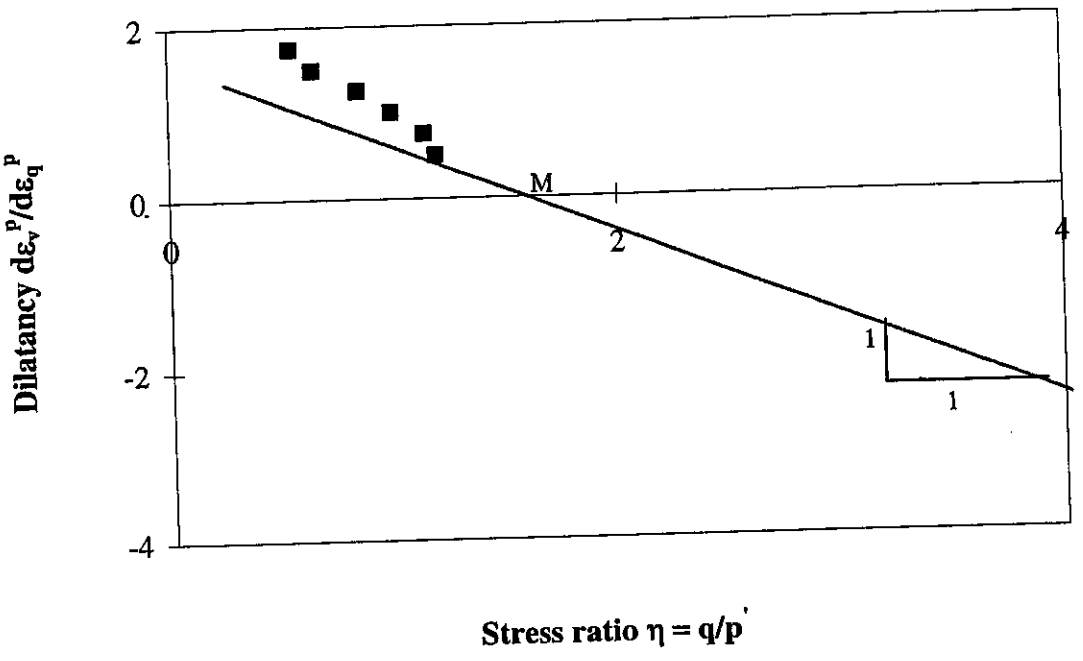

Figure 3.25 Comparison of SU1 stress-dilatancy with data for loose uncemented carbonate sand

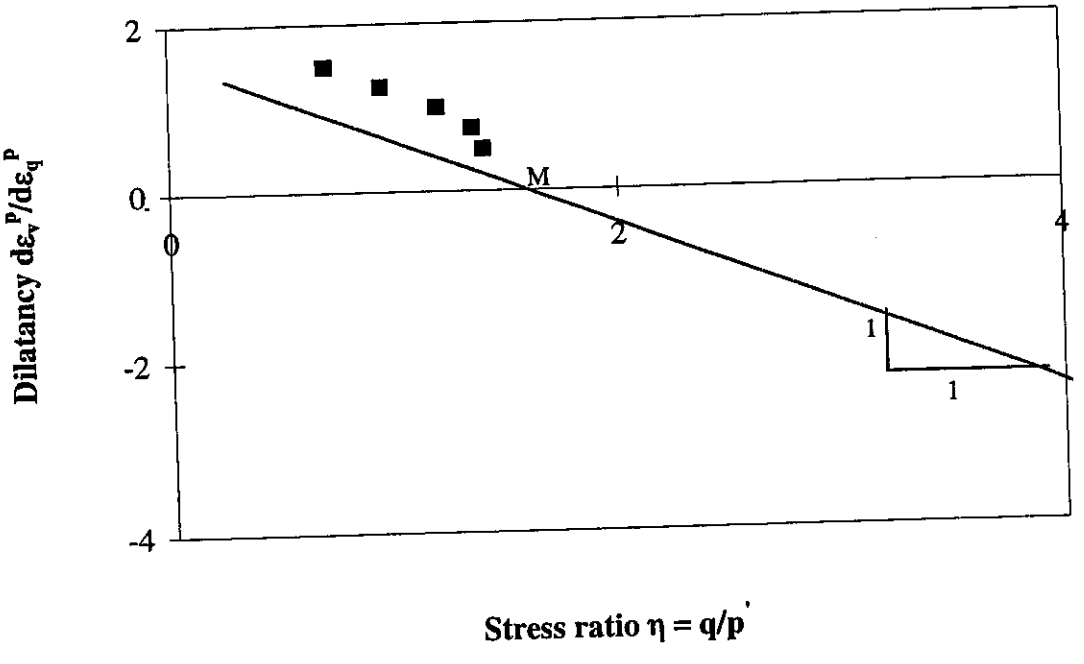

Figure 3.26 Comparison of SU1 stress-dilatancy with data for loose cemented carbonate sand

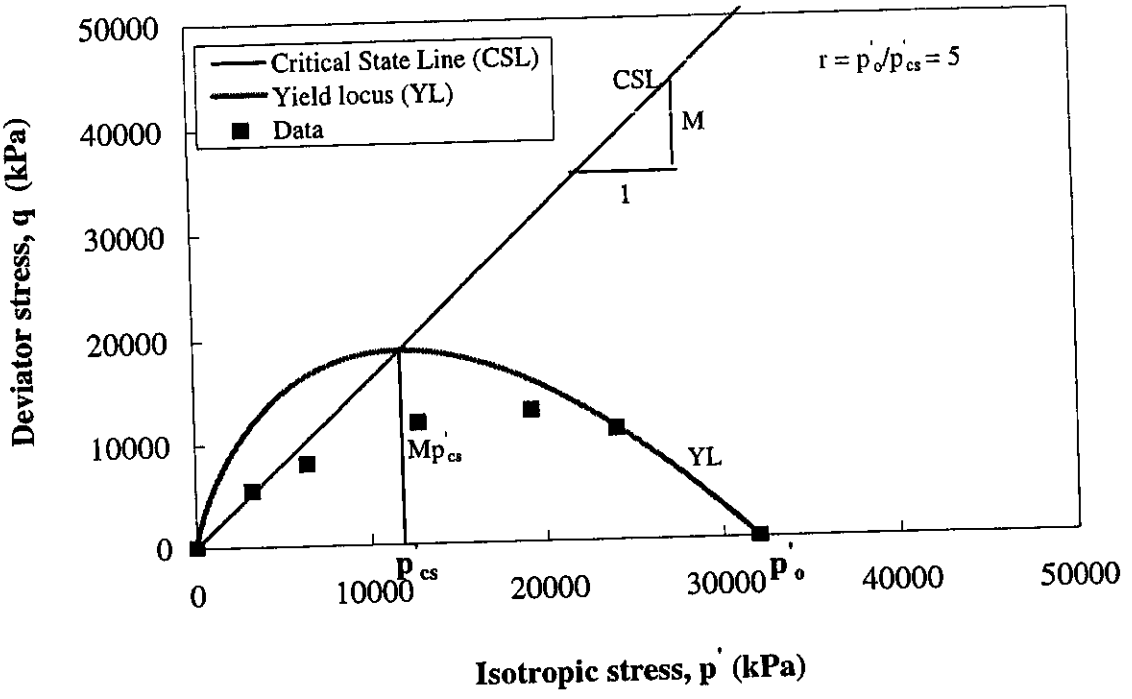

Figure 3.27 Comparison of SU1 yield locus with data for dense uncemented carbonate sand

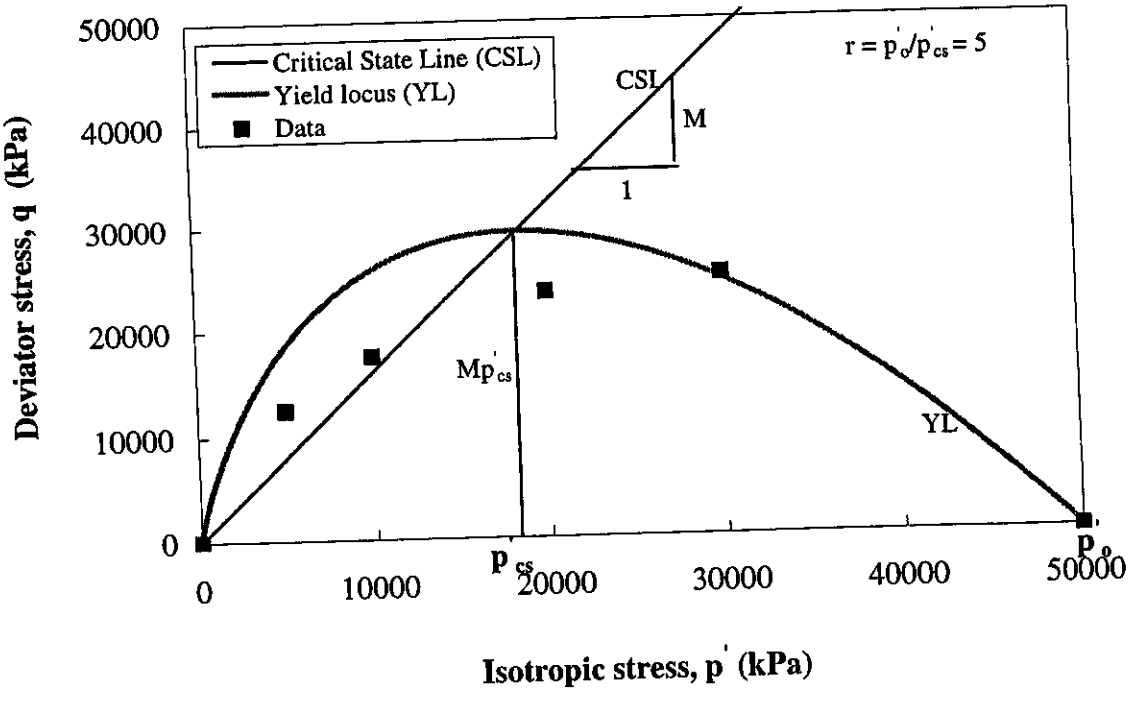

Figure 3.28 Comparison of SU1 yield locus with data for dense cemented carbonate sand

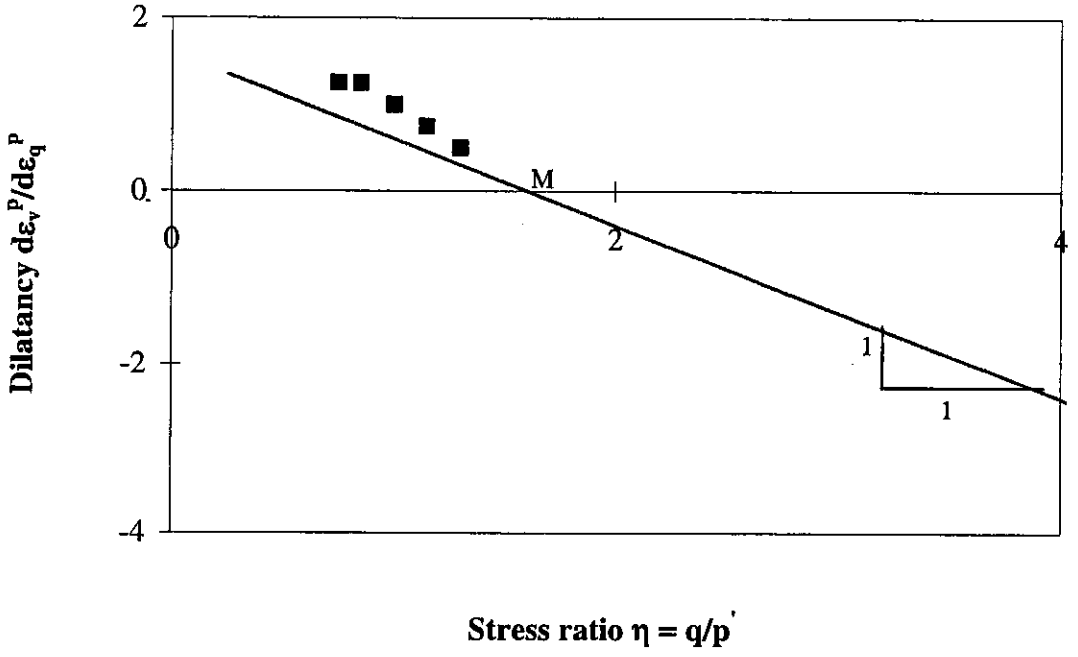

Figure 3.29 Comparison of SU1 stress-dilatancy with data for dense uncemented carbonate sand

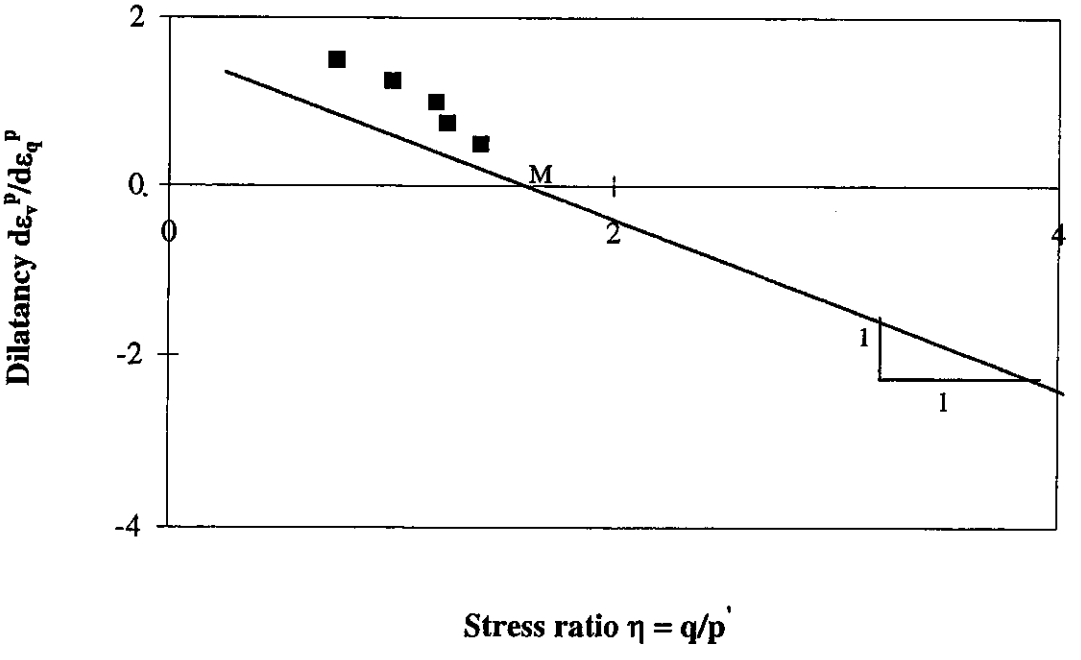

Figure 3.30 Comparison of SU1 stress-dilatancy with data for dense cemented carbonate sand

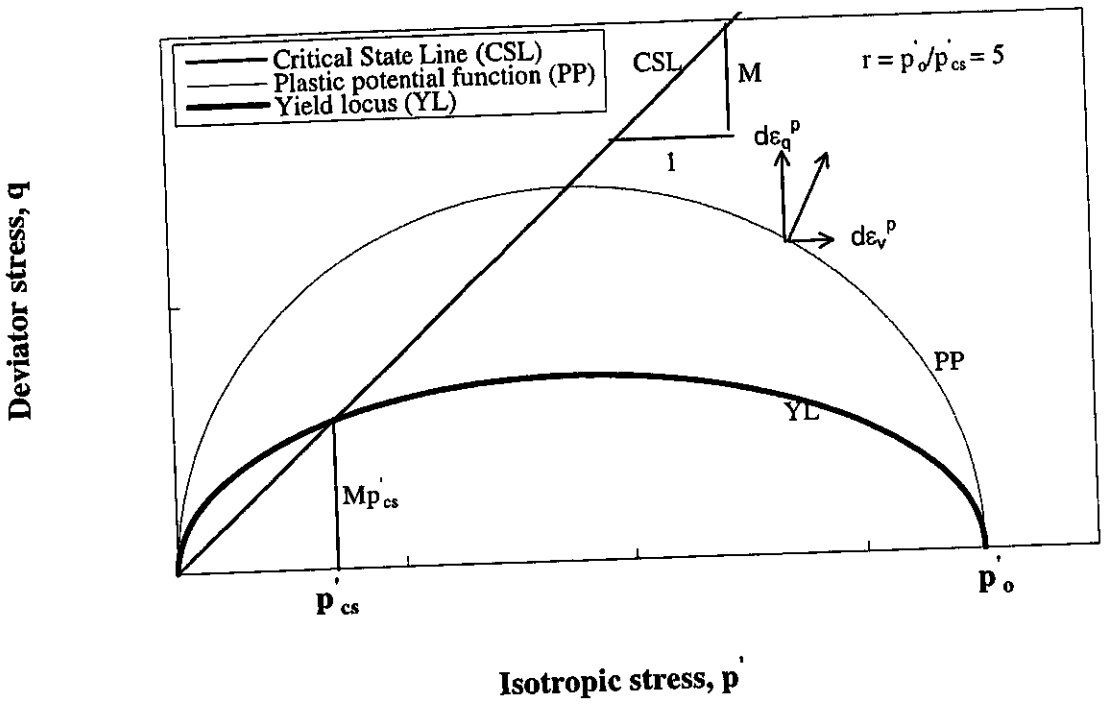

Figure 3.31 SU2 model yield locus and plastic potential function

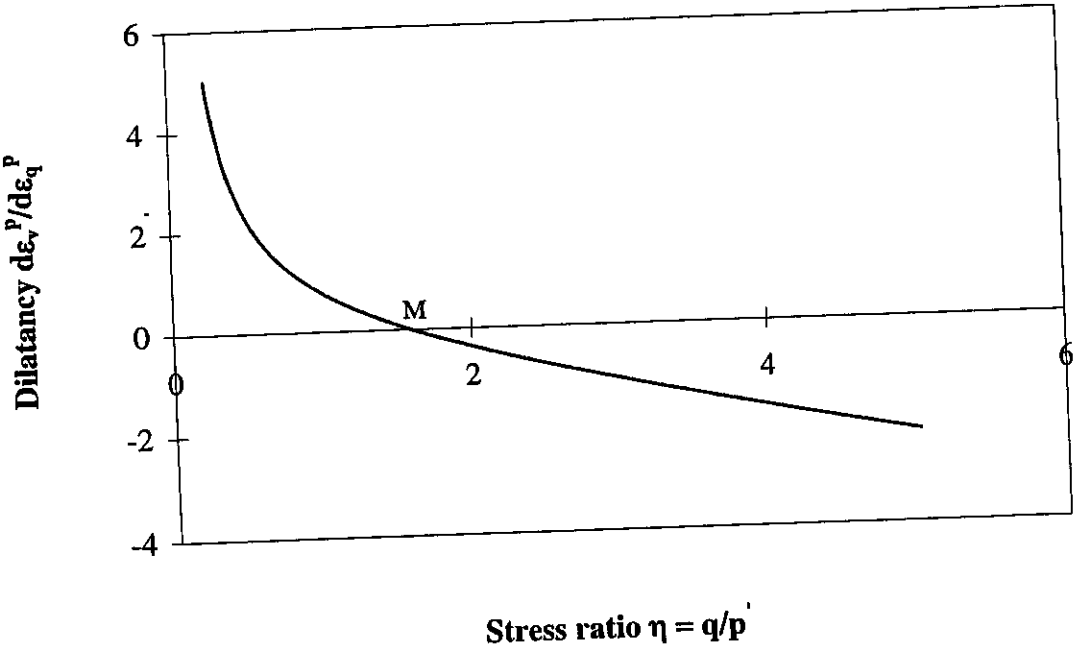

Figure 3.32 SU2 model stress-dilatancy function

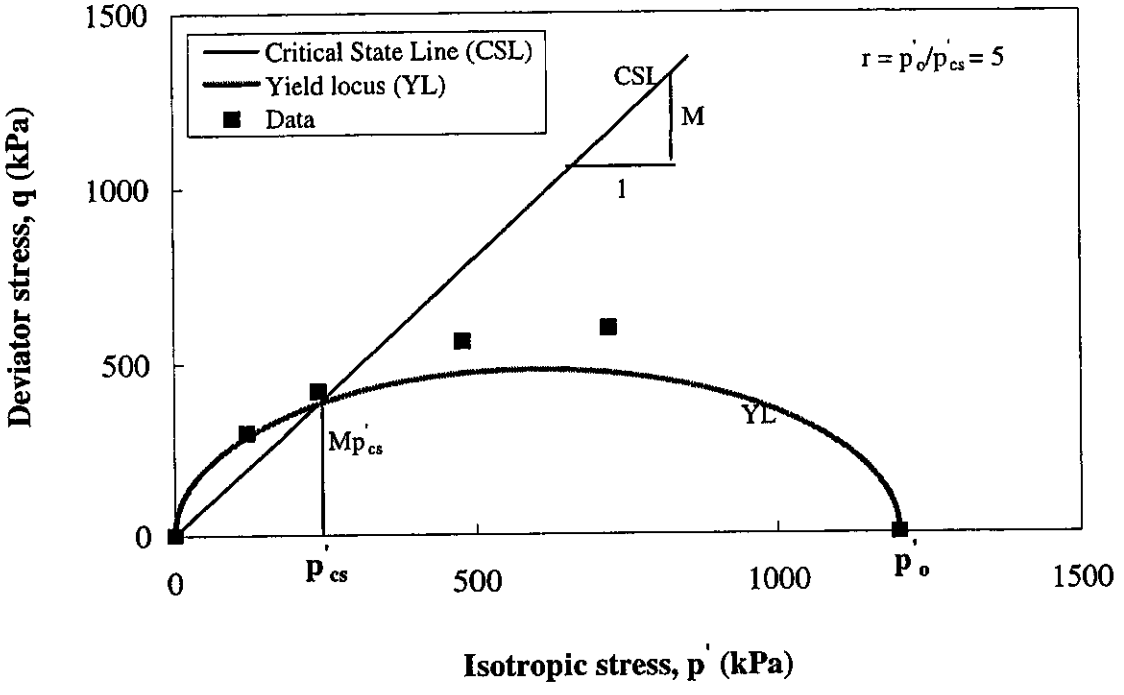

Figure 3.33 Comparison of SU2 yield locus with data for loose uncemented carbonate sand

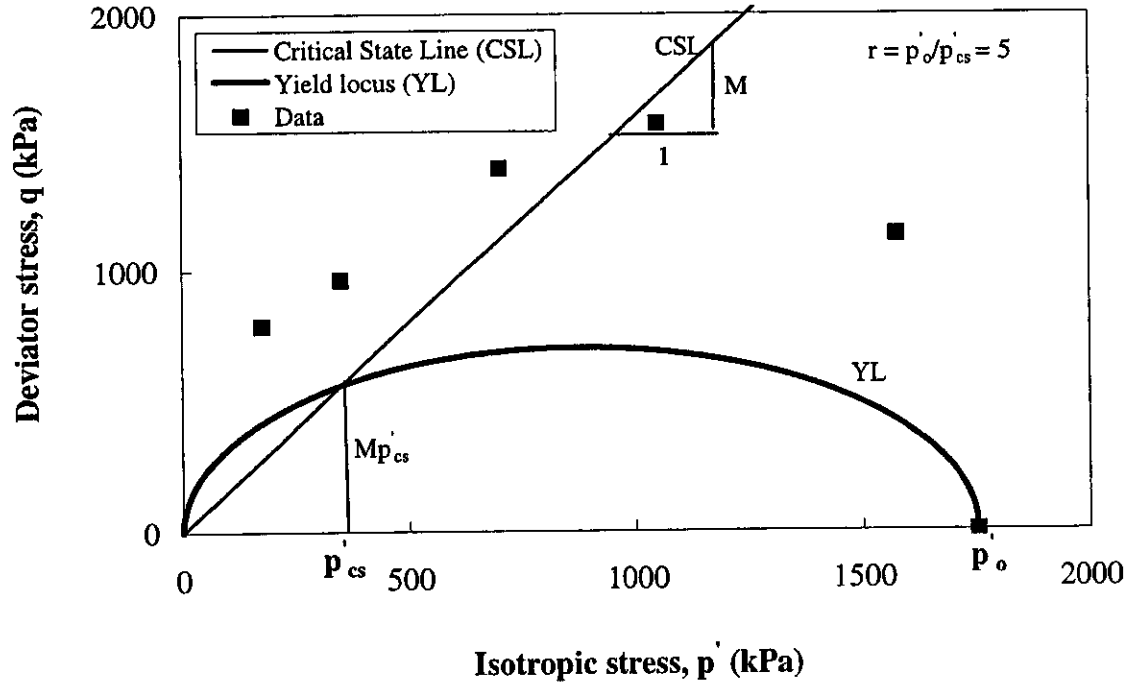

Figure 3.34 Comparison of SU2 yield locus with data for loose cemented carbonate sand

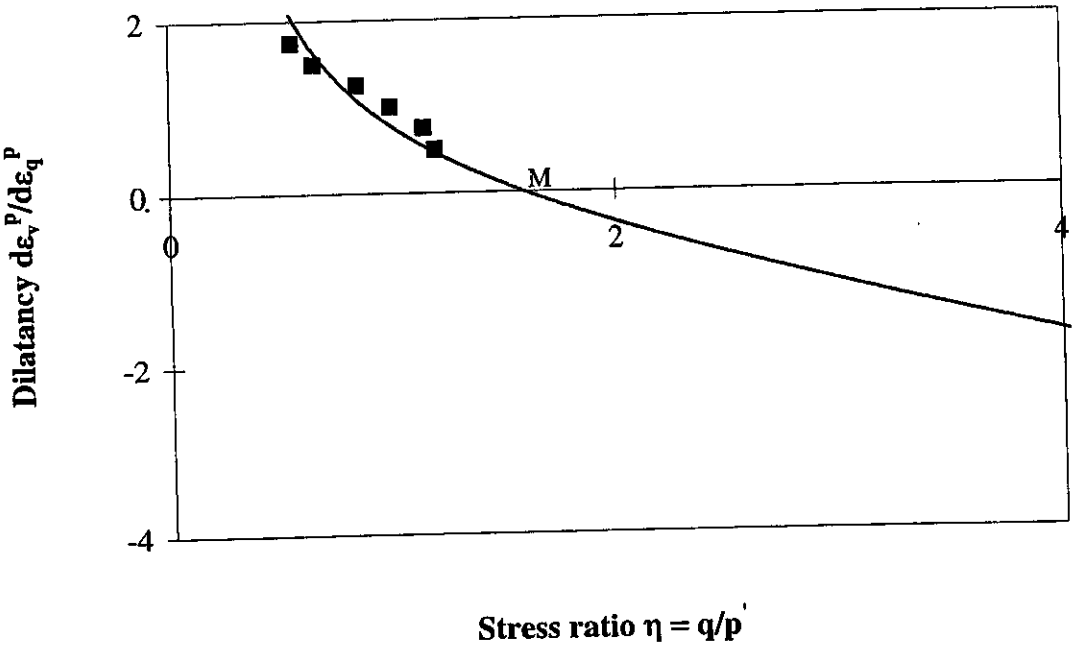

Figure 3.35 Comparison of SU2 stress-dilatancy with data for loose uncemented carbonate sand

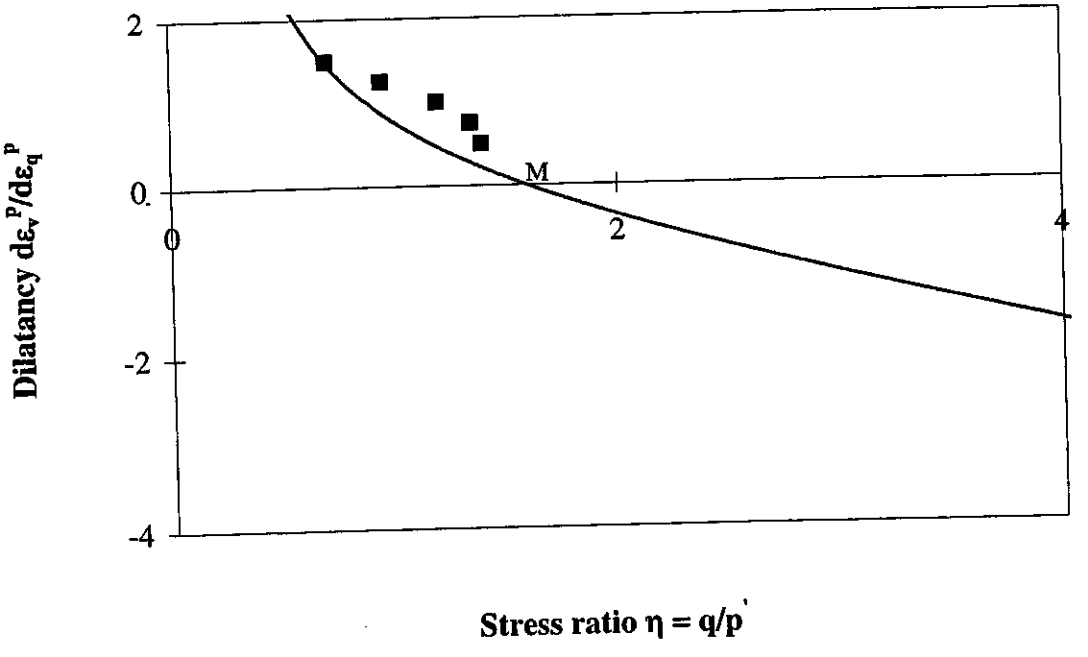

Figure 3.36 Comparison of SU2 stress-dilatancy with data for loose cemented carbonate sand

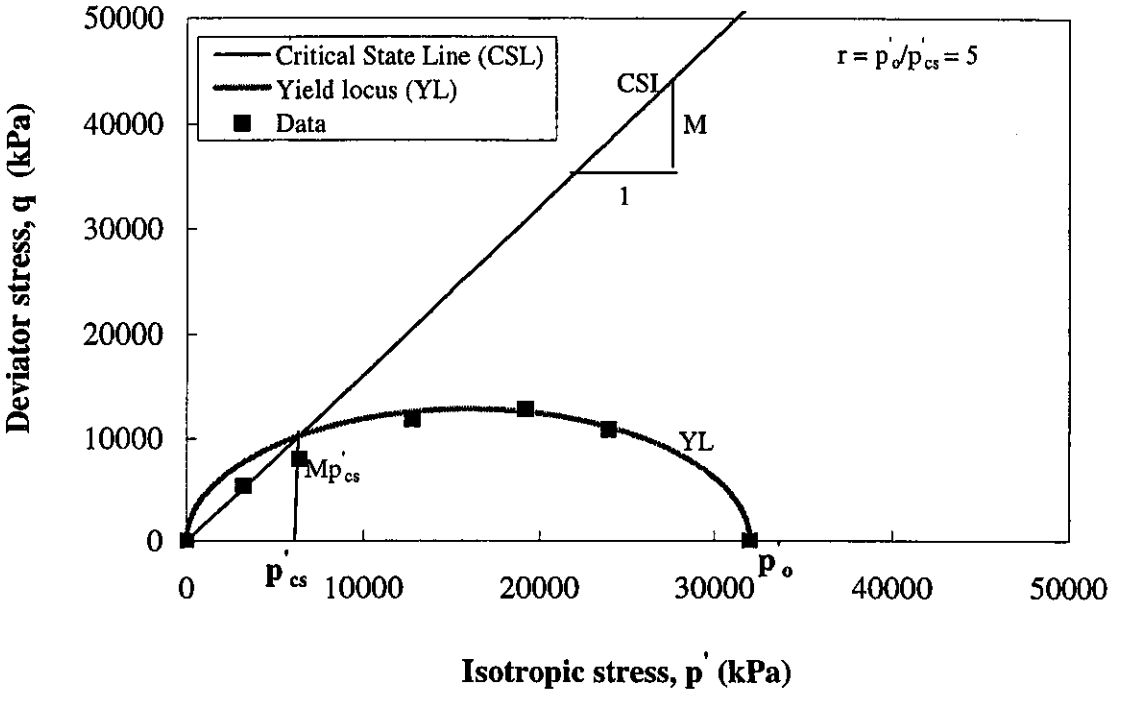

Figure 3.37 Comparison of SU2 model yield locus with data for dense uncemented carbonate sand

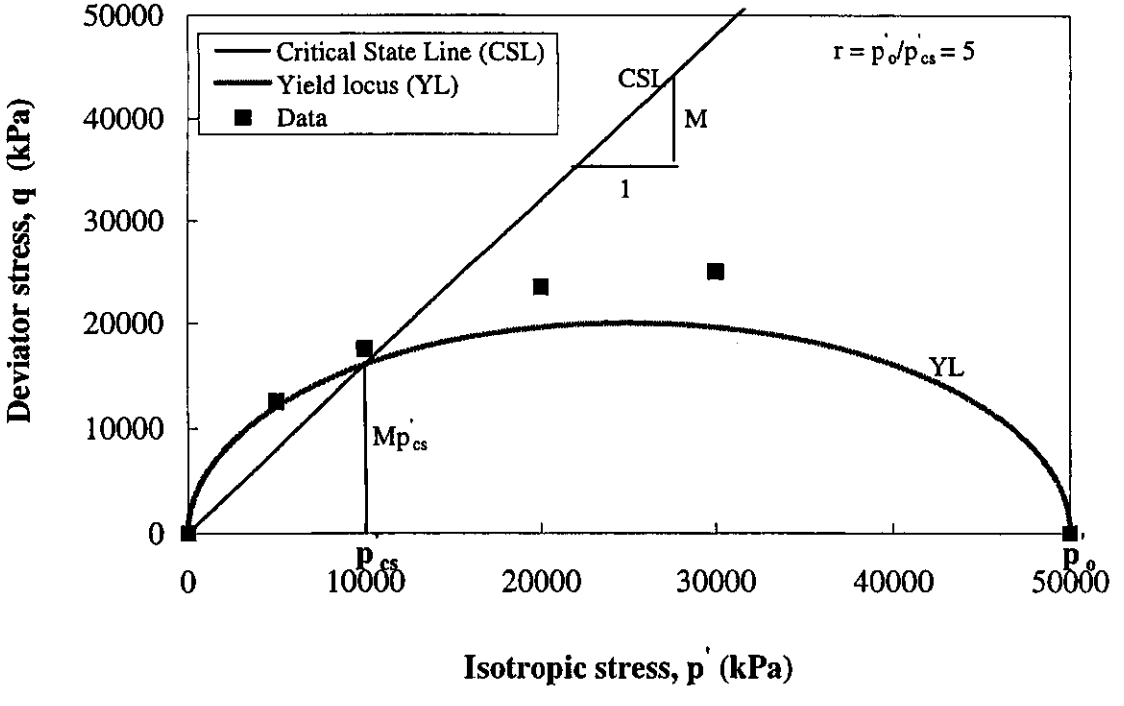

Figure 3.38 Comparison of SU2 yield locus with data for dense cemented carbonate sand

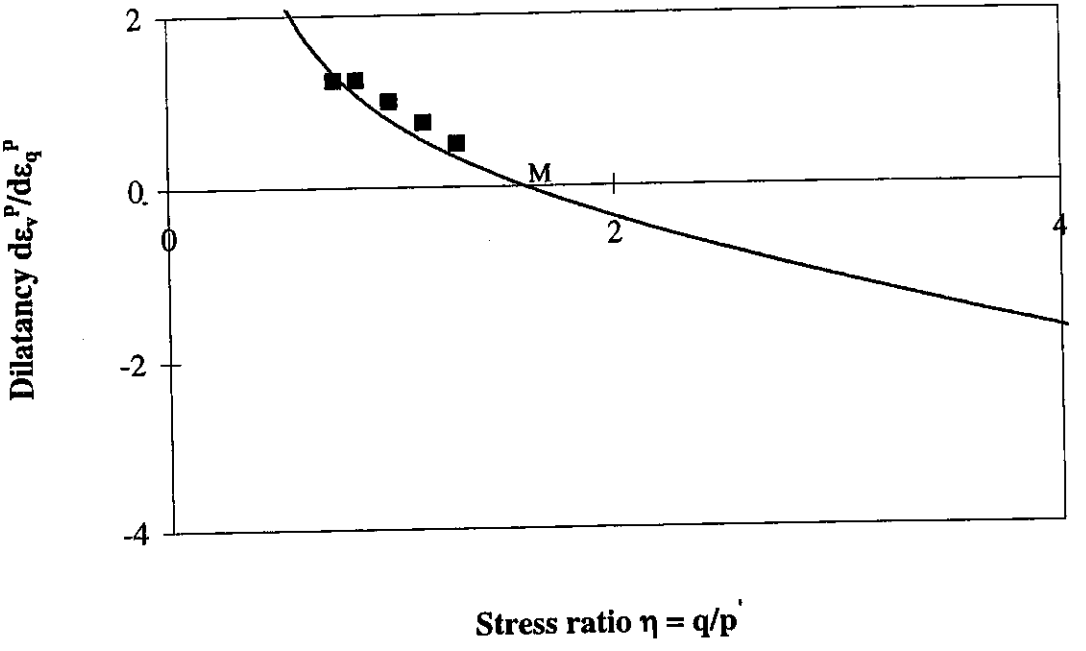

Figure 3.39 Comparison of SU2 stress-dilatancy with data for dense uncemented carbonate sand

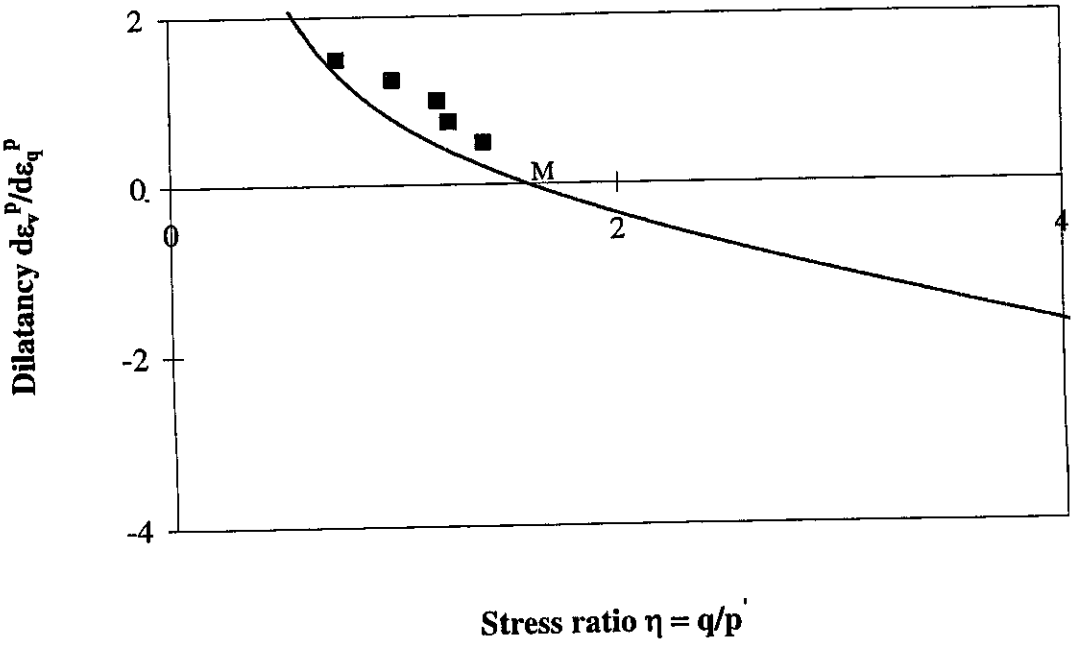

Figure 3.40 Comparison of SU2 stress-dilatancy with data for dense cemented carbonate sand

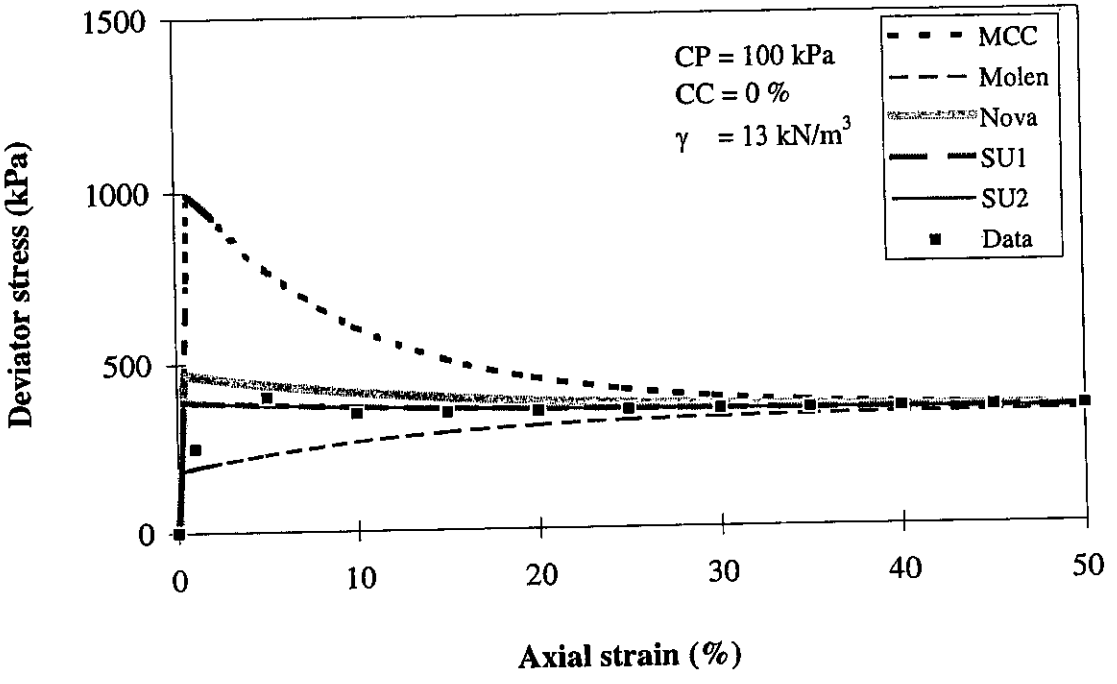

Figure 3.41 Prediction of shear behaviour of loose uncemented carbonate sand at 100 kPa cell pressure

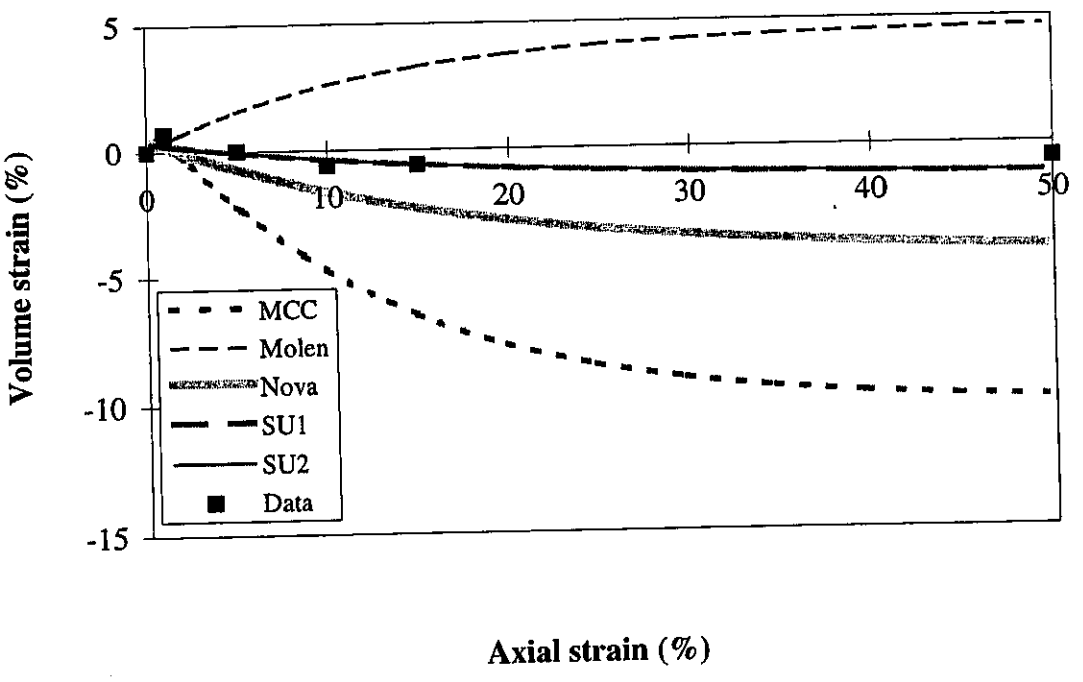

Figure 3.42 Prediction of volume strain behaviour of loose uncemented carbonate sand at 100 kPa cell pressure

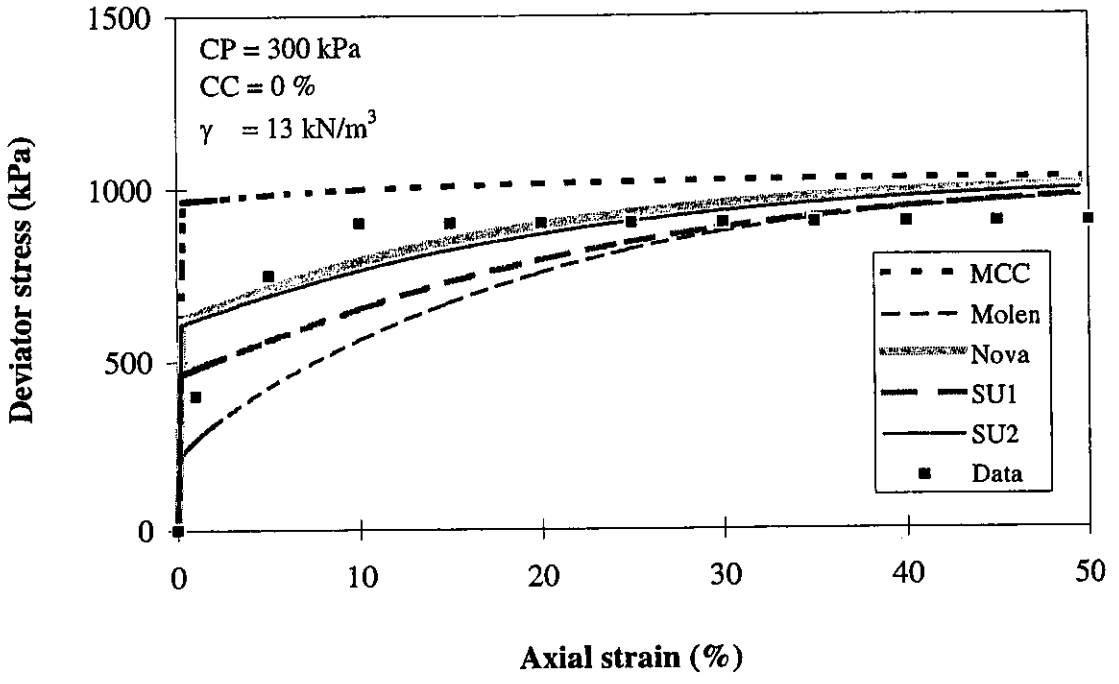

Figure 3.43 Prediction of shear behaviour of loose uncemented carbonate sand at 300 kPa cell pressure

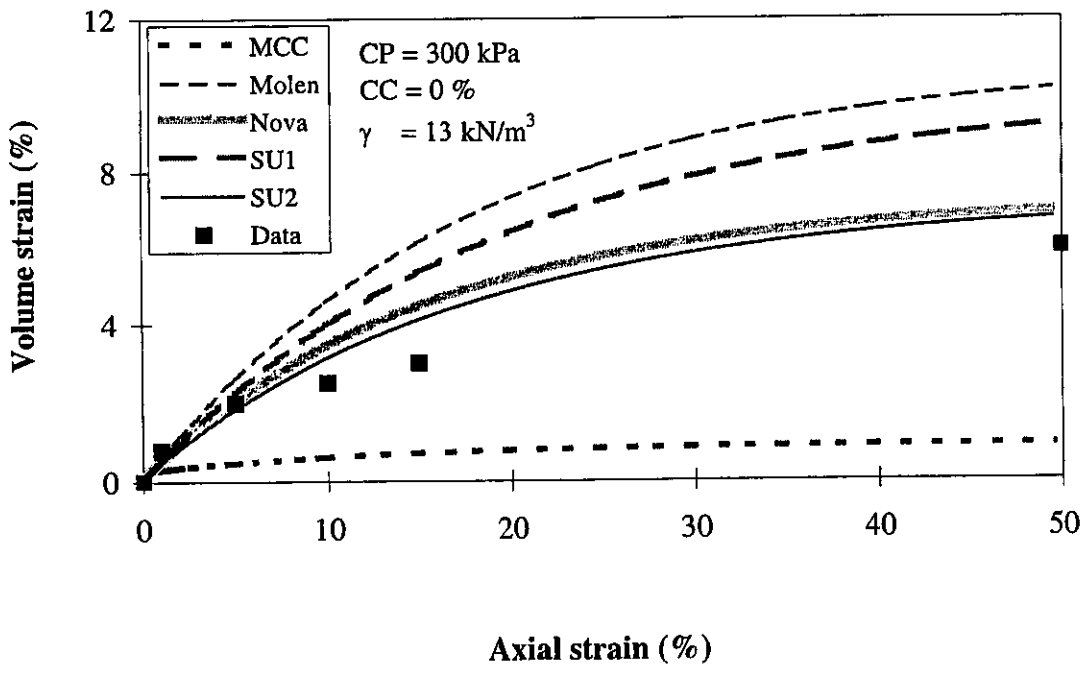

Figure 3.44 Prediction of volume strain behaviour of loose uncemented carbonate sand at 300 kPa cell pressure

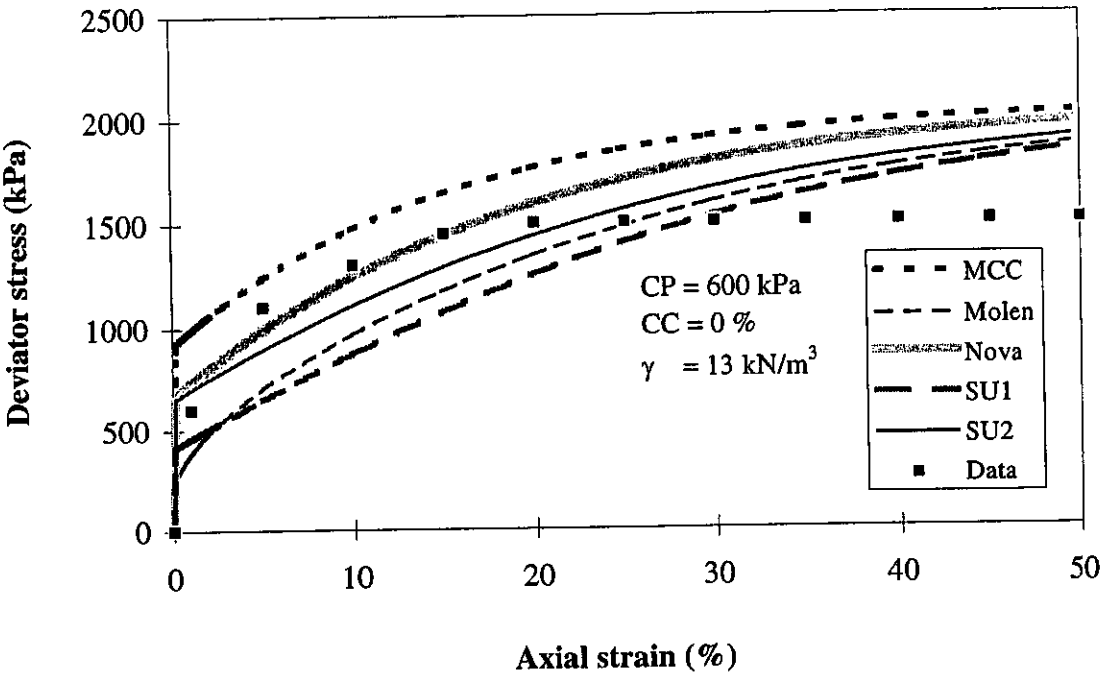

Figure 3.45 Prediction of shear behaviour of loose uncemented carbonate sand at 600 kPa cell pressure

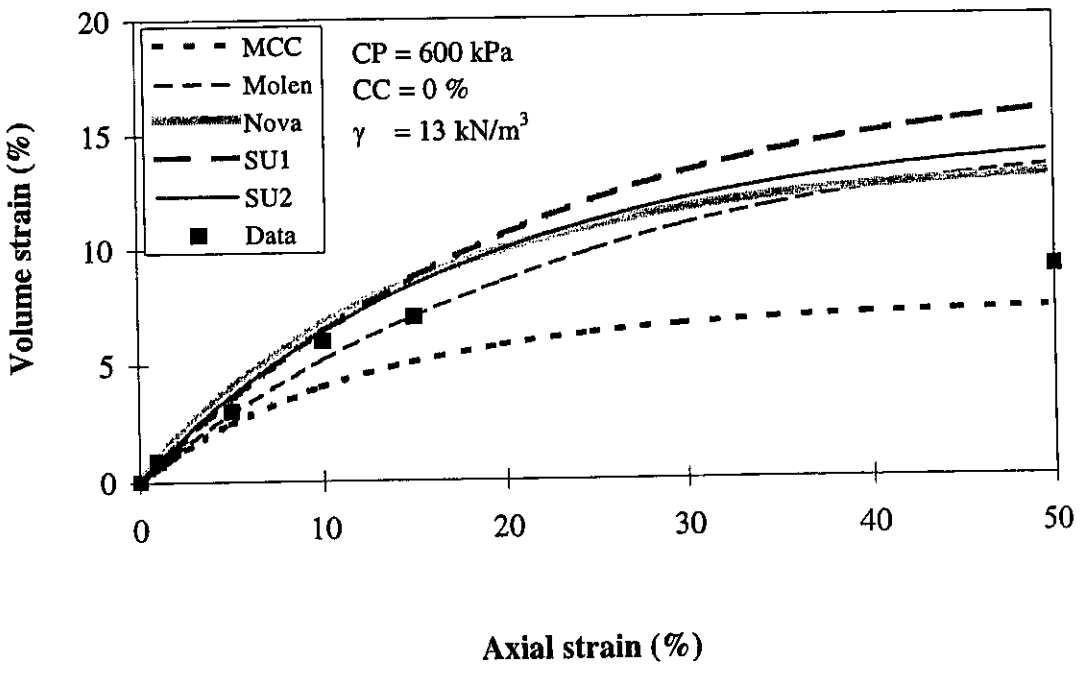

Figure 3.46 Prediction of volume strain behaviour of loose uncemented carbonate sand at 600 kPa cell pressure

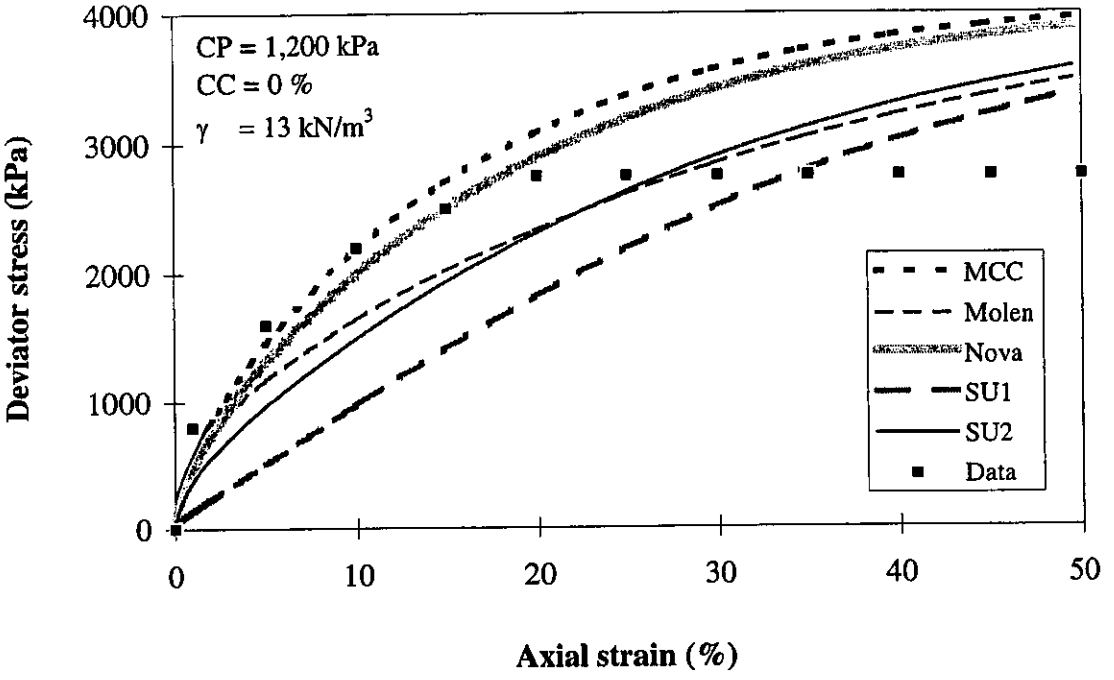

Figure 3.47 Prediction of shear behaviour of loose uncemented carbonate sand at 1,200 kPa cell pressure

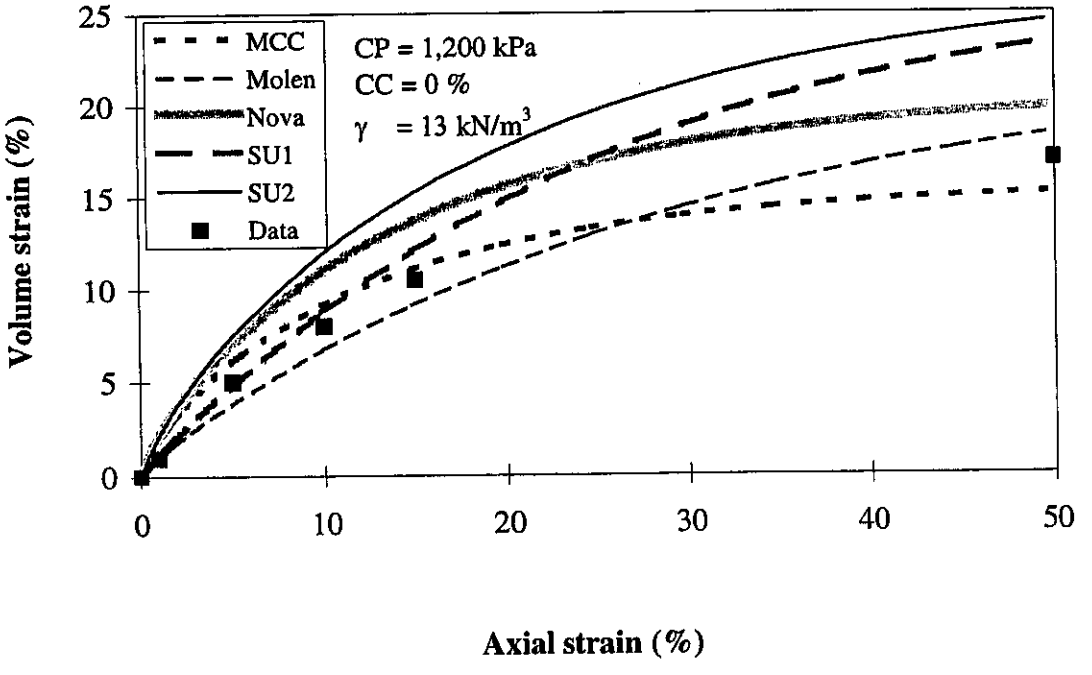

Figure 3.48 Prediction of volume strain behaviour of loose uncemented carbonate sand at 1,200 kPa cell pressure

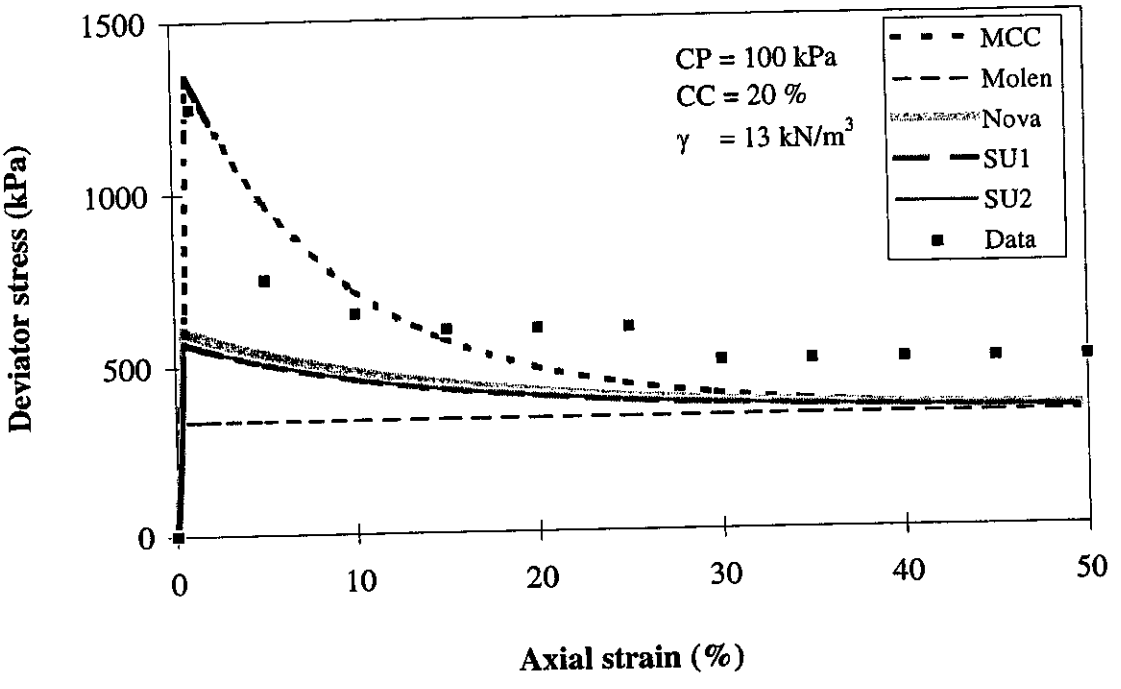

Figure 3.49 Prediction of shear behaviour of loose cemented carbonate sand at 100 kPa cell pressure

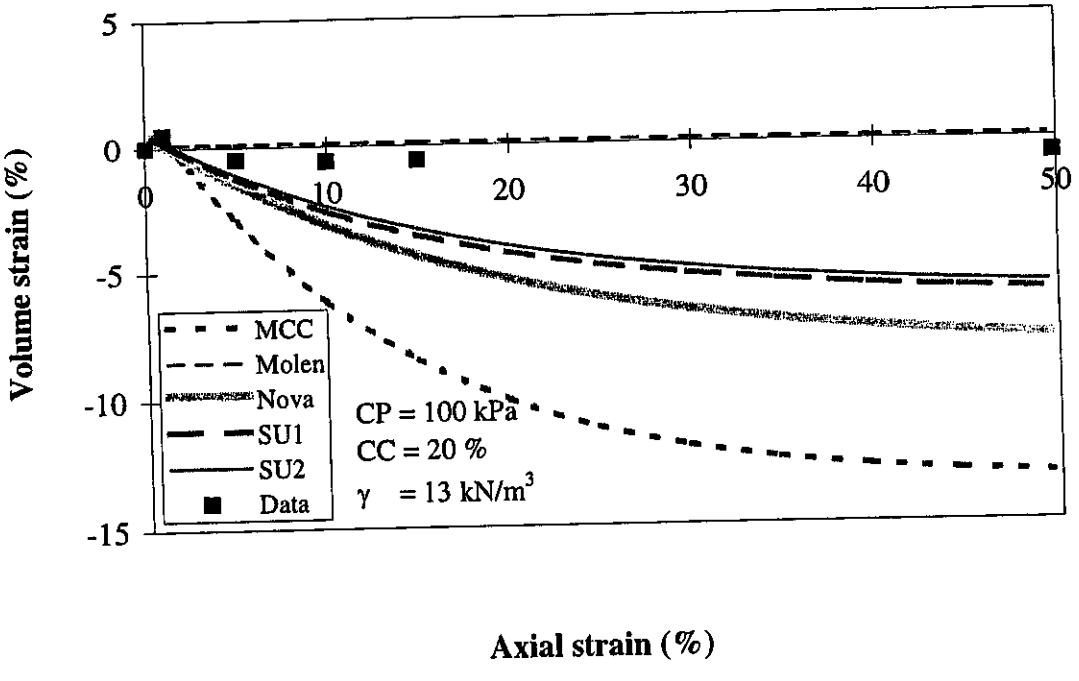

Figure 3.50 Prediction of volume strain behaviour of loose cemented carbonate sand at 100 kPa cell pressure

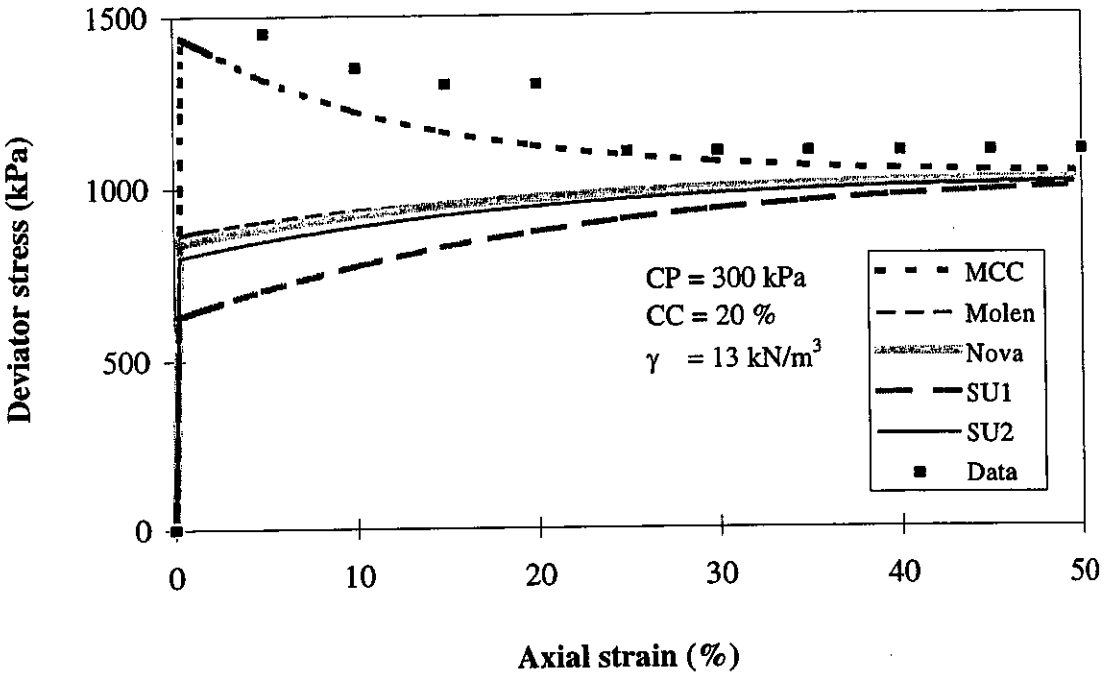

Figure 3.51 Prediction of shear behaviour of loose cemented carbonate sand at 300 kPa cell pressure

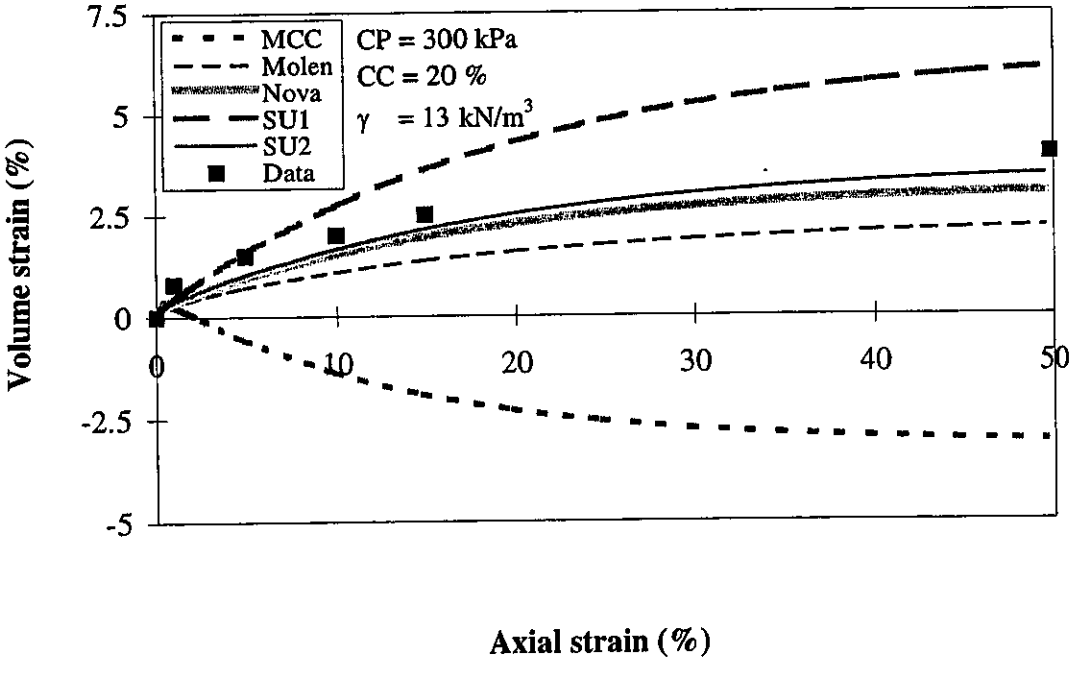

Figure 3.52 Prediction of volume strain behaviour of loose cemented carbonate sand at 300 kPa cell pressure

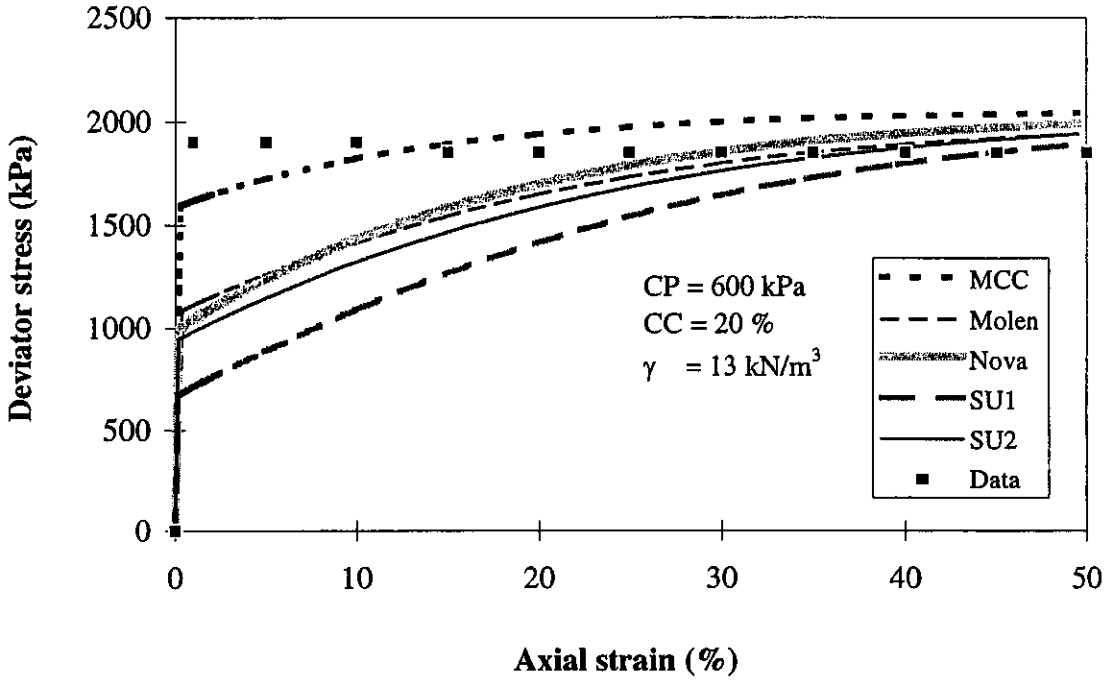

Figure 3.53 Prediction of shear behaviour of loose cemented carbonate sand at 600 kPa cell pressure

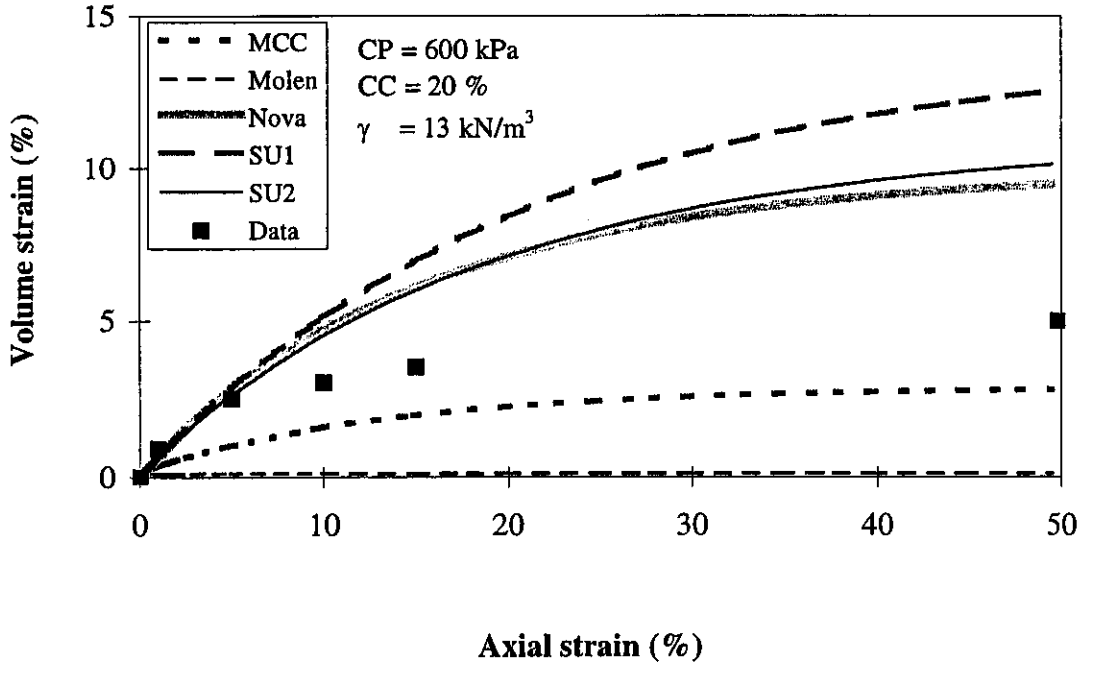

Figure 3.54 Prediction of volume strain behaviour of loose cemented carbonate sand at 600 kPa cell pressure

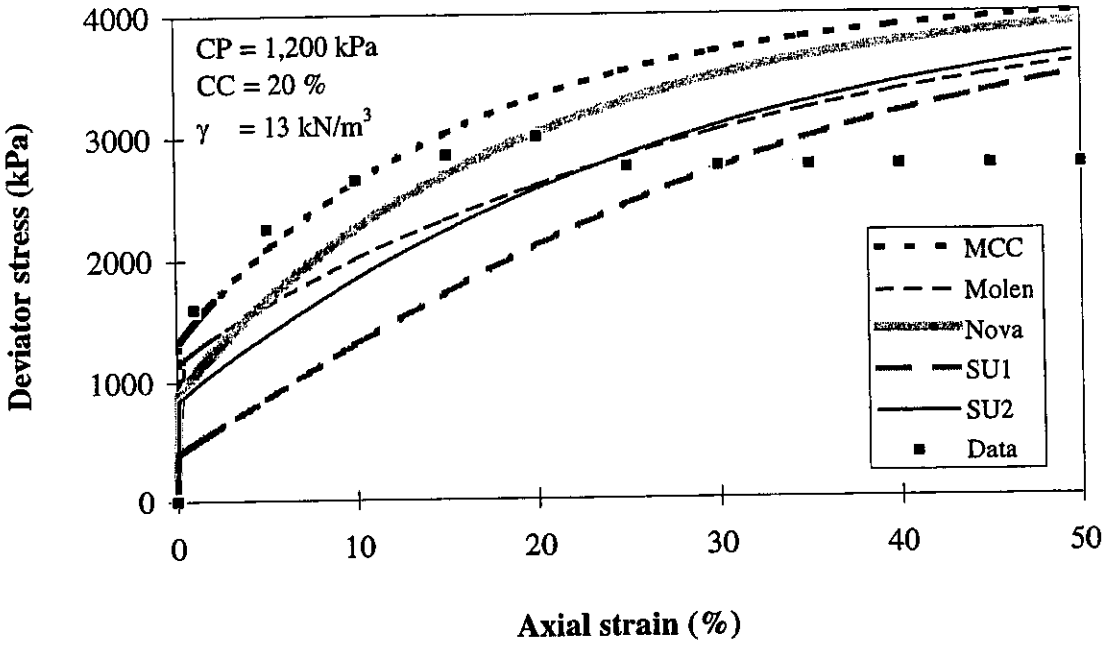

Figure 3.55 Prediction of shear behaviour of loose cemented carbonate sand at 1,200 kPa cell pressure

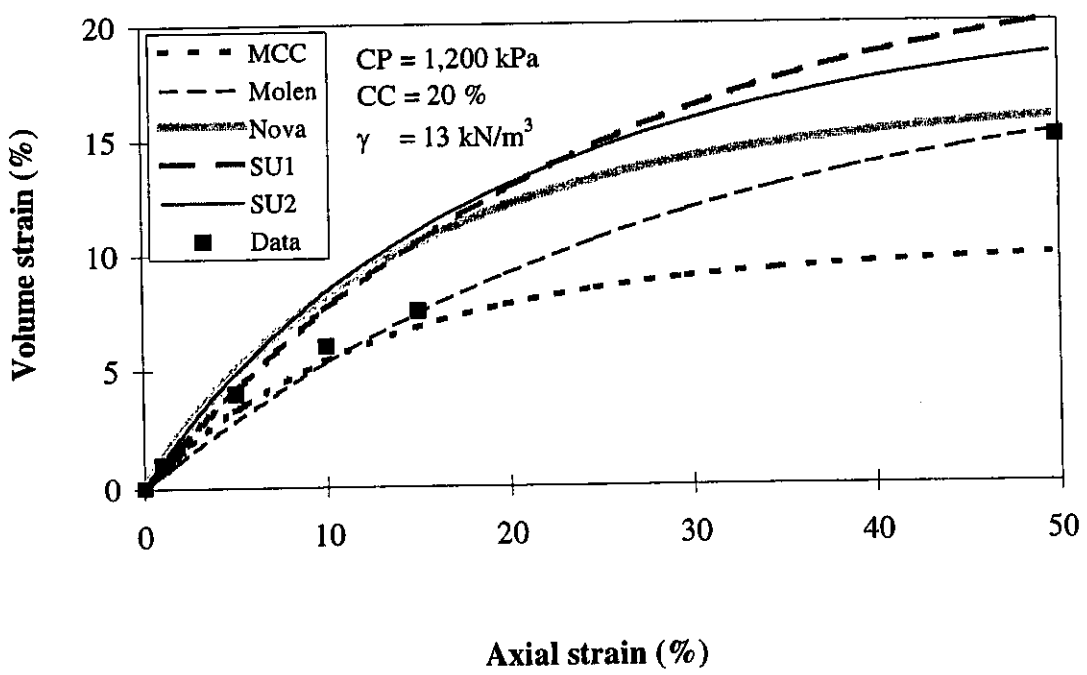

Figure 3.56 Prediction of volume strain behaviour of loose cemented carbonate sand at 1,200 kPa cell pressure

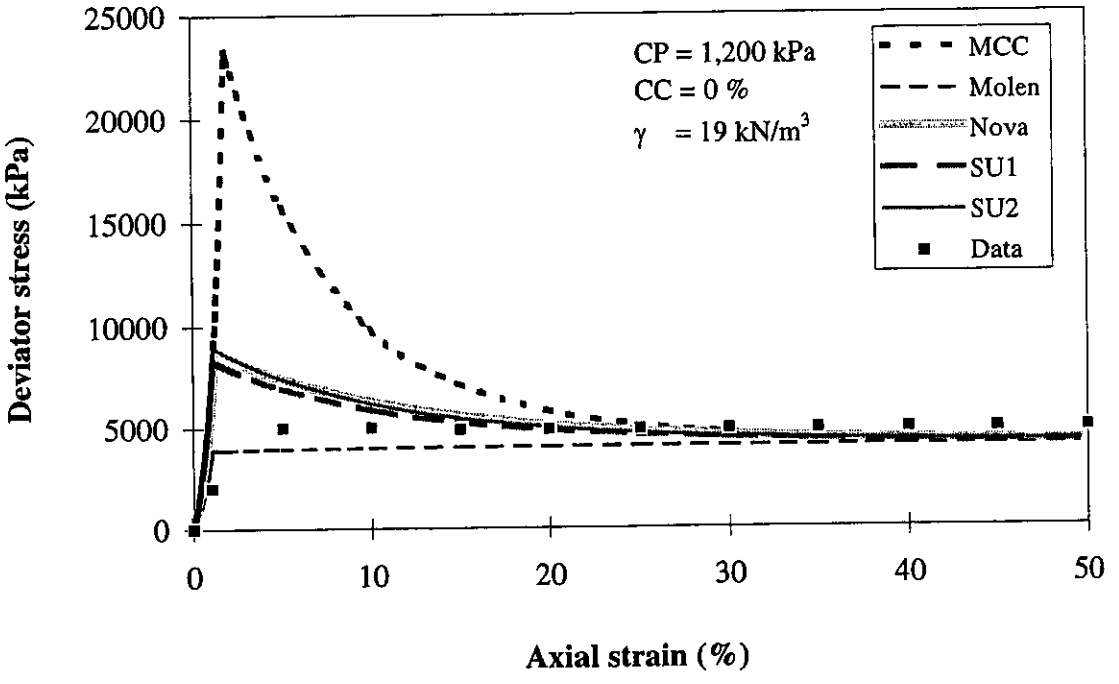

Figure 3.57 Prediction of shear behaviour of dense uncemented carbonate sand at 1,200 kPa cell pressure

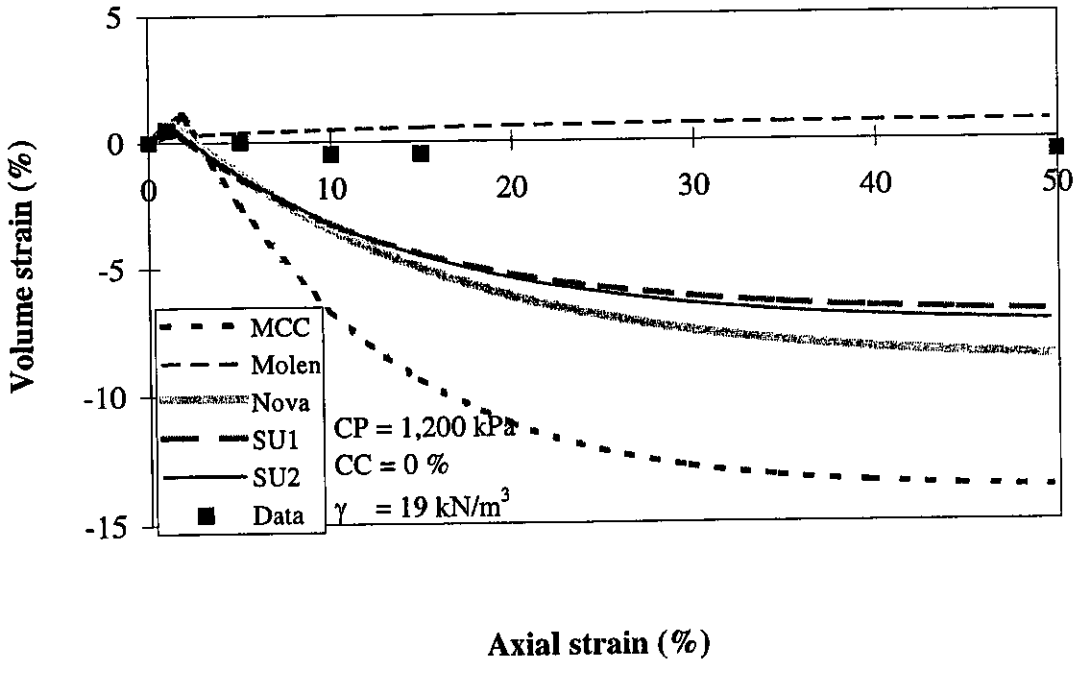

Figure 3.58 Prediction of volume strain behaviour of dense uncemented carbonate sand at 1,200 kPa cell pressure

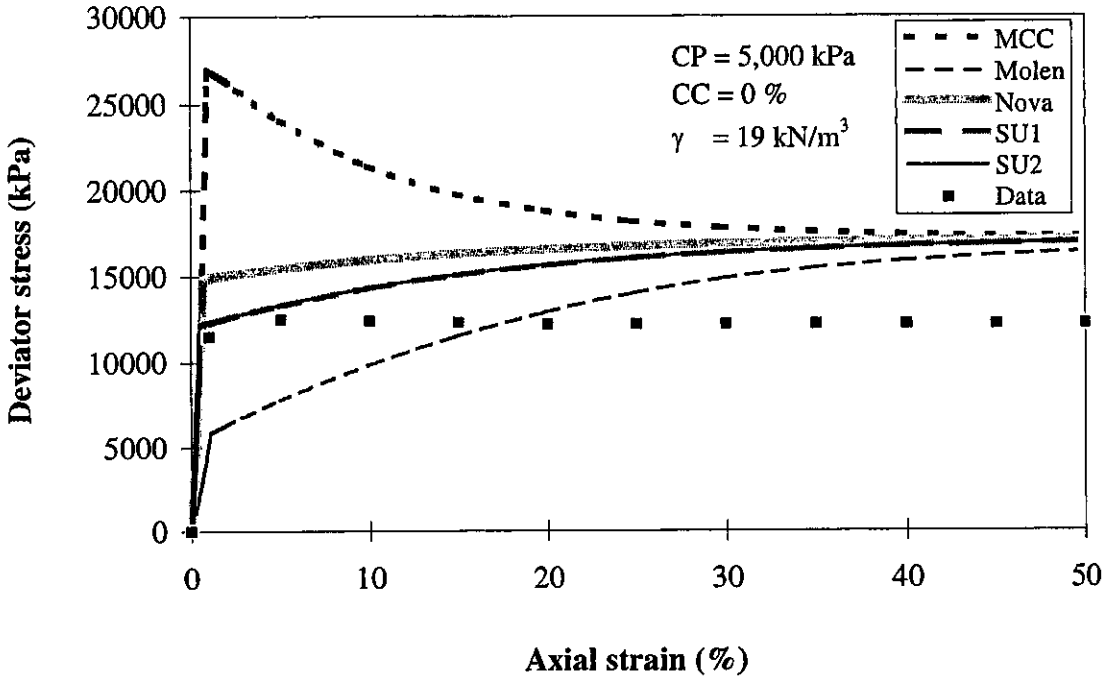

Figure 3.59 Prediction of shear behaviour of dense uncemented carbonate sand at 5,000 kPa cell pressure

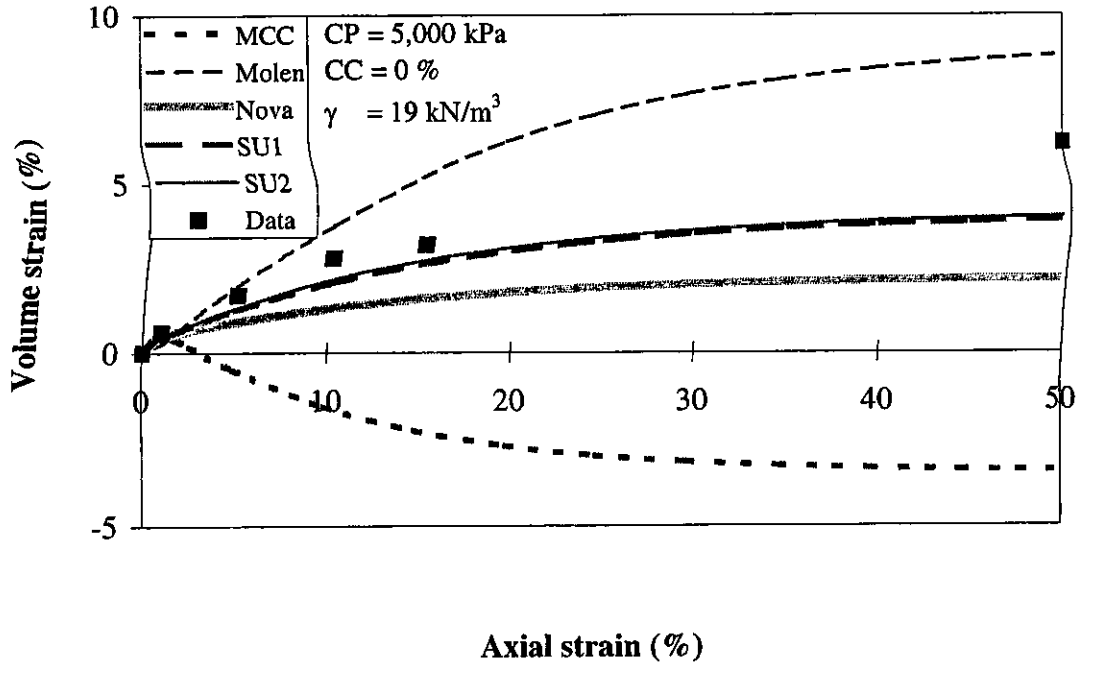

Figure 3.60 Prediction of volume strain behaviour of dense uncemented carbonate sand at 5,000 kPa cell pressure

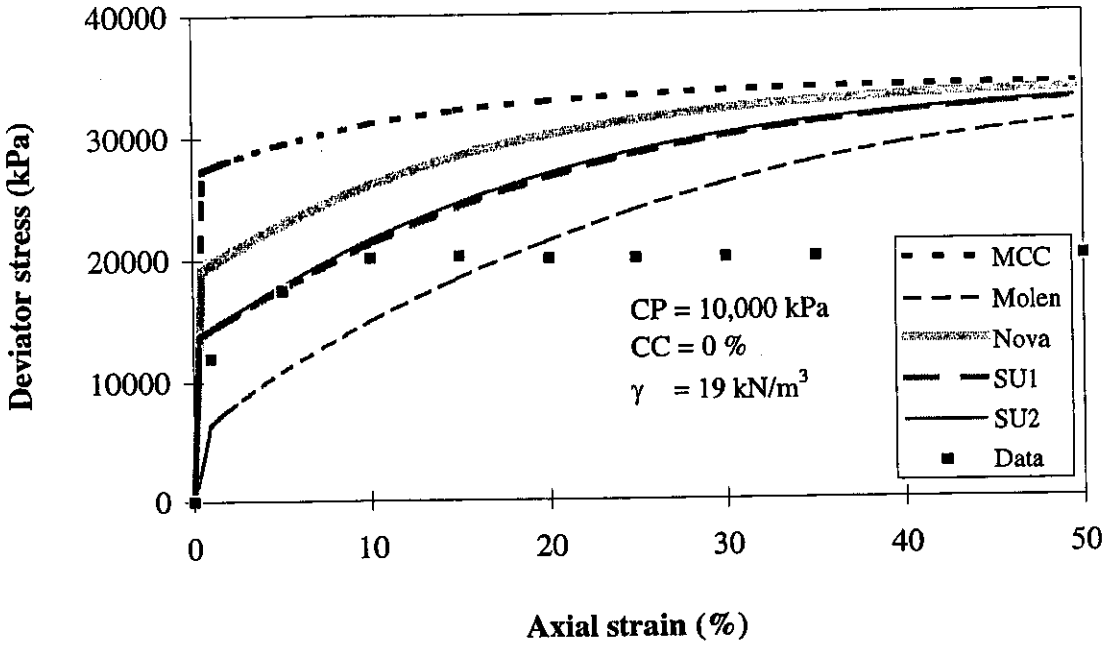

Figure 3.61 Prediction of shear behaviour of dense uncemented carbonate sand at 10,000 kPa cell pressure

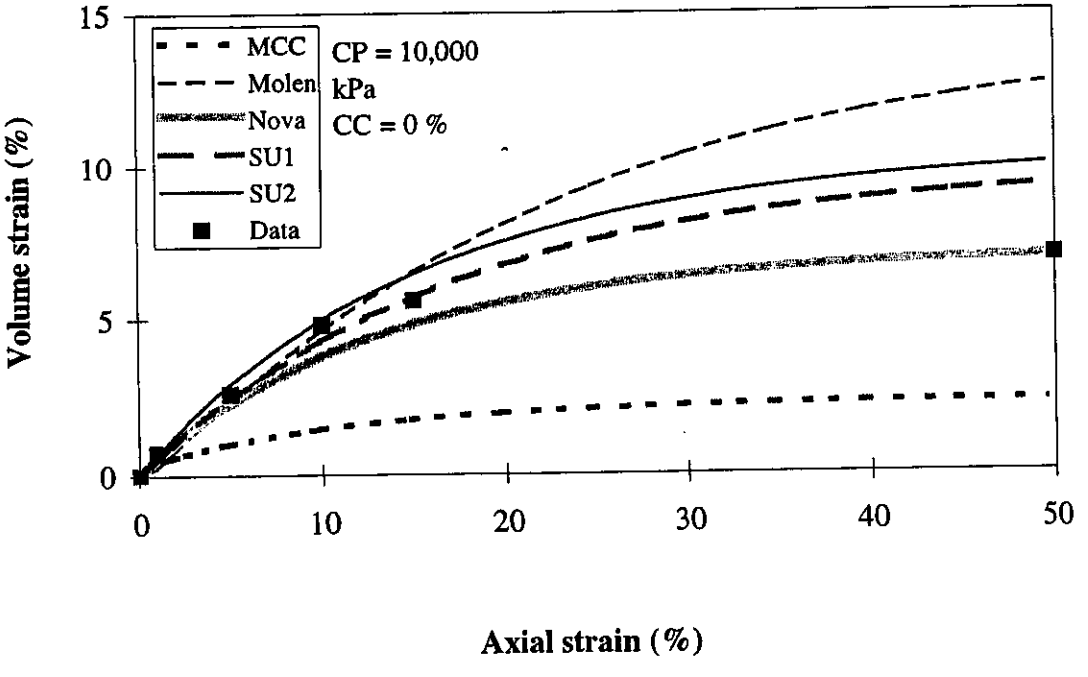

Figure 3.62 Prediction of volume strain behaviour of dense uncemented carbonate sand at 10,000 kPa cell pressure

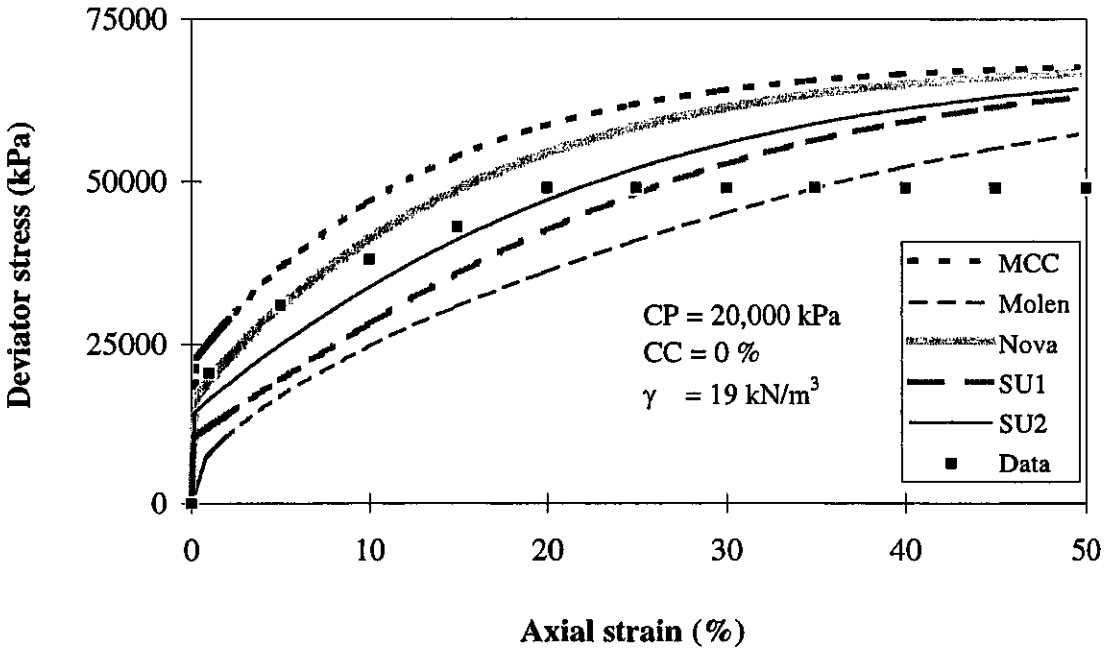

Figure 3.63 Prediction of shear behaviour of dense uncemented carbonate sand at 20,000 kPa cell pressure

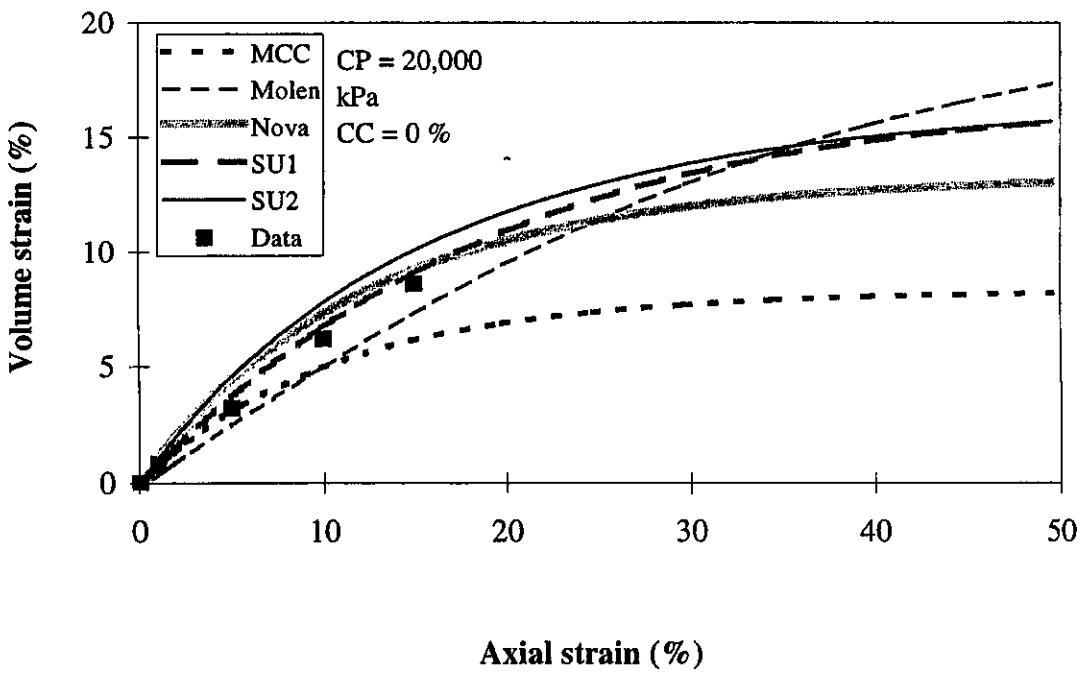

Figure 3.64 Prediction of volume strain behaviour of dense uncemented carbonate sand at 20,000 kPa cell pressure

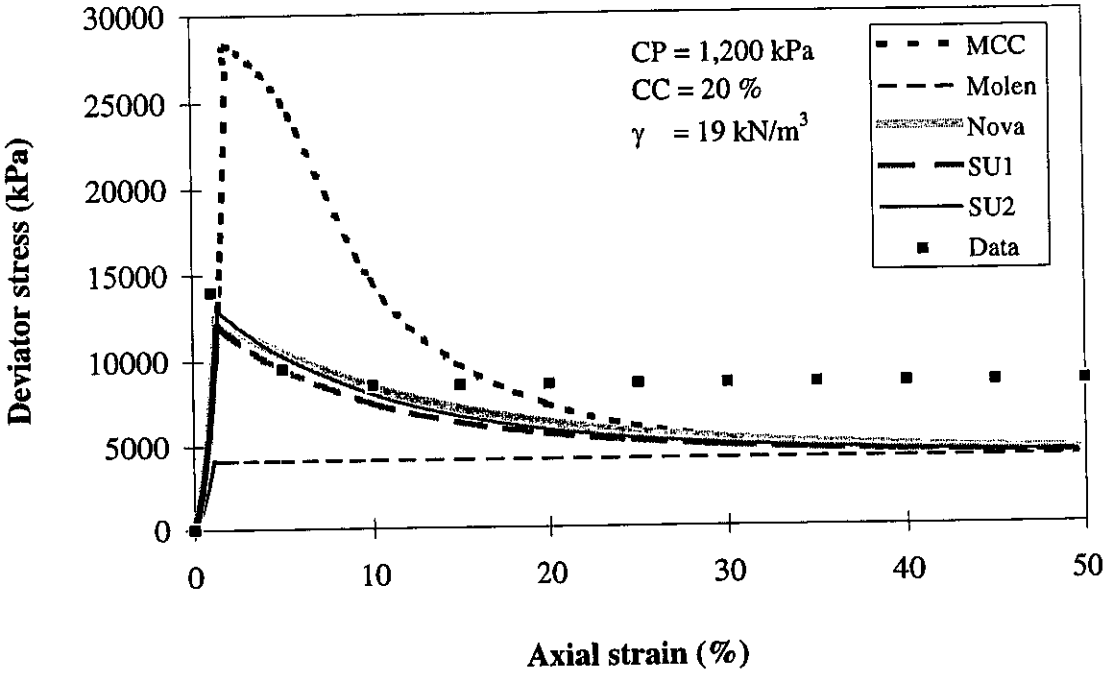

Figure 3.65 Prediction of shear behaviour of dense cemented carbonate sand at 1,200 kPa cell pressure

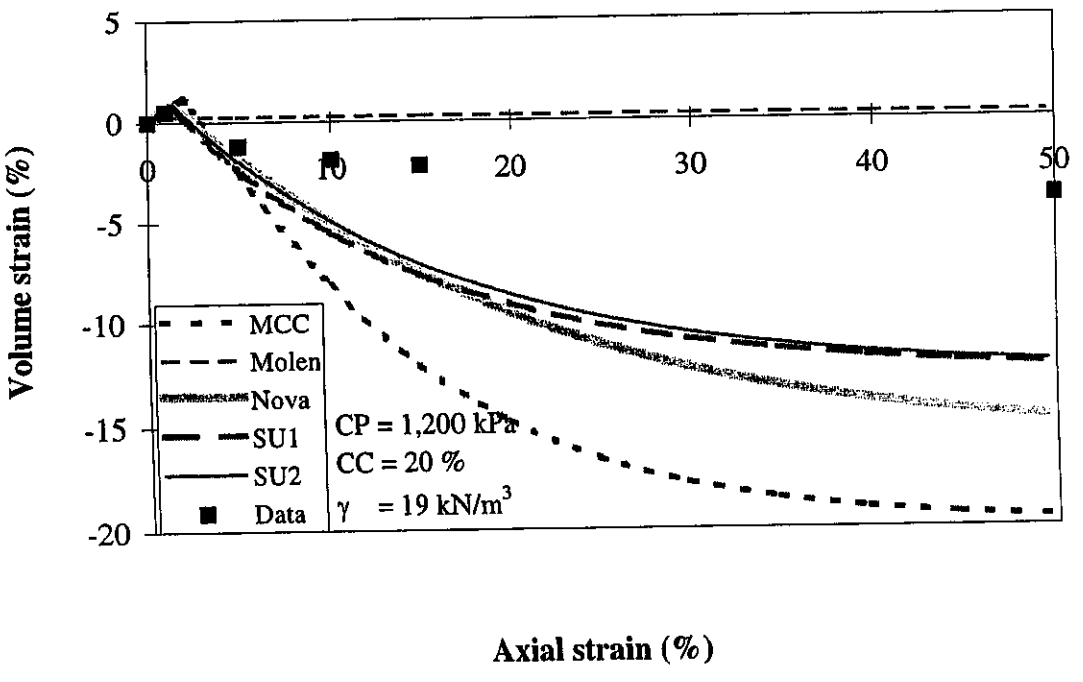

Figure 3.66 Prediction of volume strain behaviour of dense cemented carbonate sand at 1,200 kPa cell pressure

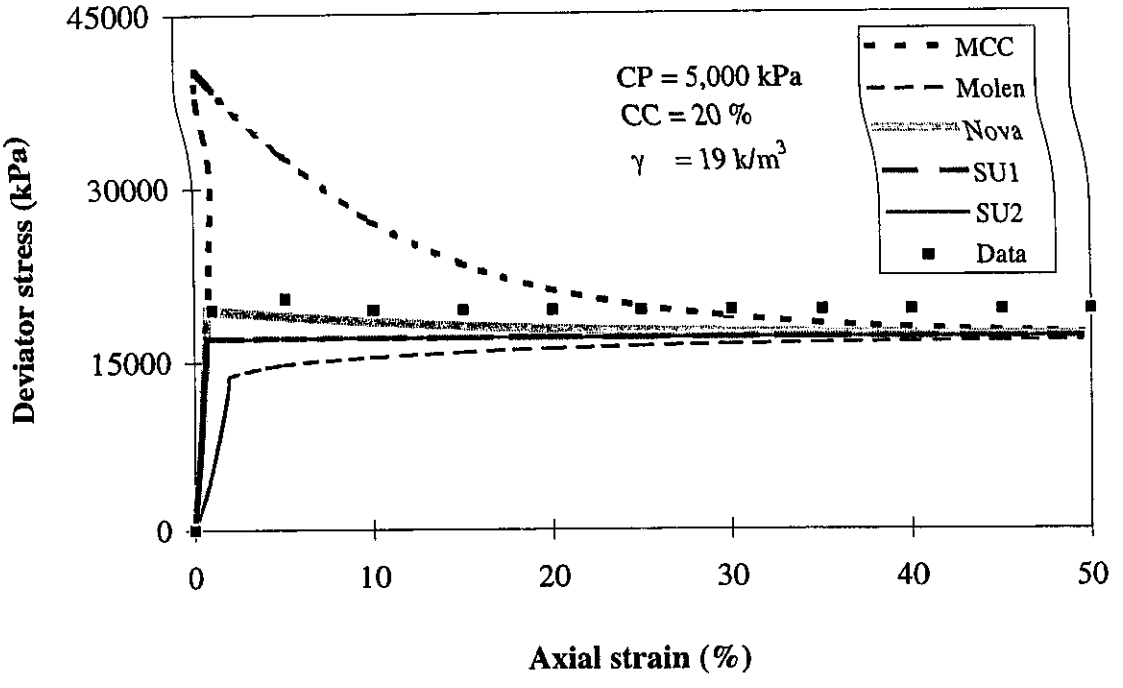

Figure 3.67 Prediction of shear behaviour of dense cemented carbonate sand at 5,000 kPa cell pressure

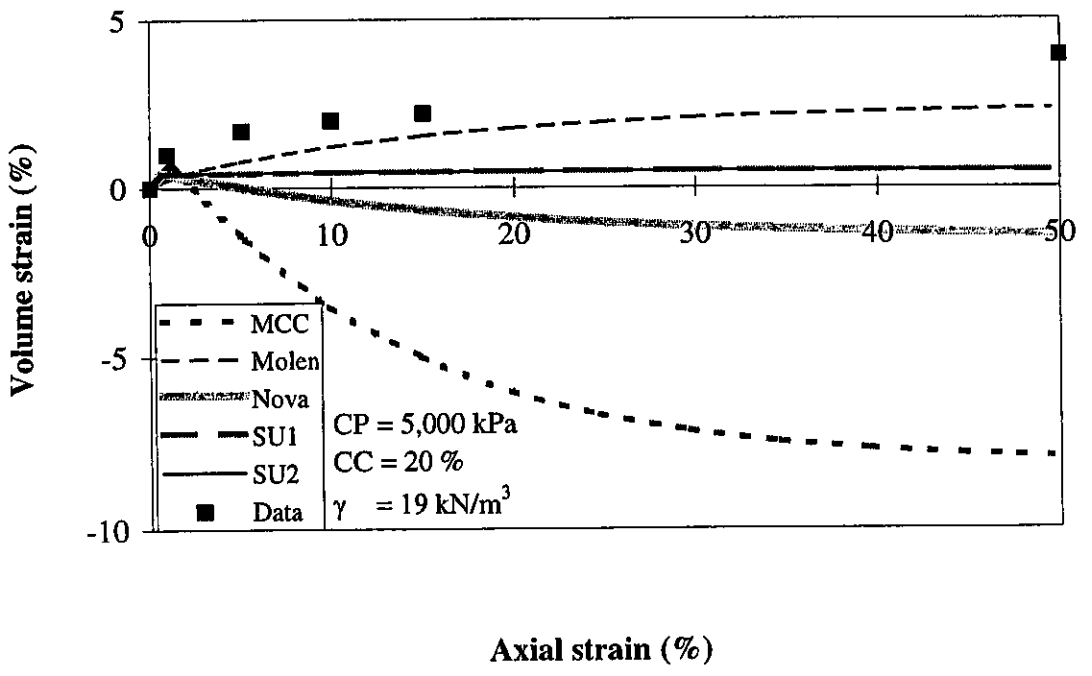

Figure 3.68 Prediction of volume strain behaviour of dense cemented carbonate sand at 5,000 kPa cell pressure

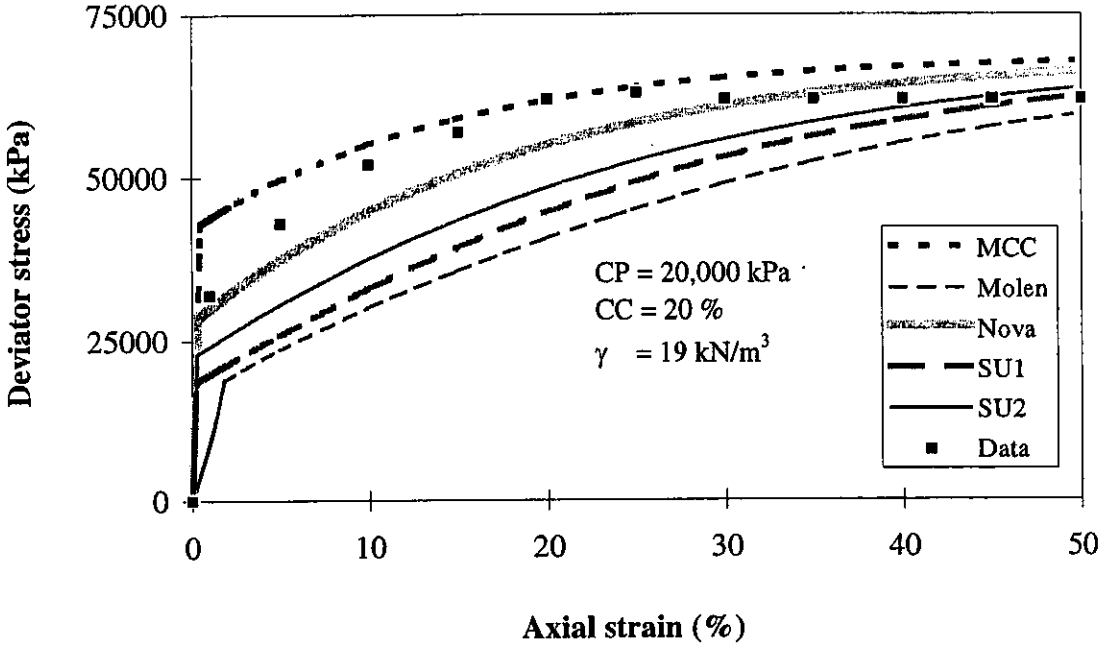

Figure 3.69 Prediction of shear behaviour of dense cemented carbonate sand at 20,000 kPa cell pressure

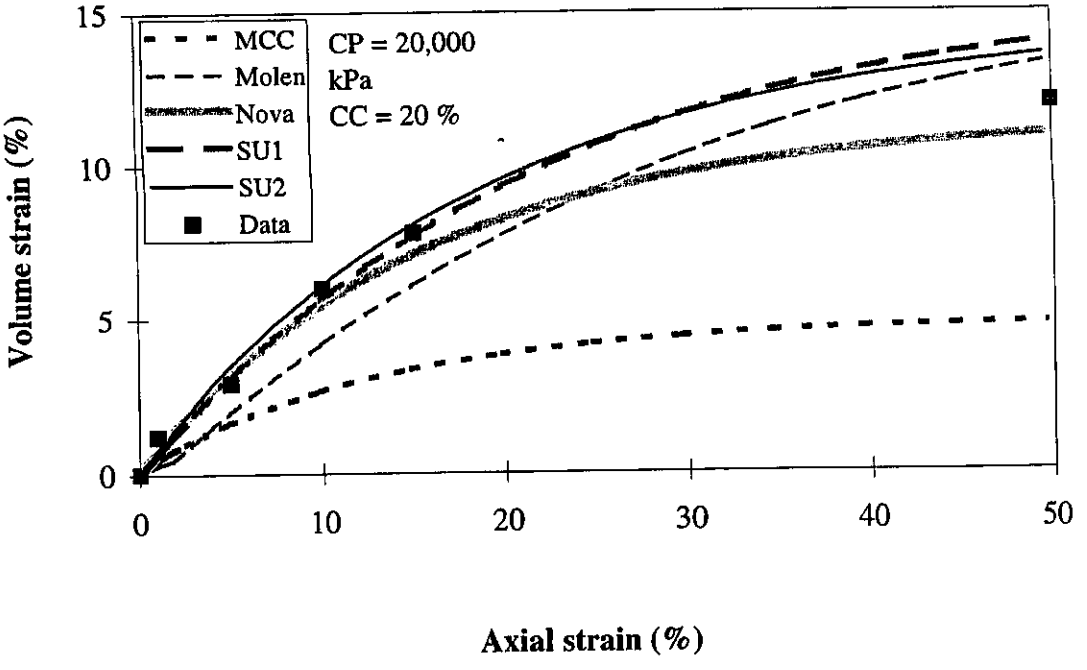

Figure 3.70 Prediction of volume strain behaviour of dense cemented carbonate sand at 20,000 kPa cell pressure

4

ELASTO-PLASTIC ANALYSIS OF CIRCULAR FOOTINGS ON CARBONATE SAND

4.1 INTRODUCTION

The predictive capability of an elasto-plastic constitutive model can be demonstrated by solving typical geotechnical problems using the finite element method. Comparing predictions with laboratory or field data may then validate the model. A typical problem used to check the performance of a constitutive model is the analysis of a uniform horizontal layer of clay or sand strata subjected to vertical loads, similar to those transmitted by a footing.

Carter and Balaam (1995) developed a finite element program named AFENA to study boundary value problems under plane strain and axisymmetric conditions. Three of the five elasto-plastic constitutive models discussed in chapter 3, viz. the Nova, SU1 and SU2 model were incorporated in AFENA by the author to predict the pressure-displacement response of a model-scale footing resting on cemented carbonate sand. In addition, the Modified Cam Clay, Molenkemp and the Mohr-Coulomb models were also used to generate the pressure-displacement response of the model-scale footing. The experimental pressure-displacement response of a model-scale footing resting on cemented carbonate sand was determined by Yeoh and Airey (1996). In this chapter, the predictions of the pressure-displacement response of footings obtained from finite element analysis using

various elasto-plastic models are presented and compared with the predictions of conventional bearing capacity theory as well as with the experimental data.

4.2 MODEL FOOTING EXPERIMENT

The experiments carried out by Yeoh and Airey (1996) on a model-scale circular footings resting on artificially cemented carbonate sand are considered here. The pressure-displacement curves obtained from these experiments were used to validate the elasto-plastic constitutive models described in chapter 3. The experimental results were also used for comparison with predictions of the Mohr-Coulomb model and conventional bearing capacity theory.

In the model footing experiment described by Yeoh and Airey (1996), displacement controlled relatively fast (3.24mm/min) and slow (0.04mm/min) monotonic tests were performed on a model footing under purely vertical load. The soil material under the footing was an artificially cemented carbonate sand. It was a mixture comprising carbonate sand with 20% by weight of gypsum cement and 43% by weight of water. The carbonate sand was obtained from the North Rankin site on the NorthWest Shelf of Australia. Prior to the footing tests, the mixture of soil, gypsum and water was one-dimensionally compressed to a predetermined unit weight of $13kN/m^3$.

Homogeneous cylindrical soil samples, 250mm in diameter and 175mm in height, were made as samples for the model footing tests. The soil cylinder was enclosed within a specially manufactured latex membrane. A geofabric membrane was placed on the top and bottom of the specimen for proper drainage, apart from the area directly under the footing. The 50mm diameter steel footing was sealed to this membrane and placed at the centre of the cylindrical soil specimen. The sample was mounted on a conventional loading frame. An MTS hydraulic actuator loaded the footing axially. The footing load was measured externally as well as internally, from the strain gauges attached to the loading ram. Deformations were measured external to the pressure vessel.

Before commencing the footing test, the samples were allowed to saturate for at least 44hrs, at an elevated back pressure of 500kPa and effective confining stress of 20kPa, and were checked for B values greater than 0.9. The samples were then allowed to consolidate for approximately 4.5 hours under an effective confining pressure of 300 kPa. In all the tests, the primary consolidation was completed within a few minutes. Complete drainage was allowed to occur at all times during the tests.

With the application of vertical load the footing punched into the soil on which it rested. The footing loads continued to increase with increased vertical displacement of the footing. In all cases, the pressure-displacement curve of the footing indicated no clear failure load even though the footings had undergone substantial vertical displacements. The soil adjacent to the footing had moved upward very slightly. In certain tests, this movement was accompanied by radial cracking of the adjacent ground surface. Penetrometer and density measurements in the region immediately below the footing, and in a depth equal to twice the footing diameter showed that the cementation in the soil was broken down. It was observed that the density of the soil immediately beneath the footing had increased to 15kN/m^3. It was also noted that the total volume change occurring in the material was practically identical to the volume of the soil displaced by the footing.

Yeoh and Airey (1996) assumed the bearing capacity of the model-scale footing as the pressure mobilised by the footing at a vertical displacement equal to 10% of the footing diameter. In the next section, the experimentally observed failure load is compared with results obtained using bearing capacity theory. In subsequent sections, the elasto-plastic models discussed in chapter 3 are used in a finite element procedure to simulate the pressure-displacement response of the model-scale footing. The comparison of this response with the experimental data is then used to validate the models.

4.3 CLASSICAL BEARING CAPACITY ANALYSIS

The modes of shear failure generally observed to occur in the soil below a footing are first discussed. The pattern of shear failure observed in the soil below the model-scale footing is then identified. An equation was proposed by Terzaghi ((1943) to determine the bearing capacity of footings on rigid perfectly plastic soils. This equation was later modified by Terzaghi to determine the bearing capacity of footings on compressible soils. In this section, the bearing capacity predicted for the model-scale footing using Terzaghi and Modified Terzaghi method is compared with the available experimental data.

4.3.1 MODE OF SHEAR FAILURE

Bearing capacity failure of shallow footings generally occurs as a shear failure of the soil supporting the footing. The three principal modes of shear failure in soils under footings are as follows: general shear failure (Terzaghi, 1943), local shear failure (Terzaghi, 1943) and punching shear failure (Vesic, 1963a). The mechanism of failure for each mode is schematically illustrated in Figure 4.1.

In the case of a general shear failure, a well-defined failure pattern consisting of a continuous slip surface from one edge of the footing to the ground surface is usually observed. A peak or ultimate load is reached at failure. It is generally accompanied by the appearance of slip lines at the ground surface. There is considerable bulging of the ground around the edges of the footing (Figure 4.1a).

In the case of a local shear failure, a failure pattern is observed only immediately beneath the footing. This pattern consists of wedge and slip surfaces originating at the edge of the footing. There is considerable vertical compression of the footing and the slip surfaces terminate within the soil layer. The slip surfaces may appear on the ground surface,

provided a large vertical displacement of the footing has occurred. In that case there is a visible bulging of the soil adjacent to the footing (Figure 4.1b).

In the punching mode of failure of a footing, no clear failure pattern is observed. The soil beneath the footing is compressed as the footing moves vertically downwards with increasing loads. No visible collapse or tilting of the footing is observed. A continuous increase of load is required to continue the movement of the footing in the vertically downward direction. The soil outside the loaded area is comparatively unaffected by the footing loads. There is practically no movement of the soil on the sides of the footing (Figure 4.1c). Such a mode of failure was observed in the footing test carried out by Yeoh and Airey (1996) on cemented carbonate sand.

In the case of local or punching shear failures, failure cannot be clearly defined in terms of an ultimate or peak load. In those cases, the loads generally continue to increase with vertical displacement of the footing. The failure mode that will occur in a particular case generally depends on the relative compressibility of the soil under the given geometric and boundary conditions. Relatively incompressible soils having finite shear strength usually exhibit general shear failure, while highly compressible soils generally exhibit failure by punching shear. Thus a footing resting on very dense sand will normally fail in general shear. The same footing resting on a loose and compressible soil such as carbonate sand will fail by punching shear.

4.3.2 BEARING CAPACITY EQUATION

The conventional theory of bearing capacity of soils used to compute the ultimate loads of a shallow footing is based on the classical theory of plasticity. It is assumed that the soil is a rigid-plastic solid and there is no deformation of the soil prior to shear failure. The soil is assumed to flow plastically at constant stress after failure. In the strict sense, the conventional bearing capacity theory can only predict the bearing capacity of relatively

incompressible soils, exhibiting the general shear failure mode. In practice, it is common to use such solutions for compressible soils as well. Empirical reduction factors are generally used to account for the effect of compressibility. This, in effect, allows for the reduced loads required to generate a limiting settlement.

The bearing capacity of a shallow footing of width B resting in a semi-infinite homogeneous soil mass is given by the Buisman-Terzaghi equation as follows:

$$q_{av} = cN_c\zeta_c + \sigma'_v N_q \zeta_q + \frac{1}{2}\gamma' B N_\gamma \zeta_\gamma \tag{4.1}$$

The soil is assumed to have an effective unit weight of γ' and the Mohr-Coulomb criterion defines its shear strength properties. The Mohr-Coulomb envelope is defined by the parameters c and ϕ. In a plot of shear versus normal stress stress, c is the intercept of the Mohr-Coulomb line on the shear axis and defines the cohesive strength of the soil. ϕ is the slope of the Mohr-Coulomb line defining the effective friction angle. The overburden pressure on the soil at depth D is represented by a uniform surcharge σ'_v, where:

$$\sigma'_v = \gamma' D . \tag{4.2}$$

N_c, N_q and N_γ are dimensionless bearing capacity factors. The equations for the bearing capacity factors as reported by Vesic (1975) are given below in Table 4.1.

Table 4.1 Bearing capacity factors

N_c	N_q	N_γ
$(N_q - 1)\cot\phi$	$e^{\pi \tan\phi} \tan^2(\pi/4 + \phi/2)$	$2(N_q + 1)\tan\phi$

Several authors have suggested different expressions for the shape factors ζ_c, ζ_q, and ζ_γ for a circular footing. Two of these are given below in Table 4.2.

Table 4.2 Shape factors for circular footing

Method	ζ_c	ζ_q	ζ_γ
Hansen (1970)	$1+\frac{N_q}{N_c}$	$1+\tan\phi$	0.60
Meyerhoff (1963)	$1+0.2N^*_\phi$	$1+0.1N^*_\phi$, $(\phi>10^o)$	$1+0.1N^*_\phi$, $(\phi>10^o)$

$* \; N_\phi = \tan^2\left(\frac{\pi}{4}+\frac{\phi}{2}\right)$

The calculation of the bearing capacity of a footing using the Terzaghi-Buismann equation is generally known as the Terzaghi method.

Currently there does not exist any rational method to analyse the bearing capacity failure of shallow footings for the local and punching shear failure mode, which is characteristic of footings on compressible soils such as carbonate sand. For compressible soils, Terzaghi (1943) proposed to use the same bearing capacity equation (4.1) with reduced strength parameters c^* and ϕ^* defined as follows:

$$c^* = 0.67c \tag{4.3}$$

$$\phi^* = \tan^{-1}(0.67\tan\phi) \tag{4.4}$$

The bearing capacity of a footing calculated using the reduced strength parameters given by equations (4.3) and (4.4) is generally known as the Modified Terzaghi method.

4.3.3 BEARING CAPACITY PREDICTION

The reduction factors proposed by Terzaghi and given by equations (4.3) and (4.4) were applied to the cohesion c and peak friction angle ϕ computed for the artificially cemented carbonate sand by Yeoh (1996). The original and reduced strength parameters computed for the peak strength of the artificially cemented carbonate sand observed in triaxial tests are given in Table 4.3 below.

Table 4.3 Original and reduced Mohr-Coulomb strength parameters

Carbonate sand	c (kPa)	ϕ (degrees)	c^* (kPa)	ϕ^* (degrees)
Cemented	400.0	23.0	266.7	15.8

For a surcharge pressure of 300 kPa, the bearing capacity of the model-scale circular footing was computed using the Terzaghi and Modified Terzaghi method. The surcharge pressure and footing diameter considered were the same as that used by Yeoh and Airey (1996) in the model footing experiments on carbonate sand described in section 4.2. The shape factors used for the circular footing are those proposed by Hansen (1970) and Meyerhoff (1963), which are given in Table 4.2. The bearing capacities computed for the model-scale footing using the Terzaghi and Modified Terzaghi method and their comparison with test data are given in Table 4.4. As no clear failure load could be observed in the footing experiment, Yeoh and Airey (1996) assumed the bearing capacity as the pressure mobilised by the model-scale footing at a vertical displacement equal to 10% of the footing diameter.

4.4.1 NUMERICAL MODEL

The footing was assumed to be a smooth, rigid and uniformly loaded plate of zero thickness resting on a finite, effectively weightless and uniform layer of carbonate sand. It was assumed that the footing is resting on a perfectly smooth base. The footing load was simulated by uniform vertical displacements that were specified incrementally on the soil surface below the footing. The rest of the top boundary of the soil cylinder was assumed to be free, without any displacements being prescribed on them. The bottom boundary of the soil strata was constrained from moving both in the vertical and lateral direction. The vertical boundary of the soil cylinder was assumed to be perfectly smooth and rigid, free to move vertically but constrained from moving in the lateral direction. The diameter of the footing was 50mm, and the depth of the soil cylinder was 175mm, which is 3.5 times the diameter of the footing. The diameter of the soil cylinder was 250mm, which is equal to 5 times the diameter of the footing. Figure 4.2 illustrates the dimensions and geometry used in the model footing experiments. An initial isotropic effective stress of 300 kPa was generated throughout the soil cylinder. An equivalent nodal load was applied at the boundaries to maintain equilibrium. The footing dimensions and isotropic pressure used in the numerical model were exactly identical to those used in the footing tests carried out by Yeoh and Airey (1996).

An incremental Euler integration scheme was used in the present analysis. In such an analysis, the tangent stiffness at the beginning of an increment is directly utilised to obtain a linear approximation of the incremental response. For some problems, the initial stiffness approach was employed. At each increment a very small displacement was used to obtain an accurate solution.

The numerical model for the footing test carried out by Yeoh and Airey (1996) has been defined. The next section describes generation of the finite element mesh used to define the problem geometry. The mesh was used for subsequent finite element simulation of the footing problem using various elasto-plastic constitutive models.

4.4.2 FINITE ELEMENT MESH

The discretisation of the domain geometry of the model-scale footing experiment using finite elements is described in this section. Such a discretisation is necessary for finite element simulation of the pressure-displacement response of the model-scale footing.

Elements consisting of 8 node quadrilaterals with quadratic interpolation functions and 15 node triangles with fourth order polynomials as interpolation functions for displacements were used to construct separate finite element meshes for the footing problem. 8 node serendipity elements have been reported to give reasonably accurate results for the general analysis of frictional, dilatant solids under plain strain as well as axisymmetric conditions (Zienkiewicz, Humpheson and Lewis, 1975: Griffiths, 1982; Smith, 1982 and de Borst and Vermeer, 1982). A mesh consisting of a total of 272 quadrilateral elements having a total of 883 nodes was used to generate the geometry of the model footing experiment. Figure 4.3 illustrates the mesh used, while Figure 4.4 shows a single 8 node quadrilateral element used in the given mesh.

Sloan and Randolph (1982) and de Borst (1982) reported that only 15 node triangular elements give accurate predictions of collapse loads for axisymmetric footings. According to Sloan and Randolph (1982), this is particularly true for undrained problems. In that case, the constant volume condition is enforced point by point at all the elements for the entire range of loading. The pressure-displacement response of the experimental model-scale footing was generated under fully drained condition. Under drained conditions, 15 node triangular elements may not be a necessary requirement to obtain accurate predictions of the response of a footing. However as a check, a mesh consisting of 544, 15 node triangular elements with a total of 4485 nodes was also used to simulate the response of the model-scale footing. Figure 4.5 illustrates the given mesh, while Figure 4.6 shows a single 15 node triangular element used in the mesh. The drained response obtained for the model-scale footing using 8 node quadrilateral and 15 node triangular elements was then compared.

Complete 3x3 Gaussian integration was employed for the quadrilateral elements. 16 point Gaussian integration was employed in case of the triangular elements. A graded mesh was used with finer mesh divisions constructed immediately adjacent to the footing. The meshes were made progressively coarser with increasing distance from the edge of the footing. This was done both laterally away and vertically downward from the footing. The finest mesh was used at the corner of the footing, where there is a singularity i.e. a sudden jump of the boundary conditions, from loading to zero loads.

The generation of the finite element mesh for the model-scale footing has been described. The next section describes the various constitutive models that were used in the finite element analysis to simulate the pressure-displacement response of the model footing.

4.5 ELASTO-PLASTIC ANALYSIS

The computation of ultimate load for a shallow footing resting on a soil mass is in principle a problem of elasto-plastic equilibrium. The most important issue in solving such a problem is to formulate a suitable mathematical or constitutive model to define the stress-strain relationship of the soil. The constitutive models and the corresponding model parameters used for finite element analysis of the model-scale footing is discussed in the following subsections.

4.5.1 CONSTITUTIVE MODELS

Six different elasto-plastic models were used to generate the pressure-displacement relation of the given footing using the finite element method, under the assumption of small strain. The following models were used in the finite element analysis:

1. The Mohr-Coulomb model

2. The Modified Cam Clay model
3. The Molenkamp model
4. The Nova model
5. The SU1 model and
6. The SU2 model

The Mohr-Coulmb is an elastic perfectly plastic model. The remaining five are critical state, isotropic strain-hardening elasto-plastic constitutive models. The five critical state models have been described in detail in chapter 3. For the finite element analysis using the Nova, SU1 and SU2 models, a stress-correction in the direction of the incremental plastic strains was applied, as suggested by Potts and Gens (1985). These models as well as their stress correction schemes were implemented in the finite element program AFENA by the author. In AFENA, stresses are corrected at constant mean pressure in the Mohr-Coulomb model. In the AFENA implementation of the Modified Cam Clay, as in other implementations, e.g. CRISP (Briito and Gunn, 1987), no true stress-correction is applied. Instead, the hardening parameter is adjusted so that the yield locus always satisfies the current state of stress. In the Molenkamp model the stresses are corrected back to the yield surface using a correction method proposed by Molenkamp (1981).

The constitutive models used to simulate the pressure-displacement response of the model footing have been described. The next section describes the assessment of the model parameters for the artificially cemented carbonate sand.

4.5.2 MODEL PARAMETERS

It is very important to generate appropriate model parameters for the artificially cemented carbonate sand used in the footing experiment. Only then can each of the constitutive models be expected to generate the appropriate pressure-displacement response of the model-scale footing. The appropriateness of the respective models may then be verified by comparing its response with experimental data.

The soil used by Yeoh and Airey (1996) for the model-scale footing experiment was carbonate sand obtained from the North West Shelf of Australia. It was artificially cemented in the laboratory with 20% gypsum. A standard and modified grading for the carbonate sand was used in their experiment. As appropriate data for determining model parameters of critical state models for the modified grading was not available, simulation for a footing resting on soil of modified grading was not generated.

For triaxial experiments, Huang (1994) used carbonate sand with the same standard grading and density. Huang (1994) artificially cemented it in the laboratory with gypsum, following a procedure identical to that of Yeoh and Airey (1996). The material parameters for each model were computed for the artificially cemented carbonate sand using the triaxial test data of Huang (1994). The parameters were generated either directly from laboratory data or by matching the model triaxial simulation with experimental results. The method of obtaining the material parameters for the critical state models has been described in detail in chapter 3. The values of the model parameters for various models for the artificially cemented carbonate sand are listed in Tables 4.5 to 4.8 below.

Table 4.5 Modified Cam Clay model parameters

λ	κ	M_g	e_{cs}	p_o' (kPa)
0.213	0.0072	1.6	2.47	1750
ν				
0.1				

Table 4.6 Molenkamp model parameters

ν	A	AP	B	BP
0.1	0.000554	0.8	0.0019	0.8
C	CP	DP	$PHIMU$	$PHICV$
0.75083	1.0	0.198	39	39
SCV	VGC	VGP	NU	EE
1000	0.0	1.0	0.0	0.247
EP	LB	N	CG	CV
2.7	0.3	7	0.8	0.8
RT	$PARCI$	$PARDI$		
0.3	3031.1	4.78		

Table 4.7 Nova model parameters

B_p	B_e	ν	γ	β
0.098	0.0034	0.1	4.77	1.4
p_o' (kPa)	ζ			
1750	0.0			

Table 4.8 SU1 and SU2 model parameters

λ	κ	M_g	e_{cs}	p_o' (kPa)
0.213	0.0072	1.6	2.28	1750
ν	r			
0.1	5.0			

The five critical state models used here do not have cohesion as a model parameter. Thus the cohesion component of the artificially cemented carbonate sand was not taken into consideration in these models. Critical state models usually use the constant volume friction angle of the soil. This was computed to be 39 degrees for the artificially cemented carbonate sand used by Yeoh and Airey (1996). The Mohr-Coulomb model, on the other hand, has both cohesion and friction angle as model parameters. The Mohr-Coulomb parameters computed by Yeoh (1996) for the artificially cemented carbonate sand have been given in Table 4.3. The friction angle of 23 degrees given in this table is the peak friction angle obtained from the Mohr-Coulomb envelope. It is not the ultimate or constant volume friction angle defined in critical state models. The model parameters used for the Mohr-Coulomb are given below in Table 4.9.

Table 4.9 Model parameters for the Mohr-Coulomb model

E (MPa)	ν	c (kPa)	ϕ (degrees)	ψ (degrees)
580.0	0.1	400.0	23.0	23.0

In Table 4.9, E is the Young's modulus of elasticity, ν is the elastic Poisson's ratio, c is cohesion, ϕ is the friction angle and ψ is the dilation angle. . An associated Mohr-Coulomb model was used in the finite element analysis $(\phi = \psi)$.

The generation of model parameters for the elasto-plastic constitutive models has been described. The next section describes the simulation of the pressure-displacement response of the model-scale footing using the various models.

4.6 PRESSURE-DISPLACEMENT CURVES

The drained pressure-displacement curve of the model-scale footing was simulated using various elasto-plastic models in the following way. Uniform vertical displacements were applied to the rigid footing in an incremental fashion. The average pressure on the footing at the corresponding displacements was computed. The response predicted by the elasto-plastic models, as well as the experimental data, were plotted with average footing pressure on the ordinate and displacement as a percent of the footing diameter, on the abscissae. The model predictions were then compared with experimental data. The comparisons of the pressure-displacement response with experimental data are described in the following subsections.

4.6.1 MOHR-COULOMB MODEL

The associated Mohr-Coulomb model showed perfectly plastic behaviour at a vertical displacement of less than 5 percent of the footing diameter. The footing collapse load was obtained using both 8 node quadrilateral and 15 node triangular elements in the finite element analysis. This was done to investigate whether there was a significant difference between the two. Some difference was observed. The collapse load obtained using the 15 node triangular element was found to be very close to the values computed from the

conventional bearing capacity equation using the shape factors for circular footings proposed by Hansen (1970). The bearing capacities obtained using these two elements and the associated Mohr-Coulomb model are compared in Table 4.10 given below.

Table 4.10 Comparison of bearing capacity obtained using 8 and 15 node elements

Mohr-Coulomb 15 node triangle (MPa)	Mohr-Coulomb 8 node quadrilateral (MPa)	Hansen (MPa)	Meyerhoff (MPa)	Test data (MPa)
14.5	15.2	14.4	13.7	5.1

Figure 4.7 shows the pressure-displacement curves obtained using the Mohr-Coulomb model and their comparison with the experimental data for the model-scale footing. The collapse load obtained using the Mohr-Coulomb model was observed to be much larger than the mobilised footing pressures obtained from the experiments.

4.6.2 STRAIN-HARDENING MODELS

The pressure-displacement curves obtained for the model-scale footing using single surface strain-hardening models such as the Modified Cam Clay, Nova, Molenkamp, SU1 and SU2 are described in this section.

As before, the pressure-displacement curve of the footing was obtained using both 8 node quadrilateral and 15 node triangular elements in the finite element analysis. The purpose was to investigate whether there was any difference between the predictions of the pressure-displacement response when using the same model. Figure 4.8 gives a comparison of the pressure-displacement curves obtained for the model-scale footing using the SU2 model. Little difference in the predictions is observed. Therefore, the drained analysis of the bearing response of circular footings using strain-hardening models was assumed to be sufficiently accurate when using 8 node quadrilateral elements.

All the critical state models exhibited an approximately bilinear type of pressure-displacement relationship (Figure 4.9). For a displacement of up to 3% to 4% of the footing diameter, the footing exhibited a stiff linear response, with the pressure-displacement curve passing through the origin. For larger displacements, the models exhibited a sharp bend in the linear pressure-displacement curve, and a consequent sharp decrease in the stiffness. The pressure-displacement responses of the footing continue to follow an approximately linear curve but with sharply decreased stiffness. The linear part of this pressure-displacement curve extrapolated backward no longer passes through the origin. Instead it has an intercept on the pressure axis.

The critical state models exhibited a continuing rise in the pressure-displacement curve, even after reaching displacements of 30% relative to the footing diameter. This behaviour is similar to that observed in the footing experiment. Although all the models simulated qualitatively similar behaviour, there was some difference in their quantitative responses. At all displacements, the Modified Cam Clay model predicted a bearing pressure larger than the other critical state models. The larger yield surface of the Modified Cam Clay compared to Nova, SU1 and SU2 possibly results in a higher yield pressure. The higher initial yield point resulted in the subsequent prediction of a larger bearing pressure at all displacements. All of the non-associated critical state models, namely Molenkamp, Nova, SU1 and SU2, exhibited pressure-displacement curves close to the experimentally observed behaviour of the footing. These models provide better predictions of the experimental data, both qualitatively and quantitatively, than the perfectly plastic Mohr-Coulomb and the Modified Cam Clay model.

It was observed from Figure 4.9 that, the SU1 and SU2 models slightly under-predict the bearing pressure mobilised by the model-scale footing. It was illustrated in the previous chapter that the SU1 and SU2 yield loci match quite well, both in size and shape, the experimental yield loci of uncemented carbonate sand. However it was shown in chapter 3 that, the yield locus of loose cemented carbonate sand at 20% cement content shows a significant increase in size, as well as a change in shape, in the deviator direction. This

change in shape and size of the yield locus in the deviator direction due to cementation is not currently taken into account in the SU1 and SU2 models. This may be a possible reason for the somewhat lower predictions of the bearing pressures when using these two models. Relatively better prediction of the pressure-displacement response of the model-scale footing is obtained using the Nova model, compared to SU1 and SU2. This is possibly due to the larger size of the initial yield locus in the deviator direction in the Nova model, which is determined by the value of the model parameter β.

The Molenkamp model has two yield surfaces and assumes deviator or shear strain hardening for the deviator yield surface. For the given surcharge pressure of 300 kPa, the artificially cemented carbonate sand used in the footing experiments was highly overconsolidated. For such a material, it is likely that the deviator yield surface of the Molenkamp model will control the plastic response of the footing. In the Molenkamp model, as the deviator yield surface strain hardens, it asymptotically approaches the Mohr-Coulomb line. The deviator yield surface then becomes identical to a non-associated Mohr-Coulomb envelope with zero dilation angle. Predictions of unstable footing response have been observed by de Borst and Vermeer (1984) when using the non-associated Mohr-Coulomb model with high friction and zero dilation angle. Thus the predictions of footing response using the Molenkamp model for a high friction angle soil, such as carbonate sand, may also be unreliable at larger displacements, where zero dilatancy applies.

It has observed that non-associated critical state models, viz. the Nova, Molenkamp, SU1 and SU2 models, can predict reasonably well the pressure-displacement response of footings on artificially cemented carbonate sands. In the next section, the bearing capacity of the model-scale circular footing predicted using each of these models is compared with experimental data.

4.7 COMPARISON OF BEARING CAPACITY PREDICTIONS

The bearing capacity of the model-scale footing was estimated from the pressure displacement curves simulated by the various elasto-plastic models. The bearing capacity was also computed using the Terzaghi and Modified Terzaghi method. These predictions were then compared with the experimental data.

Consistent with experimental observations, critical state models predict a continuously increasing pressure-displacement curve for the model-scale footing. In such cases, the bearing pressure mobilised at a displacement of 10% of the footing diameter is often defined as the bearing capacity. Based on this definition, the bearing capacity was estimated from the pressure-displacement curve predicted for the model-scale footing using the various critical state models.

In the case of the Mohr-Coulomb model, the clearly identified collapse load defines the bearing capacity. The bearing capacity for the model-scale footing was also computed using the Terzaghi and Modified Terzaghi method. The bearing capacity computed by each of these methods is compared with the experimental data in Table 4.11.

Table 4.11 Comparison of predicted bearing capacity with experimental data

Model	Bearing capacity (MPa)	Experimental data (MPa)
Mohr-Coulomb	14.5	5.1
Modified Cam Clay	7.1	
Molenkamp	5.2	
Nova	4.4	
SU1	3.6	
SU2	3.7	
Modified Terzaghi (Hansen shape factors)	5.9	
Modified Terzaghi (Meyerhoff shape factors)	5.7	

Table 4.11 shows again that the collapse load predicted by the Mohr-Coulomb model for the model-scale footing is significantly larger than the bearing capacity obtained from the experimental pressure-displacement curve. The Molenkamp, Nova, SU1 and SU2 models give reasonable estimates of the bearing capacity of the footing. It is interesting to note that the Modified Terzaghi method also provides a reasonable estimate of the bearing capacity of the model-scale footing.

Values of the bearing capacity of the model-scale footing predicted by various elasto-plastic models and the Modified Terzaghi method were compared. It was observed that the non-associated critical state models, as well the conventional bearing capacity equations taking into account compressibility effects, provide a reasonable estimate of the observed bearing capacity of the footing.

4.8 ADDITIONAL OBSERVATIONS FROM FE ANALYSIS

The spread of plastic or yield zone and the velocity fields in the soil beneath the footing, as predicted from finite element analysis using various elasto-plastic models, is investigated in the following subsections.

4.8.1 YIELD ZONE

For the perfectly plastic Mohr-Coulomb model, a Gauss point is assumed to be plastic when it touches the Mohr-Coulomb line. The Gauss point in this case will have zero incremental stiffness. For the model-scale footing, the Mohr Coulomb model shows perfectly plastic behaviour at a displacement even less than 3% relative of the footing diameter. Figure 4.10 illustrates the plastic zone observed below the footing when using the Mohr-Coulomb model. The extent of the plastic zone at 3% displacement relative to

the footing diameter was observed to be nearly identical to that at displacements of 30% relative to the footing diameter.

In the case of the critical state models, a Gauss point is assumed to be plastic as soon as it touches any point on the yield curve. Thus for such models, a Gauss point may indicate plasticity at stress ratios much lower than at critical state. In such a case, a plastic Gauss point still retains some stiffness and may be able to sustain additional loads.

The plastic zones for the single surface, volumetric strain-hardening, critical state models, at displacements equal to 3% and 30% relative to the footing diameter were plotted. Figures 4.11 and 4.12 show the extent of the plastic zones for the Modified Cam Clay, Nova, SU1 and SU2 model, which were observed to be almost identical. Figure 4.11 shows that, at displacements of 3% relative to the footing diameter the Gauss points in a small zone immediately beneath the footing have become plastic. Figure 4.12 shows that at 30% displacement relative to the footing diameter, the plastic zone increases and spreads around and underneath the footing. A significant portion of the mesh still remained elastic at such displacements. The shapes of the plastic zones beneath the footing at 3% and 30% displacement are quite similar. The shape may be idealised as a parabolic wedge. The shape is similar at all displacements but increases with footing load in size as more and more Gauss points become plastic.

Figure 4.13 shows that in the case of the Molenkamp model, a significantly larger zone below the footing becomes plastic at 3% displacement, compared to the single surface, volumetric strain-hardening, critical state-models. The shape of the plastic wedge at this displacement is however, quite similar to those models. At 30% displacement, the plastic zone of the Molenkamp model is observed to have enlarged and spread to the lateral as well as the bottom boundary of the soil domain (Figure 4.14). The spread and extent of the plastic zone at large displacement appear to be quite similar to the Mohr-Coulomb model. It was shown in chapter 3 that, as the deviatoric yield surface of the Molenkamp model strain hardens, it asymptotically approaches the behaviour of a non-associated

Mohr-Coulomb envelope having zero dilation angle. The pattern of the plastic zone below the footing at large displacements, show a similarity with the patterns observed when using a non-associated Mohr-Coulmb layer with high friction angle and zero dilation angle. It was noted in section 4.8 that such models have been observed to demonstrate unstable behaviour for footing problems, for high friction angles of the underlying sand.

The spread of the plastic zone in the carbonate sand below the model-scale footing as predicted by various elasto-plastic models has been described. The single surface critical state models show a gradual and uniform spread of the plastic zone below the footing with increasing footing displacements.

4.8.2 VELOCITY FIELDS

The deformed outline of the soil boundary and the vector plots of cumulative vertical displacements below the footing within the soil layer, as obtained for the various elasto-plastic models, are discussed in this section. The displacement vectors show the deformation and failure mechanism that is predicted to occur below the footing.

The prediction of the associated Mohr-Coulomb model is first considered. The patterns of flow in Figure 4.15 show a movement along a slip surface in the radial shearing zone through the soil under the footing. This corresponds approximately to the general shear failure pattern indicated by a rigid perfectly plastic solution. Such a shear pattern was discussed in section 4.2. The vectors subsequently move upwards around the footing edge. Figure 4.16 shows the deformed outline obtained using the Mohr-Coulomb model, indicating a significant heave of the ground surface. The ground heave is a result of the large expansive dilatancy predicted by the associated Mohr-Coulomb model. This is in contrast to experimental observation in the model-scale footing. The model-scale footing showed negligible heave of the ground surface around the footing edge. The Mohr-

Coulomb model thus appears to be inappropriate to describe the mechanism of failure or deformation of circular footings resting on cemented carbonate sand.

Figures 4.17 and 4.18 show patterns of flow in the soil and the deformed shapes of the mesh as predicted by the critical state models. A single mesh is given, as the pattern of flow predicted by the various critical state models, was observed to be qualitatively almost identical. These models show almost no heave of the ground surface around the edge of the footing. This is almost identical to the behaviour observed by Yeoh and Airey (1996) in the model-scale footing experiment. The cumulative vector plots show that most displacements occur in the vertically downward direction. They are also concentrated in a small zone located immediately beneath the footing. A few vectors near the edge of the footing show some inclination from the vertical. The vector directions do not however, indicate a slip flow pattern in a radial shearing zone, as indicated by a Terzaghi or Prandtl solution. The pattern of displacement beneath the footing confirms a punching type of shear failure occurs in the soil supporting the footing. This is similar to the behaviour observed in the model-scale footing experiment on cemented carbonate sand. In that case, the model-scale footing was observed to punch into the sand, and the total change in volume of the sand was approximately equal to the volume of sand displaced by the footing.

The Mohr-Coulomb model does not give a true picture of the mechanism of deformation below a footing resting on carbonate sand. Strain-hardening critical state models on the other hand, appear to give a correct representation of the deformation mechanism below such a footing.

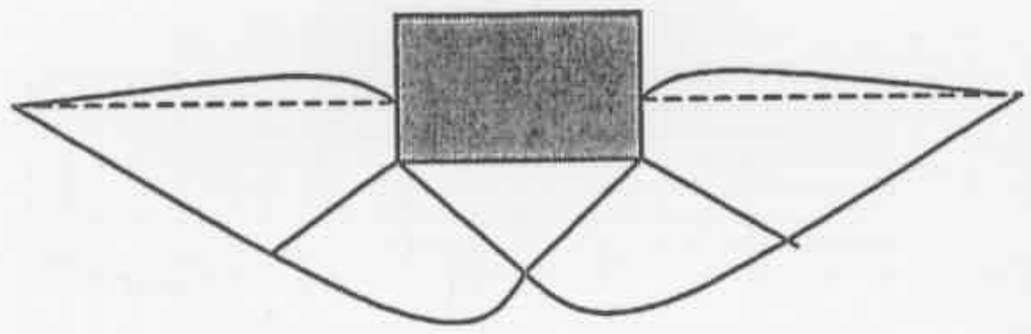

(a) General shear

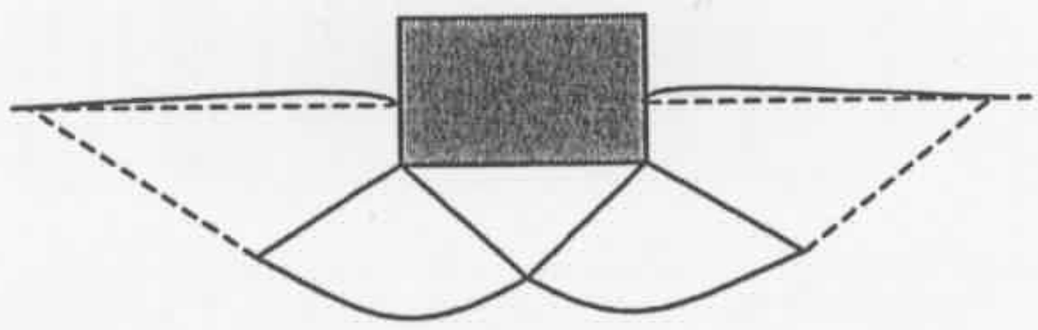

(b) Local shear

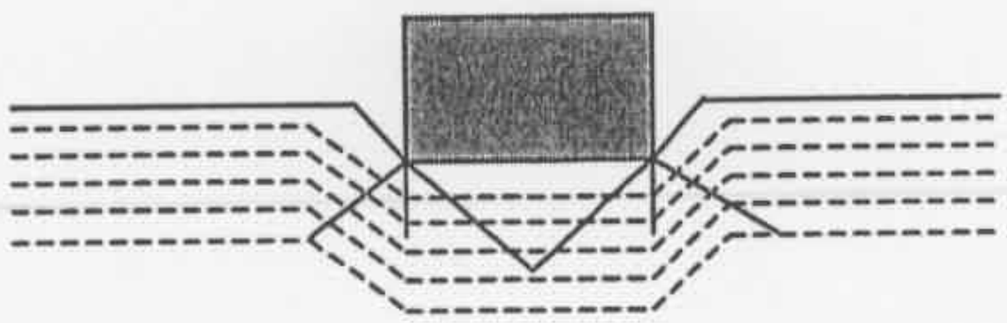

(c) Punching shear

Figure 4.1 Modes of bearing capacity failure (Vesic, 1963a)

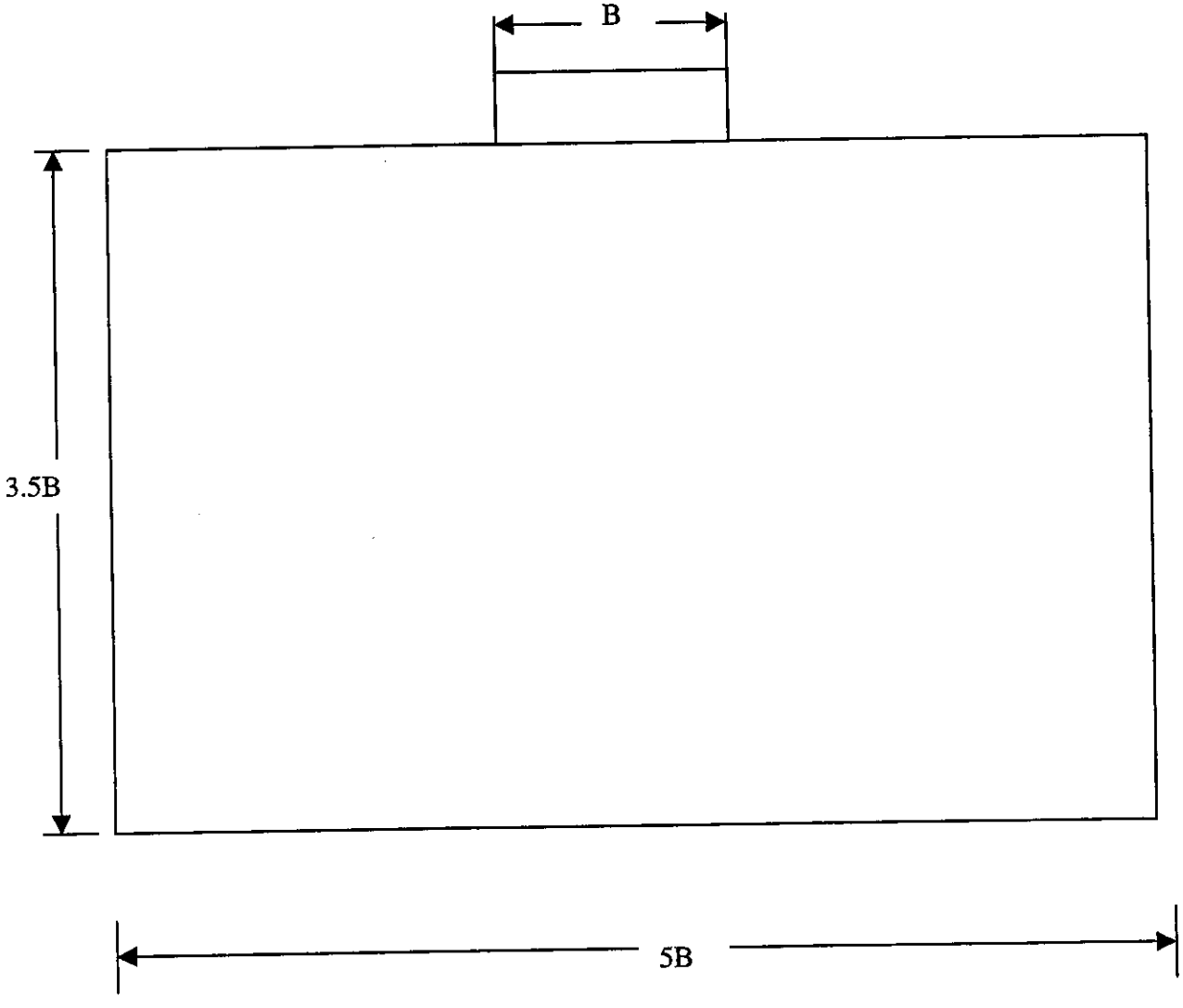

Figure 4.2 Geometry of the model footing experiment

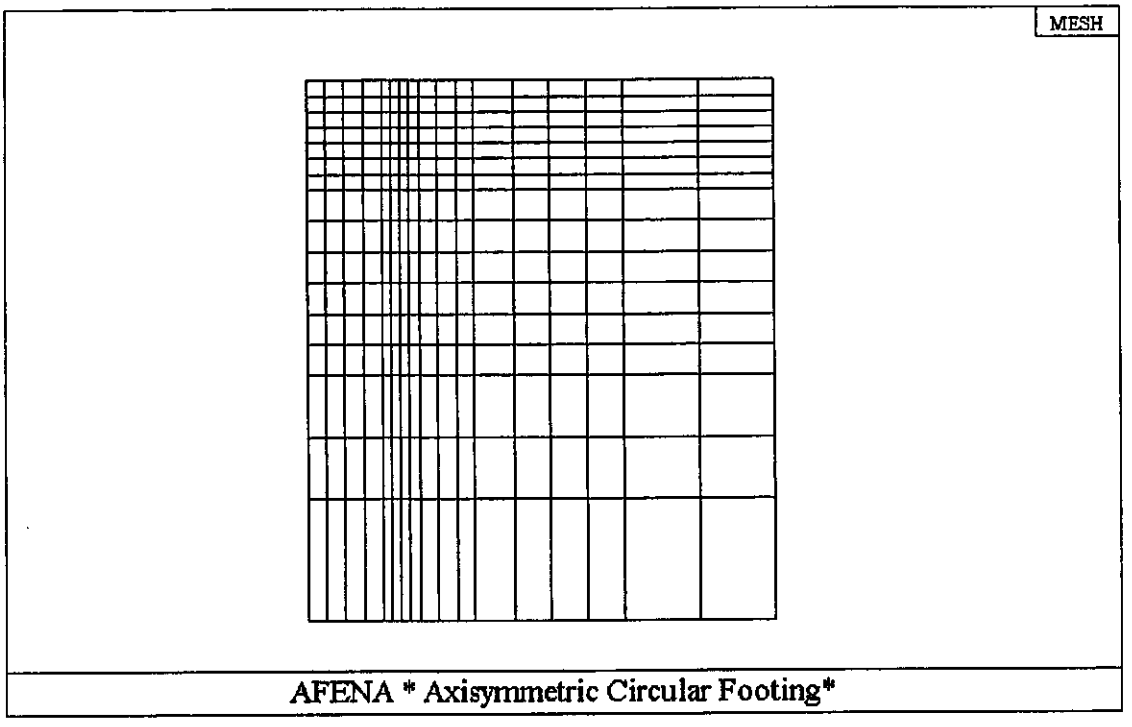

Figure 4.3 Finite element mesh for model footing using quadrilateral elements

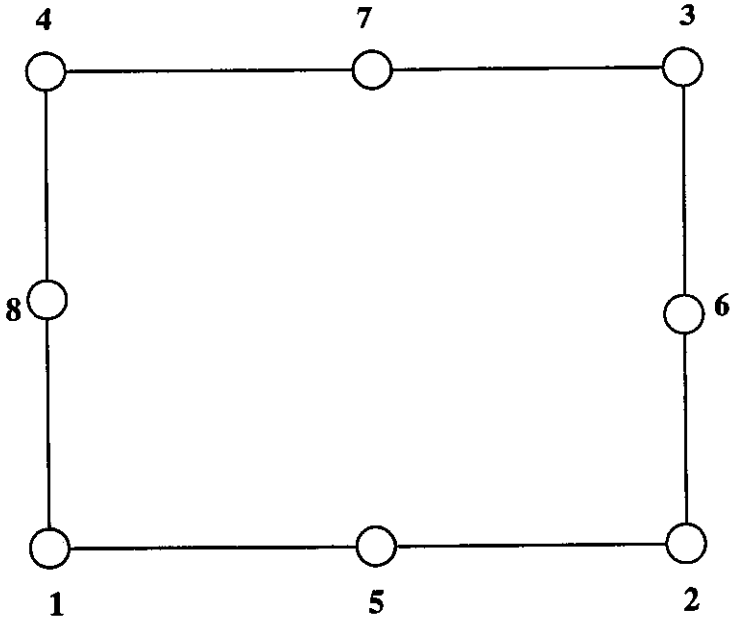

Figure 4.4 A 8 node quadrilateral element

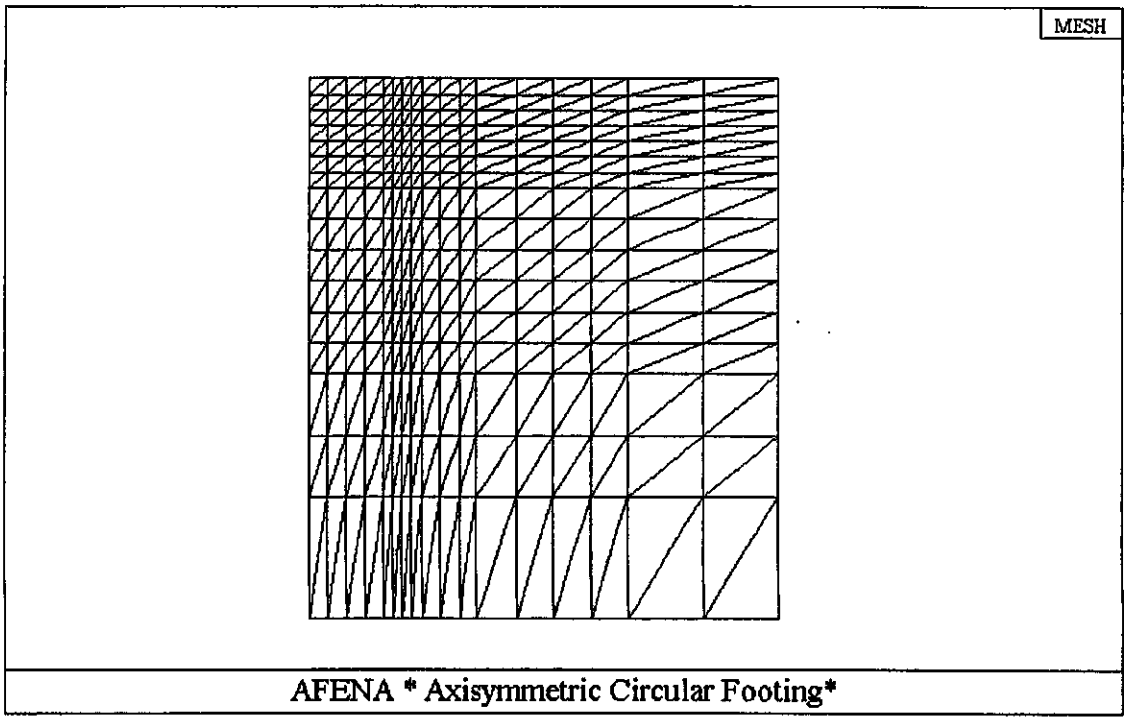

Figure 4.5 Finite element mesh for model footing using triangular elements

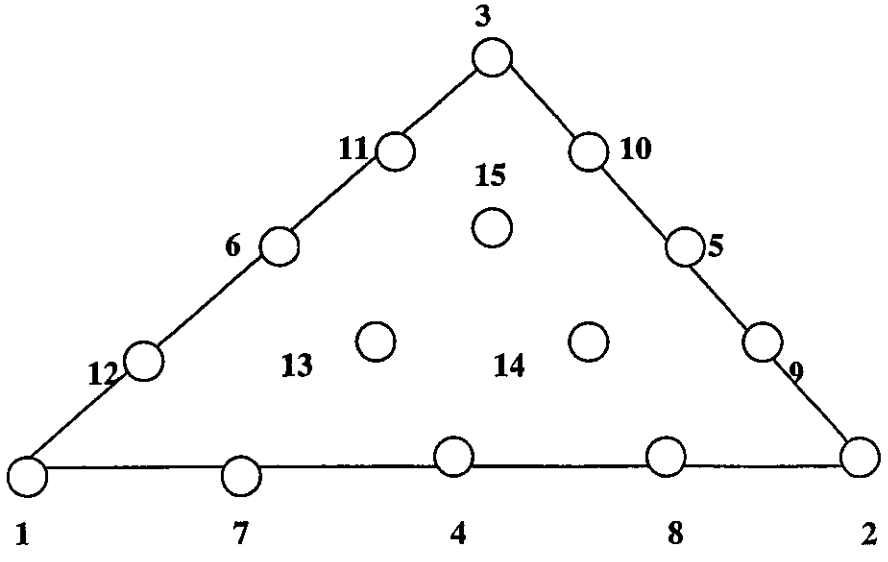

Figure 4.6 A 15 node triangular element

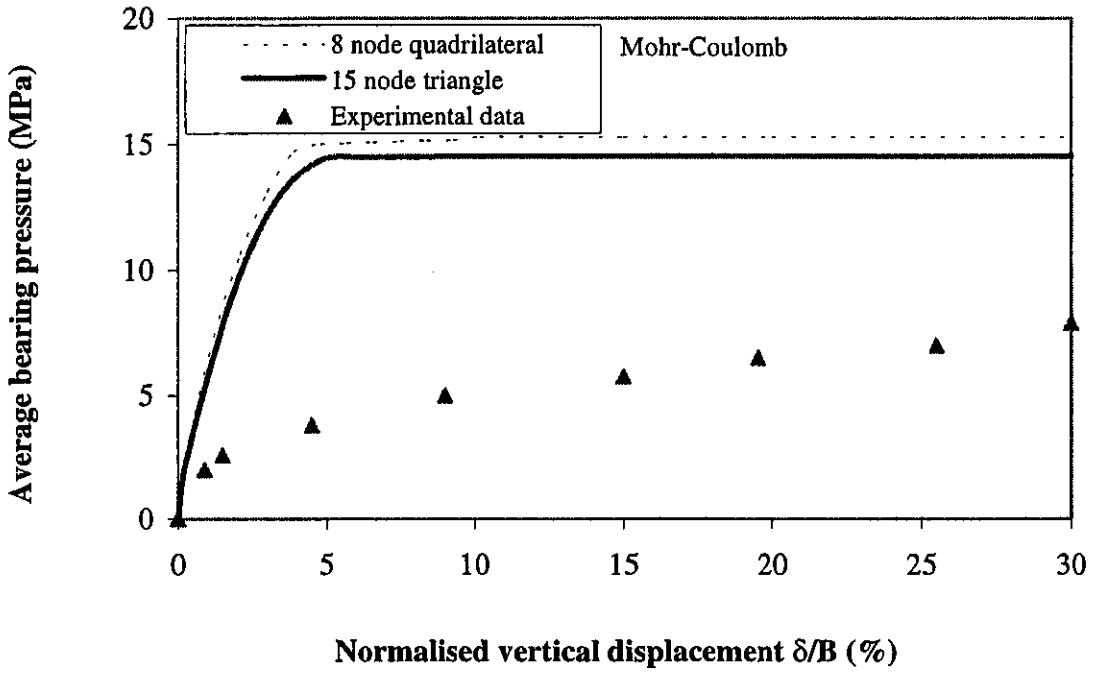

Figure 4.7 Comparison of footing simulation with 8 node quadrilateral and 15 node triangular elements using the Mohr-Coulomb model

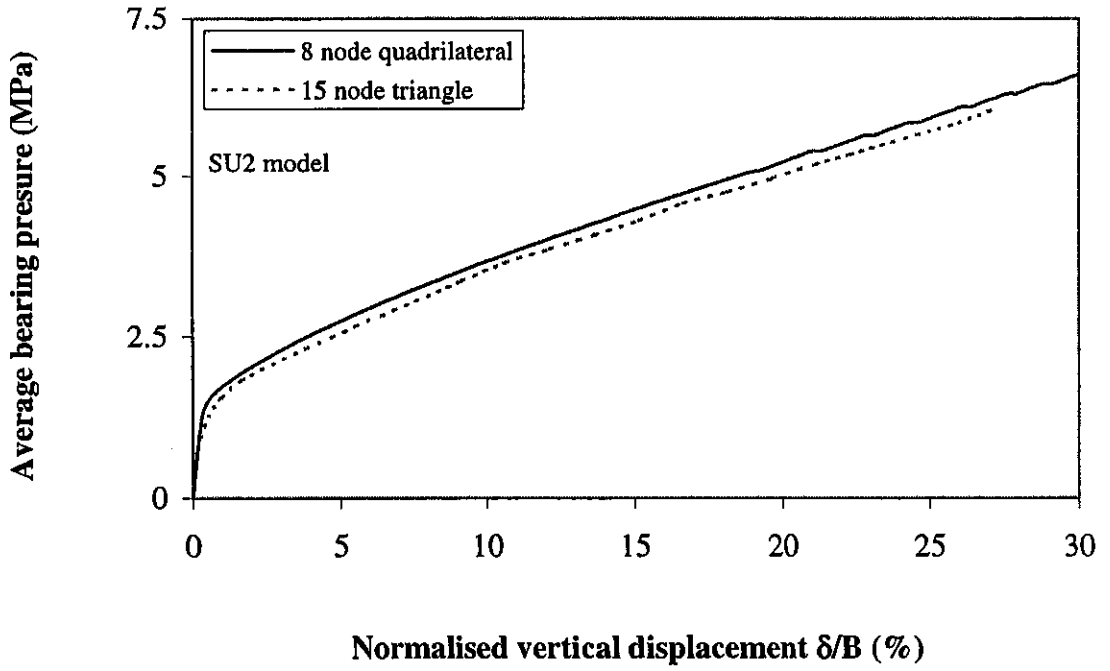

Figure 4.8 Comparison of footing simulation with 8 node quadrilateral and 15 node triangular elements using the SU2 model

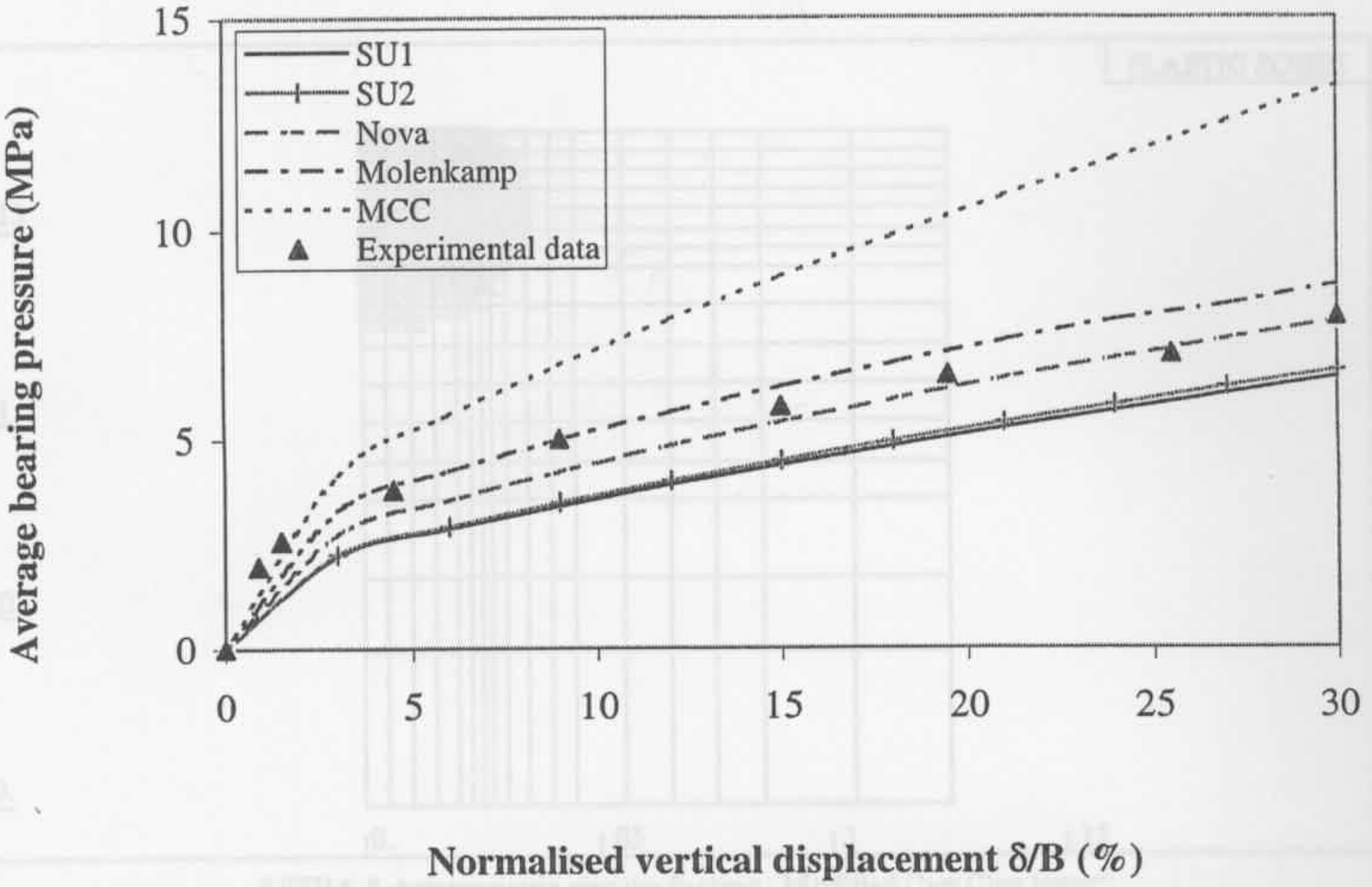

Figure 4.9 Comparison of the pressure-displacement curves simulated using various elaso-plastic constitutive models with the experimental data

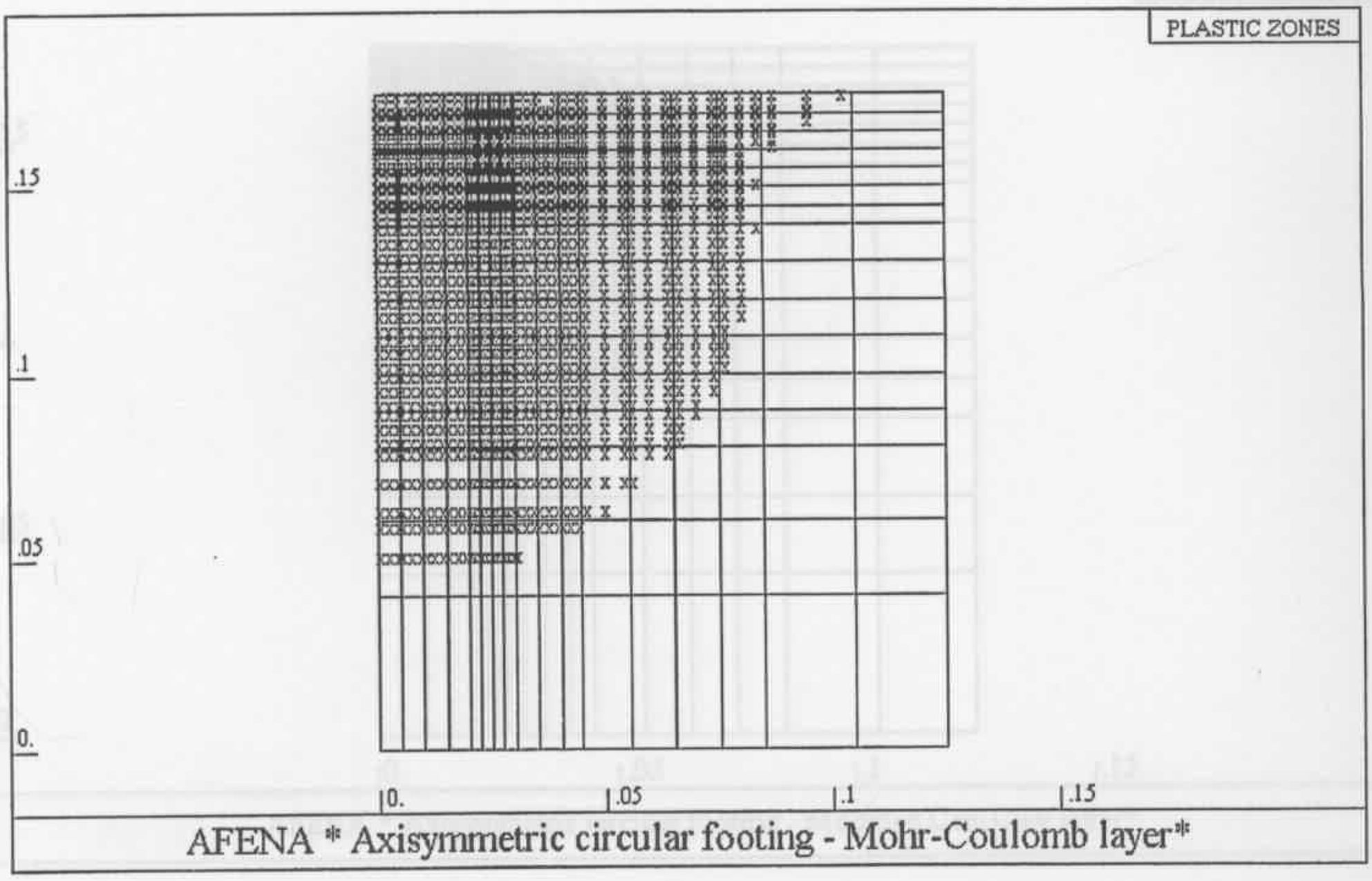

Figure 4.10 Plastic zone in a Mohr-Coulomb layer at a displacement of 3% of the footing diameter

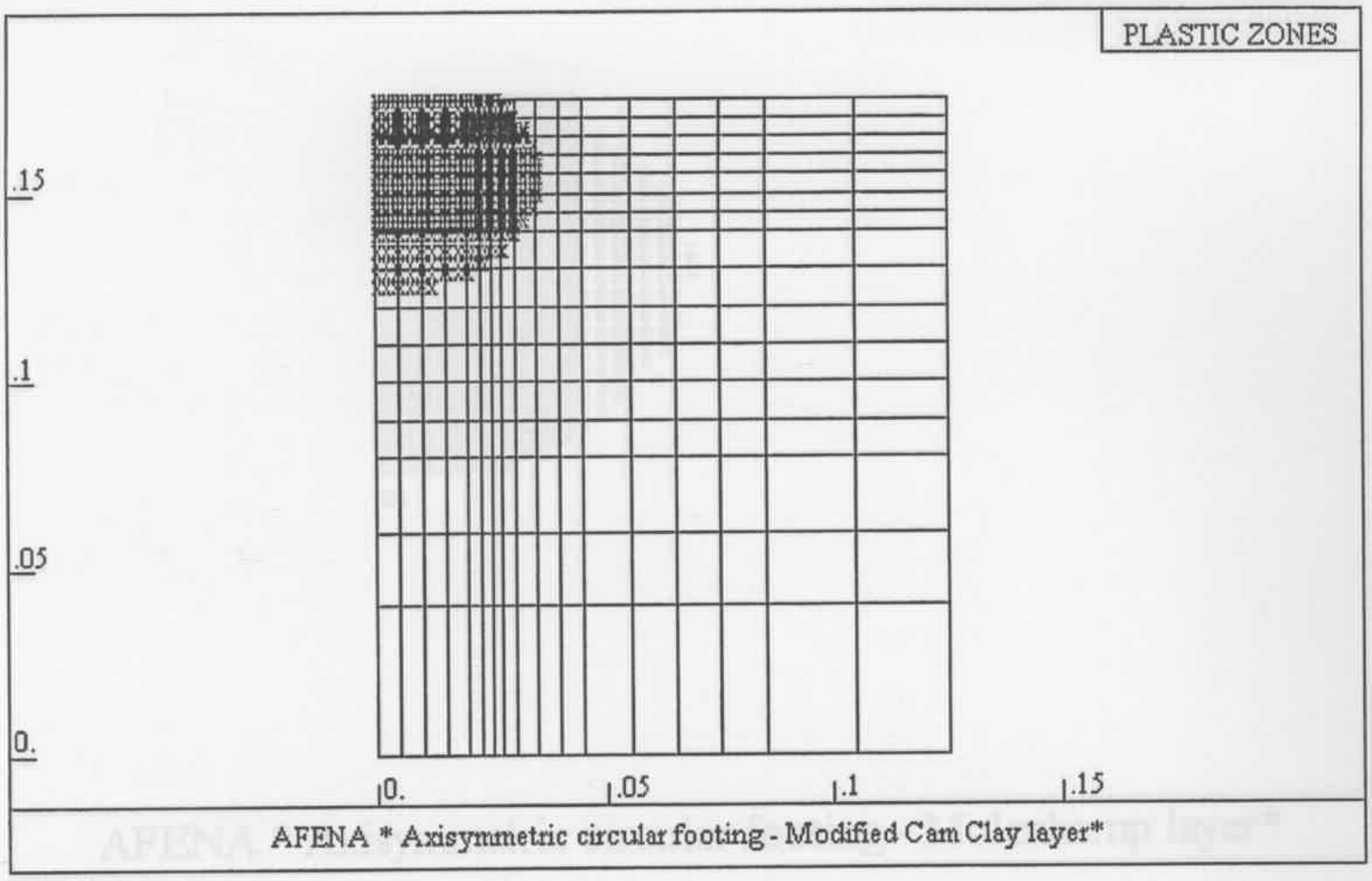

Figure 4.11 Plastic zone in a MCC layer at a displacement of 3% of the footing diameter

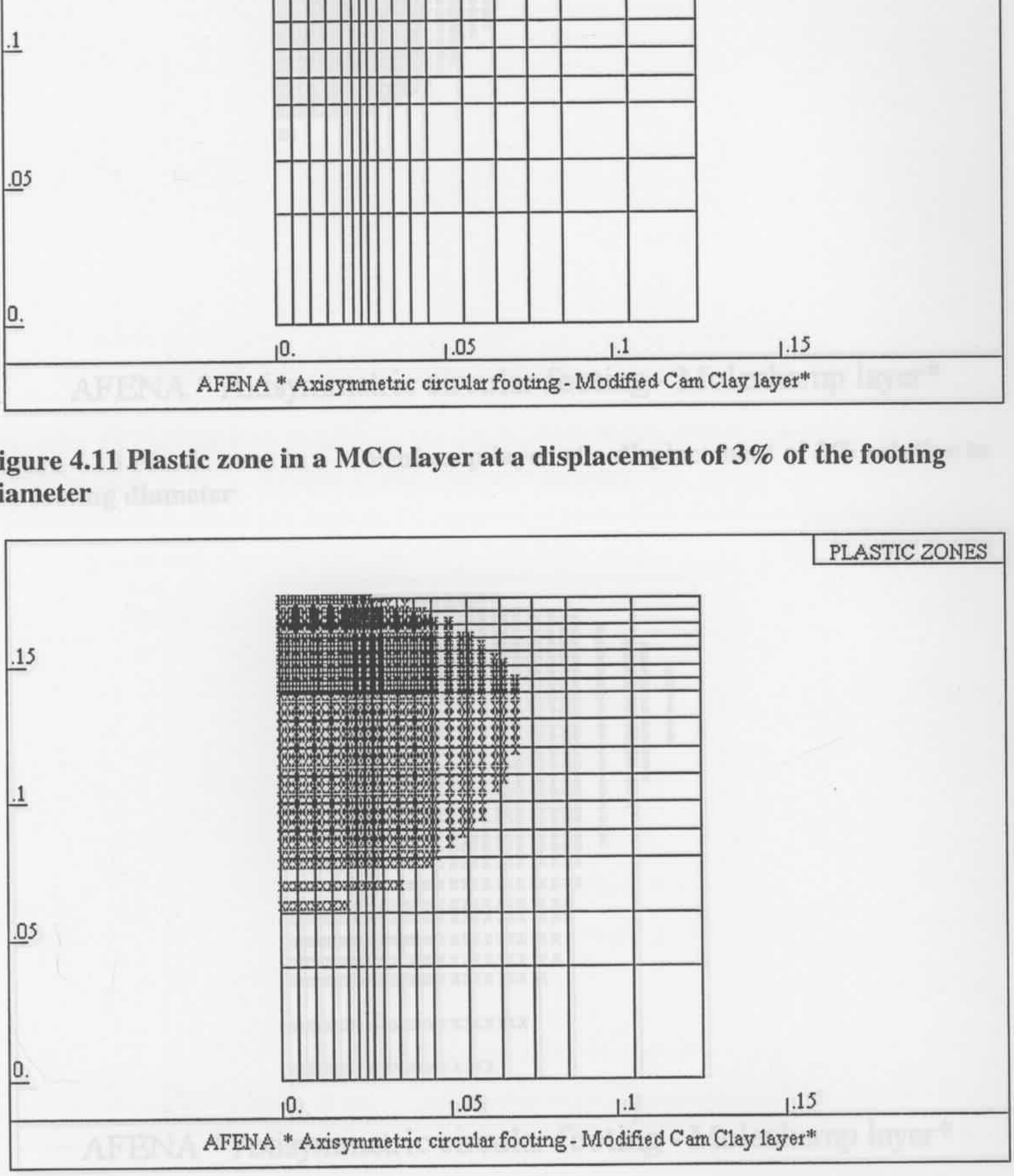

Figure 4.12 Plastic zone in a MCC layer at a displacement of 30% of the footing diameter

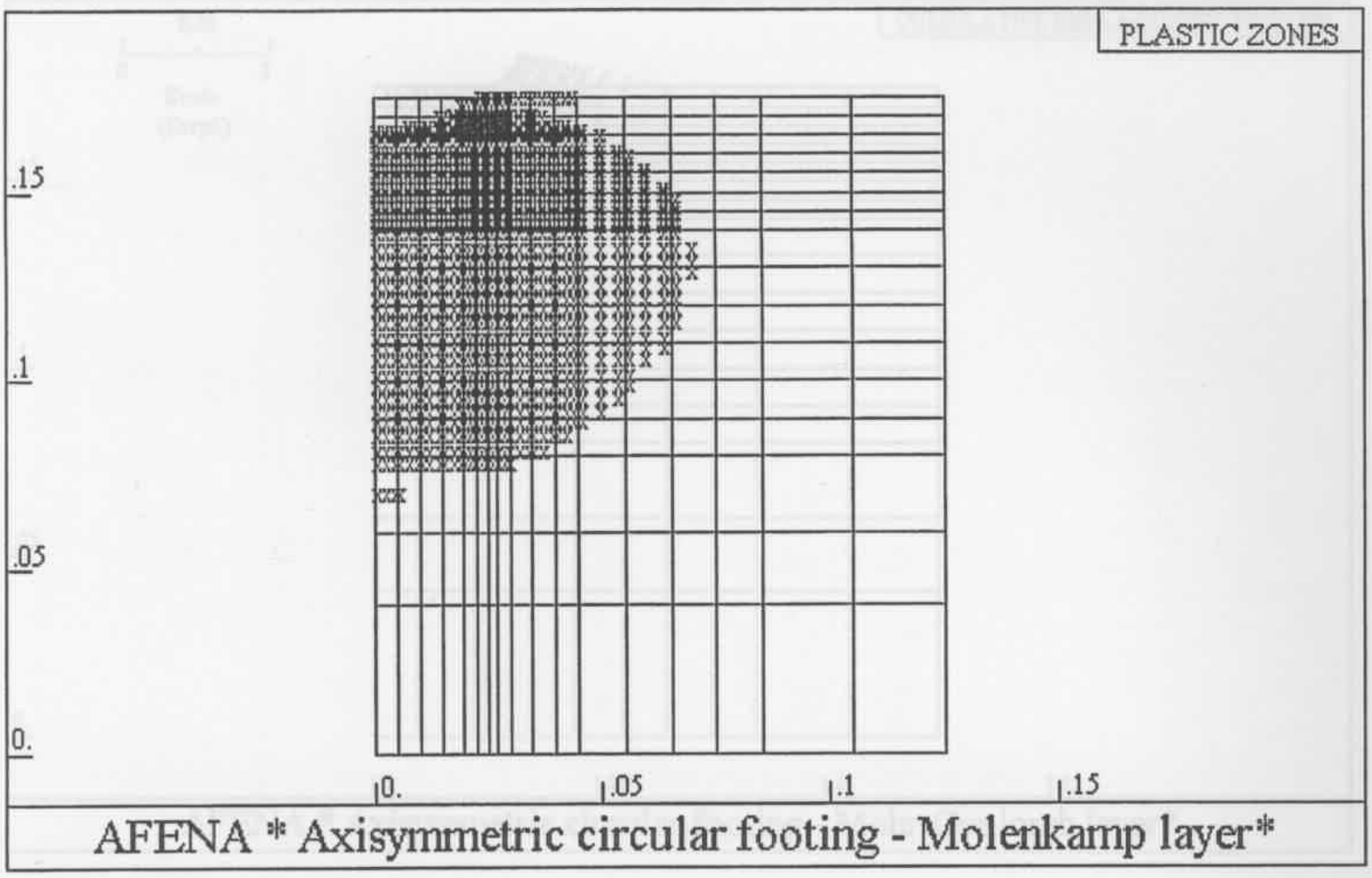

Figure 4.13 Plastic zone in a Molenkamp layer at a displacement of 3% relative to the footing diameter

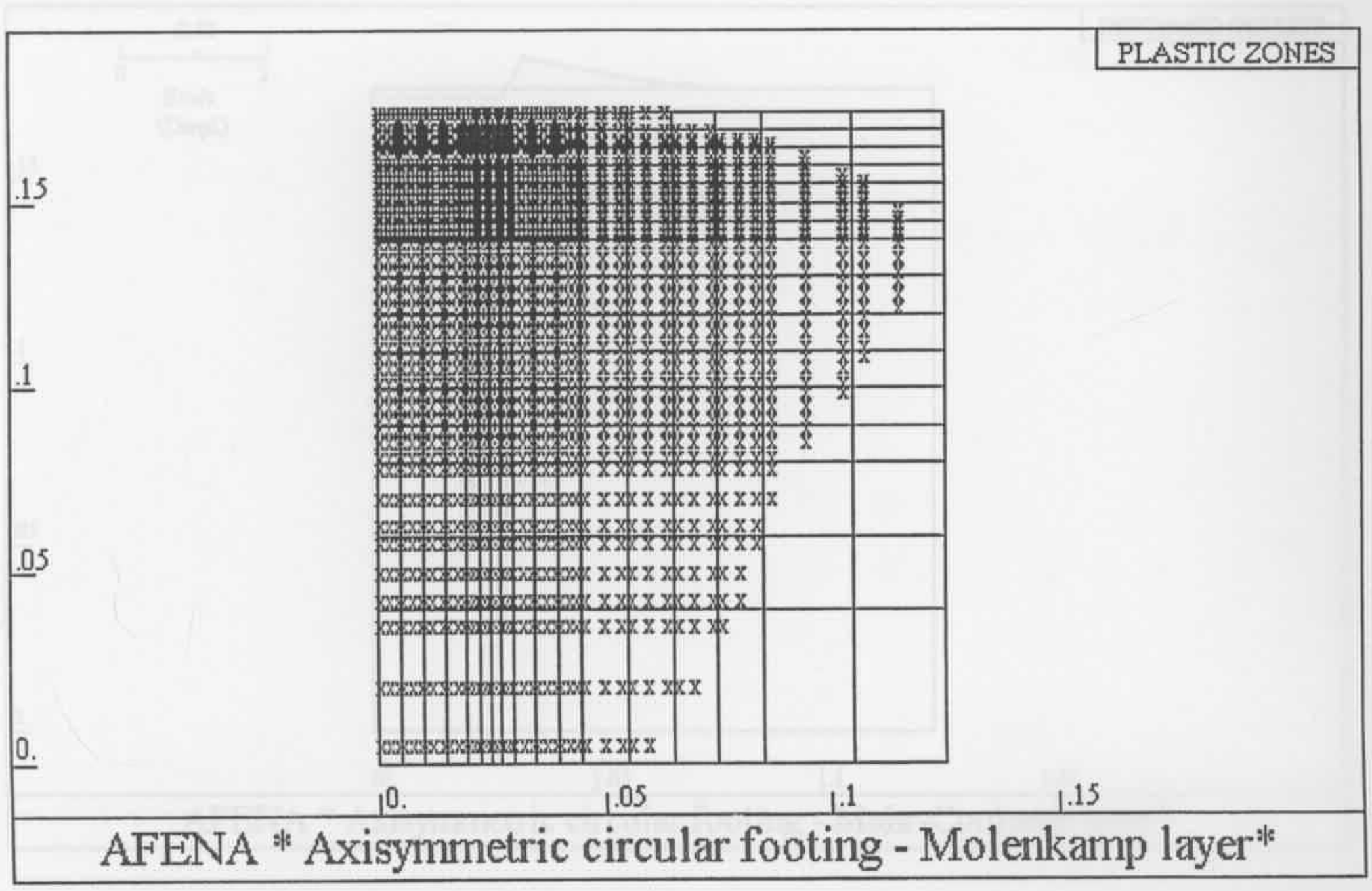

Figure 4.14 Plastic zone in a Molenkamp layer at a displacement of 30% relative to the footing diameter

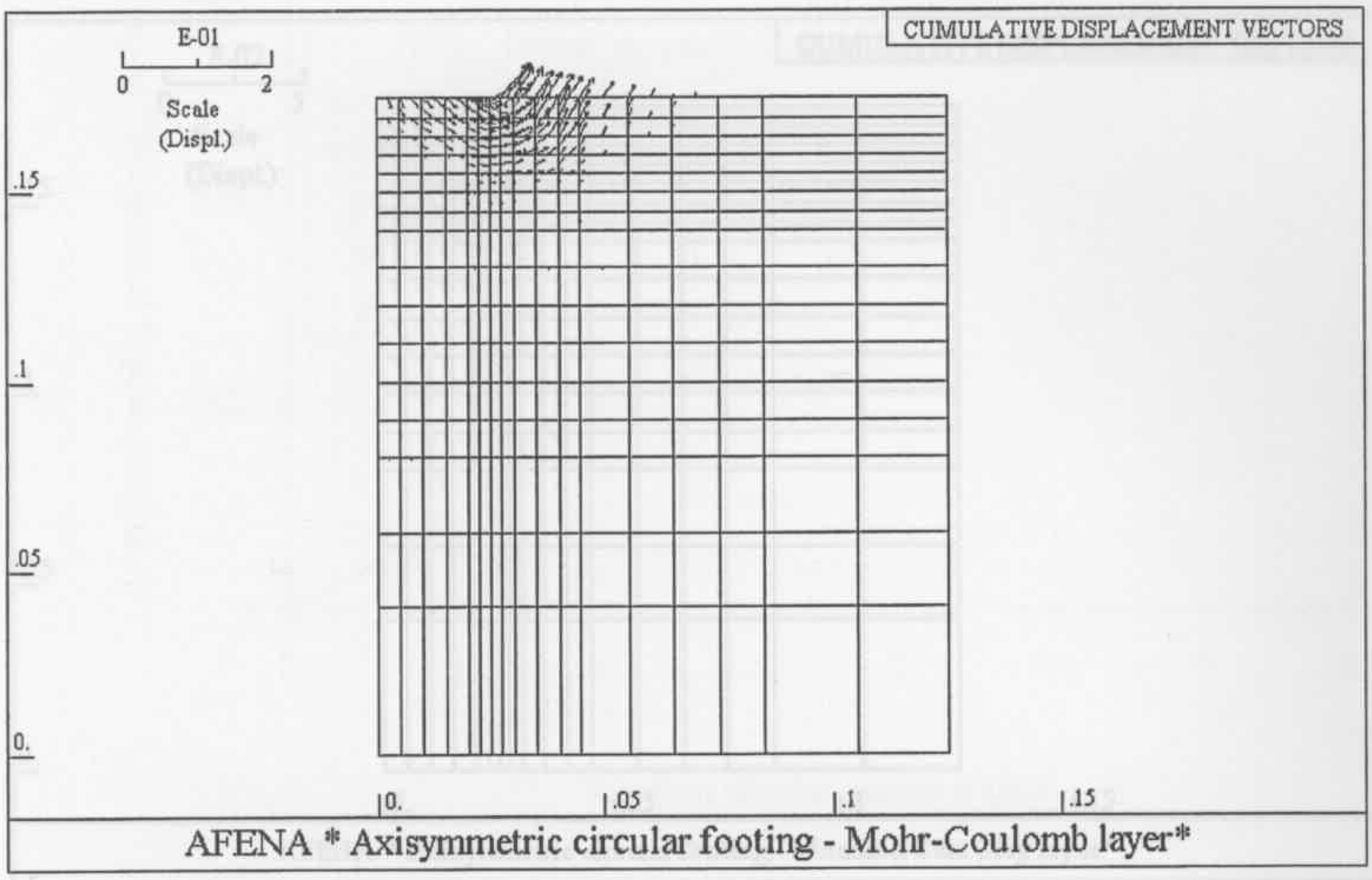

Figure 4.15 Cumulative displacement vectors in a Mohr-Coulomb layer at a displacement of 30% relative to the footing diameter

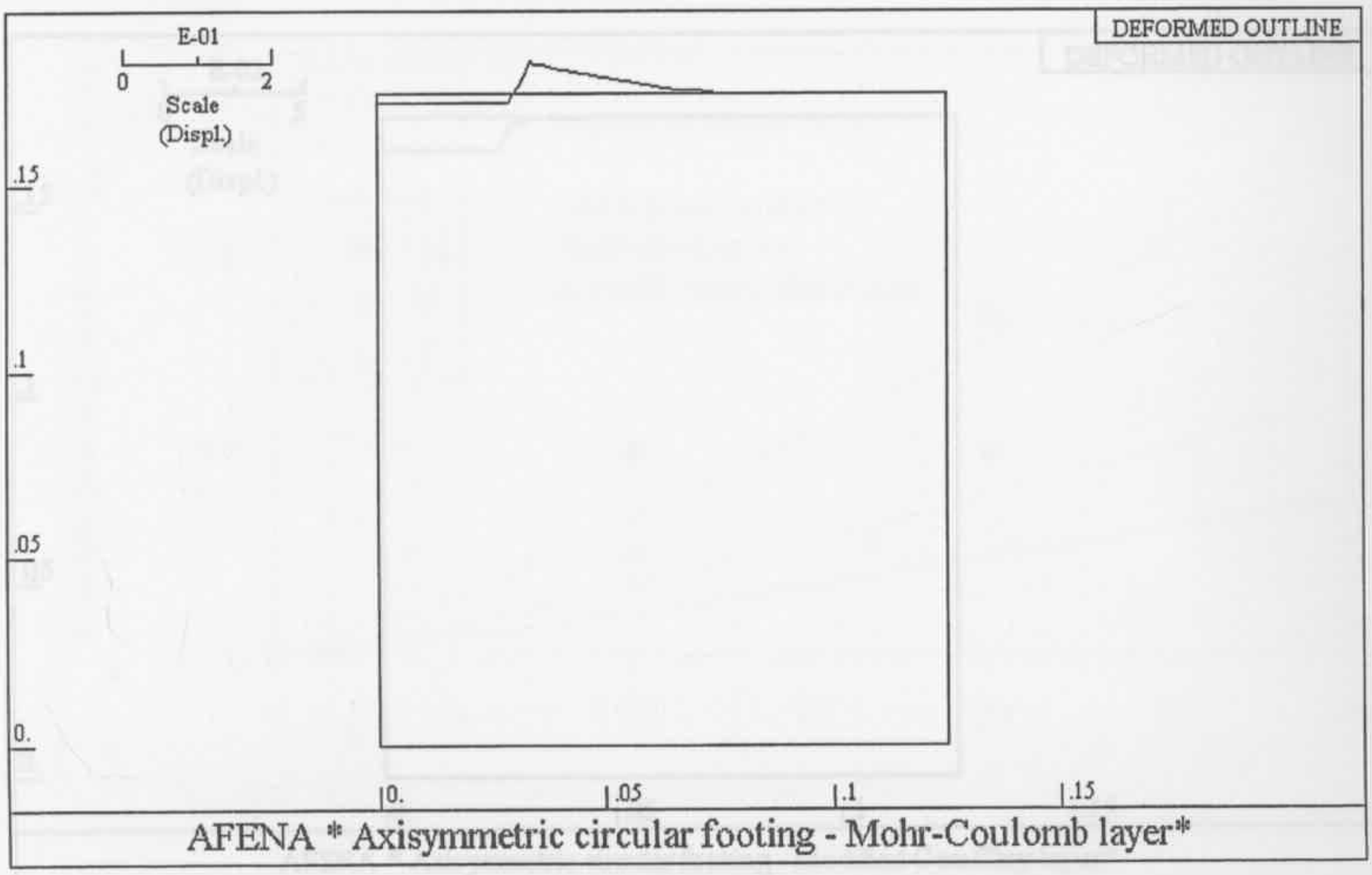

Figure 4.16 Deformed shape of a Mohr-Coulomb layer at a displacement of 30% relative to the footing diameter

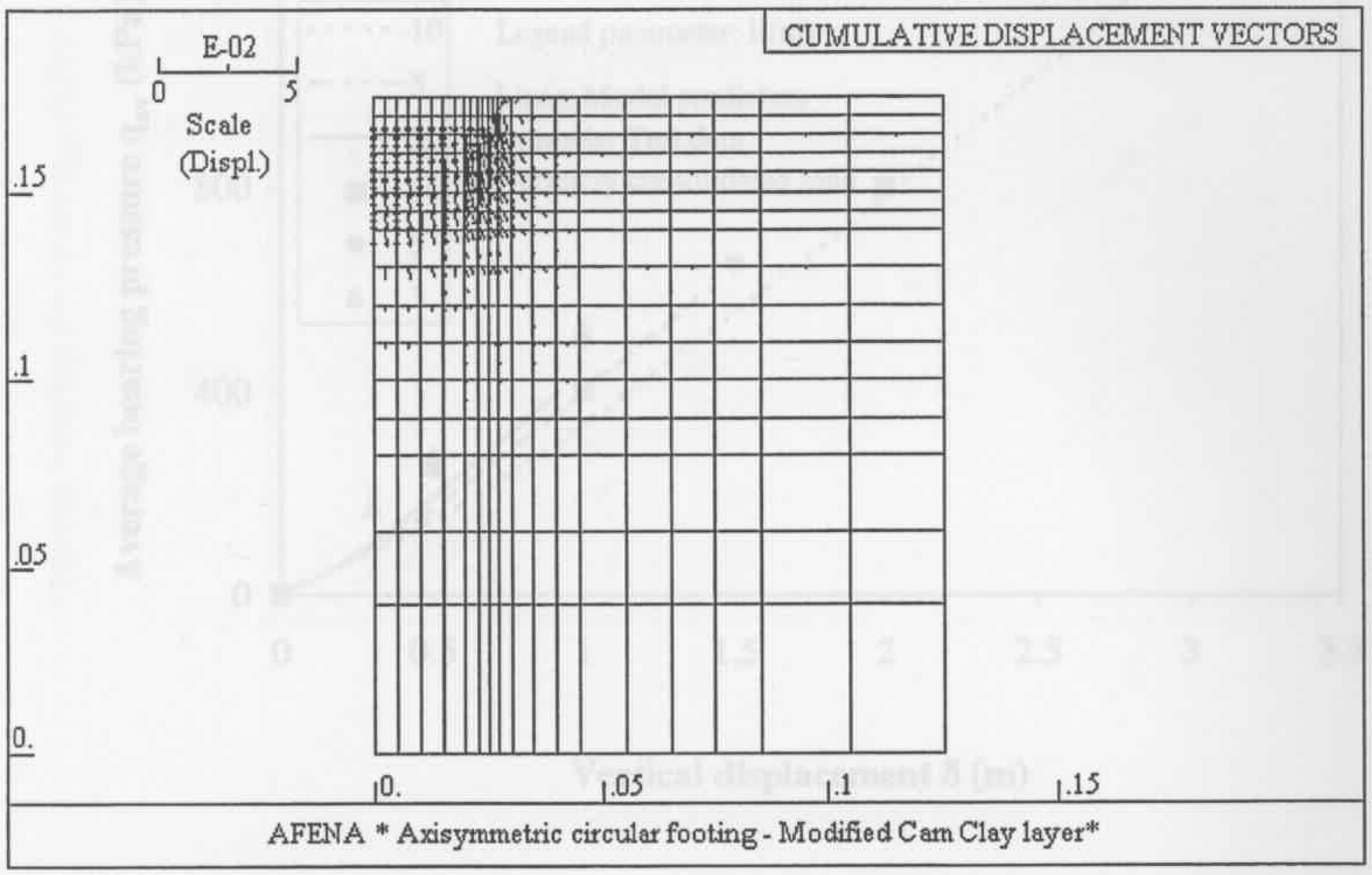

Figure 4.17 Cumulative displacement vectors in MCC, Molenkamp, Nova, SU1 and SU2 layer at a displacement of 30% relative to the footing diameter

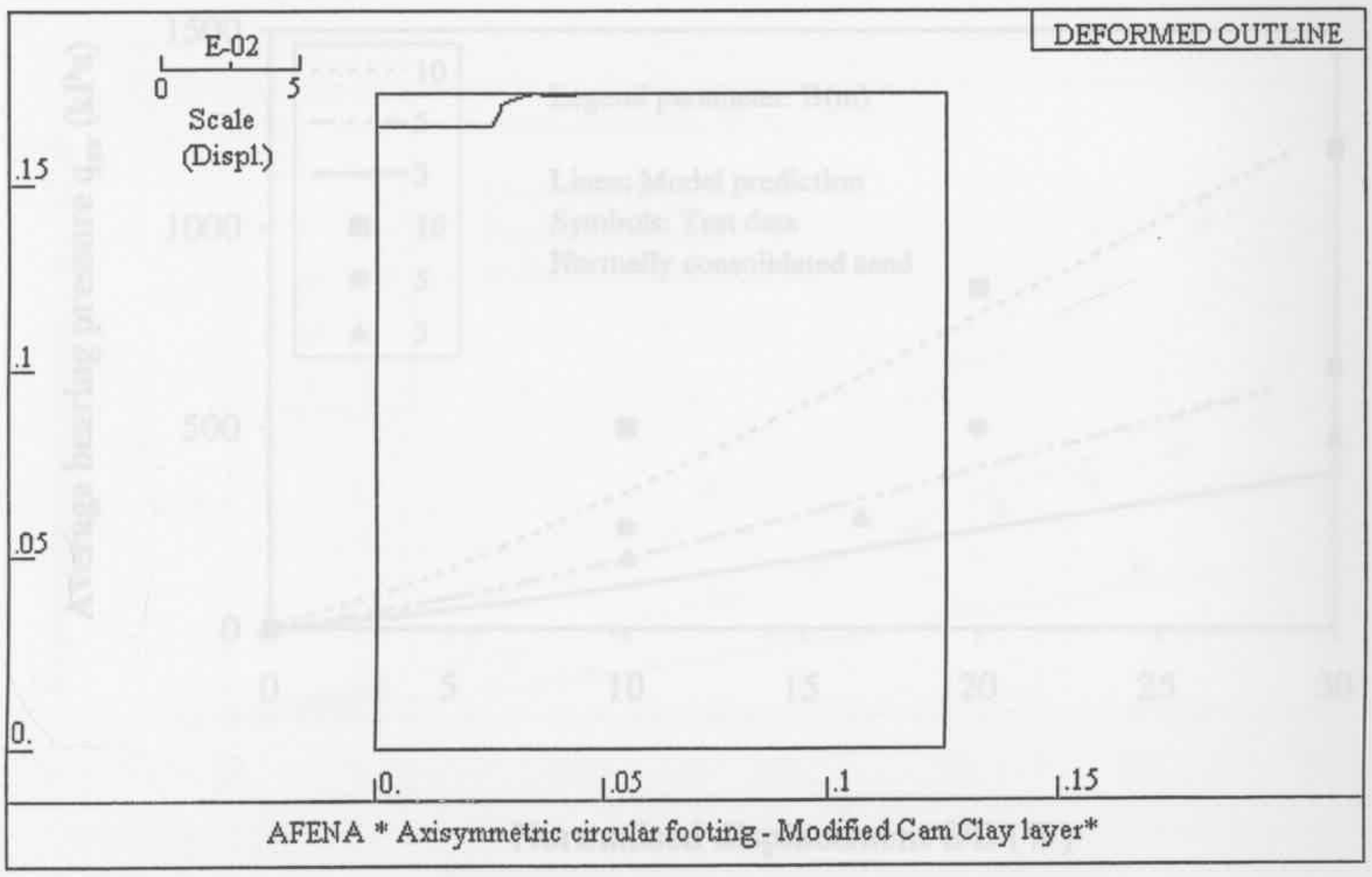

Figure 4.18 Deformed shape of MCC, Molenkamp, Nova, SU1 and SU2 layer at a displacement of 30% relative to the footing diameter

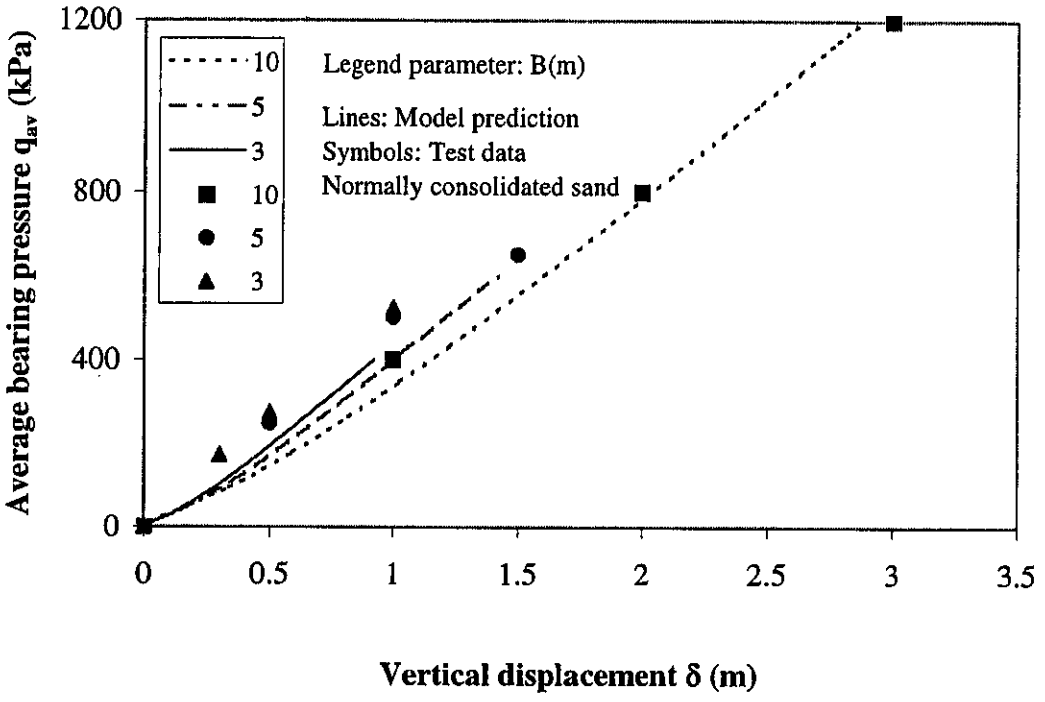

Figure 4.19 Comparison of predictions with centrifuge data for normally consolidated carbonate sand

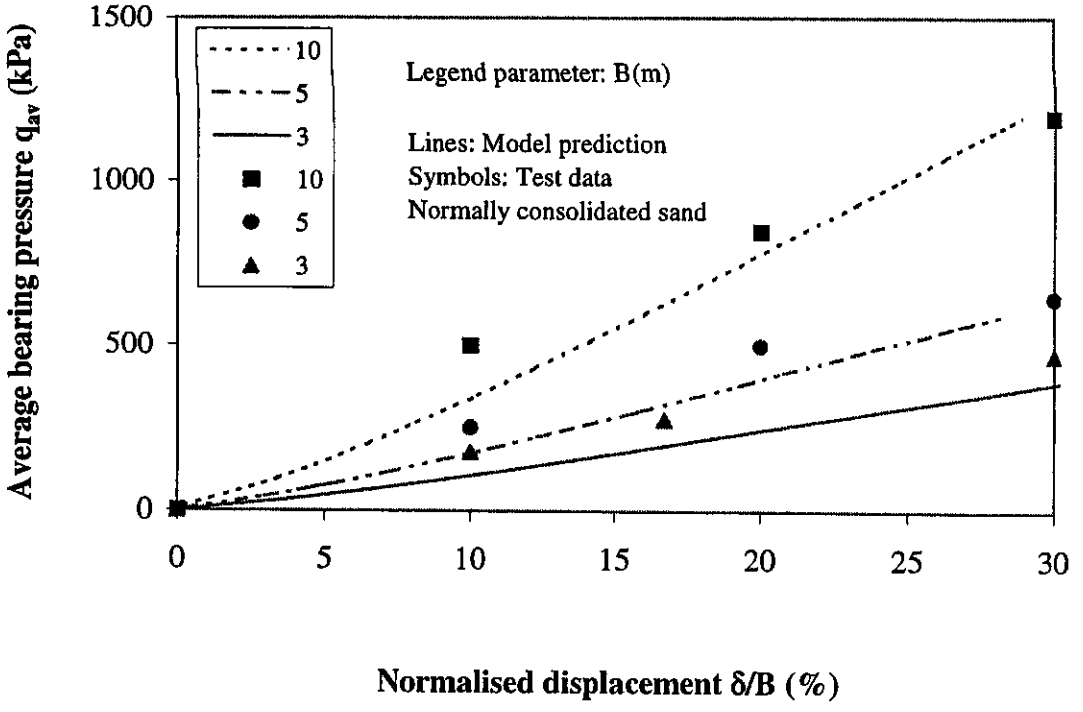

Figure 4.20 Comparison of predictions with centrifuge data for normally consolidated carbonate sand (displacement relative to footing diameter)

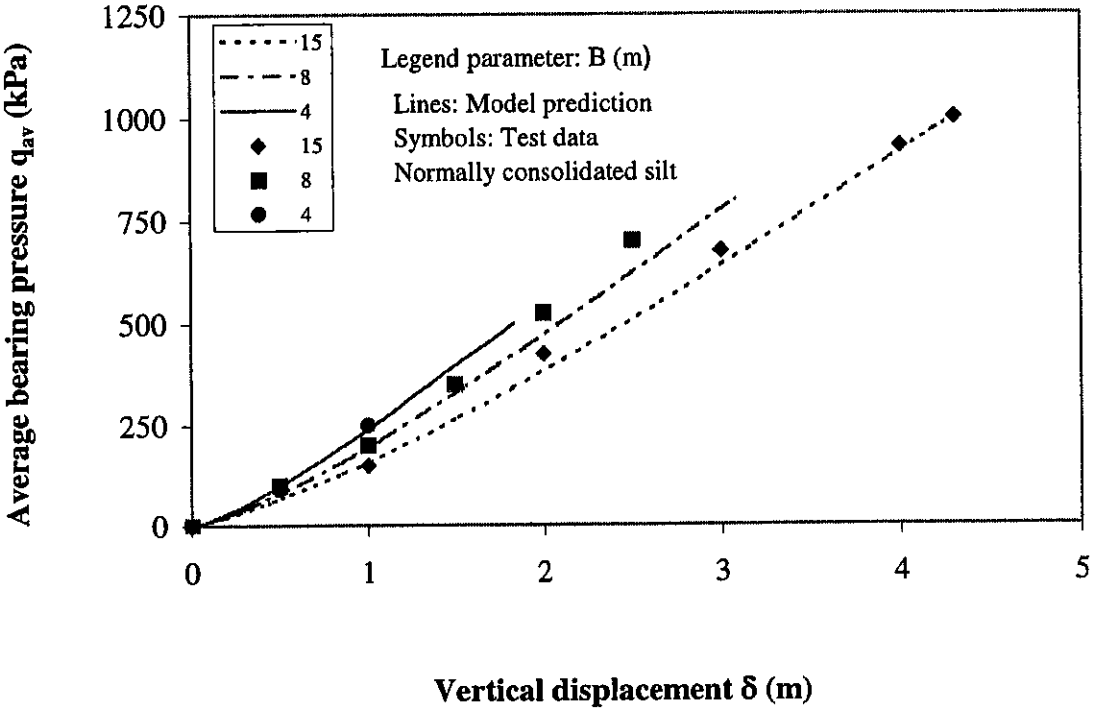

Figure 4.21 Comparison of predictions with centrifuge data for normally consolidated silt

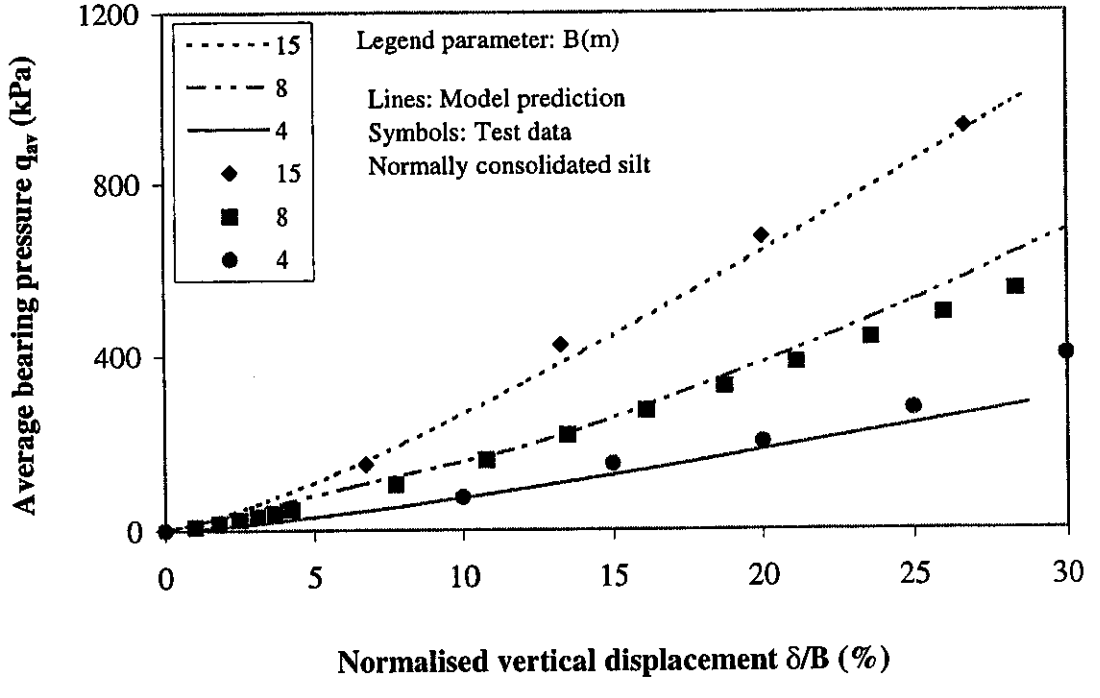

Figure 4.22 Comparison of predictions with centrifuge data for normally consolidated silt (displacements relative to the footing diameter)

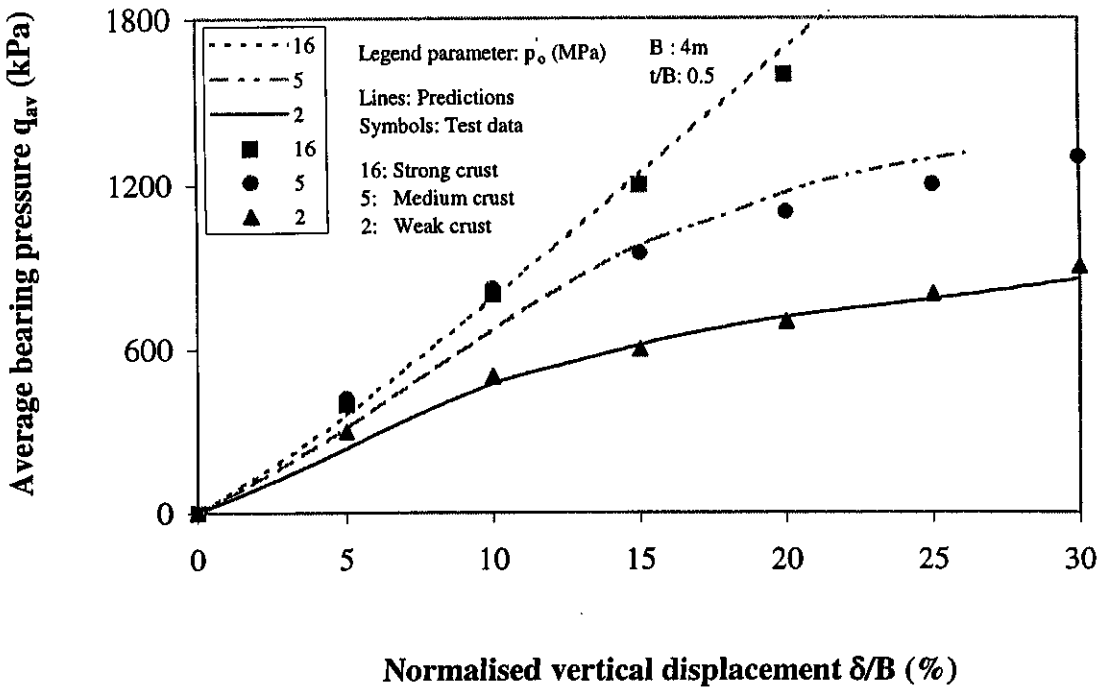

Figure 4.23 Comparison of predictions with centrifuge data for layered soil

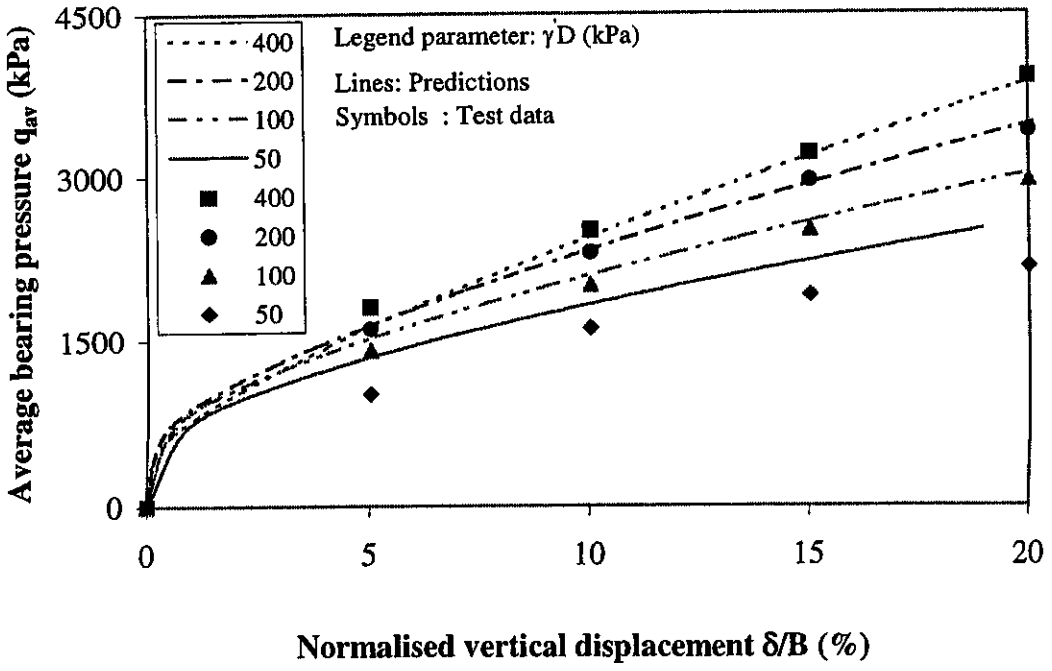

Figure 4.24 Comparison of predictions with data for model-scale footing on uncemented carbonate sand

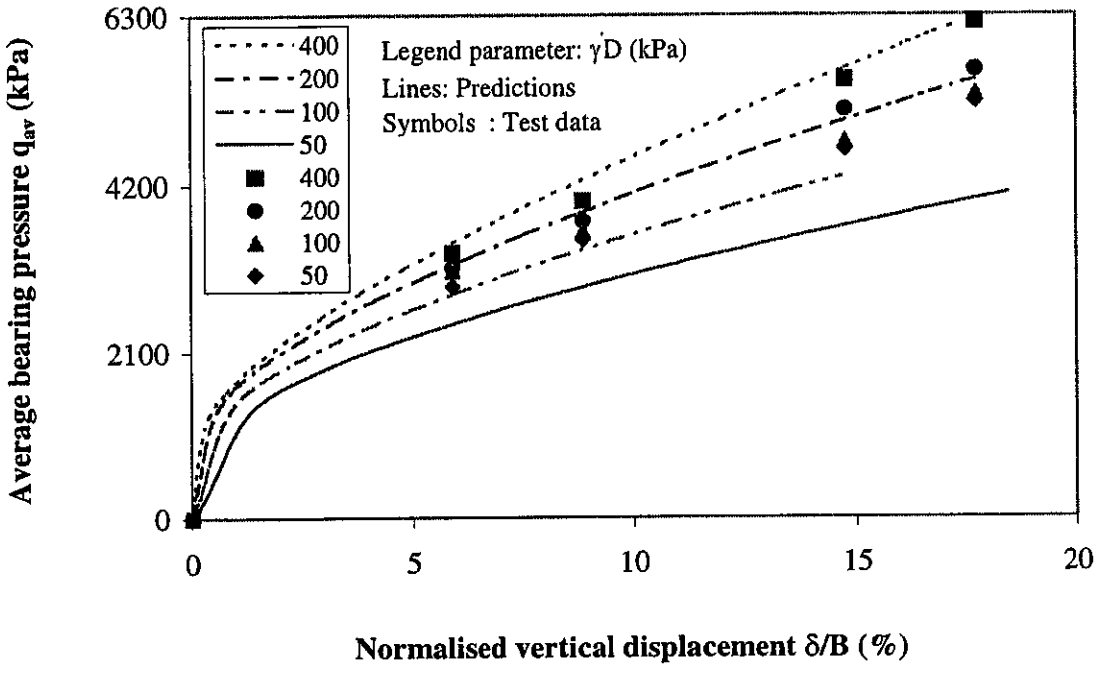

Figure 4.25 Comparison of predictions with data for model-scale footing on cemented carbonate sand

5

A PARAMETRIC STUDY OF SURFACE CIRCULAR FOOTINGS ON CARBONATE SAND

5.1 INTRODUCTION

Offshore foundations are often circular or near circular footings resting on the surface of the ocean bed. In many parts of the world, the soil layers beneath the foundation consist of carbonate sand, with or without cementation. Surface foundations on carbonate sand show a continuous increase in the mobilised bearing pressure with increased settlements. A local or punching shear mode of failure is usually seen. This behaviour is typically observed in foundations resting on compressible soils.

Currently, no rigorous analytical method exists to determine the mobilised bearing pressure curve for surface circular footings resting on compressible soils. Semi-analytical cavity expansion methods currently available can determine limit pressures for the footing, but cannot be used to obtain its mobilised pressure-displacement response. It was shown in Chapter 4 that the elastoplastic finite element analysis of circular footings using the SU2 model gives realistic predictions of the mobilised bearing pressure. In the current chapter, further experimental validation of the SU2 model is provided. A parametric study is then undertaken to demonstrate the influence of the SU2 model parameters on the predicted bearing behaviour of surface circular footings resting on carbonate sand. The results of the parametric study as well as a set of design charts are presented. The design charts can be used to determine conveniently the mobilised bearing pressure of surface circular footings

resting on carbonate sand, for a wide range of cases of practical interest. The problem of deeply buried footings will be discussed in Chapter 6.

5.2 PROBLEM DEFINITION

The purpose of the parametric study is to investigate the effect of SU2 model parameters on the predicted bearing behaviour of a surface circular footing on carbonate sand. Before undertaking such a study, the problem needs to be clearly defined.

A circular footing of diameter B is assumed to be resting on the surface of the ocean bed. Figure 5.1 shows that the initial effective vertical and horizontal stresses in the soil vary linearly with depth. The initial vertical and horizontal stress on any soil element are due to its self-weight only. Figure 5.2 shows the in-situ stress that is assumed to exist at any element of the soil at a depth h. K_o in this figure is the coefficient of earth pressure at rest.

In offshore locations, adjacent soil layers may have markedly different strengths. However, to understand clearly the effect of soil parameters on the predicted bearing behaviour of the footing, it is necessary to make simplistic idealisations of the actual soil profile. Two cases are considered. For case 1, the problem examined is that of a circular footing resting on the surface of "cemented" carbonate sand layer underlain by uncemented sand or silt. This is typically observed in many offshore locations (Finnie and Randolph, 1994). The effect of cementation is modelled as an overconsolidation ratio of the soil. It is assumed that the effect of cementation is to a great extent similar to that of overconsolidation in soils. For simplicity, it has been assumed that the transition from "cemented" to normally consolidated behaviour occurs gradually with depth. For case 2, the problem considered is that of a circular footing resting on normally consolidated carbonate sand. The behaviour of such a footing would generally give the lower limit of its response. A limited parametric study for the problem in case 2 was also carried out. The assumed soil profiles of preconsolidation pressures for both case 1 and case 2 are shown in Figure 5.3.

The major part of the parametric study was carried out for the soil profile described as case 1 in Figure 5.3, which shows that a uniform layer of "cemented" or overconsolidated material exists immediately beneath the footing to a depth H. The preconsolidation pressure of the "cemented" layer is assumed to be uniform and designated as p_o'. Figure 5.4 shows that at a depth less than H, the initial stress lies at a point C, which is located within the elliptical SU2 yield locus. Thus the soil can be considered as overconsolidated or "cemented" down to depth H. At depth H, the soil is normally consolidated, represented by the stress state at point A in Figure 5.4. Below depth H, the in-situ stress lies on the elliptical SU2 yield locus, and the self-weight stresses and preconsolidation pressure p_o' increase with depth. Thus the soil is normally consolidated below depth H. Figure 5.3 shows that below depth H, preconsolidation pressure in the soil increases linearly as a result of the increase of the in-situ stresses with depth. Under these conditions the following relations hold:

$$p_o' \propto \gamma' H \tag{5.1}$$

or

$$H \propto \frac{p_o'}{\gamma'} \tag{5.2}$$

where γ' is the effective unit weight of the soil. Thus for the problem considered, the thickness of the "cemented" layer immediately below the footing can be considered as proportional to its preconsolidation pressure p_o'.

The physical problem for which the parametric study will be carried out has now been defined. The next section discusses the pertinent details of the finite element analysis. Thereafter, details of the parametric study and the results are presented.

5.3 FINITE ELEMENT MESH

The parametric study was conducted using non-linear and incremental finite element analysis. The SU2 model was used to simulate the constitutive behaviour of the carbonate sand. Figure 5.5 shows a typical axi-symmetric finite element mesh adopted for the footing problem. The graded mesh consists of 16 rows and 17 columns with a total of 272, 8 node quadrilateral elements. There are 6 elements below the footing. A rigid footing response is simulated by a similar number of purely elastic elements above the soil surface. The elastic modulus of the footing is assumed to be several orders of magnitude higher than the underlying soil. The loading of the soil surface was applied by incrementally increasing the force applied to the rigid footing. The underside of the rigid footing was perfectly rough. The results of the parametric study are presented in subsequent sections.

5.4 IDEALISATION OF MOBILISED BEARING PRESSURE CURVE

Sharp and Seters (1988) have shown that the mobilised bearing pressure curves obtained from field plate tests on carbonate sand can be approximated by bilinear relations. Figure 5.6 shows the mobilised bearing pressure curve of a 1m diameter circular footing obtained by finite element analysis adopting the SU2 stress-strain model. It is seen that the bearing pressure curve obtained from elastoplastic finite element analysis is in fact non-linear, both in the "elastic" and in the "plastic" part. Both sections of the bearing pressure curves for footings on carbonate sand actually involve elastoplastic behaviour. However, the first section of the curve shows primarily elastic behaviour and the subsequent section shows primarily plastic behaviour. Thus, for simplicity, the initial part of the bearing pressure curve will be termed as "elastic" and subsequent part termed as "plastic" in the subsequent sections of this chapter. The bilinear idealisation of the bearing pressure curve is also shown in Figure 5.6. The bilinear curve consists of a linear "elastic" and a linear "plastic" part separated by an inflection point. The inflection point can be described in terms of a "yield pressure". The yield pressure is defined as the bearing pressure at which the slope of the mobilised pressure curve changes from "elastic" to "plastic".

It is seen in Figure 5.6 that a bilinear idealisation is a satisfactory approximation of the bearing pressure curve obtained from the finite element analysis. If the slopes of the "elastic" and "plastic" parts and the yield pressure of the bilinear curve are determined, then the complete bilinear bearing pressure curve can be plotted. During the parametric study, the "elastic" slope, the "plastic" slope and the yield pressure of the idealised bilinear bearing pressure curve was related to the SU2 model parameters, in an effort to produce simplified design charts.

5.5 VALUES OF MODEL PARAMETERS

The objective of the parametric study is to investigate the effect of SU2 model parameters on the predicted bearing response of surface circular footings on carbonate sand. Clearly, a representative range of values of the model parameters needs to be chosen to obtain realistic predictions of the footing response. Such a range of values for the model parameters was chosen after a careful review of the relevant literature.

The ranges of parameter values chosen for the study in which the Case 1 (Figure 5.3) profile was assumed are presented below in Table 5.1.

Table 5.1 Ranges of model parameters

ϕ' (deg)	κ	λ	ν	e_{cs}	p'_o (MPa)	r
35-45	0.005-0.05	0.1-0.3	0.1-0.3	2-3	0.25-25	2-5

The critical state friction angle ϕ' and plastic slope λ of the virgin consolidation line are usually quite high for carbonate sand. The range of values generally observed was considered. The elastic parameter κ generally has much lower values compared to silica sand. A larger range of values was considered to include a variety of soil types. The void ratio constant e_{cs} has a relatively high value for carbonate sands. This is because these soils generally exist in a loose state. The preconsolidation pressure

p_o' of uncemented sand and silt can be quite low. On the other hand, highly "cemented" carbonates may have high values of p_o'. North Rankin carbonate sand was found to have a spacing ratio of approximately 5.0. No direct data were available for other carbonates. Again a range of values was considered to cover a variety of soils.

In offshore conditions, the soil beneath the foundation usually exists in a completely submerged condition. The values assumed for the submerged unit weight γ' and coefficient of earth pressure at rest K_o were chosen as follows:

$$\gamma' = 7\text{kN/m}^3 \tag{5.3}$$

$$K_o = 0.5 \tag{5.4}$$

These values are considered typical for carbonate sand. The diameter B of the circular footings was varied between 1m – 100m. Such a wide range of foundation diameters may be encountered in offshore locations. Carbonate sand generally has a high void ratio and permeability. The monotonic loading of a foundation on carbonate sand is thus assumed to occur under fully drained conditions.

A separate and limited parametric study for the special case of a circular footing resting on normally consolidated carbonate sand was also carried out. The soil profile beneath the footing is illustrated as case 2 in Figure 5.3. The range of model parameters chosen for that study will be presented later.

5.6 PARAMETRIC STUDY

A range of values has been selected to conduct a parametric study of the effect of SU2 model parameters on the bearing response of a surface circular footing on carbonate sand. The effect of each model parameter is investigated in detail in subsequent subsections of this chapter.

5.6.1 EFFECT OF FOOTING DIAMETER, *B*

The effect of footing diameter on the bearing pressure mobilised by surface circular footings is investigated in this section. A constant set of values was chosen for the SU2 model parameters. The footing diameter was varied between 1m – 100m by appropriately scaling the dimensions of the finite element mesh. The values of the SU2 model parameters used to obtain the model predictions are given in Table 5.2 below.

Table 5.2 Model parameters to study effect of footing diameter

ϕ' (deg)	κ	λ	ν	e_{cs}	p'_o (MPa)	r	γ' (kN/m^3)	K_o	B (m)
35	0.005	0.1	0.1	2.5	0.25	5.0	7.0	0.5	1-100

Figure 5.7 shows plots of the mobilised bearing pressure obtained from finite element analysis in terms of the footing displacement. The bearing pressure mobilised at any displacement was observed to decrease with increased diameter of the footing. In Figure 5.8, the mobilised bearing pressures are plotted in terms of the footing settlements normalised with respect to the footing diameter. It was observed that the bearing pressure mobilised at any normalised displacement increases with the diameter of the footing. These findings are consistent with the centrifuge test results of Finnie and Randolph (1994) presented earlier. Similar patterns of behaviour were observed with significantly larger values of the preconsolidation pressure p'_o. The trends presented in Figures 5.7 and 5.8 were observed to be true for a wide range of values of other SU2 model parameters as well.

5.6.2 EFFECT OF PRECONSOLIDATION PRESSURE, p'_o

The effect of preconsolidation pressure p'_o of the "cemented" layer on the bearing response of a surface circular footing is now investigated. The preconsolidation

pressure p_o' of a soil is generally understood to represent the past maximum effective pressure that it has experienced in its geological history, or the effects of cementation. It is conventionally determined from oedometer test data by Casagrande's (1936) method. For "cemented" and structured soils, preconsolidation pressures are not necessarily equal to the maximum past pressure that the soil has experienced. They are the result of interparticle bonding, which controls the yielding level. When the total applied pressure on a specimen is larger than the preconsolidation pressure, yielding and "plastic" response is observed with consequent large changes in the void ratio. The effect of preconsolidation pressure on the response of surface circular footings is investigated in this section.

A constant footing diameter B and a constant set of values were chosen for the 6 SU2 model parameters besides p_o'. The values chosen are listed below in Table 5.3.

Table 5.3 Parameters to investigate effect of preconsolidation pressure

M	κ	λ	ν	e_{cs}	p_o' (MPa)	r	γ' (kN/m^3)	K_o	B (m)
1.42	0.005	0.1	0.1	2.5	0.25-14.0	5.0	7.0	0.5	100.0

The preconsoildation pressure p_o' of the underlying "cemented" layer was increased from a low value of 250 kPa to a high value of 14,000 kPa. The lower values are typically observed in uncemented carbonate sand and silt (Finnie, 1993). Higher preconsolidation pressures are usually observed in dense or highly "cemented" carbonate sand (Huang, 1994). In this study, higher initial values of p_o' also imply thicker "cemented" soil layers.

Figures 5.9 and 5.10 plot the mobilised bearing pressures against normalised footing displacements. It was observed that there is an increase in the mobilised bearing pressure with the preconsolidation pressure p_o'. Figure 5.9 shows that initial "elastic" and eventual "plastic" slopes of the bearing pressure curve are not significantly affected by the change in preconsolidation pressure, as would be expected. However,

the yield or inflection pressure, showing the change from largely "elastic" to largely "plastic" behaviour in the soil, is observed to increase with the preconsolidation pressure, also as expected. The mobilised bearing pressures may be normalised by the preconsolidation pressure p_o'. In Figure 5.11, the normalised bearing pressures are plotted against normalised footing displacements. It is observed that the normalised bearing pressure decreases with the preconsolidation stress. This implies that the rate of increase of the mobilised bearing resistance of the footing is less than the rate of increase of the preconsolidation pressure of the underlying soil.

In summary, it was observed that the bearing pressure mobilised by the footing increases with the preconsolidation pressure or the thickness of the "cemented" layer. However, the rate of increase of the mobilised bearing pressure is significantly less than the rate of increase in the preconsolidation pressure of the underlying soil.

5.6.3 EFFECT OF NON-DIMENSIONAL PARAMETER $\frac{\gamma' B}{p_o'}$

It is demonstrated in this section that for the given soil profile, the combined effects of three parameters on foundation response can actually be expressed by a single variable. The three parameters are respectively the effective unit weight of the soil γ', the footing diameter B and the preconsolidation pressure p_o' of the soil. These parameters may be combined together to form a single non-dimensional variable, $\frac{\gamma' B}{p_o'}$.

Equation (5.2) shows that for the soil profile described as case 1, the thickness of "cemented" layer immediately below the footing is proportional to its preconsolidation pressure, i.e., $H \propto \frac{p_o'}{\gamma'}$. It follows from equation (5.2) that

$$\frac{\gamma' B}{p_o'} \propto \frac{B}{H} \tag{5.5}$$

Thus for the soil profile considered in the study, the inverse of the parameter $\frac{\gamma' B}{p_o'}$ gives a measure of the footing diameter relative to the thickness of the "cemented" layer.

The range of values of the model parameters considered to investigate the effect of the parameter $\frac{\gamma' B}{p_o'}$ is provided below in Table 5.4.

Table 5.4 Model parameters to investigate effect of $\frac{\gamma' B}{p_o'}$

M	κ	λ	ν	e_{cs}	p_o' (MPa)	r	γ' (kN/m^3)	K_o	B (m)
1.42	0.005	0.1	0.1	2.5	0.25-25.0	5.0	7.0	0.5	1.0-100.0

The effect of the compound parameter $\frac{\gamma' B}{p_o'}$ on footing response is demonstrated by an example. The bearing responses of two footings are considered. The first footing has a diameter of 25m. It is resting on carbonate sand having a preconsolidation pressure of 250 kPa. The second footing has a diameter of 100m. It is resting on carbonate sand having a preconsolidation pressure of 1000 kPa. The effective unit weight and the values of the remaining SU2 model parameters for the two sands are assumed to be identical. Therefore the value of the parameter $\frac{\gamma' B}{p_o'}$ for the two footings is the same (0.7). Figure 5.12 shows that that the absolute bearing pressure mobilised by the larger footing at 30% displacement is approximately 4 times that of the smaller footing resting on the weaker soil. The mobilised bearing pressures of the two footings were normalised by the respective preconsolidation pressures of the "cemented" layer beneath the footings. Figure 5.13 plots the normalised bearing pressure against the normalised displacement. Almost identical curves are obtained.

Figure 5.14 shows that a similar result is obtained for a much smaller value of the parameter $\frac{\gamma' B}{p_o'}$.

The influence of the effective unit weight of the soil γ' in the compound parameter $\frac{\gamma' B}{p_o'}$ is now investigated. The preconsolidation pressure and the effective unit weight of the soil, beneath each of the two footings in the given example, were both halved. Thus the value of the parameter $\frac{\gamma' B}{p_o'}$ remain unchanged for the two footings. The non-dimensional bearing pressures plotted against non-dimensional settlements were found to be identical to Figures 5.13 and 5.14. This demonstrates that for the given soil profile, a unique value of the parameter $\frac{\gamma' B}{p_o'}$ will result in an almost unique non-dimensional bearing pressure curve, irrespective of the individual values of each of the three variables.

Figure 5.15 shows plots of the normalised bearing pressure mobilised at 10%, 20% and 30% non-dimensional displacement as a function of the non-dimensional parameter $\frac{\gamma' B}{p_o'}$. It is observed that the non-dimensional bearing pressures increase with $\frac{\gamma' B}{p_o'}$. This indicates that the influence of the parameter $\gamma' B$ on the normalised bearing pressure mobilised by a surface circular footing is greater than the preconsolidation pressure p_o' of the underlying carbonate sand.

It has been shown in this section that for the given soil profile, the bearing response of the footing can be expressed almost uniquely as a function of the compound parameter $\frac{\gamma' B}{p_o'}$. The next section investigates the effect of the elastic parameter on the bearing response of the footing.

5.6.4 EFFECT OF ELASTIC PARAMETER, κ

The effect of the elastic parameter κ on the bearing response of the footing is investigated in this section. The elastic parameter κ defines the slope of the elastic rebound line in $e - \ln p'$ space obtained from isotropic consolidation. e is the void ratio and p' is the mean effective pressure. In the SU2 model, the elastic bulk modulus is pressure dependent and inversely proportional to the elastic parameter κ. A constant Poisson's ratio is generally assumed in the model. Thus the elastic shear modulus is also inversely proportional to the elastic parameter κ.

The elastic parameter κ was varied from 0.005 to 0.05, for a wide range of values of the parameter $\frac{\gamma' B}{p'_o}$. Figure 5.16 shows that for relatively large values of $\frac{\gamma' B}{p'_o}$, the effect of κ on the bearing response of the footing is relatively small, except at very small relative displacements. This is because the "elastic" component in the bearing response is also relatively small. This is typically observed in footings resting on normally consolidated carbonate sand and silt (Finnie and Randolph, 1994). Figure 5.17 shows that for much smaller values of $\frac{\gamma' B}{p'_o}$, there is a significant "elastic" component in the bearing response. For the assumed soil profile, a smaller value of $\frac{\gamma' B}{p'_o}$ implies a thicker (relative to the footing diameter) "cemented" or overconsolidated layer exists beneath the foundation. The corresponding strong "elastic" response shown is consistent with the response of a foundation resting on a thicker layer of "cemented" or overconsolidated sand.

For a footing with a small value of $\frac{\gamma' B}{p'_o}$, Figure 5.17 shows that as κ is increased by an order of magnitude, the non-dimensional bearing pressure mobilised at 30% non-dimensional displacement is approximately halved. There is also a significant decrease in the non-dimensional "elastic" slope. Thus for relatively small values of

$\frac{\gamma' B}{p'_o}$, the elastic parameter κ has a significant influence on the "elastic" slope as well as the bearing pressure mobilised by the footing.

Figures 5.16 and 5.17 show that that the "plastic" part of the bearing pressure curves is approximately parallel for different values of κ. Thus the "plastic" response of the footing may be considered to be effectively independent of the value of κ, as expected.

The non-dimensional "elastic" slope of the bearing pressure curve is defined here as the slope of the initial part of the pressure-displacement curve of the footing, which is idealised to be linear. The pressure in this case is normalised by the preconsolidation pressure of the soil, and the displacements are expressed relative to the diameter of the footing (as fractions of the footing diameter). Figure 5.18 shows that the non-dimensional "elastic" slope decreases almost hyperbolically with κ. This is consistent with the SU2 model formulation in which the elastic bulk and shear modulus is assumed to be inversely proportional to κ.

Figure 5.19 shows that for any κ, the non-dimensional "elastic" slope increases with $\frac{\gamma' B}{p'_o}$. Thus the non-dimensional slope of the "elastic" footing response is not solely a function of the elastic parameter κ of the SU2 model. It is also dependent on the parameter $\frac{\gamma' B}{p'_o}$. Figure 5.20 shows that the non-dimensional "elastic" slope can be approximated by a single curve for different κ. This curve can be used to determine the non-dimensional "elastic" slope of the bearing pressure curve once κ and $\frac{\gamma' B}{p'_o}$ are known. Figure 5.21 plots the non-dimensional yield pressure as a function of $\frac{\gamma' B}{p'_o}$. It is observed that the yield pressure decreases with both κ and $\frac{\gamma' B}{p'_o}$, except for very

small values of $\frac{\gamma' B}{p_o'}$. The non-dimensional yield pressure is seen to lie within a narrow range, for a wide range of values of κ and $\frac{\gamma' B}{p_o'}$.

The effect of the elastic parameter κ on the bearing response of a footing was investigated. The "elastic" slope of the bearing pressure curve was found to be inversely proportional to κ. For the given soil profile, it is seen that the parameter $\frac{\gamma' B}{p_o'}$ also affects the "elastic" response of the footing. In the next section the effect of plastic volume compressibility of the soil on the footing response is discussed.

5.6.5 EFFECT OF PLASTIC PARAMETER, λ

The effect of the plastic volume compressibility of the soil on the bearing response of footings on carbonate sand is now investigated. The plastic compressibility parameter λ defines the slope of the virgin consolidation line in e-$\ln p'$ space. e is the void ratio and p' is the mean effective pressure.

The effect of λ on footing response was studied for various values of the parameter $\frac{\gamma' B}{p_o'}$. The values of the model parameters used in the parametric study are given below in Table 5.5.

Table 5.5 Model parameters to investigate the effect of λ

M	κ	λ	ν	e_{cs}	p_o' (kPa)	r	γ' (kN/m^3)	K_o	B (m)
1.42	0.005	0.1-0.3	0.1	2.5	Variable	5.0	7.0	0.5	Variable

Figure 5.22 shows that increasing the value of λ by a factor of three results in a large decrease in the bearing pressure mobilised at 30% non-dimensional

displacement. This is consistent with the conclusions of previous research which show that increased volume compressibility plays a significant role in reducing the bearing pressure mobilised by footings on carbonate sand. Figure 5.22 shows that the "elastic" responses of these footings are virtually identical. Thus the predominanly elastic response of a footing may be assumed to be approximately independent of the value of the plastic compressibility parameter λ, as expected.

Figure 5.23 plots the non-dimensional bearing pressure at 10%, 20% and 30% non-dimensional displacement. It is observed that the non-dimensional bearing pressure at any non-dimensional displacement decreases with λ, i.e. with increasing plastic volume compressibility of the sand.

The non-dimensional "plastic" slope of the bearing pressure curve is defined here as the slope of the "plastic" part of the pressure-displacement curve of the footing, which is idealised to be linear. The pressure in this case is normalised by the preconsolidation pressure of the soil, and the displacements are expressed relative to the diameter of the footing (as fractions of the footing diameter). Figure 5.24 plots the non-dimensional "plastic" slope of the bearing pressure curve as a function of λ. The plot shows a decrease in the "plastic" slope with λ. For a constant λ, a larger value of $\frac{\gamma' B}{p'_o}$ corresponds to a larger non-dimensional "plastic" slope. Figure 5.24 may be used to determine the non-dimensional "plastic" slope of the bearing pressure curve once λ and $\frac{\gamma' B}{p'_o}$ are known.

The effect of the plastic compressibility parameter λ on the bearing response of footing has been investigated. The bearing pressure and the "plastic" slope of the bearing pressure curve were found to decrease with λ. For the given soil profile, it was seen that the non-dimensional "plastic" slope of the bearing pressure curve was also dependent on the parameter $\frac{\gamma' B}{p'_o}$.

5.6.6 EFFECT OF FRICTION ANGLE, ϕ'

In conventional bearing capacity theory, the friction angle of the soil has a major influence on the drained bearing capacity of a footing. In the SU2 model, the ultimate effective friction angle defines the slope of the critical state line. This slope is termed the critical state ratio. It is identified by the symbol, "*M*". The critical state line controls the ultimate or limit state response of the soil. For triaxial compression conditions M and the ultimate friction angle ϕ' are related as follows:

$$M = \frac{6Sin\phi'}{3 - Sin\phi'} \tag{5.6}$$

The effect of friction angle or critical state ratio of the SU2 model on the bearing pressure mobilised by a surface circular footing is investigated in this section.

Figure 5.25 shows that an increase in friction angle (ϕ' or M) results in an increase in the non-dimensional bearing pressure mobilised at any non-dimensional displacement. It is obvious from the figure that the effect of friction angle occurs primarily during the "plastic" part of the response, as expected. Figure 5.26 plots the ratio of non-dimensional "plastic" slope as a function of $\frac{\gamma' B}{p'_o}$. The "plastic" slopes were calculated for two values of M. The ratio of the "plastic" slopes was observed to decrease with $\frac{\gamma' B}{p'_o}$.

In Figure 5.24, the non-dimensional "plastic" slopes are plotted as a function of λ and $\frac{\gamma' B}{p'_o}$ for M = 1.42 (ϕ' = 35°). Figure 5.26 shows that the ratio of "plastic" slopes computed for different values of M decreases with $\frac{\gamma' B}{p'_o}$. An equation is now proposed to determine the non-dimensional "plastic" slope of the bearing pressure curve for any value of M ($1.42 < M \leq 1.85$). It is given as follows:

$$S_M = \left(\frac{M}{1.42}\right)^n S_{1.42} \tag{5.7}$$

S_M = Non-dimensional "plastic" slope at critical state ratio M

$S_{1.42}$ = Non-dimensional "plastic" slope at critical state ratio of 1.42

n = An empirically determined exponent

Figure 5.27 plots the exponent n as a function of λ and $\frac{\gamma' B}{p'_o}$. The non-dimensional "plastic" slope obtained from equation (5.7) and Figures 5.24 and 5.27 is valid for any M in the range $1.42 \leq M \leq 1.85$.

The effect of M on the non-dimensional "elastic" slope appears to be negligible. Thus the non-dimensional "elastic" slope can be assumed to be independent of the value of the friction angle, as expected. The non-dimensional yield pressure was observed to increase with M. However, for simplicity, the effect of the critical state ratio M on yield pressure was ignored in the development of design charts.

In summary, for the assumed soil profile the ultimate friction angle was observed to have a significant effect on the bearing response of the footing for relatively low values of $\frac{\gamma' B}{p'_o}$. For larger $\frac{\gamma' B}{p'_o}$, the influence of ultimate friction angle on the bearing response was observed to decrease. The effect of friction angle on the "elastic" response of the footing appears to be negligible.

5.6.7 EFFECT OF POISSON'S RATIO, ν

The effect of Poisson's ratio on the bearing response of the footing is now studied. Figure 5.28 shows that for relatively large values of $\frac{\gamma' B}{p'_o}$ the effect of Poisson's ratio ν on the mobilised bearing pressure is virtually negligible. Figure 5.29 shows that

for relatively small values of $\frac{\gamma' B}{p_o'}$, the effect of Poisson's ratio ν on the bearing response of surface circular footings becomes significant. For relatively small $\frac{\gamma' B}{p_o'}$, the non-dimensional "elastic" slope is observed to decrease with ν. Overall, there is also a decrease in the bearing pressure mobilised at any displacement.

In summary, the effect of Poisson's ratio ν on the mobilised bearing pressure is negligible for relatively large values of $\frac{\gamma' B}{p_o'}$ and small for relatively small values of $\frac{\gamma' B}{p_o'}$. For simplicity, the effect of Poisson's ratio on the mobilised bearing pressure has been ignored in the remainder of this study.

5.6.8 EFFECT OF VOID RATIO CONSTANT, e_{cs}

In this section the effect of the void ratio constant e_{cs} on the bearing response of a surface circular footing is discussed. e_{cs} is defined as the void ratio at unit mean effective pressure on the critical state line, drawn in e-$\ln p'$ space. e is the void ratio and p' is the mean effective pressure. The void ratio constant determines the position of the critical state line in e-$\ln p'$ space.

Figure 5.30 shows that an increase in the value of e_{cs} results in increased non-dimensional bearing pressure being mobilised at any non-dimensional displacement. The non-dimensional bearing pressures were further normalised by $(1+e_{cs})$. It is seen in Figure 5.31 that the renormalised bearing pressure curves for different values of e_{cs} are virtually identical. This fact has been used subsequently to correct the non-dimensional "elastic" slope, yield pressure and "plastic" slope obtained respectively from Figures 5.20, 5.21 and 5.24 for a void ratio constant e_{cs} other than 2.5. The design parameters presented in these figures were computed for a void ratio constant e_{cs} of 2.5.

The results in Figures 5.30 and 5.31 were obtained for relatively large values of $\frac{\gamma' B}{p'_o}$.

Figures 5.32 and 5.33 shows that similar results are obtained for relatively small values of $\frac{\gamma' B}{p'_o}$.

Increasing the void ratio constant increases the bearing pressure mobilised at any displacement. It appears that increase in the void ratio constant and consequently the void ratio at any preconsolidation pressure, should decrease the bearing pressure mobilised at any displacement. However, critical state formulations of the Cam Clay type predict an increase of the elastic and plastic bulk modulus with void ratio, contrary to normal expectations. This is a consequence of assuming semi-logarithmic equations for the isotropic consolidation curves. Pestana and Whittle (1995) described this as a serious limitation of classical/critical state formulations. This anomaly may be corrected by assuming a log-log formulation for the normal consolidation curve, as suggested by Pestana and Whittle (1995).

5.6.9 EFFECT OF SPACING RATIO, *r*

In this section the effect of the spacing ratio parameter on footing behaviour is investigated. The spacing ratio parameter r provides a measure of the distance between the virgin consolidation line and the critical state line, measured along an elastic rebound line in e-$\ln p'$ space. The spacing ratio was computed to be approximately 5.0 for North Rankin carbonate sand. It is possible that carbonate sands at other locations may have significantly different values of the spacing ratio. There is a discernible change in spacing ratio as a result of "cementation". The change, however, is quite small.

Figures 5.34 shows the typical effect of spacing ratio on the bearing pressure mobilised by the footing. It is observed that the non-dimensional "elastic" slope of the bearing pressure curves is almost identical. The "plastic" parts of the two curves are distinct and separate but approximately parallel. The "plastic" slopes of these two

curves may be assumed to be approximately equal. Thus the non-dimensional "elastic" and "plastic" slopes obtained for footings with different values of the spacing ratio r may be assumed to be approximately same. Hence, the non-dimensional "elastic" and "plastic" slopes that may be obtained from Figures 5.20 and 5.24 are assumed to be the same for values of r other than 5.0.

The yield pressures (defining transition from primarily "elastic" to primarily "plastic" behaviour) of the bearing pressure curves in Figure 5.34 is observed to be distinctly different. The figures show that when the value of the expression $(r-1)$ is reduced by one-quarter, the yield pressure is approximately doubled. The change in the yield pressure due to a change in the spacing ratio parameter may be explained in the following way. The SU2 yield locus is defined by the following equation:

$$\left(\frac{q}{Mp'}\right)^2 = \frac{(p'_o/p')-1}{r-1} \tag{5.8}$$

In equation (5.8), q is the deviator stress, p' is the mean effective pressure, p'_o is the virgin consolidation pressure and M is the critical state ratio. It may be assumed that equation (5.8) approximates a constant mean pressure test under triaxial conditions. In that case, the deviator stress is inversely proportional to a function of the spacing ratio as follows:

$$q \propto \frac{1}{\sqrt{r-1}} \tag{5.9}$$

The ratio of the deviator stresses at first yield, for a single element of soil, at constant mean pressure with r =2 and r = 5 is given as follows:

$$\frac{q_{r=2}}{q_{r=5}} = \frac{\sqrt{5-1}}{\sqrt{2-1}} = 2 \tag{5.10}$$

This ratio is consistent with the ratio of the yield pressures observed in Figure 5.34. The behaviour of a single element of the soil thus appears to be reflected quite closely in the behaviour of the footing. The yield pressures shown in Figure 5.21 were obtained for r = 5.0. Equations (5.9) and (5.10) implies that they should be scaled by the factor $\frac{2}{\sqrt{r-1}}$, for carbonate sand having spacing ratio r other than 5.0. It is observed that for the assumed soil profile, the change in yield pressure with spacing ratio has a significant effect on the mobilised bearing pressure for relatively small $\frac{\gamma' B}{p_o'}$. The effect however, is small for relatively large $\frac{\gamma' B}{p_o'}$.

In summary, the non-dimensional "elastic" and "plastic" slopes of the bearing pressure curve were observed to be approximately independent of the value of the spacing ratio parameter r. The non-dimensional yield pressure was observed to be approximately inversely proportional to the square root of $(r-1)$.

5.7 DESIGN CHARTS

The effects of all the SU2 model parameters on the bearing response of a surface circular footing have now been investigated. The investigation was carried out for an assumed and simplified soil profile below the footing, illustrated as case 1 in Figure 5.3. In this section, design charts are suggested. These charts may be used to obtain an idealised bearing pressure curve for a surface circular footing resting on carbonate sand, with a profile of preconsolidation pressure that may be approximated as that defined as case1.

During the course of the study, the mobilised bearing pressure curve was idealised as bilinear. The bilinear curve was assumed to have a linear "elastic" part and a linear "plastic" part. A yield pressure marks the transition from "elastic" to "plastic" behaviour. The suggested design charts may be used to obtain the "elastic" slope, yield pressure and "plastic" slope of the idealised bilinear bearing pressure curve.

Once these are known, the corresponding bilinear bearing pressure curve can be drawn.

Figure 5.35 is proposed as a design chart to determine "elastic" slope of the bearing pressure curve for any κ. It incorporates correction for the void ratio constant e_{cs}. The SU2 model elastic parameter κ is assumed as known and the parameter $\frac{\gamma' B}{p'_o}$ is computed. The normalised "elastic" slope (NES) is then determined from Figure 5.35. Figure 5.36 is proposed as a design chart to determine the normalised yield pressure for any spacing ratio r and void ratio constant e_{cs}. The normalised yield pressure is the pressure at which the mobilised bearing presure curve makes a transition form primarily "elastic" to primarily "plastic" behaviour. The mobilised bearing pressure in this case is normalised by the preconsolidation pressure of the soil, and the footing displacements are expressed relative to the diameter of the footing (as fractions of the footing diameter).

Figure 5.37 is proposed as a design chart to determine the "plastic" slope for any critical state ratio M and any void ratio constant e_{cs}. The plastic compressibility parameter λ is assumed as known and the parameter $\frac{\gamma' B}{p'_o}$ is computed. Figure 5.37 is then used to obtain the normalised "plastic" slope (NPS) of the bilinear bearing pressure curve. The normalised "elastic" and normalised "plastic" slope of the bearing pressure curve has been defined earlier. The absolute "elastic" and "plastic" slopes of the bearing pressure curve may be determined from the normalised slopes in straightforward way.

The proposed design charts ignore the effect of Poisson's ratio on the non-dimensional "elastic" slope, "plastic" slope and yield pressure. They also ignore the effect of friction angle on the "elastic" slope and the yield pressure. It has been demonstrated that these effects are either negligible or small enough to be ignored

The proposed design charts may be used as a simple means of determining an approximate bilinear bearing pressure curve of a surface circular footing on

carbonate sand. A simplistic soil profile was assumed in the parametric study. Thus the design charts are only applicable for cases where this profile is a reasonable approximation to field conditions.

5.8 STUDY OF FOOTING ON NORMALLY CONSOLIDATED CARBONATE SAND

Finnie and Randolph (1994) conducted centrifuge tests of surface circular footings on normally consolidated carbonate sand and silt. They plotted the absolute bearing pressure against footing settlements. It was observed that the bearing pressure curves are relatively linear and approximately independent of the footing diameter B. The curves could be described by a single non-dimensional parameter. This parameter was termed the bearing modulus. The bearing modulus was defined as follows:

$$M_b = \frac{q_{av}}{\gamma' \delta} \tag{5.11}$$

In equation (5.11), q_{av} is the average bearing pressure mobilised at footing penetration δ and γ' is the effective unit weight of the soil.

There are several advantages of investigating the bearing pressure mobilised by a surface circular footing resting on normally consolidated sand. Surface circular footings often rest on a thin layer of "cemented" or overconsolidated material with underlying normally consolidated carbonate sand. The bearing pressure mobilised by a footing on normally consolidated carbonate sand provides a lower limit of the response under such conditions. The effects of the SU2 model parameters κ ,v, r and M on the bearing pressure were observed to be either small or negligible for relatively large values of $\frac{\gamma' B}{p_o'}$. For relatively large values of $\frac{\gamma' B}{p_o'}$, the bearing response corresponds closely to that of a footing resting on normally consolidated carbonate sand. The preconsolidation pressure profile below a surface footing resting on normally consolidated sand is effectively determined by the soil self weight

stresses. This profile is shown as case 2 in Figure 5.3. Experimental results of Finnie and Randolph (1994) and numerical simulation by the SU2 model show that the effect of the diameter B on the absolute pressure-displacement response of a surface footing is negligible. Thus the single parameter that significantly affects the bearing response of a surface circular footing on carbonate sand is the plastic volume compressibility λ.

The effect of the parameter λ on the bearing response of a surface circular footing on normally consolidated carbonate sand was investigated for reasons that should now be clear from the above discussion. Figure 5.38 is a plot of the mobilised bearing pressure against footing settlement obtained from numerical simulation for different values of λ. The plot shows that the bearing pressure curves obtained may be approximated as straight lines. It is also observed that the bearing pressure mobilised at any displacement decreases with increasing plastic compressibility. The non-dimensional bearing modulus for each of these curves was computed by fitting a straight line through the origin to each of these curves. Figure 5.39 plots the resulting bearing modulus against the plastic compressibility parameter λ. This chart may be used to determine the bearing pressure mobilised by surface circular footings resting on normally consolidated carbonate sand.

In summary, it was observed that the significant parameter that affects the bearing response of a surface circular footing on normally consolidated carbonate sand is the plastic volume compressibility λ. A design chart was proposed to determine the bearing modulus from the plastic volume compressibility. Once the bearing modulus is known, the corresponding pressure-displacement response of a surface circular footing on normally consolidated sand may be plotted.

5.9 EXAMPLE PREDICTIONS

In this section, the predicted bearing pressure curves for surface circular footings resting on carbonate sand are obtained using the proposed design charts. For the soil profile considered as case 1 (Figure 5.3), the bilinear bearing pressure curves

obtained using the proposed design charts were compared with the results of more accurate finite element analysis. The bearing pressure curves for footings resting on a thin layer of strong, medium and weakly "cemented" sand with underlying normally consolidated sand layer were obtained using the proposed chart for bearing modulus (Figure 5.39). The predicted curves were subsequently compared with experimental data of Finnie and Randolph (1994).

Consider first the case of a footing resting on a "cemented" layer overlying normally consolidated carbonate sand. The soil profile below the footing is assumed to be similar to that of case 1 in Figure 5.3. The values selected for the SU2 model parameters for the example problem are given in Table 5.6.

Table 5.6 Model parameters for example problem

M	κ	λ	ν	e_{cs}	p_o' (kPa)	r	γ' (kN/m^3)	K_o	B (m)
1.6	0.005	0.2	0.1	2.0	500.0	5.0	7.0	0.5	10.0

Figure 5.40 compares the bilinear mobilised bearing pressure curve obtained using the proposed design charts (Figures 5.35, 5.36 and 5.37) with the results of the finite element analysis. A reasonable agreement is observed between the two. The bilinear approximation is sufficiently accurate for most practical purposes. It is likely that better agreement may have been obtained if the increase in yield pressure due to the increase in frictional angle was considered. However, more investigations will be required to determine this. The detailed computation performed to obtain the mobilised bearing pressure curve from the proposed design charts is presented in Appendix 5.1.

Consider now the centrifuge data of a surface circular footing resting on strong, medium and weak "cemented" crust underlain by normally consolidated carbonate sand (Finnie and Randolph, 1994). The soil profile assumed for the underlying normally consolidated carbonate sand is similar to that shown as case 2 in Figure 5.3. The SU2 model parameters selected for the "cemented" crust and underlying

normally consolidated carbonate sand have been described already in Tables 4.12 to 4.16 in section 4.9. Figure 5.41 shows the comparison of the design chart predictions with the centrifuge test data for each of the layered materials. In each case, satisfactory agreement between model predictions and experimental data is observed.

The design chart in Figure 5.39 for normally consolidated carbonate sand was used to make predictions for the layered material in the following way. It may be assumed that the primary effect of a thin "cemented" crust overlying normally consolidated sand is to increase the apparent stiffness of the footing response. The stiff crust distributes the footing load over a larger area in the underlying normally consolidated sand, which contributes almost all the settlement. Consequently for a given footing load, the pressures and settlements of the underlying normally consolidated sand is greatly reduced and the footing shows an apparent increase in stiffness in the pressure-displacement response.

For the layered material considered, it was assumed that the thin "cemented" crust distributes the footing load on the normally consolidated sand in an area of 1.2, 2.5 and 3.0 times the area of the footing for the case of weak, medium and strong crust respectively. Similar values were reported by Finnie (1993), for a rigid foundation resting on a thin and relatively stiff "cemented" layer, overlying a soft layer. The bearing modulus for the normally consolidated sand was obtained using the design chart in Figure 5.39, which was then directly increased by factors of 1.2, 2.5 and 3.0 respectively for the weak, medium and strong crust overlying the normally consolidated material. Figure 5.41 shows that satisfactory predictions of the pressure-displacement curves were obtained for the layered material using this approach. Figure 5.42 shows the pattern of displacements obtained from finite element analysis for a thin crusted material overlying normally consolidated carbonate sand. It is obvious that the crust is behaving like a rigid plate, which punches into the underlying normally consolidated sand. Further investigations are required to relate the bearing capacity distribution factors with the physical properties of the soil as well as the soil profile. This would be necessary in order to develop a design method for more general soil profiles.

The proposed design charts have been used to predict the bearing pressure curve of a surface circular footing on carbonate sand. Satisfactory agreement could be obtained with the results of the more accurate finite element analysis as well as with experimental data for layered material.

5.10 CONCLUSION

A parametric study was carried out to investigate the effect of the SU2 model parameters on the bearing response predicted for surface circular footings on carbonate sand. In the first case, a finite layer of "cemented" material was assumed to exist immediately beneath the footing. The degree of overconsolidation was assumed to decrease gradually with depth, until at a certain depth the sand became normally consolidated. The study shows that for the assumed soil profile, the footing diameter, the preconsolidation pressure, plastic volume compressibility and the friction angle of the underlying sand exert the greatest influence on the mobilised bearing pressure. The study confirms that the bearing pressure mobilised at any displacement decreases with plastic volume compressibility. It was observed that that for the assumed soil profile, a unique value of $\frac{\gamma' B}{p'_o}$ results in almost a unique non-dimensional bearing pressure curve. Simplified design charts were proposed to determine an approximate bilinear bearing pressure curve for the footing.

It was concluded that plastic volume compressibility was the single major factor influencing the mobilised bearing pressure of a footing resting on normally consolidated carbonate sand. A design chart was proposed to determine the bearing modulus of such footings from the plastic volume compressibility. A method to modify this bearing modulus was proposed for a footing resting on a thin crust of "cemented" material underlain by normally consolidated carbonate sand. The bearing pressure curve for a footing on normally consolidated carbonate sand would generally give the lower limit of footing response. The proposed design charts have the attraction of requiring input information that is readily available. The material input data can be measured in standard laboratory tests and normally would be

obtained routinely as part of a site investigation and associated laboratory testing programme.

A practical limitation of the study was the assumption of the simplified soil profiles beneath the footing, which was necessary to determine the effect of various model parameters on the bearing response. Thus the proposed design charts should be considered to be generally unsuitable for use in cases of significant variation in the profile of the underlying sand. A simplified soil profile is probably approximately applicable for small diameter footings with a smaller depth of influence. For large diameter footings with greater a depth of influence, such simplification would no longer adequately represent reality. However, use of average or lower bound values of the significant soil parameters in the proposed design method, is expected to provide a conservative estimate of the bearing pressure mobilised by footings of large diameter.

APPENDIX 5.1 BEARING CAPACITY OF SURFACE CIRCULAR FOOTINGS USING DESIGN CHARTS

The bilinear mobilised bearing pressure curve of a 10m diameter surface circular footing was computed using the design charts proposed in Chapter 5. The details of the calculation are presented in this section. The values of the model parameters have been already given in Table 5.6, which is reproduced here for convenience:

Table 5.6 Model parameters for example problem

M	κ	λ	ν	e_{cs}	p'_o (kPa)	r	γ' (kN/m^3)	K_o	B (m)
1.6	0.005	0.2	0.1	2.0	500.0	5.0	7.0	0.5	10.0

The steps followed in the computation are listed below:

1. The parameter $\frac{\gamma' B}{p'_o}$ was determined.

$$\frac{\gamma' B}{p'_o} = \frac{7x19}{500} = 0.14$$

2. For $\kappa = 0.005$ and $\frac{\gamma' B}{p'_o} = 0.14$, the normalised "elastic" slope (*NES*) was determined from Figure 5.35.

$$NES \frac{3.5\kappa}{(1+e_{cs})} = 0.5$$

$$NES = 0.5 \frac{(1+e_{cs})}{3.5\kappa} = 86.0$$

3. For $\kappa = 0.005$ and $\frac{\gamma' B}{p'_o} = 0.14$, the normalised yield pressure (*NYP*) was determined from Figure 5.36.

$$NYP \frac{\sqrt{r-1}}{2} \frac{3.5}{(1+e_{cs})} = 0.764$$

$$NYP = 0.764 \frac{2}{\sqrt{r-1}} \frac{(1+e_{cs})}{3.5} = 0.65$$

4. For $\lambda = 0.2$ and $\frac{\gamma' B}{p'_o} = 0.14$, the normalised "plastic" slope (*NPS*) was determined from Figure 5.37. For $\lambda = 0.2$ and $\frac{\gamma' B}{p'_o} = 0.14$, the exponent n was determined from Figure 5.27.

Exponent $n = 2.8$

$$NPS \left(\frac{1.42}{M} \right)^n \frac{3.5}{(1+e_{cs})} = 7.0$$

$$NPS = 7.0 \left(\frac{M}{1.42} \right)^n \frac{(1+e_{cs})}{3.5} = 8.4$$

5. Normalised "elastic" slope (NES) = 86.0
   Normalised "plastic" slope (NPS) = 8.4
   Normalised yield pressure (NYP)= 0.65

The bilinear bearing pressure curve can be plotted once the non-dimensional "elastic" slope, "plastic" slope and the yield pressure are known.

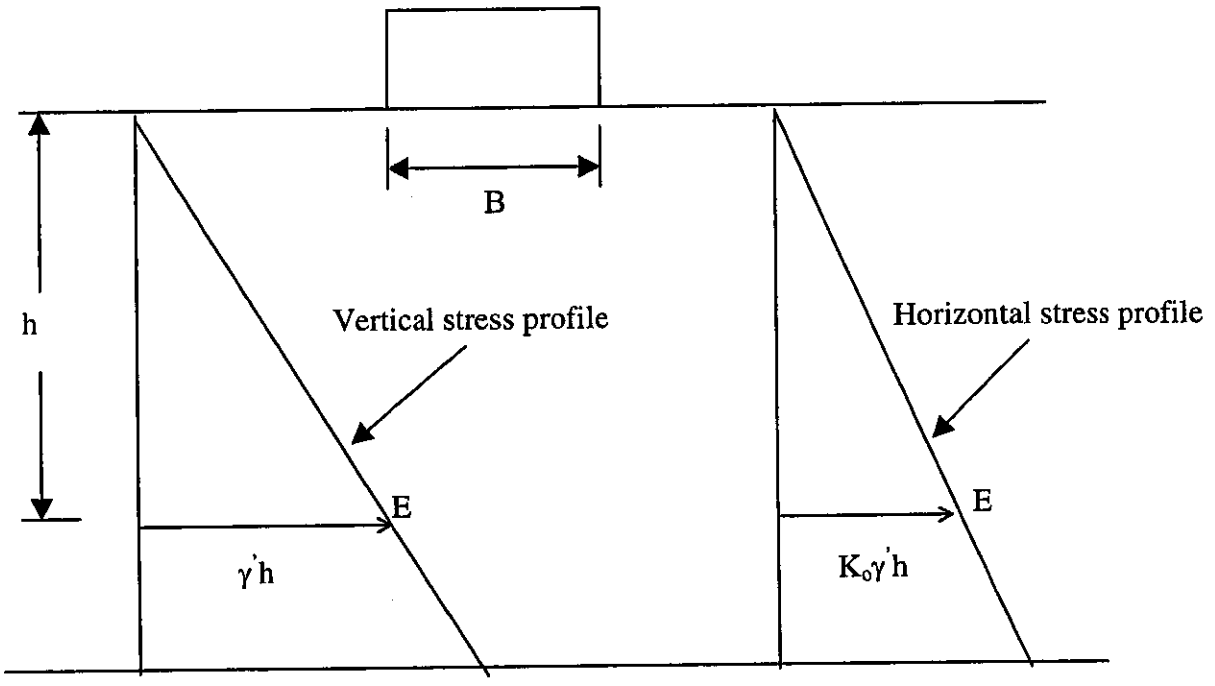

Figure 5.1 Profile of initial effective vertical and horizontal stress below surface circular footing

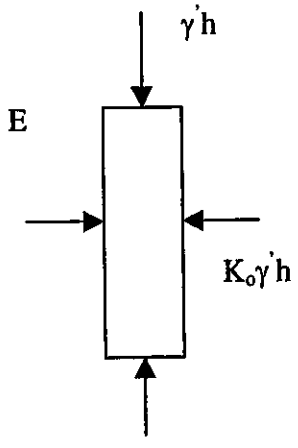

Figure 5.2 In-situ stress at any soil element at a depth *h* below footing

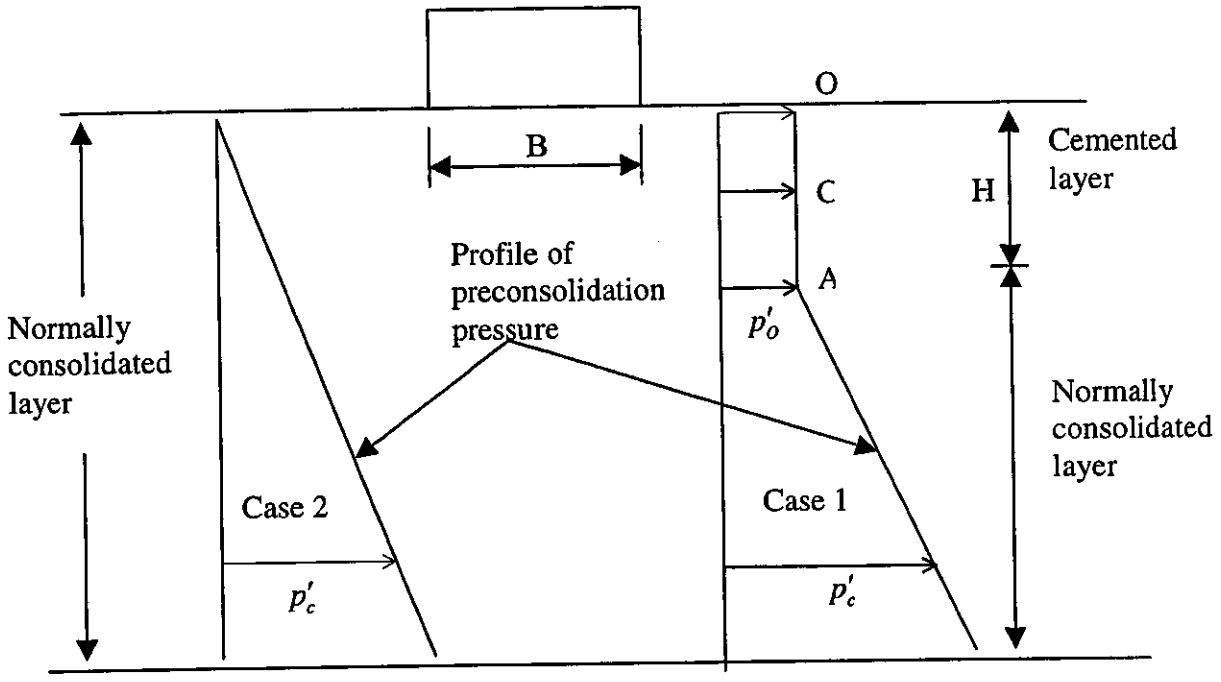

Figure 5.3 Assumed profiles of preconsolidation pressure below surface circular footing

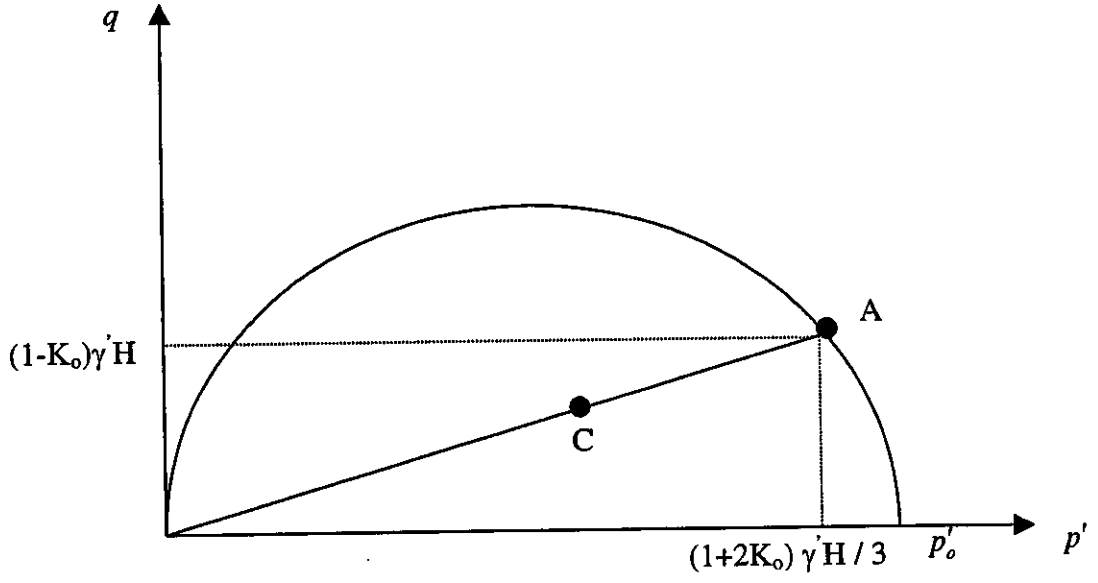

Figure 5.4 For soil profile in case 2, position of in-situ stress with respect to SU2 yield locus

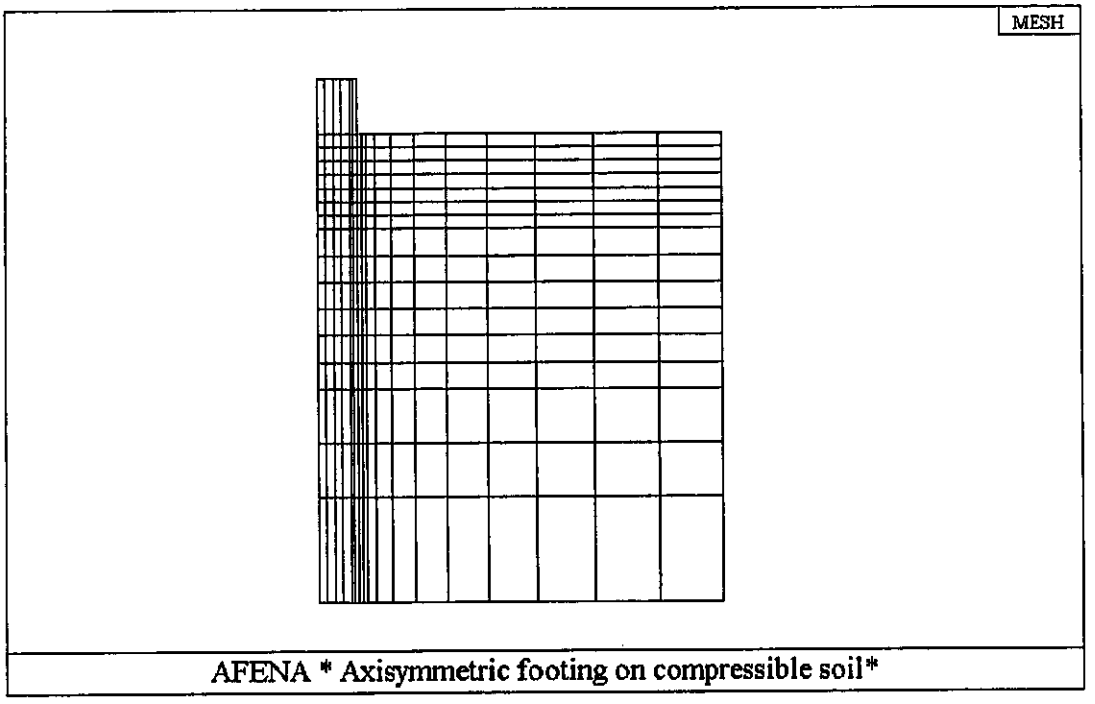

Figure 5.5 A typical axisymmetric finite element mesh for surface circular footing

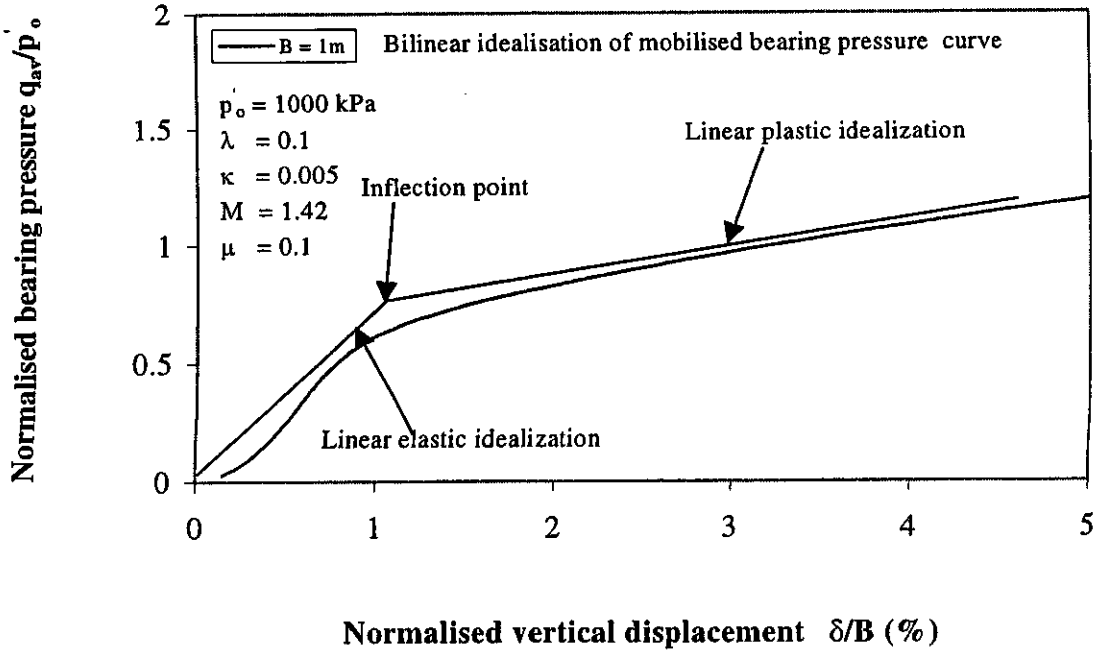

Figure 5.6 Bilinear idealisation of non-dimensional bearing pressure curve

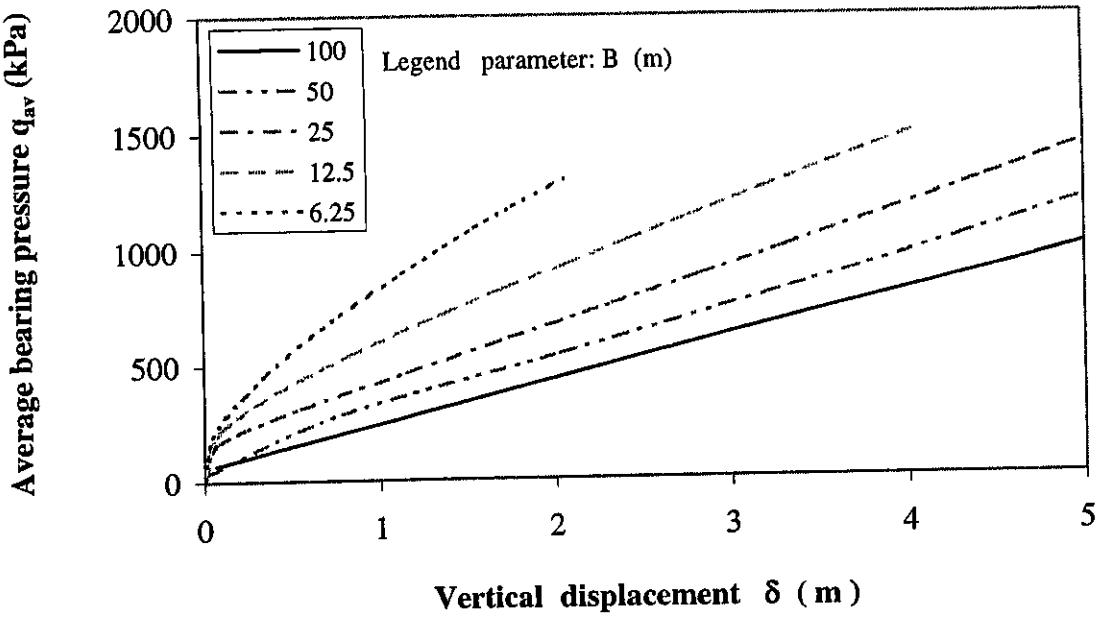

Figure 5.7 Mobilised bearing pressure as a function of absolute vertical displacement

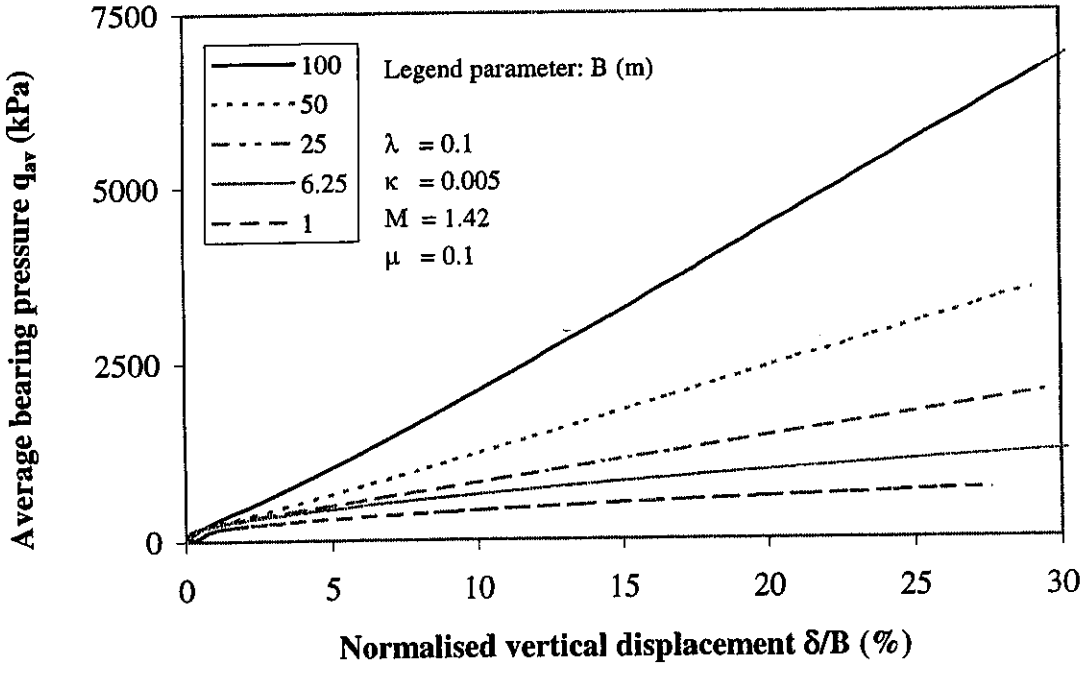

Figure 5. 8 Effect of footing diameter on the mobilised bearing pressure

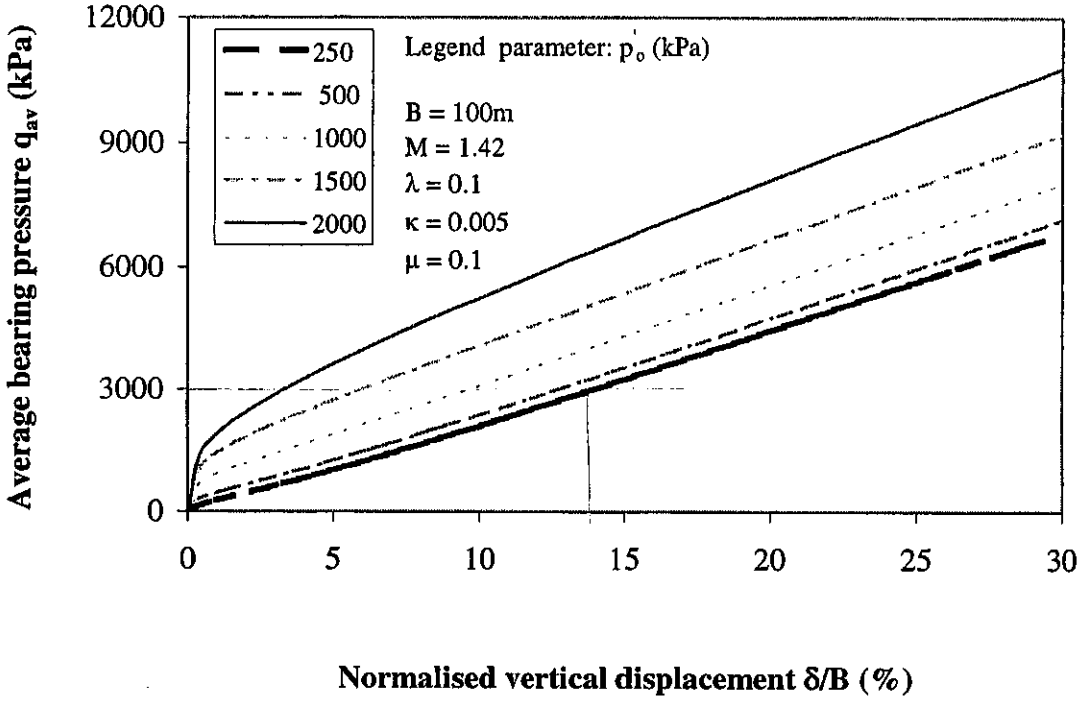

Figure 5.9 Effect of preconsolidation stress on mobilised bearing pressure

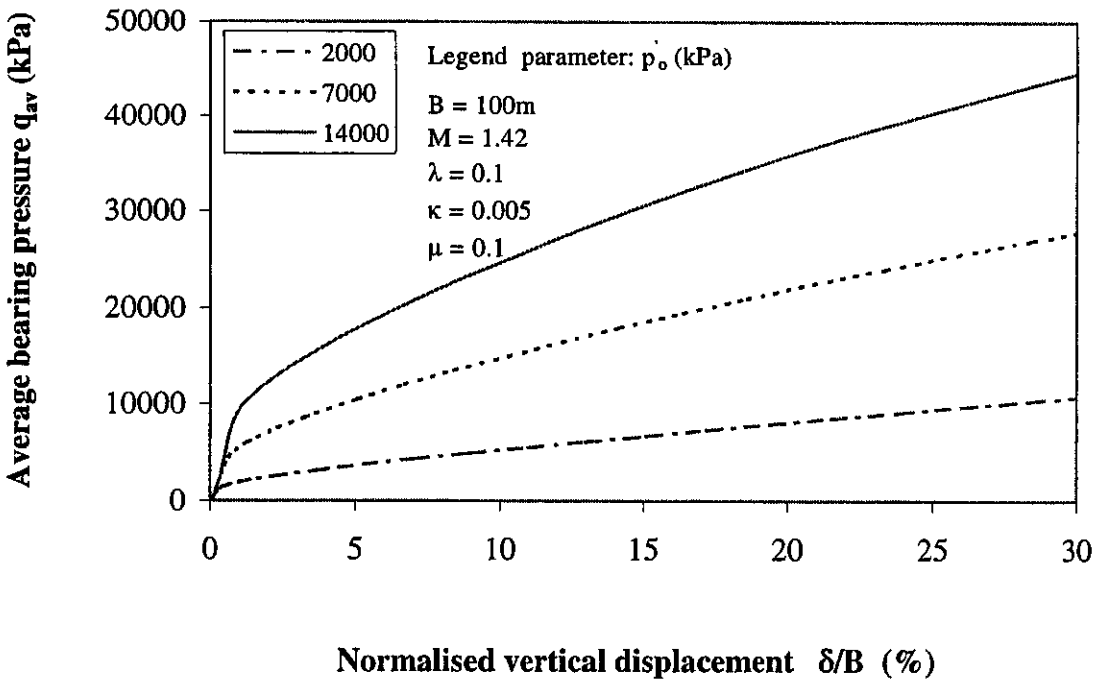

Figure 5.10 Effect of high preconsolidation stress on mobilised bearing pressure

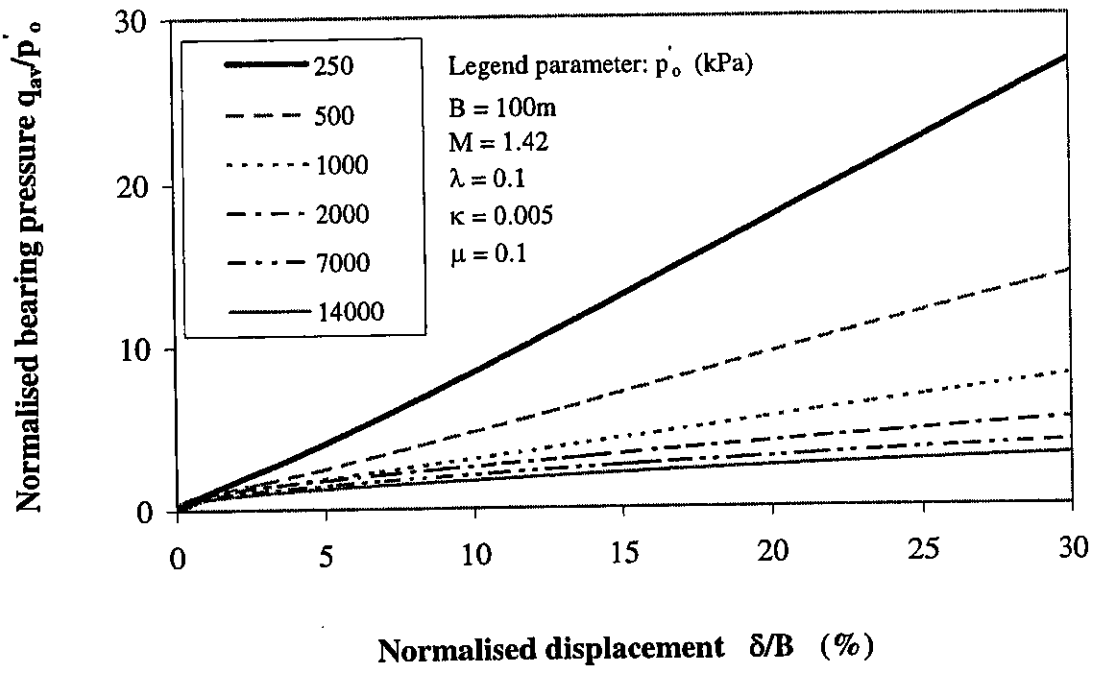

Figure 5.11 Effect of preconsolidation stress on non-dimensional bearing pressure

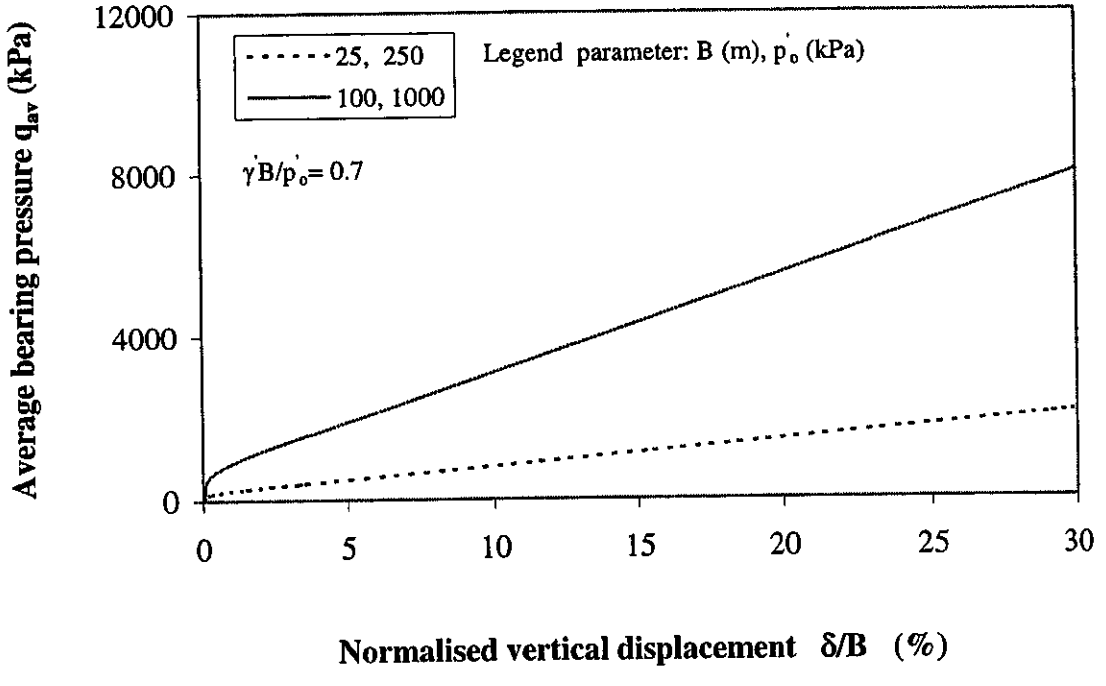

Figure 5.12 Mobilised bearing pressure for footings with equal $\frac{\gamma' B}{p'_o}$

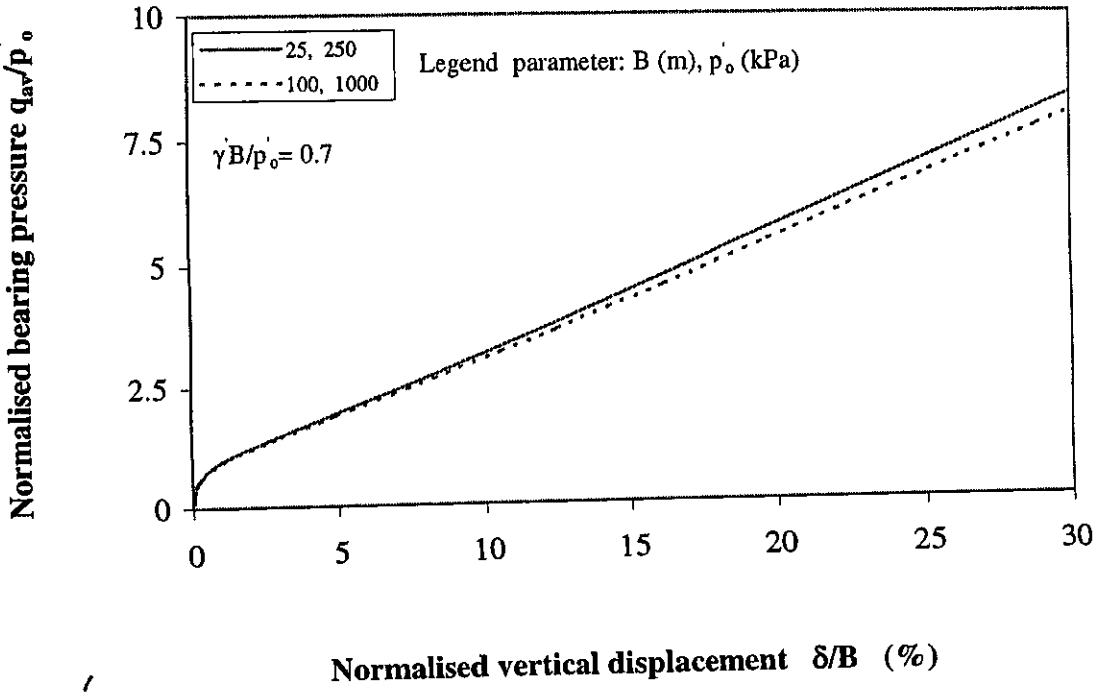

Figure 5.13 Normalised bearing pressure for footings with $\frac{\gamma' B}{p'_o} = 0.7$

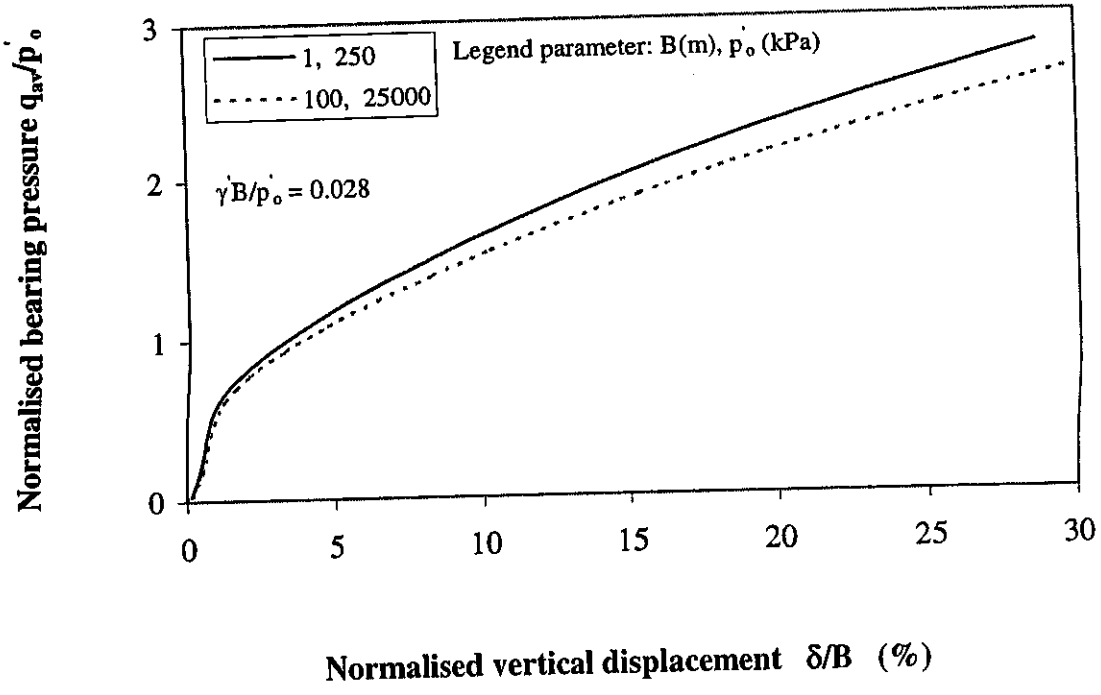

Figure 5.14 Normalised bearing pressure for footings with $\frac{\gamma' B}{p'_o} = 0.028$

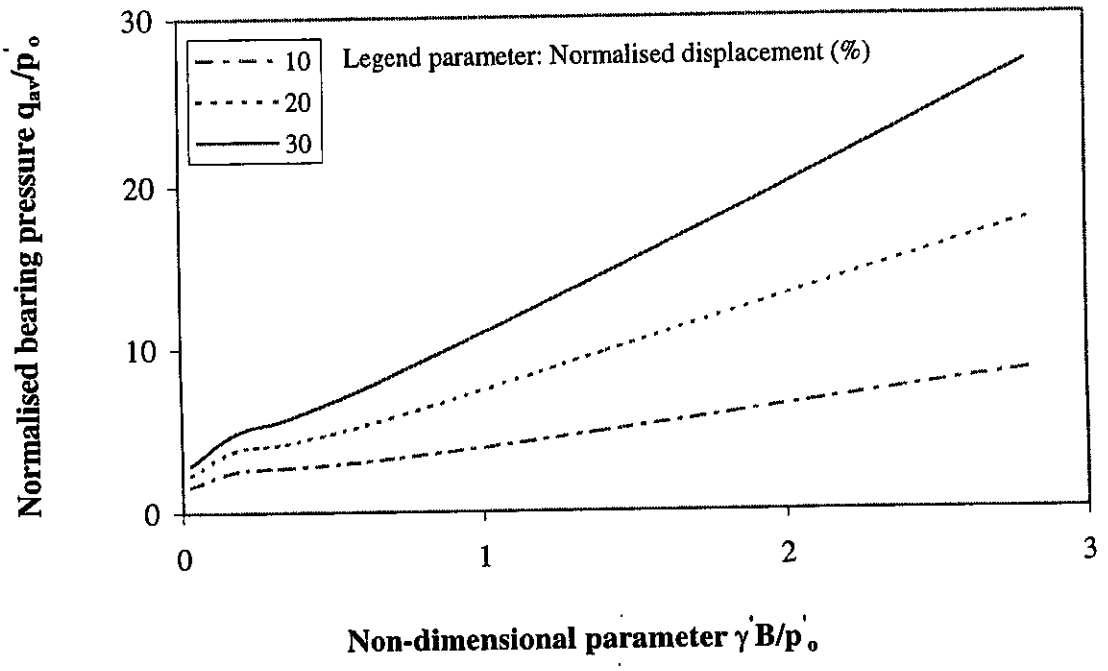

Figure 5.15 Mobilised bearing pressure as a function of $\frac{\gamma' B}{p'_o}$

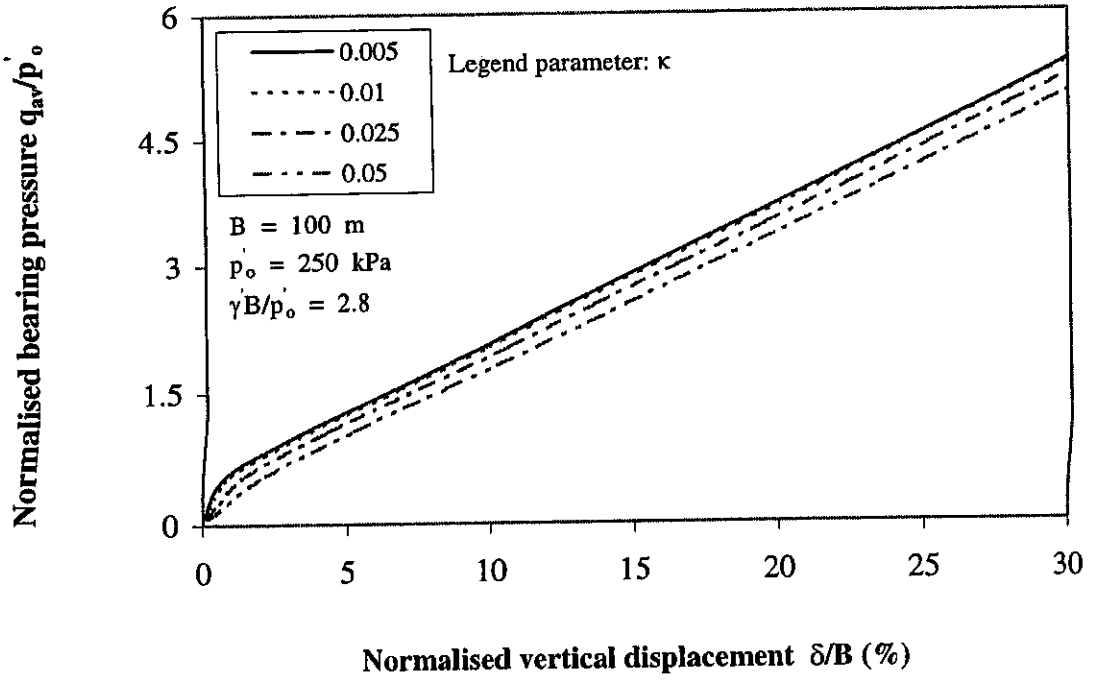

Figure 5.16 Effect of elastic parameter κ **on bearing pressure for** $\frac{\gamma' B}{p'_o} = 2.8$

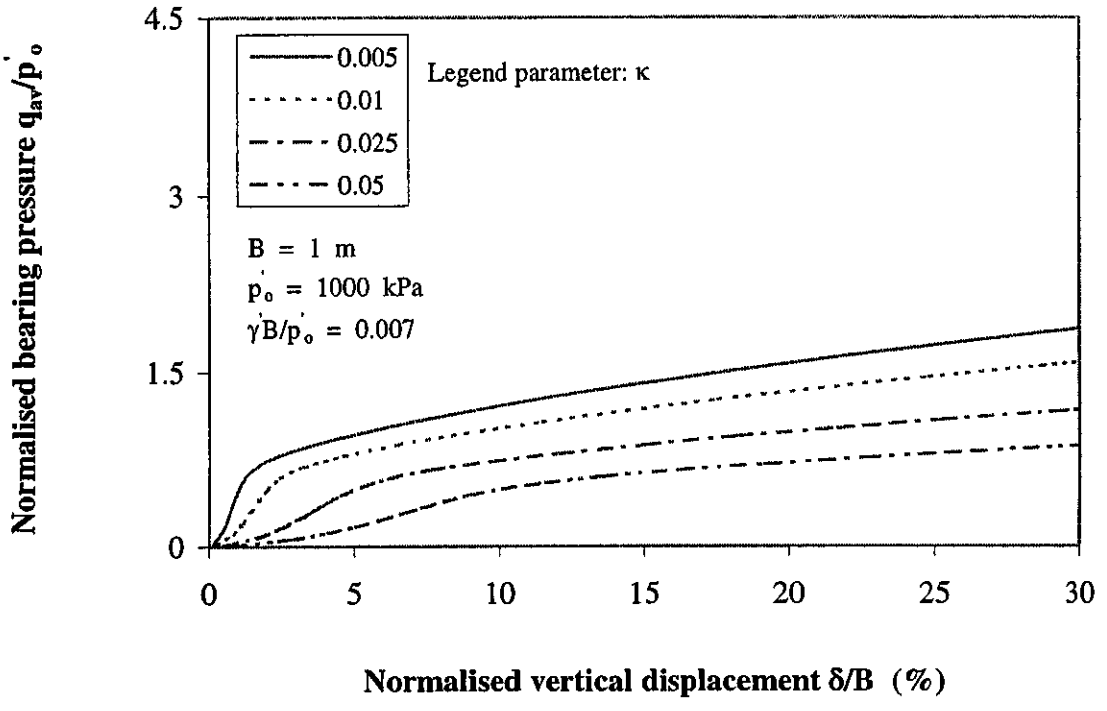

Figure 5.17 Effect of elastic parameter κ on bearing pressure for $\frac{\gamma' B}{p'_o} = 0.007$

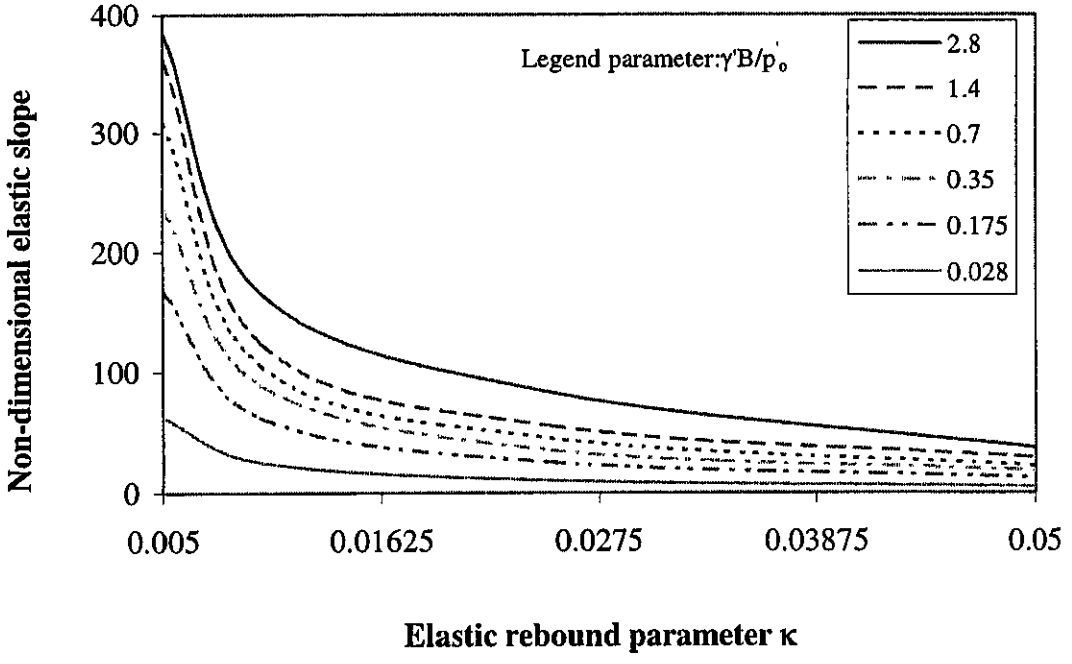

Figure 5.18 Variation of non-dimensional elastic slope with elastic parameter κ

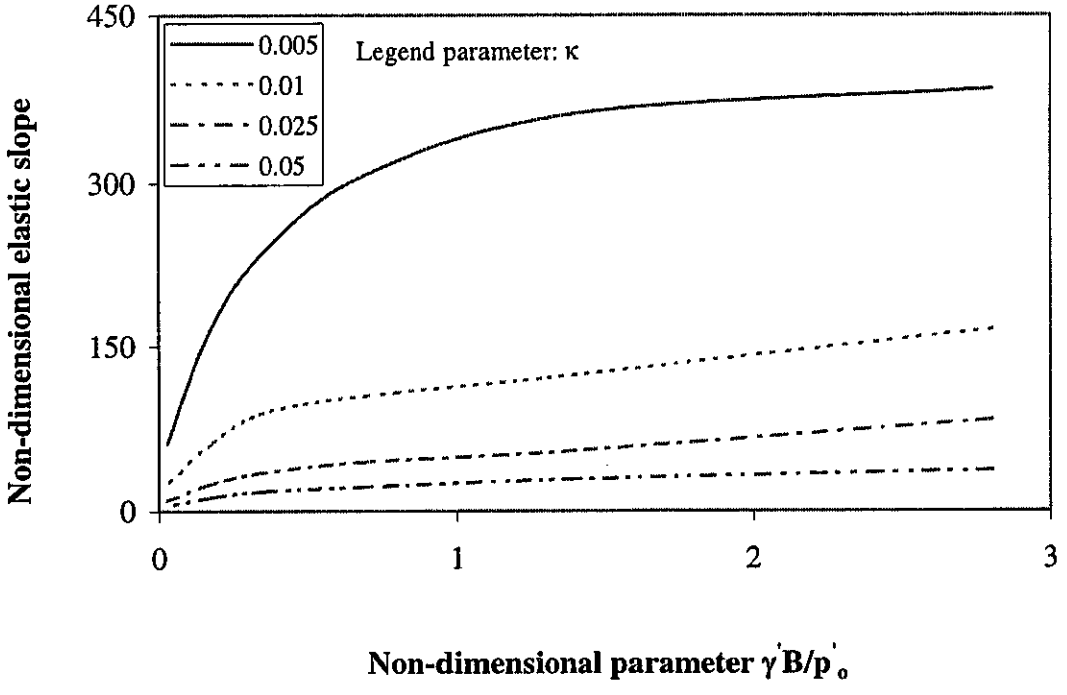

Figure 5.19 Variation of non-dimensional elastic slope with $\frac{\gamma' B}{p'_o}$

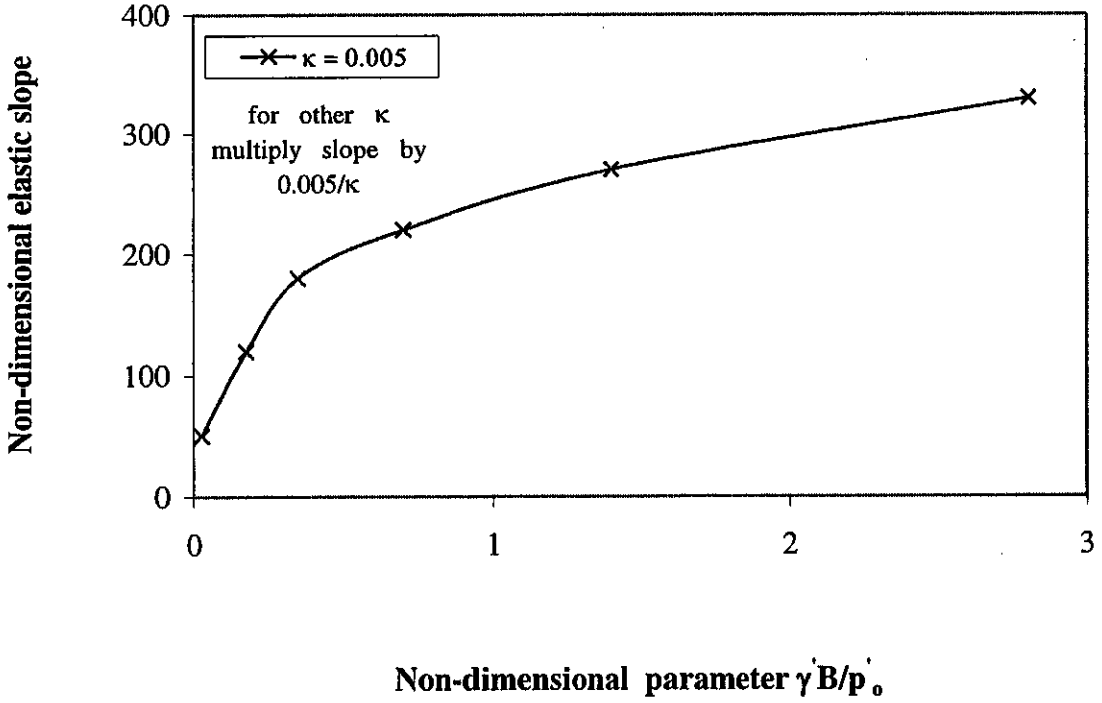

Figure 5.20 Design chart to determine elastic slope from κ and $\frac{\gamma' B}{p'_o}$

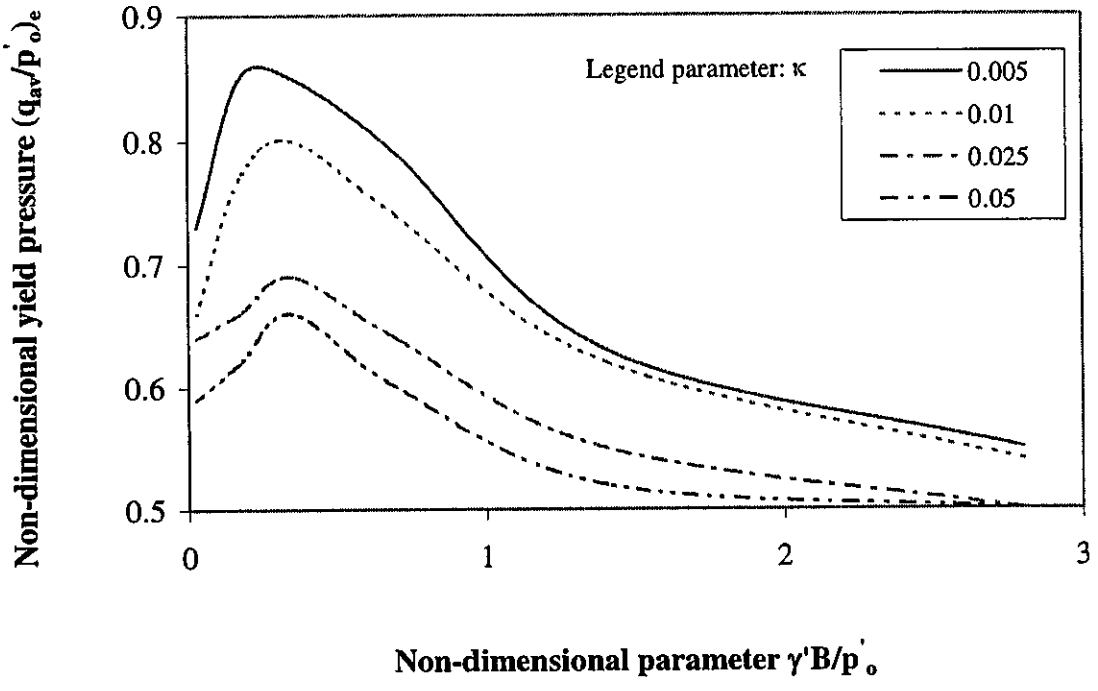

Figure 5.21 Yield pressure as a function of $\frac{\gamma' B}{p'_o}$ and κ

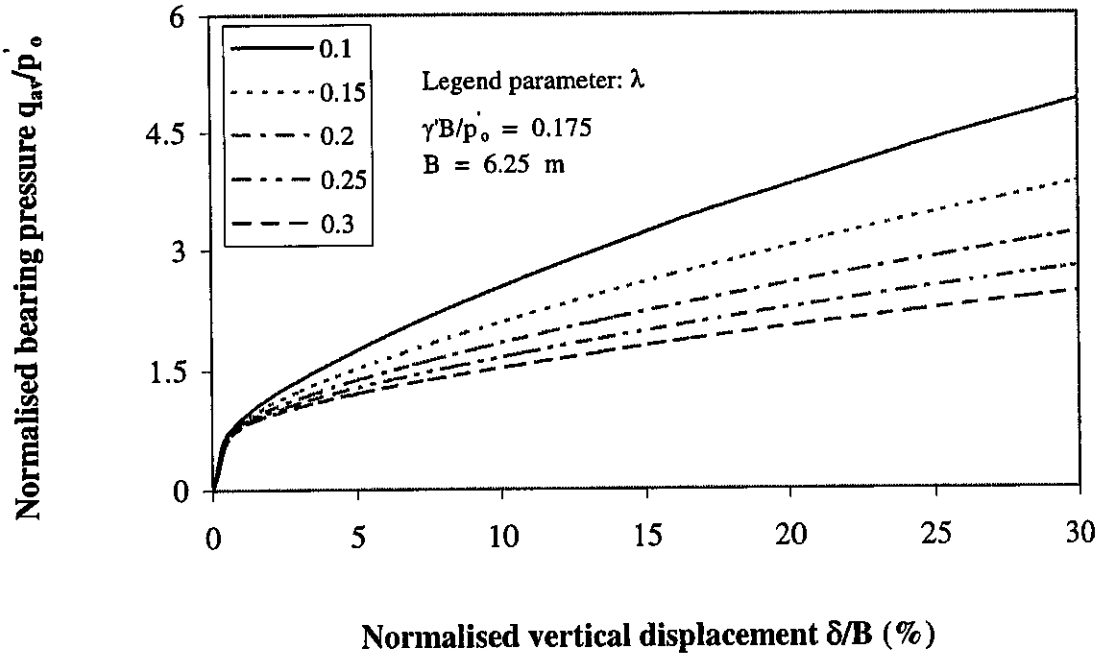

Figure 5.22 Effect of plastic parameter λ on mobilised bearing pressure

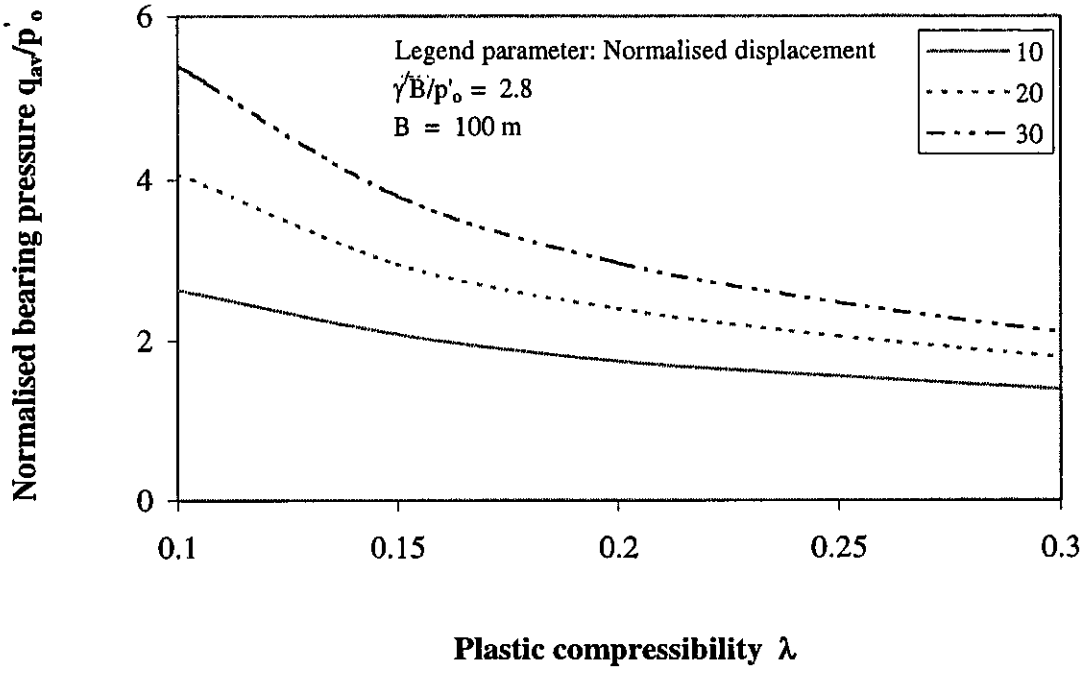

Figure 5.23 Mobilised bearing pressure as a function of λ

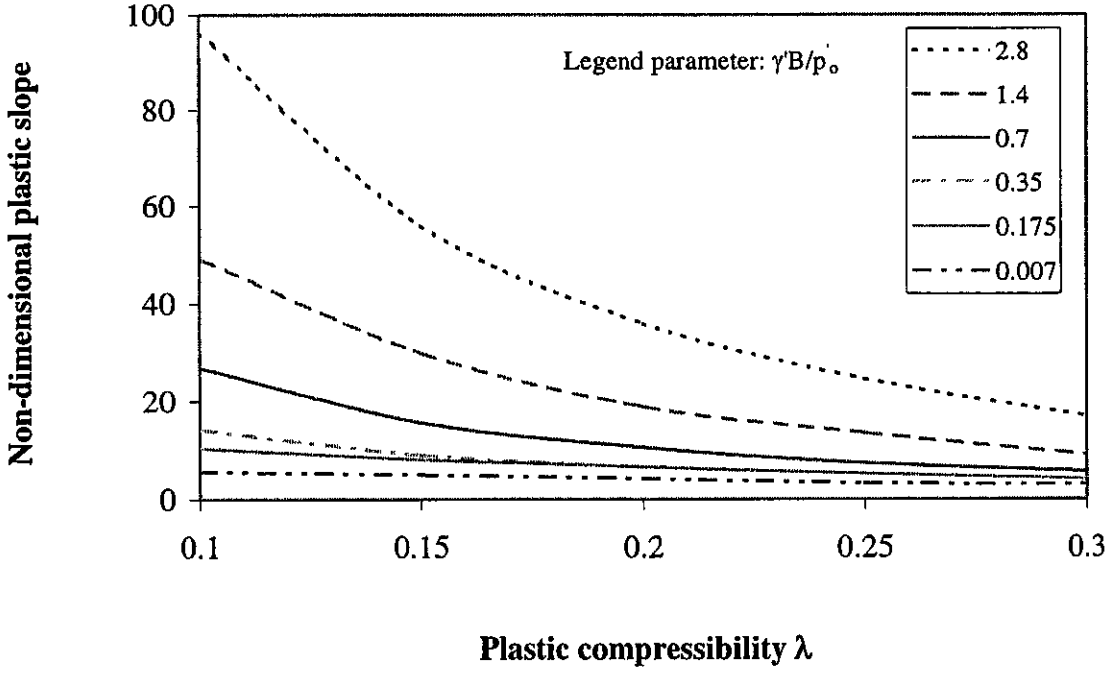

Figure 5.24 Design chart to determine plastic slope from λ and $\frac{\gamma' B}{p'_o}$

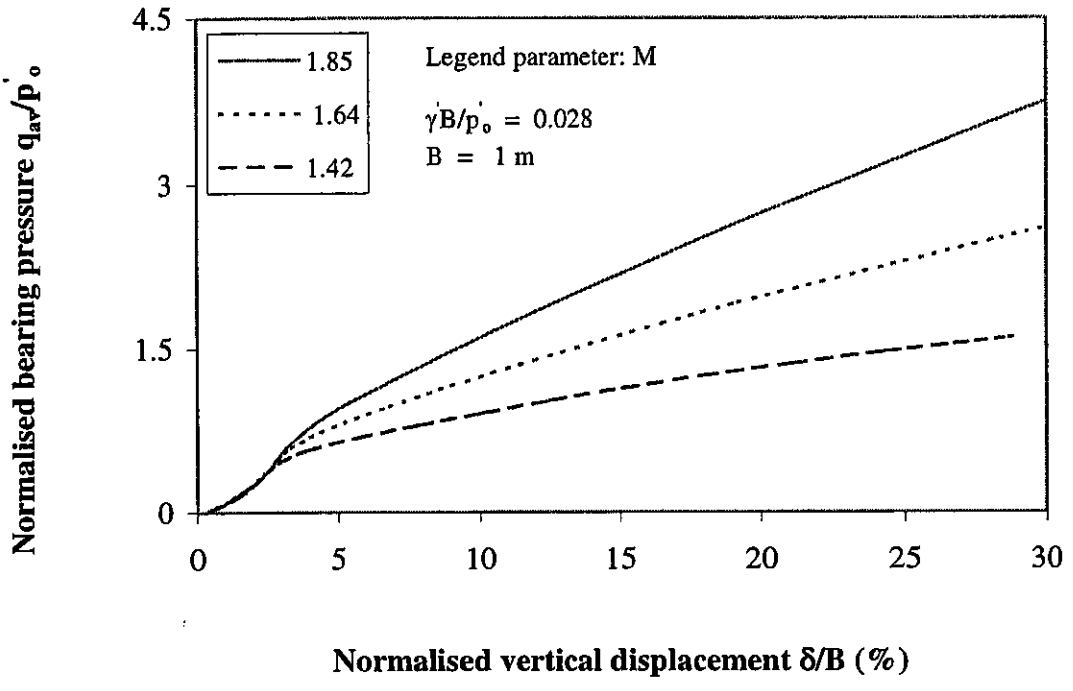

Figure 5.25 Effect of friction angle or critical state ratio *M* on bearing pressure

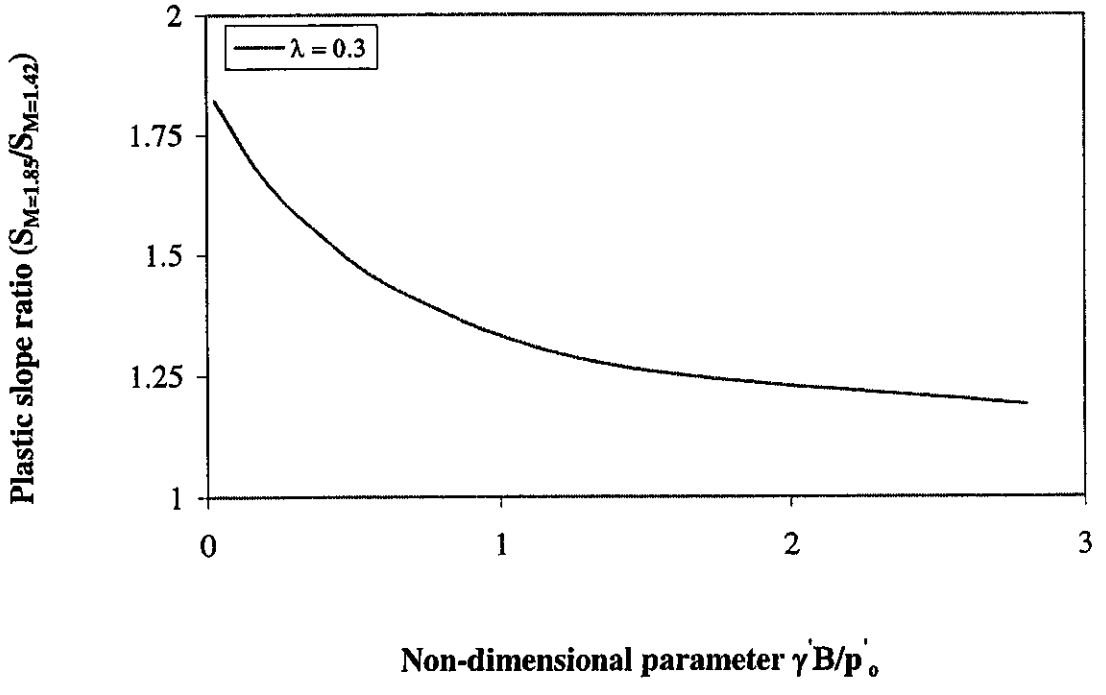

Figure 5.26 Plastic slope ratio (M = 1.85 and M = 1.42) as a function of $\frac{\gamma' B}{p'_o}$

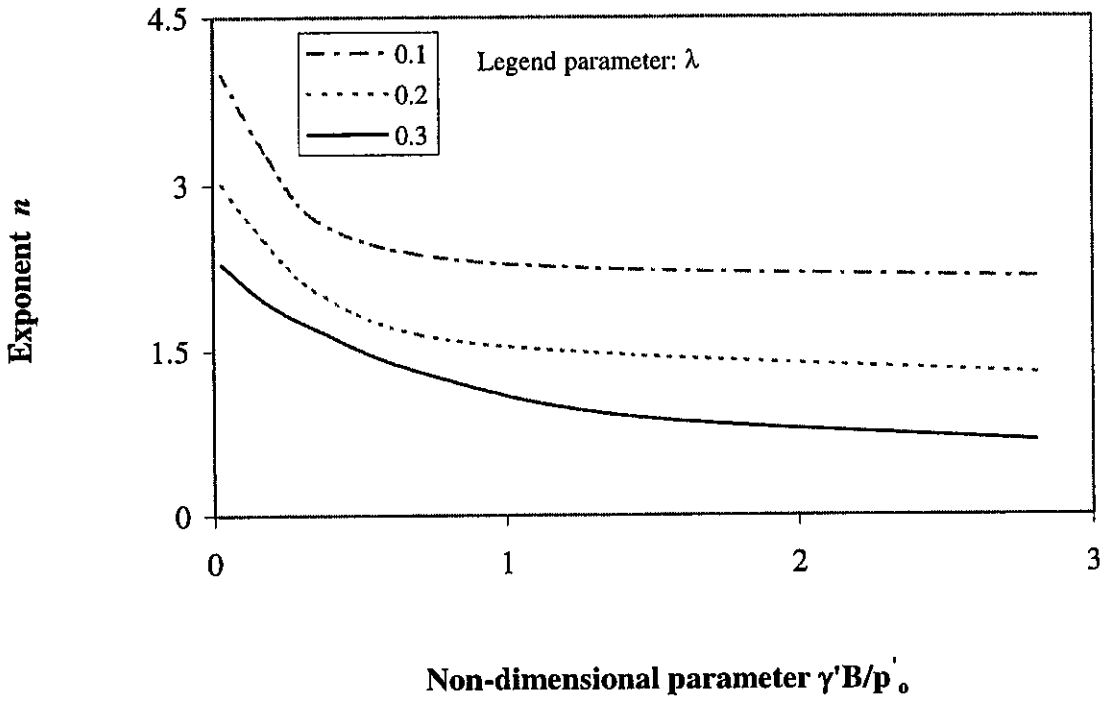

Figure 5.27 Exponent *n* to compute plastic slopes for *M*>1.42

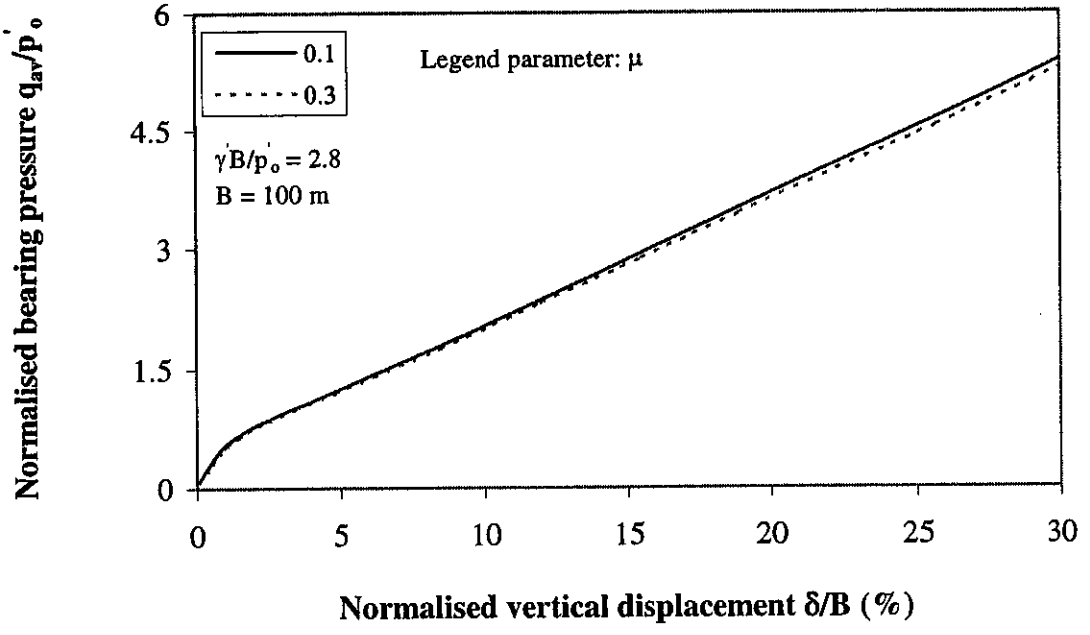

Figure 5.28 Effect of Poisson's ratio on bearing pressure for $\frac{\gamma' B}{p'_o} = 2.8$

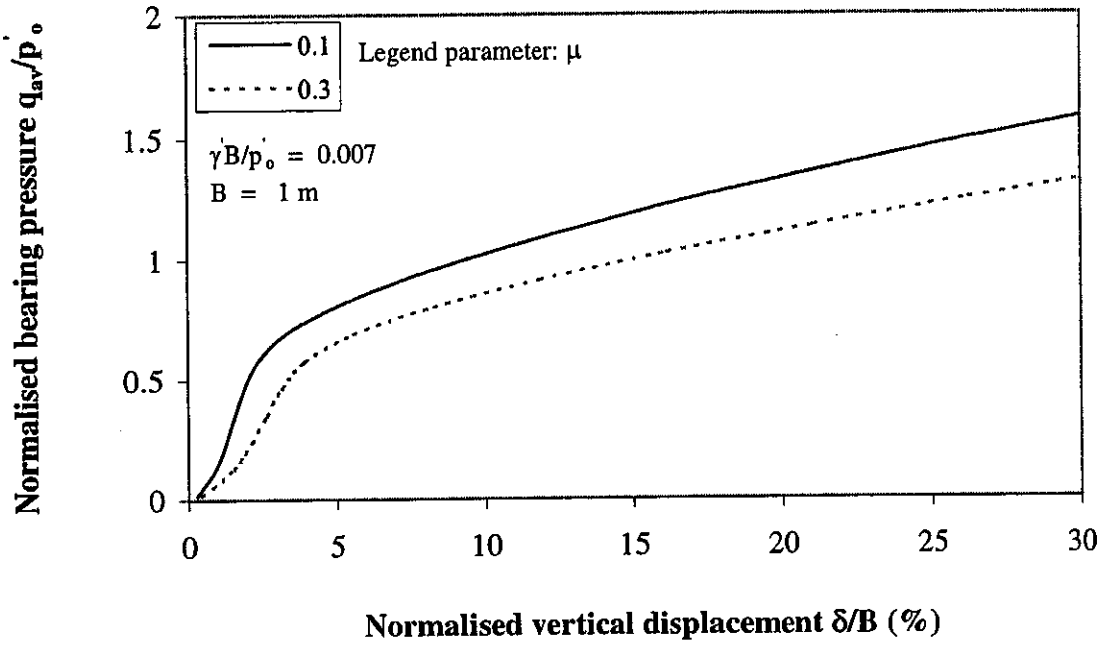

Figure 5.29 Effect of Poisson's ratio on bearing pressure for $\frac{\gamma' B}{p'_o}$ = 0.007

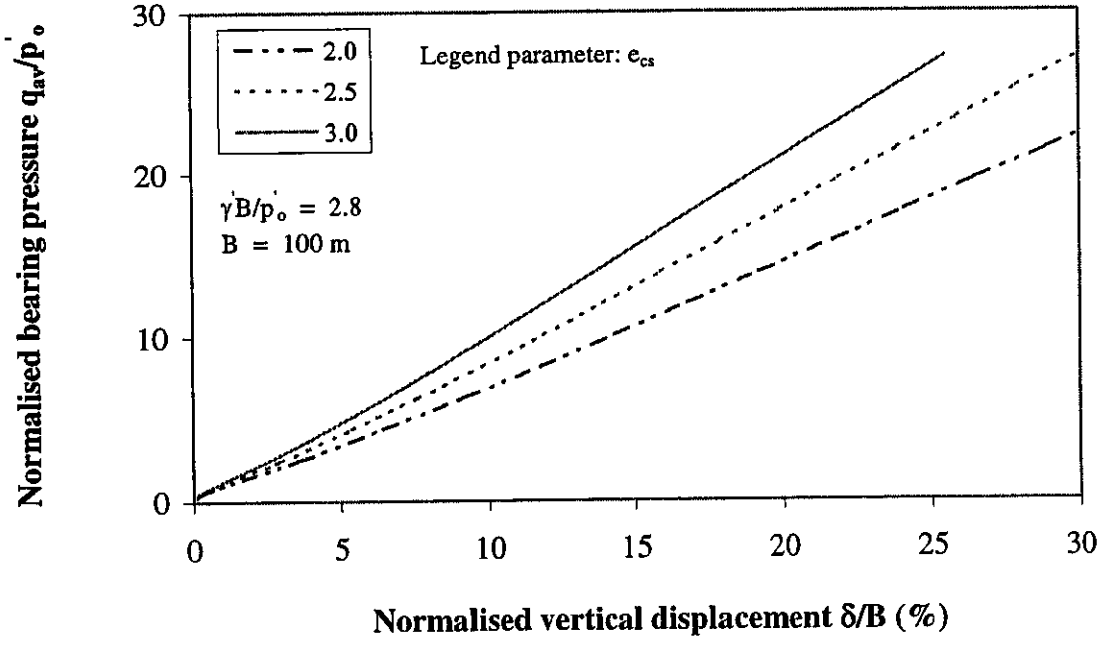

Figure 5.30 Effect of e_{cs} on bearing pressure for $\frac{\gamma' B}{p'_o}$ = 2.8

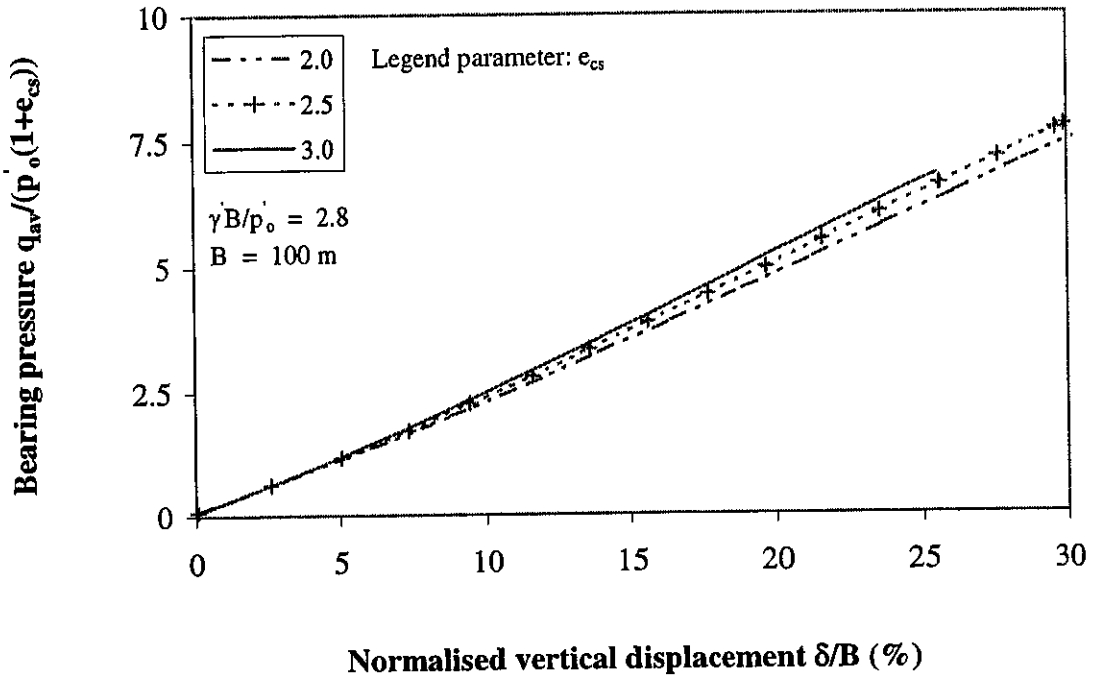

Figure 5.31 Effect of e_{cs} on the bearing pressure for $\frac{\gamma' B}{p_o'} = 2.8$

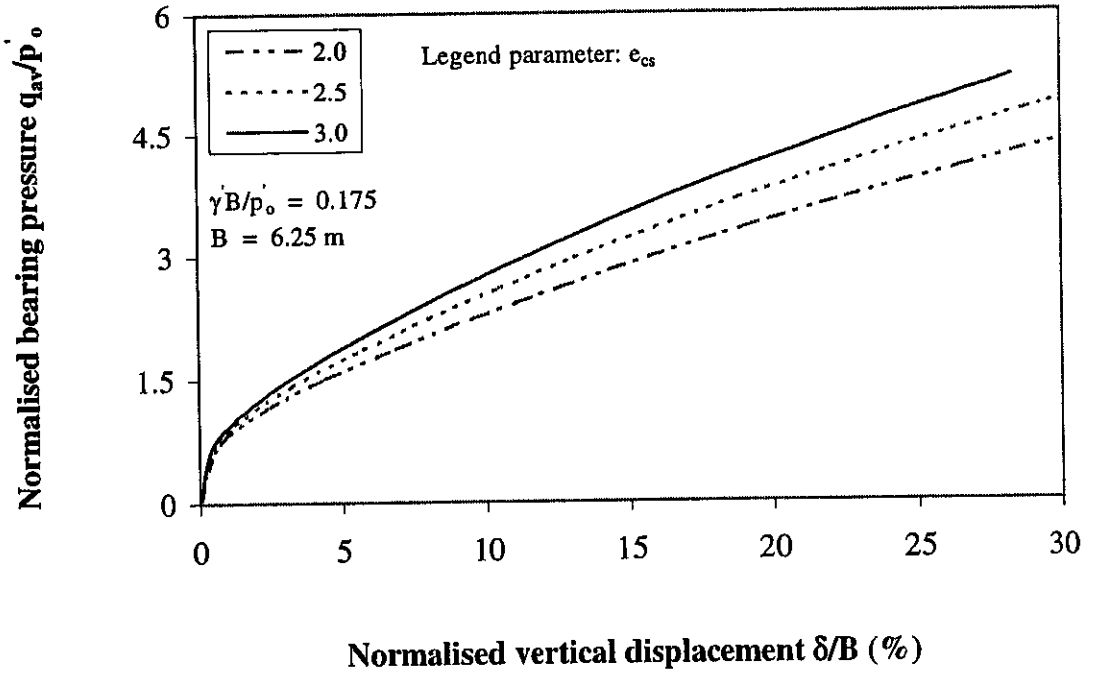

Figure 5.32 Effect of e_{cs} on bearing pressure for $\frac{\gamma' B}{p_o'} = 0.175$

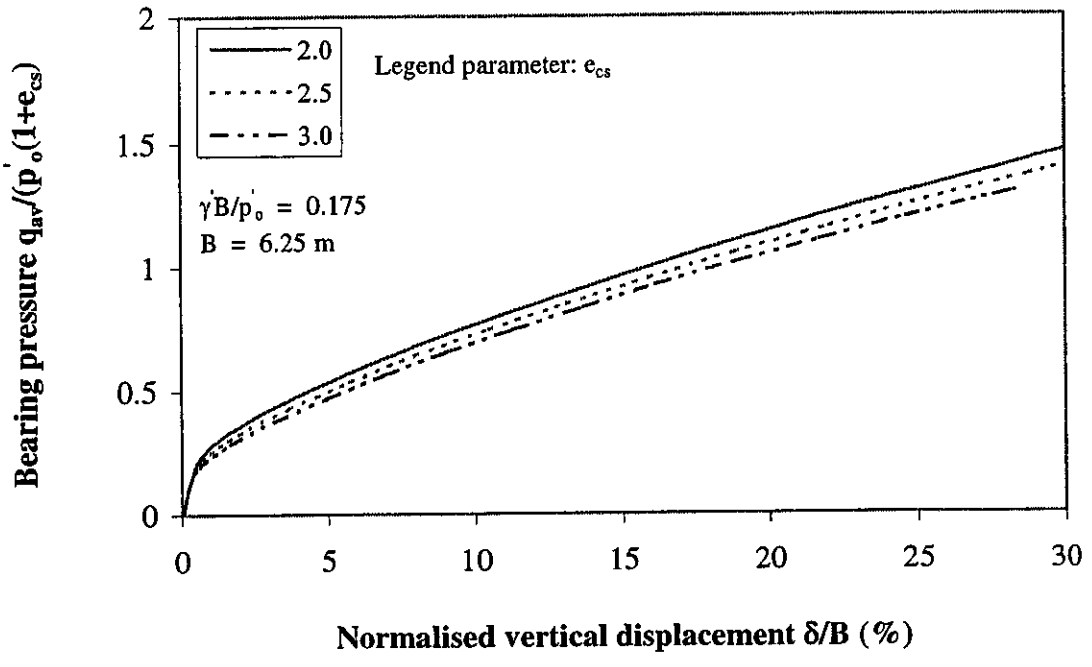

Figure 5.33 Effect of e_{cs} on the bearing pressure for $\frac{\gamma' B}{p_o'} = 0.175$

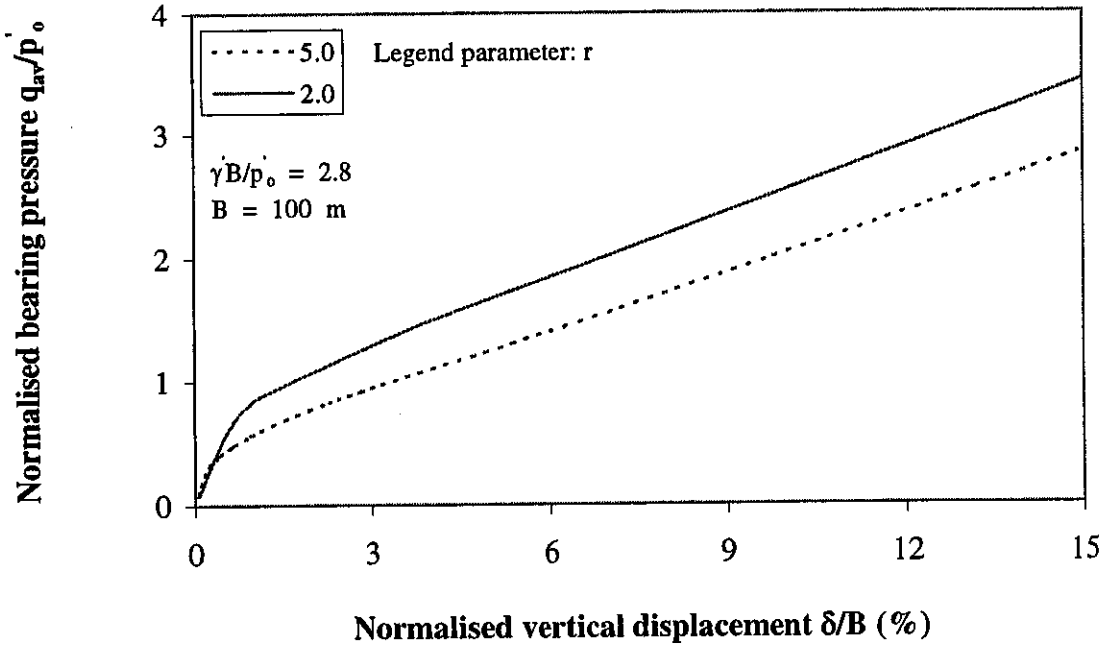

Figure 5.34 Effect of spacing ratio on bearing pressure for $\frac{\gamma' B}{p_o'} = 2.8$

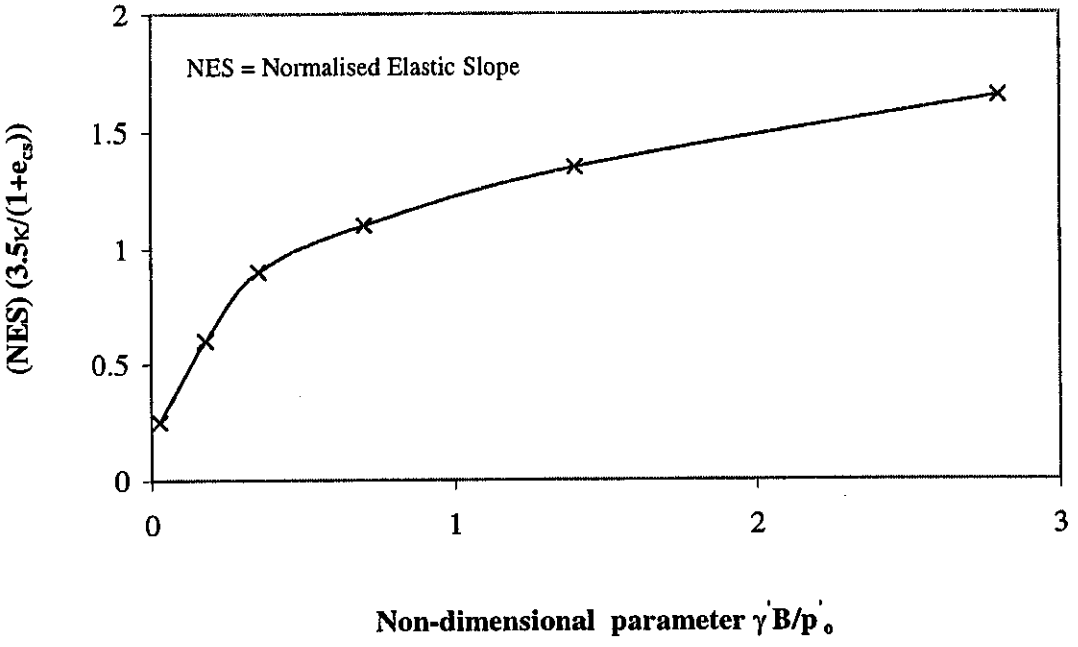

Figure 5.35 Design chart to determine elastic slope of footing response

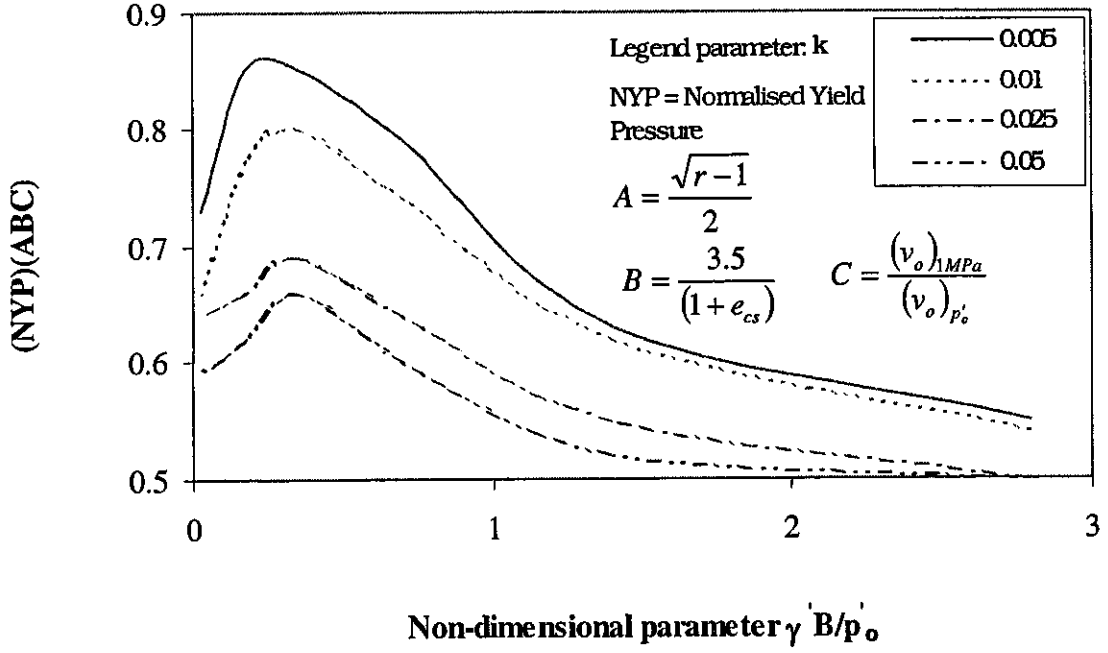

Figure 5.36 Design chart to determine yield pressure of footing response

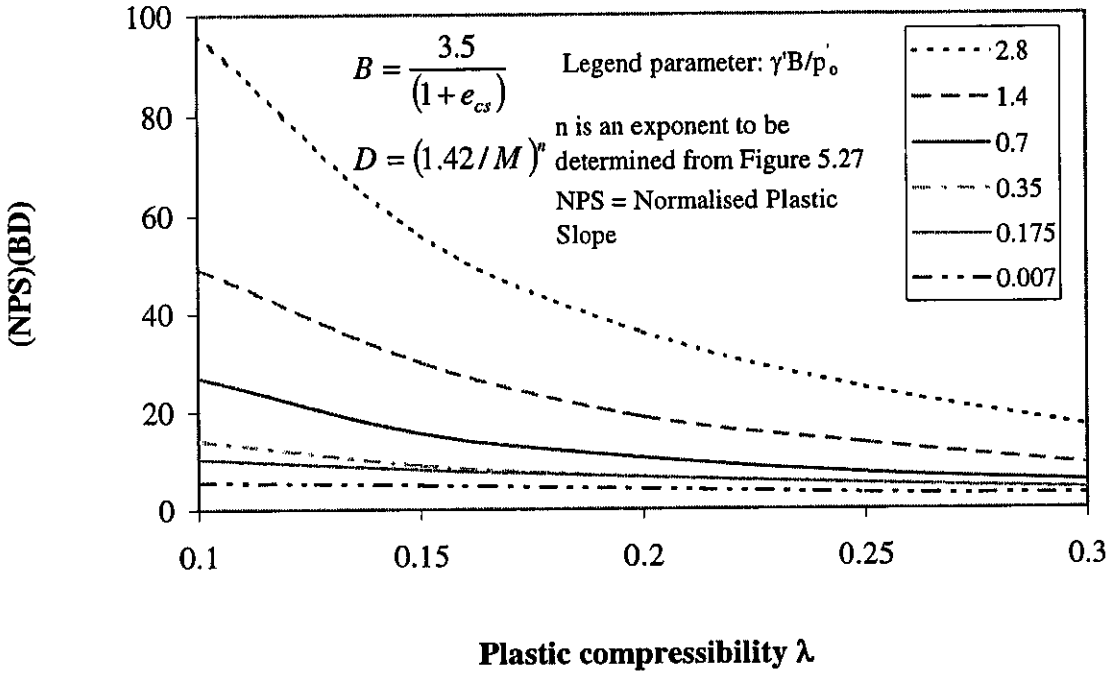

Figure 5.37 Design chart to determine plastic slope of footing response

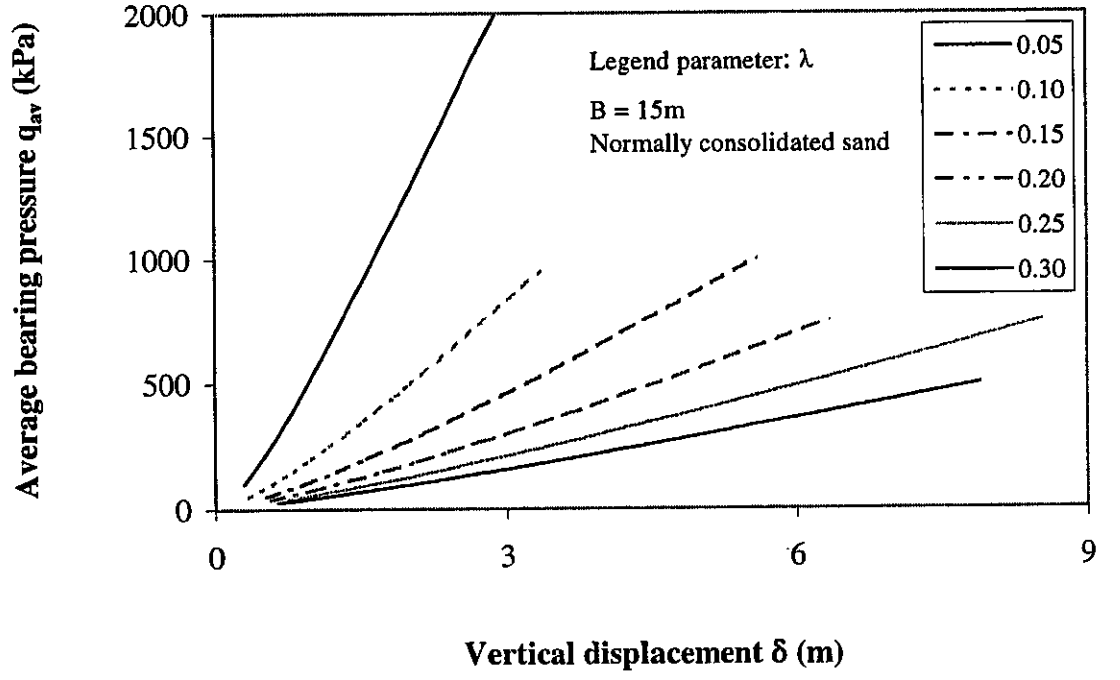

Figure 5.38 Effect of λ on bearing pressure for normally consolidated sand

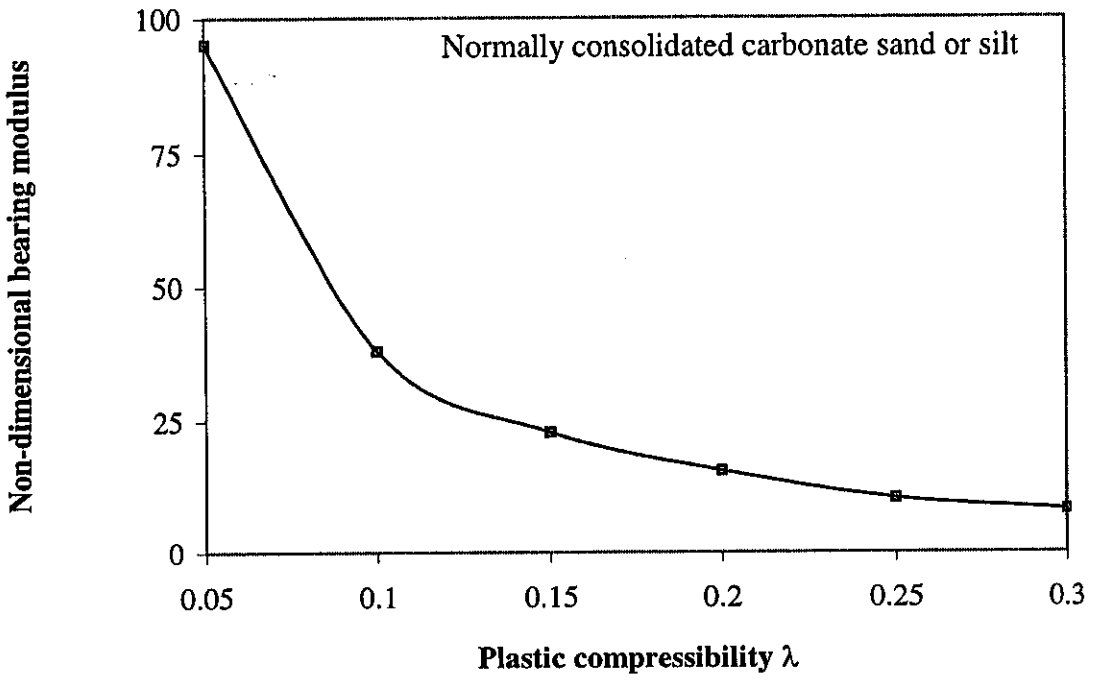

Figure 5.39 Design chart for normally consolidated sand

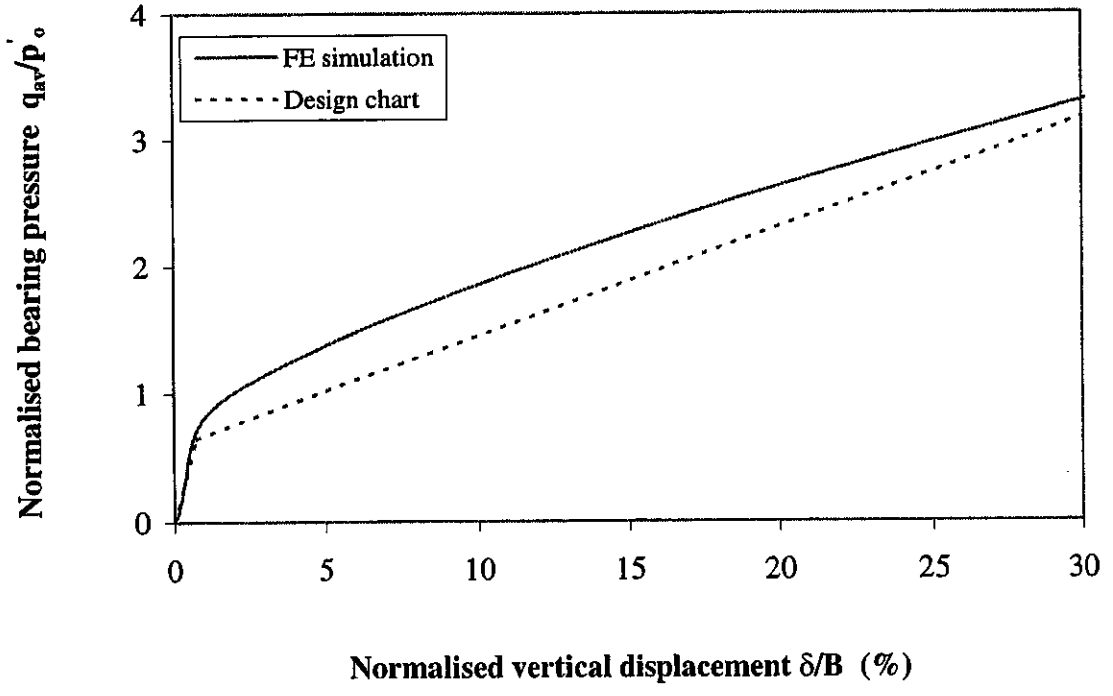

Figure 5.40 FE simulation and corresponding prediction using design chart

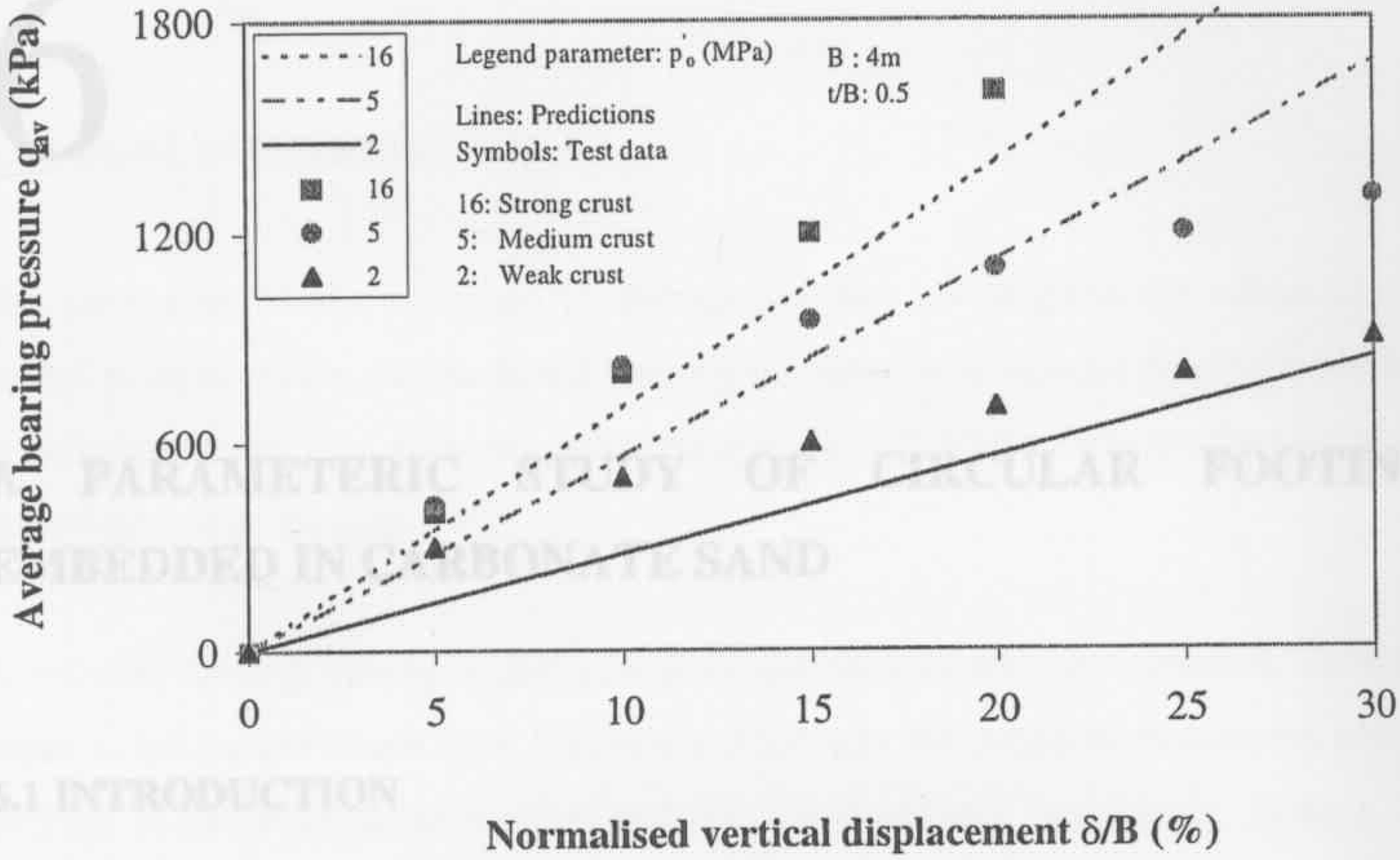

Figure 5.41 Bearing pressure predicted for layered material using design chart

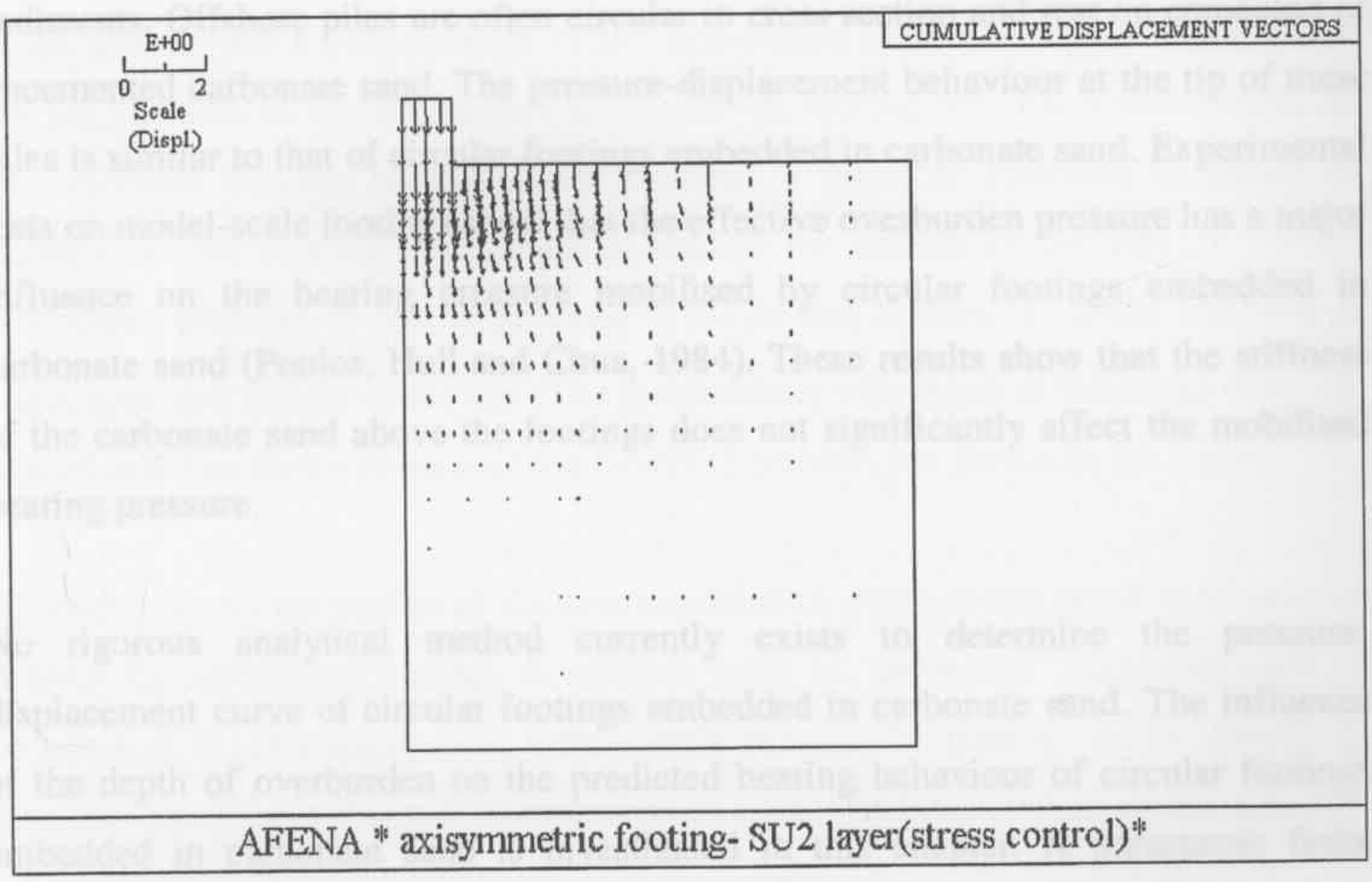

Figure 5.42 Vector of displacements below footing for strong crust underlain by normally consolidated sand

6

A PARAMETERIC STUDY OF CIRCULAR FOOTINGS EMBEDDED IN CARBONATE SAND

6.1 INTRODUCTION

Offshore piles are usually driven deep below the ocean floor. In some cases these piles derive their support primarily from the bearing pressure mobilised at the pile tip. This is because of the low frictional resistance of piles driven in carbonate sediments. Offshore piles are often circular in cross section and rest on cemented or uncemented carbonate sand. The pressure-displacement behaviour at the tip of these piles is similar to that of circular footings embedded in carbonate sand. Experimental tests on model-scale footings show that the effective overburden pressure has a major influence on the bearing pressure mobilised by circular footings embedded in carbonate sand (Poulos, Hull and Chua, 1984). These results show that the stiffness of the carbonate sand above the footings does not significantly affect the mobilised bearing pressure.

No rigorous analytical method currently exists to determine the pressure-displacement curve of circular footings embedded in carbonate sand. The influence of the depth of overburden on the predicted bearing behaviour of circular footings embedded in carbonate sand is investigated in this chapter. A parametric finite element analysis is carried out to determine the effect of the SU2 model parameters on the predicted bearing response of such footings. Finally, design charts are

proposed. These charts may be used to determine approximate bearing pressure curves of embedded footings and end bearing piles resting on carbonate sand.

6.2 PROBLEM DEFINITION

The parametric study described in this chapter has investigated the effect of SU2 model parameters on the predicted bearing response of a circular footing embedded in carbonate sand. The problem geometry and the soil profile beneath the footing are described in this section.

A circular footing having a diameter B is assumed to rest on carbonate sand at a depth D below the ocean bed. Figure 6.1 illustrates the problem considered and the profiles of initial effective vertical and horizontal stresses beneath the footing. The in-situ effective vertical and horizontal stresses increase linearly with depth. Figures 6.2 (a) and (b) show respectively the in-situ effective vertical and horizontal stresses acting in a soil element at a depth D below the soil surface and at a depth h below the bottom of the footing. In the figures, K_o is the coefficient of earth pressure at rest. These stresses are a consequence of soil self-weight only. Test results have shown that the stiffness of the carbonate sand above the footing only has a small effect on the mobilised bearing pressure. The problem is therefore idealised as shown in Figure 6.3. The footing is assumed to rest on the surface of the soil. A vertical overburden pressure of $\gamma' D$ is assumed to act on this surface. γ' is the effective or submerged unit weight of the soil. The distributions with depth of the initial effective vertical and horizontal stresses of the modified problem are shown in the figure.

Figure 6.4 shows the profile of the preconsolidation pressure that is assumed to exist beneath the embedded footing. A uniform layer of "cemented" carbonate sand of thickness H is assumed to exist immediately beneath the footing. As in Chapter 5, cementation of the soil is modelled here as an overconsolidation ratio of the soil. The preconsolidation pressure of this layer is assumed to be p_o'. Figure 6.5 shows that at depths less than H, the initial stress lies at a point C, which is located inside the SU2 yield locus. The sand is therefore, "cemented" or overconsolidated down to depth H

below the footing. At depth H, the soil is normally consolidated represented by the stress state at point A in Figure 6.5. Below depth H, the in-situ effective stress lies on the SU2 yield locus and the yield locus grows larger with depth. Thus below depth H, the soil becomes normally consolidated and the preconsolidation pressure increases linearly with depth. Under these conditions the following relations hold:

$$p_o' \propto \gamma'(H + D) \tag{6.1}$$

or

$$H \propto \frac{p_o'}{\gamma'} - D \tag{6.2}$$

Equation (6.2) implies that for the problem considered, the thickness H of the "cemented" or overconsolidated layer is dependent on the preconsolidation pressure p_o' as well as the overburden depth D. In the special case when the overburden depth equals $\frac{p_o'}{\gamma'}$, the thickness of the "cemented" or overconsolidated layer is zero. The footing in that case may be assumed to be resting on normally consolidated carbonate sand. Thus a normally consolidated soil profile is a special case of the general formulation and consequently need not be treated separately as was done in Chapter 5.

The physical problem of an embedded footing in carbonate sand for which the parametric study will be carried out has been defined. The next section discusses briefly the pertinent details of the finite element analysis, while a subsequent section considers experimental validation of the numerical model. Thereafter the effects of SU2 model parameters on the bearing pressure mobilised by the footing are investigated and the results are presented in subsequent sections of this chapter.

6.3 FINITE ELEMENT MESH

A typical mesh adopted for the finite element analysis of a footing has been already illustrated in Figure 5.5 and described in section 5.3. The effect of the depth of overburden was simulated in the finite element analysis by assuming an equivalent overburden pressure to act on the top boundary of the soil surface. The effect of the self-weight of the soil was also considered. Thus the corresponding results of the finite element analysis give the combined effect of soil self-weight and vertical overburden pressure on the bearing pressure mobilised by the footing. However, for embedment ratios greater than or equal to 1, the effect of the vertical overburden is expected to be the significant parameter in determining the bearing pressure mobilised by the footing. All analyses simulated fully drained conditions. In the next section, the SU2 model predictions of the pressure-displacement response of embedded footings are validated with experimental data.

6.4 VALUE OF MODEL PARAMETERS

The range of SU2 model parameters for carbonate sand selected for the parametric study is identical to that used in Chapter 5 for surface circular footings. For completeness, these values are repeated below in Table 6.1.

Table 6.1 Range of SU2 model parameters

ϕ' (deg)	κ	λ	ν	e_{cs}	p'_o (MPa)	r	D/B
35-45	0.005-0.05	0.1-0.3	0.1-0.3	2-3	0.25-25	2-5	1-100

The values used for the submerged unit weight γ' and coefficient of consolidation K_o were 7kN/m^3 and 0.5 respectively. The embedment ratio of large diameter footings (B>10m) would be generally quite small from practical considerations. It is likely that for such footings, the mobilised bearing pressure of the corresponding surface circular footing would give a conservative estimate of its actual value. On the

other hand, relatively large embedment or *D/B* ratios are quite likely for small diameter footings.

Most of the finite element analysis was carried out for a footing diameter *B* of 1m. The overburden depth was usually varied between 1m-100m. The embedment ratio *D/B* thus varied between 1-100. Some of the finite element analyses were carried out for footings of other diameters at embedment ratios expected in practical situations. The effect of each SU2 model parameter on the bearing response of embedded footings is described in detail in the subsequent sections.

6.5 IDEALISATION OF BEARING PRESSURE CURVE

There are two primary purposes of the parametric study. First, the effects of the SU2 model parameters on the response of an embedded footing are investigated. Second, an attempt is made to obtain simple design charts to predict the bearing pressures mobilised by such footings in an approximate way. To attain these objectives it is helpful to idealise the normalised bearing pressure curve obtained from FE analysis as bilinear, as done in Chapter 5. The bilinear bearing pressure curve is assumed to have a linear "elastic" and a linear "plastic" part. A yield pressure defines the point at which footing response changes from primarily "elastic" to primarily "plastic". A typical bearing pressure curve obtained from finite element analysis and its corresponding bilinear idealisation has been already illustrated in Figure 5.6. The bilinear bearing response can be plotted once its "elastic" slope, "plastic" slope and yield pressure are determined. In this parametric study, an attempt is made to relate the "elastic" slope, "plastic" slope and yield pressure of the assumed bilinear curve to the SU2 model parameters.

6.6 PARAMETRIC STUDY

In this section, a parametric study is undertaken to investigate the effect of SU2 model parameters on the bearing pressure mobilised by circular footings embedded in carbonate sand. However, before undertaking a separate study for embedded

footings, it needs to be first explained why a separate study is at all considered necessary. Intuitively, it appears that the analyses performed for surface circular footings (having an embedment ratio of zero), should at least be qualitatively true for footings having other embedment ratios. However, the validity of this assumption may be confirmed only after a detailed study has actually been undertaken for embedded footings. Also, it is quite reasonable to assume that design charts similar to surface circular footings may be constructed for footings having different embedment ratios. Although quite likely, using such an approach would result in three separate design charts for each value of embedment ratio. The construction of such a large series of design charts does not appear to be either feasible or practical.

Thus in the following subsections, the effect of each SU2 model parameter on the bearing response of embedded footings is investigated again. Additionally, an alternative approach for constructing a small set of design charts applicable for a wide variety of embedment ratios is investigated.

6.6.1 EFFECT OF FOOTING DEPTH, *D*

The effect of overburden depth on the bearing pressure mobilised by an embedded footing is investigated in this section. A constant set of SU2 model parameters was selected. The depth of embedment D was simulated as a surcharge pressure acting on the top boundary of the soil surface. It was varied from 1m to 100m, for a footing 1m in diameter. The values of the model parameters used to obtain the predictions are given below in Table 6.2.

Table 6.2 Model parameters to investigate effect of footing depth

ϕ' (deg)	κ	λ	ν	e_{cs}	p'_o (MPa)	r	γ' (kN/m^3)	K_o	D/B
35	0.005	0.1	0.1	2.5	Variable	5.0	7.0	0.5	1-100

Figure 6.6 shows the plots of the bearing pressure against settlements normalised by the footing diameter. The bearing pressure is observed to increase with the embedment ratio. The "elastic" slope and "plastic" slope of the corresponding idealised bilinear bearing pressure curves were computed from this data. Figures 6.7, 6.8 and 6.9 plot respectively the normalised bearing pressure, normalised "elastic" and normalised "plastic" slope as a function of $\frac{\gamma' B}{p_o'}$, for embedment ratios of 1 and 100, at 30% normalised displacement. These parameters were normalised by the preconsolidation pressure p_o'. Thus the normalised "elastic" and "plastic slopes" are the slopes of the "elastic" and "plastic" part of the bearing pressure curve, where the bearing pressures are normalised by the preconsolidation pressure p_o', and the displacements are normalised by the diameter of the footing. The values were plotted at 30% normalised displacement to illustrate clearly the increase in the mobilised bearing pressure with embedment ratio. The plots show the normalised "elastic" slope and normalised "plastic" slope also increases with the embedment ratio *D/B*. However, it is observed that the increases in normalised plastic slope are much smaller than the corresponding increase in the embedment ratio.

It must be mentioned here that for an embedment ratio of zero, the lines plotted for normalised bearing pressure, normalised "elastic" slope and normalised "plastic slope" (not shown in the graphs) are very close and similar to that for an embedment ratio of 1, in the given scale of the plot. The normalised bearing pressure, normalised "elastic" and normalised "plastic" slope of embedded footings are observed to increase with footing depth *D*. The next section investigates the effect of preconsolidation pressure on the bearing pressure mobilised by embedded footings.

6.6.2 EFFECT OF PRECONSOLIDATION PRESSURE, p_o'

The effect of the preconsolidation pressure on the bearing pressure mobilised by an embedded footing is investigated in this section. A constant footing diameter *B* and depth *D* of 1m and 100m respectively and a constant set of values of the 6 SU2

model parameters besides p_o' were chosen. The values of the model parameters used are given below in Table 6.3.

Table 6.3 Model parameters to investigate effect of preconsolidation pressure

ϕ' (deg)	κ	λ	ν	e_{cs}	p_o' (MPa)	r	γ' (kN/m^3)	K_o	D/B
35	0.005	0.1	0.1	2.5	Variable	5.0	7.0	0.5	100

Figure 6.10 shows that the bearing pressure mobilised by an embedded footing increases with the preconsolidation pressure p_o' of the overconsolidated layer immediately below it. The yield pressure is also observed to increase with p_o'. However, p_o' appears to have a negligible effect on the slope of the "elastic" part of the bearing pressure curve. Some effect of p_o' is however, observed on the slope of the "plastic" part of the curve. Figure 6.11 plots the mobilised bearing pressure normalised with p_o'. The normalised bearing pressure is observed to decrease with the preconsolidation pressure. This implies that the increase of the bearing pressure is less than the corresponding increase in the preconsolidation pressure of the underlying sand. The effect of preconsoldation pressure on the bearing behaviour of embedded footings appears to be quite similar to that for surface circular footings (Figures 5.10 and 5.11).

In summary, the bearing pressure mobilised by embedded footings was observed to increase with the preconsolidation pressure or the thickness of the "cemented" layer immediately below it. However, the increase in the mobilised bearing pressure was observed to be less than the increase in the preconsolidation pressure of the underlying carbonate sand.

6.6.3 EFFECT OF NON-DIMENSIONAL PARAMETER, $\gamma' D / p_o'$

This section shows that for the assumed soil profile, the effect of three soil parameters on footing response can actually be expressed by a single variable. The three soil parameters are respectively the unit weight of the soil γ', the embedment depth D and the preconsolidation pressure p_o' of the soil. These parameters are combined to form a single variable $\gamma' D / p_o'$.

It may be deduced from equation (6.2) that

$$\frac{p_o'}{\gamma'} \propto D + H \tag{6.3}$$

Equation (6.3) leads to the following relation:

$$\frac{\gamma' D}{p_o'} \propto \frac{D}{D+H} \tag{6.4}$$

Thus for the soil profile considered in the parametric study, the inverse of the compound parameter $\gamma' D / p_o'$ is related to the thickness of the "cemented" or overconsolidated layer H relative to the footing depth D.

The effect of the parameter $\gamma' D / p_o'$ on the bearing response of embedded footings is demonstrated by an example. The bearing responses of two embedded footings having an equal diameter of 1m are analysed. The footings are assumed to rest on a "cemented" layer of carbonate sand at depths of 10m and 100m respectively. The embedment ratio D/B is 10 in the first case, and 100 in the other. The preconsolidation pressure p_o' of the carbonate sand at a depth of 10m beneath the footing is assumed to be 1,000 kPa. The preconsolidation pressure p_o' of the carbonate sand beneath the 100m deep footing is assumed to be 10,000 kPa. Thus the value of the parameter $\gamma' D / p_o'$ is the same for both the footings.

Figure 6.12 shows that the bearing pressure mobilised at 30% normalised displacement by the 100m deep footing is more than an order of magnitude higher than the 10m deep one. The mobilised bearing pressures of the two footings were normalised by the respective preconsolidation pressures p'_o of the underlying "cemented" layers. Figure 6.13 shows that nearly identical curves are obtained for the two footings. Some deviation is observed at larger normalised displacements. The normalised bearing pressures in Figure 6.13 were further normalised by the factor $(1+e_o)$. e_o is the void ratio corresponding to the preconsolidation pressure p'_o. Figure 6.14 shows that the re-normalised bearing pressure curves are almost exactly identical.

Two footings of different diameters are now considered. The two footings are assumed to have diameters B of 1m and 100m respectively. It is assumed that the footings have identical values for the embedment ratio D/B and the parameter $\gamma' D / p'_o$. Figure 6.15 shows that although the normalised bearing pressure curves are quite close, they deviate at larger normalised displacement. The bearing pressures were further normalised by $(1+e_o)$. Figure 6.16 shows that nearly identical curves are obtained. Figures 6.17 and 6.18 show that for very small values of $\gamma' D / p'_o$, re-normalisation with $(1+e_o)$ does not result in a better matching of the bearing pressure curve of the two footings. The preceding observations may be used to obtain the corrected bearing pressures mobilised by footings of different diameters at various embedment ratios.

Figure 6.19 plots the normalised bearing pressure mobilised at 10%, 20% and 30% normalised displacement respectively as a function of $\gamma' D / p'_o$. The bearing pressure mobilised at any displacement is observed to increase with $\gamma' D / p'_o$.

It was shown that for the assumed soil profile, almost a unique normalised bearing pressure curve is obtained for a unique value of the compound parameter $\gamma' D / p'_o$. In problems where overburden pressure dominates the analysis (i.e. for relatively high values of the embedment ratio D/B), this fact may be utilised to obtain a set of three design charts only, for footings with various embedment ratios, in the following way.

Each value of the factor $\gamma' D / p'_o$ represents a combination of a value of $\gamma' B / p'_o$ and embedment ratio *D/B*. Thus three charts plotted for the "elastic" slope, "plastic slope" and yield pressure as a function of $\gamma' D / p'_o$, should essentially be equivalent to obtaining these parameters for different combinations of $\gamma' B / p'_o$ and *D/B*. For relatively small values of embedment ratio *D/B*, the effect of the overburden pressure on the mobilised bearing pressure curve may not be predominant. Thus for relatively low embedment ratios, this approach may not yield correct values of the "elastic slope", "plastic slope" and yield pressure of the mobilised bearing pressure curve. In that case, the results of the analyses of Chapter 5 may have to be used to obtain approximate and conservative estimates of the bearing pressure curves for circular footings close to the surface. The next section investigates the effect of the elastic parameter on the bearing response of embedded footings.

6.6.4 EFFECT OF THE ELASTIC PARAMETER, κ

The effect of the elastic parameter κ on the bearing response of an embedded footing is investigated in this section. The elastic parameter κ defines the slope of the elastic rebound line in $e - \ln p'$ space. Such a curve is generally obtained from isotropic consolidation tests. e is the void ratio and p' is the mean effective pressure. In the SU2 model, the elastic bulk and shear modulus of the soil is directly proportional to the mean pressure and inversely proportional to κ.

The elastic parameter κ was varied from 0.005 to 0.05 for a wide range of values of the parameter $\gamma' D / p'_o$ and for a footing diameter *B* of 1m. The values of the model parameters used are given below in Table 6.4.

Table 6.4 Model parameters to investigate effect of κ

ϕ' (deg)	κ	λ	ν	e_{cs}	p'_o (MPa)	r	γ' (kN/m^3)	K_o	*D/B*
35	0.005-0.05	0.10.3	0.1	2.5	1.0	5	7.0	0.5	0-100

Figure 6.20 plots the normalised "elastic" slope of the bearing pressure curve as a function of the elastic parameter κ. For constant $\gamma' D / p'_o$, the normalised "elastic" slope is observed to decrease with κ. This is consistent with SU2 model assumptions that elastic shear and elastic bulk modulus vary inversely with κ. Figure 6.21 plots the normalised "elastic" slope as a function of $\gamma' D / p'_o$. It is observed to increase with $\gamma' D / p'_o$. This curve gives "elastic" slopes for $\kappa = 0.005$. For any other κ, the "elastic" slope may be approximately obtained by scaling this curve by the factor $0.005/\kappa$. Figure 6.22 shows that the normalised yield pressure decrease with $\gamma' D / p'_o$. For constant $\gamma' D / p'_o$, the normalised yield pressure decreases with increasing κ. It is observed that as $\gamma' D / p'_o$ becomes greater than 0.7, the yield pressure approaches a negligible value. As a result of the overburden pressure, the carbonate sand immediately beneath the footing becomes normally consolidated in such a situation. The thickness of the "cemented" or overconsolidated layer becomes zero in such a case and the footing may be assumed to be resting on a normally consolidated layer of sand. It was shown in Chapter 5 that for such a case the bearing pressure curves are approximately straight lines passing through the origin.

The effect of elastic parameter κ on the bearing response of embedded footings was investigated. The "elastic" slope of the bearing pressure curve was found to be inversely proportional to κ. For the given soil profile, it was observed that the parameter $\gamma' D / p'_o$ also influences the "elastic" response of the footing. The effect of plastic volume compressibility λ on the response of an embedded footing is investigated in the next section.

6.6.5 EFFECT OF PLASTIC PARAMETER, λ

The effect of the plastic compressibility parameter λ on the bearing response of footings embedded in carbonate sand is now investigated. λ is the slope of the virgin consolidation in $e - \ln p'$ space. e is the void ratio and p' is the corresponding mean effective pressure.

The values of the model parameters used to investigate the effect of λ on the footing response are given below in Table 6.5.

Table 6.5 Model parameters to investigate effect of λ

ϕ' (deg)	κ	λ	ν	e_{cs}	p'_o (MPa)	r	γ' (kN/m^3)	K_o	D/B
35	0.005	Variable	0.1	2.5	1.0	5	7.0	0.5	Variable

The effect of λ on the bearing response of the footing was studied for various embedment ratios. Figure 6.23 shows that for constant embedment ratio *D/B*, the normalised bearing pressure mobilised at any normalised displacement decreases with λ. Figure 6.24 plots the normalised bearing pressure mobilised at 30% normalised displacement as a function of λ. The mobilised bearing pressure at 30% normalised displacement was used to emphasise its decrease with plastic compressibility parameter λ. This is consistent with the general observation that the bearing pressures mobilised by footings decrease with increased volume compressibility of the underlying soil. It is observed that the "elastic" component of the footing response only slightly affected by changes in λ. Thus for all practical purposes, the "elastic" response of embedded footings may be assumed to be independent of the plastic compressibility of the soil. Figure 6.25 plots the normalised "plastic" slope as a function of $\gamma' D / p'_o$. For constant $\gamma' D / p'_o$, the normalised "plastic" slope is observed to decrease with λ. For a given λ, a larger $\gamma' D / p'_o$ is observed to correspond to a larger normalised "plastic" slope. Figure 6.25 may be used to determine the normalised "plastic" slope of the bilinear bearing pressure curve once λ and $\gamma' D / p'_o$ are known.

The effect of the parameter λ on the bearing response of an embedded footing was investigated. The bearing pressure of embedded footings was observed to decrease with plastic compressibility of carbonate sand, as expected. For the assumed soil profile, the normalised "plastic" slope of the bearing pressure curve was observed to be also dependent on the parameter $\gamma' D / p'_o$.

6.6.6 EFFECT OF FRICTION ANGLE, ϕ'

The conventional bearing capacity equation shows that the friction angle of sand has a significant effect on the drained bearing capacity of an embedded footing. It was shown in section 5.6.6 of Chapter 5 that in the SU2 model, the critical state ratio M embodies the effect of friction angle on soil behaviour. In triaxial compression conditions, the critical state ratio M and ultimate friction angle ϕ' are related by equation (5.5). The influence of effective friction angle ϕ' on the bearing pressure mobilised by embedded footings was investigated by varying the critical state ratio M in the SU2 model. M was given values of 1.42, 1.64 and 1.85 respectively. This corresponds to effective friction angles ϕ' of 35°, 40° and 45° respectively. This correspondence was obtained using the relation given by equation (5.5).

Figure 6.26 shows the influence of friction angle on the bearing pressure mobilised by a footing with an embedment ratio of 5.0. The normalised bearing pressure is observed to increase with the friction angle. The normalised "plastic" slope as well as the normalised yield pressure is observed to increase with M, as expected. The increase in the yield pressure with M was, however, small. However for simplicity, the effect of M on the yield pressure was ignored in the development of design charts. It is hypothesized that the critical state parameter M has a negligible effect on the yield pressure. However, further investigations are required to confirm this hypothesis. It is seen that the slope of the "elastic" component of the response remains unchanged with friction angle. Thus the "elastic" response of an embedded footing may be assumed to be independent of the friction angle of the underlying carbonate sand.

Figure 6.27 plots the ratio of the slopes of the "plastic" component of the response for two different friction angles, as a function of $\gamma' D / p'_o$. An equation is now proposed to relate this ratio with the critical state parameter M in the following way:

$$\frac{S_M}{S_{1.42}} = \left(\frac{M}{1.42} \right)^n \tag{6.5}$$

S_M = Normalised "plastic" slope at critical state ratio M

$S_{1.42}$ = Normalised "plastic" slope at critical state ratio of 1.42

n = An empirically determined exponent

The normalised "plastic" slopes obtained from equation (6.5) and Figures 6.25 and 6.28 are valid for any M in the range $1.42 \leq M \leq 1.85$ for footings embedded in carbonate sand. Figure 6.28 plots the exponent n as a function of $\gamma' D / p'_o$ for different λ.

In summary, for the assumed soil profile the ultimate friction angle was observed to have a significant effect on the bearing response of embedded footings for relatively low values of $\gamma' D / p'_o$. For relatively larger $\gamma' D / p'_o$, the influence of the ultimate friction angle on the bearing response was observed to decrease. The ultimate friction angle has negligible effect on the "elastic" component of the footing response.

6.6.7 EFFECT OF POISSON'S RATIO, ν

This section investigates the effect of the Poisson's ratio on the bearing response of embedded footings.

Figures 6.29 and 6.30 shows that for relatively large values of $\gamma' D / p'_o$, the underlying soil is normally consolidated and the bearing responses are entirely "plastic". Consequently, the effect of the Poisson's ratio on the bearing response of embedded footings with large $\gamma' D / p'_o$ is almost negligible. For relatively smaller $\gamma' D / p'_o$, there is a finite thickness of "cemented" layer below the footing. Consequently, there is a larger range of "elastic" response of the footing. In such a case, the mobilised bearing pressure and the "elastic" slope of the response is observed to decrease with ν. For simplicity, the effect of Poisson's ratio on the mobilised bearing pressure of footings embedded in carbonate sand has been ignored in the remainder of this study.

6.6.8 EFFECT OF THE VOID RATIO CONSTANT, e_{cs}

The void ratio constant e_{cs} is defined as the void ratio at unit mean effective pressure on the critical state line, drawn in $e - \ln p'$ space. e is the void ratio and p' is the mean effective pressure. It determines the position of the critical state line in $e - \ln p'$ space. In this section the effect of the parameter e_{cs} on the bearing response of embedded footings is discussed.

Figure 6.31 shows the effect of the void ratio constant e_{cs} on the bearing pressure mobilised by a footing 1m in diameter embedded in carbonate sand at a depth of 100m. The normalised bearing pressure is observed to increase with e_{cs}. The normalised bearing pressures in Figure 6.31 were further normalised by the factor $(1+e_{cs})$. Figure 6.32 shows that virtually identical curves are obtained. This fact is subsequently used to correct the normalised "elastic" slope, yield pressure and normalised "plastic" slope obtained respectively from Figures 6.21, 6.22 and 6.25 for a void ratio constant e_{cs} other than 2.5. The values in these figures were obtained with a void ratio constant e_{cs} of 2.5.

6.6.9 EFFECT OF SPACING RATIO, r

The effect of the spacing ratio parameter r on the bearing response of embedded footings is investigated in this section. The spacing ratio has been defined and its possible range of values described in section 5.6.9 of Chapter 5.

The effect of the spacing ratio r on a 1m diameter footing resting at a depth of 20m was analysed. The spacing ratio was assumed to be 5.0 in one case and 2.0 in the other. Figure 6.33 plots the bearing pressure curves for two different values of the spacing ratio r. The "elastic" slopes of the curves were observed to be nearly identical. A small difference in the "plastic" slopes was observed. However, the yield pressure for a spacing r of 2.0 was observed to be approximately twice that for a spacing ratio r of 5.0. This is similar to observations made for surface circular footings. Thus a similar approach is used to determine the influence of the spacing

ratio on the yield pressure. For a spacing ratio r other than 5.0, it is proposed that an approximate value for the yield pressure be computed as follows:

$$\left(\frac{q_r}{p'_o}\right)_e = \frac{2}{\sqrt{r-1}}\left(\frac{q_{r=5}}{p'_o}\right)_e \tag{6.6}$$

The normalised yield pressure shown in Figure 6.22 was obtained for a spacing ratio r of 5.0. For a spacing ratio r other than 5.0, these yield pressures need to be scaled by the factor $\frac{2}{\sqrt{r-1}}$ as given by equation (6.6). The normalised "elastic" and "plastic" slopes shown in Figures 6.21 and 6.25 respectively are assumed to be approximately same for values of r other than 5.0.

Similar to surface circular footings, the normalised "elastic" and "plastic" slopes of the bearing pressure curve of embedded footings are observed to be approximately independent of the spacing ratio parameter r. The normalised yield pressure is observed to be approximately inversely proportional to the square root of *(r-1)*.

6.7 DESIGN CHARTS

The effect of the SU2 model parameters on the bearing response of footings embedded in carbonate sand has been investigated. The investigation was carried out for a simplified soil profile assumed to exist beneath the footing as shown in Figure 6.4. For the assumed soil profile, simplified design charts are suggested in this section. The design charts may be used obtain an approximate bilinear bearing pressure curve of circular footings embedded in carbonate sand. The "elastic" slope, "plastic" slope and the yield pressure of the assumed bilinear curve are obtained from these charts.

Figure 6.34 is proposed as the design chart to determine the normalised "elastic" slope (NES) of the footing response for any κ, e_{cs} and p'_o. The normalised elastic slope of the footing has been already defined in section 6.6.1. The elastic parameter

κ is assumed as known and the parameter $\frac{\gamma' D}{p'_o}$ can be computed from known information. The normalised "elastic" slope is then determined from Figure 6.34. Figure 6.35 is proposed as the design chart to determine the normalised yield pressure (NYP) of the footing response for any spacing ratio r, void ratio constant e_{cs} and preconsolidation pressure p'_o. The yield pressure is normalised by the preconsolidation pressure of the soil. For a spacing ratio r other than 5.0, the normalised yield pressure obtained from Figure 6.22 is scaled by the factor $\frac{\sqrt{r-1}}{2.0}$ in Figure 6.35. Figure 6.36 is proposed as the design chart to determine the normalised "plastic" slope of the footing response for any critical state ratio M, void ratio constant e_{cs} and preconsolidation pressure p'_o. The normalised plastic slope has also been already defined in section 6.6.1. The plastic compressibility parameter λ is assumed as known and the parameter $\frac{\gamma' D}{p'_o}$ is computed as before. The normalised "plastic" slope is then determined from Figure 6.36. The exponent n is determined from Figure 6.28 using the value of λ and $\frac{\gamma' D}{p'_o}$

The values of the normalised "elastic" slope, yield pressure and "plastic" slope in Figures 6.21, 6.22 and 6.25 respectively were computed using a fixed value of the void ratio constant e_{cs} equal to 2.5. For e_{cs} other than 2.5, the "elastic" slope, yield pressure and "plastic" slope obtained from these figures were scaled in Figures 6.34, 6.35 and 6.36 respectively by a factor of $\frac{3.5}{(1+e_{cs})}$. This follows from the observation made in Figures 6.31 and 6.32 and discussions in section 6.6.8.

The normalised "elastic" slope, yield pressure and "plastic" slope shown in Figures 6.21, 6.22 and 6.25 were computed using a constant value of the preconsolidation pressure p'_o of 1.0 MPa of the carbonate sand immediately beneath the embedded footing. To obtain correct values of these parameters in case of preconsolidation pressures other than 1.0 MPa, the values of the "elastic" slope, "plastic" slope and yield pressures in these figures were scaled by a factor $\frac{(1+e_o)_{1MPa}}{(1+e_o)_{p'_o}}$ in Figures 6.34,

6.35 and 6.36 respectively. This follows from observations made in Figures 6.13 through 6.16 and discussions in section 6.7.3.

The void ratio e_o at a preconsolidation pressure p'_o is computed as follows:

$$e_o = e_{nc} - \lambda \ln p'_o \tag{6.7}$$

In equation (6.7), e_{nc} represents the void ratio at unit pressure on the normal consolidation line. It is computed as follows:

$$e_{nc} = e_{cs} + (\lambda - \kappa)\ln r \tag{6.8}$$

e_{cs}, λ, κ and r are SU2 model parameters which have been defined before.

In the design charts proposed for footings embedded in carbonate sand the effect of Poisson's ratio on the mobilised bearing pressure was ignored. The effect of friction angle on the yield pressure was also ignored. The determination of the absolute values of "elastic slope", "plastic slope" and "yield pressure" from the corresponding normalised values is a straightforward procedure. The proposed design charts may be used as a simple method of determining an approximate bilinear bearing pressure curve for circular footings and piles embedded in carbonate sand.

6.8 EXAMPLE PREDICTIONS

In this section approximate bilinear bearing pressure curves are obtained for footings and plates embedded in carbonate sand using the proposed design charts. The bilinear bearing pressure curves are compared in one case with the results of more accurate finite element analysis and in another case with field plate load test (PLT) data.

Consider the case of a pile 1m in diameter embedded in carbonate sand at a depth of 100m below the ocean bed. The embedment ratio *D/B* is therefore 100. The model parameters assumed for the underlying carbonate sand are given below in Table 6.6.

Table 6.6 Model parameters for example problem

ϕ' (deg.)	κ	λ	ν	e_{cs}	p'_o (MPa)	r	γ' (kN/m^3)	K_o	D (m)
39	0.005	0.1	0.1	2.0	40	5	7.0	0.5	100

Figure 6.37 shows the bearing pressure curve predicted using the design charts. For comparison, the solutions obtained from finite element analysis were also plotted in the figure. Reasonable agreement is observed between the two. However, the bearing pressure predicted by the design charts appears to be somewhat lower than the corresponding FE simulations. It has been mentioned that the yield pressure is observed to increase with the friction angle. However for simplicity, the increase in yield pressure due to increased friction angle was ignored in the design charts. It is hypothesized that this results in a lower bearing pressure curve to be predicted by the proposed method. However, further investigations are required to confirm this hypothesis.

Bearing pressure curves obtained from plate load tests on carbonate sand are now predicted using the proposed design charts. Goudever et al (1988) and Sharp and Seters (1988) reported the results of plate load tests (PLT) conducted on 0.5m diameter plates at depths of 112.6m to 140.8 m below the ocean bed. The tests were carried out at the North Rankin site off Australia's NorthWest coast. Values typical for the carbonate sand at the North Rankin site are assumed for the SU2 model parameters. The assumed values are presented below in Table 6.7.

Table 6.7 Test details and assumed model parameters for North-Rankin site

PLT	D (m)	ϕ' (deg)	κ	λ	ν	e_{cs}	p'_o (MPa)	r	γ' (kN/m^3)	K_o
1	117	35	0.005	0.3	0.1	2.5	2.4	5.0	7.0	0.5
2	118	35	0.005	0.3	0.1	2.5	5.0	5.0	7.0	0.5
3	125	35	0.005	0.1	0.1	2.5	6.0	5.0	7.0	0.5
6	140	35	0.005	0.3	0.1	2.5	1.4	5.0	7.0	0.5

The preconsolidation pressure of the carbonate sand immediately beneath the plate was obtained from its correlation with the corresponding cone penetration (CPT) value. Figure 6.38 gives the CPT profile and locates the depth of the PLT' s at the test site. The correlation proposed between CPT and preconsolidation pressure p'_o for carbonate sand by Randolph, Joer and Airey (1999) is as follows:

$$p'_o = 0.1 q_c \tag{6.9}$$

In equation (6.9), p'_o is the preconsolidation pressure of carbonate sand corresponding to the cone penetration value q_c. An estimate of the friction angle of the carbonate sand could also be obtained from its standard correlation with q_c. Figure 6.39 shows the comparison of four PLT data with the predicted bilinear bearing pressure curves obtained using the proposed design charts. Reasonable agreement is observed between predictions and experimental data.

It is observed that lower yield pressures and stiffer "elastic" slopes are generally predicted by the proposed design charts. It is well known that cementation in carbonate sand increases the size of the yield locus in the deviator direction. The SU2 model, in its current form, does not take this into account. This may be a reason for the prediction of consistently lower yield pressures. A second reason may be the use of a constant Poisson's ratio, ν equal to 0.1, in obtaining the design charts. This may lead to the overprediction of "elastic" slopes and yield pressures for carbonate sand having a Poisson's ratio greater than 0.1. This has been demonstrated in section 6.7.7

and Figure 6.30. However, despite such shortcomings, the design charts appear to provide a reasonable first approximation of the PLT data.

6.9 CONCLUSION

The suitability of the SU2 model for predicting the behaviour of circular footings on carbonate soils subjected to overburden pressure was established. For this, the SU2 model predictions were validated with test data for model-scale footings. It was shown that the overburden depth increases the bearing pressure mobilised by footings embedded in carbonate sand. It was observed that three of the SU2 model parameters viz. λ, κ and M had the major influence on the bearing pressure mobilised by circular footings embedded in carbonate sand. It was shown that for the assumed soil profile, a unique value of the parameter $\frac{\gamma' D}{p'_o}$ results in a unique normalised bearing pressure curve. Similar to surface footings, volume compressibility of carbonate sand was observed to decrease the bearing pressure mobilised by deep footings.

Design charts were proposed to predict the bearing pressure of embedded footings and end bearing piles in carbonate sand. It was shown that approximate bilinear pressure curves obtained using the design charts provide a realistic first estimate of the bearing pressure curve of deep footings and piles embedded in carbonate sand.

A major limitation of the study is the assumption that an idealised soil profile with uniform soil properties exists beneath the foundation. For the smaller diameters usual for deep footings and piles, the assumption of such a profile with uniform soil properties may be considered to be a reasonable approximation of reality. Another limitation of the proposed approach is that although this method will work for small embedment ratios, it will not work for surface circular footings when the embedment ratio and $\frac{\gamma' D}{p'_o}$ becomes equal to zero.

APPENDIX 6.1 BEARING CAPACITY OF EMBEDDED FOOTINGS USING DESIGN CHARTS

The bilinear bearing pressure curve of an end bearing pile 1m in diameter and 100m deep was computed using the proposed design charts. The details of the calculation are presented in this appendix. The values of the model parameters used for the example problem have been already given in Table 6.6. It is reproduced below for convenience:

Table 6.6 Model parameters for example problem

ϕ' (deg.)	κ	λ	ν	e_{cs}	p'_o (MPa)	r	γ' (kN/m^3)	K_o	B (m)	D (m)
39	0.005	0.1	0.1	2.0	40	5	7.0	0.5	1	100

The steps followed in the computation are listed below:

1. The parameter $\gamma' D / p'_o$ was computed.

$$\frac{\gamma' D}{p'_o} = \frac{7x100}{40{,}000} = 0.0175$$

2. For κ = 0.005, λ = 0.1 and $\gamma' D / p'_o$ = 0.0175, the normalised "elastic" slope (*NES*), the normalised yield rressure (*NYP*) and the normalised "plastic" slope (*NPS*) for the bilinear bearing pressure curve were computed as follows:

Exponent n = 4.5 (Figure 6.28)

$$NES \frac{3.5\kappa}{(1+e_{cs})} \frac{(1+e_o)_{1MPa}}{(1+e_o)_{p'_o}} = 0.175 \quad \text{(Figure 6.34)}$$

$$NYP \frac{\sqrt{r-1}}{2.0} \frac{3.5}{(1+e_{cs})} \frac{(1+e_o)_{1MPa}}{(1+e_o)_{p'_o}} = 0.7 \quad \text{(Figure 6.35)}$$

$$NPS\left(\frac{1.42}{M}\right)^n \frac{3.5}{(1+e_{cs})} \frac{(1+e_o)_{1MPa}}{(1+e_o)_{p'_o}} = 7.0 \quad \text{(Figure 6.36)}$$

3. The carbonate sand has a void ratio constant e_{cs} of 2.0. Thus

$$\frac{3.5}{(1+e_{cs})} = \frac{3.5}{3.0} = 1.167$$

4. The carbonate sand has a preconsolidation pressure p'_o of 40 MPa. Thus

$$e_{nc} = e_{cs} + (\lambda - \kappa)\ln r = 2.0 + (0.1 - 0.005) \text{ x } \ln 5.0 = 2.16$$

$$e_o|_{1MPa} = e_{nc} - \lambda \ln p'_o = 2.16 - 0.1 \text{ x } \ln 1000 = 1.47$$

$$(1+e_o)_{1MPa} = 1.0 + 1.47 = 2.47$$

$$e_o|_{40MPa} = e_{nc} - \lambda \ln p'_o = 2.16 - 0.1 \text{ x } \ln 40,000 = 1.1$$

$$(1+e_o)_{40MPa} = 1.0 + 1.1 = 2.1$$

Hence,

$$\frac{(1+e_o)_{1MPa}}{(1+e_o)_{p'_o}} = 1.176$$

5. The final design parameters were

Normalised "elastic" slope	= 25.5
Normalised yield pressure	= 0.51
Normalised "plastic" slope	= 8.76

6. Computation of average bearing pressure mobilised at 30% normalised displacement:

   Normalised displacement at yield = 0.51/25.5 = 0.02

   Mobilised normalised bearing pressure at 30% normalised displacement = 8.76 x (0.3 – 0.02) + 0.51 = 2.96

   Mobilised bearing pressure at 30% normalised displacement = 2.96 x 40,000.0 = 118,400 kPa = 118.4 MPa.

   The mobilised normalised bearing pressure multiplied by the soil preconsolidation pressure gives the absolute values of the bearing pressure mobilised by the pile as a function of settlement relative to the pile diameter.

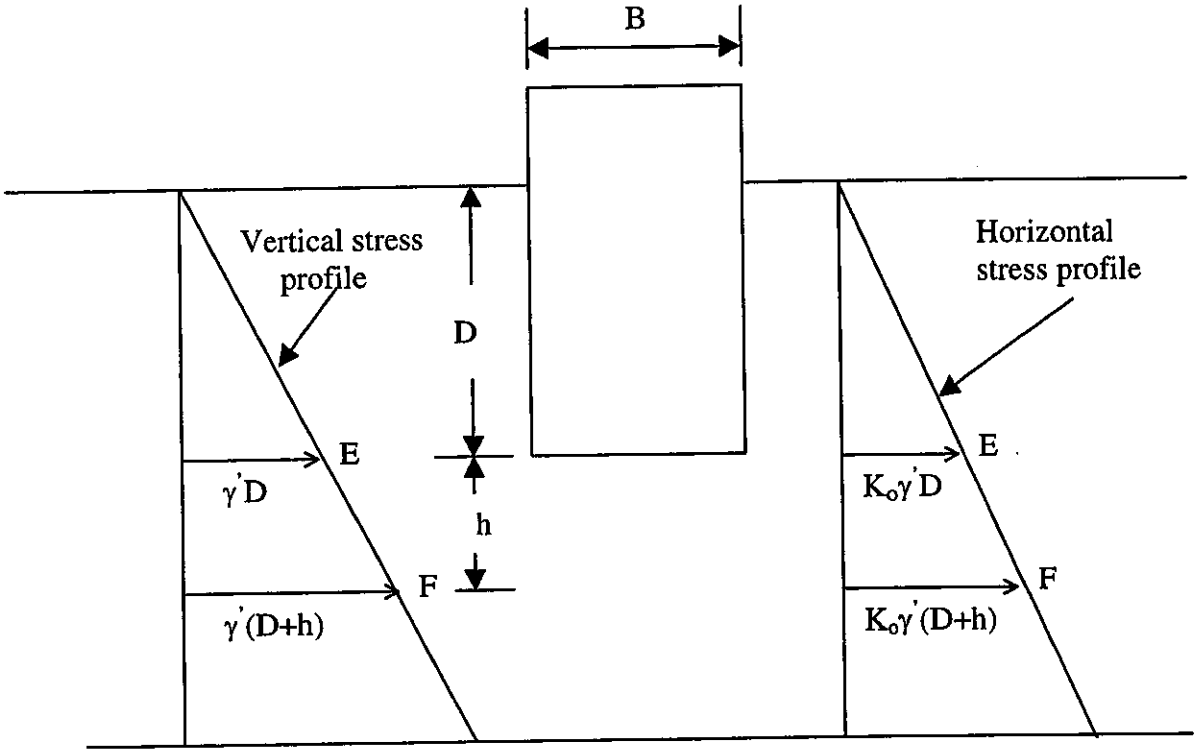

Figure 6.1 Profile of effective in-situ vertical and horizontal stress in soil

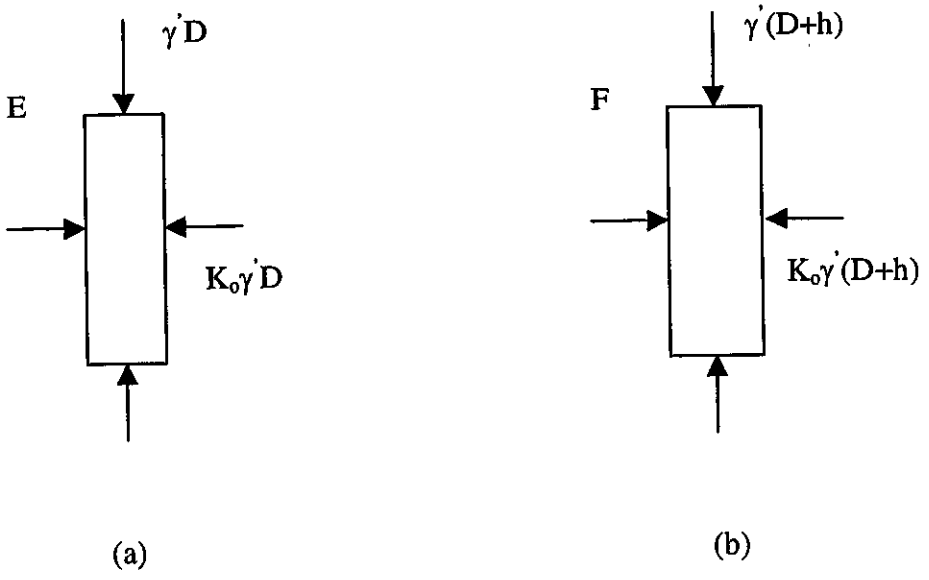

Figure 6.2 In-situ stress at a soil element respectively at a depth *D* and *(D+h)* below the footing

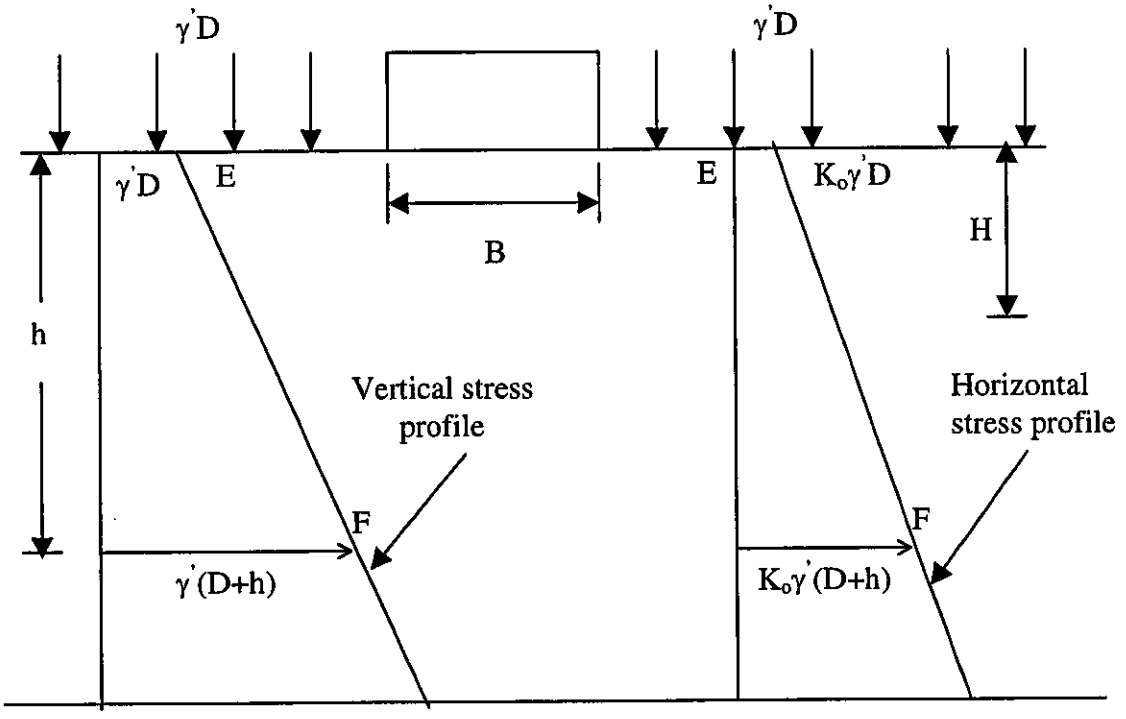

Figure 6.3 Modified problem formulation and corresponding in-site effective vertical and horizontal stress profile

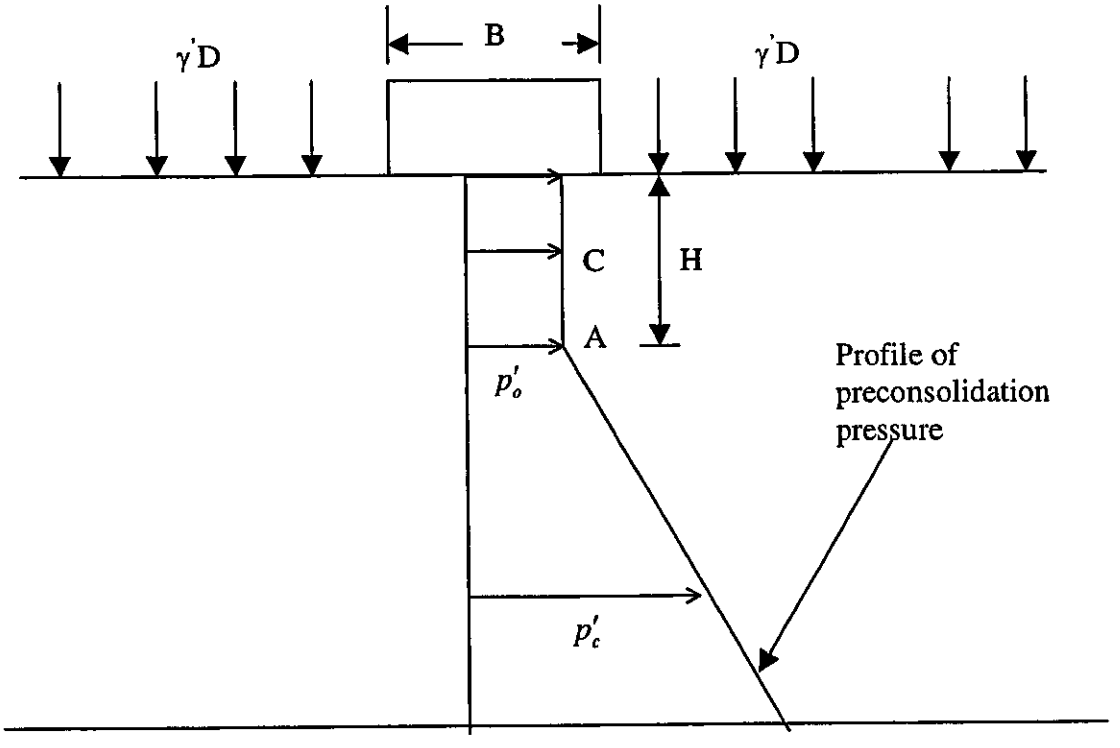

Figure 6.4 Profile of preconsolidation pressure below the footing

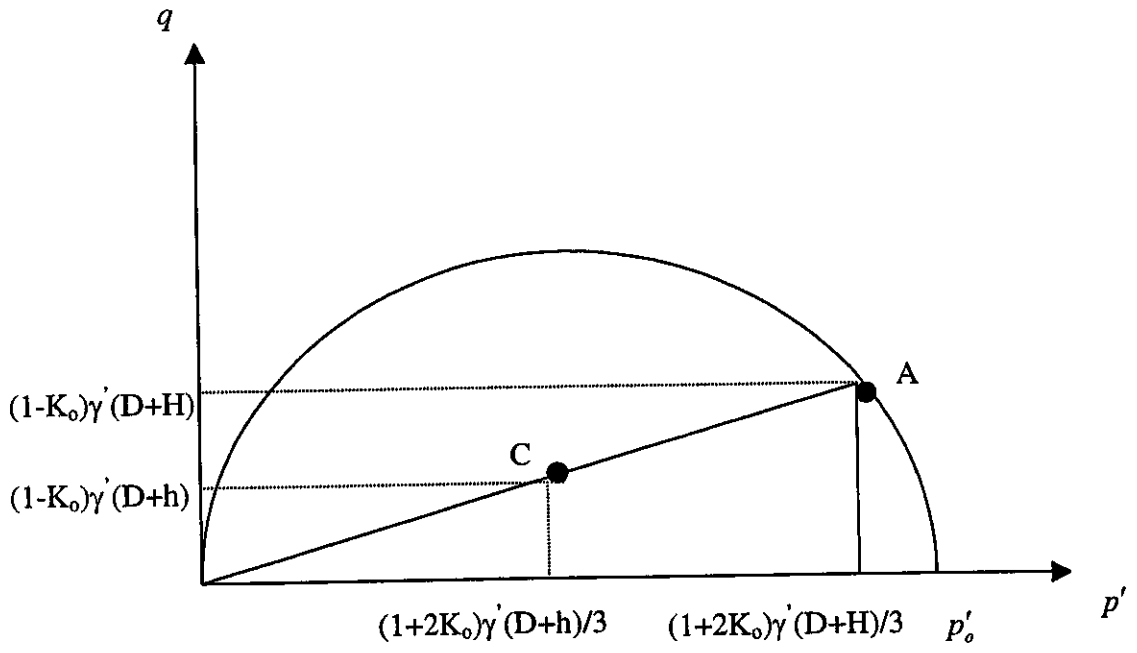

Figure 6.5 Position of in-situ stress with respect to the SU2 yield locus

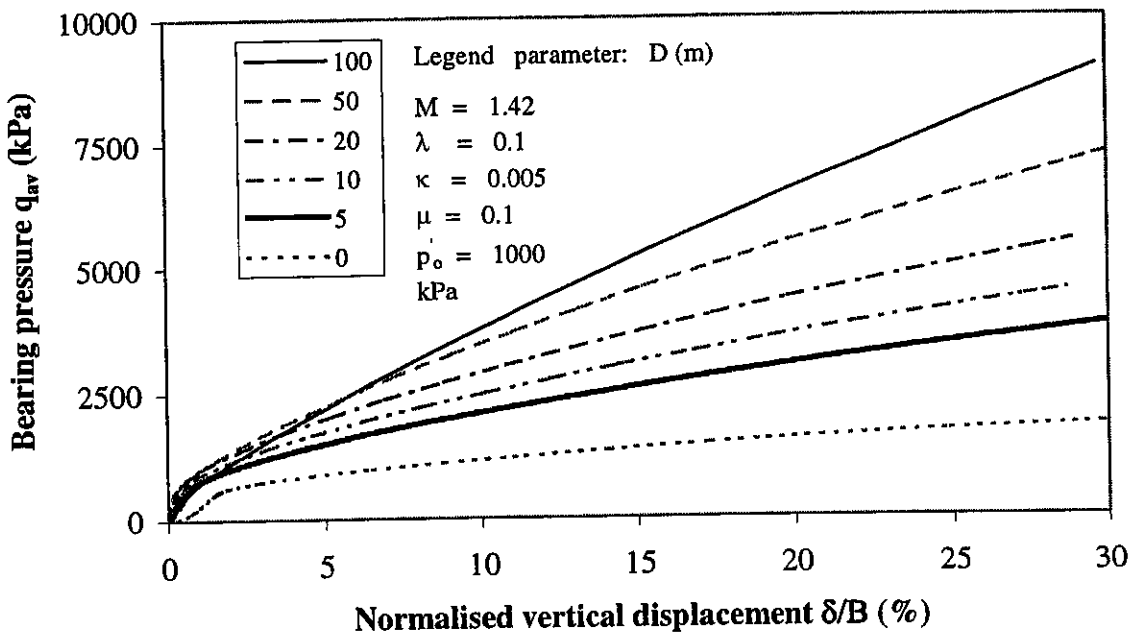

Figure 6.6 Effect of footing depth on the mobilised bearing pressure

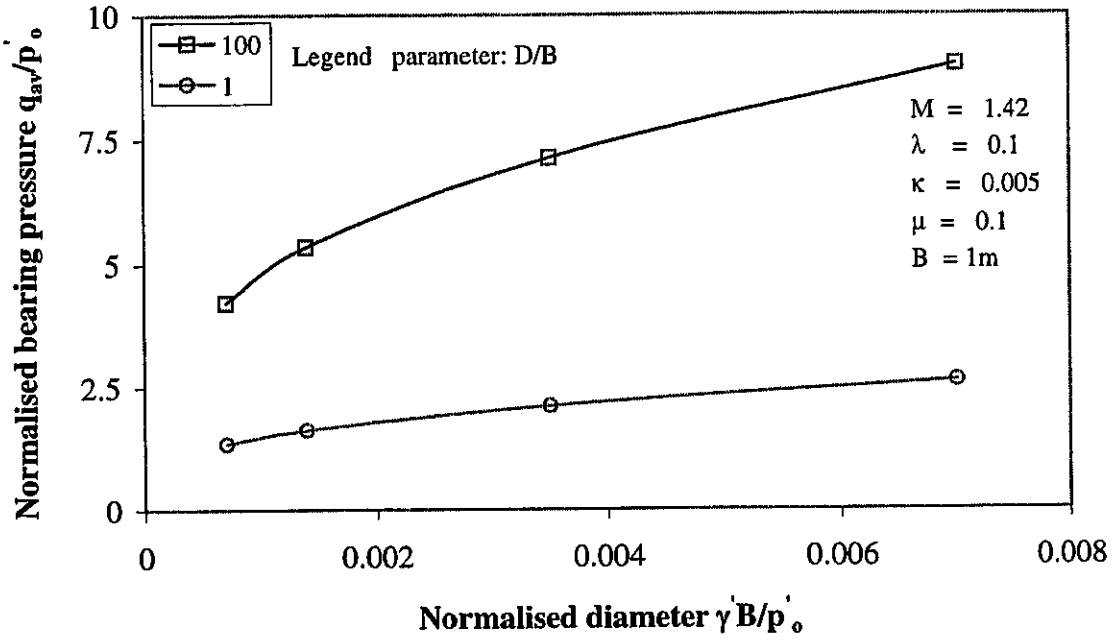

Figure 6.7 Effect of embedment ratio on mobilised bearing pressure

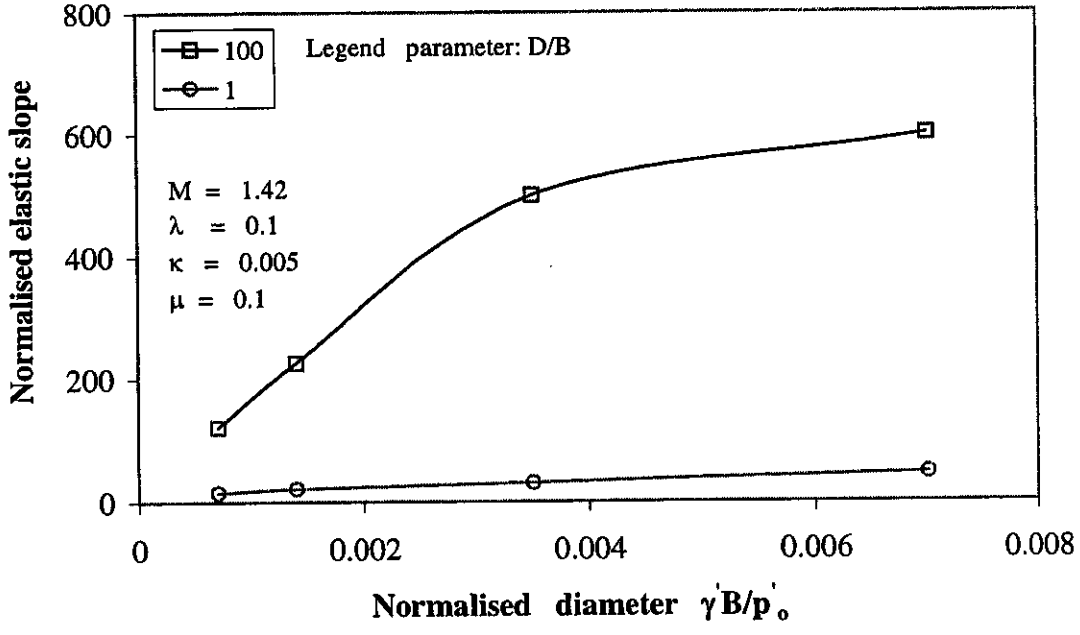

Figure 6.8 Effect of embedment ratio on elastic slope

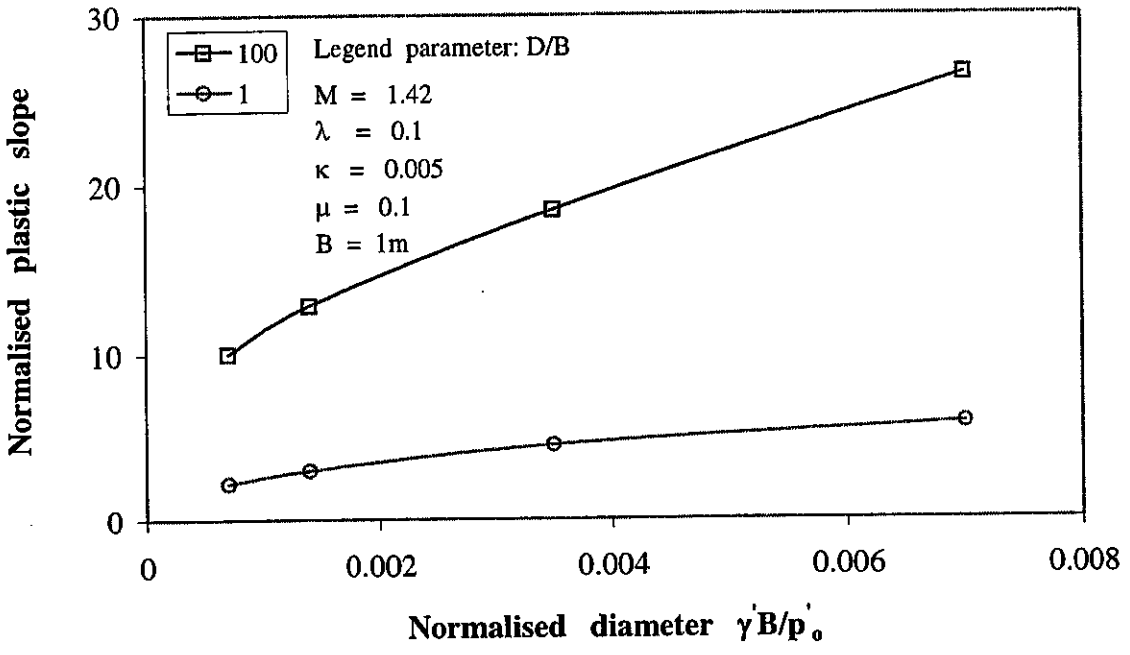

Figure 6.9 Effect of embedment ratio on plastic slope

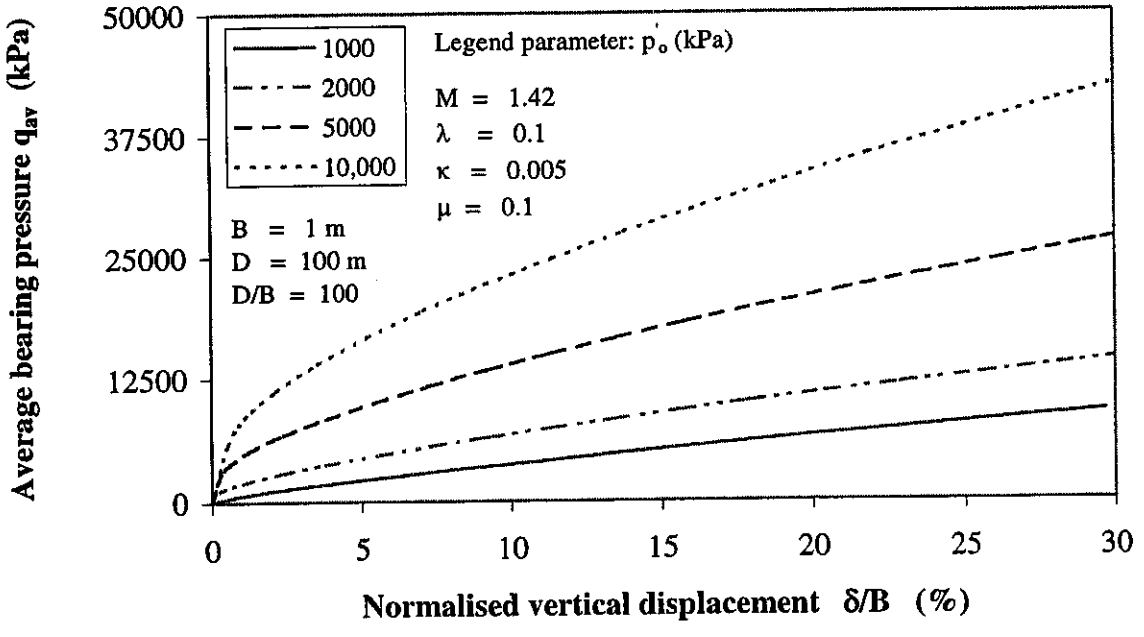

Figure 6.10 Effect of preconsolidation stress on bearing pressure

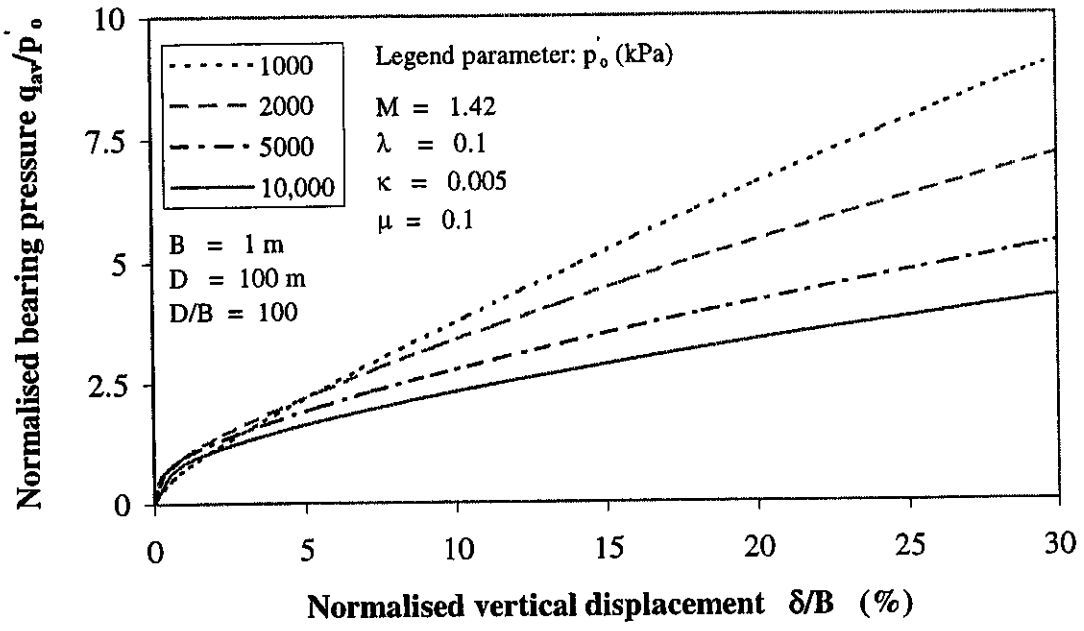

Figure 6.11 Effect of preconsolidation stress on normalised bearing pressure

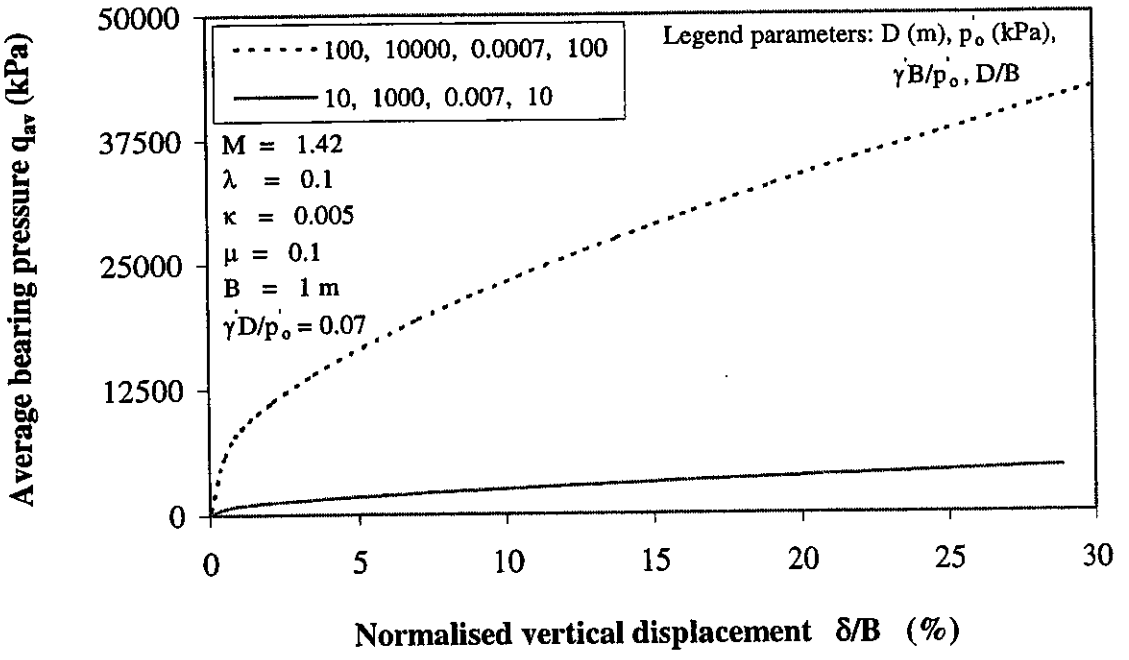

Figure 6.12 Mobilised bearing pressure for footings with equal $\frac{\gamma' D}{p_o'}$

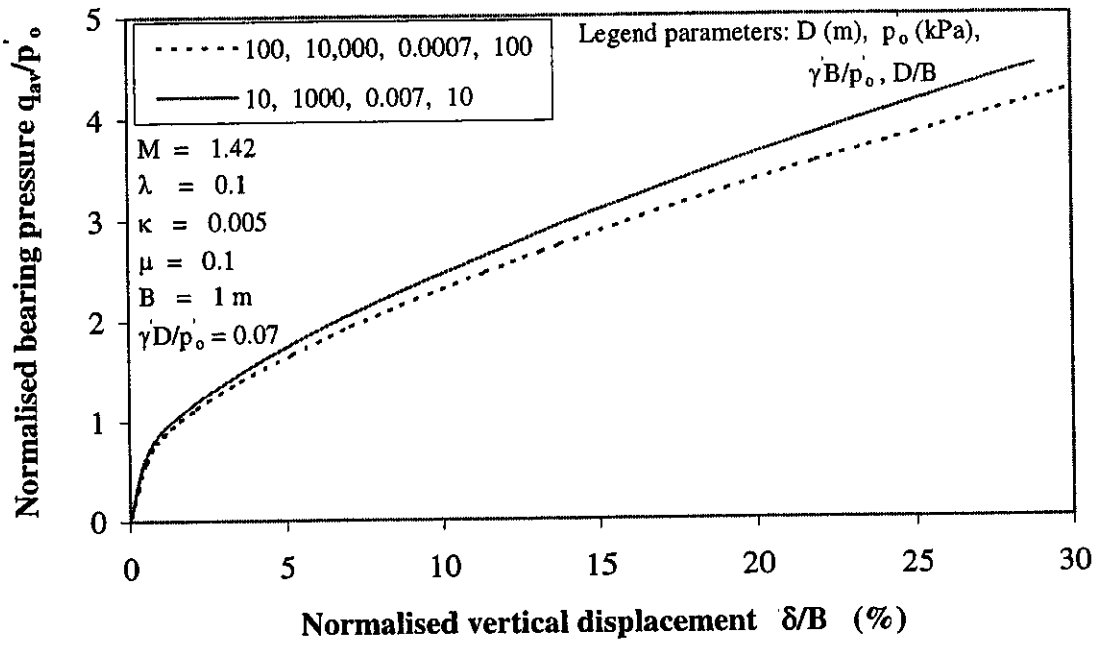

Figure 6.13 Normalised bearing pressure for footings with equal $\frac{\gamma' D}{p'_o}$

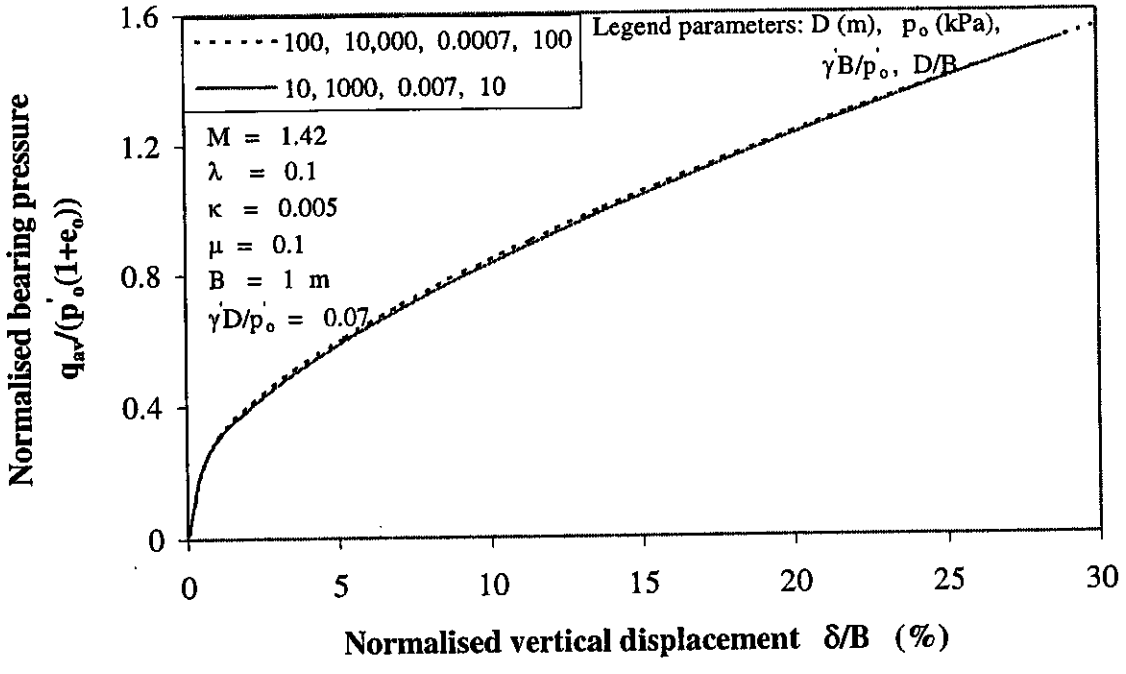

Figure 6.14 Bearing pressure normalised with $p'_o(1+e_o)$ **for footings with equal** $\frac{\gamma' D}{p'_o}$

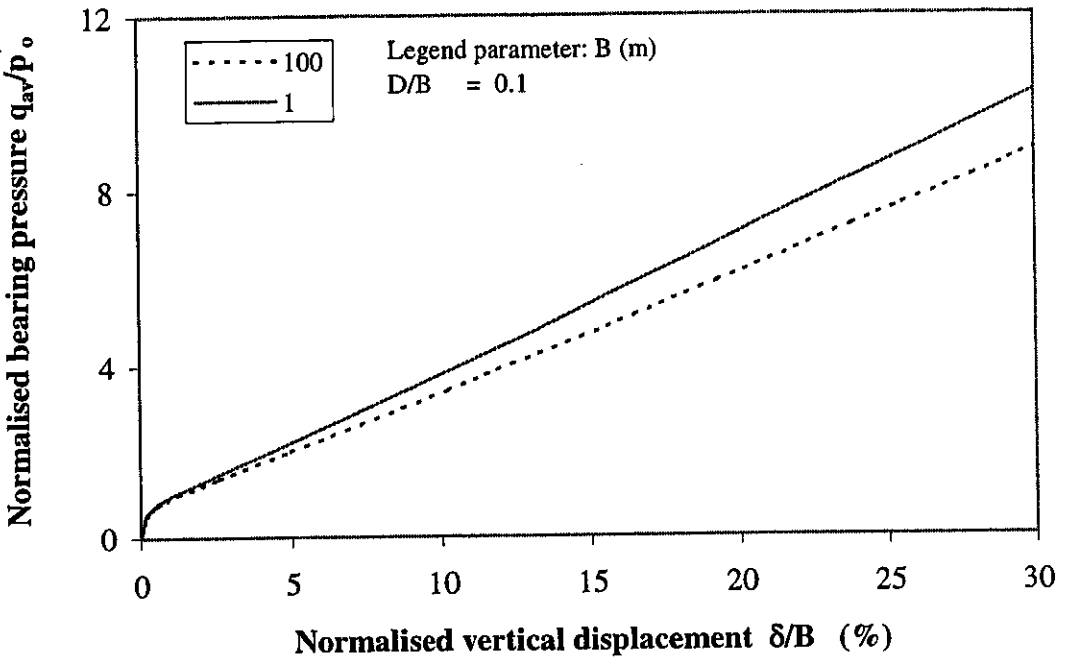

Figure 6.15 Normalised bearing pressure for footings of different diameter having equal embedment ratio

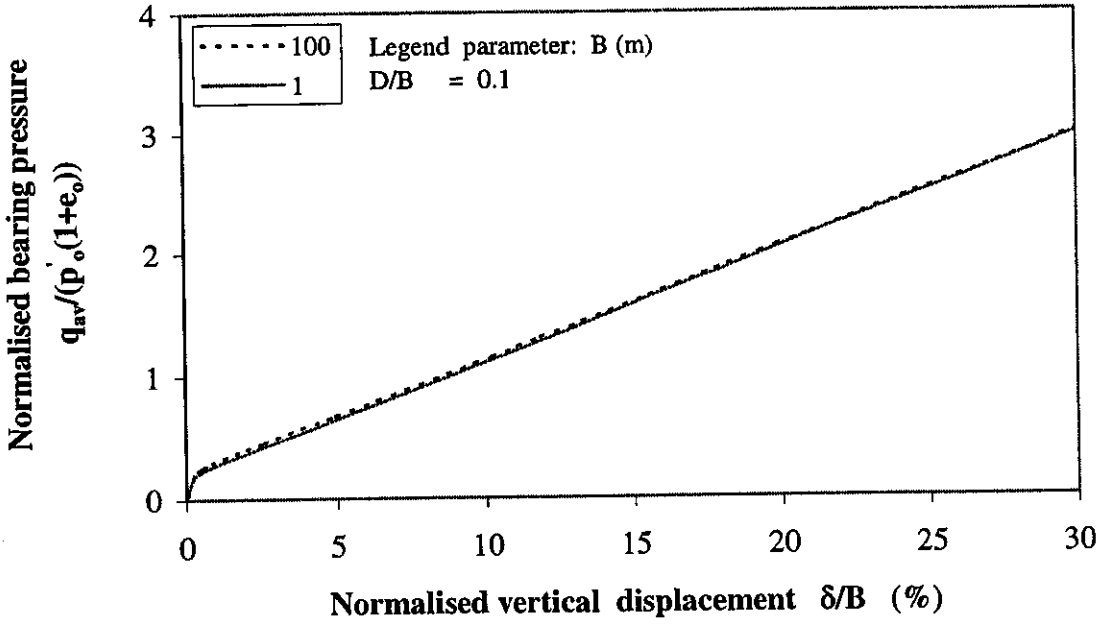

Figure 6.16 Bearing pressure normalised with $p'_o(1+e_o)$ for footings of different diameter having equal embedment ratio

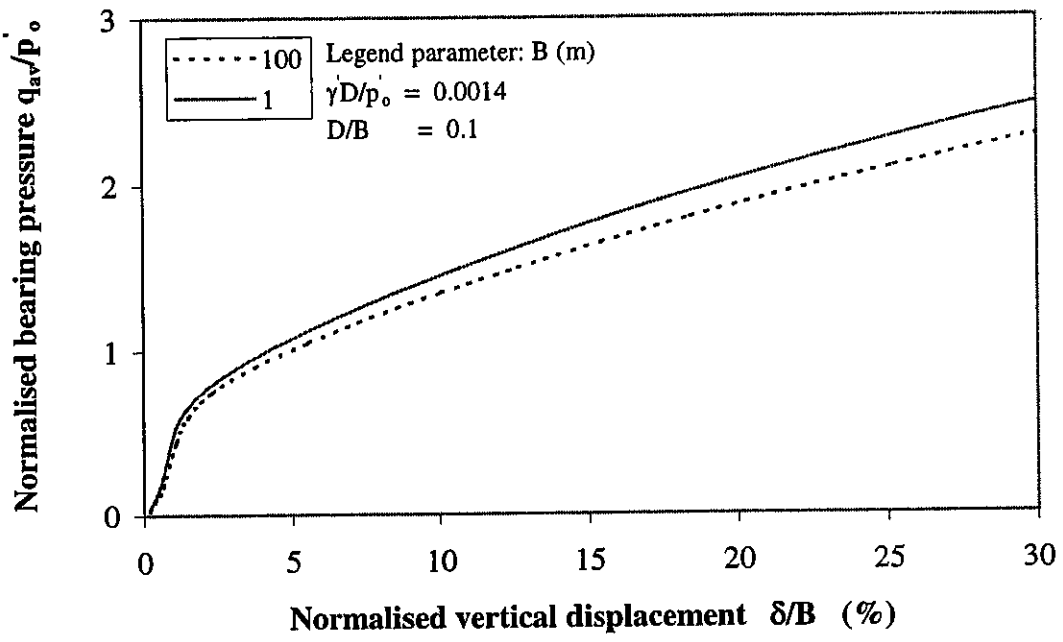

Figure 6.17 Normalised bearing pressure for footings of different diameter with relatively small $\frac{\gamma' D}{p_o'}$

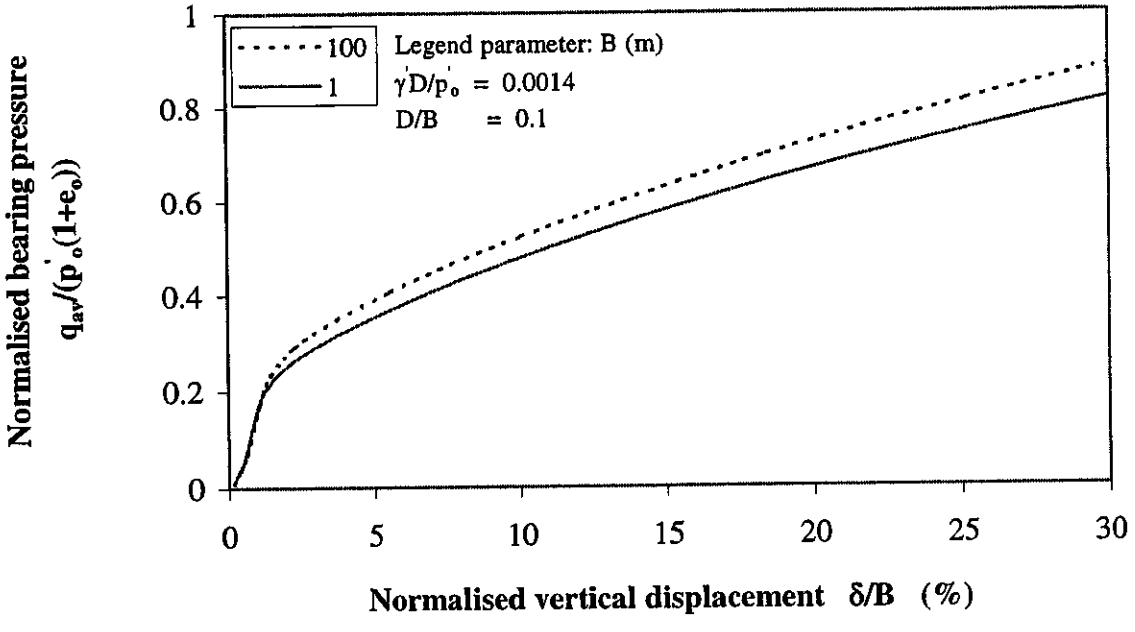

Figure 6.18 Bearing pressure normalised with $p_o'(1+e_o)$ for footings of different diameter with relatively small $\frac{\gamma' D}{p_o'}$

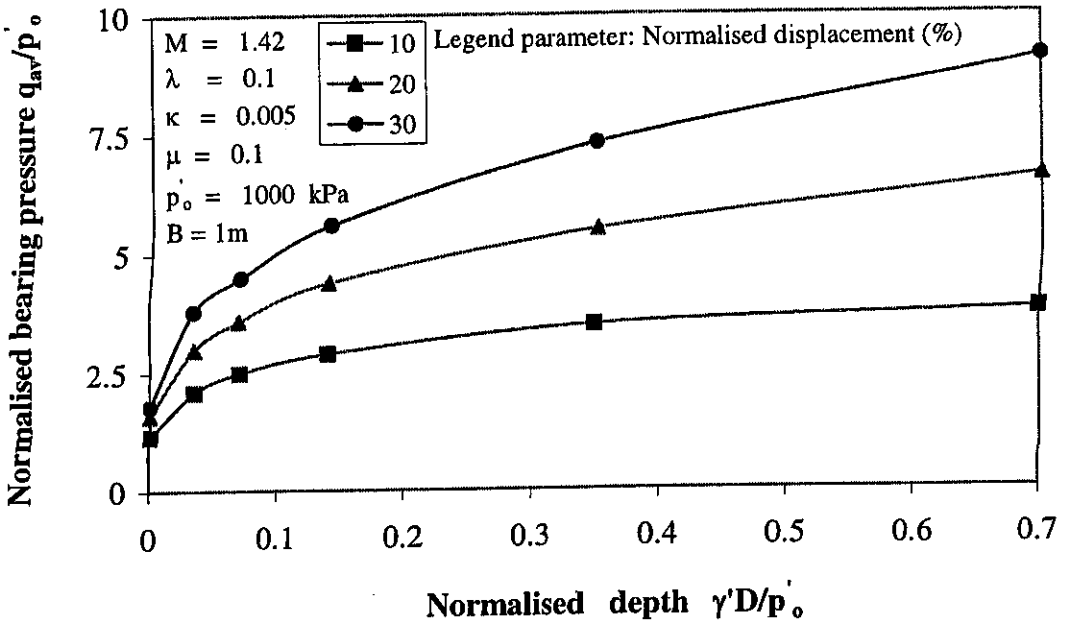

Figure 6.19 Increase in mobilised bearing pressure with normalised depth $\frac{\gamma' D}{p'_o}$

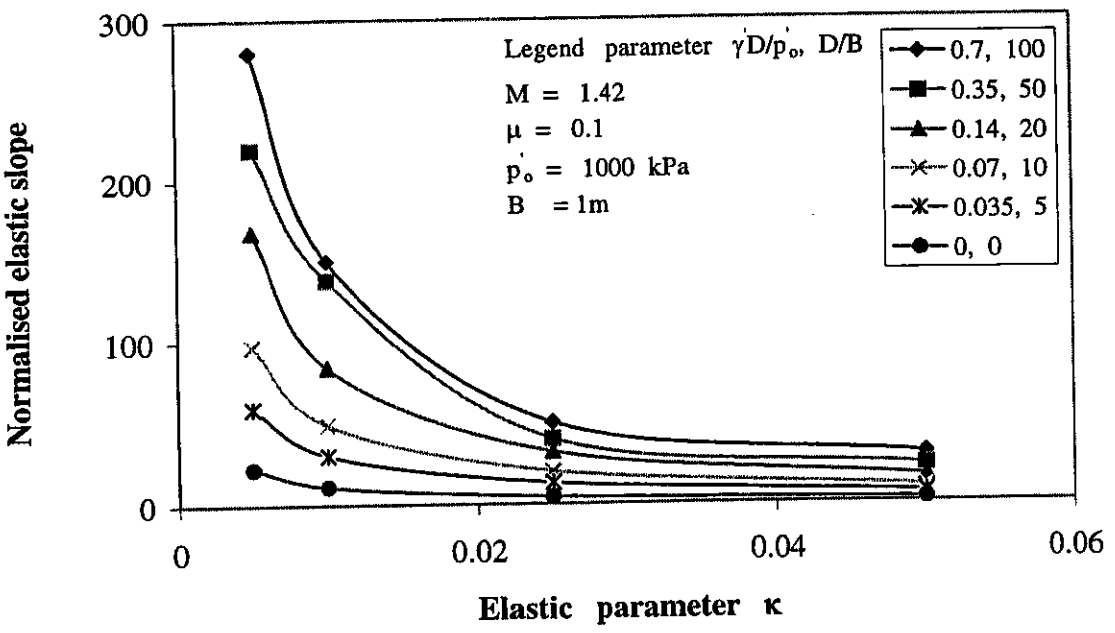

Figure 6.20 Variation of normalised elastic slope with elastic parameter κ

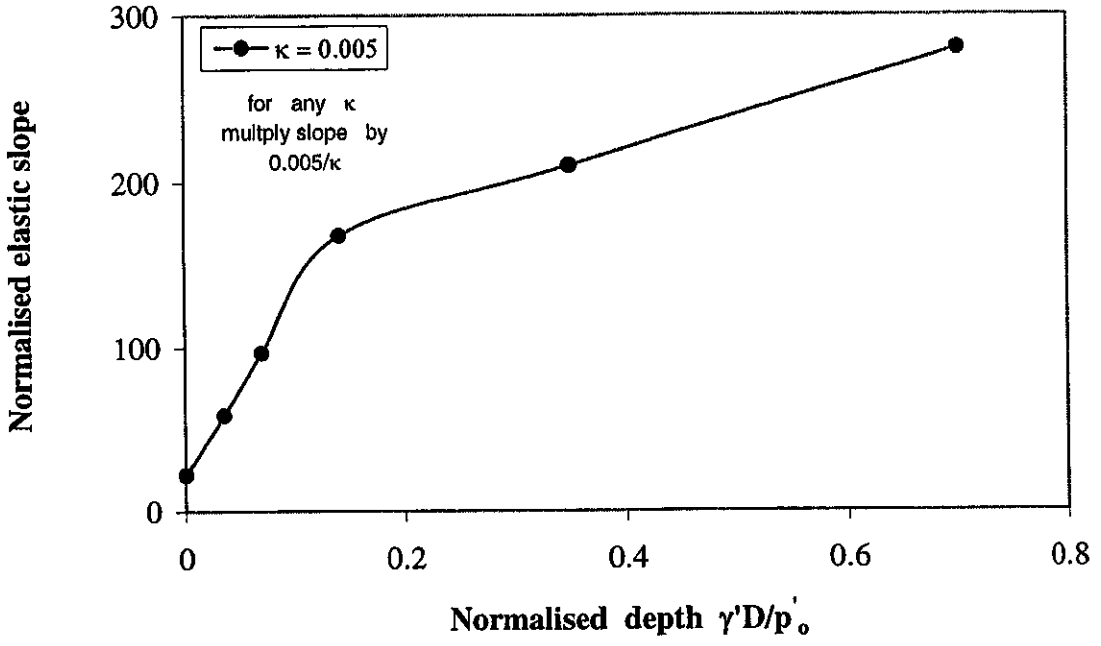

Figure 6.21 Variation of normalised elastic slope with normalised depth $\frac{\gamma' D}{p'_o}$

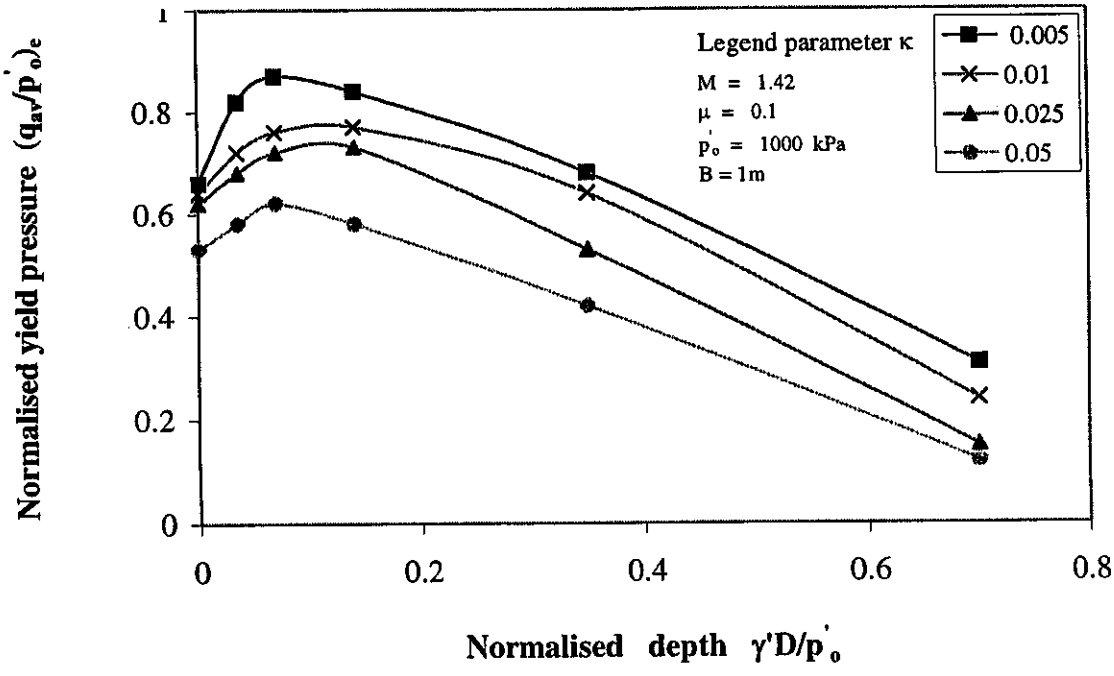

Figure 6.22 Variation of normalised yield pressure with elastic parameter κ and normalised depth $\frac{\gamma' D}{p'_o}$

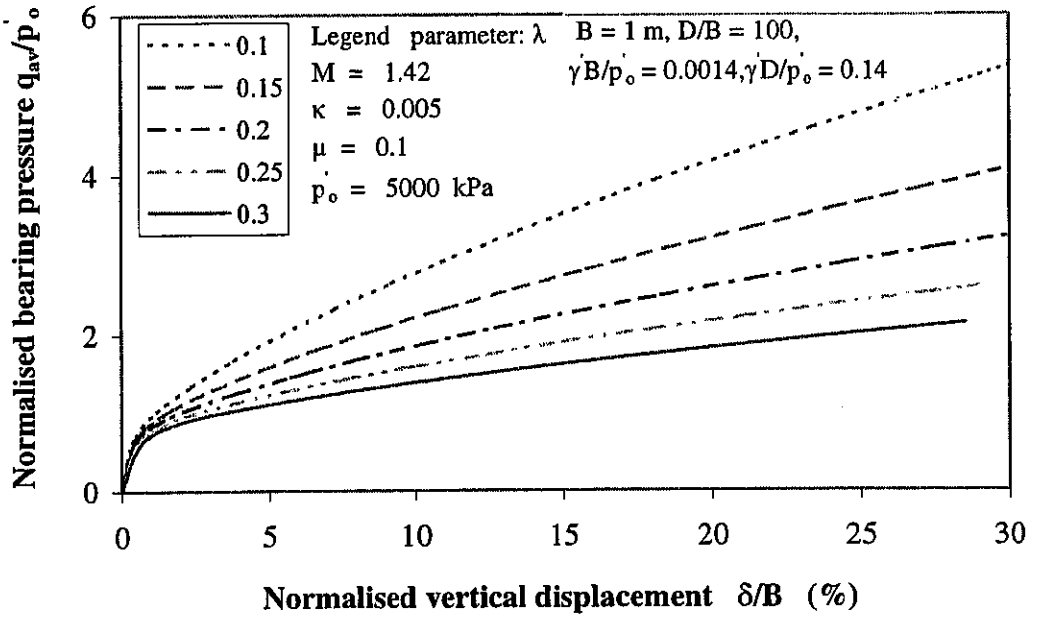

Figure 6.23 Effect of plastic compressibility on normalisedbearing pressure curve

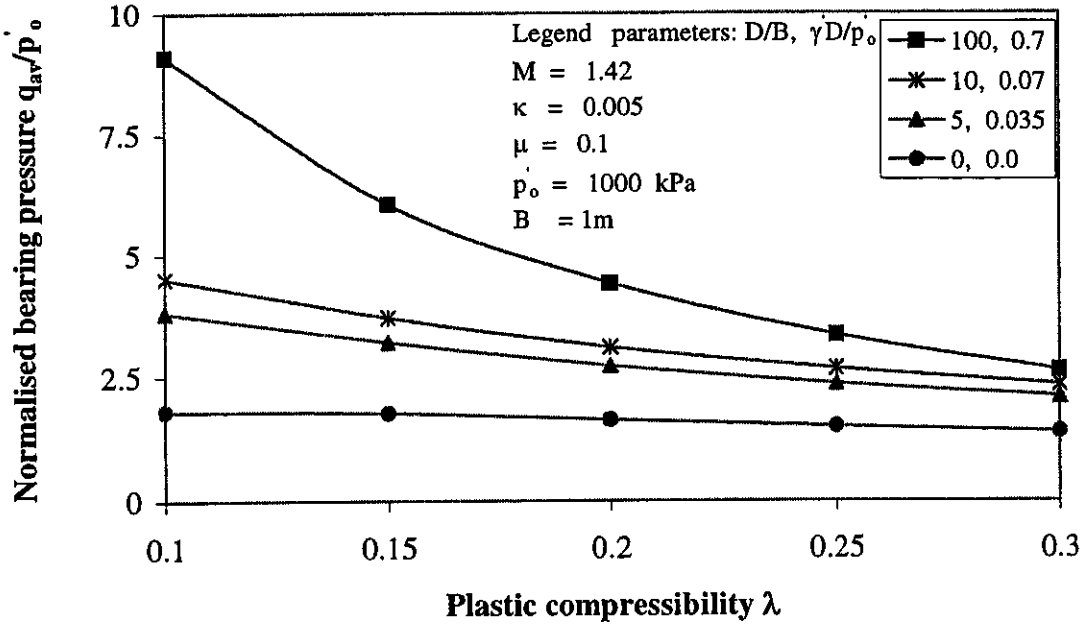

Figure 6.24 Effect of plastic compressibility on normalised bearing pressure mobilised at 30% normalised displacement

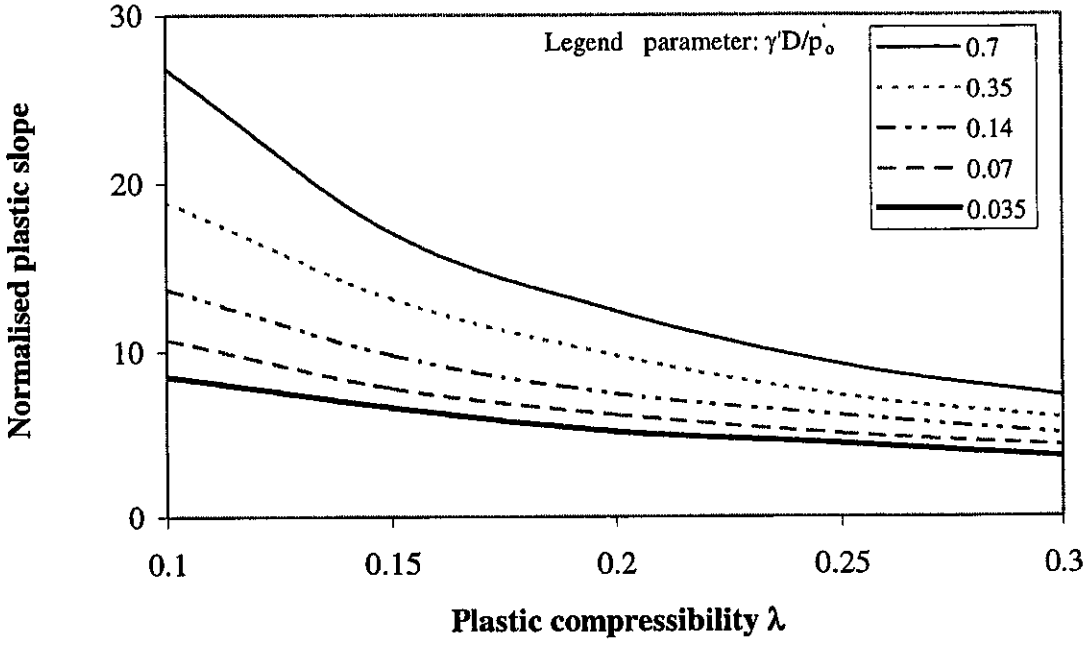

Figure 6.25 Change of normalised plastic slope with λ and $\frac{\gamma' D}{p'_o}$

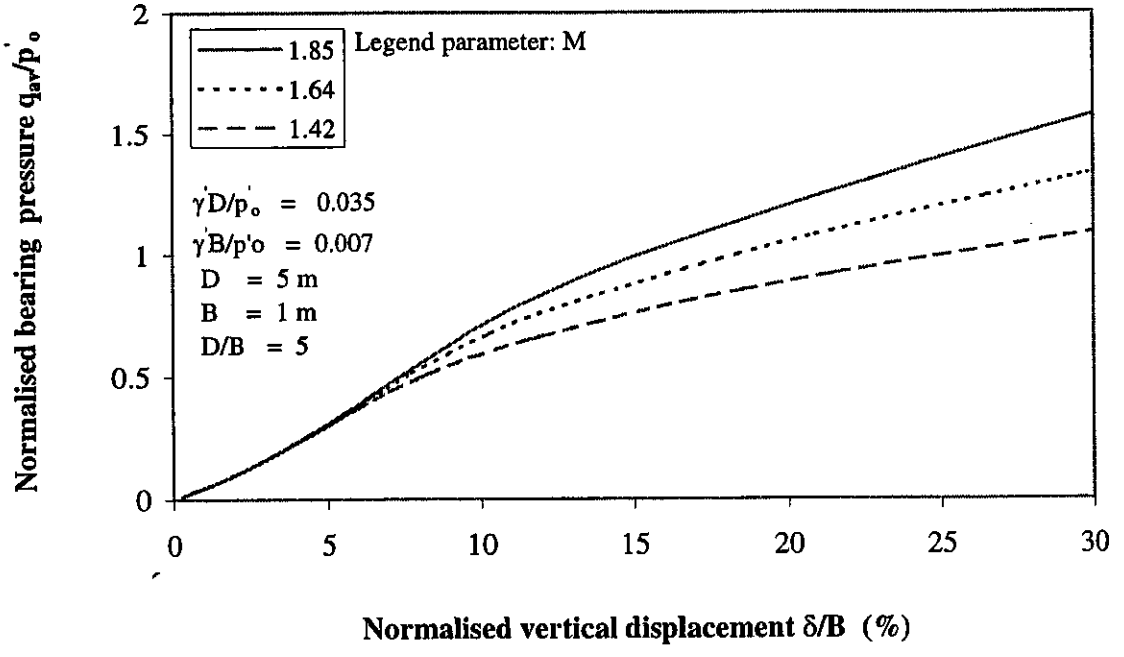

Figure 6.26 Effect of friction angle on bearing pressure curve for relatively small $\frac{\gamma' D}{p'_o}$

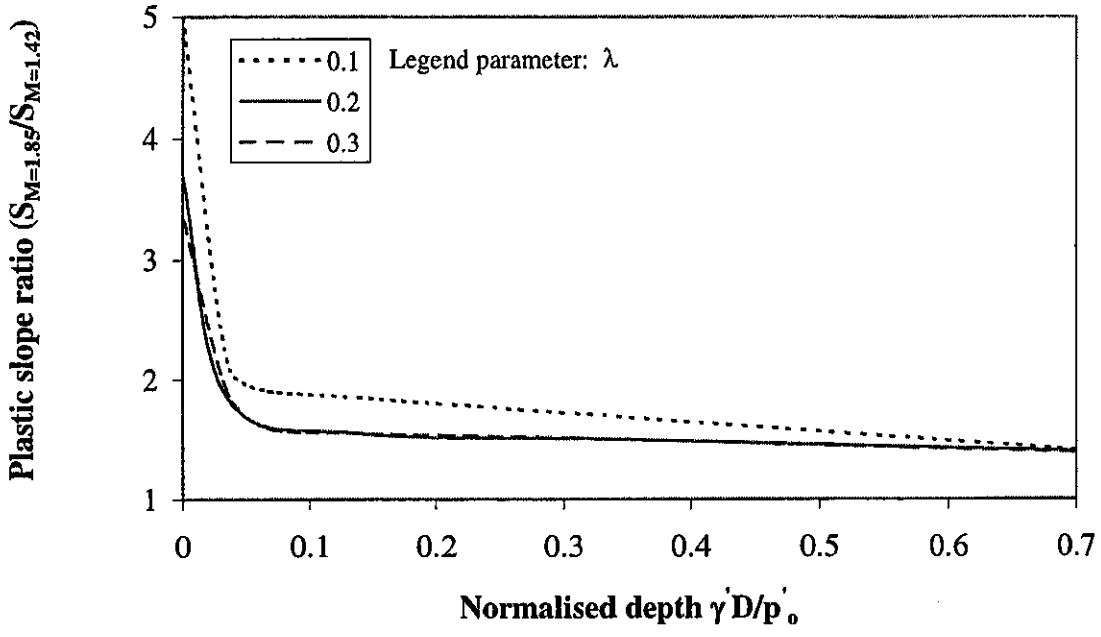

Figure 6.27 Change of plastic slope ratio with normalised depth $\frac{\gamma' D}{p'_o}$

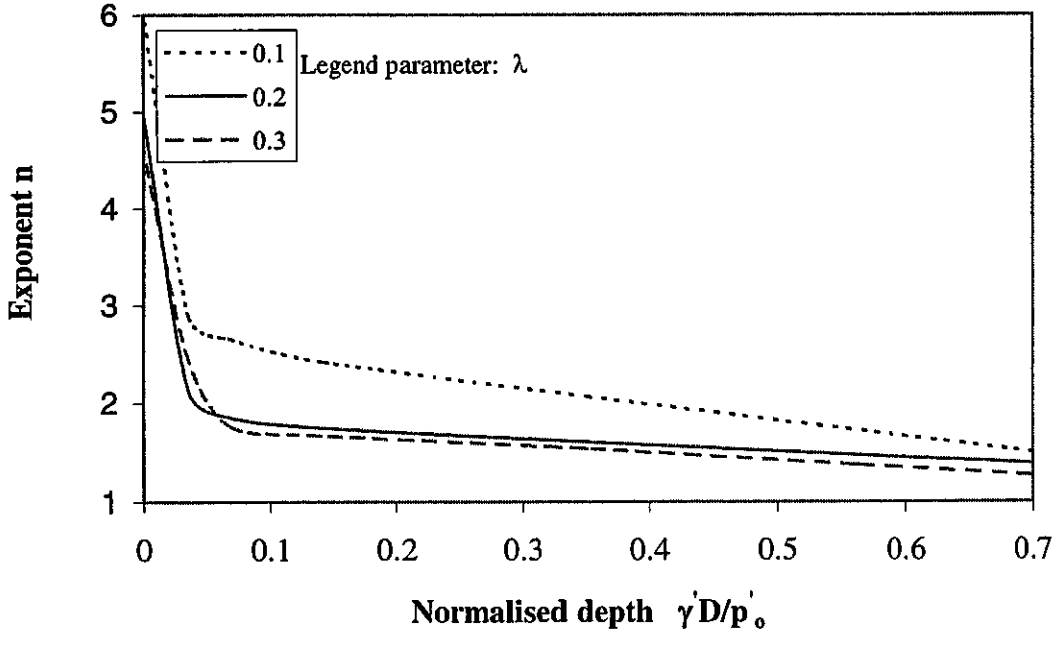

Figure 6.28 Exponent *n* as a function of normalised depth $\frac{\gamma' D}{p'_o}$

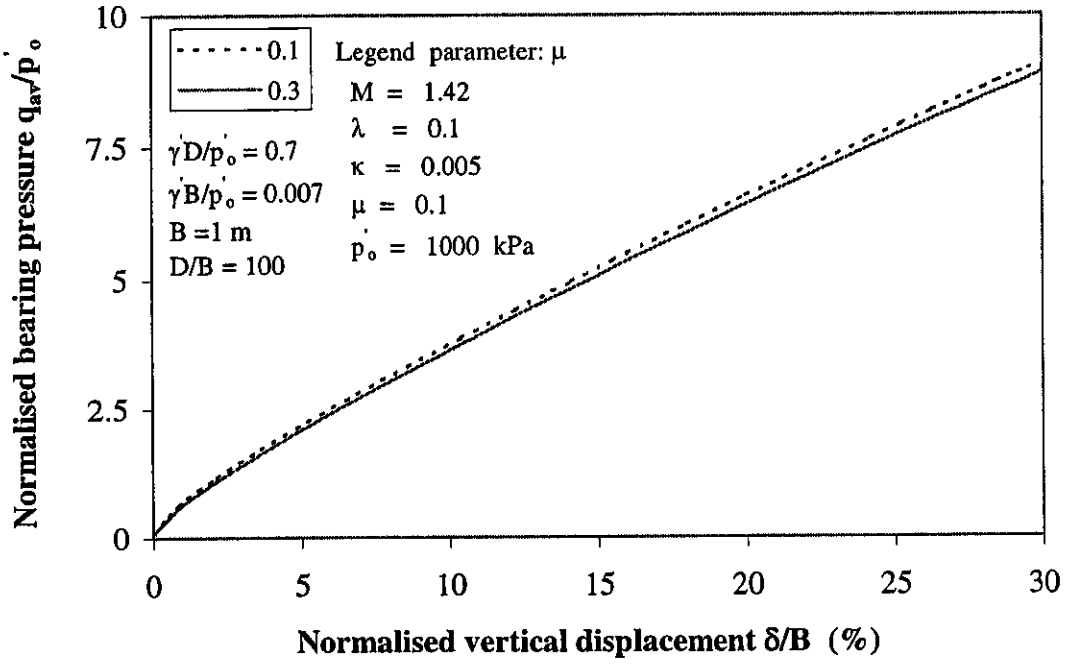

Figure 6.29 Effect of Poisson's ratio on bearing pressure for relatively large $\frac{\gamma' D}{p'_o}$

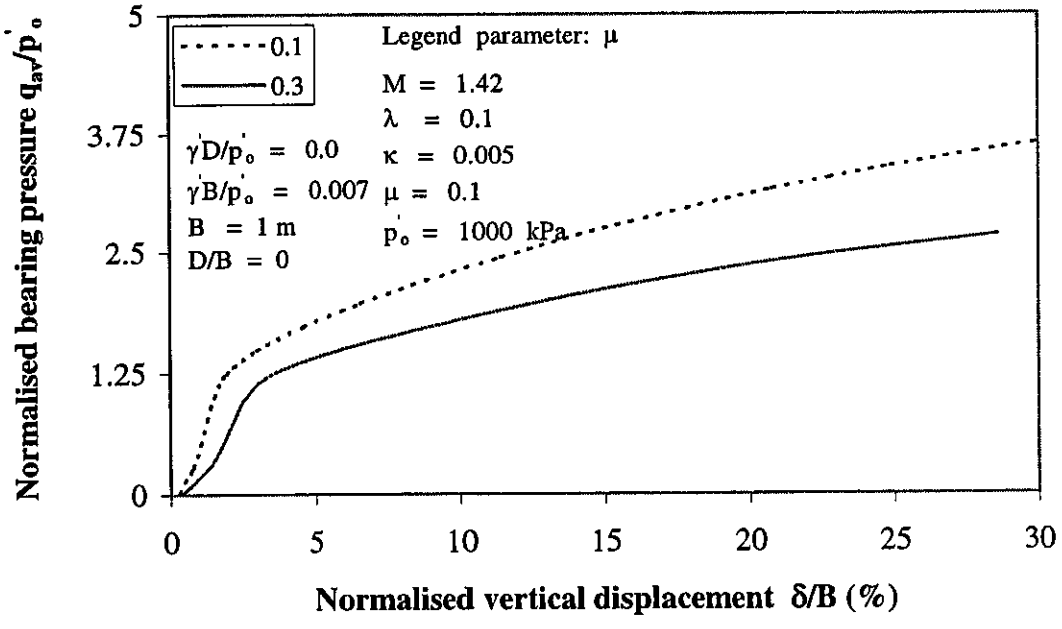

Figure 6.30 Effect of Poisson's ratio on bearing pressure for relatively small $\frac{\gamma' D}{p'_o}$

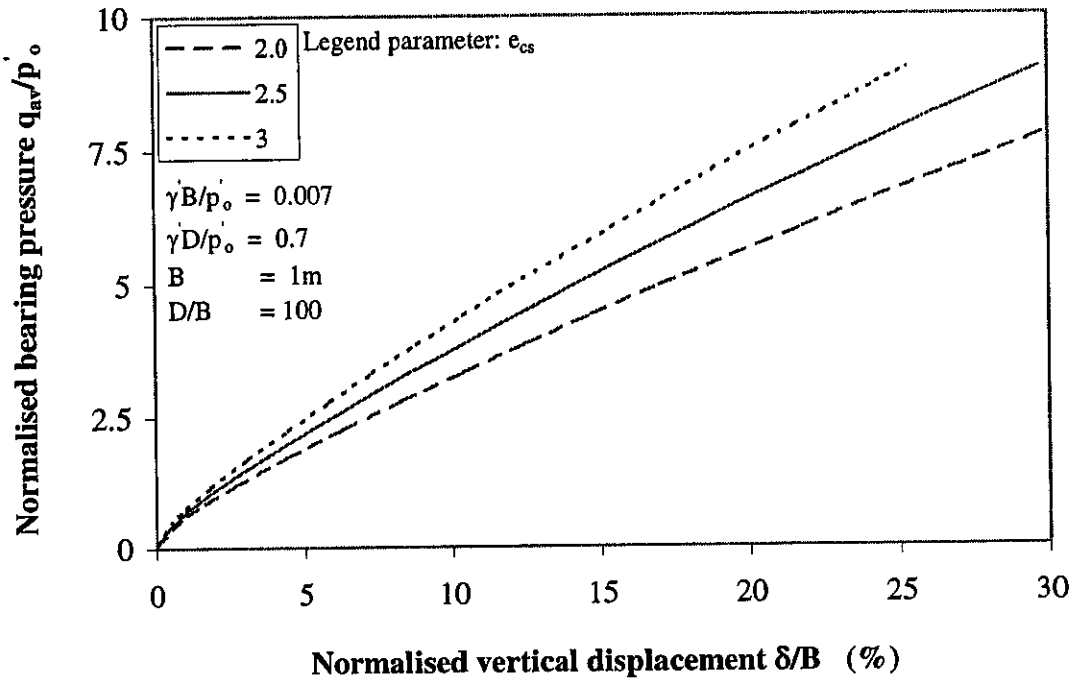

Figure 6.31 Effect of void ratio constant e_{cs} on bearing pressure curve

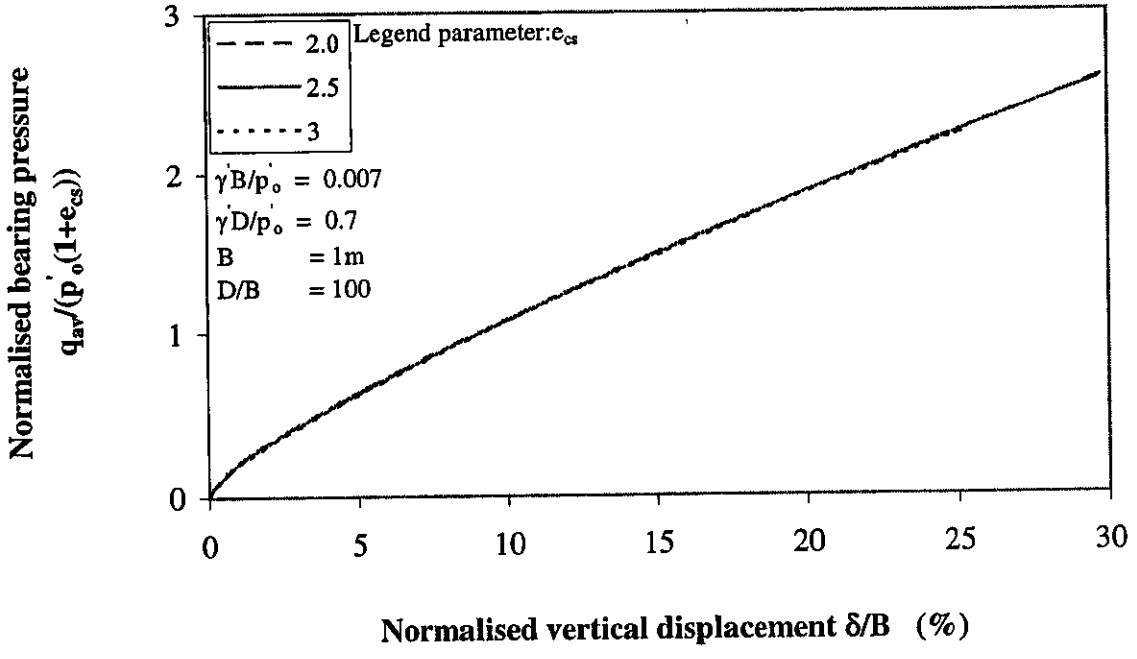

Figure 6.32 Normalisation of bearing pressure curve with $p'_o(1+e_{cs})$

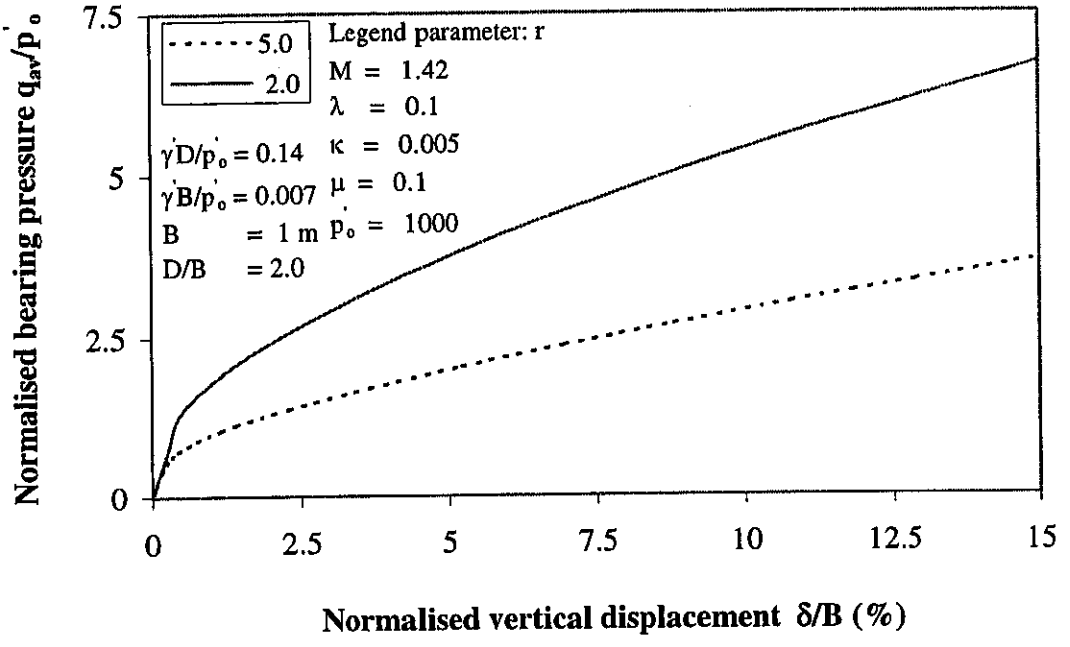

Figure 6.33 Effect of spacing ratio on bearing pressure curve

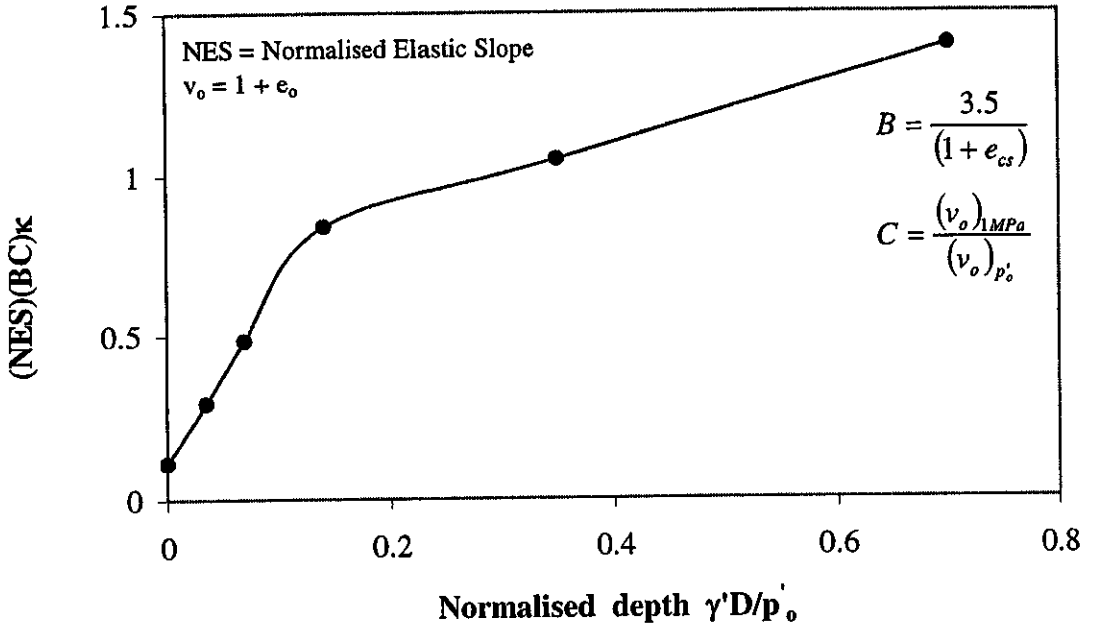

Figure 6.34 Design chart to determine the elastic slope of footing response

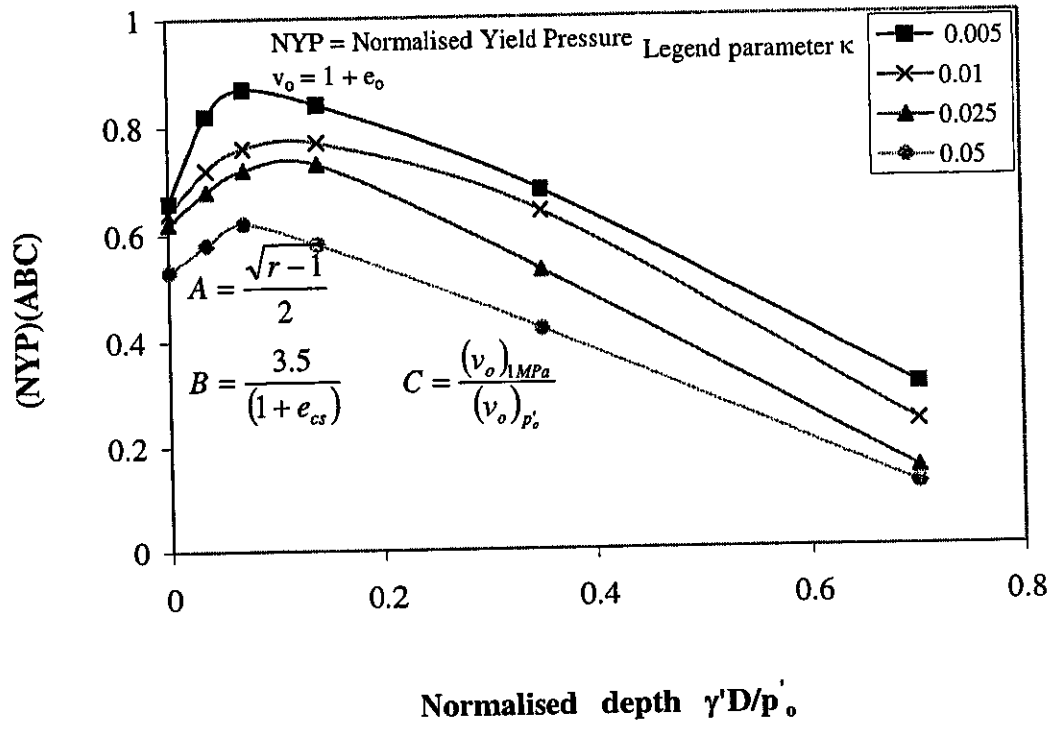

Figure 6.35 Design chart to determine yield pressure of footing response

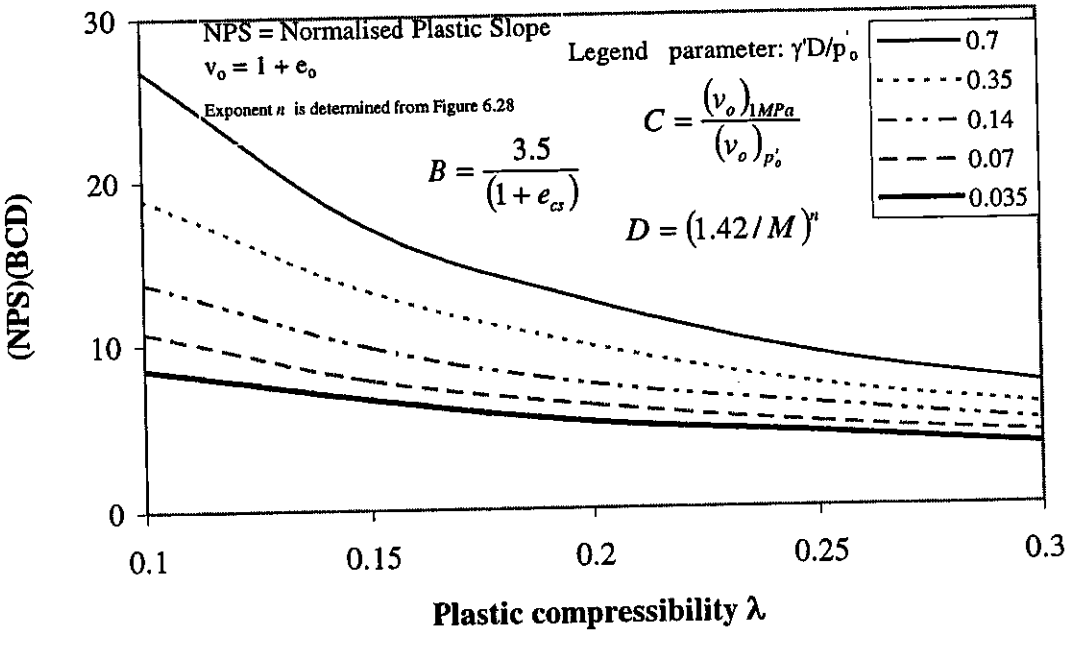

Figure 6.36 Design chart to determine plastic part of footing response

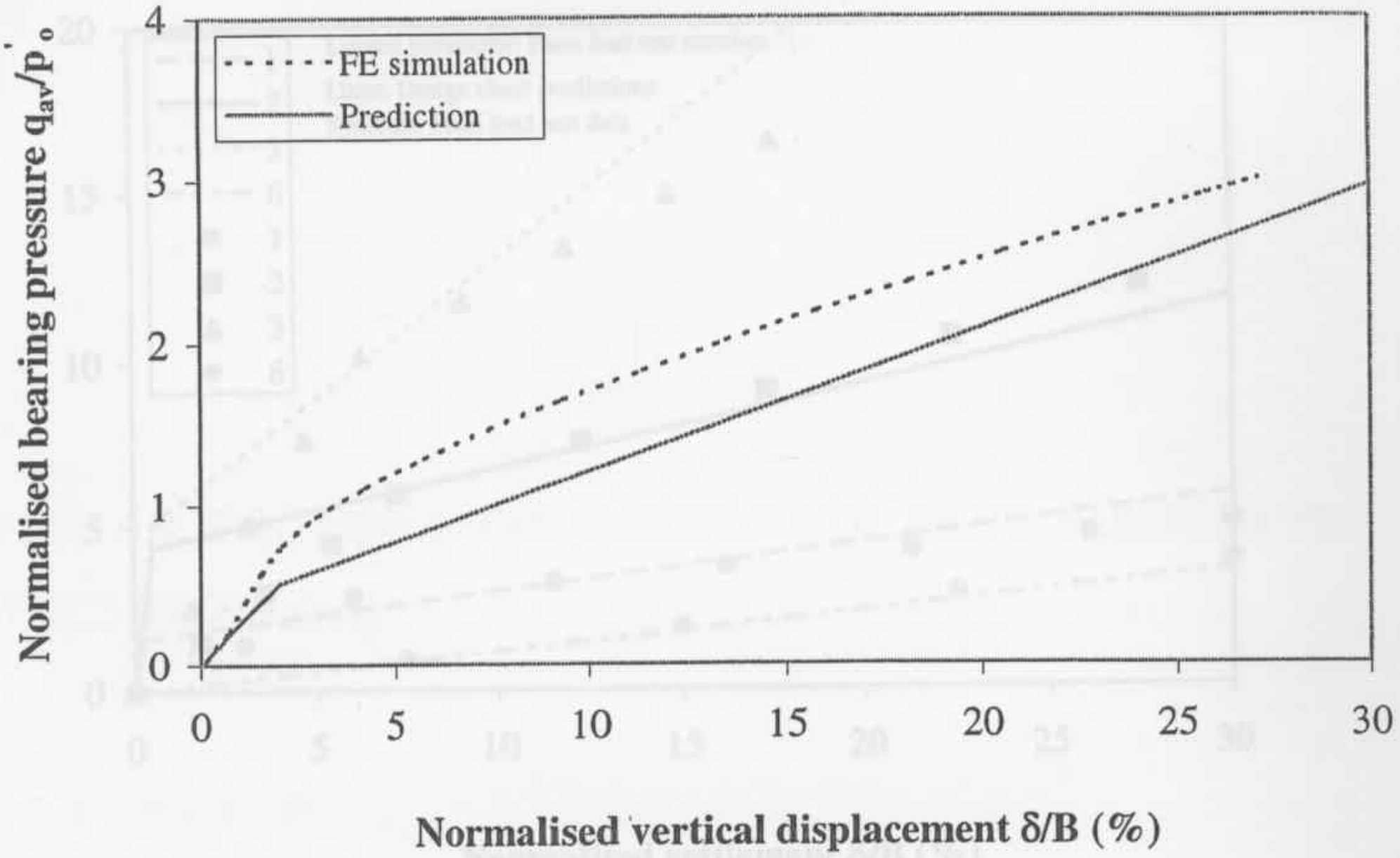

Figure 6.37 FE simulation and corresponding prediction using design chart

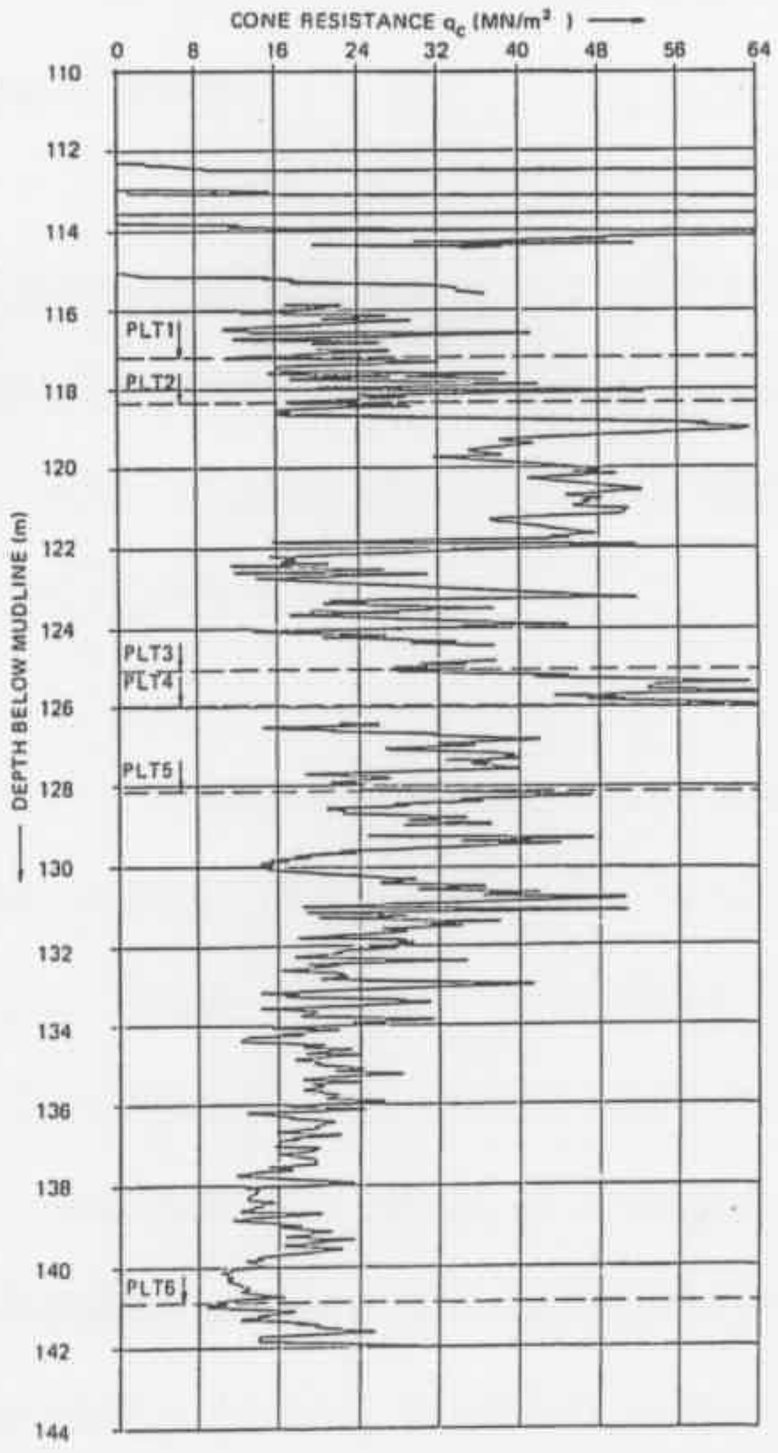

Figure 6.38 CPT profile of PLT site at North Rankin (Sharp and Seters, 1988)

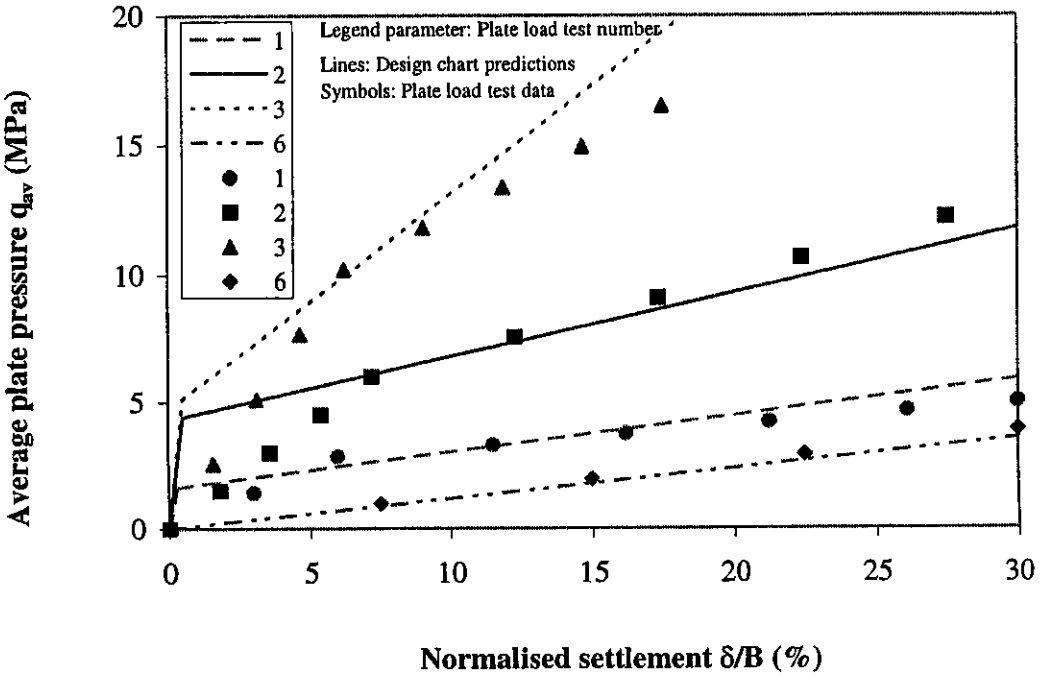

Figure 6.39 Prediction of plate load test data using proposed design charts

7

CIRCULAR FOOTINGS ON CARBONATE SAND SUBJECTED TO INCLINED LOAD

7.1 INTRODUCTION

Foundations of offshore structures are subjected to combined vertical, horizontal and moment loading due to environmental load effects on the superstructure. In order to predict the behaviour of offshore structures subjected to combined loading, it is necessary to develop analytical and numerical methods to predict the response of individual foundations to such loads.

Pan (1999) carried out experimental studies of a model-scale circular footing resting on carbonate sand subjected to inclined load at zero eccentricity. The experimental data and its comparison with results of empirical and plasticity based bearing capacity theory are presented in this chapter.

Taiebat (1999) developed a semi-analytical three-dimensional finite element procedure for elasto-plastic solids. The SU2 model was implemented in this semi-analytical three-dimensional finite element procedure, which was then used to simulate the behaviour of the experimental model-scale footing. A limited parametric study was carried out to investigate the effect of selected SU2 model parameters on the bearing pressure mobilised by surface circular footings subjected to inclined load. Finally, a simplified elasto-plastic footing model is proposed. The model was used to predict the bearing pressure mobilised by circular footings under inclined load. The

predictions of the footing model were compared with the results of the more sophisticated finite element analysis.

7.2 MODEL-SCALE FOOTING TEST

Pan (1999) carried out experimental studies of a model-scale footing on carbonate sand subjected to inclined load at zero eccentricity. The experiments and the results obtained are briefly described in this section.

The model steel footing was 25mm in diameter and 20mm in thickness. The footing was placed on the top of a cylindrical specimen of carbonate sand. The sand cylinder was 250mm in diameter and 175mm in thickness. The carbonate sand was subjected to a uniform isotropic pressure of 50 kPa. Vertical and horizontal loads at zero eccentricity were gradually applied on the footing.

The change of traction with load inclination was measured. Traction is defined here as the total load applied to the model footing divided by its plan area. The results obtained for artificially cemented and uncemented carbonate sands are presented below in Tables 7.1 and 7.2.

Table 7.1 Experimental data for footing on artificially cemented carbonate sand

Inclination (degrees)	$(q_{av})_{10\%}$ (MPa)	$(q_{av})_{20\%}$ (MPa)	$(q_{av})_{30\%}$ (MPa)	$\left(\frac{q_{av}}{q_o}\right)_{10\%}$	$\left(\frac{q_{av}}{q_o}\right)_{20\%}$	$\left(\frac{q_{av}}{q_o}\right)_{30\%}$
0	6.33	8.28	9.49	1.0	1.0	1.0
10	6.17	NA*	NA*	0.97	NA*	NA*
20	4.26	6.58	7.81	0.67	0.79	0.82
30	3.25	5.20	6.38	0.52	0.63	0.67

*NA implies not available

Table 7.2 Experimental data for footing on uncemented carbonate sand

Inclination (degrees)	$(q_{av})_{10\%}$ (MPa)	$(q_{av})_{20\%}$ (MPa)	$(q_{av})_{30\%}$ (MPa)	$\left(\frac{q_{av}}{q_o}\right)_{10\%}$	$\left(\frac{q_{av}}{q_o}\right)_{20\%}$	$\left(\frac{q_{av}}{q_o}\right)_{30\%}$
0	4.15	5.88	7.15	1.0	1.0	1.0
10	2.59	4.23	5.44	0.62	0.72	0.76
20	1.91	3.13	3.92	0.46	0.53	0.55
30	0.82	1.33	2.02	0.19	0.23	0.28

In Tables 7.1 and 7.2, q_{av} is the traction mobilised at displacements of 10%, 20% and 30% of the footing diameter, under inclined load. q_o is the bearing pressure under purely vertical load, mobilised at 10%, 20% and 30% vertical displacement relative to the footing diameter.

The experimental data for model-scale footings resting on uncemented and artificially cemented carbonate sand subjected to inclined load have been presented in tabular form. The subsequent sections compare this data with predictions obtained using classical, plasticity and semi-analytical 3D finite element analysis.

7.3 FOOTINGS UNDER INCLINED LOAD

Analyses of shallow foundations subjected to combined loading have been formulated using approximate and empirical methods by Meyerhoff (1953, 1963), Hanna and Meyerhoff (1981) and Hansen (1970). Their formulations are presented in this section. The inclined bearing capacity of model-scale circular footings resting on carbonate sand was computed using these methods. The computed results were then compared with the experimental data presented in the previous section.

7.3.1 CLASSICAL ANALYSIS

The bearing capacity q_{av} of a shallow footing of any shape resting on a rigid perfectly plastic solid subjected to inclined load is usually described by the following equation:

$$q_{av} = cN_c\zeta_c\zeta_{ci} + \sigma'_v N_c N_q \zeta_q \zeta_{qi} + \frac{1}{2}\gamma' B N_\gamma \zeta_\gamma \zeta_{\gamma i} \tag{7.1}$$

In equation (7.1), c is the cohesion, σ'_v is the effective surcharge pressure, B is the footing width and γ' is the effective unit weight of the soil. N_c, N_q, N_γ are the usual bearing capacity factors, ζ_c, ζ_q, ζ_γ are correction factors for foundation shape and ζ_{ci}, ζ_{qi}, $\zeta_{\gamma i}$ are correction factor for load inclination. Hansen (1970) and Meyerhoff (1953, 1963) proposed empirical expressions for the inclination and shape factors. The shape and load inclination factors relevant for a circular footing are given below in Tables 7.3 and 7.4.

Table 7.3 Shape factors for circular footing

Method	ζ_c	ζ_q	ζ_γ
Hansen (1970)	$1+\frac{N_q}{N_c}$	$1+\tan\phi$	0.60
Meyerhoff (1963)	$1+0.2N_\phi$	$1+0.1N_\phi$, $(\phi > 10^o)$	$1+0.1N_\phi$, $(\phi > 10^o)$

$N_\phi = \tan^2\left(\frac{\pi}{4}+\frac{\phi}{2}\right)$

Table 7.4 Inclination factors

Method	ζ_{ci}	ζ_{qi}	$\zeta_{\gamma i}$
Hansen (1970)	$\zeta_{qi} - \dfrac{1-\zeta_{qi}}{N_c \tan\phi}$	$\left[1 - \dfrac{H}{V + B'L'c\cot\phi}\right]^n$	$\left[1 - \dfrac{H}{V + B'L'c\cot\phi}\right]^{n+1}$
Meyerhoff (1963)	$\left(1-\theta/90^o\right)^2$	$\left(1-\theta/90^o\right)^2$	$\left(1-\theta/\phi\right)^2$

ϕ is the friction angle of the sand and θ is the angle of inclination (in degrees) of the applied load with respect to the vertical. V and H are the vertical and horizontal loads and B' and L' are the effective width and length of the footing allowing for eccentricity of loading. If inclination of the load is in the direction of the shorter side B of the foundation, then:

$$n = \frac{2 + B'/L'}{1 + B'/L'} \tag{7.2}$$

If inclination of the load is in the direction of the longer side L of the foundation, then:

$$n = \frac{2 + L'/B'}{1 + L'/B'} \tag{7.3}$$

For compressible soils, Terzaghi (1943) proposed a reduction of the cohesion c and friction angle ϕ to c^* and ϕ^* as follows:

$$c^* = 0.67c \tag{7.4}$$

$$\phi^* = \tan^{-1}(0.67\tan\phi) \tag{7.5}$$

Carbonate sand is highly compressible. The reduction factors proposed by Terzaghi (1943) and given by equation (7.4) and (7.5) were used to compute the reduced

cohesion and friction angle for carbonate sand. The original and reduced strength parameters computed for carbonate sand are given below in Table 7.5. Data for c and ϕ have been measured by Yeoh (1996) using the peak strength Mohr-Coulomb envelope for cemented carbonates and those of uncemented carbonates were measured using the Huang's (1994) triaxial test data at ultimate stress states.

Table 7.5 Original and reduced Mohr-Coulomb strength parameters

Carbonate sand	c (kPa)	ϕ (degrees)	c^* (kPa)	ϕ^* (degrees)
Cemented	400.0	23.0	266.7	15.8
Uncemented	0.0	39.0	0.0	28.4

Pan (1999) used a surcharge pressure of 50 kPa in his footing experiments. For a surcharge pressure of 50 kPa, the resultant bearing capacity of the model-scale footing was computed using equation (7.1) and the shape and inclination factors proposed by Hansen (1970) and Meyerhoff (1963). The computed bearing capacities were compared with the traction mobilised by the model-scale footing at a resultant displacement of 10% of the footing diameter. These comparisons are presented in Tables 7.6 and 7.7 below.

Table 7.6 Comparison of classical analysis with data for footing on artificially cemented carbonate sand

Inclination / Method	0° q_{av} (MPa)	10° q_{av} (MPa)	20° q_{av} (MPa)	30° q_{av} (MPa)	10° $\left(\frac{q_{av}}{q_o}\right)$	20° $\left(\frac{q_{av}}{q_o}\right)$	30° $\left(\frac{q_{av}}{q_o}\right)$
Hansen	4.51	3.40	2.53	1.85	0.75	0.56	0.41
Meyerhoff	4.42	3.54	2.84	2.27	0.80	0.64	0.51
Experiment	6.33	6.17	4.26	3.25	0.97	0.67	0.52

Table 7.7 Comparison of classical analysis with data for footing on uncemented carbonate sand

Inclination / Method	0° q_{av} (MPa)	10° q_{av} (MPa)	20° q_{av} (MPa)	30° q_{av} (MPa)	10° $\left(\frac{q_{av}}{q_o}\right)$	20° $\left(\frac{q_{av}}{q_o}\right)$	30° $\left(\frac{q_{av}}{q_o}\right)$
Hansen	1.27	0.96	0.68	0.40	0.76	0.54	0.32
Meyerhoff	1.09	0.86	0.68	0.54	0.79	0.62	0.49
Experiment	4.15	2.59	1.91	0.82	0.62	0.46	0.19

q_{av} is the resultant bearing capacity (traction) under inclined load and q_o is the bearing capacity (pressure) under purely vertical load. For the model-scale footing, the traction mobilised at 10% resultant displacement relative to the footing diameter was adopted as the nominal bearing capacity of the footing at various load inclinations.

It is observed that the conventional bearing capacity equations together with their modifications for shape and load inclination, as suggested by Hansen (1970), Meyerhoff (1963) and Terzaghi (1943), predict significantly lower bearing resistance for footings on uncemented and artificially cemented carbonate sand. Hansen's (1970) method predicts larger changes of the bearing resistance with load inclination for artificially cemented carbonate sand than are measured. The change in bearing resistance predicted by Meyerhoff's (1963) method for larger load inclinations appears to be quite close to that observed in the experiments for footings on artificially cemented carbonate sand. For footings on uncemented carbonate sand, the change in bearing resistance with load inclination predicted by both the Hansen and Meyerhoff methods appear to be significantly different from that actually observed in the footing experiments.

7.3.2 FOOTINGS UNDER INCLINED LOAD: PLASTICITY ANALYSIS

In recent times researchers such as Butterfield (1980) put forward the idea of analysing the foundation by means of the interaction domain between forces acting on it. Montrasio and Nova (1988) considered the interaction of the soil and foundation as a macroelement with an elasto-plastic strain-hardening law. This idea was extended by Nova and Montrasio (1991). Butterfield and Gottardi (1994), Gottardi and Butterfield (1993), and Georgiadis and Butterfield (1988) also used the new plasticity based approach to determine the bearing capacity of footings subjected to inclined load. Their proposed method is described in this section. The bearing capacity predicted by this approach is compared with the experimental data for model-scale footings.

A strip footing of width B subjected to an inclined load Q at zero eccentricity is considered. The resultant applied load Q, with inclination θ, is assumed to cause bearing capacity failure of the footing. Q is transformed into its statically equivalent components of vertical load V and horizontal load H. The interaction diagram for the failure locus of the footing is represented by a non-linear equation, expressed as follows:

$$F(V,H,V_M) = \frac{H}{mV_M} - \frac{V}{V_M}\left(1-\frac{V}{V_M}\right)^{\beta} = 0 \qquad (7.6)$$

Georgiadis and Butterfield (1988) proposed equation (7.6) for footings on silica sand. In equation (7.6), V_M is the bearing capacity under purely vertical load and m and β are parameters. The parameter β determines the position of the maximum horizontal load. For β = 1.0, the above equation is a parabola. In that case, H has a maximum value when $V = V_M/2$. m is the slope of the tangent to the interaction locus at the origin. It is a function of the soil-footing interface friction angle and is defined by the following equation:

$$H = mV \qquad (7.7)$$

Nova and Montrasio (1991) observed that for $\beta = 0.95$ or values slightly less than 1.0, the tangent to the loading function on the V-axis is vertical. This gives realistic predictions of vertical displacements only for footings subjected to pure vertical loading. A better fit of the failure locus with the experimental data is also obtained.

The reduction in the resultant bearing resistance for inclined loading of footings was computed using equation (7.6) for $\beta = 1.0$ and $\beta = 0.95$. In the absence of actual data, the soil-footing interface friction angle was assumed to be equal to the friction angle of the soil. The parameter m was thus computed directly from the friction angle ϕ of the carbonate sand. The bearing capacity for the model footing was defined as the traction mobilised at a resultant displacement equivalent to 10% of the footing diameter. The results obtained were compared with experimental data, which are presented below in Table 7.8.

Table 7.8 Comparison of plasticity analysis with test data

Inclination / Method	10° $\frac{q_{av}}{q_o}$	20° $\frac{q_{av}}{q_o}$	30° $\frac{q_{av}}{q_o}$
Georgiadis and Butterfield (1988)	0.79	0.59	0.33
Nova and Montrasio (1991)	0.78	0.56	0.31
Experimental data (Cemented sand)	0.97	0.67	0.52
Experimental data (Uncemented sand)	0.62	0.46	0.19

In Table 7.8, q_{av} is the traction or resultant bearing resistance under inclined load and q_o is the bearing capacity under vertical load.

It is observed that that the change in traction with load inclination predicted by the plasticity based approaches does not compare well with the experimental data for model-scale circular footings resting on uncemented and artificially cemented carbonate sand.

7.4 THREE-DIMENSIONAL SEMI-ANALYTICAL FINITE ELEMENT

In many practical problems, the applied loading is three-dimensional while the geometry is axisymmetric. This is especially true for a circular footing subjected to inclined load. In such cases, a semi-analytical finite element approach is useful and efficient. Lai and Booker (1991) and Runneson and Booker (1982, 1983) used the discrete Fourier series approach to analyse the non-linear behaviour of axisymmetric solids under true three-dimensional loading conditions. Taiebat (1999) extended this approach and developed a semi-analytical finite element procedure for a three-dimensional elasto-plastic solid. The computation time for such an analysis has been shown to be less than 5% of the computation time required for a full three-dimensional finite element analysis. The bearing response of the model-scale circular footings under inclined load was simulated using the SU2 model, which was implemented in the semi-analytical 3D FE procedure.

In this method, the field quantities are represented as discrete Fourier series. The axisymmetric body is divided into N identical wedges (Figure 7.1). The body then exhibits a polar periodicity with period N. The field quantities are written in terms of Fourier coefficients as:

$$\left(u_r,u_z,u_\theta,q,f\right)_j=\frac{1}{\sqrt{N}}\sum_{k=0}^{N-1}\left(U_r,U_z,U_\theta,Q,F\right)_k e^{ijk\alpha} \tag{7.8}$$

In the above equation $\left(u_r,u_z,u_\theta\right)_j$ denote the nodal displacements of wedge j, q_j are the excess pore pressures at nodes on wedge j and f_j are nodal forces applied to wedge j. $\left(U_r,U_z,U_\theta,Q,F\right)_k$ are the kth Fourier coefficients of nodal displacements, porewater pressures and external applied load. The inverse relations are defined by:

$$(U_r, U_z, U_\theta, Q, F)_K = \frac{1}{\sqrt{N}} \sum_{j=0}^{N-1} (u_r, u_z, u_\theta, q, f)_j e^{-ijk\alpha} \tag{7.9}$$

The details of the derivation are available in Taiebat (1999). The SU2 model was also implemented in the above semi-analytical three-dimensional finite element procedure. The SU2 model was then used to simulate the drained response of a circular model-scale footing resting on carbonate sand subjected to inclined load.

7.5 FINITE ELEMENT FORMULATION FOR MODEL-SCALE FOOTING

The experiments regarding the inclined loading of a model-scale circular footing have been described in section 7.2. The 3D FE simulation of those experiments is described in this section.

7.5.1 NUMERICAL MODEL

The circular model footing was simulated as a rigid elastic material. The elastic modulus of the footing was assumed to be several orders of magnitude higher than the underlying sand. It was assumed that the rigid footing, having a perfectly rough base, was resting at the top surface of a weightless cylindrical soil sample (Figure 7.1). The stress-strain behaviour of the soil was simulated using the SU2 model. The footing was loaded by a uniform traction applied incrementally at its surface. The vertical traction was applied at the top nodes of the footing element, while the lateral traction was applied to the nodes at the bottom. This ensured the gradual application of an inclined load on the footing centre at zero eccentricity, i.e., with no moment about the centre of the footing-soil interface.

The vertical boundary of the cylindrical soil sample was assumed to be perfectly smooth. However, it was constrained from moving in the lateral and circumferential directions. Except for the area in contact with the footing, the top boundary of the soil sample was subjected to uniform vertical surcharge of 50 kPa. The bottom

boundary was constrained from moving in the vertical, lateral and circumferential directions.

All analyses simulated fully drained conditions. An initial isotropic stress of 50 kPa was generated throughout the soil layer. This is consistent with the conditions applied in the experiments. Equivalent nodal forces were applied at the boundaries to maintain equilibrium. The finite element mesh constructed to simulate the 3D geometry of the problem is described in the next section.

7.5.2 FINITE ELEMENT MESH

The three dimensional geometry of the cylindrical soil-footing domain was generated using 12 identical cylindrical wedges (Figure. 7.1). Elements consisting of 20 node cubes (Figure. 7.2), with quadratic interpolation functions for displacements, were used to discretise each wedge. Figure 7.3 shows the angle of inclination of the applied load. Figure 7.4 represents a diametrical cross section through the cylindrical domain. A graded mesh was used with progressively coarser element size being constructed laterally away and vertically downward from the footing. 2x2x2 reduced Gaussian integration was used for all calculations

7.6 CALIBRATION OF SU2 MODEL IN 3D FINITE ELEMENT

The purpose of this section is to validate the results obtained using the SU2 implementation of the 3D finite element procedure with those of corresponding 2D finite element analyses. Once the SU2 implementation in 3D finite element has been validated, it may then be used to predict the response of model-scale footings under inclined load.

Single element SU2 model simulations of triaxial tests were generated using the 3D semi-analytical finite element program. The predictions were compared with the corresponding simulations of 2D finite element analysis. Figures 7.5 and 7.6 show close agreement between the results obtained using the two methods. The 2D and 3D

finite element programs were used to generate the SU2 model simulations of the pressure-displacement curve for a circular footing subjected to vertical load. Figure 7.7 shows that the pressure-displacement curves are nearly identical. This indicates that the SU2 model implementation is working properly in the 3D finite element program.

Even a semi-analytical 3D finite element program incorporating a highly non-linear constitutive model is computation intensive. From practical considerations, it is important to use a minimum number of load increments consistent with an accurate solution. To determine the optimum number of load increments, a boundary value problem simulating the model-scale footing was solved. The number of increments to reach a relative displacement of 30% was varied. Figure 7.8 shows that sufficient accuracy is achieved using 3,000 steps. The initial stiffness method was used in all cases.

Numerical instability was often observed when using the SU2 model in the 3D program to generate the response of the model-scale footing subjected to inclined load. Pressure-dependent non-linear elasticity is normally assumed in the SU2 model. In order to reduce some numerical instability, the SU2 model was modified so that constant linear elasticity was incorporated in the model. The behaviour of the model-scale footings resting on overconsolidated carbonate sand was thus simulated using the SU2 model modified for constant linear elasticity. When using pressure-dependent elasticity under inclined load, elements in front of the footing developed significantly higher pressures and elastic moduli, while elements behind the footing developed lower pressures and consequently lower elastic moduli. When the initial stiffness approach is employed, it is likely that such widely varying responses may result in problems in stress correction and solution stability. It is however possible, that increasing significantly the number of increments may resolve the problem. However, this may result in unacceptably long computation time to solve a boundary value problem. The numerical simulation of the bearing response of the model-scale footing is described in the following section. It is hypothesized at this point, that the relative change of the mobilised bearing pressure with load inclination (which is the main focus of this chapter) would not be significantly affected whether constant or pressure dependent elasticity is assumed in the SU2 model.

7.7 MODEL VALIDATION FOR INCLINED LOADING

In this section, 3D finite element simulations of the model-scale circular footing are compared with the experimental data. The comparisons show the strengths and weaknesses of the SU2 model in predicting the response of footings subjected to inclined load.

The values of the SU2 model parameters for the uncemented and artificially cemented carbonate sand were chosen in the following way. The values assumed for friction angle ϕ', plastic compressibility λ, Poisson's ratio ν, spacing ratio r and coefficient of consolidation K_o were those generally observed for North Rankin carbonate sand. The values of elastic shear modulus were chosen by best fitting the overall pressure-displacement curve of the experimental model footing subjected to vertical load. A consolidation pressure of 3 MPa was applied by Pan (1999) to the uncemented sand to reach the desired density. Assuming a preconsolidation pressure of 3 MPa provided a good fit with the pressure-displacement curve of the experimental footing resting on uncemented sand subjected to vertical load. A preconsolidation pressure of 3.5 MPa was assumed for the cemented sand, as this fits the experimental pressure-displacement curve of the footing resting on cemented sand and subjected to vertical load. The values of the SU2 model parameters used to simulate the behaviour of cemented and uncemented carbonate sand below the model-scale footing are given below in Tables 7.9 and 7.10.

Table 7.9 SU2 model parameters for artificially cemented carbonate sand

ϕ' (deg)	G (MPa)	λ	ν	e_{cs}	p_o' (MPa)	r	γ' (kN/m^3)	K_o	B (mm)
39	75.0	0.213	0.2	2.28	3.5	5.0	7.0	0.5	25.0

Table 7.10 SU2 model parameters for uncemented carbonate sand

ϕ' (deg)	G (MPa)	λ	ν	e_{cs}	p'_o (MPa)	r	γ' (kN/m^3)	K_o	B (mm)
39	37.5	0.213	0.2	2.28	3.0	5.0	7.0	0.5	25.0

Figures 7.9 and 7.10 show comparisons of the finite element predictions of the response of the model-scale footing with experimental data. It is observed that the SU2 model cannot predict satisfactorily the change in traction with load inclination for footings on cemented carbonate sand, particularly at small strains. The predictions of the change in traction with load inclination for the model-scale footing resting on uncemented sand is even poorer. Figures 7.11 and 7.12 show the mobilised traction normalised by a reference pressure to make it dimensionless. The normalising pressure used in this case is the bearing resistance mobilised at a displacement of 30% of the footing diameter under vertical load. The change in traction with load inclination predicted by the SU2 model appears to be in good agreement with the experimental data for cemented carbonate sand. The agreement with the data for uncemented carbonate sand is not entirely satisfactory.

The SU2 model predictions of the traction q_{av} mobilised at 10% resultant displacement and its change with load inclination are compared with the experimental data for the model-scale footing resting on uncemented and artificially cemented carbonate sand. The comparisons are given in Table 7.11 below.

Table 7.11 Comparison of SU2 model predictions with test data

Inclination / Method	0° q_o (MPa)	10° $(q_{av})_{10\%}$ (MPa)	20° $(q_{av})_{20\%}$ (MPa)	30° $(q_{av})_{30\%}$ (MPa)	10° $\left(\frac{q_{av}}{q_o}\right)_{10\%}$	20° $\left(\frac{q_{av}}{q_o}\right)_{10\%}$	30° $\left(\frac{q_{av}}{q_o}\right)_{10\%}$
3D FE, SU2 Cemented	5.72	5.49	4.75	3.77	0.96	0.83	0.66
Test data Cemented	6.33	6.17	4.26	3.25	0.97	0.67	0.52
3D FE, SU2 Uncemented	4.25	4.10	3.60	2.91	0.96	0.85	0.69
Test Data Uncemented	4.15	2.59	1.91	0.82	0.62	0.46	0.19

It is observed that satisfactory predictions of the pressure-displacement response of circular footings subjected to inclined load are obtained using the SU2 model, for footings on artificially cemented sand. However the predictions of the inclined load response for footings on uncemented sand, are not entirely satisfactory. For footings on uncemented sand subjected to inclined load, the mean pressures in the soil at the back of the footing (opposite to the direction of horizontal footing displacement) decrease rapidly to or near to zero. The soil in this region undergoes a kind of tensile failure, and does not contribute to footing bearing capacity. The SU2 model as used here does not take into account the tensile failure of the soil and the consequent loss of soil stiffness. This may be a possible reason for the unsatisfactory predictions of the SU2 model. Additionally, the soil-footing interface behaviour under inclined loading may be significantly different than that predicted by the SU2 model.

7.8 EFFECT OF LOAD INCLINATION ON SOIL DOMAIN

The 3D finite element predictions of the distribution of effective stress, displacement and plastic zones in the carbonate sand beneath the footing are now considered.

These distributions help to understand what happens in the soil immediately below and around the footing when it is subjected to inclined loads.

Figure 7.13 (a) shows the direction and plane of the applied load and some selected elements in this plane immediately beneath the footing. The elements in wedge 1 and 7 are intersected by the vertical plane of the applied load and located opposite to one another. The discrete wedges for the 3D footing problem are shown in plan view in Figure 7.13 (b). The applied load moves the footing towards the soil element 102 in wedge 1, which is located immediately ahead of the footing. This is expected to compress this element and increase its mean confining pressure. Simultaneously, the footing moves away from the corresponding element in wedge 7, which is element 214. Element 214 is located immediately behind the footing. This movement is expected to decrease the mean confining pressure in this element. Figures 7.14 and 7.15 plot the stress path of selected Gauss points in elements 102 and 214, respectively. An isotropic pressure of 50 kPa was applied on the soil cylinder before the beginning of load application. Thus Figures 7.14 and 7.15 show zero deviatoric stress, q, at an initial mean effective pressure p' of 50 kPa. As expected, the mean effective pressure in element 102 at any stage of loading is observed to be significantly larger than in element 214. The deviator stress mobilised at a particular Gauss point in element 102 is also observed to be significantly larger than that at the equivalent point in element 214. At theses Gauss points in elements 102 and 214, no significant differences in inclination of the stress path due to load inclination are observed. Other Gauss points in these elements show similar responses.

Figures 7.16 and 7.17 plot the stress path at a particular Gauss point in element 100 in wedge 1 and for the corresponding element and Gauss point in element 212 in wedge 7. Both the elements are located immediately beneath the footing. Figures 7.16 and 7.17 show a zero deviatoric stress at an initial mean pressure of 50 kPa. It is observed that the deviator at the Gauss points within these elements increase and the stress paths are steeper with load inclination. It is observed that larger the load inclination or shear stress applied to the footing, the greater is the deviatoric stresses mobilised within these elements.

Figure 7.18 shows that for a footing subjected to vertical load, the largest displacements occur in a small zone immediately beneath the footing. The displacements are aligned essentially in the vertically downward direction. Figure 7.19 shows that for a footing subjected to inclined load, the largest displacements are still concentrated in a small zone immediately beneath the footing. However, the displacements are aligned essentially in the direction of applied load in the plane of load application. The displacement vectors show some small outward movement of the soil immediately ahead of the footing at larger load inclinations. This is consistent with experimentally observed behaviour.

Figure 7.20 shows the plastic zone (the region bounded by a contour value of 1) below the footing at a displacement of 30% of the footing diameter. Figure 7.21 shows that when inclined load is applied, the plastic zone in the plane of load application is shifted in the direction of the applied load.

The effects in the soil domain predicted by SU2 model appear to be logical and consistent with intuitive reasoning, although the model overpredicts the initial stiffness when the footing is subjected to inclined load. The next section presents a limited parametric study of the effect of selected SU2 model parameters on the response of circular footings subjected to inclined load.

7.9 PARAMETRIC STUDY

A limited parametric study is now carried out using the SU2 model. The effect of selected SU2 model parameters on the pressure-displacement curve of a surface circular footing subjected to inclined load at zero eccentricity is investigated.

The problem considered is that of a surface circular footing 25m in diameter resting on carbonate sand. The effect of the following SU2 model parameters on the footing response was investigated: $\frac{\gamma' B}{p_o'}$, λ and M. γ' is the effective unit weight of the soil,

B is the footing diameter, p_o' is the preconsolidation pressure and M is the critical state ratio, a function of the ultimate friction angle of the soil.

7.9.1 EFFECT OF PARAMETER $\frac{\gamma' B}{p_o'}$

The effect of the parameter $\frac{\gamma' B}{p_o'}$ on the bearing pressure mobilised by surface circular footings under inclined load has been investigated in this section. The soil profiles assumed to exist below the circular footing are shown in detail in Figures 7.22 through 7.24. The profile of preconsolidation pressure assumed in this case is shown as case 1 in Figure 7.24. It was shown in Chapter 5 that for such a profile, $\frac{\gamma' B}{p_o'}$ represents a measure of the thickness of the cemented or overconsolidated layer immediately beneath the footing relative to the footing diameter. Figure 7.25 shows the position of the in-situ stresses at locations A and C below the footing with respect to the SU2 yield locus. While point A is normally consolidated, point C is overconsolidated, both being at K_o consolidated condition.

The SU2 model parameters chosen to simulate the footing response are presented below in Table 7.12.

Table 7.12 SU2 model parameters to investigate effect of parameter $\frac{\gamma' B}{p_o'}$

ϕ' (deg.)	G (MPa)	λ	ν	e_{cs}	p_o' (MPa)	r	γ' (kN/m^3)	K_o
40	20	0.20	0.1	2.5	Variable	5.0	7.0	0.5

A footing diameter of B = 25.0m was used in the finite element analysis. Figures 7.26 shows the traction-displacement curves for the 25m diameter surface circular footing subjected to inclined load and resting on overconsolidated carbonate sand

with $\frac{\gamma' B}{p_o'}$ of 0.175. The traction curves obtained appear to be qualitatively similar to those observed for the model-scale footing resting on artificially cemented carbonate sand.

The change in the traction mobilised at 10% resultant displacement, as predicted by finite element analysis for different values of the parameter $\frac{\gamma' B}{p_o'}$, is presented below in Table 7.13.

Table 7.13 Effect of $\frac{\gamma' B}{p_o'}$ on reduction of bearing pressure with load inclination

Inclination / $\frac{\gamma' B}{p_o'}$	10° $\left(\frac{q_{av}}{q_o}\right)_{10\%}$	20° $\left(\frac{q_{av}}{q_o}\right)_{10\%}$	30° $\left(\frac{q_{av}}{q_o}\right)_{10\%}$
0.175	0.98	0.90	0.78
0.7	0.98	0.95	0.89
2.8	0.98	0.92	0.86

In Table 7.13, q_{av} is the traction mobilised at 10% resultant displacement. q_o is the bearing pressure mobilised at 10% vertical displacement for a footing subjected to purely vertical load. It is observed that the change in traction with load inclination is larger at very small $\frac{\gamma' B}{p_o'}$.

The effect of the compound parameter $\frac{\gamma' B}{p_o'}$ on the change of traction with load inclination was investigated. It was observed that the change in traction with load inclination was larger for comparatively smaller $\frac{\gamma' B}{p_o'}$ (0.175). However, no consistent

pattern was observed of the change in traction with load inclination as a function of $\frac{\gamma' B}{p'_o}$.

7.9.2 EFFECT OF PLASTIC COMPRESSIBILITY, λ

The effect of plastic volume compressibility λ of the soil on the change in mobilised traction with load inclination is investigated. Normally consolidated carbonate sand was assumed to exist below the footing. The profile of preconsolidation pressure assumed to exist below the footing is shown as case 2 in Figure 7.24.

The SU2 model parameters chosen for the parametric study are presented in Table 7.14 below.

Table 7.14 SU2 model parameters to investigate the effect of plastic compressibility λ

ϕ' (deg.)	κ	λ	ν	e_{cs}	p'_o	r	γ' (kN/m^3)	K_o
40	Variable	Variable	0.1	2.5	NC	5.0	7.0	0.5

A footing diameter of B = 25.0m was used in the finite element analysis. NC in Table 7.14 implies normally consolidated carbonate sand. The parameter λ was varied in the numerical analysis. Figure 7.27 shows the change in footing traction with load inclination. Although the actual pressures mobilised by the footing is affected by the plastic compressibility λ, it appears to have no major effect on the change of traction with load inclination. Table 7.15 summarises the results.

Table 7.15 Effect of λ on reduction of bearing pressure with load inclination

Inclination / λ	10° $\left(\frac{q_{av}}{q_o}\right)_{10\%}$	20° $\left(\frac{q_{av}}{q_o}\right)_{10\%}$	30° $\left(\frac{q_{av}}{q_o}\right)_{10\%}$
0.1	0.96	0.86	0.71
0.2	0.96	0.83	0.68
0.3	0.96	0.86	0.73

7.9.3 EFFECT OF FRICTION ANGLE, ϕ'

The effect of friction angle on change of mobilised traction with load inclination was investigated. Normally consolidated carbonate sand was assumed to exist below the surface circular footing. The SU2 model parameters selected for the study are presented below in Table 7.16.

Table 7.16 SU2 model parameters to investigate effect of friction angle ϕ'

ϕ' (deg.)	κ	λ	ν	e_{cs}	p'_o	r	γ' (kN/m^3)	K_o
Variable	0.02	0.2	0.1	2.5	NC	5.0	7.0	0.5

A footing diameter of B = 25.0m was used in the finite element analysis. NC in Table 7.16 implies normally consolidated carbonate sand. The change in traction with load inclination obtained for various friction angles assumed for the carbonate sand is presented below in Table 7.17.

Table 7.17 Effect of friction angle on change of traction with load inclination

Inclination / ϕ'	10° $\left(\frac{q_{av}}{q_o}\right)_{10\%}$	20° $\left(\frac{q_{av}}{q_o}\right)_{10\%}$	30° $\left(\frac{q_{av}}{q_o}\right)_{10\%}$
35°	0.95	0.81	0.64
40°	0.96	0.83	0.68
45°	0.96	0.87	0.72

It is observed that the smaller the friction angle of the soil, the greater is the change in the bearing resistance with load inclination. This is consistent with the expectation that the footing would either fail by sliding or develop very large horizontal displacements, as the load inclination approaches the ultimate friction angle of the underlying carbonate sand.

7.10 SIMPLIFIED ELASTO-PLASTIC FOOTING MODEL

Georgiadis and Butterfield (1988), Gottardi and Butterfield (1993, 1994) and Montrasio and Nova (1991) have proposed elasto-plastic models for inclined loading of footings on sand. The proposed models can predict the load-displacement curve and the bearing capacity of strip footings on silica sand subjected to inclined load. No model has been proposed to predict the bearing response for inclined loading of footings on carbonate sand under drained conditions. This is because only limited experimental data is available for inclined loading of footings on carbonate sand. However, 3D finite element simulation of inclined loading of footings using the SU2 model, gives at least a qualitative indication of its response. The elasto-plastic footing models mentioned above were modified and a simple footing model was proposed, to predict the response of circular footings on carbonate sand subjected to inclined load. The predictions of the simplified footing model were compared with results obtained from finite element analysis.

The simplified footing model assumes the load-displacement curve at any inclination to be bilinear as shown in Figure 7.28. The incremental horizontal and vertical displacements at the centre of the footing may be expressed as the sum of their elastic and plastic components as follows:

$$dh' = dh'_e + dh'_p \tag{7.10}$$

$$dv' = dv'_e + dv'_p \tag{7.11}$$

dh'_e and dh'_p are the incremental elastic and plastic horizontal displacements and dv'_e and dv'_p are the incremental elastic and plastic vertical displacements of the footing.

For a given increment of applied horizontal traction and vertical pressure (dH', dV'), the corresponding increment of horizontal and vertical displacements (dh', dv') at the centre of the footing are computed. The load-displacement curve of the footing for any load inclination is obtained by summing the corresponding incremental values. Thus for a horizontal and vertical traction (H', V') applied at the centre of the footing, the horizontal displacements h' and vertical displacement v' may be expressed as follows:

$$h' = h'_e + h'_p \tag{7.12}$$

$$v' = v'_e + v'_p \tag{7.13}$$

h'_e and h'_p are the elastic and plastic horizontal displacements and v'_e and v'_p are the elastic and plastic vertical displacements at the centre of the footing. The elastic and plastic components of the vertical displacement of the footing are shown in Figure 7.28. The details of the proposed model are described in the subsequent sections.

7.10.1 ELASTIC RESPONSE

The initial response of a footing on carbonate sand is approximately linear and "elastic". This response is assumed to be identical to that of a rigid circular footing resting on a homogeneous elastic half-space. The corresponding elastic pressure-displacement relation may be described by the following equations:

$$V_e' = K_{ve} v_e' \tag{7.14}$$

$$H_e' = K_{he} h_e' \tag{7.15}$$

where

$$V_e' = \frac{V_e / (\pi B^2 / 4)}{q_{ref}} \tag{7.16}$$

$$H_e' = \frac{H_e / (\pi B^2 / 4)}{q_{ref}} \tag{7.17}$$

$$v_e' = \frac{v_e}{B} \tag{7.18}$$

$$h_e' = \frac{h_e}{B} \tag{7.19}$$

V_e and H_e are respectively the applied vertical and horizontal loads at the footing centre and V_e' and H_e' are the corresponding vertical and horizontal components of the applied traction. The components of the applied traction are normalised here by a reference pressure q_{ref} to make them independent of the units of measurement. The bearing pressure mobilised by the footing at a displacement of 30% of the footing diameter under purely vertical load, have been used here as the reference pressure, q_{ref}. The elastic vertical and horizontal displacements v_e and h_e at the centre of the footing are normalised by the footing diameter B to give dimensionless vertical and

horizontal displacements v_e' and h_e' respectively. K_{ve} and K_{he} are respectively the vertical and horizontal elastic stiffness of the footing, with each having the units of pressure.

V_e and H_e are assumed to be given by the elasticity equations for circular footings reported in Poulos and Davis (1974) as follows:

$$V_e = \left[\frac{4GR}{1-\nu}\right] v_e \tag{7.20}$$

$$H_e = \left[\frac{32GR(1-\nu)}{7-8\nu}\right] h_e \tag{7.21}$$

In equations (7.20) and (7.21), V_e is the vertical and H_e is the horizontal elastic component of the inclined load, G is the elastic shear modulus of the soil, ν is the Poisson's ratio of the soil and R is the footing radius.

Using equations (7.20) and (7.21), it can be shown that

$$K_{ve} = \frac{8}{\pi}\frac{1}{q_{ref}}\frac{G}{1-\nu} \tag{7.22}$$

$$K_{he} = \frac{64G}{\pi}\frac{1}{q_{ref}}\frac{1-\nu}{7-8\nu} \tag{7.23}$$

For simplicity, a constant value for the elastic shear modulus and Poisson's ratio is assumed in the footing model. Equations (7.20) and (7.21) thus define a constant vertical and horizontal elastic stiffness for a circular footing, independent of the state of stress. The function of the reference pressure q_{ref} in equations (7.22) and (7.23) is to make the elastic footing stiffnesses K_{ve} and K_{he} independent of the units of measurement. Subsequent sections describe the equations for obtaining the plastic components of displacement of the footing. This includes equations for the hardening function, yield locus, plastic potential function and plastic hardening modulus.

7.10.2 HARDENING FUNCTION

The hardening function in a volumetric strain hardening plasticity model describes the change of the hardening parameter p_o' with plastic volumetric strains $d\varepsilon_v^p$ of the soil. In the proposed footing model, the hardening function defines the change in the vertical bearing pressure V_o' (the hardening parameter) with plastic vertical displacements v_p' at the centre of the footing. In this case, the vertical bearing pressure V_o' may be considered to be analogous to the preconsolidation pressure p_o' and the plastic vertical displacements v_p' may be considered to be analogous to plastic volumetric strains $d\varepsilon_v^p$ of the soil.

The bearing pressure curve of the footing under vertical load is idealised to be bilinear as shown in Figure 7.28. It is assumed to be analogous to the isotropic consolidation curve for a soil. The linear elastic and linear plastic part of the bilinear bearing pressure curve shown in Figure 7.28 may be defined by the following equations:

$$V_o' = N + K_{ve} v_e' \tag{7.24}$$

$$V_o' = \Gamma + K_{vep} v' \tag{7.25}$$

In equations (7.24) and (7.25), V_o', v_e' and v' are respectively the bearing pressure, elastic vertical displacement and total vertical displacement at the centre of the footing subjected to vertical load. The bearing pressure is normalised by a reference pressure and the displacements are normalised by the diameter of the footing to make them dimensionless. K_{ve} is the stiffness of the linear elastic part and K_{vep} is the stiffness of the linear plastic part of the footing response under purely vertical load. The slopes K_{ve} and K_{vep} are shown in Figure 7.28. The constant N in equation (7.24) is in general non-zero. It is the pressure represented by the intercept of the unload-reload line with the ordinate or V_o' axis. . The constant Γ in equation (7.25) is the

pressure at the intersection of the linear plastic part of the bearing pressure curve with the ordinate or V_o' axis.

The incremental plastic vertical displacement dv_p' is basically the difference between the incremental vertical displacement dv' and incremental elastic vertical displacement dv_e'. Thus,

$$dv_p' = dv' - dv_e' \tag{7.26}$$

Differentiating equation (7.24) and (7.25) and using the incremental relation (7.26), the incremental hardening function for the footing may be derived as follows:

$$dV_o' = K_{vp} dv_p' \tag{7.27}$$

where

$$K_{vp} = \frac{K_{vep} K_{ve}}{K_{ve} - K_{vep}} \tag{7.28}$$

In equations (7.27) and (7.28), K_{vp} is the plastic stiffness of the footing under vertical load.

The incremental hardening function of the footing model was derived from the equation of the linear plastic part of the idealised bilinear bearing pressure curve. This equation defines the change in the vertical bearing pressure V_o' (the hardening parameter for footing model) with plastic vertical displacements v_p'. The hardening function is used to define the hardening rule for the footing yield locus described in the subsequent section.

7.10.3 YIELD LOCUS

The yield locus for a footing subjected to inclined load defines the limit of its elastic response in $H'-V'$ space. H' and V' are respectively the applied horizontal and vertical traction at the centre of the footing. They are made dimensionless by normalising them with a standard pressure q_{ref}. The yield locus in a footing model may be defined either as contours of plastic resultant displacement or contours of plastic vertical displacement of the footing centre in $H'-V'$ space. Figure 7.29 shows the contours of plastic resultant displacement of the footing centre and Figure 7.30 shows the contours of plastic vertical displacement. The yield loci were drawn from the results of 3D finite element simulations of the model-scale footing obtained using the SU2 model. For simplicity, the contours of normalised plastic vertical displacement as shown in Figure 7.30 are chosen as the footing yield locus in the proposed footing model. The intersection of the cap yield loci with the V' axis in Figures 7.29 and 7.30 represents the bearing pressure V_o' mobilised by the footing under vertical load (also shown in Figure 7.28).

Two separate yield loci have been defined in the footing model. The first yield locus is defined by a cap function, which represents the contours of plastic vertical displacement in $H'-V'$ space. It is approximated by an equation given as follows:

$$H'^2 = m^2(V_o' - aV') \tag{7.29}$$

$$m = \tan\phi' \tag{7.30}$$

V_o' is the normalised bearing capacity under purely vertical load, H' and V' are the normalised applied horizontal traction and vertical pressure respectively, ϕ' is the friction angle of the soil and a is a model parameter.

It is observed from Figure 7.30 that the proposed cap yield locus may be fitted quite well with the yield locus obtained using the results of 3D finite element simulation for the model-scale footing for a=1. The intersection of the cap yield locus with the

V' axis represents the bearing pressure V_o' under vertical load. When the horizontal and vertical component H' and V' respectively of the normalised applied footing traction touch the cap yield locus, the load-displacement behaviour of the footing changes from elastic to elasto-plastic. For loading beyond this point, there will be a sudden decrease in the footing stiffness and the footing response is predicted to change from linear elastic to linear elasto-plastic by the proposed footing model. With increasing plastic vertical displacements v' of the footing, the cap yield locus expands isotropically in $H'-V'$ space. For constant load inclinations, the cap yield locus will expand indefinitely predicting increasing footing displacements with load. This appears to be in agreement with experimentally observed behaviour for footings on carbonate sand. As the bearing resistance for the footing under vertical load has been assumed as bilinear, the proposed footing model prediction for traction under inclined load will also be bilinear.

A second deviator yield or failure function fixed in $H'-V'$ space is postulated for the footing. It is approximated by an equation given as below:

$$H' = mV' \tag{7.31}$$

Figure 7.31 shows the cap and deviator yield locus in $H'-V'$ space. It is assumed that infinite horizontal displacements occur when the footing pressures H' and V' touches the deviator yield locus given by equation (7.31). The footing is then assumed to fail by sliding along the soil-footing interface. Experimental results of Pan (1999) show that large horizontal displacements occur when footings on carbonate sand are subjected to load inclination close to the friction angle of the sand. The next section defines the stress-dilatancy relation and plastic potential function of the footing model.

7.10.4 STRESS-DILATANCY AND PLASTIC POTENTIAL

The relative magnitudes of the incremental plastic vertical and horizontal displacements of a footing subjected to inclined load may be termed as the dilatancy

ratio. 3D finite element results show that the dilatancy ratio of the footing may be expressed as a function of the load inclination. This function is termed here as the stress-dilatancy relation for the footing. The integration of this incremental function gives the plastic potential function for the footing model. The gradients of the plastic potential function give the relative magnitudes of the incremental plastic vertical and horizontal displacement of the footing as a function of load inclination or $\frac{H'}{V'}$.

A simple stress-dilatancy relation for a circular footing on carbonate sand is proposed as follows:

$$\frac{dv'_p}{dh'_p} = \frac{m^2 - n^2}{kn} \tag{7.32}$$

where

$$n = \frac{H'}{V'} = \tan\theta \tag{7.33}$$

$$m = \tan\phi' \tag{7.34}$$

ϕ' is the friction angle of the carbonate sand, θ is the angle of load inclination and k is a model parameter. Figure 7.32 plots the proposed stress-dilatancy function for k = 1 and compares it with predictions obtained for the model-scale footing from 3D finite element analysis. Reasonable agreement is observed between the two.

For k = 1, the stress-dilatancy relation can be integrated to obtain the equation for the footing plastic potential function as follows:

$$\left(\frac{H'}{mV'}\right)^2 + \ln\left(\frac{V'}{V'_o}\right)^2 = 0 \tag{7.35}$$

For $k \neq 1$, the following expression is obtained for the plastic potential function of the footing:

$$\ln\left\{1+k\left(\frac{H'}{mV'}\right)^2\right\}+\frac{2k}{k+1}\ln\left(\frac{V'}{V'_o}\right)=0 \tag{7.36}$$

Figure 7.31 plots the plastic potential function given by equation (7.35).

The plastic potential function for the proposed footing model has now been defined. The gradients of the plastic potential function define the relative magnitudes of the incremental horizontal and vertical plastic displacements of the footing at any given load inclination. The plastic hardening modulus may now be obtained from the equations of the yield locus and plastic potential function.

7.10.5 PLASTIC HARDENING MODULUS

The plastic hardening modulus defines the plastic stiffness of a circular footing resting on carbonate sand subjected to inclined load. It is computed from the plastic consistency condition using the equations for yield locus and plastic potential function described in the previous sections. The consistency condition is described as follows:

$$df = 0 \tag{7.37}$$

The expression for the plastic hardening modulus may be obtained from the consistency condition and is given as follows:

$$H_{\text{mod}} = -\frac{\partial f}{\partial V'_o}\frac{\partial V'_o}{\partial v'_p}\frac{\partial g}{\partial V'_o} \tag{7.38}$$

where H_{mod} is the plastic hardening modulus, f is the yield function, g is the plastic potential function, V'_o is bearing pressure mobilised under purely vertical load at a

plastic vertical displacement of v'_p. The value of $\frac{\partial V'_o}{\partial v'_p}$ may be obtained from equation (7.27).

The equations for the yield locus, plastic potential function and plastic hardening modulus of the footing model have been derived. These equations may be used to obtain the incremental plastic displacements of the footing for a given increment of vertical and horizontal traction. This is described in the next section.

7.10.6 INCREMENTAL PLASTIC DISPLACEMENT

The equations for the yield locus, plastic potential function and plastic hardening modulus for the footing model have now been described. The horizontal and vertical incremental plastic displacements at the centre of the footing for a given increment of applied horizontal and vertical traction (dH', dV') may now be computed as follows:

$$dh'_p = d\lambda \frac{\partial g}{\partial H'} \tag{7.39}$$

$$dv'_p = d\lambda \frac{\partial g}{\partial V'} \tag{7.40}$$

where

$$d\lambda = \frac{1}{H_{\text{mod}}}\left(\frac{\partial f}{\partial V'}dV' + \frac{\partial f}{\partial H'}dH'\right) \tag{7.41}$$

$d\lambda$ is the proportionality factor defining the magnitude of incremental plastic displacements at the footing centre for a given increment of vertical and horizontal traction on the footing. The remaining terms used in the above equations have been described already in the previous sections.

7.10.7 LOAD-DISPLACEMENT CURVE

The load-displacement curve for a circular footing subjected to inclined load may be computed using the simplified footing model in the following way. The horizontal and vertical stiffness of the footing are first computed using equations (7.22) and (7.23) from the constant elastic shear modulus and Poisson's ratio of the underlying carbonate sand. The elastic vertical and horizontal displacements of the footing may then be calculated using equations (7.14) and (7.15). It is assumed that the bearing pressure curve of the footing and its bilinear idealisation under vertical load, as shown in Figure 7.28, is known. The bearing pressure curve may be obtained using finite element analysis. A hand method for predicting this curve was given in Chapter 5. The initial yield pressure, marking the transition from linear elastic to linear plastic behaviour in Figure 7.28 is assumed as the initial value of V_o'. A value for the parameter a is assumed (generally 1.0). Once V_o' and a are known, the initial cap yield locus is fixed in $H'-V'$ space, as defined by equation (7.29). The deviator yield locus given by equation (7.31) is defined once the friction angle for the underlying carbonate sand is known. This fixes the deviator yield locus in $H'-V'$ space. The position of the initial cap and deviator yield locus are now defined in $H'-V'$ space.

When the stress state given by the horizontal and vertical traction (H',V') of the footing touches the cap yield locus, incremental plastic horizontal and vertical displacements of the footing are assumed to take place, and their magnitudes are given by equations (7.39) and (7.40). The hardening and expansion of the cap yield locus with plastic vertical displacements of the footing is defined by the hardening function given by equation (7.27). K_{vp} in equation (7.27) is determined from equation (7.28). In equation (7.28), K_{ve} is determined using equation (7.22) and K_{vep} is determined from Figure 7.28 as the slope of the linear plastic part of the bearing pressure curve under vertical load.

The incremental elastic and plastic, vertical and horizontal displacements of the footing can now be obtained for any given increment of vertical and horizontal traction applied at the centre of the footing. The bilinear load-displacement curve for

any load inclination is then obtained from the integration of the applied incremental traction and corresponding incremental displacements at the centre of the footing.

7.11 PREDICTIONS USING SIMPLIFIED FOOTING MODEL

The approximate bilinear load-displacement curves under inclined load for the experimental footing 25mm in diameter resting on cemented sand as well as that of a 25m diameter surface circular footing on normally consolidated sand, were predicted using the simple footing model. The values of the footing model parameters a and k were assumed to be 1.0 for both the cases. The predictions were compared with results obtained from 3D finite element analysis.

Values of the parameters chosen to obtain predictions for the load-displacement response of the 25mm diameter experimental footing on cemented carbonate sand are provided below in Table 7.18. The reference pressure q_{rsf} chosen to normalise all traction terms was the bearing pressure of 9.5 MPa mobilised by the experimental footing at a displacement of 30% of the footing diameter, under purely vertical load.

Table 7.18 Footing model parameters for model-scale footing

ϕ' (deg)	G (MPa)	ν	V_o'	K_{vep}	a	k
39.0	75.0	0.2	0.43	2.04	1.0	1.0

The value of the parameter V_o' was obtained from the idealised bilinear bearing pressure curve of the footing under vertical load. It was normalised by the reference pressure of q_{ref} = 9.5 MPa. The value of the elastic shear modulus was chosen by best fitting the initial part of the experimental pressure-displacement curve of the model footing subjected to purely vertical load. The dimensionless value of K_{vep} was determined as the slope of the linear plastic part of the bilinear bearing pressure curve under vertical load as illustrated in Figure 7.28. In determining K_{vep}, the

bearing pressures were normalised by the reference pressure of q_{ref} = 9.5 MPa and footing displacements were normalised by the footing diameter.

Figures 7.33 and 7.34 compare the average resultant and vertical traction mobilised by the experimental footing at different load inclinations, as predicted by the simple footing model and 3D finite element analysis. Although reasonable agreement is observed at large strains, satisfactory agreement could not be obtained at small strains. Figure 7.35 compares the predicted horizontal and vertical displacements with the results obtained from 3D finite element analysis. A reasonable fit could be obtained for most load inclinations. Deviation of the horizontal displacement from 3D finite element predictions is observed at larger load inclinations. This implies that at larger load inclinations, the simplified footing model stress-dilatancy relation given by equation (7.32) does not fit the stress-dilatancy predicted by 3D finite element analysis of the problem.

The simple footing model was also used to predict the load-displacement curve of a 25m diameter surface circular footing resting on normally consolidated carbonate sand and subjected to inclined load. The values of the footing model parameters chosen to obtain the predictions are provided below in Table 7.19. For a footing on normally consolidated sand, there is no purely elastic part for the footing response under vertical load. The value of the parameter V_o' was thus assumed to be zero. A normalising pressure of q_{ref} = 250 kPa was used. This was the bearing pressure mobilised by the footing at a displacement of 30% of the footing diameter under vertical load, as obtained from 2D finite element analysis. The value of K_{vep} is the slope of the linear plastic part of this bearing pressure curve. In determining K_{vep}, the bearing pressures were normalised by the reference pressure of q_{ref} = 250 kPa and footing displacements were normalised by the footing diameter.

Table 7.19 Footing model parameters for 25m diameter footing

ϕ' (deg)	G (MPa)	ν	V_o'	K_{vep}	a	k
40.0	37.5	0.2	0.0	9.15	1.0	1.0

Figure 7.36 compares the predicted load-displacement curves with results of 3D finite element analysis. It is observed that at larger load inclinations, smaller tractions are predicted by the simple footing model than the corresponding 3D finite element analysis. A better fit may have been obtained by adjusting the parameters a and k of the simple footing model to match the yield locus and plastic potential functions as obtained from 3D finite element analysis.

Elasto-plastic models proposed for inclined loading of footings on silica sand were modified and a simple elasto-plastic footing model was formulated. The simplified model was used to predict the response of circular footings on carbonate sand subjected to inclined load. It was demonstrated that such a model could be used to fit the pressure-displacement curves of circular footings on carbonate sand subjected to inclined load at zero eccentricity. However, the simplified model is unable to predict the strongly non-linear elasto-plastic response observed in model-scale experimental footings on carbonate sand subjected to inclined load, even at small footing displacements. Elasto-plasticity needs to be introduced within the yield locus of the simplified footing model as well the constitutive soil model to predict more accurately the inclined pressure-displacement response of circular footings on carbonate sand at small displacements.

7.12 CONCLUSION

The SU2 model appears to provide satisfactory predictions of the bearing behaviour of a model-scale circular footing resting on cemented carbonate sand and subjected to inclined load. The change of the mobilised bearing resistance with load inclination is reasonably well predicted by this model. Most carbonate sands, as obtained in nature, are usually cemented to some extent. However, the SU2 model could not predict satisfactorily the change of bearing resistance with load inclination for a model-scale footing resting on uncemented carbonate sand. There may be several reasons for such unsatisfactory predictions. In the finite element analysis it was assumed that the constitutive response of the soil-footing interface was exactly similar to the underlying soil. However, in reality the interface behaviour may be significantly different from the response within the soil domain. The unsatisfactory

prediction may also be due to certain limitations of the SU2 model itself. The model in its present form does not take into account soil anisotropy effects and rotation of principal stresses with load inclination (incorporating the effect of Lode angle in the constitutive model), which may affect the footing behaviour under inclined load.

A simple elasto-plastic footing model was proposed for a footing on carbonate sand subjected to inclined load. The proposed footing model has a small number of model parameters. The predictions of the simplified footing model agree quite well with predictions from 3D finite element analysis. In particular, the model can simulate in a simple way, a continuously increasing but lowered bilinear bearing pressure curve for a footing subjected to inclined load. Such a response is observed for footings on carbonate sand. However, the simplified footing model was tested only for simple stress paths and for inclined load of circular footings at zero eccentricity. Also, the response of the simplified footing model at small displacements is not entirely satisfactory and needs further development. However, the development of a simple footing model may serve as a useful tool for approximating the response of soil-structure interaction problems of offshore platforms. It also has the convenience of being easily programmed, for example using a spreadsheet.

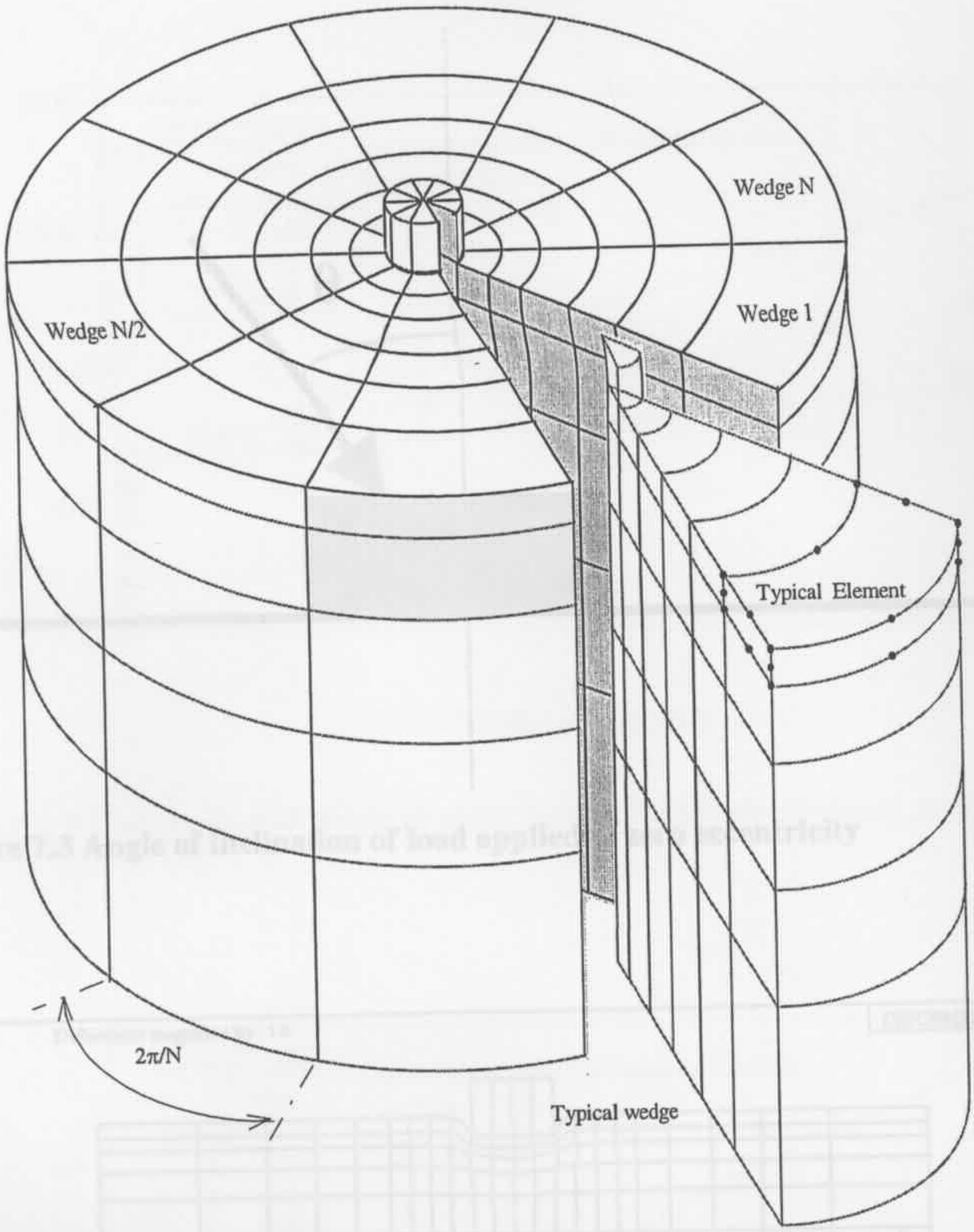

Figure 7.1 Mesh discretisation in semi-analytical 3D FE (Taiebat, 1999)

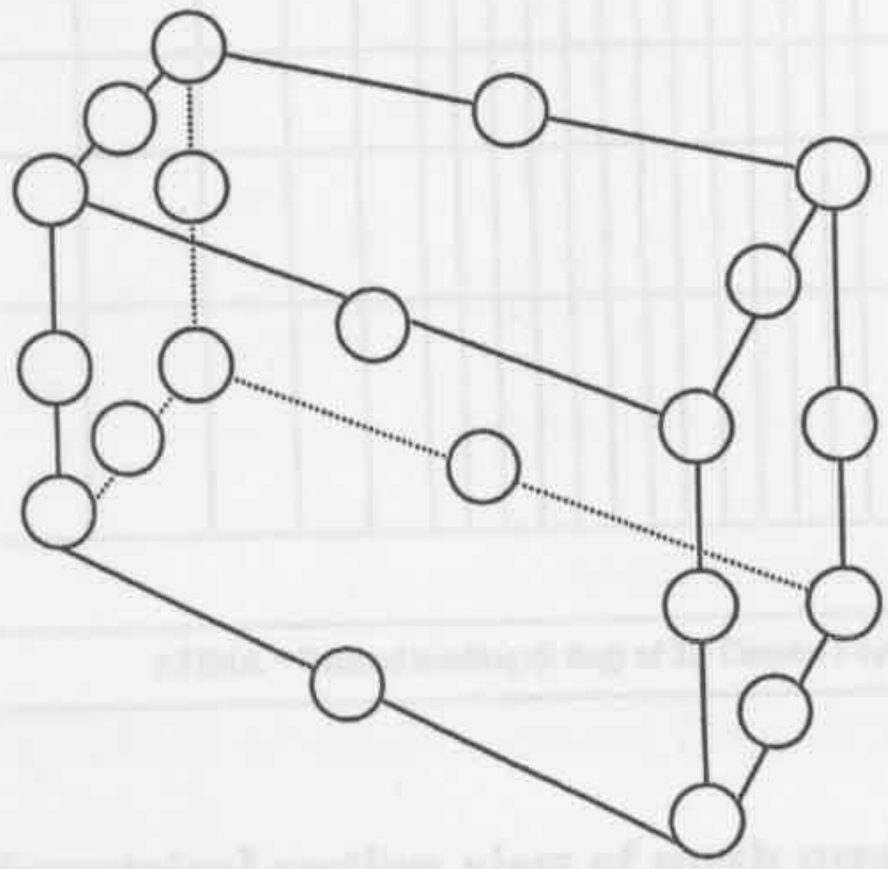

Figure 7.2 20 node cubic element used in 3D FE mesh

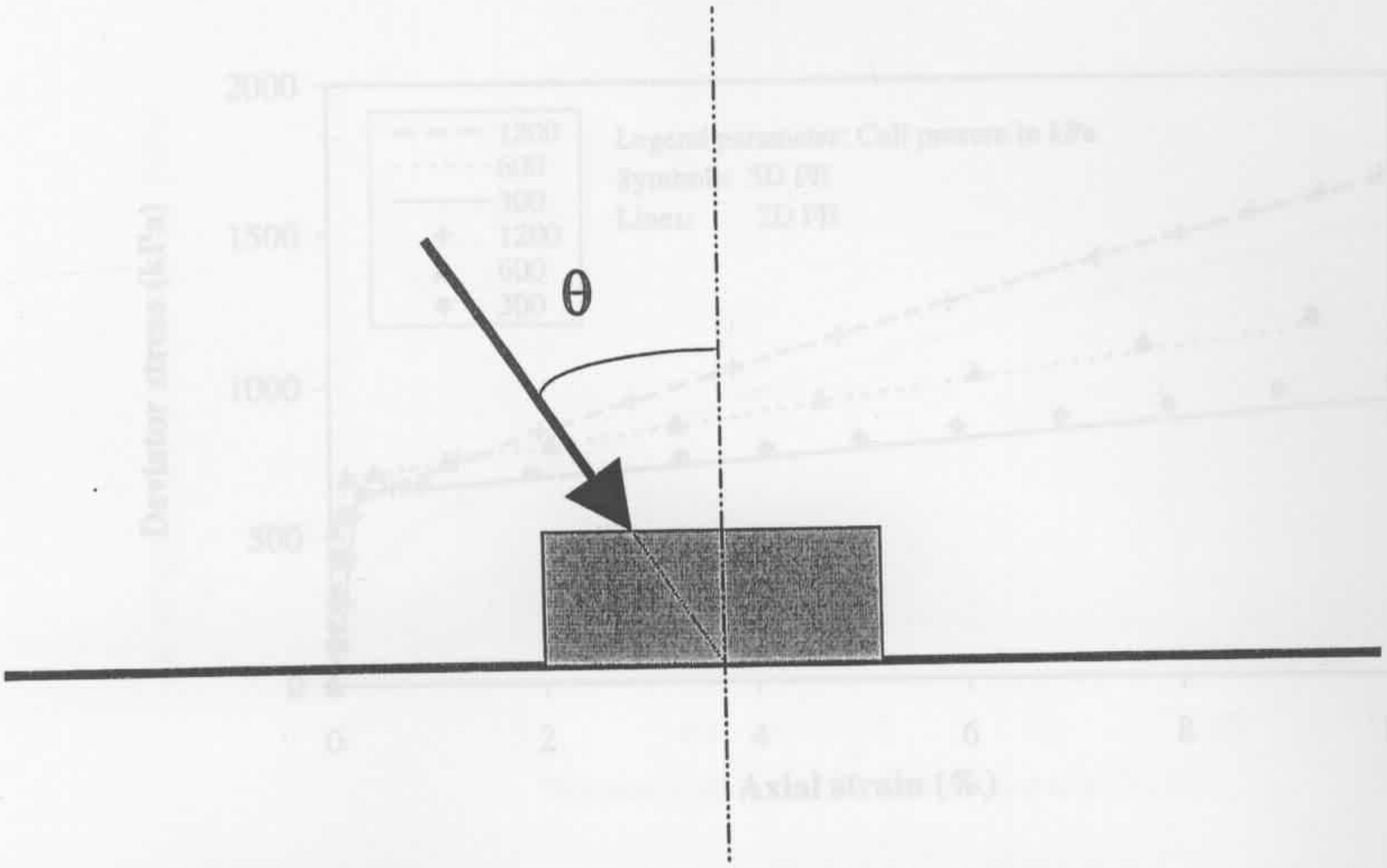

Figure 7.3 Angle of inclination of load applied at zero eccentricity

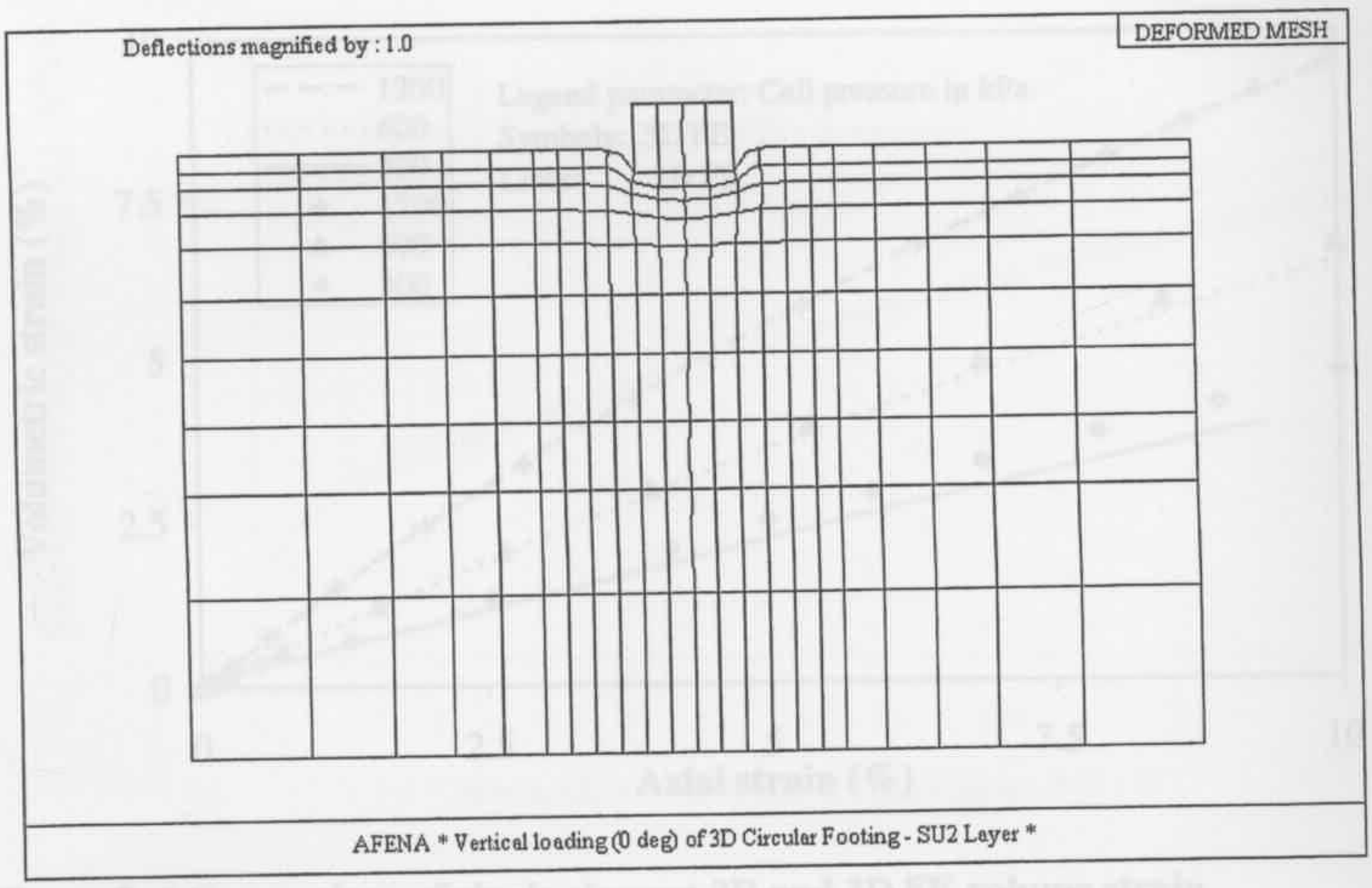

Figure 7.4 A diametrical section view of mesh used in 3D FE

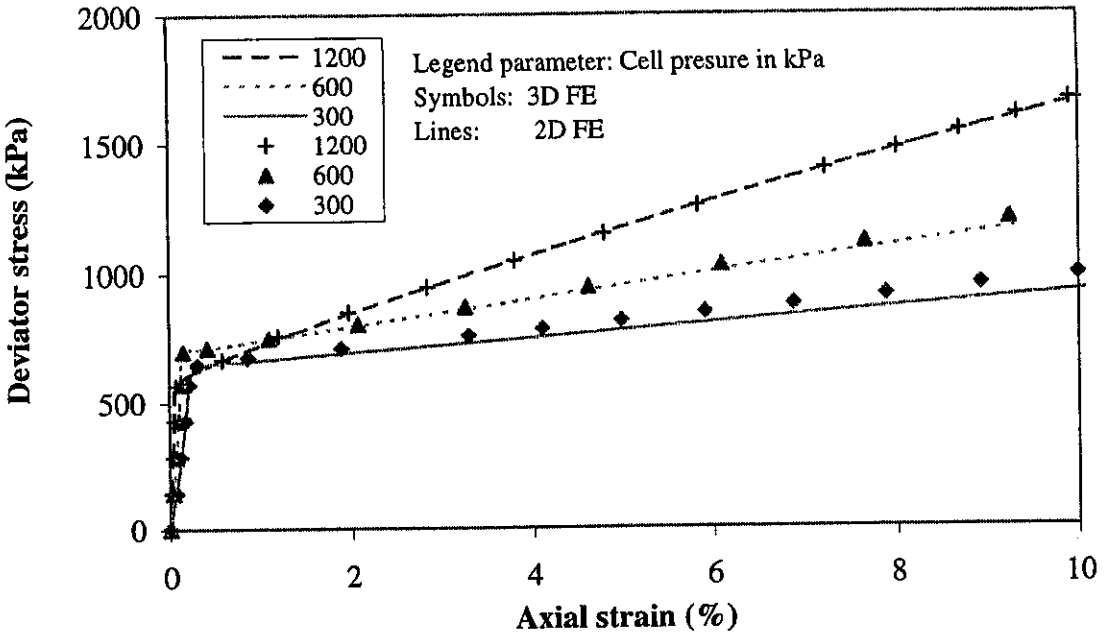

Figure 7. 5 Comparison of single element 2D and 3D FE stress-strain prediction

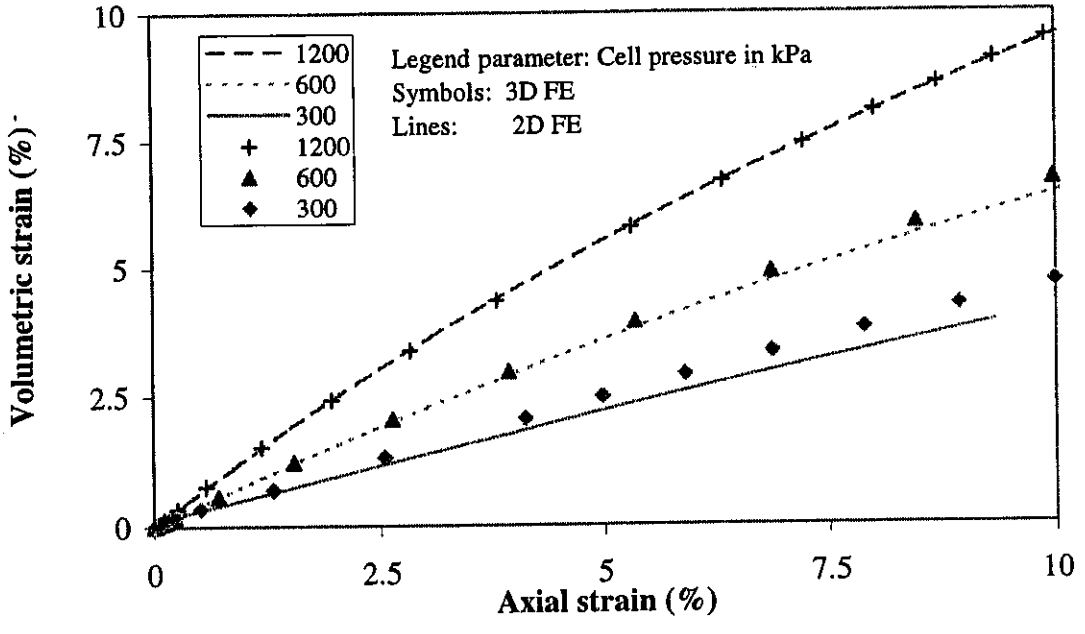

Figure 7. 6 Comparison of single element 2D and 3D FE volume strain predictions

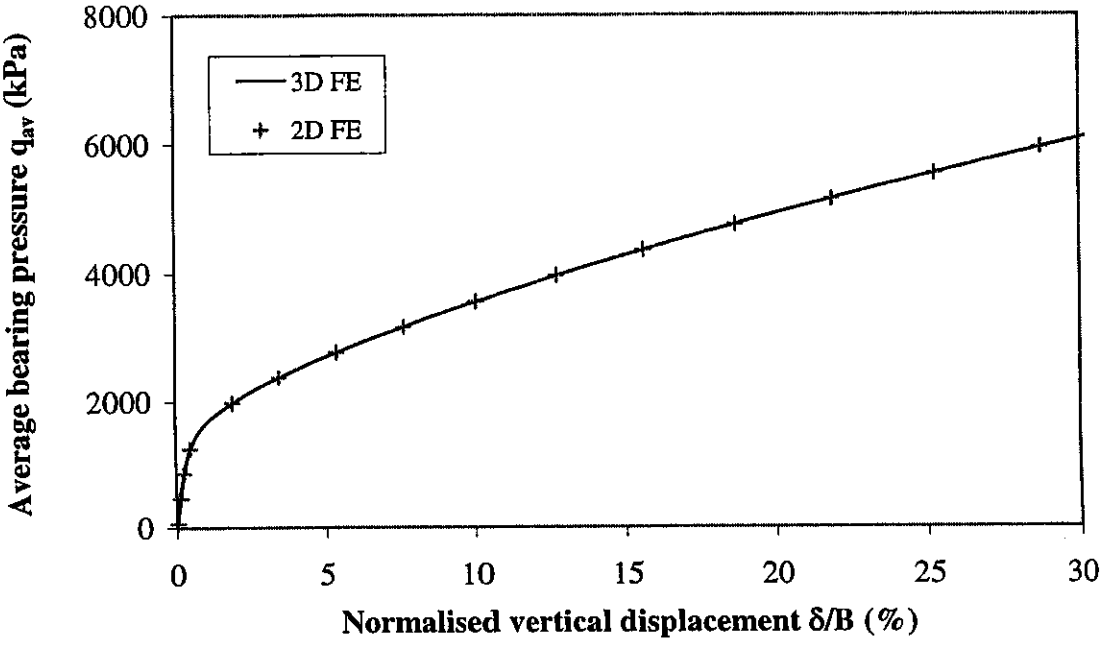

Figure 7.7 Comparison of 3D FE prediction of pressure-displacement curve of a footing under vertical load with 2D FE predictions

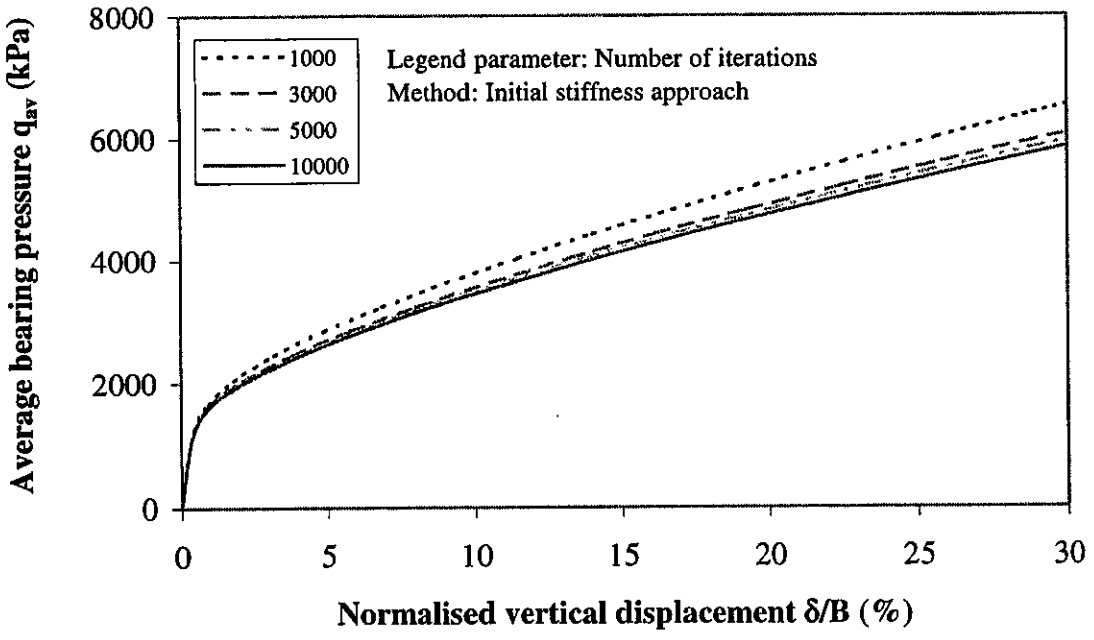

Figure 7.8 Load increments required for convergence of pressure-displacement curve

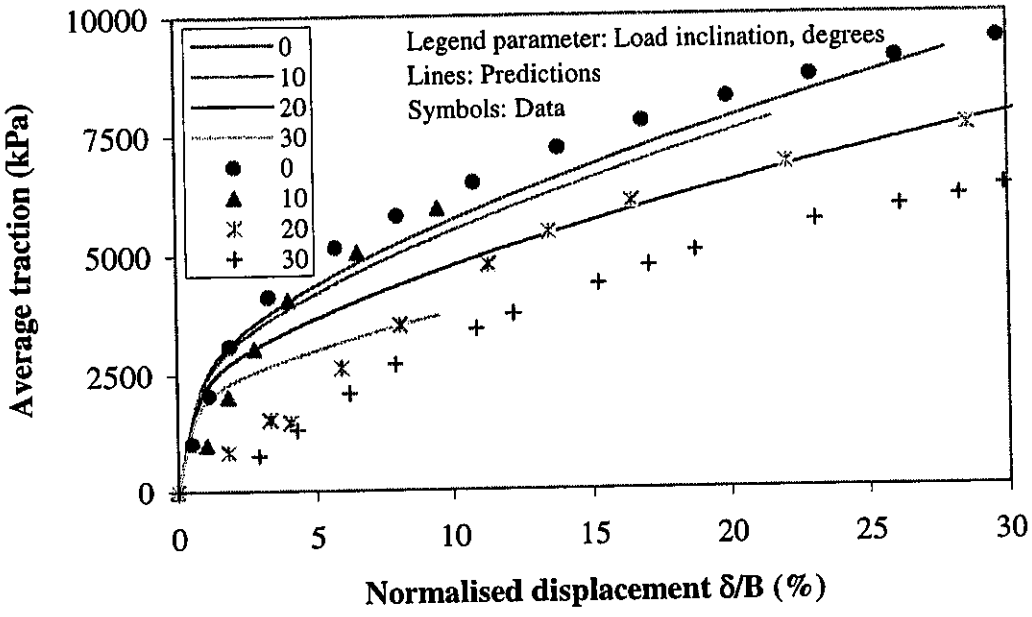

Figure 7.9 Comparison of 3D FE predictions with experimental data for footing on artificially cemented carbonate sand

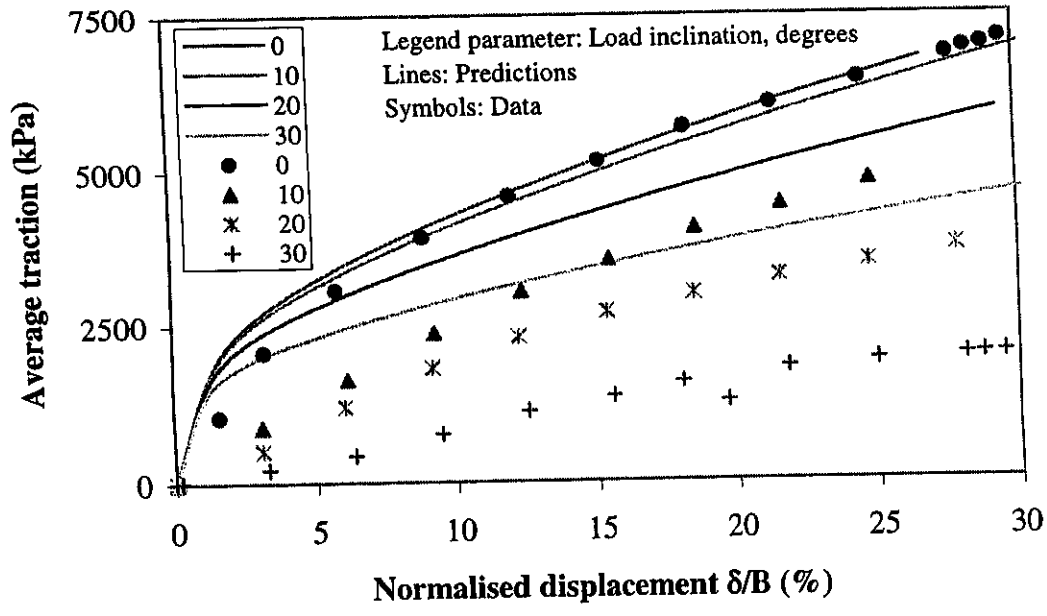

Figure 7.10 Comparison of 3D FE predictions with experimental data for footing on uncemented carbonate sand

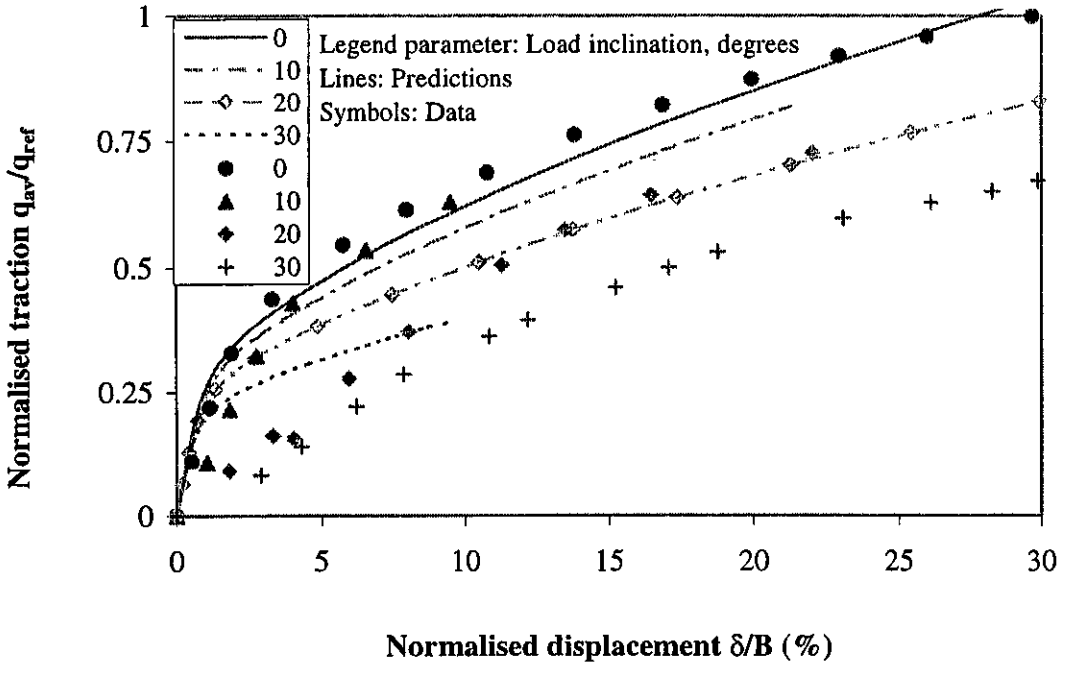

Figure 7.11 Comparison of predictions of change of footing traction with load inclination with data for footing on artificially cemented carbonate sand

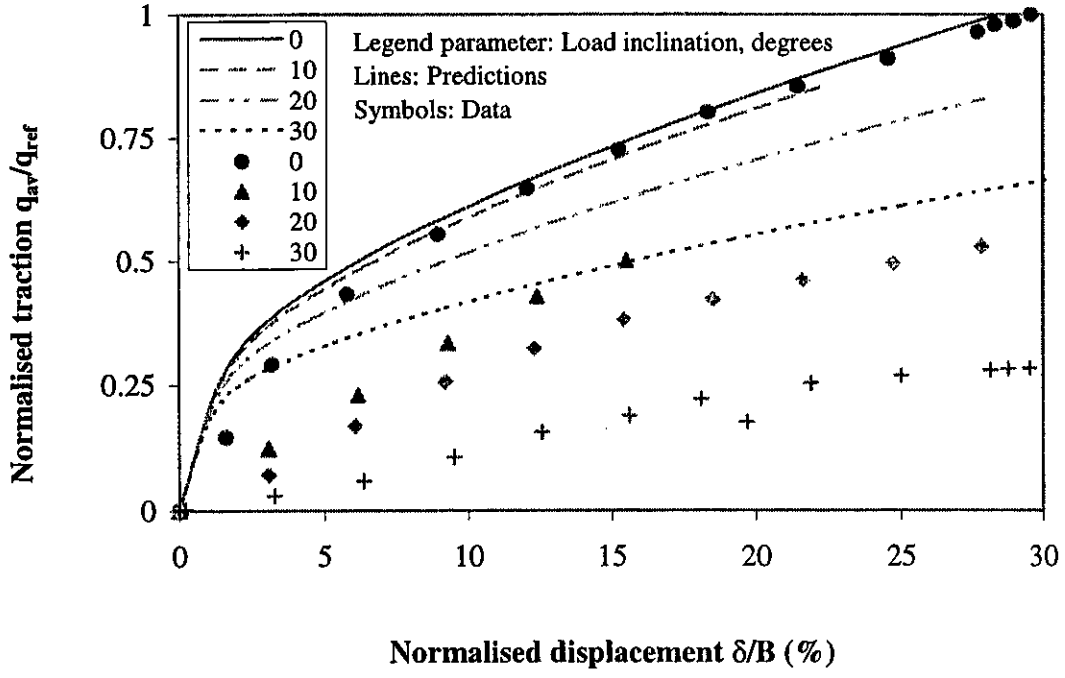

Figure 7.12 Comparison of predictions of change of footing traction with load inclination with data for footing on uncemented carbonate sand

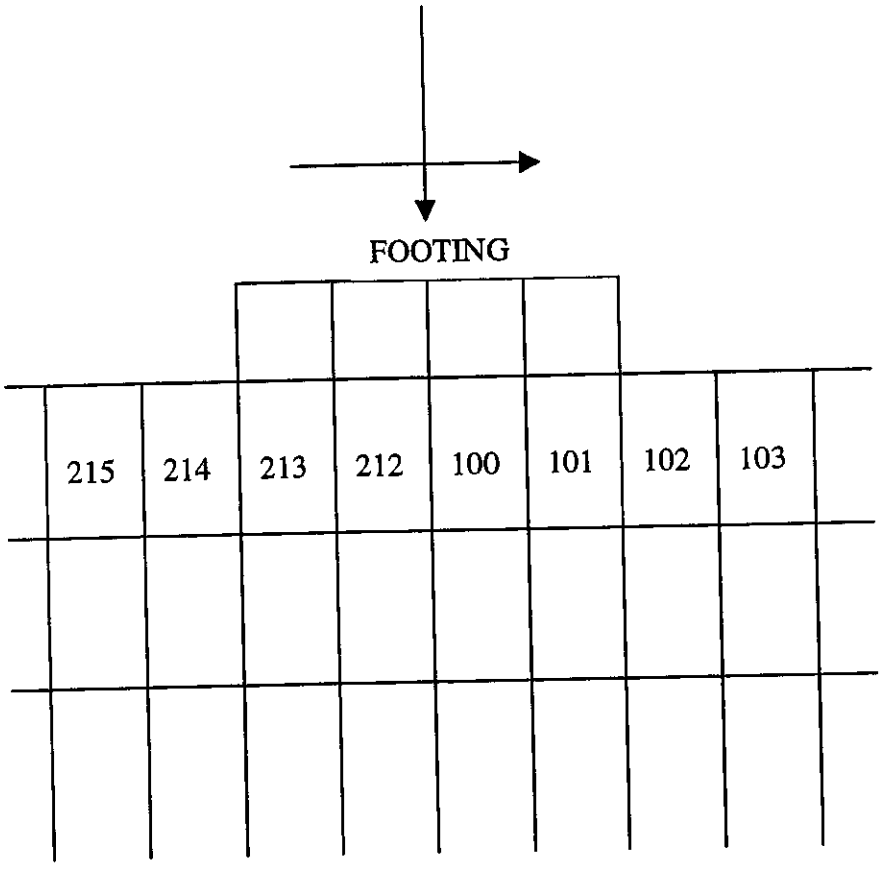

7.13 (a)

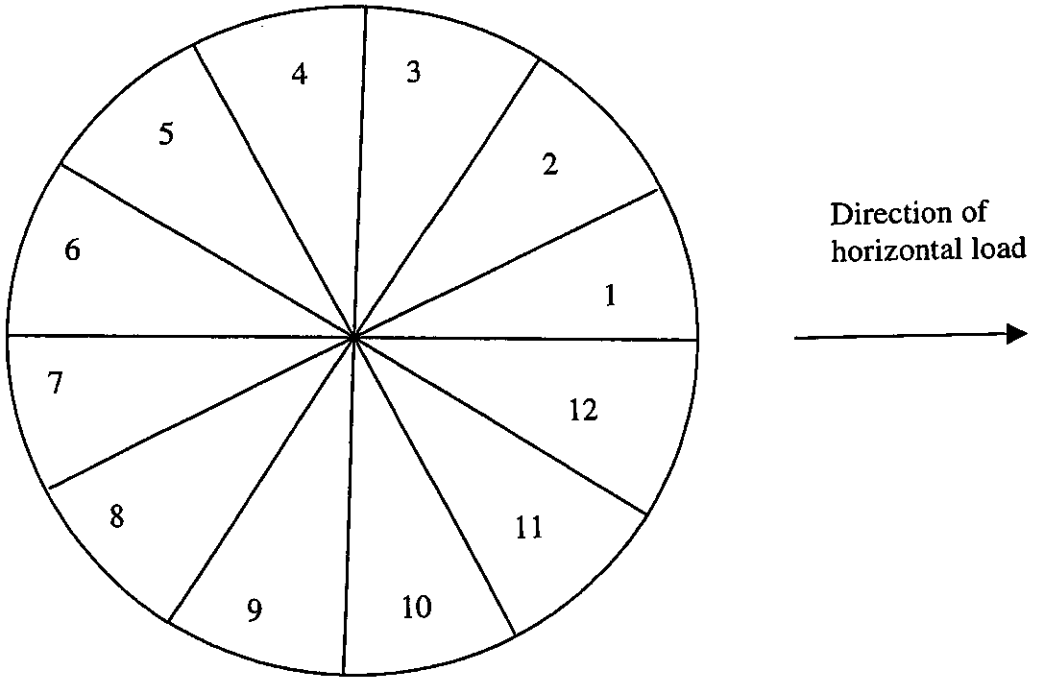

7.13 (b)

Figure 7.13 (a) Selected elements below the footing in the plane of applied load which is the vertical bisector of wedges 1 and 7 (b) Plan view of the wedges

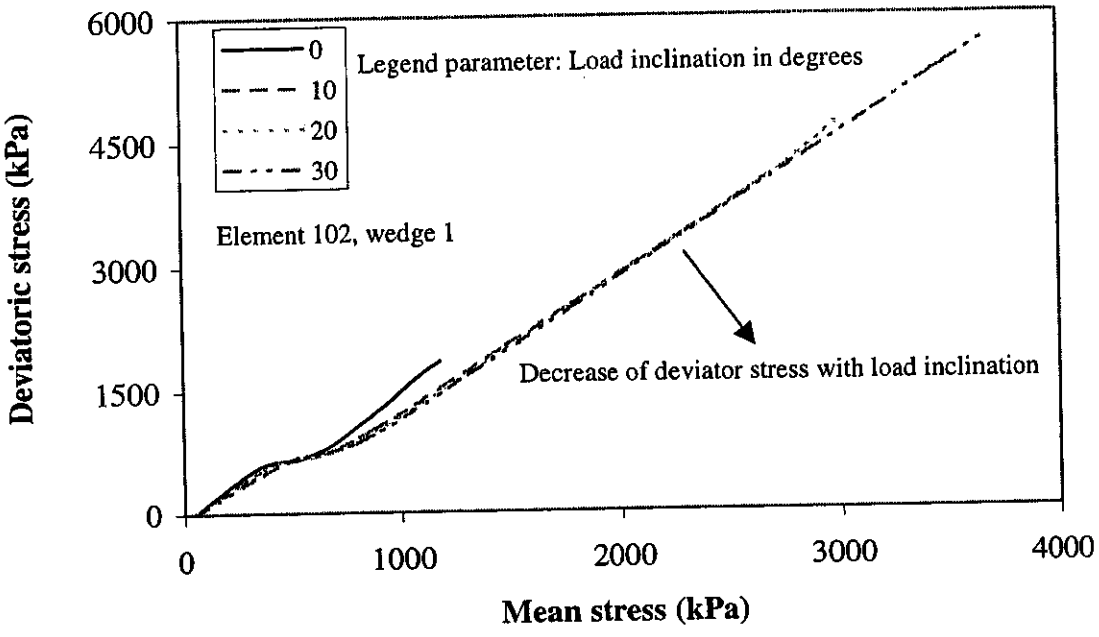

Figure 7.14 Average stress path in wedge 1, element 102 of circular footing

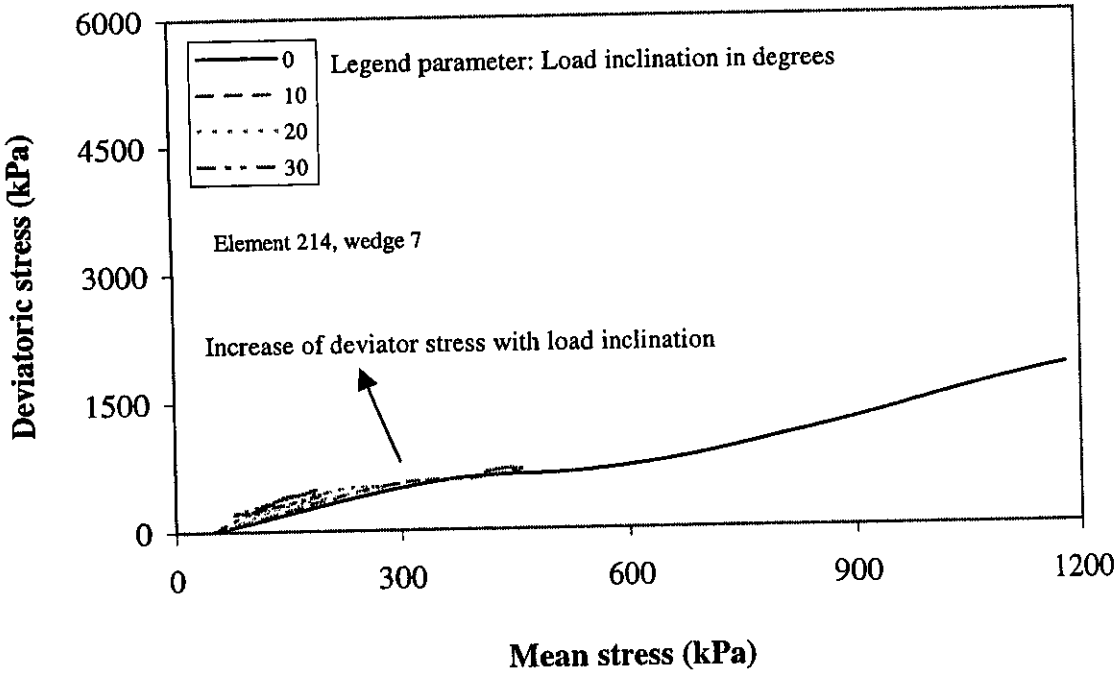

Figure 7.15 Average stress path in wedge 7, element 214 of circular footing

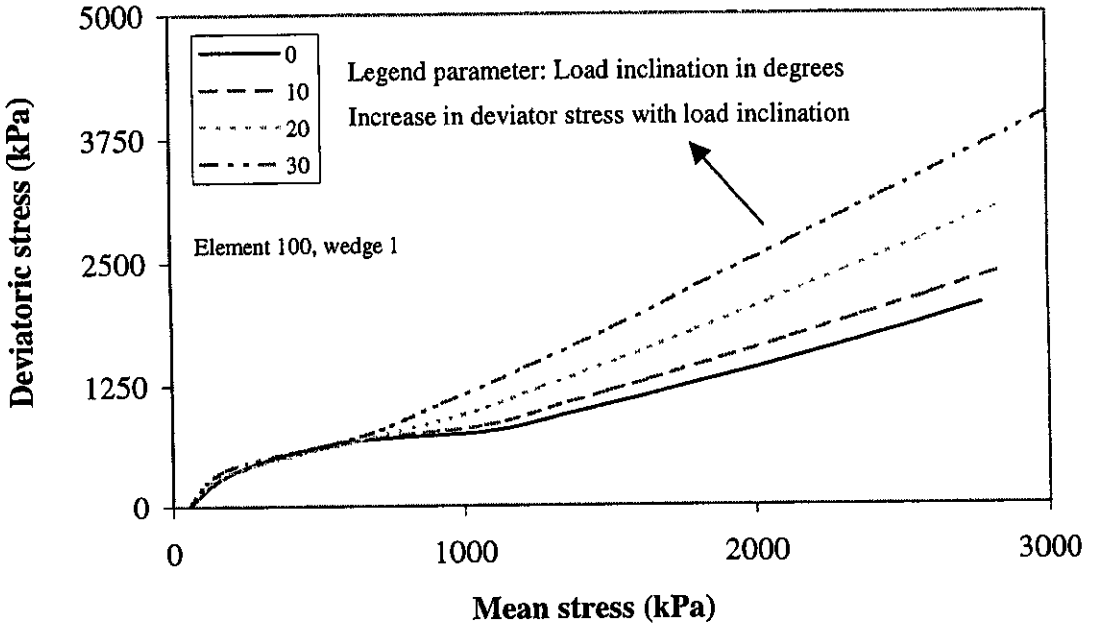

Figure 7.16 Average stress path in wedge 1, element 100 of circular footing

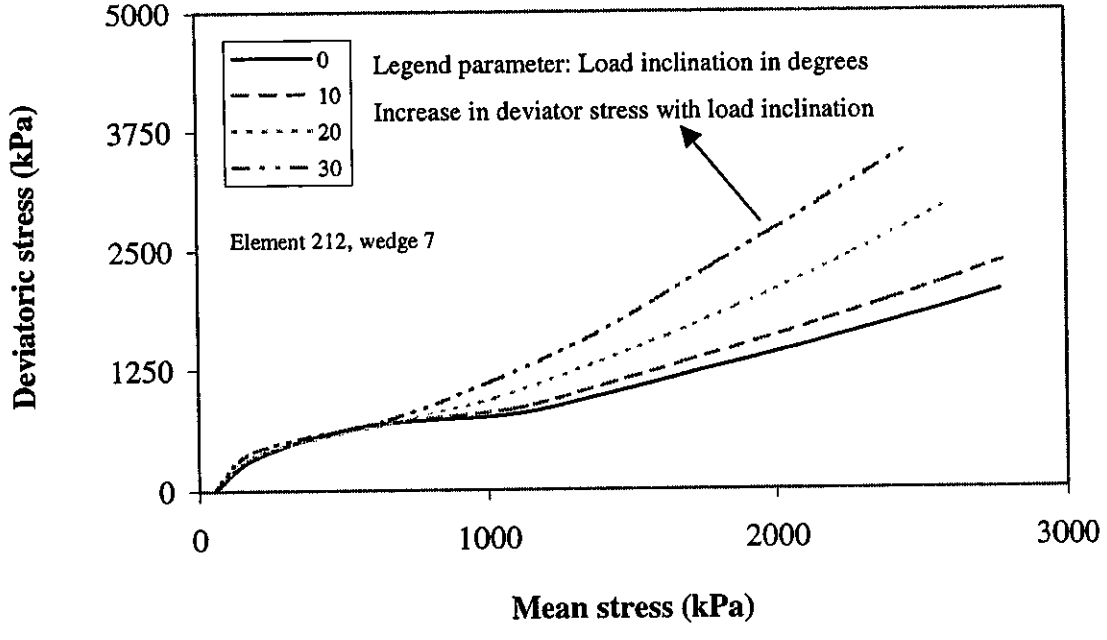

Figure 7.17 Average stress path in wedge 7, element 212 of circular footing

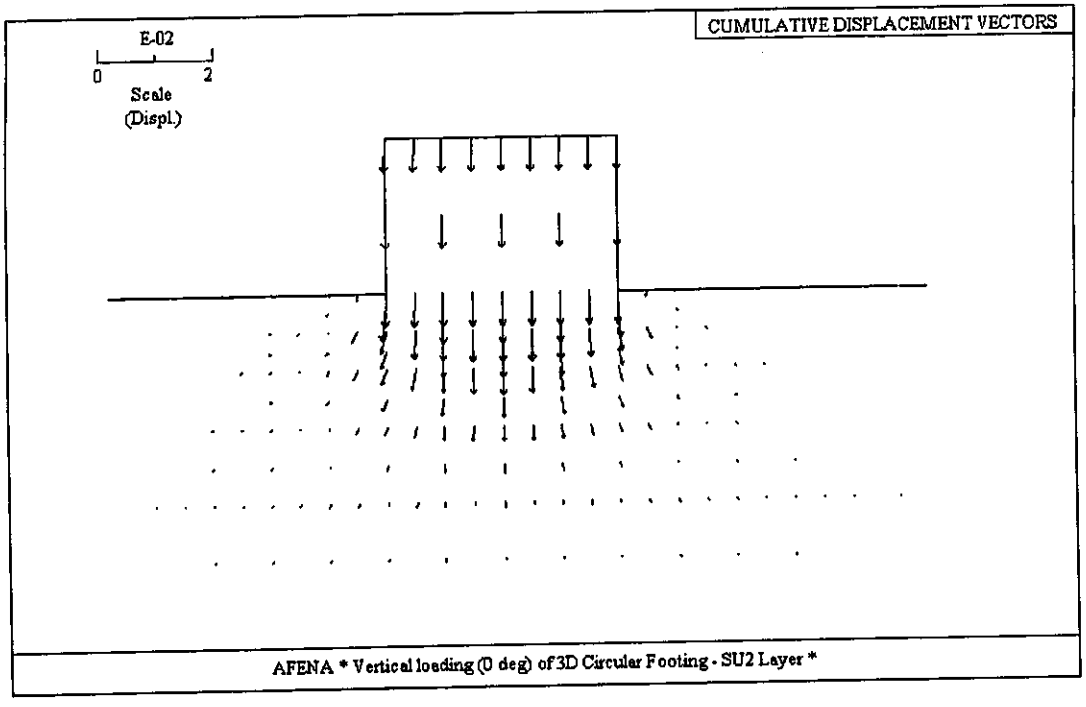

Figure 7.18 Cumulative nodal displacement vectors under vertical load

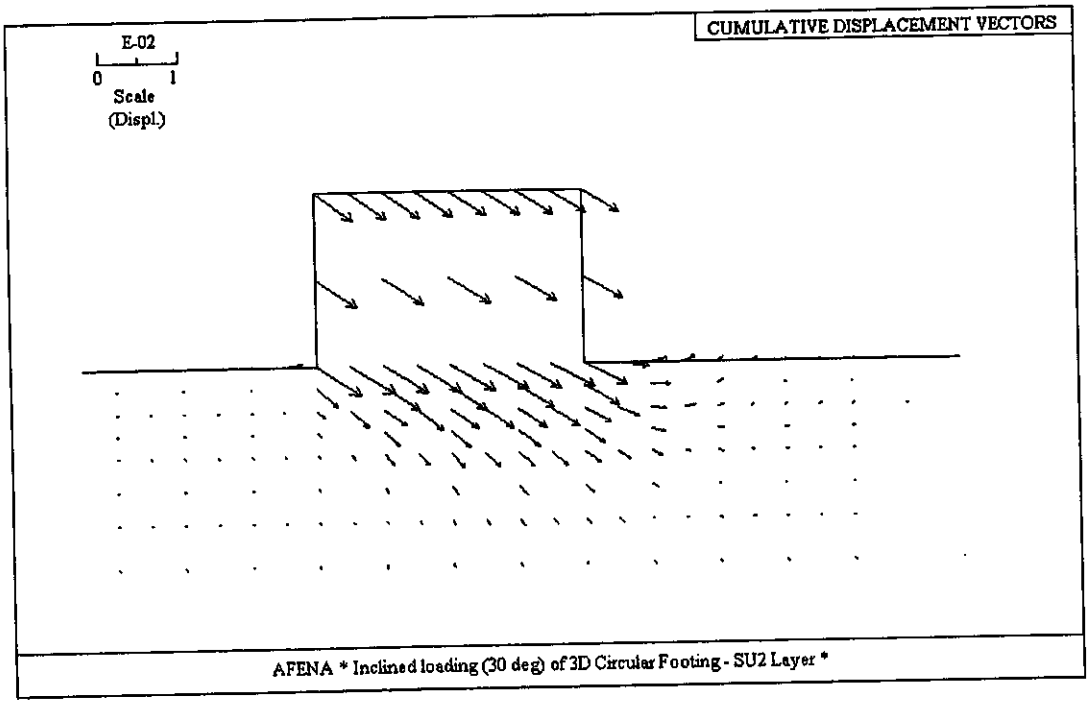

Figure 7.19 Cumulative nodal displacement vectors under inclined load

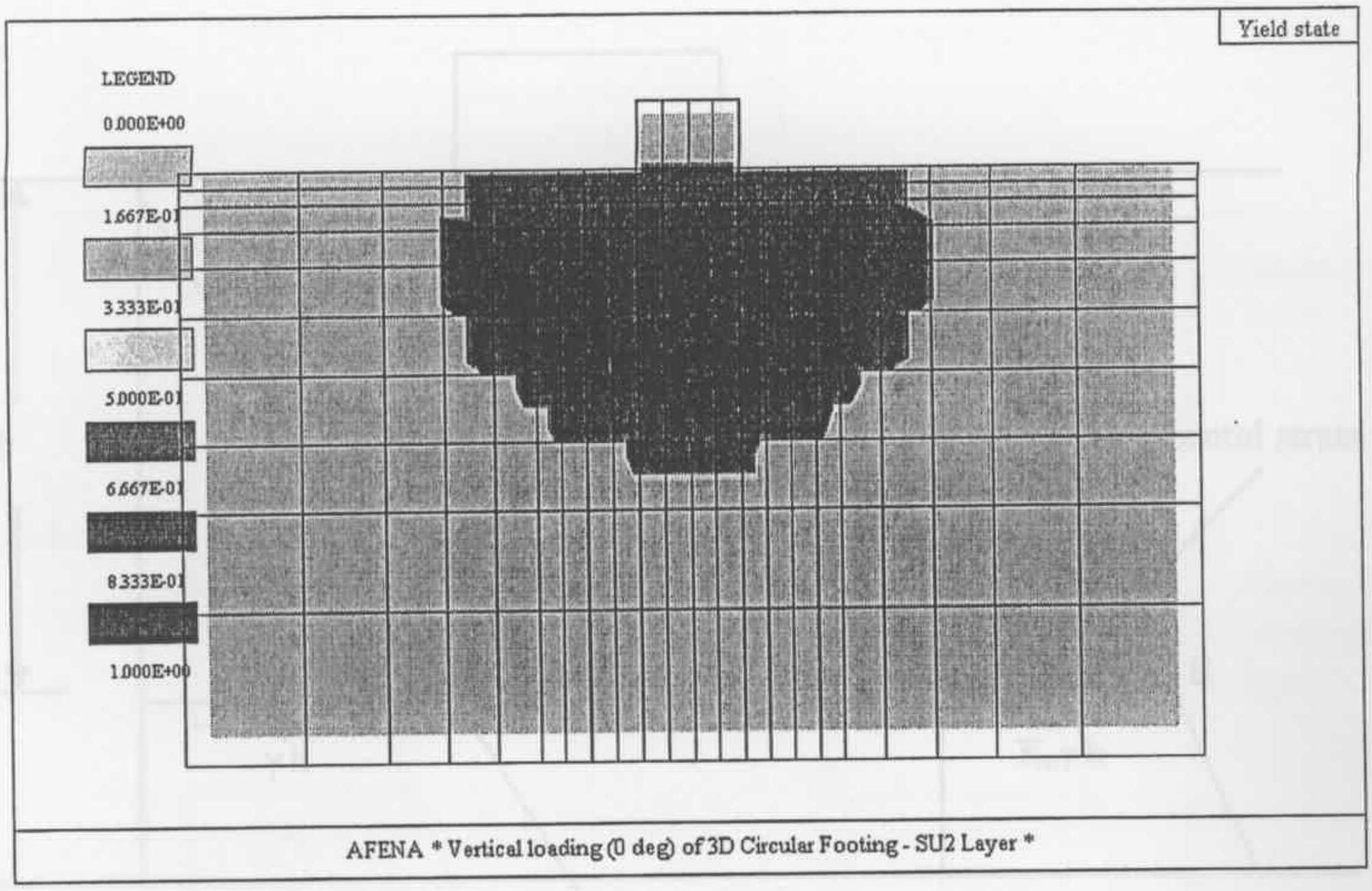

Figure 7.20 Yield zone at large displacement for vertical load of footing

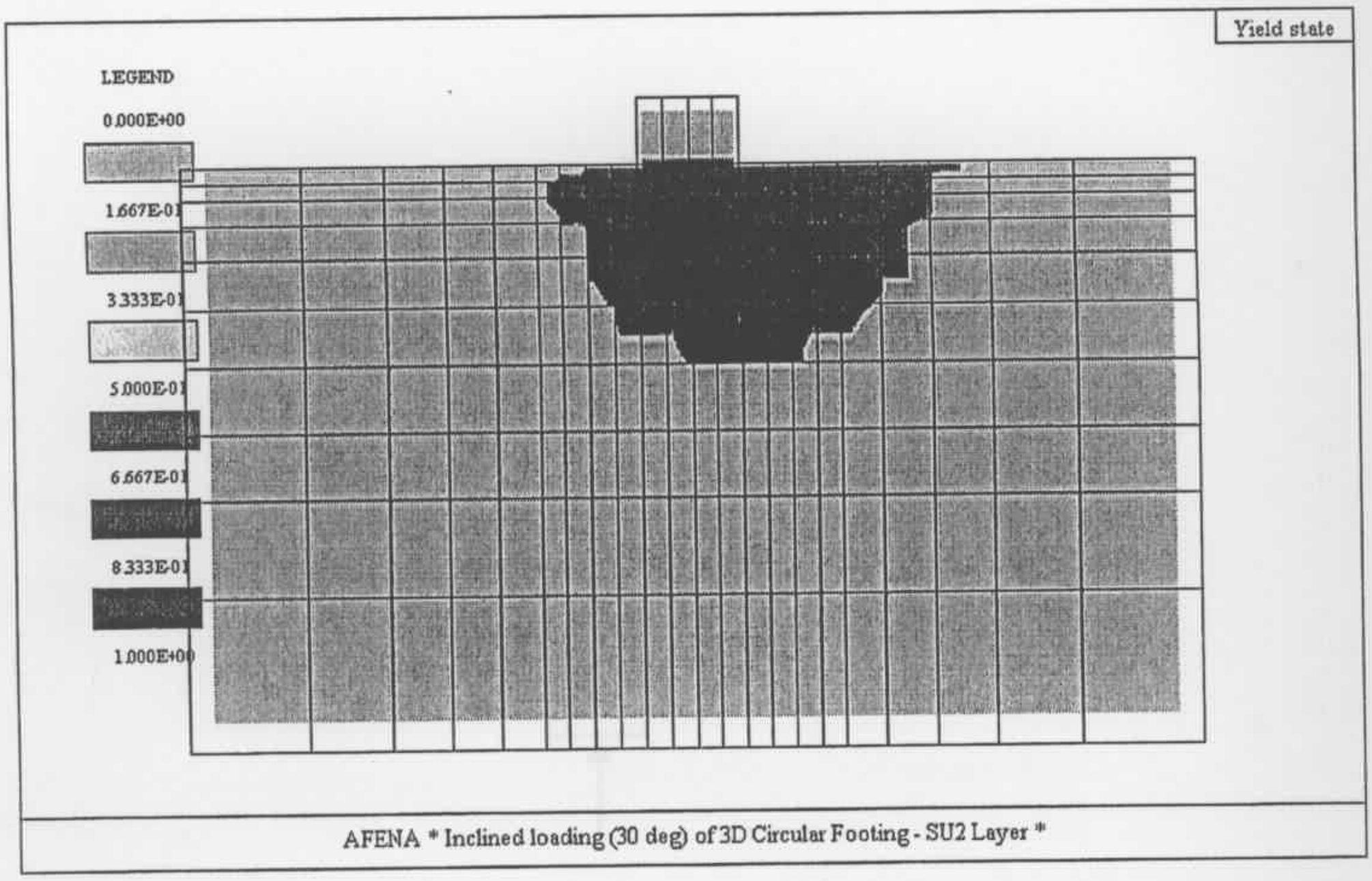

Figure 7.21 Shift of yield zone along loading plane for inclined load of footing

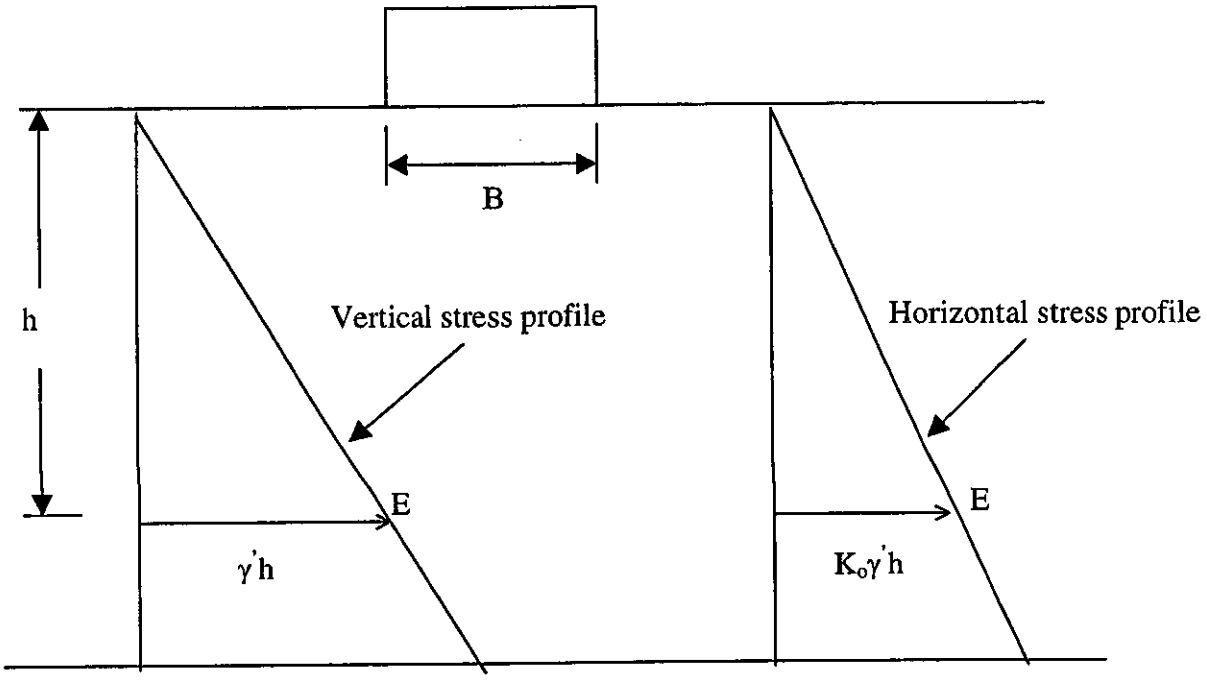

Figure 7.22 Profile of initial effective vertical and horizontal stress below surface circular footing

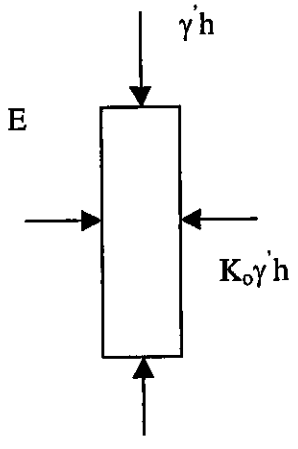

Figure 7.23 In-situ stress at any soil element at a depth *h* below footing

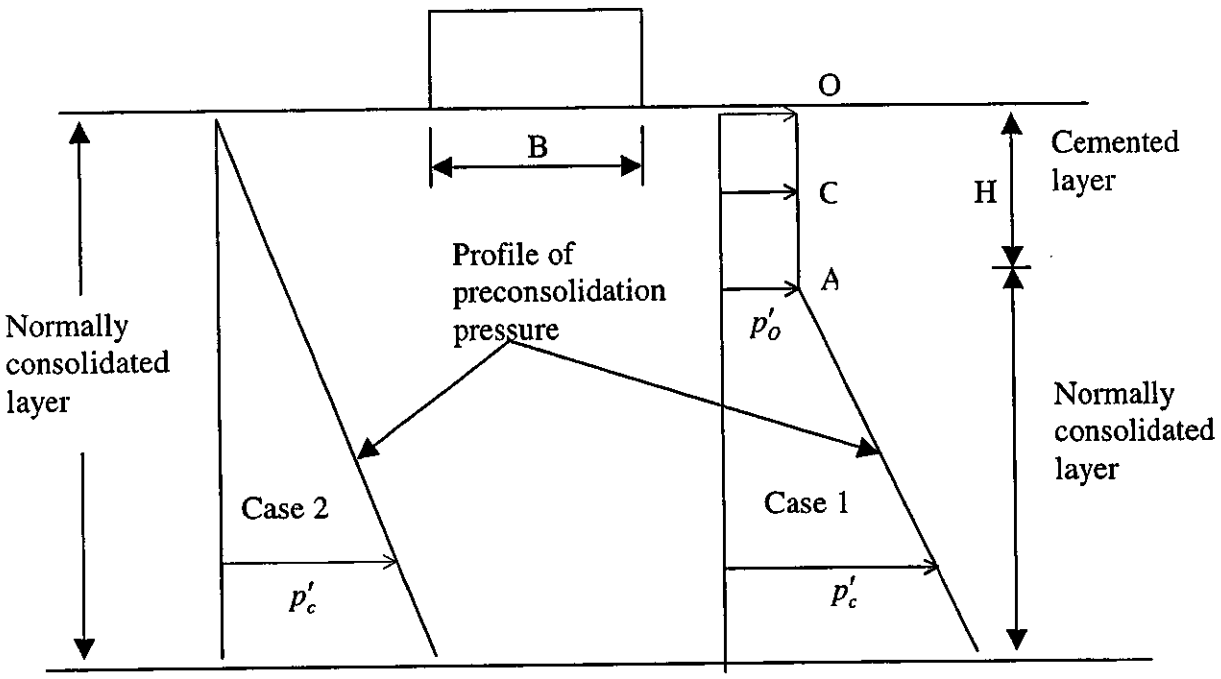

Figure 7.24 Assumed profiles of preconsolidation pressure below surface circular footing

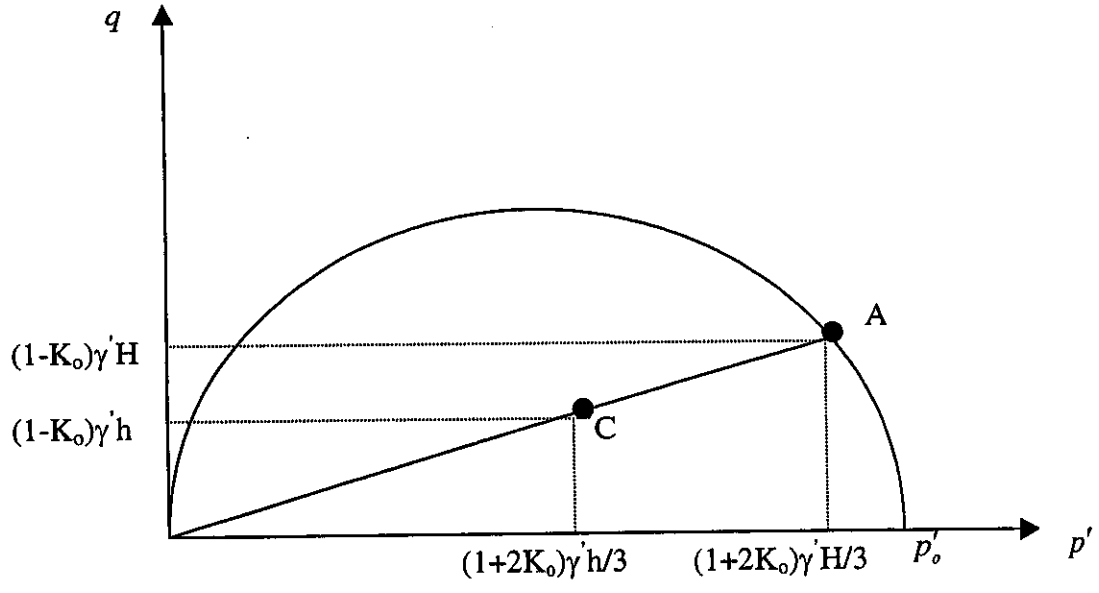

Figure 7.25 For soil profile in case 2, position of in-situ stress with respect to SU2 yield locus

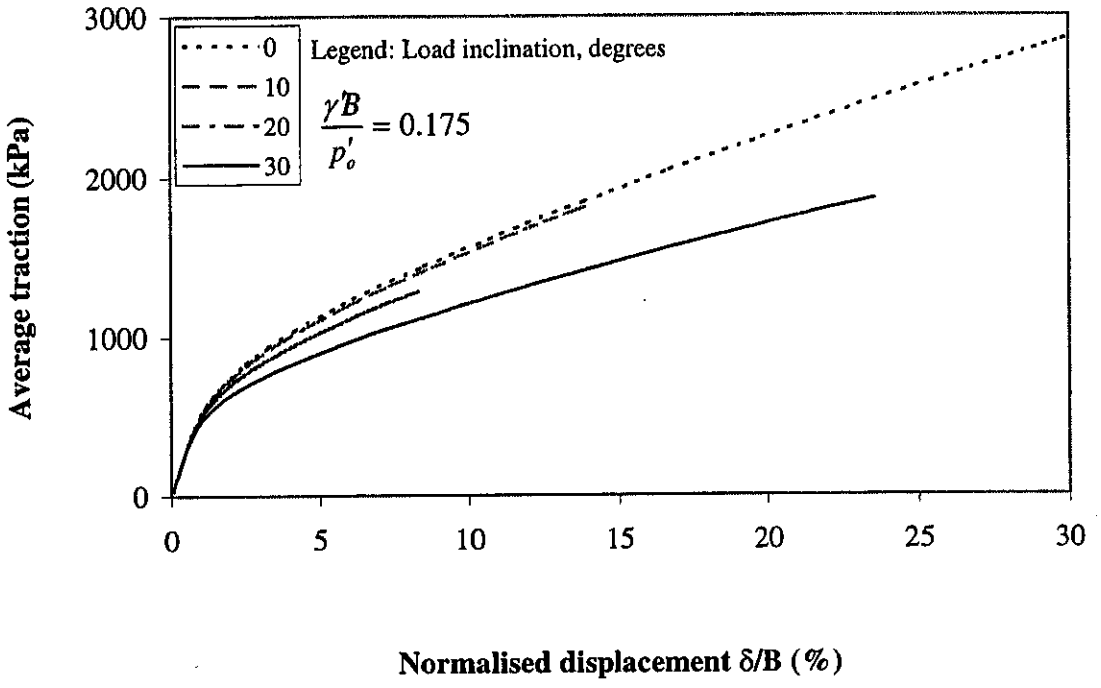

Figure 7.26 FE prediction of the behaviour of a 25m surface circular footing on overconsolidated carbonate sand subjected to inclined load

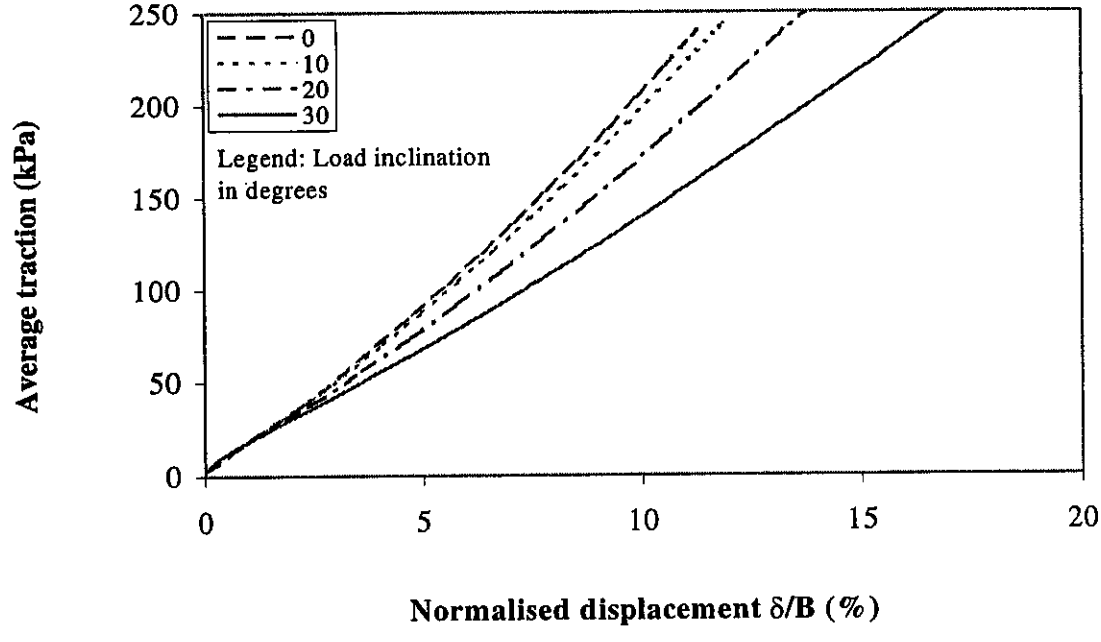

Figure 7.27 FE prediction of the behaviour of a 25m surface circular footing on normally consolidated carbonate sand subjected to inclined load

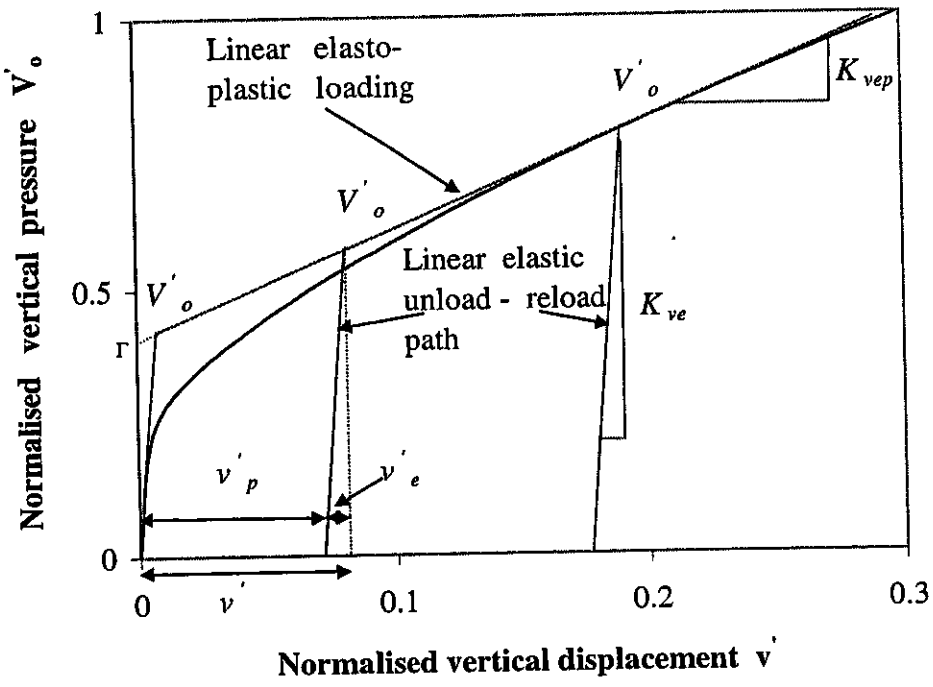

Figure 7.28 Idealised bilinear bearing pressure curve for circular footing on carbonate sand

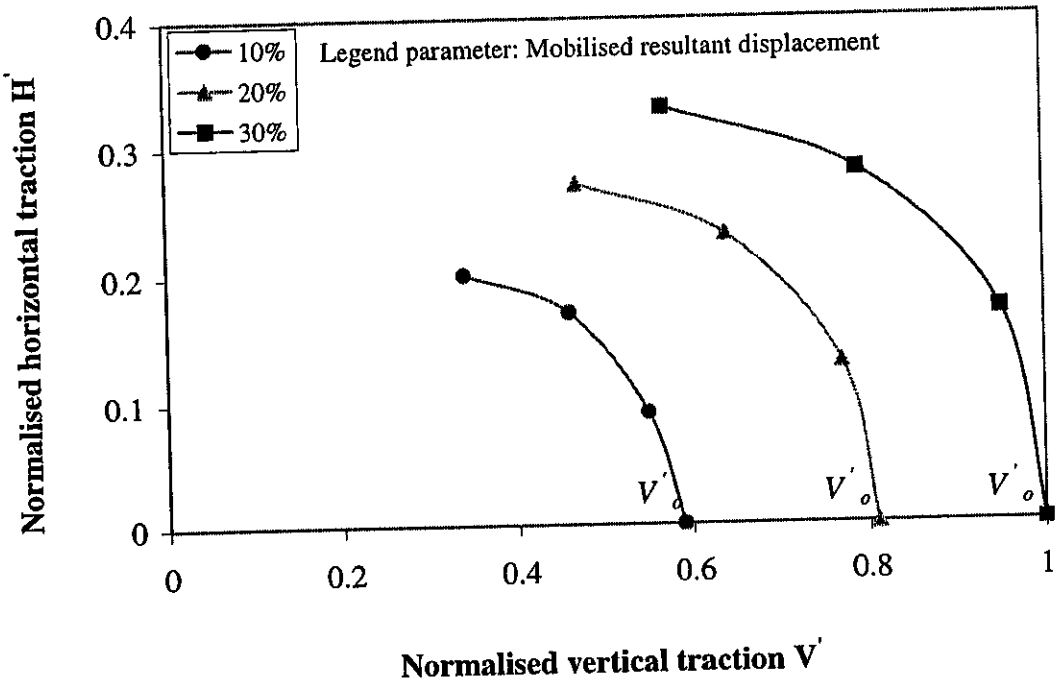

Figure 7.29 Contours of plastic resultant displacement obtained from 3D FE

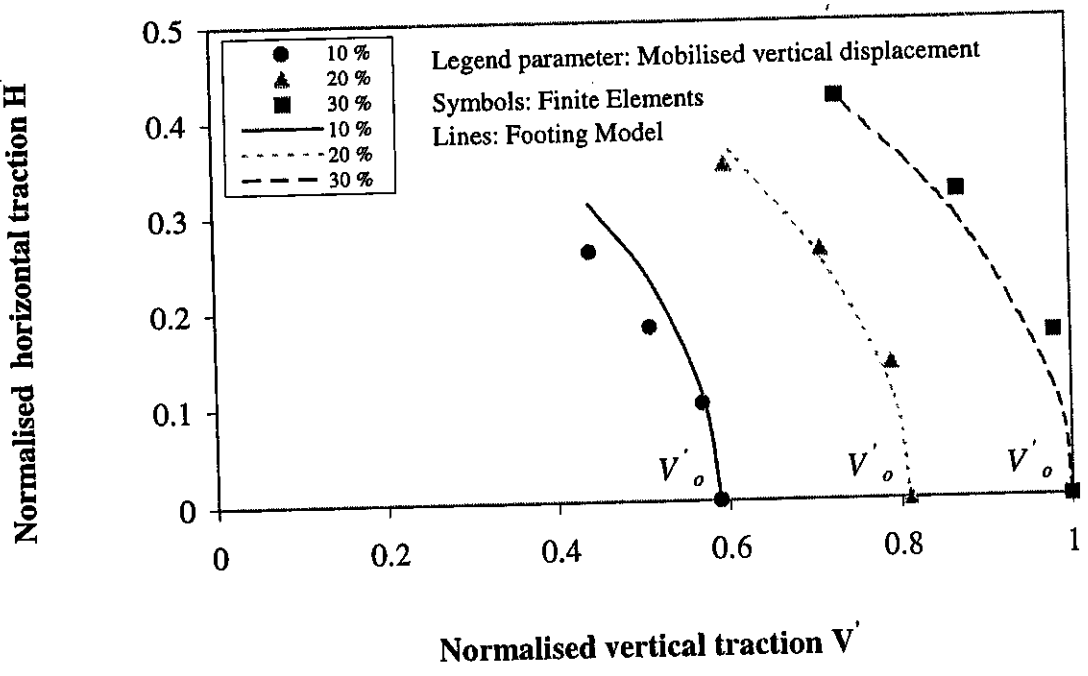

Figure 7.30 Comparison of proposed footing yield loci with contours of plastic vertical displacement obtained from 3D FE

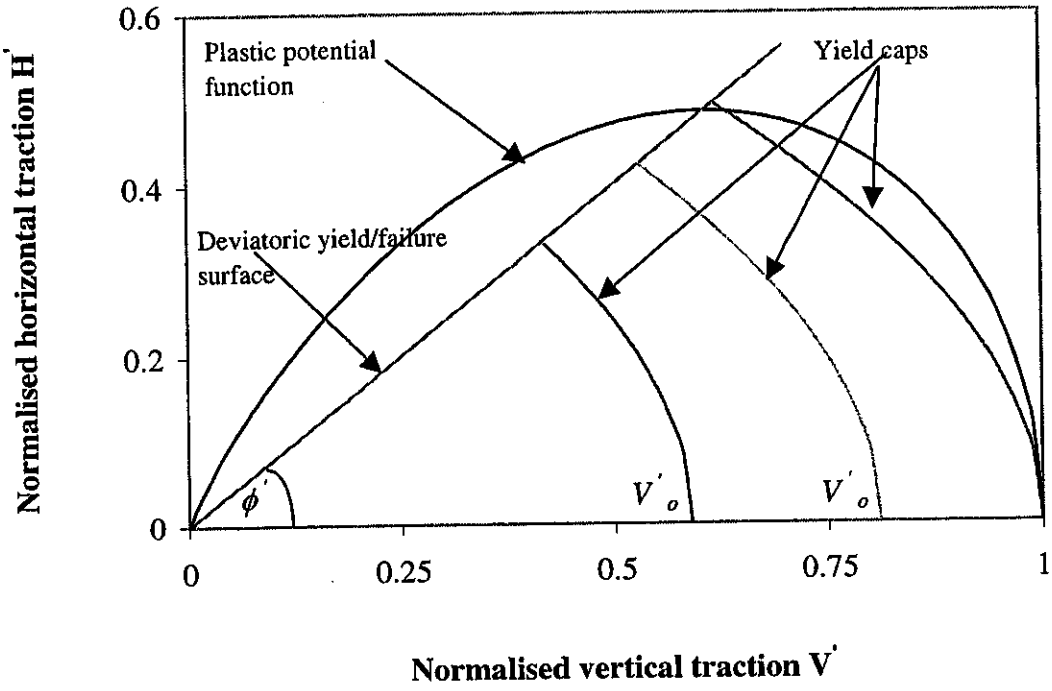

Figure 7.31Yield cap, deviator locus and plastic potential function (k=1) for proposed footing model

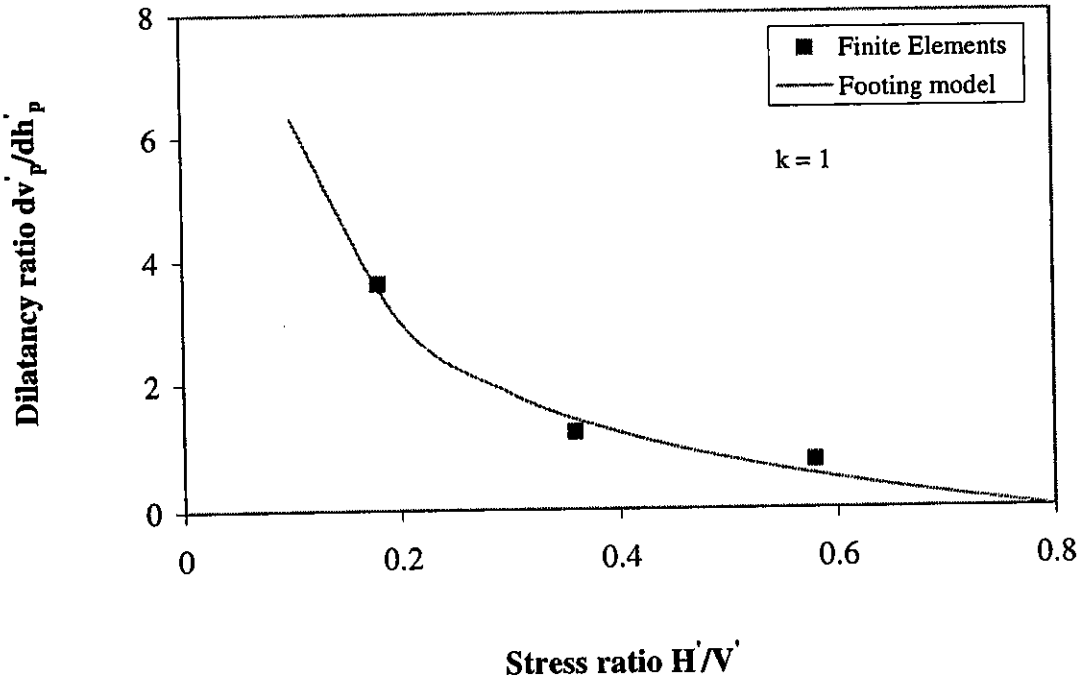

Figure 7.32 Comparison of footing model stress-dilatancy with results obtained from 3D FE simulation of model-scale footing

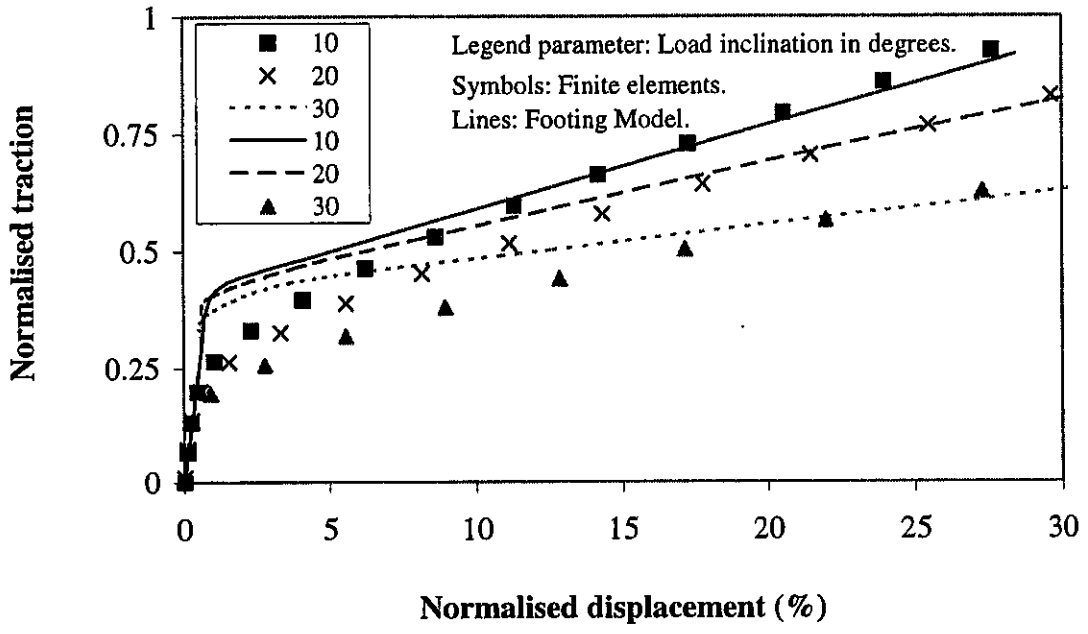

Figure 7.33 Comparison of footing model prediction with 3D FE prediction of the traction mobilised by a model-scale footing subjected to inclined load

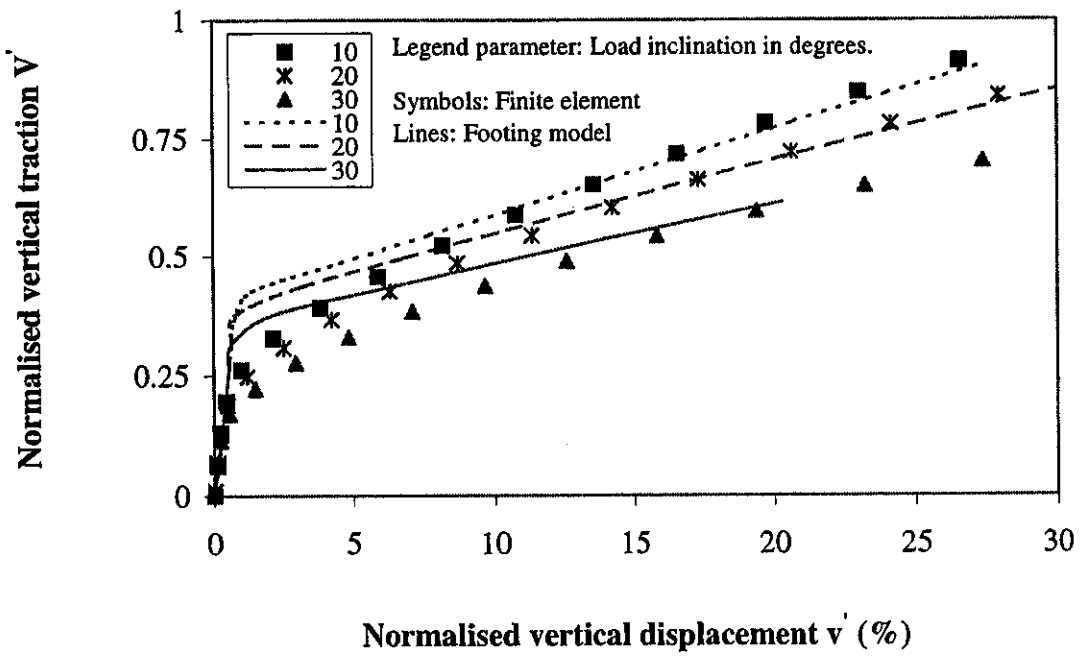

Figure 7.34 Comparison of footing model prediction with 3D FE prediction of the vertical bearing pressure mobilised by a model-scale footing

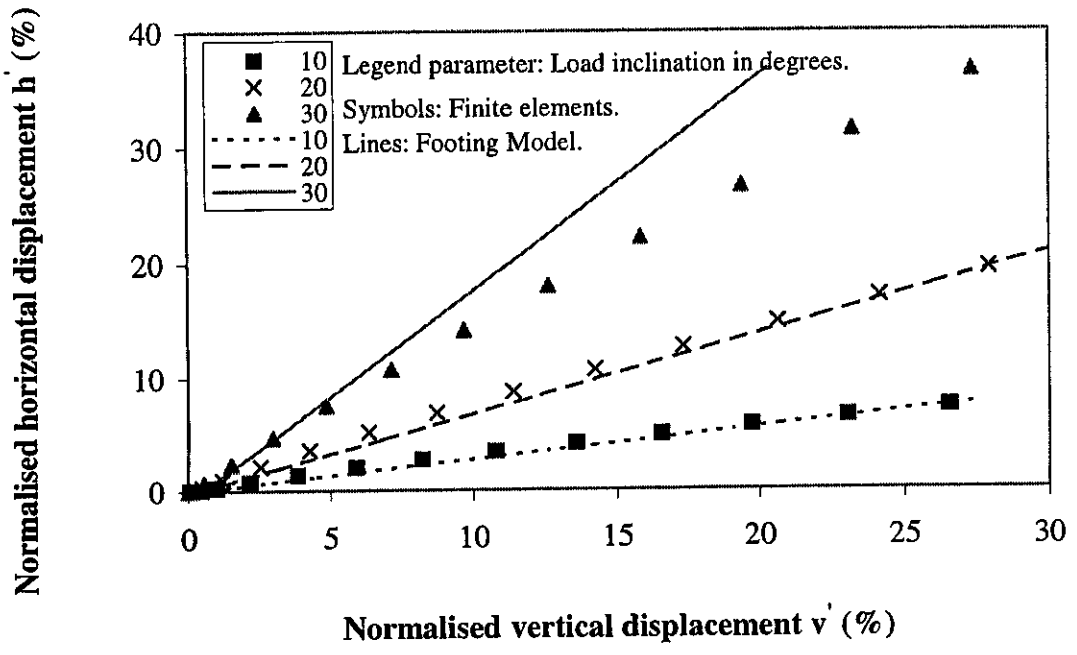

Figure 7.35 Comparison of footing model predictions with 3D FE predictions of the displacements mobilised by a model-scale footing

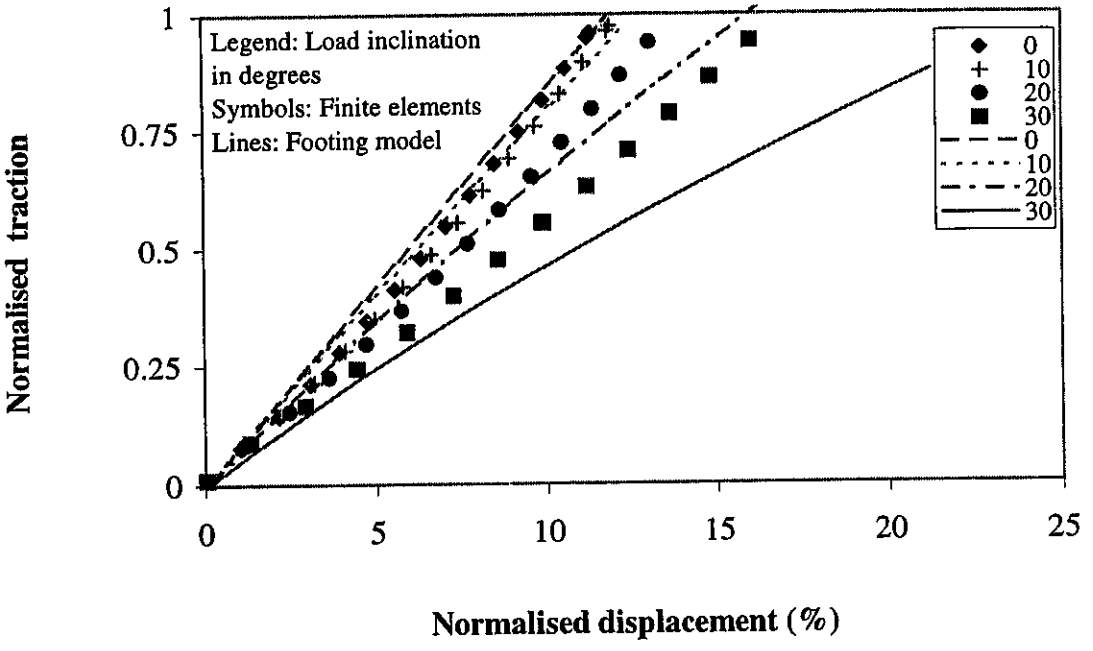

Figure 7.36 Comparison of footing model predictions with 3D FE predictions of the average traction mobilised by a 25m diameter surface circular footing

8

CONCLUSIONS

8.1 INTRODUCTION

A numerical study of constitutive behaviour of carbonate sand was carried out. Existing constitutive models based on the framework of critical state soil mechanics were used to simulate the triaxial response of carbonate sands under drained conditions. Two models were proposed. One of the proposed models was used in a finite element procedure to simulate the response of surface circular footings and footings embedded in carbonate sand. The model was also used in a semi-analytical three dimensional finite element procedure to simulate the response of circular footings on carbonate sand subjected to inclined load.

In this chapter, the results obtained and observations made from the numerical study regarding the triaxial behaviour of carbonate sands and the response of footings resting on these sands is summarised. Based on these observations, certain recommendations and propositions are put forward for further investigation of the stress-strain behaviour of carbonate sands and the response of footings on such sands.

8.2 CONCLUDING OBSERVATIONS

Several existing constitutive models based on critical state soil mechanics were used to simulate the triaxial response of carbonate sand under drained condition. It was observed that some of the existing models could predict reasonably well both the stress-strain and volume strain behaviour of carbonate sands. However, the Modified

Cam Clay model was unable to predict correctly the stress-strain and volume strain response of carbonate sands. Two models were proposed for carbonate sands as relatively simple modifications of the Cam Clay and Modified Cam Clay model respectively. In the proposed models, the yield locus of the Cam Clay and Modified Cam Clay model was scaled down using the spacing ratio parameter. The concept of spacing ratio is not new. However in the proposed models, a new approach was taken and the spacing ratio was used to determine the degree of difference between the yield locus and plastic potential function. A significant improvement was observed in predicting the yield locus, stress-strain and volume strain behaviour for uncemented carbonate sand using the proposed models. The volume compression behaviour of uncemented carbonates at a wide range of cell pressures could be rationally explained using the proposed models. The behaviour of dense artificially cemented carbonates was also well predicted by the proposed models. However, the yield loci, stress-strain and volume strain response of loose cemented samples was not well predicted using any of the existing critical state models including the ones proposed.

Using finite element analysis, several critical state models were used to simulate the pressure-displacement response of a model-scale circular footing resting on artificially cemented carbonate sand under drained conditions. It was observed that some of the existing critical state models, as well as those newly proposed, predict quite well both qualitatively and quantitatively, the drained pressure-displacement response of circular footings on carbonate sand. Contours obtained from finite element analysis show the displacements in the soil to be mostly in the vertically downward direction and concentrated in a small zone immediately below the footing. The displacement contours were consistent with observed experimental behaviour and those expected for a footing resting on a compressive non-dilational soil. It appears that strain hardening critical state models, which properly take into account the plastic stress-dilatancy and volume compression response exhibited by carbonate sand, predict reasonably well the pressure-displacement response of such footings under drained conditions.

It was observed that one of the proposed models chosen for detailed study in this thesis (called the SU2 model) could predict quite well the pressure-displacement response observed in centrifuge tests involving surface circular footings resting on

normally consolidated carbonate sand and silt under fully drained conditions. The SU2 model could also predict the centrifuge test results of surface circular footings resting on cemented carbonates underlain by normally consolidated carbonate sands. A parametric study of surface circular footings on normally consolidated carbonate sands was carried out using the SU2 model. The study shows plastic volumetric compressibility to have the significant influence on the drained pressure-displacement response of such footings. The parametric study, as well centrifuge test results, show that footing diameter has no significant effect on the pressure-displacement response of such footings.

A parametric study of surface circular footings and footings embedded in carbonate sand was carried out assuming an idealised profile of preconsolidation pressure to exist below the footing. It was assumed that the carbonate sand immediately below the footing has a uniform preconsolidation pressure. Below depths at which the soil self weight stresses touched the yield locus of the proposed model, the preconsolidation pressure was assumed to increase with depth, as for a normally consolidated soil. The parametric analysis shows that for the assumed soil profile, the footing diameter, preconsolidation pressure, unit weight, plastic compressibility, constant volume friction angle, spacing ratio and the void ratio constant all have some influence on the pressure-displacement response of surface circular footings. The Poisson's ratio appears to have an effect on footing behaviour only in the case of a strong elastic response, as expected. Similar observations were made for footings embedded in carbonate sand. It was observed that the response of both surface circular footings and footings embedded in carbonate sand could be approximated as bilinear curves. An outcome of the parametric study was the development of simplified design charts for circular footings on carbonate sand having an idealised soil profile. Design charts were also proposed for circular footings resting on normally consolidated carbonate sand. The proposed design charts can be used to obtain approximate pressure-displacement curves once the SU2 model parameters for the soil are known, without recourse to a finite element procedure.

The SU2 model was incorporated in a semi-analytical three dimensional finite element procedure to predict the response of circular footings resting on carbonate sand subjected to inclined load. It was observed that the SU2 model could predict

quite well the mobilised bearing resistance of circular footings resting on cemented carbonate sand. However, the prediction of the mobilised bearing resistance of circular footings resting on uncemented carbonate sand was not satisfactory. The exact reason for satisfactory predictions in one case and unsatisfactory predictions in the other could not be ascertained. A simplified footing model was proposed to predict the bearing resistance of a circular footing resting on carbonate sand. The simplified footing model could be used to predict the mobilised bearing resistance once the SU2 model parameters and the traction-displacement response of a footing under vertical load was known. The predictions of the simplified footing model were observed to agree reasonably well with the results of semi-analytical three dimensional finite element procedure.

8.3 RECOMMENDATIONS FOR FURTHER RESEARCH

The effects of cementation have been simulated in the proposed SU2 model by the increased preconsolidation pressure of cemented carbonate sands. A simple experimental approach is now proposed to investigate whether aspects of cementation other than the increase of preconsolidation pressure have a significant effect on the mechanical behaviour of cemented carbonates. It is proposed that uncemented carbonate sand should be isotropically consolidated to the same preconsolidation pressure as that assumed for the artificially cemented carbonate sands considered in the present study. Isotropic consolidation, triaxial shear and model-scale footing tests should then be conducted on these two sand samples. Such tests will show whether other aspects of cementation, such as change in shape and size of the yield loci in the deviator direction and breakdown of cementation with plastic strains, have a significant effect on the mechanical response of such sands. The test results will also indicate the significance of incorporating these aspects of cemented soil behaviour in the proposed SU2 or other critical state soil models.

The SU2 model could be modified to simulate in greater detail the triaxial response of cemented carbonate sands. The following modifications are suggested:

- modelling the increase in elastic stiffness within the yield locus using constant elasticity
- incorporating cohesion and tensile strength components within the yield locus that occurs with cementation
- incorporating the expansion in size and change in shape of the yield loci in the deviator direction that occurs with cementation.

The first two have been incorporated already in the model proposed by Lagioia and Nova (1993,1995) to simulate the triaxial response of highly cemented natural calcerinites. However, the increase in size and shape of the yield locus in the deviator direction with cementation is presumed to have a significant effect on its behaviour. These effects can be easily incorporated in the SU2 model using additional model parameters. It would be of interest to see what such modifications have on the predictions of the triaxial response of cemented and natural carbonates as well as on the behaviour of circular footings resting on such sands.

Breakdown of cementation could be incorporated in the SU2 model in a manner similar to that suggested by Lagioa and Nova(1993, 1995). It is assumed in these models that the yield locus shrinks in size with cementation breakdown. Additionally, it may be assumed that with cementation breakdown, the yield locus changes in shape and gradually approach the shape of the yield locus of uncemented carbonates. It may be interesting to simulate different rates of breakdown of cementation by appropriate modification of the SU2 model and observe its effects both on the triaxial response of cemented carbonates as well as on the behaviour of circular footings resting on these sands.

It was observed that the pressure-displacement response of surface circular footings resting on normally consolidated carbonate sands was approximately linear and the slope of this curve was primarily affected by the plastic volume compressibility of the sand. The behaviour of such footings could be investigated in greater detail in order to develop closed form solutions for the pressure-displacement curve of such footings.

Further parametric study may be carried out, both for surface circular footings and footings embedded in carbonate sand, using the SU2 model. Circular footings resting on soil profiles of practical interest other than those assumed here, and footings resting on layered media could also be investigated in greater detail.

Interface elements with separate constitutive properties could be introduced between the soil and footing to investigate the behaviour of circular footings on carbonate sand subjected to inclined load. The SU2 model could be used in the semi analytical 3D FE procedure to model the soil behaviour. This may help to simulate more appropriately the experimental behaviour of model-scale footings resting on carbonate sand and subjected to inclined load.

REFERENCES

Airey, D.W., Randolph, M.F., and Hyden, A.M. (1988). The strength and stiffness of two calcareous sands. Engineering for Calcareous Sediments, Jewell and Andrews (eds.), *Proceedings International Conference on Calcareous Sediments*, Perth, Vol. 1, Balkema, Rotterdam, pp. 43-50.

Allman, M.A. (1988). Piles in cemented calcareous soil, *Ph.D. thesis*, University of Sydney.

Allman, M.A. and Poulos, H.G. (1988). Stress-strain behaviour of an artificially cemented calcareous soil, Engineering for Calcareous Sediments, Jewell and Andrews (eds.), *Proceedings International Conference on Calcareous Sediments*, Perth, Vol. 1, Balkema, Rotterdam, pp. 51-60.

Allman, M.A., Poulos, H.G., Carter, J.P. and Yeung, S.K. (1988). Model footing tests on artificially cemented calcareous soil. *5th ANZ Conference on Geomechanics*, Sydney, Australia, pp. 268-272.

Atkinson, J.H. and Bransby, P.L. (1975). *The mechanics of soils – An introduction to critical state soil mechanics*, McGraw Hill, New York, NY, pp. 375.

Atkinson, J.H. and Little, J.A. (1988). Undrained triaxial strength and stress-strain charactersitics of a glacial till, *Canadian Geotechnical Journal*, Vol. 25, pp. 428-439.

Balmer, G.G. (1958). Strength and elastic properties of soil cement mixtures under triaxial loading, *ASTM Proc. 58*, pp. 1187-1204.

Been, K and Jefferies, M.G. (1985). A state parameter for sands. *Geotechnique* 35, No. 2, pp.99-112.

Boey, C.Y. (1990). Modelling of the behaviour of natural calcerinite, *Ph.D. thesis*, School of Civil and Mining Engineering, University of Sydney, Australia.

Butterfield, R. and Gottardi, G. (1994). A complete three dimensional failure envelope for shallow footings on sand. *Geotechnique* 44, No. 1, pp. 181-184.

Brown, E.T. and Yu, H.S. (1988). A model for the ductile yield of porous rock. *International Journal for Numerical and Analytical Methods in Geomechanics*, Vol 12, pp. 679-688.

Carter, J.P. and Balaam, N.P. (1995). *AFENA - A Finite Element Numerical Algorithm*, Users' Manual, Centre for Geotechnical Research, University of Sydney.

Carter, J.P., Booker, J.R. and Yeung, S.K. (1986). Cavity expansion in cohesive frictional soils. *Geotechnique 36*, pp. 349-358.

Carter, J.P., Johnston, I.W., Fahey, M., Chapman, G.A., Novello, E.A. and Kaggwa, W.S. (1988). Triaxial testing of North Rankine calcerinite, Engineering for Calcareous Sediments, Jewell and Andrews (eds.), *Proceedings International Conference on Calcareous Sediments*, Perth, Vol. 2, Balkema, Rotterdam, pp. 515-530.

Carter, J.P and Yeung, S.K. (1985). Analysis of cylindrical cavity expansion in strain-weakening materials. *Computers Geotech.*, 1, pp. 161-180.

Casagrande, A. (1936). Determination of the preconsolidation load and its practical significance, *Proceedings 1st ICSMFE*, Cambridge, Massachussets, Vol. pp 60-64.

Chen, W.F. and Mizuno, E. (1990). *Nonlinear analysis in soil mechanics*, Elsevier Science Publishers B.V., New York, USA.

Chiu, H.K. and Johnstone, I.W. (1984). The application of critical state concepts to Melbourne mudstone. *4th ANZ Conference on Geomechanics*, Vol. 1, pp. 107-120.

Clough, G.W., Sitar, N., Bachus, R.G. and Reed, N.S. (1981). Cemented sand under static loading. *Journal of Geotech. Engg. Div.*, ASCE, Vol. 107, GT6, pp. 797-817.

Coop, M.R. (1990). The mechanics of uncemented carbonate sands, *Geotechnique 40*, No. 4, pp. 607-626.

Coop, M.R. and Atkinson, J.H. (1993). The mechanics of cemented carbonate sands, *Geotechnique 43*, No. 1, pp. 53-67.

Datta, M., Gulhati, S.K. and Rao, G.V. (1980b). An appraisal of the existing practice of determining the axial load capacity of deep penetration piles in calcareous sands. *Proceedings 12th Annual Offshore Technical Conference*, Houston, Paper No. OTC 3867, pp. 119-130.

de Borst, R. and Vermeer, P.A. (1984). Possibilities and limitations of finite elements for limit analysis, *Geotechnique 34*, No. 2, pp. 199-210.

de Borst, R. and Vermeer, P.A. (1982). Finite element analysis of static penetration tests, *Proc. 2nd Eur. Symp. Penetration Testing (eds. A. Verruijt, F.L. Beringen and E. H. de Leeuw)*, pp. 457-462, Balkema, Rotterdam.

Di Prisco, C., Matiotti, R. and Nova, R. (1992). A mathematical model of grouted sand behavior. *Proceedings 4th International Symposium on Numerical Models in Geomechanics*, pp. 25-35. Rotterdam, Balkema

Dimaggio, F.L. and Sandler, I.S. (1971). Material model for granular soils. *Journal. ff Engineering Mechanics. Division.*, ASCE, 97(EM3), pp. 935-950.

Drescher, A. Birgison, B. and Shah, K. (1995). A model for water saturated loose sand. In G.N. Pande and S. Pietrusczak (eds.), *Proc. of the 5th International Conference in Geomechanics*, A.A. Balkema, Rotterdam, pp. 109-112.

Drucker, D.C. (1959). A description of stable inelastic material. *Jour. Appl. Mech.*, 26, pp. 101-126.

Drucker, D.C. (1956). On uniqueness in the theory of plasticity. *Quart. Appl. Math*, 14, pp. 35-42.

Drucker, D.C. and Prager, W. (1952). Soil mechanics and plasticity analysis or limit design. *Quart. Appl. Math.*, 10(2): pp. 157-175.

Elliot, G.M and Brown, E.T. (1986). Yield of a soft high porosity rock, *Geotechnique 33*, No. 4, pp. 413-433.

Finnie, I.M.S. (1993). Performance of shallow foundations in calcareous soils, *Ph.D. thesis*, The University of Western Australia.

Finnie, I.M.S. and Randolph, M.F. (1994). Punch through and liquefaction induced failure of shallow foundations on calcareous sediments, *Research Report No. G1126*, Geomechanics Group, Department of Civil Engineering, University of Western Australia.

Fookes, P.F. and Higginbottom, I.E. (1975). The classification and description of near-shore carbonate sediments for engineering purposes, *Geotechnique*, Vol. 25, pp. 406-411.

Fookes, P.F. (1988). The geology of carbonate soils and rocks and their characterisation and description. *Engineering for Calcareous Sediments, Jewell and Andrews (eds.), Proceedings International Conference on Calcareous Sediments*, Perth, Vol. 2, Balkema, Rotterdam, pp. 787-806.

Frantziokonis, G., Desai C.S. and Somasundaram, S. (1986). Constitutive model for non-associative behaviour, *Journal of Engineering Mechanics*, Vol. 112, No. 9, pp. 932-946.

Gens, A. and Nova, R. (1993). Conceptual bases for a constitutive model for bonded soils and weak rocks. *Proceedings of the International Symposium on Geotechnical Engineering of Hard Soils-Soft Rocks*, pp. 485-494. Rotterdam, Balkema.

Gens, A. and Potts, D.M. (1988). Critical state models in computational Geomechanics, *Engineering computations*, Vol. 5, pp. 178-197.

Georgiadis, M. and Butterfield, R. (1988). Displacement of footings on sand under eccentric and inclined loads. *Canadian Geotechnical Journal*, 25, 199-212.

Gottardi, G. and Butterfield, R. (1994). A complete three-dimensional failure envelope for shallow footings on sand. *Geotechnique* 44, No. 1, pp. 181-184.

Gottardi, G. and Butterfield, R. (1993). On the bearing capacity of surface footings on sand under general planar loads. *Soils and Foundations*, Vol. 33, No, 3, pp. 68-79.

Goudoever, P., Deane, R.B., Shade, D.S. and Sharp, D.E. (1988). Development and implementation of plate load tests. Engineering for Calcareous Sediments, Jewell and Andrews (eds.), *Proceedings International Conference on Calcareous Sediments*, Perth, Vol. 2, Balkema, Rotterdam, pp. 463-472.

Griffiths, D.V. (1982). Elastoplastic analysis of deep foundations in cohesive soil, *International Journal for Numerical and Analytical Methods in Geomechanics*, Vol. 6, pp. 211-218.

Hanna, A.M. and Meyerhoff C.G. (1981) Experimental evaluation of bearing capacity of footings subjected to inclined loads. *Canadian Geotechnical Journal*, Vol.18, pp. 599-603.

Hansen, J.B. (1970). A revised and extended formula for bearing capacity. *Danish Geotechnical Institute*, Copenhagen, Denmark, Bulletin 28, pp.5-11.

Henkel, D.J. (1960). The relationship between water content and effective principal stress in saturated clays, *Geotechnique 10*, pp. 41-54.

Hicks, M. A. (1990). Numerically modelling the stress-strain behaviour of soils, *Ph.D. thesis*, University of Manchester.

Huang, J.T. (1994). The effect of density and cementation on cemented sands, *Ph.D. thesis*, University of Sydney, Australia.

Huang, J.T. and Airey, D.W. (1998). Properties of artificially cemented carbonate sand. *Journal of Geotechnical and Geoenvironmental Engineering*, Vol. 124, No. 6, pp. 492-499.

Hull, T.S., Poulos, H.G. and Alehossein, H. (1988). The static behaviour of calcareous sediments. *Engineering for Calcareous Sediments, Jewell and Andrews (eds.), Proceedings International Conference on Calcareous Sediments*, Perth, Vol. 1, Balkema, Rotterdam, pp. 87-96.

Jefferies, M.G. (1993). Nor-Sand: A simple critical state model for sand. *Geotechnique* 43, No. ?, pp. 92-103.

Kavvadas, M., Anagnostopoulos, A. and Kalteziotis, N. (1993). A framework for the mechanical behaviour of cemented Corinth marl. *Geotechnical Engineering of Hard Soils-Soft Rocks*, Anagnostopoulos et al (eds.), 1993, Balkema, Rotterdam, pp. 577-583.

Kim, M.K. and Lade, P.V. (1988). Single hardening constitutive model for frictional materials, I: Plastic potential function, *Computers and Geotechnics*, Vol. 5, No. 4, pp. 307-324.

King, R. and Lodge, M. (1988). North West Shelf development – The foundation engineering challenge. Engineering for Calcareous Sediments, Jewell and Andrews (eds.), *Proceedings International Conference on Calcareous Sediments*, Perth, Vol. 2, Balkema, Rotterdam, pp. 333-342.

Ladanyi, B. (1967). Expansion of cavities in a brittle media. *International Journal of Rock Mechanics and Mining Science*, Vol. 4, pp. 301-328.

Lade, P.V. (1977). Elastoplastic stress-strain theory for cohesionless soils with curved yield surfaces. *Int. Jour. Of Solids and Structures*, Vol. 13, No. 11, pp. 1019-1035.

Lade, P.V. and Duncan, J.M. (1976). Stress path dependent behaviour of cohesionless soils. *Journal of Geotechnical Engineering Division*, ASCE, Vol. 102, No. 1, pp. 51-56.

Lade, P.V. and Duncan, J.M. (1975). Elastoplastic stress-strain theory for cohesionless soil. *J. Geotech. Engg. Div.*, ASCE, 101(GT10), pp. 1037-1053.

Lade, P.V. and Duncan, J.M. (1973). Cubical triaxial tests on cohesionless soils. *J. Soil Mech. And Found. Div.*, ASCE, 99(SM10), pp. 793-812.

Lade, P.V. and Kim, M.K. (1988a): Single hardening constitutive model for frictional materials, III: Comparison with experimental data, *Computers and Geotechnics*, Vol. 6, No. 1, pp. 30-47.

Lade, P.V., Nelson, R.B. and Ito, Y.M. (1988). Instability of granular materials with non-associated flow. *Journal of Engineering Mechanics*, Vol. 114, No. 12, pp. 2173-2191.

Lade, P.V. and Prabucki, M. (1995). Softening and preshearing effects in sand, *Soils and Foundations*, Vol. 35, No. 4, pp. 93-104.

Lagioia, R. and Nova, R. (1995). An experimental and theoretical study of the behaviour of a calcerinite in triaxial compression. *Geotechnique 45*, No. 4, pp. 633-648.

Lagioia, R. and Nova, R. (1993). A constitutive model for soft rocks. *Geotechnical Engineering of Hard Soils-Soft Rocks*, Anagnostopoulos et al (eds.), 1993, Balkema, Rotterdam,pp. 625-632.

Lai, J.Y. and Booker, J.R. (1991). Application of discrete Fourier series to the finite element stress analysis of axisymmetric solids. *International Journal of Numerical Methods in Engineering.*, 31, 619-647.

Lama, R.D. and Vutukuri, V.S. (19780. *Handbook on mechanical properties of rocks*, Vol. 2, TransTech Clansthal, Germany.

Liu, M.D., Carter, J.P. and Airey, D.W., (1996). A plasticity model for cemented carbonate sediments, *2nd International Conference on Soft Soil Engineering*, Nanjing.

Matsuoka, H. (1976). On the significance of the spatial mobilized plane. *Soils and Foundations*, Vol. 16, No. 1. Japanese Society of Soil Mechanics and Foundation Engineering.

Matsuoka, H. and Nakai, T. (1974). Stress deformation and strength characteristics of soil under three different principal stresses, *Proceedings of the JSCE*, No. 232.

McClelland, B. (1988). Calcareous sediments: an engineering enigma, Opening Address. *Proceedings International Conference on Calcareous Sediments*, Perth, Australia, Vol. 2, pp. 777-786.

Meyerhoff, C.G. (1963). Some recent research on the bearing capacity of foundations. *Canadian Geotechnical Journal*, 1, No. 1, pp. 16-26.

Meyerhoff, C.G. (1953). The bearing capacity of footings under eccentric and inclined loads. *Proceedings 3 rd ICSMFE*, Zurich, pp. 440-445.

Molenkamp, F. (1981). Elasto-plastic double hardening model MONOT. *LGM Report Co- 218595: Delft Geotechnics.*

Montrasio, L. and Nova, R. (1988). Assestamenti di una fondazione modello sotto carico inclinato: risultati sperimentali e modellazione matematica. *Rivista Italiana di Geotechnica*, 22, No. 1, pp. 35-50.

Nova, R. (1988). Sinofonietta classica: An exercise on classical soil modelling. *Constitutive equations for granular non-cohesive soils.* Saada and Bianchini (eds.), Balkema, Rotterdam, pp. 501-519.

Nova, R. (1992). Mathematical modelling of natural and engineered geomaterials. *General Lecture, 1st E.C.S.M. Munchen, Eur. J. Mech. A/Solids,* 11, Special Issue, pp. 135-154.

Nova, R. and Montrasio, L. (1991). Settlements of shallow foundations on sand. *Geotechnique* 41, No. 2, pp. 243-256.

Nova, R. and Wood, D.M. (1979). A constitutive model for sand. *Int. Jour. Num. and Analy. Meth. Geomech.*, Vol. 3, pp. 255-278.

Nova, R. and Wood, D.M. (1978). An experimental program to define yield function for sands. *Soils and Foundations*, Vol. 18(4), pp. 77-86.

Novello, E.A. (1988). Geomechanics and the critical state, *Ph.D. thesis*, Civil Engineering Department, Monash University.

O'Rourke, T.D. and Crespo, E. (1988). Geotechnical properties of cemented volcanic soil, *Journal of Geotechnical Engineering*, Vol. 114, No. 10, pp. 1126-1147.

Pan, J.P. (1999).The behaviour of shallow foundations on calcareous soil subjected to inclined load, *Ph.D. thesis (submitted)*, University of Sydney.

Pastor M., Zienkiewicz, O.C. and Chan, A.H.C. (1990). Generalized plasticity and modeling of soil behavior. *International Journal for Numerical and Analytical methods in Geomechanic*s, Vol. 14, pp. 151-190.

Pastor, M., Zienkiewicz, O.C., Chan, A.H.C. (1988). Generalized plasticity model for three-dimensional sand behaviour. *Constitutive equations for granular non-cohesive soils*, Saada and Bianchini (eds.), pp. 535-549. Rotterdam, Balkema.

Pastor, M., Zienkiewicz, O.C., Dou, X.G. (1992). Constitutive modeling of sand behaviour. *Numerical models in Geomechanics*, Pande and Pietruszczak (eds.), pp. 15-23. Rotterdam, Balkema.

Pestana, J.M. and Whittle, A.J. (1995). Compression model for cohesionless soils, *Geotechnique 45*, No.4, pp. 611-631.

Pooroshasb, H.B., Holubec, I. And Sherbourne, A.N. (1967). Yielding and flow of sands in triaxial compression: Parts II and III, *Canadian Geotechnical Journal*, Vol. IV, No. 4, pp. 376-397.

Pooroshasb, H.B., Holubec, I. and Sherbourne, A.N. (1966). Yielding and flow of sands in triaxial compression: Part I, *Canadian Geotechnical Journal*, Vol. III, No. 4, pp. 179-190.

Potts, D.M. and Gens, A. (1985). A critical assessment of methods of correcting for drift from the yield surface in elasto-plastic finite element analysis,

International Journal for Numerical and Analytical Methods in Geomechanics, Vol. 9, pp. 149-159.

Poulos, H.G. (1989). The mechanics of carbonate sediments, *Research Report No. 595*, School of Civil and mining Engineering, University of Sydney.

Poulos, H.G. (1988). The mechanics of calcareous sediments, Jaeger memorial lecture, *Australian Geomechanics*, pp. 8-39.

Poulos, H.G. (1980). The mechanics of calcareous sediments, *Jaeger memorial lecture*, Australian Geomechanics, pp. 8-39.

Poulos, H.G. (1980). A review of the behaviour and engineering properties of carbonate soils. *Research Report No. 381*, School of civil and mining engineering, University of Sydney.

Poulos, H.G. and Chua, E.W. (1985). Bearing capacity of foundations on calcareous sand. *Proceedings of the 11th International Conference on Soil Mechanics and Foundation Engineering*, Vol. 3, pp. 1619-1622.

Poulos, H.G. and Davis, E.H. (1974). *Elastic Solutions for Soil and Rock Mechanics.* New York, N.Y., John Wiley.

Poulos, H.G., Hull, T.S. and Chua, E.W. (1984). Foundation Behaviour in Calcareous Sands. *Proceedings 9th Australasian Conference on the Mechanics of Structures and Materials*, pp.28-32.

Poulos, H.G., Uesugi, M. and Young, G.S. (1982). Strength and deformation properties of Bass Strait carbonate sands, *Geotechnical Engineering*, Vol. 13, pp. 189-211.

Randolph, M.A., Joer, H.A. and Airey, D.W. (1998). Foundation design in cemented soils, Keynote Lecture (*In Press??*), *2nd International Symposium on Hard Soils-Soft Rocks*, Naples, Italy.

Rendulic, L. (1936). Relation between void ratio and effective principal stress for a remoulded silty clay. *Proc. 1st Int. Conf. SMFE*, Harvard, 3, pp. 48-51.

Roscoe, K.H. and Burland, J.B. (1968). On the generalized stress-strain behaviour of wet clay, *Engineering Plasticity*, J. Heyman and F.A. Leckie (eds.), Cambridge University Press, Cambridge, England, pp. 535-609.

Roscoe, K.H, Schofield, A.N. and Thurairajah, A. (1963). Yielding of clays in states wetter than critical, *Geotechnique 13(3)*, pp. 211-240.

Rowe, P.W. (1962). The stress-dilatancy relation for static equilibrium of an assembly of particles in contact, *Proceedings, Series A, Vol. 269, Royal Society of London*, pp. 500-527.

Runesson, K. and Booker, J.R. (1983). Finite element analysis of elasto-plastic layered soil using discrete Fourier series expansion. *International Journal of Numerical Methods in Engineering*, 19, pp. 473-478

Runesson, K. and Booker, J.R. (1982). Efficient finite element analysis of 3D consolidation, *4th International Conference in Numerical Methods in Geomechanics*, Edmonton, pp. 359-364.

Schofield, A. and Wroth, C.P. (1968). *Critical state soil mechanics*, Mcgraw Hill, London..

Semple, R.M. (1988). State of the art report on mechanical properties of carbonate sands, Engineering for Calcareous Sediments, Jewell and Andrews (eds.), *Proceedings International Conference on Calcareous Sediments*, Perth, Vol. 2, Balkema, Rotterdam, pp. 807-836.

Shah, K.R. (1997). An elasto-plastic constitutive model for brittle-ductile transition in porous rocks. *International Journal of Rock mechanics and Mineral Science*, Vol. 34, No.3-4.

Sharp, D.E. and Seters, A.J. (1988). Results and evaluation of plate load test results. Engineering for Calcareous Sediments, Jewell and Andrews (eds.), *Proceedings International Conference on Calcareous Sediments*, Perth, Vol. 2, Balkema, Rotterdam, pp. 473-483.

Simpson, B. (1970). Modelling materials for engineering mechanics, *Int. J. of Rock. Mech. Min. Sci.*, Vol. 7, pp. 77-121.

Smith. I.M. (1982). *Programming the finite element method*, New York: Wiley.

Smith, I.M., Hicks, M.A., Kay, S. and Cuckson, J. (1988). Undrained and partially drained behaviour of end bearing piles and bells founded in untreated calcerinite, Engineering for Calcareous Sediments, Jewell and Andrews (eds.), *Proceedings International Conference on Calcareous Sediments*, Perth, Vol. 2, Balkema, Rotterdam, pp. 663-679.

Sweet, J. (1988). Estimation of the drained bearing capacity of calcareous material, Engineering for Calcareous Sediments, Jewell and Andrews (eds.), *Proceedings International Conference on Calcareous Sediments*, Perth, Vol. 2, Balkema, Rotterdam, pp. 655-661.

Taeibat, H. (1999). Three dimensional liquefaction analysis of offshore foundations, *Ph.D. thesis*, University of Sydney.

Tatsuoka, F. and Ishihara, K. (1974). Yielding of sand in triaxial compression, *Soils and Foundations*, Japanese Society of Soil Mechanics and Foundation Engineering, Vol. 14, No. 2, pp. 63-76.

Terzaghi, K. (1943). *Theoritical Soil Mechanics*, John Wiley & Sons, NewYork.

Vermeer, P.A. (1978). A double-hardening model for sand. *Geotechnique*, Vol. 28, No. 4, pp. 413-433.

Vesic, A.S. (1975). Bearing capacity of shallow foundations, *Foundation Engineering Handbook*, 1st edition, H.F. Winterkorn and H.Y. Fang (eds), Van Nostrand Reinhold Company Inc., New York, N.Y.

Vesic, A.S. (1972). Expansion of cavities in infinite soil mass. *Journal of Soil Mechanics and Foundations Division,* ASCE, Vol. 98, No. SM3, pp. 265-290.

Vesic, A.S. (1963a) Bearing capacity of deep foundations in sand, *National Academy of Sciences, National Research Council, Highway Research Record*, 39, pp,112-153.

Yamada, Y. and Ishihara, K.(1979). Anisotropic deformation characteristics of sand under three dimensional stress conditions. *Soils and Foundations*, Japanese Society of Soil Mechanics and Foundation Engineering 19, pp. 79-94.

Yeoh, C.K. (1996). Cyclic response of cemented soils and foundations, *Ph.D. thesis*, University of Sydney.

Yeoh, C.K. and Airey, D.W. (1996). The response of model footings on artificially cemented calcareous soil. *Proceedings of the 7th ANZ Conference on Geomechanics*, pp. 720-725.

Yeung, S.K. and Carter, J.P. (1989). An assessment of the bearing capacity of calcareous and silica sands. *International Journal for Numerical; and Analytical Methods in Geomechanics*, Vol. 13, pp.19-36.

Yu, H.S. (1998). CASM: A unified state parameter model for clay and sand. *International Journal for Numerical; and Analytical Methods in Geomechanics*, Vol. 22, pp. 621-653.

Yu, H.S. (1995). A unified constitutive model for clay and sand, *Research Report No. 112.08.1995*, Department of Civil Engineering and Surveying, University of Newcastle.

Zienkiewicz, O.C., Humpheson, C. and Lewis, R.W. (1975). Associated and non-associated viscoplasticity and plasticity in soil mechanics, *Geotechnique 25*, No. 4, pp. 671-689.

This thesis has been accepted for the award of the degree in the Faculty of Engineering